



HAL
open science

Comparative studies of the structural and alteration controls on gold mineralization in the Wa-Lawra region, NW Ghana.

Prince Ofori Amponsah

► **To cite this version:**

Prince Ofori Amponsah. Comparative studies of the structural and alteration controls on gold mineralization in the Wa-Lawra region, NW Ghana.. Mineralogy. Université Toulouse III Paul Sabatier, 2016. English. NNT: . tel-01320937

HAL Id: tel-01320937

<https://theses.hal.science/tel-01320937>

Submitted on 24 May 2016

HAL is a multi-disciplinary open access archive for the deposit and dissemination of scientific research documents, whether they are published or not. The documents may come from teaching and research institutions in France or abroad, or from public or private research centers.

L'archive ouverte pluridisciplinaire **HAL**, est destinée au dépôt et à la diffusion de documents scientifiques de niveau recherche, publiés ou non, émanant des établissements d'enseignement et de recherche français ou étrangers, des laboratoires publics ou privés.



Université
de Toulouse

THÈSE

En vue de l'obtention du

DOCTORAT DE L'UNIVERSITÉ DE TOULOUSE

Délivré par l'Université Toulouse III – Paul Sabatier

Discipline ou spécialité : Géologie structurale et métallogénie

Présentée et soutenue par *Prince Ofori Amponsah*

Le 12 Janvier 2016

Titre :

*Etude comparative des structures et des altérations associées aux
minéralisations aurifères de la région de Wa-Lawra, NW Ghana*

JURY

Pr. Anne-Sylvie Andre Mayer	G2R, ENSG, Univ. Lorraine, Nancy	Rapporteur
Dir. Rech. Alain Chauvet	Geoscience, Montpellier	Rapporteur
Pr. Didier Béziat	GET, UPS, Toulouse	Directeur de thèse
Pr. Olivier Vanderhaege	GET, UPS, Toulouse	Membre
Dir. Rech. Mark Jessell	CET, Univ. Western Australia	Membre
Pr. Michel Faure	ISTO, Univ. Orléans	Membre
CR Lenka Baratoux	GET, UPS, Toulouse	Invité
CR Stefano Salvi	GET, UPS, Toulouse	Invité
DR Luc Siebenaller	GET, UPS, Toulouse	Invité

Ecole doctorale : *Sciences de l'Univers, de l'Environnement et de L'Espace (SDU2E)*

Unité de recherche : *Géosciences Environnement Toulouse (GET)*

Directeur(s) de Thèse : *Didier Beziat (directeur de thèse),*

Lenka Baratoux (co-directeur de thèse)

Résumé

L'objectif de ce travail de thèse était de réaliser une étude structurale détaillée des minéralisations et des zones d'altération associées, de trois gisements d'or situés au Nord-Ouest du Ghana, sur la marge orientale du Craton Ouest Africain: Kunche et Bepkong, situés dans la ceinture de Wa-Lawra, et Julie situé dans la ceinture de Julie. Ces trois gisements présentent de multiples différences d'ordre géologique, structural, tectonique et géochimique, mais leur caractéristique commune est que leur minéralisation est associée à un métamorphisme de faciès schiste vert.

A Julie, la minéralisation aurifère est encaissée dans des granitoïdes de composition tonalite-trondhjemite-granodiorite (TTG) alors qu'à Kunche et Bepkong elle est localisée au sein de formations sédimentaires volcanoclastiques et de schistes graphiteux fortement silicifiés. Cette minéralisation est associée à un réseau de veines souvent boudinées de quartz formées en relation avec une zone de cisaillement orientée Est-Ouest à Julie, mais N à NNO à Kunche et Bepkong, constituant un couloir de déformation de 0.5 à 3,5 km de longueur et de 20 à 300 m de puissance suivant les gisements.

La paragenèse d'altération dominante de la zone minéralisée est à séricite, quartz, carbonate et sulfures, et suivant la nature de la roche hôte se rajouteront par exemple la tourmaline dans les granitoïdes et la chlorite dans les schistes ou les métavolcanites. A Julie, l'or est étroitement associé à la pyrite alors qu'à Kunche et Bepkong l'or est associé à l'arsénopyrite. Deux générations d'or sont distinguées ; la première correspond à de l'or invisible associé aux zones de croissance primaire des cristaux de pyrite à Julie et d'arsénopyrite à Bepkong, et de l'or visible tardif en inclusion et plus fréquemment en remplissage de fractures.

Abstract

The objective of this thesis was to perform a detailed structural, mineralization and associated alteration studies of three gold deposits located in northwest Ghana, on the eastern margin of the West African Craton. Thus, the Kunche and Bepkong deposits, located in the Wa-Lawra belt and Julie deposit located in the Julie belt. These three deposits have multiple differences in terms of geological, structural, tectonic and geochemical characteristics but gold mineralization in these deposits are all associated with a green schist facies metamorphism.

In Julie, the gold mineralization is hosted in granitoids with its composition akin to tonalite-granodiorite-trondhjemite (TTG) whereas in the Kunche and Bepkong deposits, the gold mineralization are localized within volcanoclastic sedimentary formations and strongly silicified graphitic schists. The gold mineralization is associated with a network of quartz veins often boudinaged and formed in connection with a shear zone, oriented E-W in the Julie deposit and N to NNW at Kunche and Bepkong deposits.

The dominant alteration in the mineralized zone is sericite, quartz, carbonate and sulfides with influences from the host rock. For example, the granitoid is influenced by tourmaline and chlorite in the schists or in the metavolcanic rocks. At Julie, gold is closely associated with pyrite whereas Kunche and Bepkong gold is associated with arsenopyrite. Two generations of gold are distinguished; the first corresponds to the invisible gold associated with primary growth areas in the pyrite crystals in Julie and arsenopyrite in Kunche and Bepkong, and late visible gold inclusions which are frequently found in fracture fillings.

In Julie, the mineralizing fluid is rich in CO₂, and has low to moderate salinity (NaCl-H₂O-CO₂ system), trapped in P / T conditions around 220 ° C and <1 kbar; whilst in Bepkong, the mineralizing fluid is associated with quartz and is rich in CH₄, with a low salinity (CH₄-CO₂-SO₂-H₂O system) which indicates that the visible trapping temperatures is around 320°C.

Acknowledgement

My sincerest gratitude goes to Azumah Resources Limited, the owners of Julie, Bepkong and Kunche gold deposits in NW Ghana, for allowing me to use their deposits as the focus of my study and also financing the field work. This thesis would not have been possible without the support of the WAXI (West African Exploration Initiative) project. Many people near and afar supported me in immeasurable ways throughout this PhD. It is impossible to keep track of their generosity, hospitality and kindness.

I am greatly indebted to Prof. Mark Walter Jessell for the confidence he had in me, proposing this PhD project and further went ahead to take me on as his student and nurturing my interest in metallogeny. I would like to thank Stefano Salvi, Didier Béziat, Lenka Baratoux and Luc Siebenaller for taking me on as their student and imparting some of their colossal knowledge in Geology on to me. I cannot thank them enough for their patience, excellent supervision, extraordinary insight, guidance and critical revision of my thesis.

Special thanks goes to John Miller, Sylvain Block, Prosper Mackenzie Nude and the entire geological staff of Azumah Resources Limited for their insightful geological discussions about the various deposits I was dealing with. I will like to extend my gratitude to Nick Franey and Stephen Stone for taking the great risk to support and finance this work even with the downturn of global gold prices. I say “kudos” to Andrew Chubb for his valuable contributions towards my manuscripts.

I would like to thank my family, especially my parents Peter Ofori Amponsah and Dorothy Akoi-Appiah, my sisters, my auntie Esther Akoi-Appiah and my in-laws Mr and Mrs Laud Mansfield Baddoo and their entire family for their immense support and prayers.

I would also want to thank all the staff and workers of Azumah Resources Limited for their enormous support towards making this work a reality. Thanks to all my dear friends Manuel Dela Eli, Miriam Yahaya-Shiru, Wendy Annan, Kofi Eghan-Ekuban, Jennifer Agbetsoamedo, Emmanuel Abitty and Daniel Kwayisi for their support.

Finally, I say ‘ayekoo’ to my dear and lovely wife, Mrs. Laudetta Amponsah for her steadfast love, support, patience and for providing me the motivation to complete this work.

This thesis is dedicated to God almighty and my loving wife, *Laudetta Awulaa Naa Lamiley Amponsah* in appreciation of her love, patience and encouragement.

Table of Contents

Résumé	i
Abstract	ii
Acknowledgement	iii
Introduction.....	1
Cadre général de la thèse	3
Géographie	6
La zone d'étude et accessibilité.....	6
Relief et réseau hydrographique.....	8
Végétation, sols et climat.....	9
Cartographie de terrain.....	10
Background and Justification.....	10
Geography.....	12
Study area and Accessibility	12
Relief and Drainage	12
Vegetation, Soils and Climate	13
Field work.....	13
References.....	14
Chapter 1.....	17
1.0 Overview of Orogenic Gold mineralization.....	19
1.1 Introduction.....	19
1.2 Spatial and temporal distribution of Orogenic gold	21
1.3 Control on relative and absolute timing	23
1.4 Global gold grade and tonnages associated with metamorphic gold.....	26
1.5 Tectonic controls on Orogenic Gold mineralization	28
1.6 Orogenic gold ore body geometry and ore body controls	30
1.7 Metamorphic grade	32
1.8 Hydrothermal alteration	34
1.9 Sources of Gold	35
1.10 Fluid chemistry.....	36
1.11 Reference	38
Chapter 2.....	43
2.1 Introduction.....	45
2.2 Summary of geological framework of the West African Craton.....	45
2.2.1 The Shields.....	48
2.2.1.1 Summary of the Reguibat shield.....	48

2.2.1.2 Summary Leo-Man Shield	49
2.2.1.3 Summary of the sedimentary basins in the WAC.....	50
2.2.1.4 Summary of the Pan African Belts	52
2.3 The Birimian Overview of Ghana	53
2.3.1 Birimian Architecture in Ghana	54
2.3.2 Birimian Sediments and Volcanics	55
2.3.3 Tarkwaian Sediments	55
2.3.4 Birimian Terrane Plutonism and metamorphism	56
2.3.5 Tectonic Evolution and Eburnean Orogeny.....	56
2.4 Geological setting of the Study area	58
2.4.1 Structural and metamorphic framework of NW Ghana	59
2.5 Gold deposits in the West African Craton.....	60
2.6 References.....	63
Chapter 3.....	71
The Julie Deposit.....	71
Introduction.....	73
3. 1 Geology and geochemistry of the shear-hosted Julie gold deposit, NW Ghana.....	74
3. 2 Shear related gold mineralization in Northwest Ghana: The Julie deposit.....	94
Chapter 4.....	101
The Kunche Deposit	101
Introduction.....	103
4.0 Geological, structural and geochemical controls of Gold Mineralization in the Wa-Lawra belt, NW Ghana: A case study from the Kunche deposit	104
4.1 Introduction.....	105
4.2 Regional Geology	105
4.3 Methodology	107
4.4 Geology of the Kunche Deposit.....	108
4.5 Geochemistry.....	110
4.5.1 Volcanoclastic sediments	110
4.5.2 Microdiorite.....	113
4.6 Deformation History.....	116
4.6.1 D _{K1}	116
4.6.2 D _{K2}	117
4.6.3 D _{K3}	117
4.7 Quartz veins.....	119
4.8 Alteration.....	120
4.9 Ore body characteristics and geometry.....	121
4.10 Ore Mineralogy	122

4.11 Mineral paragenesis	126
4.12 LA-ICP-MS profile character of the arsenopyrite	126
4.13 Discussion.....	128
4.13.1 Structural controls and timing of gold mineralization in the Kunche deposit	130
4.13.2 Insight on ore genesis	132
4.13.3 Source of gold.....	133
4.14 Conclusions	133
Acknowledgement	133
Reference	134
Chapter 5.....	137
The Bepkong Deposit	137
Introduction.....	139
5.0 Gold mineralization in the Wa-Lawra greenstone belt, NW Ghana; The Bepkong deposit.....	139
Abstract	140
5.1 Introduction.....	140
5.2 Regional geology of the Wa-Lawra Belt	141
5.3 Methodology	144
5.4 Local Geology- the Bepkong deposit	145
5.4.1 Main Lithologies	145
5.4.1.1 Geochemistry.....	148
5.4.2 Deposit scale structures.....	153
5.4.2.1 D _{B1} deformational phase	154
5.4.2.2 D _{B2} deformational phase	155
4.2.2 D _{B3} deformational phase	155
5.4.3 Quartz veins.....	156
5.4.3.1 Type-1	156
5.4.3.2 Type-2 quartz veins	158
5.4.4 Alteration, ore body geometry and mineralogy.....	158
5.4.4.1 Alteration.....	158
5.4.4.2 Ore body geometry and mineralization style.....	159
5.4.4.3 Ore mineralogy	160
5.4.4.4 Trace element Geochemistry of sulphides	163
5.4.4.5 Gold occurrence in Arsenopyrite	167
5.4.5 Arsenopyrite geothermometry	168
5.4.6 Fluid inclusions.....	173
5.5 Discussion.....	179
Acknowledgement	182
5.6 Reference	183

5.7 The Bepkong gold deposit, northwestern Ghana.....	189
Chapter 6.....	197
Discussion and Conclusion.....	197
6.1 Discussion	199
6.1.1 Host Rocks	199
6.1.2 Structures.....	199
6.1.3 Mineralization style and alteration	203
6.1.4 Fluid inclusions.....	204
6.1.5 Sulphide characterization.....	204
6.2 Genetic Model.....	205
6.2.1 The Kunche and Bepkong deposits	205
6.2.2 Implication on gold endowment within the two deposit in the Wa-Lawra belt.....	207
6.2.3 Genetic model for gold mineralization in the Julie deposit	207
6.3 Resituating the three gold deposit in NW Ghana into craton-scale mineral systems context	209
6.3.1 Space and time constrains.....	211
6.3.2 Structures.....	211
6.3.3 The nature of the fluids	212
6.4 Exploration Guide in the Wa-Lawra region	214
6.5 Conclusion.....	215
6.6 References.....	216
6.7 Conclusion générale.....	219
APPENDIX.....	221
APPENDIX A.....	222
APPENDIX B.....	242
Julie structural measurement.....	242
Kunche deposit measurement.....	252
Bepkong deposit measurement.....	255

Introduction

Cadre général de la thèse

L'augmentation du prix de l'or durant la dernière décennie a été le point de départ de très nombreuses recherches sur les minéralisations aurifères aussi bien dans le domaine académique qu'industriel dans le but de mieux comprendre les processus de formation des gisements de ce métal précieux. En effet, il reste encore de très nombreuses réponses à apporter concernant la distribution irrégulière des minéralisations au niveau d'un gisement ou d'une région et de façon générale concernant la complexité des processus conduisant à des concentrations économiques. Afin de répondre à ces questions, il a été mis en place un programme de recherche appliqué aux gisements aurifères de l'Afrique de l'Ouest, le West African Exploration Initiative (WAXI) qui a pour objectif d'étudier la géologie et la métallogénie du Craton Ouest-Africain (COA), notamment dans les parties sud-ouest du Burkina Faso et nord-ouest du Ghana. Le projet WAXI est un programme de collaboration en Sciences de la Terre entre l'industrie minière, les universités et les services géologiques en Afrique de l'Ouest et les Universités en France et en Australie. Le projet est essentiellement financé par l'industrie minière qui opère en Afrique de l'Ouest, avec une contribution des gouvernements Français et Australien. L'objectif du WAXI est d'effectuer une analyse détaillée des formations géologiques afin d'améliorer la compréhension des domaines paléoprotérozoïques du Craton Ouest Africain et de leur minéralisation associée, mais aussi d'offrir une formation aux étudiants et aux géologues ouest-africains qui viennent des universités, des services géologiques, et même des sociétés minières.

Depuis de nombreuses années, les compagnies minières qui s'intéressent à l'or, font de l'exploration au niveau des « vieux » continents, appelés cratons. Ces cratons ont été excessivement étudiés en Amérique de Nord et en Australie (Goldfarb et al., 1993 ; Goldfarb et al., 1997 ; Goldfarb et al., 1998 ; Bierlein et al., 2004 ; Goldfarb et al., 2005 ; Dube & Gosselin, 2007). De nombreuses études ont contraint et classifié l'évolution métallogénétique de ces cratons, en distinguant par exemple les divers types de minéralisations aurifère: i) associées à des filons de quartz (type orogénique); ii) disséminée dans des formations magmatiques felsiques parfois en association avec le cuivre (type porphyre) ; iii) associées à des niveaux de sulfures massifs au sein de formations volcaniques (type VMS); et iv) dans des conglomérats et sédiments fluvio-deltaïques (type placer). Toutefois, il faut savoir que le Craton Ouest-Africain est fortement sous-exploré par rapport à ces homologues nord-américain et australien, d'où la nécessité de la mise en place de nouveaux programmes scientifiques d'exploration, comme le programme WAXI.

Plus de 100 Moz d'or a été produit par les divers pays du craton Ouest-Africain, notamment du Ghana (anciennement Gold Coast) depuis l'Antiquité. Durant le XVIème siècle, la Gold Coast a produit à elle seule 35% de la production mondiale (Amedofu, 1995). Mais par la suite, la production d'or n'a cessé de diminuer jusqu'au XXème siècle et ce n'est que vers les années 1980 que l'on a assisté à une reprise de l'exploration en raison d'un contexte économique devenu plus favorable. Mais c'est surtout à partir des années 2000 avec la mise en place de nouveaux codes miniers et en raison des très nombreux investissements par des compagnies minières internationales qu'une nouvelle "ruée" vers l'or a vu le jour sur tout le craton ouest-africain. L'amélioration continue de notre compréhension des systèmes de minéralisation présents dans le COA a également fortement contribué à cette attractivité car elle augmente bien évidemment les chances de découvrir de nouveaux gisements. C'est alors

dans ce même ordre d'idée qu'on m'a proposé comme sujet de thèse de faire l'étude détaillée de gisements d'or peu connus situés au nord du Ghana dans la ceinture de Wa-Lawra. Cette thèse a été coordonnée avec celle de Sylvain Block de l'Université de Toulouse (Block, 2015) qui a caractérisé l'évolution tectonique et métamorphique régionale ainsi que sur la systématique pétrologique, géochimique et géochronologique des granitoïdes de la partie nord du Ghana (Block et al., 2015). Elle fera également référence aux travaux de thèse de Vaclav Metelka qui traitent de la géologie de la ceinture de Boromo située au sud-ouest du Burkina Faso, et qui représente l'extension septentrionale de la ceinture Wa-Lawra (Metelka, 2011).

La ceinture des roches vertes Lawra et le domaine des granitoïdes adjacent (Domaine de Koudougou-Tumu) sont les cibles principales de cette étude ; elles font partie du Craton Ouest-Africain et sont explorées pour l'or par Azumah Resources Limited (Fig. A). L'exploration dans cette région a abouti à la découverte d'un gisement de 2.2 Moz d'or, se subdivisant en une ressource mesurée de 1.35 Moz et supposée de 0.85 Moz, avec une teneur moyenne de 1.8 g/tonne (Azumah Resource announcement, 2013). Bien qu'un gisement d'or économique soit découvert dans la ceinture de Wa-Lawra et le domaine de granitoïdes adjacent, la géologie (architecture structurale, métamorphisme, métallogénie) et l'évolution géodynamique n'ont pas été suffisamment étudiées.

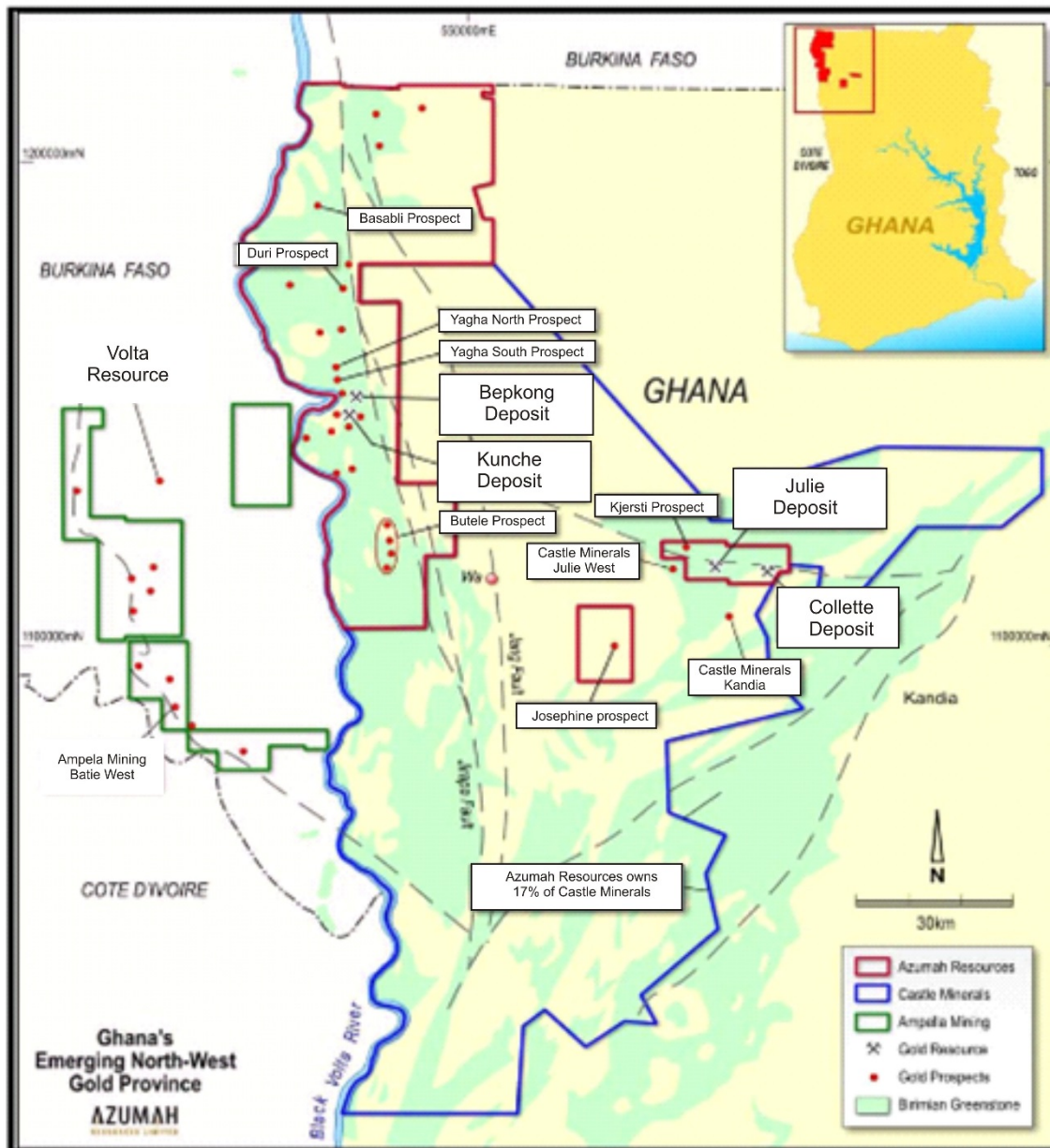


Fig. A. Carte de la partie nord du Ghana montrant les permis d'Azumah ; en haut et à droite la carte du Ghana (Azumah Resources Limited, 2015).

L'objectif principal de cette thèse est de comprendre la métallogénie de trois gisements d'or (Julie, Bepkong et Kunche), appartenant à Azumah Resources Ltd., situés dans la ceinture de Wa-Lawra et les granitoïdes adjacents. Plus précisément, cette thèse vise à répondre aux questions suivantes :

1. Quel est le cadre géologique de la zone d'étude, le cadre structural/tectonique et la nature de la minéralisation associée ?
2. Quelle est la nature des relations et la chronologie relative entre la déformation, le métamorphisme et la minéralisation aurifère ?

La thèse sera divisée en deux parties : la première partie présentera une synthèse concise des gisements d'or orogénique (1^{er} Chapitre) et de la géologie du Craton Ouest-Africain avec un accent mis sur la géologie du Birimien de la partie occidentale du Ghana et plus précisément de la zone d'étude (2^{ème} chapitre). La deuxième partie sera constituée de trois chapitres, chacun s'appuyant sur une publication publiée ou soumise dans une revue scientifique internationale, qui détailleront les caractéristiques des 3 gisements étudiés, plus particulièrement la géologie et la géochimie des fluides dans le cas du gisement de Julie (3^{ème} chapitre), l'architecture tectonique et la géochimie du gisement pour le gisement de Kunche (4^{ème} chapitre) et la géologie (étude structurale, géochimie d'altération, étude des inclusions fluides) du gisement de Bepkong (5^{ème} chapitre). Les trois gisements seront comparés en termes de structures, géochimie d'altération, style de minéralisation en or, nature des fluides (modalités de circulation et de transport de l'or) et un modèle métallogénique général sera proposé dans le 6^{ème} chapitre.

Géographie

La zone d'étude et accessibilité

La zone d'étude se situe dans la région nord-ouest du Ghana, plus précisément dans les districts de Lawra, Nandom, Lambussie, Jirapa, Wa East et la municipalité de Wa. Elle couvre une surface de 8000 km² et elle est délimitée par les coordonnées 2.8° E, 9° N to 2° E, 11° N de longitude/latitude de l'ellipsoïde WGS 84. D'un point de vue géologique, la zone d'étude couvre la ceinture de Wa-Lawra et les granitoïdes du domaine adjacent dénommé Koudougou-Tumu et la ceinture de Julie (Fig. C). Cette région se situe à 480 km de Kumasi (par la voie bitumée) et à 320 km de Ouagadougou. La plupart des villes et villages de la région sont connectés par un bon réseau de routes bitumés ou rurales, et la ville de Wa possède une petite piste d'atterrissage de 2km, ce qui rend la région facilement accessible.



Fig. B. Carte topographique simplifiée du Ghana (Nation Online project, 2015). La zone en rouge représente la zone d'étude.

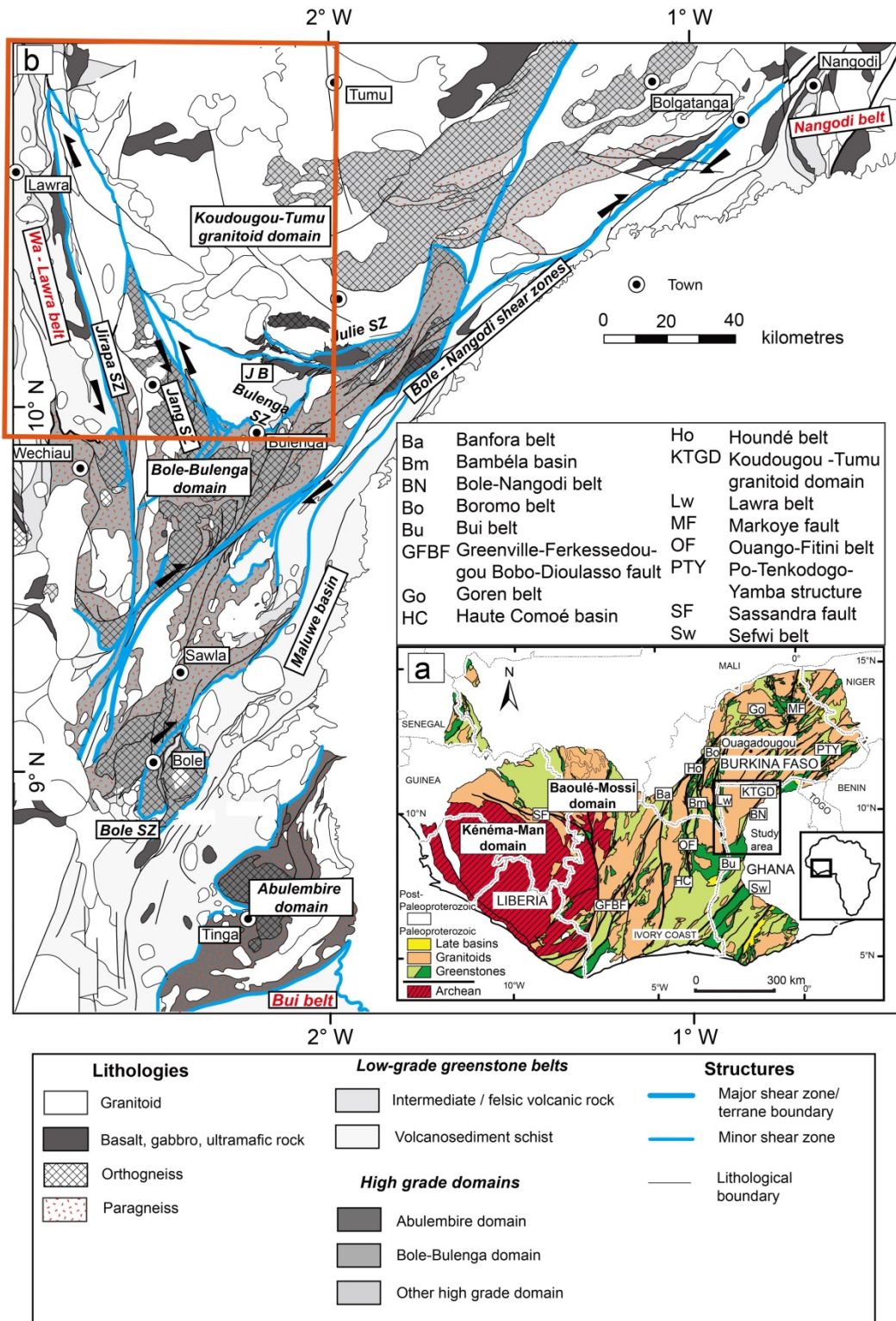


Fig. C. (a) Carte géologique d'Afrique de l'Ouest (d'après Milési et al., 2004) ; la zone d'étude est indiquée par le cadre noir, (b) carte géologique du nord-ouest du Ghana (Block et al., 2015); le cadre rouge représente la zone d'étude qui englobe la ceinture de Wa-Lawra et le domaine granitique adjacent de Koudougou-Tumu.

Relief et réseau hydrographique

La région a été aplanie par une érosion extensive qui a laissé seulement quelques collines dispersées orientées N-S, avec une altitude moyenne de 350m à 450m. La région est drainée par le Volta Noir à l'ouest, qui marque également la frontière entre le Burkina Faso et le Ghana. Le Volta Noir est alimenté par plusieurs affluents qui ont pour noms Bepkong, Kulpaw et Felin.

Végétation, sols et climat

La zone d'étude se situe dans la zone végétale de type savane guinéenne qui est caractérisée par les herbes de différentes hauteurs alternant avec les petits arbustes résistant au feu (Fig. D) (Ghana Government, 2015). Les sols principaux sont les latérites qui sont développés sur les roches birimiennes sous-jacentes (Dickson & Benneh, 1988).



Fig. D. Photographie montrant la végétation typique de la zone d'étude (type savane guinéenne).

Le climat dans la zone d'étude est tropical et est dominé par une saison sèche entre octobre et avril, février, mars et avril étant les mois les plus chauds de l'année (Ghana Government, 2015) et une saison de pluies entre mai et septembre avec le maximum de précipitations en juin. Les précipitations annuelles moyennes sont de 1033 mm. La moyenne annuelle de la température, de l'humidité relative, de la vitesse de vent, du nombre d'heures d'ensoleillement et de l'irradiation solaire quotidienne sont respectivement de 28.1 °C, 61 %, 138 Km/jour, 7,3 heures et 19.6 MJ/m²/jour (Environmental Protection Agency, Ghana, 2002).

Cartographie de terrain

Les travaux de terrain effectués dans le cadre de cette thèse ont été menés essentiellement en 2013 et 2014, pour une période de 6 mois chaque année. En début de 2013 (du janvier jusqu'au mars), j'ai réalisé une cartographie de reconnaissance des trois gisements d'or (i.e. Julie, Kunche et Bepkong) sur les permis d'Azumah Resources Limited. Cette cartographie a été cruciale car elle m'a permis d'identifier les lithologies principales, le cadre structural, les assemblages métamorphiques présents et le système de fluides dans la zone d'étude. Les derniers trois mois des travaux de terrain pendant la dernière année ont été consacrés à une cartographie géologique détaillée à l'échelle de 1 :10000 afin de tester les hypothèses faites à partir des travaux précédents. En 2014, j'ai « logué » les forages disponibles (éclats ou cuttings produits par la méthode de forage « Reverse Circulation » et les carottes de forages au diamant) des trois gisements. Ces travaux m'ont procuré une base solide et m'ont permis de placer les données géologiques obtenues par le logging dans un contexte tridimensionnel et de proposer un modèle de contrôle structural et d'altération sur la minéralisation aurifère. Au total, 209 forages (circulation inversée et diamant) qui représentent 15 fences ont été logués sur les trois gisements. De plus, j'ai participé à une formation de terrain sur l'évolution tectonique du nord-ouest du Ghana organisée par Sylvain Block en 2014. Cette formation m'a permis de relier les observations à l'échelle du gisement à un modèle tectonique à l'échelle régionale.

Background and Justification

The surge in gold price over the past decade has provided an incentive for both industry and academia to direct their efforts in the search and also in understanding the occurrence of this precious metal.

For this reason, the West African Exploration Initiative (WAXI) program launched the study of Geology and Metallogeny in key regions of the West African Craton (WAC) which includes SW Burkina Faso and NW Ghana. The WAXI program is a collaborative research program amongst industries, universities and geological surveys across the West African sub-region and their equivalents in France and Australia. The funding for this project is mainly from mining industries actively exploring and mining in West Africa with contributions from the French and Australian Governments. The objective of the WAXI program is to undertake detailed analysis, increase the geological knowledge base in key areas within the Paleoproterozoic terranes of the WAC, and build capacity between West African students, geologists from universities, geological surveys and to address particular demands of industry.

Over the years, gold has been explored and extracted by mining companies from the oldest part of the continents called cratons. The cratons of the North American and Australian continents have been studied in detail (Goldfarb et al., 1993; Goldfarb et al., 1997; Goldfarb et al., 1998; Bierlein et al., 2004; Goldfarb et al., 2005; Dubé & Gosselin, 2007). As a result of these studies, the metallogenesis of gold in these cratons in these regions have successfully been classified and constrained into different classes. For example 1. Gold associated with quartz veins (Orogenic type); 2. Gold disseminated in felsic magmatic formations and sometimes associated with copper (Porphyry type); 3. Gold associated with massive levels of sulphide in volcanic formations (VMS type); 4. Gold in conglomerates and sea-river deltaic sediments (placer type). The West African Craton is under-explored and less well studied compared to its North American and Australian counterparts, hence the need for the establishment of new scientific exploration programs, including the WAXI program.

Over 100 Moz of gold have been produced by various countries of the West African craton since ancient times, notably Ghana (formerly the Gold Coast). During the sixteenth century, the Gold Coast alone produced 35% of world gold production (Amedofu, 1995) but in later times production steadily declined, until the twentieth century (in the 1980s) when gold exploration experienced an upturn again throughout the world as a result of the favourable economic conditions surrounding the commodity. The establishment of new mining laws in many West Africa countries in the early 2000's have attracted increased investment from international mining companies (what was called the "new gold rush" in West Africa) into exploring for gold throughout the craton. Continuous upgrading of our understanding of the various mineral systems present in the WAC can help transform and maximize our chances of new discoveries.

For this reason, this PhD work was designed to study the lesser known economic gold deposits in NW Ghana in the Wa-Lawra belt. This thesis is coordinated with that of Sylvain Block at the University of Toulouse III who worked on the regional tectonics and metamorphic rock records as well as on the petrological and geochemical systematics of the granitoids in NW Ghana, (Block, 2015). It will also draw upon the results of the PhD findings of Vaclav Metalka who worked in the Boromo Belt in SW Burkina Faso, which is the northern extension of the Wa-Lawra belt in that country (Metelka, 2011).

The Wa-Lawra greenstone belt and its adjacent granitoid domain, also known as the Koudougou-Tumu domain, is the main focus of this study. This belt has been actively explored for gold by Azumah Resources Limited since 2006 (Fig. A). Exploration work done in this area so far, has yielded about 2.2 million ounces (Moz) of gold, with measured and indicated gold being 1.35 Moz and 0.85 Moz of inferred resource at an average grade of 1.80 gram per tonne (g/t; Azumah Resource announcement, 2013). Even though economic gold has been discovered by Azumah Resources Limited in the Wa-Lawra belt and its adjacent granitoid domain, the geology (tectonics or geodynamics, structural architecture, metamorphism and metallogeny) is not fully resolved.

The main purpose of this research is to understand and compare the metallogeny of the Julie, Bepkong and Kunche deposits held by Azumah Resources Limited in the Wa-Lawra Belt and the adjacent TTGs, and specifically to answer the following questions:

1. What is the geological setting of the area, the structural/tectonic framework and the nature of the associated mineralization?
2. What is the nature of relationship and the relative timing between the deformation, metamorphism and gold mineralization?

The thesis is divided into two parts, the first part deals with a brief review of orogenic gold (Chapter 1) and the geology of the West African Craton with emphasis on the Birimian of the western part of Ghana and the study area (Chapter 2).

The second part consists of a succession of papers detailing the geology and fluid geochemistry of the Julie deposit (Chapter 3), the tectonic architecture and geochemistry of the Kunche deposit (Chapter 4) and the geology (structural study, alteration geochemistry and fluid inclusion studies) of the Bepkong deposit (Chapter 5). All these three gold deposits are discussed and compared by way of their structures, alteration geochemistry, gold mineralization and fluid inclusion characteristics (fluid flow, transportation model; chapter 6).

Geography

Study area and Accessibility

The study area (Fig. B) is located in the Upper West Region of Ghana with notable towns such as the Lawra, Nandom, Lambussie, Jirapa, Wa East districts and the Wa municipality. It covers a total area of 8000 km² bounded by the coordinates 2.8° E, 9° N to 2° E, 11° N of the longitude/ latitude WGS 84 datum ellipsoid. The study area straddles the Wa-Lawra belt and its adjacent granitoids in the Koudougou-Tumu domain and Julie belt (Fig. C). The area under study is about 480 km from Kumasi via a bitumen road and also 320 km from Ouagadougou. All the major towns and villages in the study area are connected with good network of bitumen and feeder roads, with a 2 km air strip in Wa, which makes the area highly accessible.

Relief and Drainage

Extensive erosion has levelled the area, leaving only few scattered north-south trending hills with heights ranging from 350 to 450 m. The area is well drained by the Black Volta River to the west which also serves as a boundary between Ghana and Burkina Faso. The Black Volta

is fed by many affluent rivers such as the Bepkong, Kulpawn and Felin (Dickson & Benneh, 1988).

Vegetation, Soils and Climate

The study area lies within the Guinea savannah vegetation zone and is typified by grasses of different heights interspersed with fire resistant, shorter deciduous trees (Fig. D) (Ghana Government, 2015). The main soil in the area is laterite and is developed from the underlying Birimian rocks (Dickson & Benneh, 1988).

The Climate in the study area is tropical and experiences a prolonged dry season from October to April with February to April being the hottest months (Ghana Government, 2015) and a uni-modal rainfall regime from May to September that peaks in June. The mean annual rainfall is 1033 mm. The average annual temperature, relative humidity, wind speed, sunshine hours, solar radiation are 28.1 °C, 61 %, 138 km/day, 7.3 hours and 19.6 MJ/m²/day respectively (Environmental Protection Agency, Ghana, 2002).

Field work

Field work pertaining to this thesis was executed mostly in 2013 and 2014 and ran about 6 months each year. In the early part of 2013 (thus, from January to March), reconnaissance mapping was undertaken on the various deposits (Julie, Kunche and Bepkong) owned by Azumah Resources Limited. This was critical, as it provided a framework for the geology in terms of host lithologies the local structural architectural framework, the metamorphic assemblages present and the fluid plumbing systems in the area. The last three months of field work of that year was focussed on detailed geological mapping up to the scale of 1:10,000 to decipher field relationships.

The year 2014 was used to log available borehole materials (reverse circulation chips and diamond drill core) of the three gold deposit mentioned above. This provided the necessary foundation needed to place the logged geological data in a three-dimensional context by way of structural, lithological and alteration controls on the gold mineralization. In all, about 209 boreholes (RD and DD combined), representing 20 fences, were logged on the three gold deposits. A field excursion was organised by Sylvain Block, in 2014 on the whole tectonic evolution of NW Ghana which helped to relate local-scale observations to the regional scale context.

References

- Amedofu, S. K., 1995. Gold in Ghana. *Pangea* 23, 1-14.
- Azumah Resources Limited, 2015. [Online] Available at: <http://www.azumahresources.com.au/projects-wa-gold.php>. [Accessed 26 May 2015].
- Azumah Resources Limited, 2013. Azumah resources resource announcement (unpublished report)
- Bierlien, F.P., Christie, A.B., and Smith, P.K., 2004. A comparison of orogenic gold mineralization in central Victoria (AUS), western South Island (NZ) and Nova Scotia (CAN)—implications for variations in the endowment of Paleozoic metamorphic terrains. *Ore Geology Reviews* 25, 125–168
- Block, S, 2015. Evolution géodynamique du craton Ouest Africain au nord du Ghana. PhD thesis, University of Toulouse III (unpublished), 415.
- Dickson, K.B., Benneh, G., 1988. *A New Geography of Ghana*. Longman Group Limited. 1-177.
- Dubé, B., Williamson, K., McNicoll, V., Malo, M., Skulski, T., Twomey, T., and Sanborn-Barrie, M., 2004. Timing of gold mineralization in the Red Lake gold camp, northwestern Ontario, Canada: New constraints from U-Pb geochronology at the Goldcorp high-grade zone, Red Lake mine and at the Madsen Mine. *Economic Geology*, 99, 1611-1641.
- Environmental Protection Agency, Ghana, 2002. National action program to combat drought and desertification. EPA, Ghana.
- Ghana Government, 2015. <http://lawra.ghanadistricts.gov.gh>. [Online]. Available at: <http://lawra.ghanadistricts.gov.gh>. [Accessed 15 September 2015].
- Goldfarb, R.J., Baker, T., Dubé, B., Groves, D.I., Hart, C.J.R., Robert, F., and Gosselin, P., 2005, World distribution, productivity, character, and genesis of gold deposits in metamorphic terranes, in Hedenquist, J.W., Thompson, J.F.H., Goldfarb, R.J., and Richards, J.P., eds., *Economic Geology One Hundredth Anniversary*. Society of Economic Geologists, 1905-2005, 407-450.
- Goldfarb, R.J., Miller, L.D., Leach, D.L., and Snee, L.W., 1997. Gold deposits in metamorphic rocks of Alaska. *Economic Geology Monograph* 9, 151–190.
- Goldfarb, R.J., Phillips, G.N., and Nokleberg, W.J., 1998. Tectonic setting of synorogenic gold deposits of the Pacific Rim. *Ore Geology Reviews*, 13, 185–218.

Goldfarb, R.J., Snee, L.W., and Pickthorn, W.J., 1993. Orogenesis, high-T thermal events, and gold vein formation within metamorphic rocks of the Alaskan Cordillera. *Mineralogical Magazine*, 57, 375–394.

Nation Online project, 2015. [Online]. Available at:
www.nationsonline.org/oneworld/map/ghana_map.htm. [Accessed 3 September 2015].

Chapter 1

Overview of Orogenic gold

1.0 Overview of Orogenic Gold mineralization

1.1 Introduction

Gold has sustained livelihoods and economies in the world from times of old until today, due to its commercial value when explored and exploited. The commodity has seen its value increase massively (e.g. from \$271.04 in 2001 to 1571.52 at the end of 2011) and consequently during 2012, 4477 tonnes of it were produced globally with a net worth of approximately \$140 billion (Price water house Coopers LLP, 2012). Owing to the extended profitability of the commodity, it has been well studied over the years. These studies include: the regions where they form; their mode of occurrence; their formative periods; their geochemical signatures; their mineral structures; their exploration and exploitation methods and their classification.

Classification schemes have been proposed by various authors (Robert et al., 2005; Groves et al., 1998; Gebre-Mariam et al., 1995; Sillitoe et al., 1991; Heald et al., 1987). These classifications are based on geological environments, structural settings and geological processes. Amongst all these classifications, the one of importance to this issue or PhD work is that of Orogenic gold.

Orogenic gold type makes up about 41% of the global gold endowment (thus 9,145 Moz of past production + resource + reserves and paleoplacers, (Lipson, 2014). Fig. 1.1 shows the global endowment of gold, thereby making the orogenic gold type an important target when it comes to gold targeting and exploration.

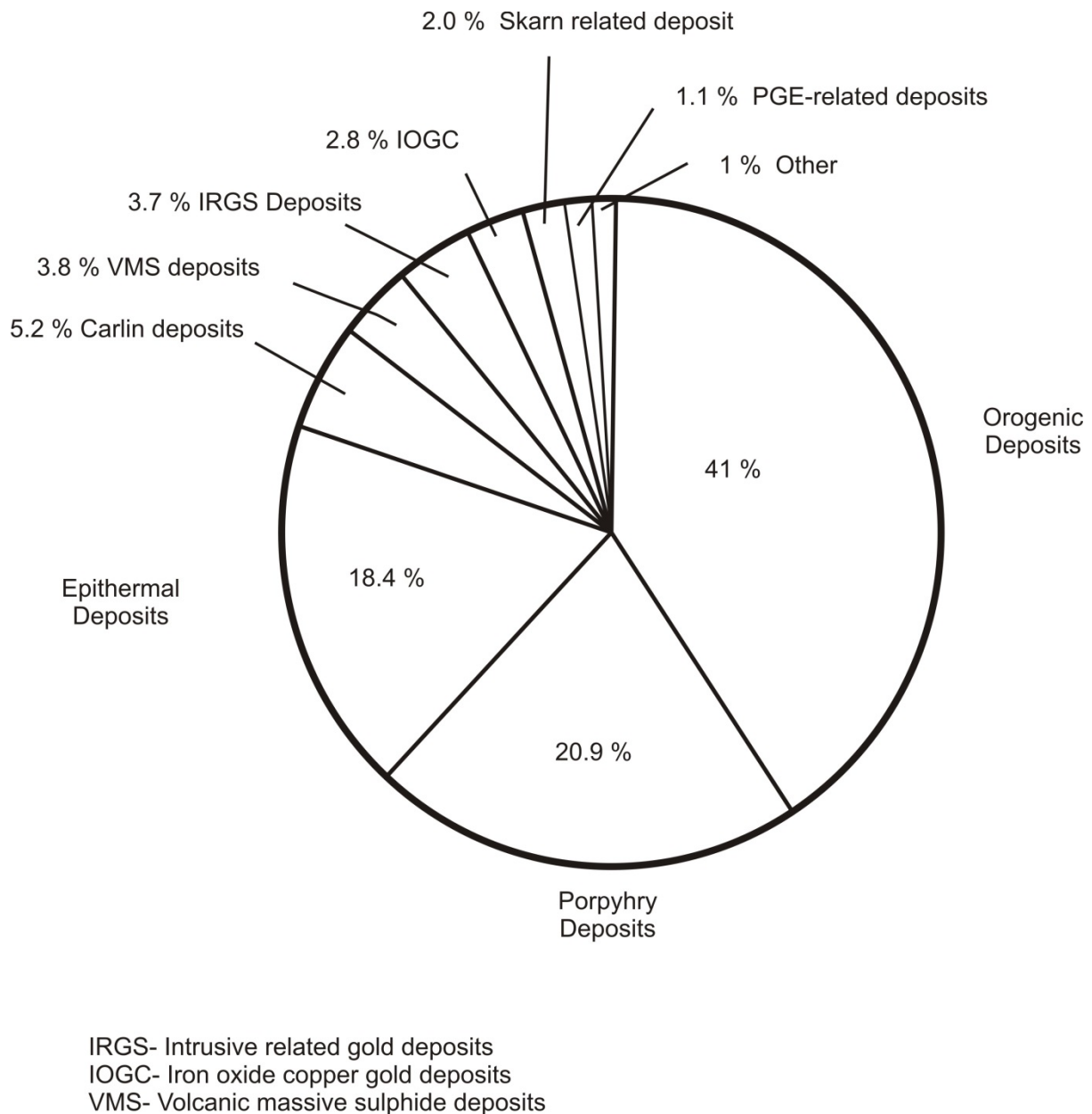


Fig. 1.1. Pie chart showing the cumulative gold endowment through time in the various gold deposit types in the world as at December, 2013 (Lipson, 2014)

The term orogenic gold was proposed by Böhlke (1982) and further expanded by Groves et al. (1998) to describe all quartz-carbonate lode-gold deposits formed in metamorphic rocks, in mid to shallow crust (5 to 15 km) (Tomkins, 2013), accretionary and collisional orogens (Groves et al., 1998) in the world. Orogenic gold, prior to 1998 has been referred to by various names such as synorogenic, mesothermal, lode gold or reef type and the likes. The proliferation of such names for the same single quartz-carbonate Au-Ag deposit in mainly greenstone belts can be quiet confusing.

Böhlke (1982) was the first person to recognise and describe some broad features common to many moderate temperature and intermediate depths gold quartz (carbonate) vein deposit of various ages which occur in orogenic belts worldwide. Most Orogenic gold (metamorphic-hosted) deposits described by Böhlke (1982) incorporated most of Lindgren's early 1900's description of mesothermal to hydrothermal vein deposits. He recognised that all the gold quartz veins are considered to represent a syn- or late metamorphic stage gold concentration which is distinct from the stratiform syn-depositional stages represented in Archean Au-bearing iron formation of carbonate or sulphide facies.

Böhlke's (1982) term 'orogenic' allows for the complete gradation from stratabound low-grade polymetallic deposit, through metamorphic segregation lodes to fissure filling hydrothermal gold quartz-veins with metasomatic haloes.

1.2 Spatial and temporal distribution of Orogenic gold

Orogenic gold occurs mainly in deformed metamorphic greenstone terranes of all ages (Fig. 1.2) which are associated in space and time with accretionary tectonics. Orogenic gold, was deposited during the Archean, Proterozoic and Phanerozoic times (Fig. 1.2). Even though orogenic gold does occur in Palaeozoic and tertiary terranes, they are mostly concentrated in Precambrian terranes and particularly those of late Archean age (Dubé & Gosselin, 2007).

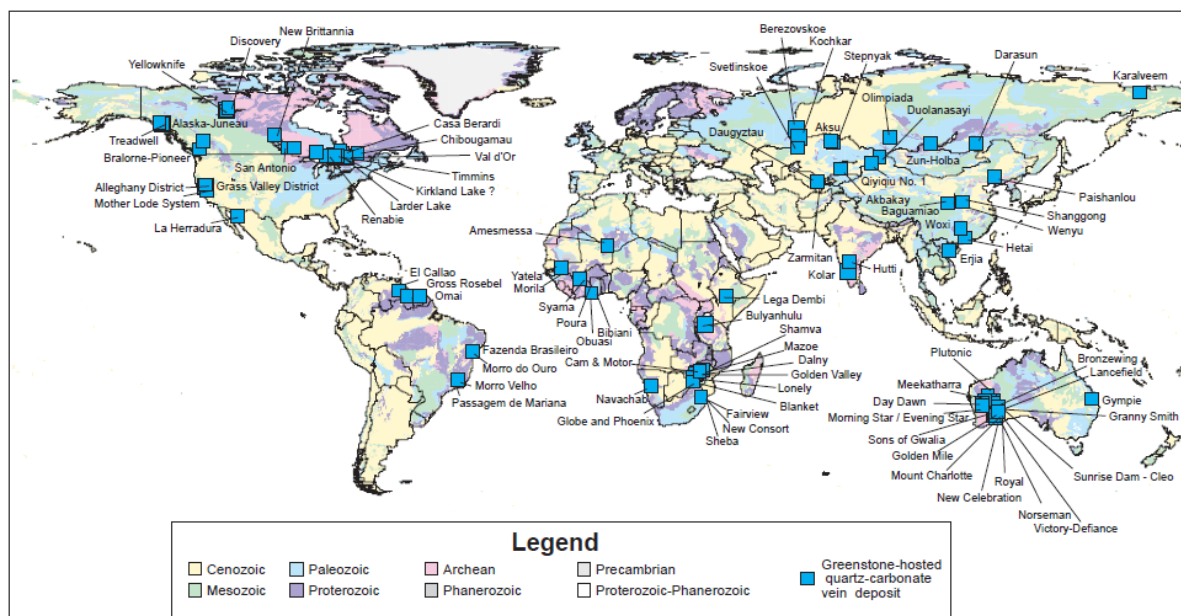


Fig. 1.2. World distribution of orogenic gold deposit across all geological terranes and ages modified after (Dubé & Gosselin, 2007).

Most Archean orogenic gold deposit can be found in Archean terranes in Canada, the Kaapvaal Craton in South Africa, the Indian Craton and Yilgarn Shield in Australia (Fig. 1.2). In Canada, all the orogenic gold deposits are of late Archean age except the Bralorne-Pioneer in the Abitibi greenstone belt (Fig. 1.3).

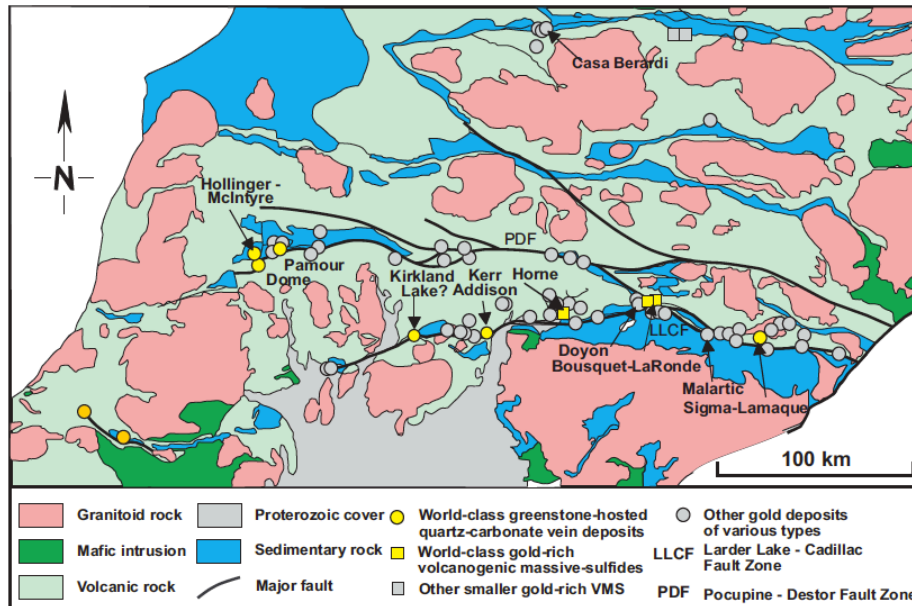


Fig. 1.3. Simplified map of the Abitibi greenstone belt showing the distribution of Major shear zones and Archean gold deposits modified after (Poulsen et al., 2000; Robert et al., 2005)

Gold concentration in Archean terranes has been interpreted in terms of continental growth and a number of late large-scale collisions between continental fragments and associated development of major faults and large scale hydrothermal fluid flows during the super continental cycle and plume events (Goldfarb et al., 2001a; Dubé & Gosselin, 2007; Barry & Groves, 1992).

Generally, Archean orogenic gold is hosted in granitoid-greenstone terrane in a wide range of rocks such as the iron rich tholeiitic basalts, differentiated gabbros, dolerites, ultramafic/mafic rocks, and granitoids can also occur in banded iron formations as well as calcareous sediments in greenstones. Examples are the Superior province deposits hosted in porphyry dykes, the Golden mile in Kalgoorlie in the Yilgarn Craton is hosted in dolerite sills, Perron-Beaufort/North Pascalis deposit is hosted in intrusive complexes and the Val D’or in the Bourlamaque batholith (Dubé & Gosselin, 2007).

In the Proterozoic and Phanerozoic periods, orogenic gold were hosted in accreted oceanic metasedimentary sequences with subordinate mafic volcanics which are interbedded with shales and greywackes (Goldfarb et al., 1998) with close spatial and temporary association with collisional orogenies or subduction zones (Fig. 1.4). According to Goldfarb et al. (1998), deposits of these ages reflect the synchronous sedimentation and or the oceanic arc or ridge volcanism prior to collision. The magmatic roots of such collision are rarely observed in

suture zones, appearing as minor ultramafic or mafic plutonic bodies. Examples of deposits that formed during this periods are the Mother Lode deposits in the USA, Ashanti in Ghana, Sukhoi Log in the Russia Far East, Eastern Cordillera in South America, Tasman deposit in Australia, the Otago deposits and the Homestake deposit in the USA.



Fig. 1.4. Continental reconstruction showing sites and examples of orogenic gold deposits and accretionary or subduction zones in Late (Neo) Proterozoic and Palaeozoic periods (Goldfarb et al., 2005).

1.3 Control on relative and absolute timing

Orogenic gold deposits have are believed to have formed late, during deformation and metamorphism of volcano-plutonic terranes as a result of focussed fluid flow (Groves et al., 1998; Kerrich et al., 2000). Based on the relative timing constrains across the geologic periods, this type of gold mineralization is formed late relative to the structural framework of individual deposits and as a broad generalization, are consistent with regional compressional settings (Hagemann & Cassidy, 2000) which facilitates the transfer of hot gold bearing fluids from deeper crustal levels (Goldfarb et al., 1998; Goldfarb et al., 2005; Tomkins, 2013). Geochronological studies on world class orogenic deposits of all ages are consistent with the interpretation made above:

1. In the superior province in Canada, the rocks are middle to late Archean in age, with spatial magmatic age ranging from 2.72 to 2.61 Ga., and the age of gold mineralization ranging from 2.72 to 2.40 Ga. (Kerrich & Wyman, 1994; Kerrich & Cassidy, 1994; Powell et al., 1991).
2. Ages of rocks in the Yilgarn Craton, Australia range from 2.75 to 2.69 Ga. with ages of the vein of gold mineralization ranging from 2.65 to 2.57 Ga (Kent & McDougall, 1996; Kent et al., 1996).
3. The Ashanti belt in Ghana, has rocks of Birimian age (2.18 to 2.15 Ga) with the age of mineralization around 2.1 Ga (Hirdes et al., 1996).
4. Rocks in Queensland, NE Australia have ages ranging from Silurian to Devonian with the ages of mineralization and quartz veining being 408 ± 30 Ma (Solomon & Groves, 1994)
5. Rocks in the southern Appalachians in the USA are Palaeozoic in age but have gold mineralization formed between 343 to 294 Ma.
6. Rocks in the Russian Far East are late Palaeozoic to Middle Mesozoic in age with ages of mineralization ranging from 135 to 100 Ma (Goldfarb et al., 1998).

From the dates and ages of the rock shown above there is a considerable overlap between time of deformation and gold mineralization suggesting the rocks and gold is usually a single product of a large scale crustal thermal event (Goldfarb et al., 1998).

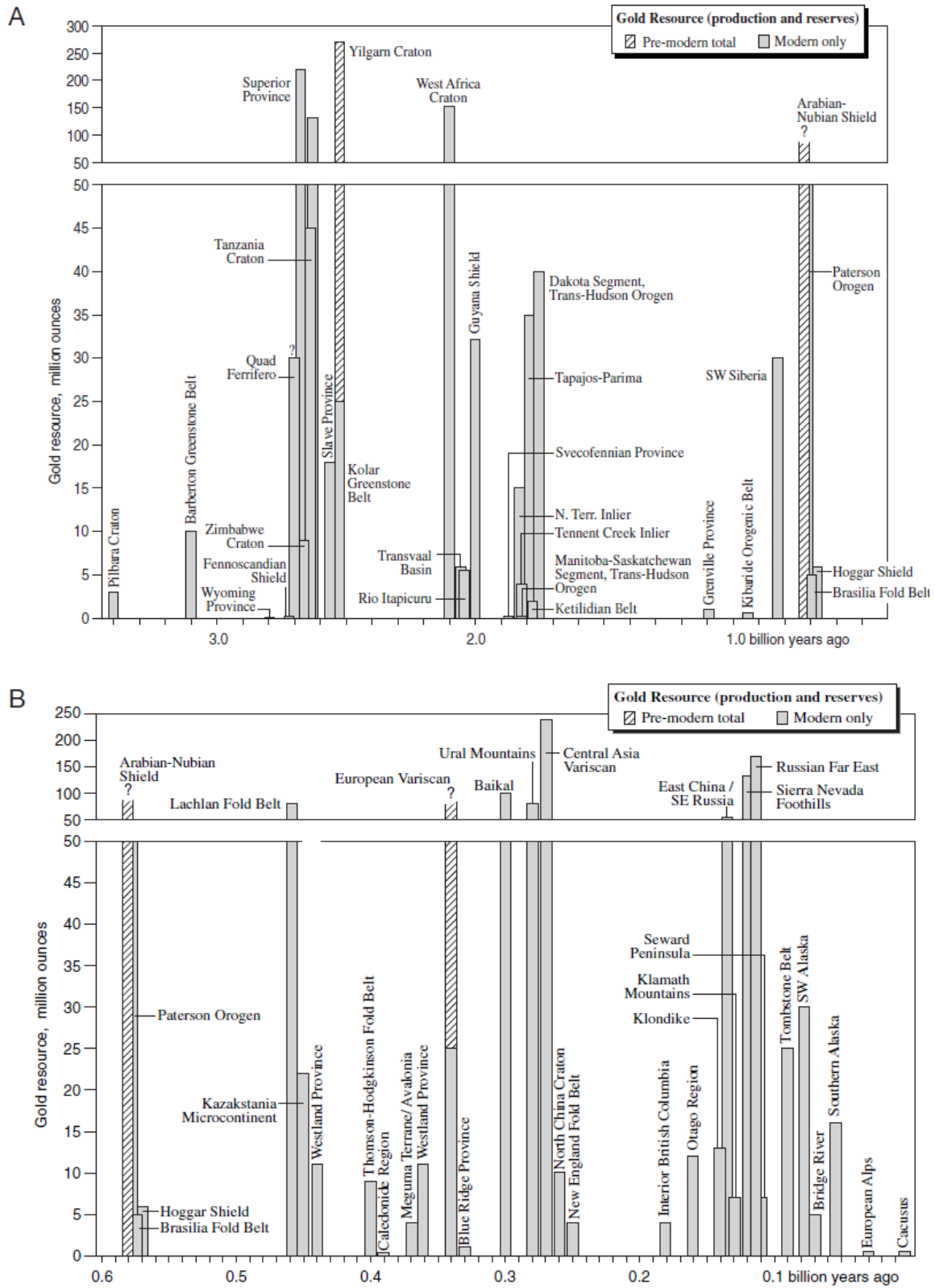


Fig. 1.5. The distribution of Orogenic gold through time (a) Orogenic gold with its associated placers in the late Archean to early Proterozoic periods (b) orogenic gold distribution through the Phanerozoic to tertiary times (Goldfarb et al., 2001a; Goldfarb et al., 2005).

1.4 Global gold grade and tonnages associated with metamorphic gold

Several world class orogenic gold deposits in metamorphic terranes have defined well over 500 t of gold (Fig. 1.5; Dubé & Gosselin, 2007; Goldfarb et al., 2005). These deposits span from Archean to Palaeozoic terranes (Fig. 1.5), including late Archean gold in the Canadian Shield (McIntyre-Hollinger), the Yilgarn Craton in Australia (Golden Mile), the Paleoproterozoic deposits in West Africa (Ashanti) and the Palaeozoic deposits in Asia (Muruntau).

The average gold grade in the Archean, Proterozoic and Palaeozoic times were above 10 g/t with higher tonnages (Fig. 1.6) whilst there is significant drop in the gold grade and tonnage (due to the number of orogenic deposit) in the Cenozoic periods (Fig. 1.7). Gold productivity associated with the Mesozoic-Cenozoic periods is very low but does not take the huge resource potential from orogenic gold (Fig. 1; Goldfarb et al., 2005).

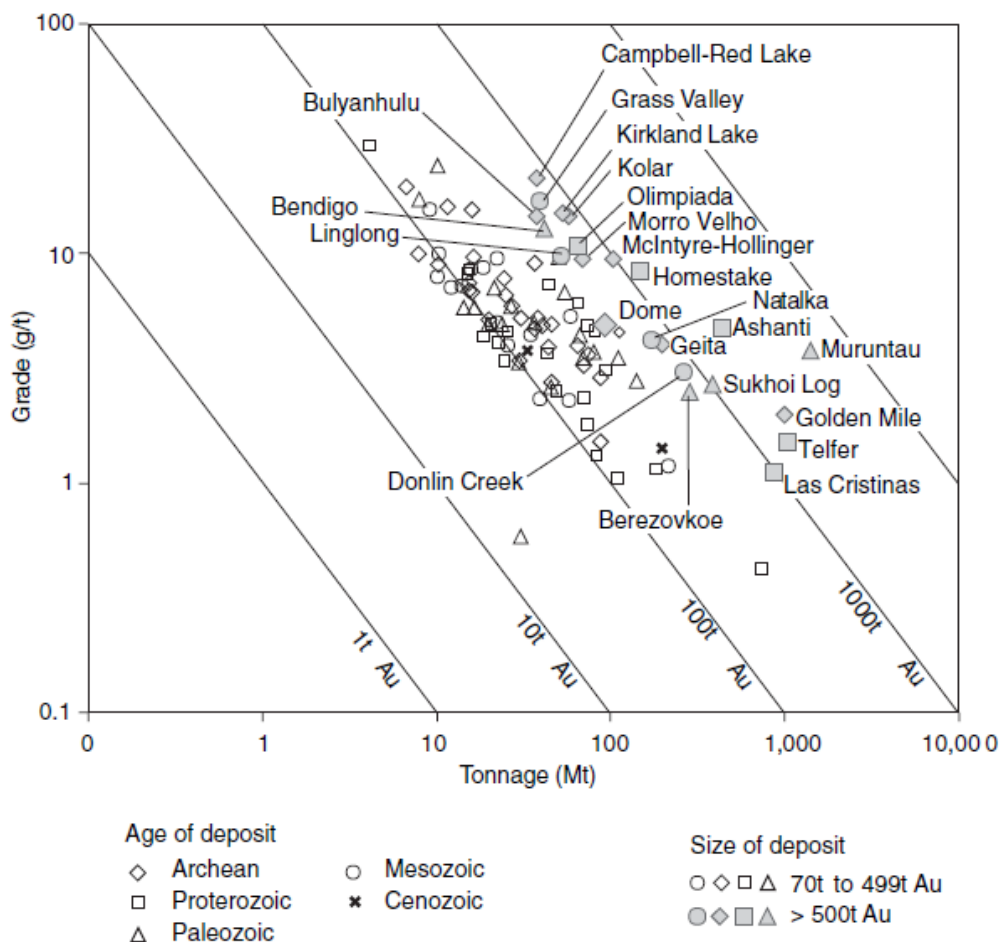


Fig. 1.6. Tonnage vs grade relationship of world class orogenic gold deposits in the world modified after (Goldfarb et al., 2005).

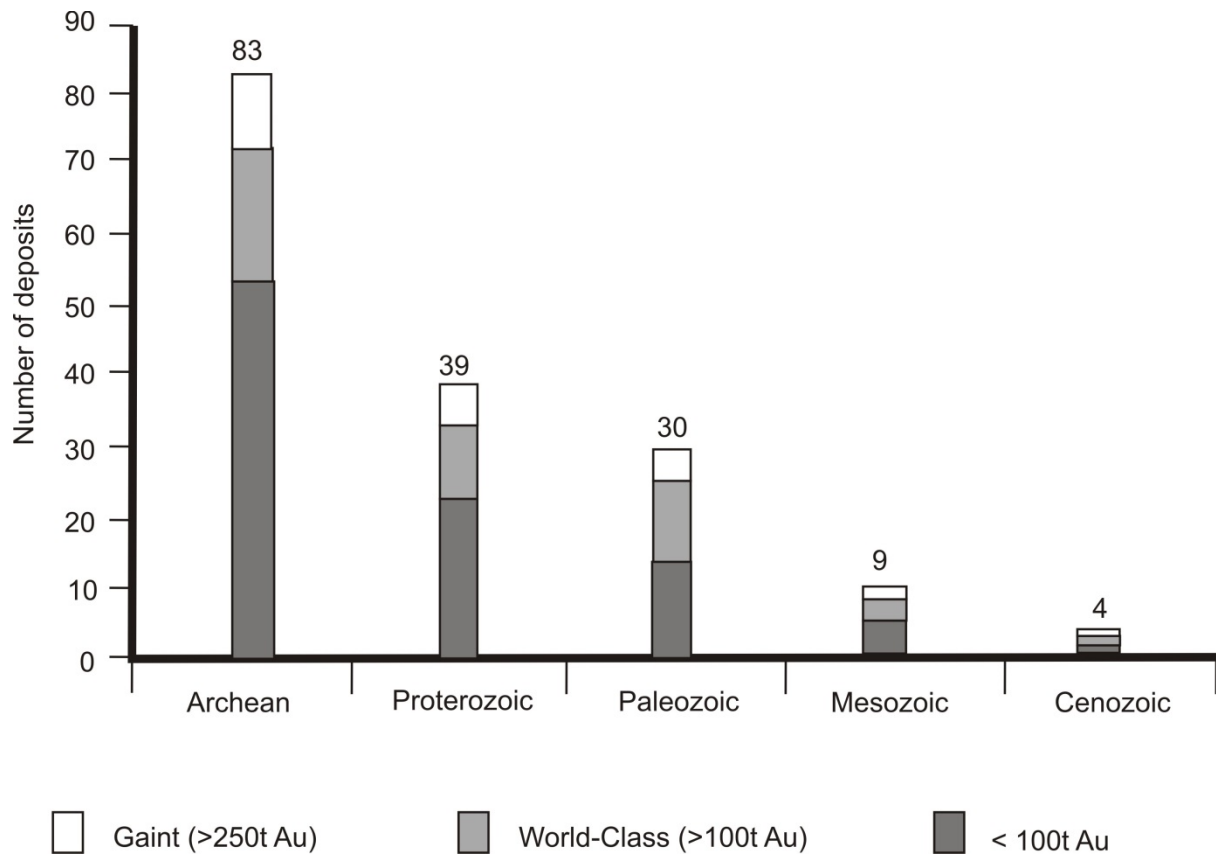


Fig. 1.7. Number of deposits containing at least 31 t of gold defined by time periods and deposit types. Modified after (Goldfarb et al., 2005; Dubé & Gosselin, 2004; Dubé & Gosselin, 2007).

With the global increase in gold prices in the early 2000's and with improved methods for gold extraction, the definition of what is economically viable deposits has evolved. In the 1950's the average gold grade mined in Ghana, USA, Canada, and Australia was 12 g/t whereas what is mined today can be as low as 3 g/t. In many discoveries, mined from 2011, the grade is as low as 1.17 g/t (Fig. 1.8).

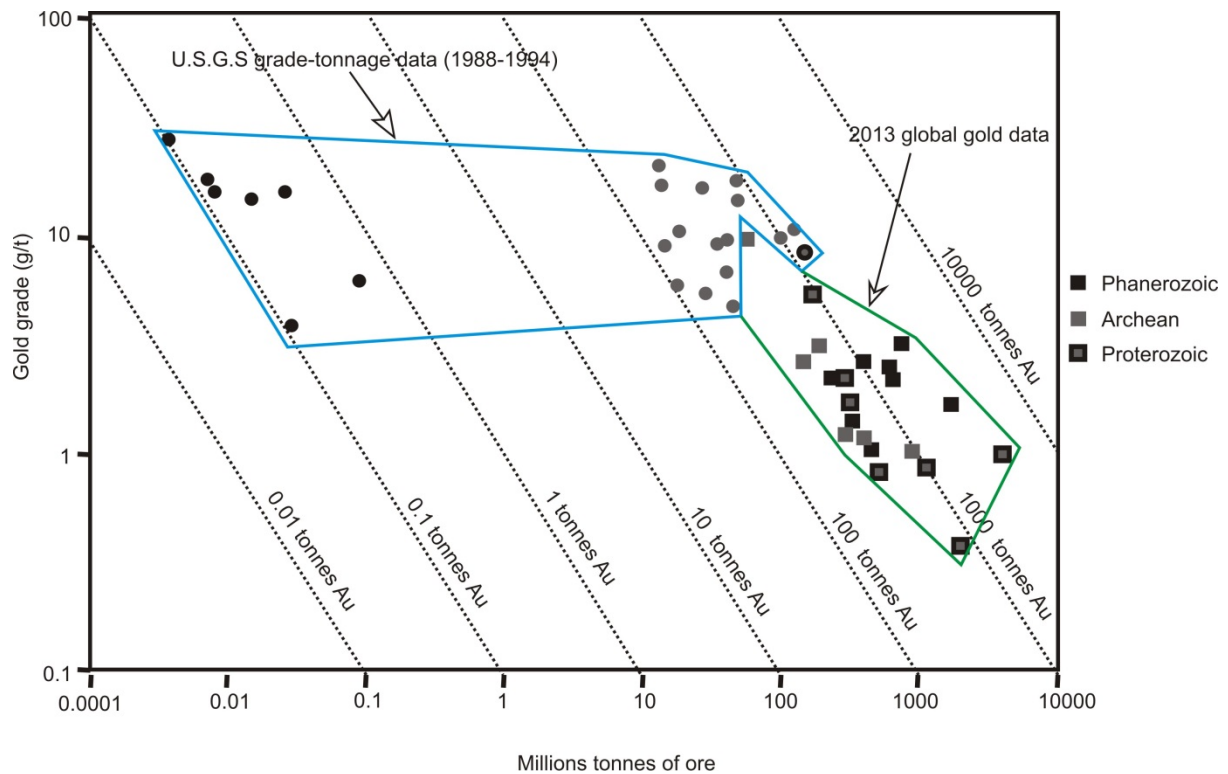


Fig. 1.8. Tonnage vs grade relationships today as compared to what it was in 1988 to 1994 (Dubé & Gosselin, 2007).

1.5 Tectonic controls on Orogenic Gold mineralization

Economic geologists have long recognised that hydrothermal gold deposits have a spatial relationship with faults and structural breaks or discontinuities (Grove et al., 1998; Sillitoe, 2000; Bierlein et al., 2004). The empirical relationships between orogenic gold and major structures play an important role by providing a pathway for fluids to be focussed into the upper crust due to its high permeability and low strengths.

Orogenic gold deposits are near to first-order transcrustal structures, generally bounding tectonically juxtaposed metamorphic supracrustal sequences or tectonostratigraphic terranes of all ages (Groves & Foster, 1991; Goldfarb et al., 1993; McCuaig & Kerrich, 1998).

Examples of such first-order transcrustal structures are the Kirkland lake-Cadillac faults, Destor-Porcupine faults in the Abitibi Archean province in Canada, the Archean Norseman-Wiluna belt associated with the Kalgoorlie deposits in Australia, the Proterozoic Ashantibelt in Ghana in West Africa hosting the Obuasi, Ahafo and Kunche deposits respectively, the Hercynian suture in Uzbekistan which hosts the largest deposit of this type (Muruntau), the Mesozoic Foot hill metamorphic belt in California hosting the Mother lode province (McCuaig & Kerrich, 1998) and the Cenozoic Coast range megalineament hosting the Juneau deposits in Alaska (Goldfarb et al., 1993; Goldfarb et al., 1997).

General characteristics of first-order geological structures that cut across orogenic terranes of all ages are;

1. They exhibit anastomosing shear zones at the brittle-ductile transition
2. They are several hundreds of kilometres in length, and they are not single faults, but segmented structures that shows multiple events
3. Show doubly plunging folds
4. Exhibit mega boudinage
5. Have L-S tectonic fabrics with lineations ranging from steeply dipping to sub-horizontal attitudes and
6. Metamorphic grade (McCuaig & Kerrich, 1998).

These faults are parallel to the volcanic and sedimentary sequences in Precambrian terrains and have complex and long-lived structural history, which commences with shortening and high angle reverse movements (Goldfarb et al., 2005). Reverse faults do have the higher degree of misorientation with respect to the strike of the fault plane during compressional regime, with higher level of fluid over pressure, making it susceptible to a high fluid flux.

Although, orogenic gold deposits associated with first-order structures are rare, dilatational jogs and anti-dilatational jogs, fault bifurcations and thrust duplexes on these transcrustal structures are known to host some gold deposits. Examples are the New Celebrations gold deposits in Australia and shear zones such as the Archean Mount Monger fault (Goleby et al., 2002), the Proterozoic Ashanti shear zones (Allibone et al., 2002), the Paleozoic South Armorican shear zone (Jegouzo, 1980) and the Mesozoic Gawk fault (Walker & Jackson, 2002).

Although orogenic gold have spatial association with first order crustal scale structures (McCuaig & Kerrich, 1998; Bierlien et al., 2004; Goldfarb, 2012), the first order structures appears to have little or no hydrothermal mineralization in them, but are instead hosted in second or third order structures that splay or bifurcate of the major first order structure. This geometrical relationship is observed in all orogens of varying ages.

Examples of gold deposits are the Kunche and Bepkong deposits in the Wa-Lawra belts which are formed in second order structures that splay off the first order Jirapa shear zone (Amponsah et al., 2015); the Kirkland Lake and Val D'or deposits on the Kirkland-Cadillac fault and the Gaint gold deposit on the Kalgoorlie-Kumbalda trend in Australia. According to McCuaig & Kerrich, (1998), this is a result of:

1. A temperature gradient exist laterally away from the first order structure

2. The first order structures are largely aseismic, largely due to their ductile character and the development of micas on the shear planes, but second and third order structures flanks the rocks seismically active, leading to greater fluid pressure fluctuations
3. Permeability and fluid flux are greater in rocks flanking first order structures because these are zones of low mean stress.

Orogenic gold mineralization also forms in areas where faults intersect, anticlines or uplifts and zones of competency contrast. The percentage of gold formed at this structural sites are not readily known.

1.6 Orogenic gold ore body geometry and ore body controls

Orogenic gold deposits are typified by quartz vein system, usually dominated by quartz with 3 to 5% sulphide content and 5 to 15% carbonate minerals (Goldfarb et al., 1998). Many studies have shown that gold lodes within orogenic systems have a direct relationship with a structural and/or lithological trap and have a variety of geometries (Cox et al., 1991). The quartz veins carrying the gold are usually situated in dilatational zones caused by changes in structural attitudes, lithological contacts, splay and intersections (McKinstry, 1955; Hodgson, 1989).

Favourable sites for orogenic gold are areas of low mean stress for shear and tensile failure, within a large strain zone or in areas of tensile stress. The splay or horse tails generate tensional fields which causes reduction in the local mean stress at the point of the splay (Chinnery, 1960a) and splay can suggest a focal point of seismicity, dilatation and heat flow (Seagall & Pollard, 1980).

Orogenic gold can form also along regional structural anticlines as in Damang (Fig. 1.9), Ghana (White et al., 2014) especially along the fold hinge zones, in tight fold slate belts in Ballarat and open folds in Telfer in Australia. According to United States Geological Survey (USGS) Open File Report 01-151, changes in the structural attitude of a rock or conduit serves as favourable loci for dilatation and the dip sense are attributed to reverse or normal kinks on properly oriented S- and -Z symmetry in the fissure plane.

Rheological and chemical favourable rocks such as banded iron formation (BIFs) are key to ore body controls. Iron or carbon rich rocks along flow paths have proven to be important sinks for the release of gold from hydrothermal solutions (Goldfarb et al., 2005). An example of this type of chemical trap is the stratabound Homestake BIF formation (Fig. 1.10) in South Dakota (Caddy et al., 1990; Ladeira, 1991a) and the BIF-hosted deposits in the Yilgarn block.

Also chemical favourable lithologies such as the Fe-rich tholeiitic basalts in Kalgoorlie in Western Australia (Golden Mile and the Campbell-Red Lake deposits; McCuaig and

Kerrich, 1998) favour the deposition of orogenic gold, by serving as desulphidation sinks for gold transporting fluids.

In Phanerozoic terranes, carbonaceous pelitic sediments or sequences are thought to have served as important reducing agent of the fluids and producing focii of high grade ore (Cox, et al., 1991; Goldfarb, et al., 2005).

Lithological contacts also play a major role in the distribution, shape and orientation of ore bodies.

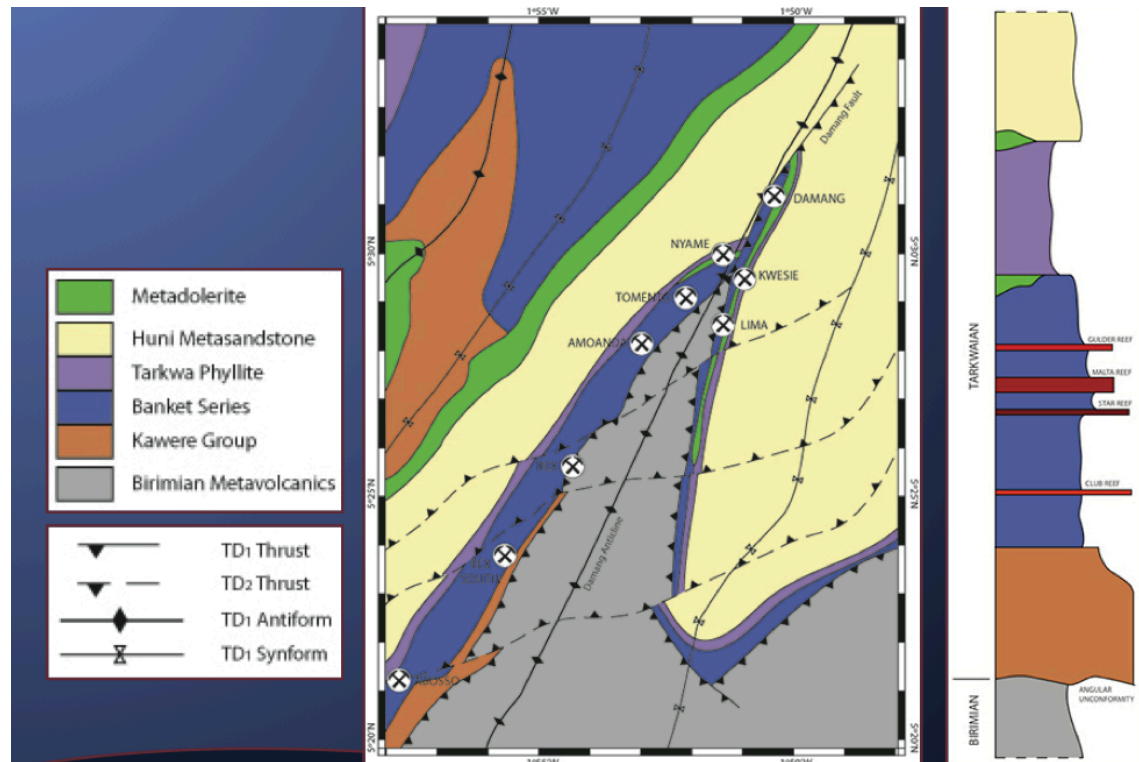


Fig. 1.9. Map showing orogenic gold deposits along the hinges of a regional anticline in Damang (Southern Ghana, West Africa) and the other deposit at the limbs of the fold. Map modified after White et al. (2014).

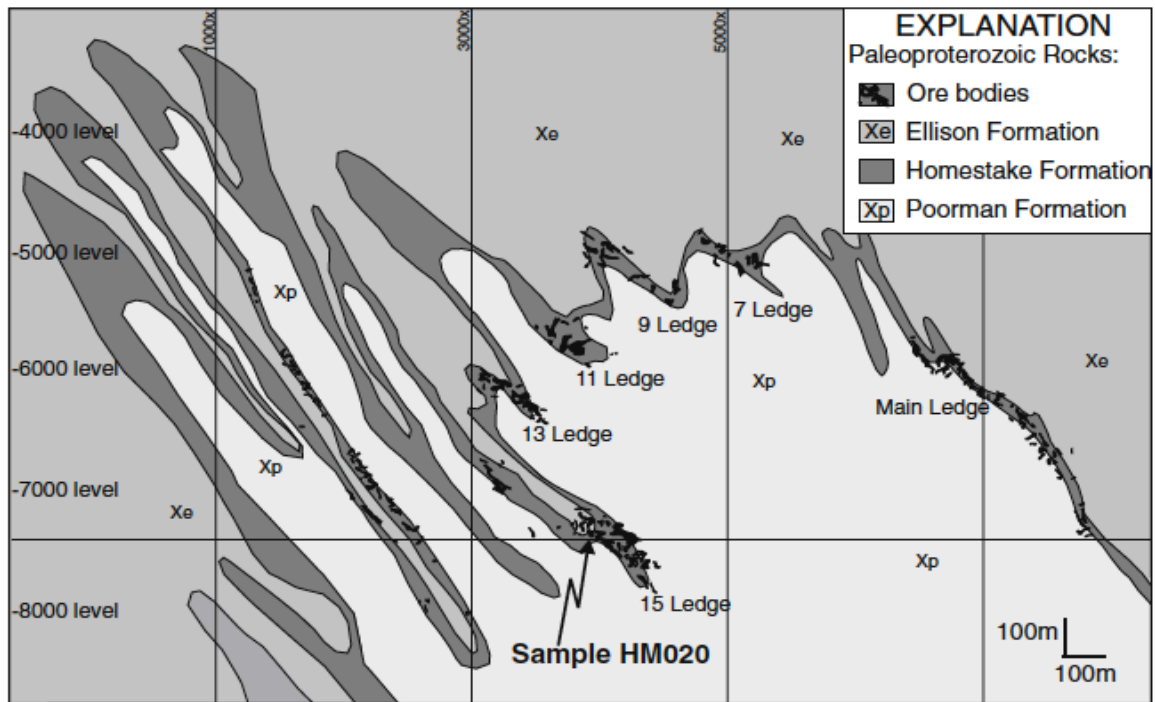


Fig. 1.10 Mine face map showing favourable chemical and anticlinal trap hosting gold in the BIF's in the Homestake Formation, USA. Map modified after Caddy et al. (1991).

1.7 Metamorphic grade

Greenschist facies in orogenic accretionary terranes (e.g. greenstone belts) have a spatial relationship with gold mineralization of Precambrian and Phanerozoic ages. It is a well-established fact that gold in Precambrian greenstones belts (eg. Yilgarn and Superior Lode gold provinces; Fig. 1.11) and Phanerozoic orogens (Juneau deposit; Fig. 1.12) have a spatial association with greenschist facies and the majority of orogenic gold deposit have an ambient pressure and temperature in mid-crustal conditions (Boyle, 1979; Goldfarb, et al., 2005).

The exact reason why gold is spatially associated with greenschist facies rocks is not well established, but Goldfarb et al. (2005) suggested the following reasons;

- (1) Within the transition of greenschist and amphibolite facies, large quantities of fluids are created and released
- (2) Favourable structures hosting orogenic gold (usually at the brittle-ductile transition) lie within the greenschist facies zone.
- (3) Fluid focusing and phase separation are mostly likely to occur as fluids ascend into greenschist-amphibolite facies regime due to pressure and temperature drops.
- (4) Gold solubility shows a sharp drop under greenschist temperatures and pressure

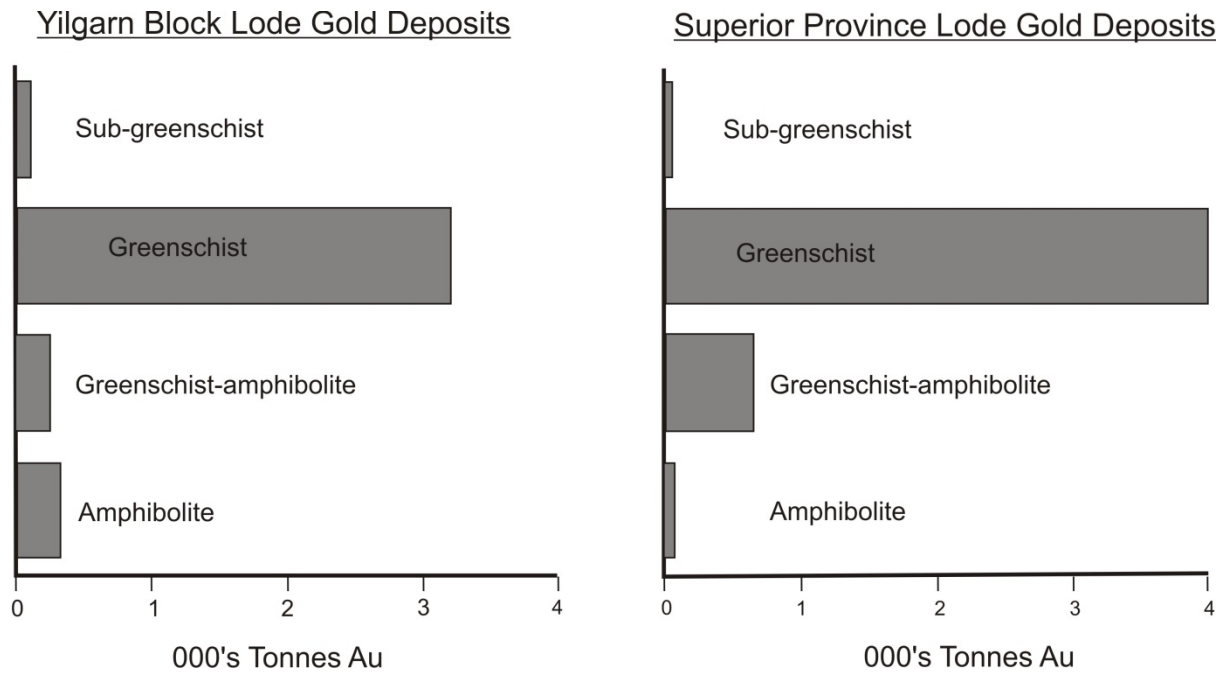


Fig. 1.11. Diagram showing the spatial association of gold mineralization with metamorphic facies in Precambrian terranes, for example the Yilgarn block and Superior Province Lode gold deposits.

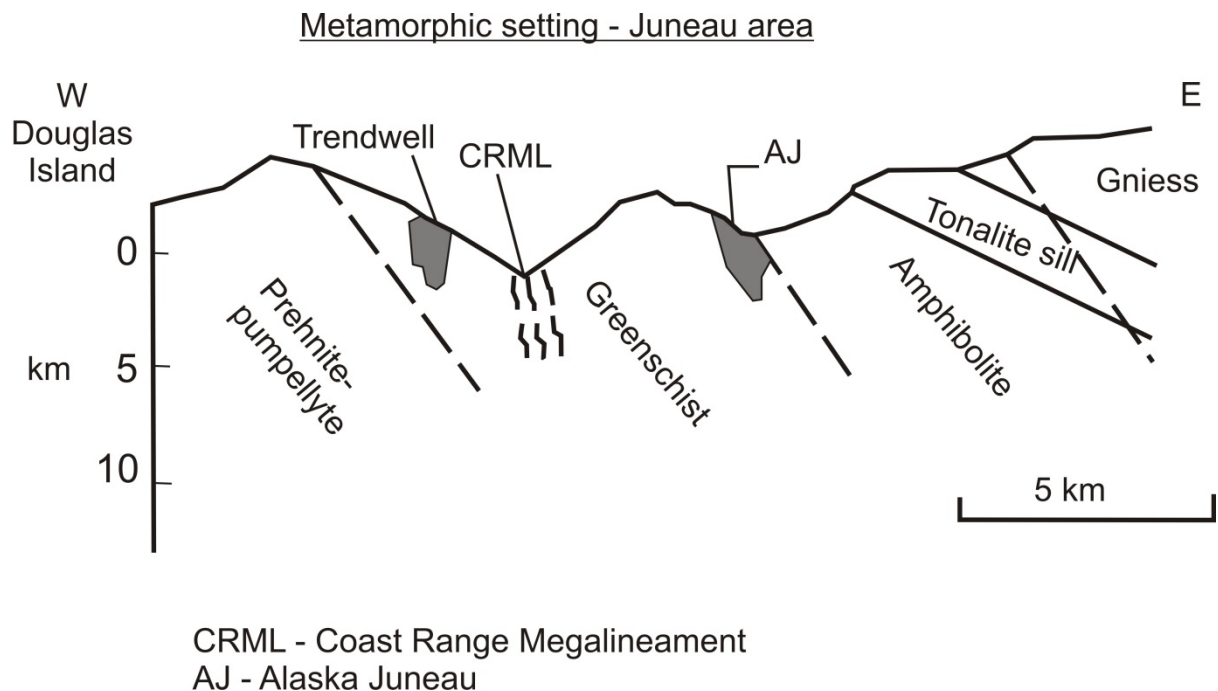


Fig. 1.12. Cross section showing the distribution of the various metamorphic isogrades in the Juneau area. The Trendwell and the Alaska Juneau deposits were formed within greenschist facies environment (Newberry & Brew, 1987).

Veins that fill extensional fractures form more readily under greenschist facies metamorphic conditions. Examples of gold deposits by Goldfarb et al. (2005) that formed under greenschist to amphibolite facies conditions are:

1. The Paleoproterozoic Ashanti deposit formed under greenschist conditions and defined by chlorite, sericite, calcite mineral assemblages
2. Archean age Golden Mile deposit (greenschist)
3. Proterozoic age Homestake mine (greenschist-amphibolite transition),
4. Archean age McIntyre-Hollinger mine (greenschist facies conditions)
5. Sukhoi Log Mine (greenschist metamorphic conditions)
6. Morro Velho deposit (greenschist metamorphic conditions)
7. Prestea mines (greenschist conditions)
8. Kirkland lake mine (lower greenschist conditions)
9. Natalka mines (greenschist conditions)
10. Campbell-Red Lake (middle greenschist to lower amphibolite conditions).

1.8 Hydrothermal alteration

Hydrothermal alteration assemblages in quartz-hosted orogenic gold deposit in shear and fault zones show evidence of having been open systems (Goldfarb et al., 2005). The chemical and isotopic metasomatic interaction of fluid and adjacent wall rock (McCuaig & Kerrich, 1998) usually reflects the interaction of a $\text{H}_2\text{O}-\text{CO}_2-\text{H}_2\text{S}$ ($\pm \text{CH}_4$ and N_2) fluids with different rock types at various temperatures (Goldfarb et al., 2005; Diamond 2000). McCuaig & Kerrich (1998) showed that the movement of hydrothermal fluids into wall rocks as well as the hydrothermal alteration mineralogy is dependent on the geometry of the hydrothermal plumbing system and the deformation mechanism operating within it. Many authors have recognised that the paragenetic minerals for orogenic gold deposits of all ages are similar (McCuaig & Kerrich, 1998; Goldfarb, et al., 2005). Quartz and carbonates precipitate over a relative wider range of temperatures, whereas silicates (mica, chlorite, and plagioclase) and sulphides (arsenopyrites, pyrites, pyrrhotite, sphalerite, and galena), oxides (ilmenite, rutile) and gold have more restrictive temperatures of deposition (McCuaig & Kerrich, 1998). Gold in many orogenic deposits around the world usually have one or more stages of deposition, but the last stage is typically associated with the late brittle structures and considered to be a remobilization of the early formed gold within the paragenetic sequence (Kerrich & Cassidy,

1994; McCuaig & Kerrich, 1998). According to McCuaig & Kerrich (1998), the hydrothermal minerals associated with orogenic gold varies and zonation occurs over a wide range of scale.

1.9 Sources of Gold

The genesis of orogenic gold is still a subject of debate for a while now, as there is no reliable marker or pathfinder of the source (Groves et al., 1998; Tomkins, 2013; Phillips, 2013). The two most likely sources of gold as suggested by Tomkins (2013), are:

1. Metamorphic rocks: Fluids are generated out of these rocks as a result of increasing temperatures.
2. Magmas: during the crystallization process of felsic and intermediated magmas, there is usually large release of fluids.

Orogenic gold deposits are formed in metamorphic rocks at about 3-5 km at depth in accretionary and collisional setting during compressional and transpressional deformational processes (Fig. 1.13a) and this enables the transfer of fluids from deeper levels of the crust. Seismic events usually control weakly oxidized, low salinity fluids to the site of gold mineralization and allow these fluids to flow in thin relatively thicker crust (Tomkins, 2013; Cox, 2005; Sibson et al., 1998).

The rapid rise through the crust takes the fluids out of equilibrium with its surroundings, thereby promoting the destabilization of gold carrying hydrosulphide complexes ($\text{Au}(\text{HS})_2^-$ and AuHS ; Tomkins, 2013). As the fluid rises, temperature and pressure decreases and this aids in precipitation of gold. The exact temperature and pressure for the precipitation to occur varies from place to place depending on the rock fluid reaction. Precipitation of gold can also be expedited by fluid boiling, fluid mixing and chemisorption on the surfaces of sulphides (Tomkins, 2013).

Groves et al., (2000) proposed a crustal continuum model for gold occurrence, which suggested that orogenic gold extends over a continuum of depth (Fig. 1.13b) in growing fore arc regions at a temperature ranging from 100-750 °C.

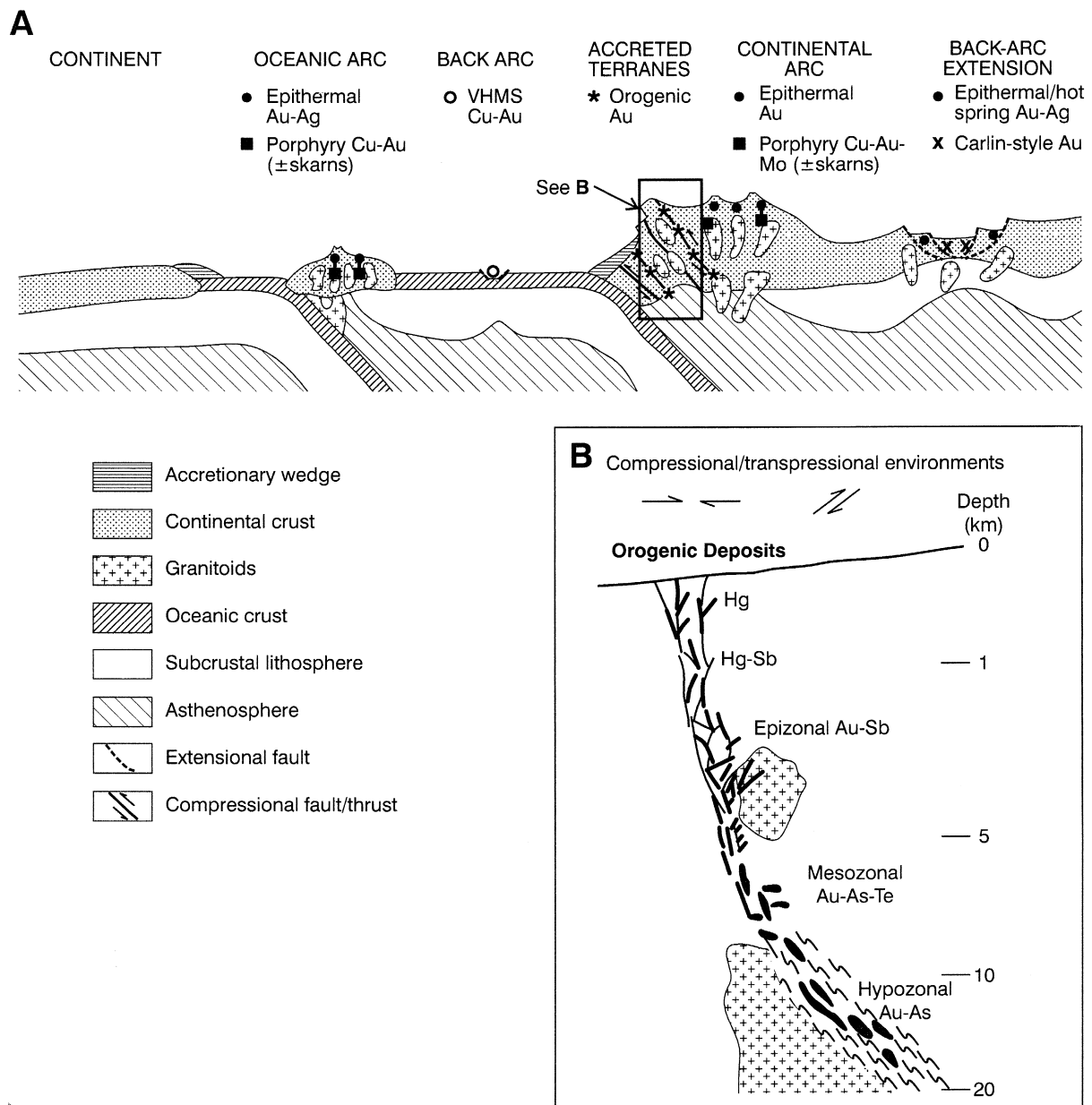


Fig. 1.13. The setting and nature of orogenic gold. (a) Plate tectonic diagram showing the environment of formation of orogenic gold. The black insert show they are basically form in accretionary terranes (b) Depth profile of orogenic gold (Groves et al., 2000)

1.10 Fluid chemistry

Fluids associated with orogenic gold are alike between orogenic gold of all ages (Kerrick & McCuaig, 1998; Groves et al., 2000). These studies have shown that orogenic gold ore fluids are CO₂ rich, thus 5 mol% of CO₂ to equal amounts of H₂O and CO₂ (Goldfarb et al., 1986; Groves et al., 2000). The substantial CO₂ content in these fluids, are responsible for the widespread carbonate alteration (Groves et al., 2000). Since most orogenic gold occurs in metasedimentary rock, the fluid interaction with the wall rocks gives fluids with signatures

which reflects a H₂O-CO₂-H₂S (\pm CH₄ and N₂) system. The variable CO₂/H₂O/CH₄ ratios are commonly caused by phase separation during extreme pressure fluctuations (Sibson et al., 1988; Groves et al., 2003). The transport of ore fluids associated with these fluid inclusion system is facilitated by reduced sulphur complexes (Goldfarb et al., 1989, Groves et al., 2000). Work done on fluid inclusions by many authors in orogenic gold deposits shows that the general temperature-pressure (T/P) conditions for the formation of this ore are 150 to 700 °C and 0.5 to 5 kbars respectively, but the majority lies within 250 °C to 350 °C and 1 to 3 kbar respectively. According to McCuaig & Kerrich (1998), fluid inclusion data from high temperature and pressure deposits (eg. 500-750 °C and 4-5 kbars) are difficult to interpret for several reasons; (1) it is difficult to preserve fluid inclusions at these temperatures due to the high recovery rates of quartz (2) most fluid inclusion will be modified as a result of the uplift and cooling episodes these fluids experience (3) the retrogression of higher temperature assemblages in these deposits, indicating post mineralization movements through the rocks.

Salinities reported in Precambrian terranes are less than 6 wt. eq. NaCl. Low salinities are responsible for the low base metal concentrations associated with orogenic gold but in rare cases, where there are high salinities with abundant base metal like the Sabie-Pilgrims Rest in the Transvaal basin in South Africa, the spatial association of the ore and the basin sedimentary sequence is very important (Boer et al., 1995, Groves et al., 2000).

1.11 Reference

Allibone, A.J., McCuaig, T.C., Harris, D., Etheridge, M., Munroe, S., Byrne, D., Amanor, J., Gyapong, W., 2002. Structural controls on gold mineralization at the Ashanti Gold Mine, Obuasi, Ghana, vol. 9. Society of Economic Geologists Special Publication, 65–93.

Amponsah, P.O., Salvi, S., Beziat, D., Baratoux, L., Siebenaller, L., Nude, P.M., Nyarko, R.S., Jessell, M.W., in press. The Bepkong deposit, Northwestern Ghana. *Ore Geology Reviews*. <http://dx.doi.org/10.1016/j.oregeorev.2015.06.022>

Barley, M. E., Groves, D. I., 1992. Supercontinental cycles and the distribution of metal deposits through time. *Geology*, 20, 291-294.

Bierlien, F.P., Christie, A.B., and Smith, P.K., 2004. A comparison of orogenic gold mineralization in central Victoria (AUS), western South Island (NZ) and Nova Scotia (CAN)—implications for variations in the endowment of Paleozoic metamorphic terrains. *Ore Geology Reviews* 25, 125–168.

Böhlke, J.K., 1982, Orogenic (metamorphic-hosted) gold-quartz veins. U.S. Geological Survey Open-file Report 82-795, 70–76.

Boer, R.H., Meyer, F.M., Robb, L.J., Graney, J.R., Vennemann, T.W., and Kesler, S.E., 1995. Mesothermal-type mineralization in the Sabie-Pilgrim's Rest gold field, South Africa. *Economic Geology*, 90, 860–876.

Boyle, R.W., 1979. The geochemistry of gold and its deposits. Geological Survey of Canada Bulletin 280, 584.

Caddy, S.W., Bachman, R.L., Campbell, T.J., Reid, R.R., and Otto, R.P., 1991. The Homestake mine, an Early Proterozoic iron-formation-hosted gold deposit, Laurence County, South Dakota. U.S. Geological Survey, Bulletin 1857-J, 67.

Chinnery, M.A., 1960a. Some physical aspects of earthquake mechanism. *Journal of Geophysical Research*, 65, 3852-3854.

Cox, S.F., Wall, V.J., Etheridge, M.A., and Potter, T.F., 1991. Deformational and metamorphic processes in the formation of mesothermal vein-hosted gold deposits: Examples from the Lachlan fold belt in central Victoria, Australia. *Ore Geology Reviews*, 6, 391–423.

Dubé, B., and Gosselin, P., 2007, Greenstone-hosted quartz-carbonate vein deposits, in Goodfellow, W.D., ed., *Mineral Deposits of Canada: A Synthesis of Major Deposit-Types*,

District Metallogeny, the Evolution of Geological Provinces, and Exploration Methods. Geological Association of Canada, Mineral Deposits Division, Special Publication 5, 49-73.

Dubé, B., Williamson, K., McNicoll, V., Malo, M., Skulski, T., Twomey, T., and Sanborn-Barrie, M., 2004. Timing of gold mineralization in the Red Lake gold camp, northwestern Ontario, Canada: New constraints from U-Pb geochronology at the Goldcorp high-grade zone, Red Lake mine and at the Madsen Mine. *Economic Geology*, 99, 1611-1641.

Gebre-Mariam, M., Hagemann, S.G., and Groves, D.I., 1995. A classification scheme for epigenetic Archaean lode-gold deposits. *Mineralium Deposita*, 30, 408-410.

Goldfarb, R.J., Baker, T., Dubé, B., Groves, D.I., Hart, C.J.R., Robert, F., and Gosselin, P., 2005. World distribution, productivity, character, and genesis of gold deposits in metamorphic terranes, in Hedenquist, J.W., Thompson, J.F.H., Goldfarb, R.J., and Richards, J.P., eds., *Economic Geology One Hundredth Anniversary*. Society of Economic Geologists, 1905-2005, 407-450.

Goldfarb, R.J., Groves, D.I., and Gardoll, S., 2001a. Orogenic gold and geologic time: A global synthesis. *Ore Geology Reviews*, 18, 1-75.

Goldfarb, R.J., Miller, L.D., Leach, D.L., and Snee, L.W., 1997. Gold deposits in metamorphic rocks of Alaska. *Economic Geology Monograph* 9, 151-190.

Goldfarb, R.J., Phillips, G.N., and Nokleberg, W.J., 1998. Tectonic setting of synorogenic gold deposits of the Pacific Rim. *Ore Geology Reviews*, 13, 185-218.

Goldfarb, R.J., Snee, L.W., and Pickthorn, W.J., 1993. Orogenesis, high-T thermal events, and gold vein formation within metamorphic rocks of the Alaskan Cordillera. *Mineralogical Magazine*, 57, 375-394.

Goleby, B.R., Korsch, R.J., Fomin, T., Bell, B., Nicoll, M.G., Drummond, B.J., and Owen, A.J., 2002. Preliminary 3-D geological model of the Kalgoorlie region, Western Australia, based on deep seismic reflection and potential field data. *Australian Journal of Earth Sciences*, 49, 917-933.

Groves, D.I., Foster, R. P., 1991. Archaean lode gold deposits. In *metallogeny and exploration*. R. P. Foster (eds) Glasgow: Blackie, 63-103.

Groves, D.I., 1993. The crustal continuum model for late-Archaean lode gold deposits of the Yilgarn block, Western Australia. *Mineralium Deposita*, 28, 366-374.

Groves, D.I., Goldfarb, R.J., Gebre-Mariam, M., Hagemann, S.G., and Robert, F., 1998. Orogenic gold deposits: A proposed classification in the context of their crustal distribution and relationship to other gold deposit types. *Ore Geology Reviews*, 13, 7–27.

Groves, D.I., Goldfarb, R.J., Knox-Robinson, C.M., Ojala, J., Gardoll, S., Yun, G., and Holyland, P., 2000. Late-kinematic timing of orogenic gold deposits and significance for computer-based exploration techniques with emphasis on the Yilgarn block, Western Australia. *Ore Geology Reviews*, 17, 1–38.

Hagemann, S.G, Cassidy, K.F., 2000. Archean orogenic lode gold deposits. *Economic Geology Reviews*, 13, 9-68.

Heald, P., Hayba, D.O., Foley, N.K., 1987. Comparative anatomy of volcanic-hosted epithermal deposits: acid-sulfate and adularia-sericite types. *Economic Geology*, 82, 1-26.

Hirdes, W., Davis, D.W., Ludtke, G., Konan, G., 1996. Two generations of Birimian (Paleoproterozoic) volcanic belts in northeastern Cote d'Ivoire (West Africa): consequences for the 'Birimian controversy'. *Precambrian Research* 80, 173–191.

Hodgson, C.J., 1989. Patterns of mineralization. *Geological Association of Canada Short Course Notes*. 6, 51–88.

Jegouzo, P., 1980. The South Armorican Shear zone. *Journal of structural geology*, 2, 39-47

Kent, A. J. R., McDougall, I., 1996. ^{40}Ar - ^{39}Ar and U-Pb age constraints on the timing of gold mineralization in the Kalgoorlie gold field, Western Australia. *Economic Geology*, 91, 795-799.

Kent, R.W., Hardarson, B.S., Saunders, A.D., Storey, M., 1996. Plateaux ancient and modern: Geochemical and Sedimentology perspectives of Archean oceanic magmatism. *Lithos* 37, 129-142.

Kerrick, R., and Cassidy, K.F., 1994. Temporal relationships of lode gold mineralization to accretion, magmatism, metamorphism and deformation. Archean to present: A review. *Ore Geology Reviews*, 9, 263–310.

Kerrick, R., and Wyman, D., 1994. The mesothermal gold-lamprophyre association: Significance for an accretionary geodynamic setting, supercontinent cycles, and metallogenic processes: *Mineralogy and Petrology*, 51, 147–172.

Kerrich, R., Goldfarb, R.J., Groves, D.I., and Garwin, S., 2000. The geodynamics of world-class gold deposits: Characteristics, space-time distribution, and origins. *Economic Geology Reviews*, 13, 501–551.

Ladeira, E.A., 1991a. Genesis of gold in the Quadrilatero Ferrifero—a remarkable case of permanency, recycling and inheritance—a tribute to Djalma Guimaraes, Pierre Routhier, and Hans Ramberg, in Ladeira, E.A., ed., *Brazil Gold '91—the geology, geochemistry and genesis of gold deposits*. Rotterdam, Balkema, 11–30.

Lipson R 2014. The promise and perils of porphyry deposits in the future of gold production. *Society of Economic Geology Newsletter* 98

McCuaig, T.C., and Kerrich, R., 1998. P-T-t-deformation-fluid characteristics of lode gold deposits: Evidence from alteration systematics. *Ore Geology Reviews*, 12, 381–454.

McKinstry, H. E., 1955. *Mine Geology*. Geology Series, Prentice Hall, Inc, New York, 680.
Peters, S.G. Use of Structural Geology in Exploration for and mining of sedimentary rock-hosted Au deposits. USGS open file Report 01-151.

Newberry, R. J., Brew, D.A., 1987. The Alsaka-Juneau gold deposit; remobilized syngenetic verses exotic epigenetic origin, in Hamilton, T. D., and Galloway, J. P., edits, *Geologic studies in Alaska by the U.S Geological Survey during 1986*. U.S. Geological Survey Circular 988, 128 -131.

Price Water House Coopers, LLP, 2012. 2012 Gold report. Keeping up with the price of gold. Price Water House Coopers, 19.

Poulsen, K.H., Robert, F., and Dubé, B., 2000. Geological Classification of Canadian Gold Deposits. Geological Survey of Canada, Bulletin 540, 106.

Powell, R., Will, T.M., and Phillips, G.N., 1991. Metamorphism in Archean greenstone belts: Calculated fluid compositions and implications for gold mineralization. *Journal of Metamorphic Geology*, 9, 141-150.

Robert, F., Poulsen, K.H., Cassidy, K.F., and Hodgson, C.J., 2005. Gold metallogeny of the Yilgarn and Superior cratons, in Goldfarb, R.J., and Richards, J.P., eds., *Economic Geology One Hundredth Anniversary*. Society of Economic Geologists, 1905-2005, 1001-1033.

Segall, P., Pollard, D. D., 1980. Mechanics of discontinuous faults. *Journal of Geophysical Research*, 85, 4337-4350.

Sibson, R.H., Robert, F., and Poulsen, K.H., 1988. High-angle reverse faults, fluid-pressure cycling, and mesothermal gold-quartz deposits. *Geology*, 16, 551-555.

Sillitoe, R.H., 1991. Intrusion-related gold deposits, in Foster, R.P., ed., *Gold metallogeny and exploration Glasgow*. Blackie and Son, 165-209.

Solomon, M., and Groves, D.I., 1994. The geology and origin of Australia's mineral deposits. *Oxford Monographs on Geology and Geophysics*, 24, 951.

Tomkins, A.G., 2013. On the source of orogenic gold. *Geology, Geological Society of America*, 41, 1255-1256.

Walker, R., Jackson, J.A., 2002. Offset and evolution of the Gowk fault, S.E. Iran: a major intra-continental strike-slip system. *Journal of Structural Geology*, 24, 1677-1698.

White, A., Burgess, R., Charnley, N., Selby, D., Whitehouse, M., Robb, L., Waters, D., 2014. Constrains on the timing of the late-Eburnean metamorphism, gold mineralisation and regional exhumation of the Damang mine, Ghana. *Precambrian Research*, 243, 18-38.

Chapter 2

Geology and summary of Gold deposits in the West African Craton

2.1 Introduction

This thesis chapter gives a general insight of the various tectono-metamorphic domains of the West African Craton which are conserved in the rock record as major geological events from 3.7 Ga to 1.7 Ga. It also shows how the West African Craton was reshaped during the Jurassic period as a result of continental breakup of the West Africa (WAC) from South American craton (São Luís craton) and the tectonic process that took place.

This chapter also sheds some light on the nature and distribution gold deposits in the West African craton. Most of the mines are found within the greenstone belts of the craton. Deposits discussed here have reserves more than 1 million ounces.

2.2 Summary of geological framework of the West African Craton

The 'guitar shape' West African Craton (WAC) is made up Archean and Proterozoic nuclei or basement rocks covered with sediments ranging from Mesoproterozoic to the present time and entirely surrounded by several Pan African belts. The WAC is located on the northwestern margin of Gondwana (Villeneuve & Cornee, 1994). The São Luís craton in NE Brazil and N Guyana are considered to be fragments of the West African Craton which were rifted apart during the Jurassic period (Fig. 2.1; Klein & Moura, 2008). The Archean and Proterozoic basements were stabilized around 1700 Ma during the period of extreme quiescence (Black & Liégeois, 1993). The Precambrian basement rocks outcrops in two principal zones. These zones are the Reguibat shield to the north and the Man Shield to the south (Fig. 2.2). The Western portions of these two principal zones are Archean in age and the eastern portions are Proterozoic in age. Between these two shields are two small windows known as the Kenieba and Kayes inlier (Fig. 2.3; Assie, 2008). Rocks of the West African Craton outcrop in Ghana, Mauritania, Morocco, Algeria, Burkina Faso, Niger, Ivory Coast, Guinea, Sierra Leone, Liberia, Mali, Togo and Senegal.

The WAC is bounded to the north by the by the Anti-Atlas belt (685 to 615 Ma), to the east by the Hoggar shield, to the southeast by the Benin-Nigerian shield and to the west by the Mauritanides, Rockilides, Bassarides of Pan African age (800-530 Ma; Fig. 2.2) and to the south by the Gulf of Guinea . The basement is covered by three main sedimentary basins; namely the Tindouf basin (in the north), the intracratonic Taoudeni basin in the central part and the Volta basin located in the Southeastern part. The Taoudeni basin is filled with sediments of both Proterozoic and Palaeozoic age, whiles the Tindouf basin is composed mainly of Palaeozoic sediments and the Volta basin by mainly Proterozoic sediments (Fig. 2.2; Villeneuve & Cornee, 1994; Bessoles, 1977).

The West African Craton has experienced five orogenic cycle events which have overprinted each other in space and time (Assie, 2008; Yacé, 1984). These are from the oldest to the

youngest: the Leonean (3500 to 2900 Ma), the Liberian event (2900 to 2400 Ma), the Eburnean Orogeny (2400 to 1900 Ma), Kiberian (1600 to 900 Ma) and the last orogenic event is the Pan African (900 to 450Ma). The Leonean, Liberian and Eburnean orogenies are related to major crustal growth and cratonization of Africa (Assie, 2008; Yacé, 1984).

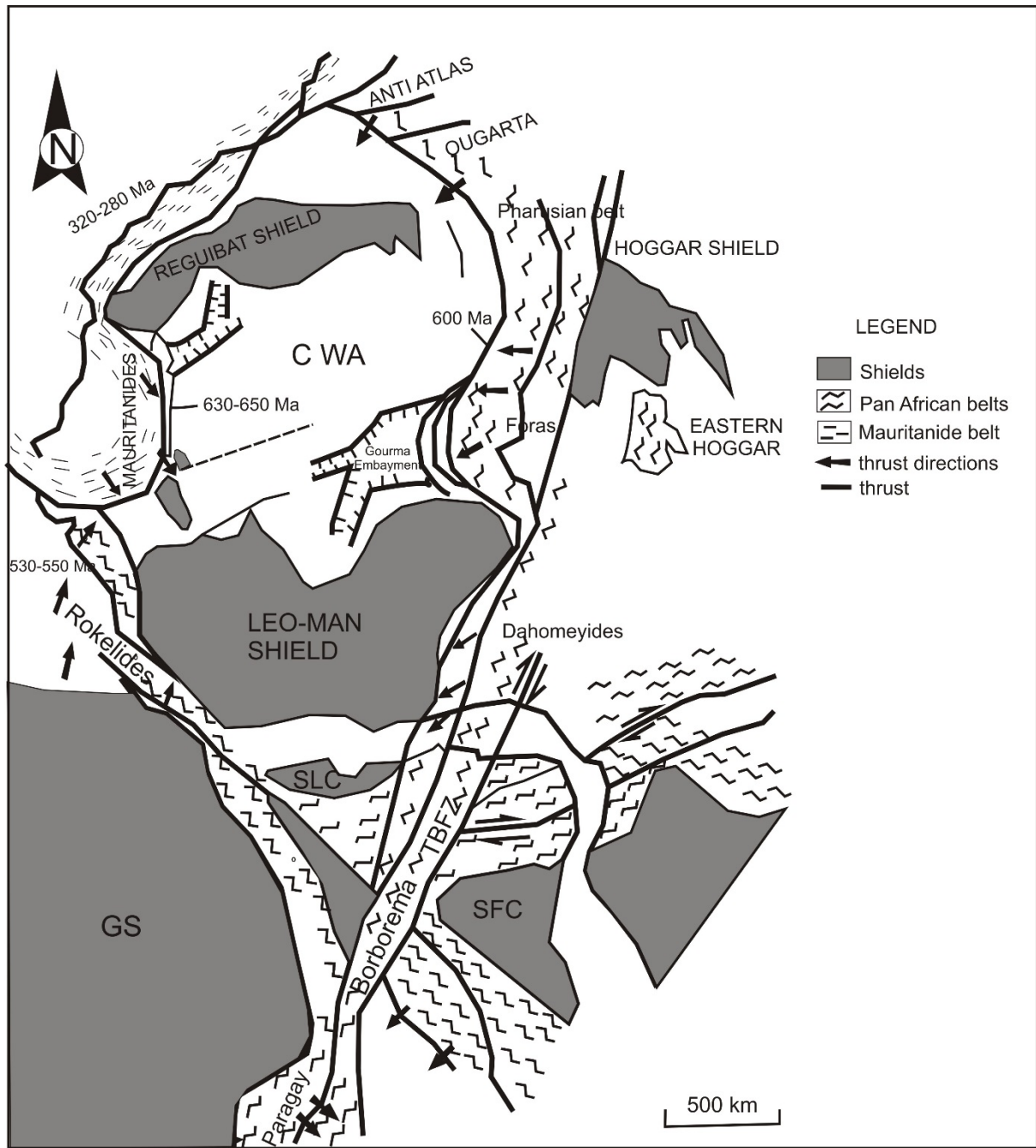


Fig. 2.1. The structural features of the West African Craton with its surrounding structures in Gondwana during the late Precambrian time (Modified after Villeneuve & Cornee, 1994). GS- Guyana shield, SLC- São Luís Craton, SFC- São Francisco Craton.

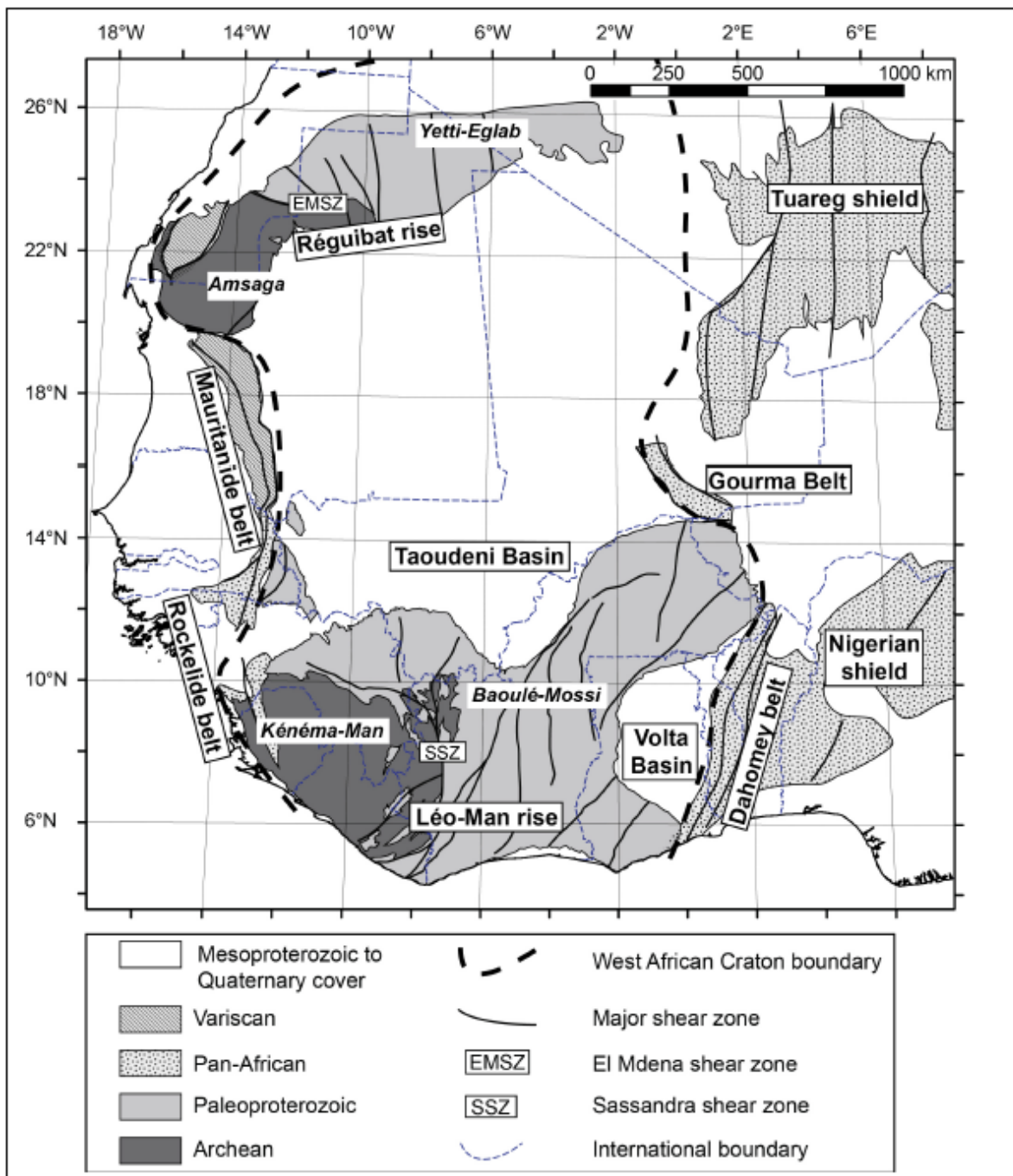


Fig. 2.2. (a) Simplified geological map of the West African craton showing the various sub-terrains (modified after Feybesse et al., 2006)

2.2.1 The Shields

The West African Craton consists of the Reguibat shield or rise and the Leo-Man shield or rise. They both have an Archean nucleus to the west and a Proterozoic nucleus (Fig. 2.2) to the east (Potrel et al., 1998; Feybesse & Milési, 1994; Boher et al., 1992; Liégeois et al., 1991; Abouchami et al., 1990). Their boundaries are marked by a major almost N-S shear zone or faults with a mylonitic character called the Sassandra fault in the Leo-Man shield found in Ivory Coast (Cahen et al., 1984) and the El Mdena shear zone in Mauritania (Attoh & Ekwueme, 1997). The Archean nucleus is composed of geological formations sutured by the Leonean and Liberian orogens.

2.2.1.1 Summary of the Reguibat shield

The Reguibat shield is bounded to the north and east by a Phanerozoic cover and to the west by the Hercynian Mauritanides and coastal basin, and to the south by the gently dipping Taoudeni basin. It is exposed in Southern Morocco, Mauritania and Southern Algeria (Fig 2.2). The Archean nucleus, found to the west in the Reguibat Shield, also known as Amsaga-Tiris-Ouassat domain (Fig 2.2; Goodwin, 1996; Keys et al., 2008), is composed of polycyclic TTG- type migmatitic orthogneisses, meta volcanic and metasedimentary rocks composed of ironstone and marbles, greywackes, metapelites, banded iron formations, ultramafic rocks (Kimberlites) and amphibolites. The gneisses are 3.52 Ga to 2.85 Ga and intruded by 2.99 to 2.83 Ga charnockitic gneisses. The Reguibat shield was affected by a 2.74 Ga. polyphase deformation and high grade metamorphism associated with the Liberian Orogeny followed by the emplacement of late granites of 2.73 to 2.72 Ga (Potrel et al, 1998; Attoh & Ekwueme, 1997).

The Proterozoic nucleus found east of the Reguibat shield also known as the Yetti domain (Goodwin, 1996). The Yetti domain, straddles the Mauritania-Algeria boarder (Fig. 2.2) and is composed of 2.1 to 1.9 Ga metasupracrustal migmatitized plutonic complexes (Chegga group; Fig. 2.3) and volcanoclastic-detrital sequences which has been intruded by Eburnean (1.97 to 1.76 Ga.) granitoid plutons. The unfolded and unmetamorphosed post orogenic Guelb el Habib molasses locally overlies the older orogenic assemblages, but has also been intruded by the 1.7 Ga granitoid plutons. The Guelb Habib group has been locally unconformably overlain by sediments of the Hank supergroup (1.05 Ga). The Hank supergroup is the oldest part of the Taoudeni cover sequences (Fig. 2.3; Goodwin, 1996).

2.2.1.2 Summary Leo-Man Shield

The Leo-Man shield of the West African craton covers an area extent of about 1700 km from Ghana in the east to Sierra Leone in the west with an average width of about 800 km. It is bordered to the north by the Proterozoic-Palaeozoic Taoudeni basin and to the east by the Volta basin and South east by the Dahomeyide orogenic belt (Fig. 2.2; Fig. 2.3).

The Archean nucleus of the Leo-Man shield outcrops in Liberia, Sierra Leone and Guinea and is smaller in size compared to the Proterozoic nucleus (Fig. 2.2). The Archean nucleus is composed of high grade felsic and mafic gneisses, phlogopite lamproites, alkaline igneous complexes (Culver & Williams, 1979) associated with narrow greenstone belts of lower metamorphic grade. The narrow greenstone belts are composed of supracrustal rocks consisting of tholeiitic basalts and metasediments. The metasediments consist of turbidites, conglomerates and extensive banded iron formation (Jessell et al., 2012) of two ages. These are (1) the rare 3.0 Ga Loko belts and (2) the wide spread 2.7 Ga old banded iron formations which constitute the Kambui belts (Goodwin, 1996).

The Paleoproterozoic nucleus also known as the Birimian or Baoulé Mossi domain was formed between 2250 to 1980 Ma (Feybesse et al., 2006) and is bounded to the north and east of the Archean domain (Fig. 2.2; Bessoles, 1977). The dominant structural grain of this nucleus was formed during the Eburnean Orogeny (Baratoux et al., 2011; Bonhomme, 1962). Rocks found here are characterised by typical Archean-like greenstone granitoid assemblages which are composed of volcanic, volcano sedimentary and sedimentary sequences separated by tonalite-trondhjemite-granodiorite and granite provinces (Jessell et al., 2012; Boher et al., 1992). Radiometric dating of the volcanic units places the peak Birimian volcanism at around 2190-2160 Ma (Jessell et al., 2012; Lüdtke et al., 1998; Davis et al., 1994) whereas some detrital zircon found in the Birimian in NW Ghana are as young as 2130 Ma (Agyei Duodu et al., 2009) supporting the idea that the sedimentary basins postdates the principal volcanic activity (Baratoux et al., 2011; Hirdes et al., 1996; Davis et al., 1994). The volcanic activity in the Paleoproterozoic nucleus is bimodal, with tholeiitic and calc-alkaline affinities. The tholeiitic basalts predates the calc alkaline series and represents an immature volcanic arc setting (Béziat et al., 2000; Lüdtke et al., 1998; Ama Salah et al., 1996). Other workers have shown that the Birimian of West Africa craton formed in an ocean plateau setting related to mantle plumes (Baratoux et al., 2011; Boher et al., 1996; Abouchami et al., 1990). The molassic sediments of the earlier Birimian rocks deposited on top of the greenstone sequences and are regarded as the youngest units in the Paleoproterozoic Birimian terrane (Davis et al., 1994; Leube et al., 1990) and deposited around 2120 Ma. These molassic sediments are known as the Tarkwaian units (Whitelaw, 1929). The Tarkwaian units are composed of quartzites, phyllites, conglomerates and sandstone sequences.

2.2.1.3 Summary of the sedimentary basins in the WAC

The sedimentary basins in the WAC consist of the Tindouf, Taoudeni and the Volta basins. The 8 km deep Tindouf basin outcrops in the northern edge of the fore lands of the Anti-Atlas fold belt and in the Zemmour area in Morocco beneath the Hercynian thrust (Fig. 2.3). It covers a land area of about 150,000 km² as an open syncline. The sediments here are composed of schisto-quartzitic formations with interbedded ultrabasic rocks, tillites, argillites and volcanic intrusions, molassic deposits. These rocks have been overlain by Cambrian age shallow marine sediments. The eastern and western portions of the Tindouf basin are mostly deformed (Villeneuve & Cornee, 1994 and reference there in).

The 2,000,000 km² Taoudeni basin extends along the whole central cratonic depression of the West African craton and divides it into two: the Reguibat shield to the north and the Leo-Man shield to the south. The basin is composed of late Proterozoic and early Palaeozoic sedimentary strata composed of tillites and sandy sequences (Trompette, 1973). These sequences represent the foreland equivalents of sediments involved in all or parts of the Pan African mobile belts that surrounds the West African craton (Goodwin, 1996).

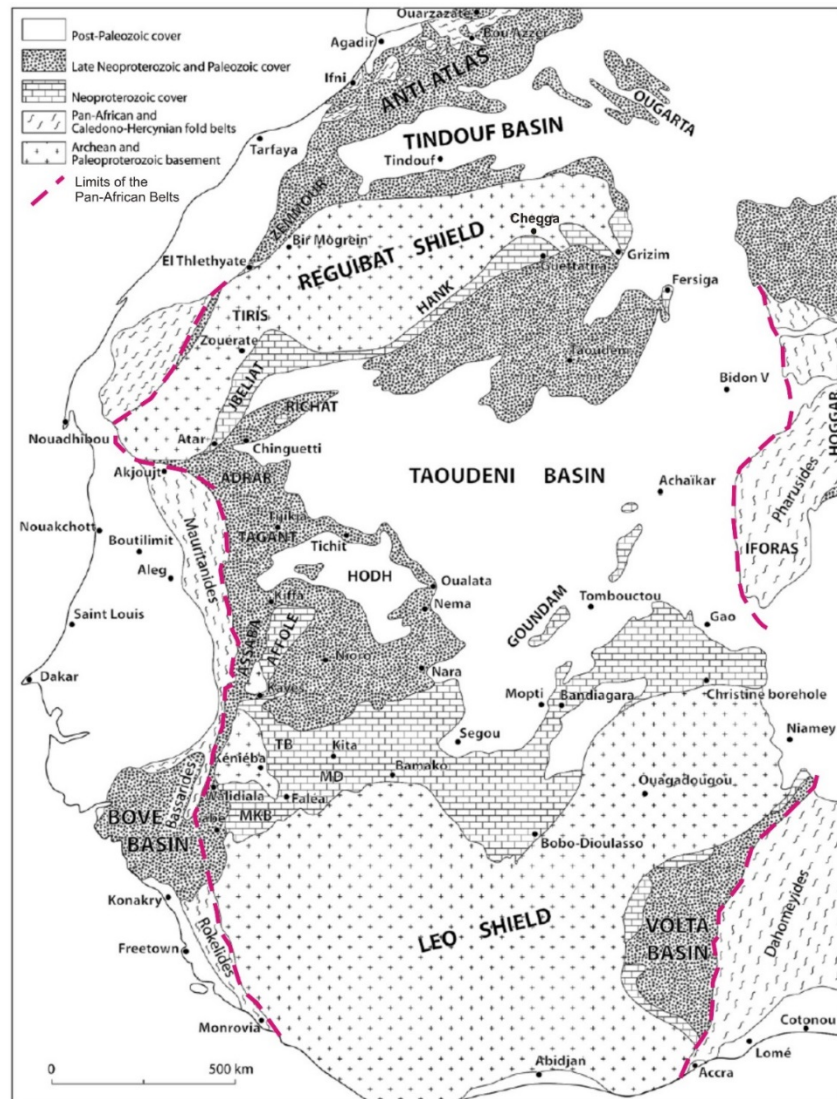


Fig. 2.3. Regional extent of the West African Craton, showing the extent of all the basins, shields and the poly cyclic orogenic belts (modified after Kah et al., 2012)

The youngest formation in the Taoudeni basin is within the centre of the basin and is characterized by a typical regressive sequence. The north western part of the basin is a probable aulacogen generally striking NNE and contains about 4 km thick sediments. The Gourma embayment (Fig. 2.1) which is on eastern side of the Taoudeni basin is composed of an 8 km thick terrigenous clastic and carbonate sediments and is interpreted as a failed triple point which have evolved into an aulacogen (Goodwin, 1996; Black, 1980).

The Volta Basin is the foreland of the Man shield (Fig. 2.3) and occupies an area size of >115, 000 km². The Volta Basin is composed of 5 to 7 km succession of flat lying Neoproterozoic to Palaeozoic sandstones, siltstones and mudstones with subordinate proportions of limestones (Kalsbeek & Frei, 2010). The basin outcrops mostly in Ghana and

in minor areas in Togo, Niger, Burkina Faso and Benin. The Basin unconformably overlies the deformed Paleoproterozoic Birimian rocks (Boher et al., 1992). Sedimentation of early sandstone in the basin syncline began around 1035 Ma and ended with tillites sequences dated around 620 Ma (Goodwin, 1996). In Ghana, the Volta Basin has been subdivided into the Obosum Group, Oti group and the Bombouaka group. This basin represents a subsidence on the southeastern flank of the West African craton and is partly up-thrust westward onto the Man shield (Goodwin, 1996).

2.2.1.4 Summary of the Pan African Belts

The Pan African orogenic belts surround the WAC on its eastern and western sides (Fig. 2.2; Fig. 2.3). The Pan African orogeny induced a partial remobilization on the West African Craton boundaries, inducing a metacratonic evolution (Ennih & Liégeois, 2008). The western margins are composed of the Mauritanides, Bassarides and Rokelides. The Mauritanides and the Bassarides are of the same aged (660 Ma) but are largely reworked by the Hercynian orogen (Villeneuve & Dallmeyer, 1987). The Mauritanides thrusts onto the West African Craton. The northern external nappes of the Mauritanides were thrust over the Palaeozoic Taoudeni Basin (Bassot, 1966). In Liberia and Sierra Leone the Rokelides overthrust the Archean Man shield (Villeneuve & Cornee, 1994; Thorman, 1976).

The 1035 to 500 Ma Anti-Atlas domain forms north of the Tindouf basin (Fig. 2.3) and generally unconformably overlies the Proterozoic basement inliers called the Berberides. The Berberides is disconformably overlain by glaciogenic sediments which deposited through to the Carboniferous time. The nearby El Graara ophiolites at Bou Azzer (Fig. 2.3) to the east of the belt is dated 787 Ma and abducted onto the West African craton by 685 Ma (Goodwin, 1996; Leblanc, 1980).

The Trans-Sahara mobile belt, which includes the Benin-Nigeria shield and the Tuareg shield (Fig. 2.2) is located at the eastern margin of the West African craton and is about 2500 km long. The belt is composed of Pan-African plutonic components, representing basement reactivation, coupled with passive granitoid plutonism, metamorphism and deformation mainly around 650-550 Ma (Goodwin, 1996). The Benin-Nigerian shield contacts the West African craton to the east in a form of a frontal thrust known as the Gourma-Dahomeyan components (Fig. 2.2). The Benin-Nigerian shield is dominated by amphibolite facies banded gneisses, migmatites, amphibolites, marble and quartzites. The Pharusides component of the TSMB also up-thrusts westward onto the West African craton. Their contact is marked by rocks of the Gourma embayment in Mali (Goodwin, 1996).

The 500,000 km² Tuareg shield is composed of the Hoggar region together with its southwestern and southeastern extensions, the Air, the Adrar and Iforas found south of the Hoggar (Fig. 2.2). The shield is composed of huge sub-ridional slices structural architecture

composed of weakly and strongly metamorphosed rocks separated by major shield wide wrench fault. The central Hoggar is home to some 3.5 Ga rock remnants. The south of the Hoggar region is composed of 3.2-3.0 Ga rocks, metamorphosed to the granulite facies and gave rise to long slender, and fault bounded charnokitic rich rock in the Ouzzal-Iforas domain (Fig. 2.2). This event is called the Ouzzal event. Early Proterozoic sediments on the Tuareg shield are widely intruded and metamorphosed by the 2.2-1.8 Ga. Eburnean orogeny rocks. These are overlaid by Meso Proterozoic pelitic sequences and extensive granitic intrusions which were all folded around 1.1 Ga. The Hoggar tectono-thermal event occurred around 660 to 604 Ma, which involved widespread granitoid intrusion and metamorphism.

2.3 The Birimian Overview of Ghana

The Birimian terrane in Ghana forms an extensive part of the Paleoproterozoic domain of the West African Craton (Vidal et al., 2009; Davis et al., 1994; Einslohr & Hirdes, 1991), and covers the western part of Ghana (Fig. 2.4). This Paleoproterozoic domain composed of granite-greenstone assemblages juxtapose against the Archean nucleus to the east and north (Perrouy et al., 2012).

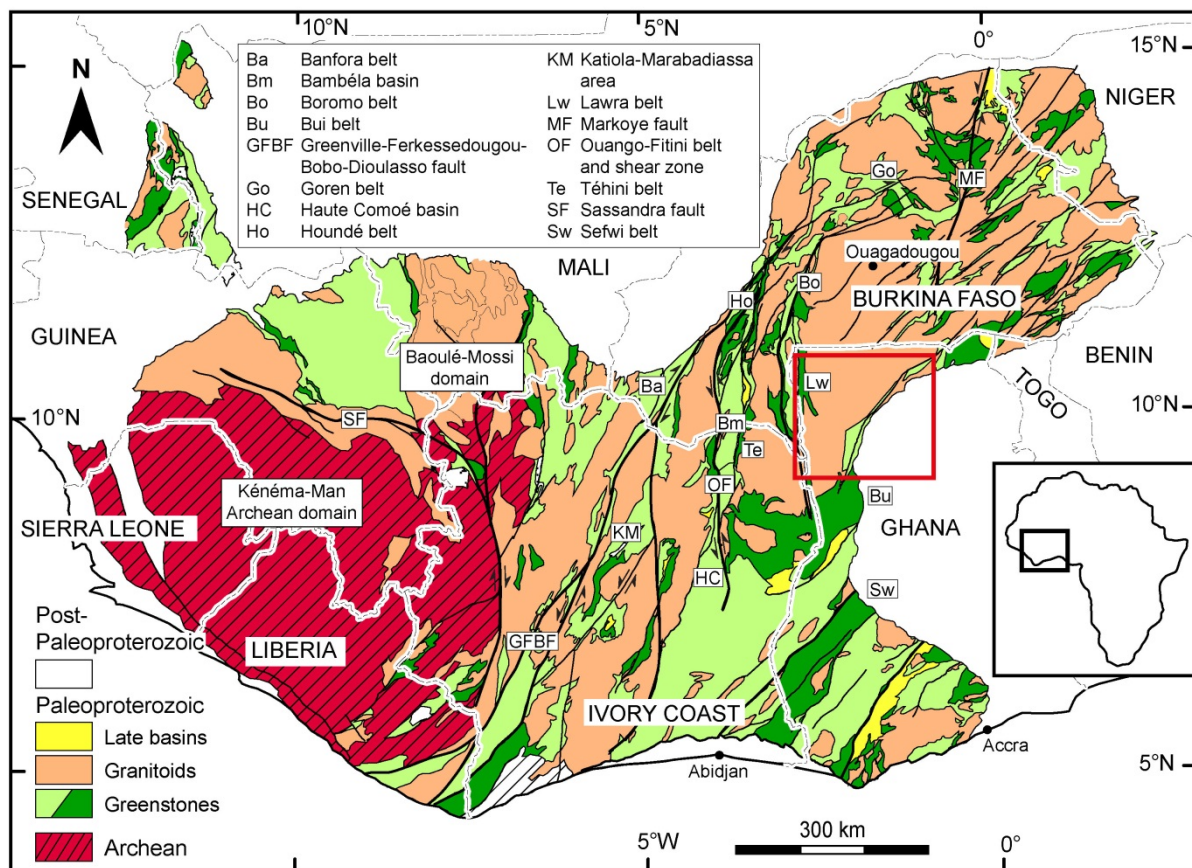


Fig. 2.4. Regional geological map of West African Craton (Milési et al., 2004)

2.3.1 Birimian Architecture in Ghana

The Birimian terrane in Ghana consists of five northeast-southwest trending and one north-south trending greenstone belts with intervening sedimentary basins (Davis et al., 1994). From the south to north, the greenstone belts in Ghana are the Kibi-Winneba, Ashanti, Sefwi, Bui, Bole-Navrongo and Wa-Lawra (Fig. 2.5).

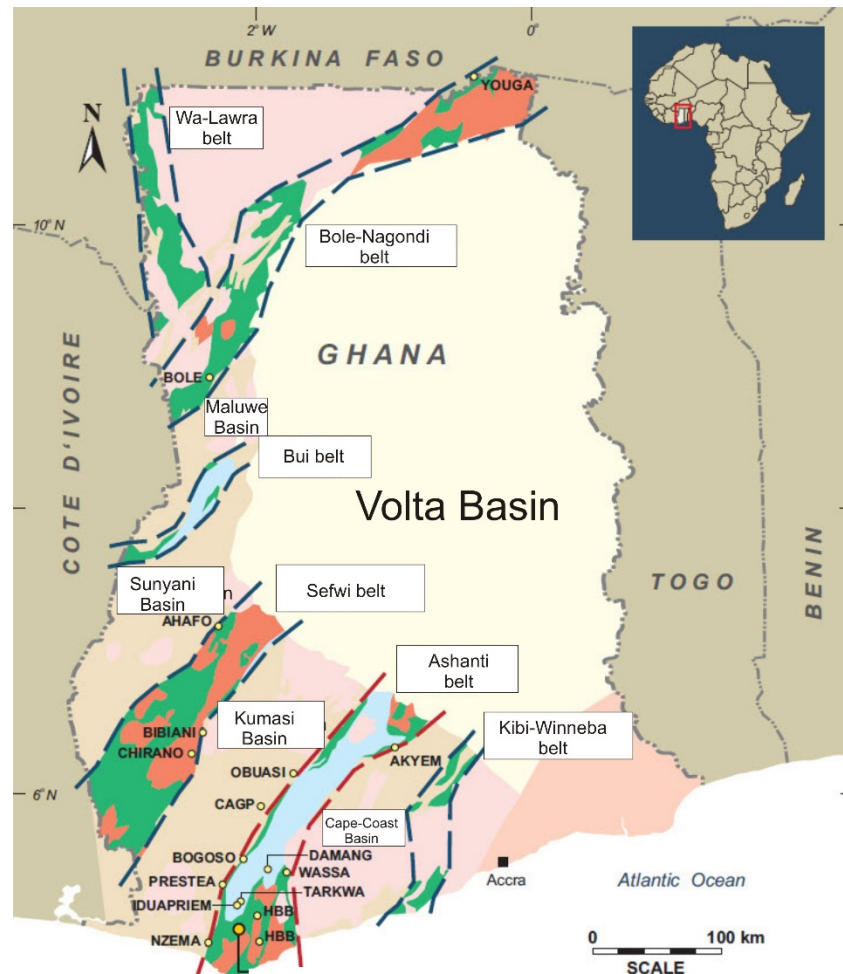


Fig. 2.5. Simplified geological map of Ghana showing the structural architecture of the greenstone belts and intervening basin (Castle Mineral Resources, 2013)

Interpretation of gravity and magnetic data showed north-easterly extension of these greenstone belts below the Neoproterozoic/Palaeozoic Voltaian sediments and in adjoining countries, thus reaching several 100 kilometres in length (Leube et al., 1990; Hastings, 1983). These belts are 15-40 km wide and 60-90 km apart, trend northeast-southwest and decrease in width north-westward across the country (Taylor et al., 1992) with intervening sedimentary basins. These basins and belts have been intruded by various granitoids. Four

types of Paleoproterozoic granitoids suites are present in Ghana (Hirdes et al, 1992) known as the Winneba, Cape Coast, Dixcove and Bongo granitoids (Junner, 1940; Kesse, 1985). The Birimian terrane is highly eroded, therefore giving the terrane a general flat topography (Dickson & Benneh, 1988).

2.3.2 Birimian Sediments and Volcanics

The name Birimian was introduced by Kitson (1928) to describe the Paleoproterozoic rocks in the valley of the Birim River in Ghana. The early research into the stratigraphic designation of the Birimian terrane defined an Upper and Lower Birimian. The Lower Birimian was thought to be made up primarily of sedimentary rocks and the Upper Birimian of volcanic rocks (Kitson, 1928; Junner, 1935, 1940; Hastings, 1982, Kesse, 1985, Milési et al., 1992). The stratigraphy of the Birimian established by early authors was an issue of debate, due to different evidence seen in various countries where the Birimian is exposed. This stratigraphy has undergone considerable review due to the subsequent use of relative dating methods. Leube et al. (1990) suggested contemporaneous age facies equivalence between the metasediments and metavolcanics even though flysh sedimentary sequence underlain by volcanics has been observed (Tigani, 1971, 1972; Vidal & Alric, 1994; Baratoux et al., 2011).

The sediments within the lower Birimian outcropped mainly within the basins. These are the Cape-Coast, Kumasi, Sunyani and the Maluwe Basins (Fig. 2.5). The metasediments are composed of volcanoclastic rocks, turbidity related greywackes, argillitic rocks and chemical sediments whilst the metavolcanics been characterized by tholeiitic and alkaline compositional varieties with the tholeiitic basalt predating the calc alkaline series. Loh (1999) reported ages of 2162 ± 6 Ma and 2266 ± 2 Ma for the metavolcanics.

A range of tectonic models for the Birimian terrane have been proposed by various authors. Abouchami et al. (1990), Boher et al. (1992), Dia et al. (1997), Pouclet et al. (2006) and Lompo (2010) all proposed a Paleoproterozoic juvenile continental crust formed during the Eburnean orogenic event, most probably from oceanic materials in an intraplate ocean plateau. Alternatively intra-cratonic rift to oceanic spreading and accretion related settings have been proposed (Leube et al., 1990). Dia (1988), Sylvester & Attoh (1992), Ama Salah et al. (1996), Lüdtke et al. (1998), Béziat et al. (2000) Condie (2005) and Dampare et al. (2008) also proposed an immature island arc environment built on an oceanic crust due to the slight compositional difference that exists within the volcanics.

2.3.3 Tarkwaian Sediments

Kitson (1928) and Whitelaw (1929) originally identified the Tarkwaian in Ghana. The Tarkwaian is composed of four sedimentary units. The base of the unit is made up of 250-700 m thick Kawere group composed of sandstone and conglomerates. This is overlain by the gold bearing Banket series with an approximate thickness of 600 m. This is made of conglomerated and interbedded sandstone layers. Following the Banket series is the 400 m thick Tarkwa phyllites and subsequently overlaid by the 1300 m Huni Sandstone. Goodwin (1991) proposed the Tarkwaian being deposited in graben structures formed by rifting.

An age of ~2120 Ma defined by detrital zircon reported by various writers suggest that the Tarkwaian was deposited after that age, thereby making it the youngest deposition in the greenstone sequence (Leube et al., 1990; Castaing et al., 2003; Feybesse et al., 2006; Baratoux et al., 2011).

2.3.4 Birimian Terrane Plutonism and metamorphism

The granitoids intruding the Birimian terrane intruded both the greenstone belts and sedimentary basins. Earlier workers group them into basin type for those that intruded the basins and belt type granitoids for those granitoids which intruded the belt (Kesse, 1985; Taylor et al., 1988; Mauer, 1990; Leube et al., 1990; Oberthür et al., 1996). Hirdes et al. (1992) described the belt granitoids as metaluminous, hornblende rich and medium size plutons and have geochemical characteristics similar to tholeiitic basalts whilst the basin granitoids are peraluminous, biotite rich and with no basaltic similarities. With the onset of relative dating two episode of granitoid plutonism has been recognised and described by several authors. The earlier episode occurred within 2205 Ma and 2130 Ma (Boher et al., 1992; Hirdes et al., 1992, Oberthür et al., 1998) during Eburnean I (Allibone et al., 2004) and Eoeburnean (deKock et al., 2011). The second episode of granitoid magmatism occurred within 2116 Ma to 2088 Ma during Eburnean II.

Most of the volcanic and sedimentary suite has experienced metamorphism from the lower to upper greenschist facies (Feybesse et al., 2006; Křibek et al., 2008). Regional amphibolite facies has been reported by John et al. (1999) with regional metamorphic temperature and metamorphic pressure conditions of 500-600 °C and 5-6 kbars. Leube et al. (1990) and Debat et al. (2003) said amphibolite facies occur sporadically but most around the margins of granitoid bodies.

2.3.5 Tectonic Evolution and Eburnean Orogeny

The structural evolution of the Birimian terrane has been described by many workers as polycyclic events (Cozens, 1988; Ledru et al., 1990; Milési et al., 1992; Eisenlohr & Hirdes, 1992; Feybesse et al., 2006).

Ledru et al. (1988), Cozens (1988) and Milési et al. (1992) proposed that there were two major phases of deformation; the Pre-Tarkwaian (D_1) and Post Tarkwaian (D_2). Eisenlohr & Hirdes (1992) also recognised two phases or intensities of deformation. They recognised low strain and high strain phases of deformation. In the low strain phase, the rocks developed northeast-trending subvertical foliation (S_1). This is sub-parallel, or at a small angle, to bedding and contain a subhorizontal intersection lineation (L_1). Rocks belonging to the high strain phase occur predominantly along the north-western margins of the volcanic belts and are characterized by the presence of a penetrative north-eastern trending foliation (S_2) and a south-west plunging stretching lineation.

Feybesse et al. (2006) distinguished three phases of deformation within the Birimian terrane in Ghana. The D_1 deformation was defined by S_1 foliation parallel to the axial plane of microfolds and by an L_1 stretching lineation. Penetrative fabrics developed during this stage vary according to the intensity of metamorphism and the relative proportion of co-axial strain associated with the deformation. Where the evidence of co-axial deformation was pronounced, weak stretching lineations and symmetrical pressure shadows were produced and the bedding was not transposed. The D_2 deformational phase, represents the maximum strain, which is manifested by F_2 folds with horizontal or slightly plunging hinges, associated with a general east-northeast to west-southwest striking S_2 cleavages and north-east to south-west sinistral ductile faults with reverse components. D_3 is defined by folds generally associated with brittle shears, indicating that the crust was already exhumed to higher structural levels.

The Eburnean in Ghana has been grouped into two phases by Allibone et al. (2002), thus the Eburnean I and Eburnean II. Allibone et al. (2002) Eburnean I spans within the periods 2200 Ma to 2150 Ma and is characterized by a phase of magmatism and metamorphism liable for the emplacement of granitoids and metavolcanics in the Sefwi group (Perrouty et al., 2012). Eburnean II (2116 Ma to 2088Ma) is associated to the periods of deformation in the Birimian and Tarkwaian sediments. Feybesse et al. (2006) also described a magmatic accretion periods between 2135 Ma to 2100 Ma and that ended during the development of the Sunyani and Kumasi-Afema basin. deKock et al. (2011) also proposed two phases of the Eburnean evolution in northern Ghana, thus the Eoeburnean and Eburnean. The Eoeburnean occurred between 2160 to 2150 Ma and associated with the emplacement of rocks with volcanic and volcanoclastic origin. His Eburnean was from 2148 to 2090 Ma. It started with the rifting of the Bole-Navrongo crust in 2148 to 2125 Ma to form the Maluwe basin, followed by younger magmatic episodes from 2122 Ma to 2118 Ma. Crustal thickening between 2114 Ma to 2090 Ma was responsible for the hydrothermal alteration and the epidote-amphibolite-grade metamorphism. Broadly, deKock et al. (2011) Eoeburnean and Eburnean defined in the northern Ghana has the same correlation with what has been defined in the south by Allibone et al. (2002).

2.4 Geological setting of the Study area

According to [Block et al. \(2015\)](#), the geology of NW Ghana can be divided into 5 domains, thus the Wa-Lawra belt, the Koudougou-Tumu domain, the Bole-Bulenga domain, the Julie belt and the Bole-Nangodi belt.

The Wa-Lawra belt, the southern extension of the larger Boromo belt in Burkina-Faso ([Amponsah et al. in press](#)) is fault-bounded to the east by the Koudougou-Tumu domain. The Wa-Lawra belt can be divided into two parts (thus the eastern and western parts) by the crustal scale transcurrent (> 200 km) shear zone known as the Jirapa shear zone formed during the Paleoproterozoic period. The eastern part is composed of regionally metamorphosed and deformed sediments such as shales, greywackes, volcanosediments and volcanic rocks ([Block et al., 2015](#), [Amponsah et al. in press](#)) of 2139 ± 2 Ma (dating of detrital zircon using U-Pb dating in the volcanoclastics; [Agyei Duodu et al., 2009](#)) age and early syn-tectonic (2212 ± 1 Ma to 2153 ± 4 Ma; [Sekyi et al., 2014](#); [Agyei Duodu et al., 2009](#)) granitoids. These rocks have been intruded by the late 2104 ± 4 Ma granitoids which remain apparently undeformed. The western half is composed of 2187 ± 3 Ma high grade gneisses and granitoids. The rocks have been metamorphosed up to amphibolite facies.

The east of the Wa-Lawra belt is bounded by the Koudougou-Tumu domain. This domain is just-posed to the Wa-Lawra belt by the Jang fault. The domain is composed of 2162 ± 1 Ma to 2134 Ma gneisses and gabbro which have been intruded by 2128 late porphyritic granites ([Agyei Duodu et al., 2009](#); [Feng et al., in press](#); [Amponsah et al., in press](#)).

South of the Koudougou-Tumu domain is the Julie belt and the Bole-Bulenga domain. The Julie belt is composed to basalts, volcanosediments and TTG's with granodioritic affinities ([Amponsah et al., in press](#)) which have all been metamorphosed to the greenschist facies. Dating by [Block et al. \(2015\)](#) in the volcanoclastics gave an age of 2129 ± 7 Ma.

The Bole-Bulenga domain is composed of high grade paragneisses which have been intruded by orthogneisses with crystallization ages between 2195 Ma and 2135 Ma. Bounded the south of the Bole-Bulenga domain and the Julie belt is the Bole-Nangodi shear zone. The boundary is marked by NE-SW crustal scale shear zones ([Block et al., 2015](#)). The belt is composed of shales, volcanoclastics, granites, gneisses with crystallization ages between 2196 ± 1 Ma and 2118 ± 3 Ma ([Agyei Duodu et al., 2009](#); [de Kock et al., 2011](#)).

2.4.1 Structural and metamorphic framework of NW Ghana

The Birimian terrane in the West African Craton has been characterized by many workers to have a polyphase deformation character and has therefore grouped these phases by their ages of occurrence and field relationships (Milési et al, 1989; Milési et al., 1992; Hirdes et al., 1996; Allibone et al., 2004; Feybesse et al., 2006; Baratoux et al. 2011; Block et al. 2015).

The Koudougou-Tumu orogenic phase corresponds to the Eburnean I as described by Allibone et al. (2002), D₁ by Block et al. (2015), Feybesse et al. (2006), Ledru et al. (1991), Milési et al. (1989). D₁ in NW Ghana is marked by thrust faults forming E-W S₁ foliation fabrics and L₁ stretching lineation. This deformation affected the basalts, volcanosediments and the TTG in the Julie belt and the Koudougou-Tumu terrane. According to Block et al. (2015) the regional S₁ contains mineral assemblages characteristic of the regional metamorphism and therefore also occurred during the 2139 to 2123 Ma tectono-metamorphic evolution. The D₁ event in NW Ghana is marked by amphibolite facies metamorphism retrograde into greenschist facies metamorphism (Block et al., 2015). The amphibolite facies regional metamorphic overprint has pressures not exceeding 11 kbars and temperatures < 600°C, with retrogressing of greenschist facies between 230°C to 350°C and pressures between 1 to 3 kbar with peak metamorphism occurring between 2144 to 2123 Ma. The greenschist facies mineral assemblages are composed of mainly chlorite, calcite and muscovite whilst those of the amphibolite facies are epidote, biotite and quartz.

D₂ in NW Ghana is marked by extensional features as a result of the collapse of some of the crustal thickened nappe (Block et al., 2015). This is marked by N-S down-dip oriented lineation and is also marked by the exhumation of lower crustal materials as observed within the Bulenga area. One of the most persuading arguments for extension in this area is the contrasting metamorphic grades between migmatite and greenschist facies separated by a shear zone.

D₃-D₄ events described by Allibone et al. (2002) and Feybesse et al. (2006) which corresponds to regional D₁ by Baratoux et.al. (2011) took place between 2130-2110 and 2090 to 1980 Ma. The Wa-Lawra (southern portion of the larger Boromo belt) belt has been affected by D₃ regional scale N to NNW trending transcurrent faults or shear zones which affected all the Birimian volcanic and volcano-sedimentary units and structured most of the syn-tectonic intrusion and early magmatic rock which was formed around 2160 Ma (Baratoux et al., 2011). D₃ event is associated with S₃ vertical dipping metamorphic penetrative foliation and parallel to primary bedding. These shear zones are mainly sinistral. Gold mineralization has been reported by Allibone et al. (2002) and Feybesse et al. (2006) to form along these late orogenic shear zones.

D₄ deformation (Block et al., 2015) in NW Ghana which corresponds to regional D₂ of Baratoux et al. (2011) consist of anastomosing steeply dipping NNE to ENE oriented dextral transcurrent S₄ shear zones with shallowly dipping lineations. The majority of the D₄ shear

zones operates under lower greenschist facies conditions. The S₄ shear zones are generally brittle to ductile compared to most of S₃ which is mostly ductile and schistose in nature, suggesting S₄ shear zones operated at lower temperatures with respect to D₃. This deformational event is associated to gold bearing mineralization event.

The regional D₅ (Block et al., 2015) which is regional D₃ of Baratoux et al. (2015) deformational phase is characterized by the development of crenulation cleavages and kink folds. The S₅ space cleavage and kink folds are generally steeply dipping and cross-cut S₃ and S₄ at high angles (Baratoux et al., 2011).

D₆ is characterized late NE-SW steeply dipping faults. These faults are observed in geophysical images. The structural pattern of the D₆ is consistent to the overall N-S compression according to Block et al. (2015). These late faults were described as brittle with a limited extension than then main transcurrent shear zones in D₃. They intersect and offset all the older structures and mark the final manifestation of the deformation (Feybesse et al., 2006).

2.5 Gold deposits in the West African Craton

This subsection summaries the features of gold deposit found within the West African craton, based on their rock type, structure, mineral paragenesis and the ore body geometry. The major gold deposits in the West African craton is mainly restricted to the Paleoproterozoic Birimian and Tarkwaian terranes (Fig. 2.6). A map showing the distribution of this map is below in Figure 2.6.

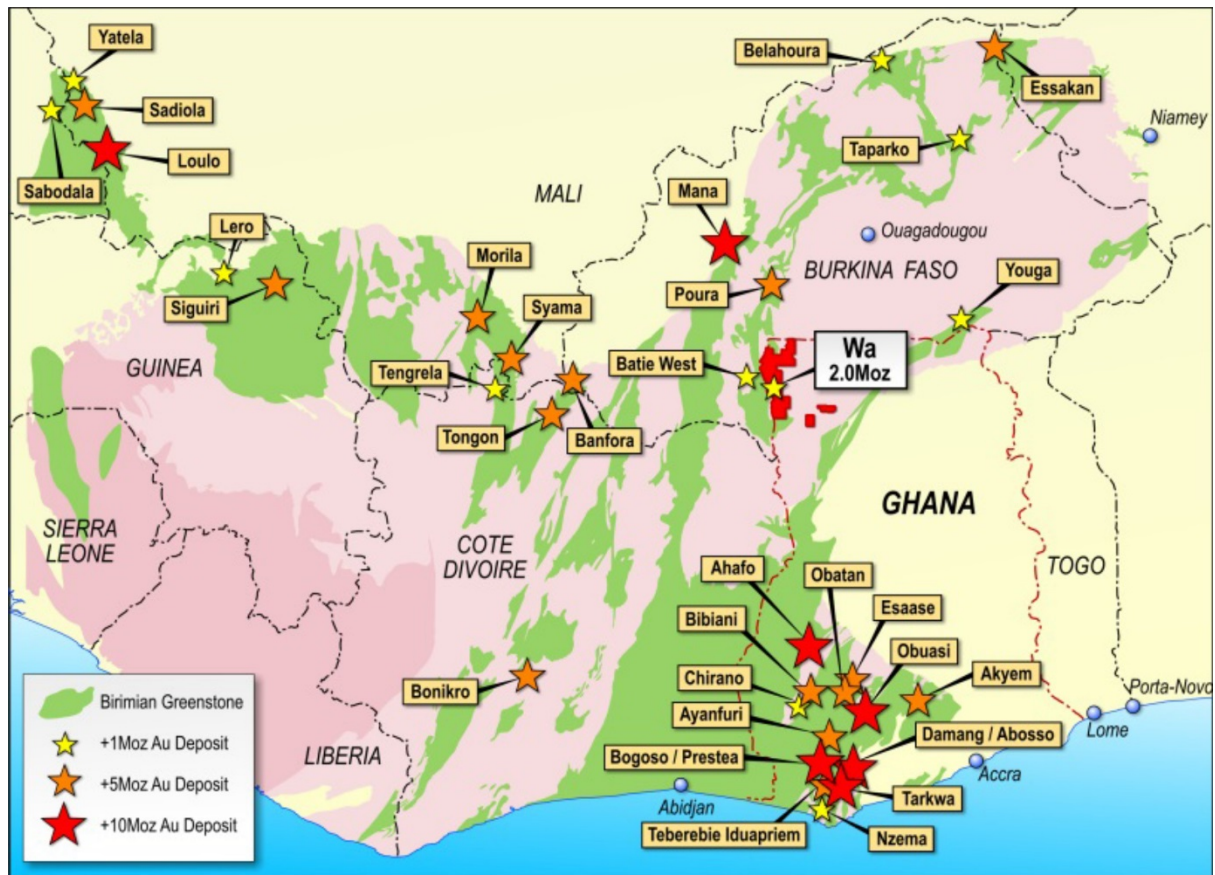


Fig. 2.6. A Map of the Leo-Man shield of the West African craton showing the distribution of gold deposits and mines (modified after Milési et al., 2004). Insert in red is the Wa-Gold project owned by Azumah Resources limited which is the focus of this PhD.

Ghana

There are numerous gold mines or deposits in Ghana but the notable deposits are the Obuasi mines (AngloGold Ashanti limited), The Konongo mines (Owere mines), Wassa mines (Golden star Resources Limited) and the Chirano mines (Kinross), Damang and Tarkwa mines (Goldfields). These are world class deposits that occur in lithologies such as metasediments (volcaniclastics, greywackes, shales and chemical facies, defined by cherts, manganese and carbon-rich sediments), volcanics and intrusive rocks. According to Allibone et al. (2002, 2004), these deposits are found along or within the NE trending faults that defined the regional structural architecture. The gold found in these deposits in Ghana are associated with disseminated gold bearing arsenopyrites mainly within the metasedimentary rocks and in quartz veins and stock works associated with free gold and polymetallic sulphides such as pyrrhotite, pyrite, chalcopyrite, galena. Gold in Ghana is also found in the molasses paleoplacers of the Birimian terrane termed as the Tarkwaian deposits in Ghana. The gold here, is hosted in conglomerate rock. For example in the Iduaprem and Teberebe mines

(AngloGold Ashanti Limited) gold is mined in the Banket series or reefs of the Tarkwaian. Free gold is sometime associated with the iron rich conglomeratic horizons. Also of interest to this PhD is the Wa gold project owned by Azumah resources (Fig. 2.6). This deposit is found on the N-S oriented Wa-Lawra belt and a total resources of about 2.2 million ounces (Moz).

Ivory Coast

Prominent deposits in Ivory Coast are Aniuiri and Asupiri in the Afema gold district, Bonikro (Newcrest Mining Limited) and the Ity deposits (Endeavour mining). The Aniuiri and Asupiri are main associated with metasedimentary rocks, volcanics and felsic intrusives. They are generally found along a NE-SW structural corridor and commonly associated with disseminated gold bearing arsenopyrites and quartz veins and stock works with free gold and polymetallic sulphides (Assie, 2008). The Ity deposit is a saprolitic hosted skarn deposit with gold mineralization found within the regolith profile (Béziat et al., 2015).

Senegal

The main deposit in Senegal is the Sabodala mines (Teranga Gold Coperation). The gold mineralization is associated with metasedimentary (conglomerates, sandstones), volcanic rocks and granites. The gold here is generally associated with quartz veins with polymetallic sulphides, cupo-argentiferous sulphosalts and native gold (Assie, 2008).

Burkina Faso

The notable mines in Burkina are the Poura, Inata (Avocet mining), Kalsaka (Cluff Mining), Essekané mine (IAMGOLD Corporation) and the Mana mines (SEMAFO Inc.). The gold in these deposits are associated with metasediments, volcanics and granitic rocks. The gold here is generally associated with quartz veins with polymetallic sulphides, cupo-argentiferous sulphosalts and native gold (Assie, 2008).

Mali

The notable mines in Mali are the Loulo and Morila (Randgold Resources Limited), Sandiola (AngloGold Ashanti Limited), Yatela (IAMGOLD Corporation) and Syama mines (Resolute Mining limited). The Loulo gold deposit is associated with tourmalinized turbidite formation (sandstones and conglomerates). The highest ore grade is found within the tourmalinized sulphide (pyrrhotite, pyrite, arsenopyrite and gersdorffite) horizons. Syama deposit is associated with mafic tholeiitic, volcanites, lamprophyres and metasediments. Gold is associated with sulphides and visible gold occur as infilled fractures in breccia zones, related to the late E-W compression in the Syama belt. Pyrites and chalcopyrites are abundant with minor pyrrhotite and magnetite.

2.6 References

- Abouchami, W., Boher, M., Michard, A., Albarede, F., 1990. A major 2.1 Ga event of mafic magmatism in West Africa: an early stage of crustal accretion. *Journal of Geophysical Research* 95, 17605–17629.
- Agyei Duodu, J., Loh, G.K., Boamah, K.O., Baba, M., Hirdes, W., Toloczyki, M., Davis, D.W., 2009. Geological map of Ghana 1:1 000 000. Geological Survey Department of Ghana (GSD)
- Allibone, A., Hayden, P., Cameron, G., Duku, F., 2004. Paleoproterozoic gold deposits hosted by albite- and carbonate-altered tonalite in the Chirano District, Ghana, West Africa. *Economic Geology and the Bulletin of the Society* 99, 479–497.
- Allibone, A., Teasdale, J., Cameron, G., Etheridge, M., Uttley, P., Soboh, A., Appiah-Kubi, J., Adanu, A., Arthur, R., Mamphey, J., Odoom, B., Zuta, J., Tsikata, A., Pataye, F., Famiyeh, S., Lamb, E., 2002. Timing and structural controls on gold mineralization at the Bogoso Gold Mine, Ghana, West Africa. *Economic Geology* 97, 949–969.
- Ama Salah, L., Liegeois, J.-P., Pouclet, A., 1996. Evolution d'un arc insulaire oceanique birimien precoce au Liptako nigerien (Sirba): geologie, geochronologie et geochemie. *Journal of African Earth Sciences* 22, 235–254.
- Amponsah, P. O., Salvi, S., Béziat, D., Jessell, M., Siebenaller, L., Baratoux, L., 2015. Geology and geochemistry of shear hosted Julie gold deposit, NW Ghana. *Journal of African Earth Science* (In press). <http://dx.doi.org/10.1016/j.jafrearsci.2015.06.013>
- Amponsah, P.O., Salvi, S., Beziat, D., Baratoux, L., Siebenaller, L., Nude, P.M., Nyarko, R.S., Jessell, M.W., in press. The Bepkong deposit, Northwestern Ghana. *Ore Geology Reviews*. <http://dx.doi.org/10.1016/j.oregeorev.2015.06.022>
- Assie, K.E., 2008. Lode gold mineralization in the Paleoproterozoic (Birimian) volcanosedimentary sequence of the Afema gold district, southeastern Cote d'Ivoire. PhD thesis dissertation). Technical University of Clausthal (unpublished)
- Attoh, K., Ekwueme, B., 1997. The West African shield. In: De Wit, M.J., Ashwall, L.D. (Eds.), *Greenstone Belts*. Oxford University Press, 517–528.
- Baratoux, L., Metelka, V., Naba, S., Jessell, M.W., Grégoire, M., Ganne, J., 2011. Juvenile Paleoproterozoic crust evolution during the Eburnean orogeny (2.2–2.0Ga), Western Burkina Faso. *Precambrian Research* 191, 18–45.

Bassot, J.P., 1966. Etude géologique du Sénégal oriental et de ses confins guinéo-maliens. Mem. Bur. Rech. Geol. Min, Paris, 40, 322

Bessoles, B., 1977. Geologie de l'Afrique. Le craton Ouest-Africain, Memoires BRGM, Paris, 88.

Béziat, D., Bourges, F., Debat, P., Lompo, M., Martin, F., Tollon, F., 2000. A Palaeoproterozoic ultramafic-mafic assemblage and associated volcanic rocks of the Boromo greenstone belt: fractionates originating from island-arc volcanic activity in the West African craton. *Precambrian Research* 101, 25–47.

Béziat, D., Bourges, F., Debat, P., Lompo, M., Martin, F., Tollon, F., 2000. A Palaeoproterozoic ultramafic-mafic assemblage and associated volcanic rocks of the Boromo greenstone belt: fractionates originating from island-arc volcanic activity in the West African craton. *Precambrian Research* 101, 25–47.

Black R., Liégeois J. P., 1993. Cratons, mobile belts, alkaline rocks and continental lithospheric mantle: the Pan-African testimony. *Journal of the Geological Society*, London 150, 89–98.

Block, S., Baratoux, L., Jessell, M., Ailleres, L., Bruguier, O., Zeh, A., Bosch, D., Caby, R., Ganne, J., Mensah E., (2015). Lower crust exhumation during Paleoproterozoic (Eburnean) orogeny, NW Ghana, West African Craton: interplay of coeval contractional deformation and extensional gravitational collapse. *Precambrian Research*.

Block, S, 2015. Evolution geodynamique du craton Ouest Africain au nord du Ghana. PhD thesis, University of Toulouse III (unpublished)

Boher, M., Michard, A., Albarede, F., Rossi, M., Milesi, J.P., 1992. Crustal growth in West Africa at ca 2.1 Ga. *Journal of Geophysical Research* 97, 345–369.

Bonhomme, M., 1962. Contribution à l'étude géochronologique de la plate-forme de l'Ouest africain. Thesis, Ann. Fac. Sci. Univ. Clermont-Ferrand, Geol. Mineral. 5, 62.

Cahen, L., Snelling, N.J., Delhal, J. and Vail, J.R. (1984). *The Geochronology and Evolution of Africa*. Oxford University Press, New York

Castaing, C., Billa, M., Milesi, J.P., Thieblemont, D., Le Mentour, J., Egal, E., Donzeau, M., Guerrot, C., Cocherie, A., Chevremont, P., Tegye, M., Itard, Y., Zida, B., Ouedraogo, I., Kote, S., Kabore, B.E., Ouedraogo, C., Ki, J.C., Zunino, C., 2003. Notice explicative de la carte géologique et minière du Burkina Faso à 1/1 000 000. BRGM, BUMIGEB, 147.

- Clifford, T.N., 1970. The structural framework of Africa. In T.N. Clifford and I.G. Gas (eds) *African magmatism and tectonic*, Oliver and Boyd Edinburgh, 1-26
- Condie, K.C. 2005. High field strength element ratios in Archean basalts - a window to evolving sources of mantle plumes? *Lithos*, 79, 491-504
- Cozens, B., 1988. On the structure of the Konongo gold mines, the structural fabric of Ghana and their implication in gold exploration. Abstract, International Conference on the Geology of Ghana with special emphasis on Gold Comm. 75th Anniversary of the Geological Survey Department Accra.
- Culver, S.J., William, H.R., 1979. The late Precambrian and Phanerozoic geology of Sierra Leone. *Journal of Geological Society of London*, 136, 605-618
- Dampare, S.B., Shibata, T., Asiedu, D.K., Osae, S., Banoeng-Yakubo, B., 2008. Geochemistry of Paleoproterozoic metavolcanic rocks from the southern Ashanti volcanic belt, Ghana: Petrogenetic and tectonic setting implications. *Precambrian Research* 162, 403-423.
- Davis, D.W., Hirdes, W., Schaltegger, U., Nunoo, E.A., 1994. U-Pb age constraints on deposition and provenance of Birimian and gold-bearing Tarkwaian sediments in Ghana, West Africa. *Precambrian Research* 67, 89-107.
- de Kock, G.S., Armstrong, R.A., Siegfried, H.P., Thomas, E., 2011. Geochronology of the Birim Supergroup of the West African craton in the Wa-Bole region of westcentral Ghana: implications for the stratigraphic framework. *Journal of African Earth Sciences* 59, 1-40
- Debat, P., Nikiema, S., Mercier, A., Lompo, M., Beziat, D., Bourges, F., Roddaz, M., Salvi, S., Tollon, F., Wenmenga, U., 2003. A new metamorphic constraint for the Eburnean orogeny from Paleoproterozoic formations of the Mansfield (Aribinda and Tampilga countries, Burkina Faso). *Precambrian Research* 123, 47-65.
- Dia, A., 1988. Caracteres et significations des complexes magmatiques et metamorphiques du secteur de Sandikounda-Laminia (Nord de la boutonniere de Keidougou, Est Senegal). Un modele geodynamique du Birimien de l'Afrique de l'Ouest. UCAD, Dakar.
- Dia, A., Van Schmus, W.R., Kroner, A., 1997. Isotopic constraints on the age and formation of a Palaeoproterozoic volcanic arc complex in the Kedougou Inlier, eastern Senegal, West Africa. *Journal of African Earth Sciences* 24, 197-213.
- Dickson, K.B., Benneh, G., 1988. *A New Geography of Ghana*. Longman Group Limited. 1-177.

Eisenlohr, B. N., Hirdes, W., 1992. The structural development of the early Proterozoic Birimian and Tarkwaian rocks of southwest Ghana, West Africa. *Journal of Earth Sciences* 14, 313-325.

Eisenlohr, B. N., Hirdes, W., 1992. The structural development of the early Proterozoic Birimian and Tarkwaian rocks of southwest Ghana, West Africa. *Journal of Earth Science*, 14, 3, 313-325

Ennih, N., Liegeois, J-P, 2008. The boundaries of the West African Craton, with special reference to the basement of the Moroccan metacratonic Anti-Atlas belt. *The Geological Society of London*, 297, 1-17

Feng, X., Amponsah, P. O., Martin, R., Ganne, J., Jessell, M.W., 2015. 3-D numerical modelling of the influence of pre-existing faults and boundary conditions on the distribution of deformation: example of North-Western Ghana. *Precambrian Research* (in press). <http://dx.doi.org/10.1016/j.precamres.2015.06.006>

Feybesse, J.-L., Billa M., Guerrot C., Duguey E., Lescuyer, J., Milési, J.P., Bouchot., 2006. The Paleoproterozoic Ghanaian province: Geodynamic model and ore controls, including regional stress modeling. *Precambrian Research* 149, 149-196.

Feybesse, J.L., Milesi, J.P., 1994. The Archaean/Proterozoic contact zone in West Africa: a mountain belt of decollement thrusting and folding on a continental margin related to 2.1 Ga convergence of Archaean cratons? *Precambrian Research* 69, 199–227.

Goodwin, A., 1996. *Principles of Precambrian Geology*. Academic Press,

Hasting, D. A., 1982. On the tectonics and metallogensis of West Africa: a model incorporating new geophysical data. *Geoexploration*, 20, 295-327.

Hirdes, W., Davis, D.W., Eisenlohr, B.N., 1992. Reassessment of Proterozoic granitoid ages in Ghana on the basis of U/Pb zircon and monazite dating. *Precambrian Research* 56, 89–96.

Jessell, M.W., Amponsah, P.O., Baratoux, L., Asiedu, D.K., Loh, G., Ganne, J., 2012. Crustal- scale transcurrent shearing in the Paleoproterozoic Sefwi-Sunyani-Comoe region, West Africa. *Precambrian Research* 212-213, 155- 168.

John, T., Klemd, R., Hirdes, W., Loh, G., 1999. The metamorphic evolution of the Paleoproterozoic (Birimian) volcanic Ashanti belt (Ghana West Africa). *Precambrian Research* 98, 11–30.

Junner, N.R., 1935. *Gold in the Gold Coast*. Gold Coast Geological Survey Memoir 4, 1–67.

Junner, N.R., 1940. Geology of the Gold Coast and western Togoland (with revised geological map). Gold Coast Geological Survey Bulletin 11, 1–40.

Kalsbeek, F., Frei, R., 2010. Geochemistry of the Precambrian sedimentary rocks used to solve stratigraphical problems: An example from the Neoproterozoic Volta Basin, Ghana. *Precambrian Research*, 176, 65–76

Kesse, G., 1985. The mineral and rocks resources of Ghana. A.A. Balkema, Rotterdam, Boston, 609.

Kesse, G., 1985. The mineral and rocks resources of Ghana. A.A. Balkema, Rotterdam, Boston, p. 609.

Key, R.M., Loughlin, S.C., Horstwood, M.S.A., Gillespie, P.J.E, Henrey, P.J., Crowley, Q.G., Del Rio, M., Darbyshire, D.P.F., 2008. Two Mesoarchean terrane in the Reguibat shield of NW Mauritania. *Geological society*, 1–23.

Kitson, A.E., 1918. Annual Report. Gold Coast Geological Survey for 1916/17, Accra. (Not published), Accra.

Křibek, B., Sykorova, I., Machovič, V., Laufek, F., 2008. Graphitization of organic matter and fluid-deposited graphite in Paleoproterozoic (Birimian) black shales of the Kaya-Goren greenstone belt (Burkina Faso, West Africa). *Journal of Metamorphic Geology* 26, 937–958.

Ledru, P., Milési, J. P., Vinchon, C., Ankrah, P.T., Johan, V and Marcoux, E., 1988. Geology of the Birimian Series of Ghana. Abstr., International Conference and workshop on the Geology of Ghana and Exploration in Ghana and in selected other Precambrian terrians. 75th Anniversary, Ghana Geological Survey Department. Accra, 26–27.

Leube, A., Hirdes, W., Mauer, R., Kesse, G.O., 1990. The early Proterozoic Birimian Supergroup of Ghana and some aspects of its associated gold mineralization. *Precambrian Research* 46, 139–165.

Liegeois, J.P., Claessens, W., Camara, D., Klerkx, J., 1991. Short-lived Eburnian orogeny in southern Mali. Geology, tectonics, U–Pb and Rb–Sr geochronology. *Precambrian Research* 50, 111–136.

Lompo, M., 2010. Paleoproterozoic structural evolution of the Man-Leo Shield (West Africa). Key structures for vertical to transcurrent tectonics. *Journal of African Earth Sciences* 58, 19–36.

- Lüdtke, G., Hirdes, W., Konan, G., Kone, Y., Yao, C., Diarra, S., Zamble, Z., 1998. Geologie de la region Haute Comoe Nord—feuilles Kong (4b et 4d) et Tehini-Bouna (3a á 3d), Direction de la Geologie Abidjan Bulletin, 178.
- Milési, J.P., Feybesse, J.L., Pinna, P., Deschamps, Y., Kampunzu, H., Muhongo, S., Lescuyer, J.L., Le Goff, E., Delor, C., Billa, M., Ralay, F., Henry, C., 2004. Geological map of Africa 1:10,000,000, SIGAfrique project. In: 20th Conference of African Geology, BRGM, Orleans, France, 2–7 June, <http://www.sigafrique.net> (last accessed 14/12/2010).
- Milesi, J.-P., Feybesse, J.L., Ledru, P., Dommagnet, A., Ouedraogo, M.F., Marcoux, E., Prost, A., Vinchon, C., Sylvain, J.P., Johan, V., Tegye, M., Clavez, J.Y., Lagny, Ph., 1989. Mineralisations auriferes de l’Afrique de l’ouest, leurs relations avec l’evolution litho-structurale au Paleoproterozoïque inférier. *Chron. Rech. Min.* 497, 3–98.
- Milési, J.-P., Ledru, P., Feybesse, J.-L., Dommagnet, A., Marcoux, E., 1992. Early Proterozoic ore deposits and tectonics of the Birimian Orogenic belt, West Africa. *Precambrian Research*, 58, 305–344.
- Oberthur, T., Schmidt Mumm, A., Vetter, U., Simon, K., Amanor, J.A., 1996. Gold mineralization in the Ashanti Belt of Ghana. Genetic constraints of the stable isotope geochemistry. *Economic Geology* 91, 289–301.
- Oberthür, T., Vetter, U., Davis, D. W., Amanor, J.A., 1998. Age constrains on gold mineralization and Paleoproterozoic crustal evolution in the Ashanti belt of Southern Ghana. *Precambrian Research* 89, 129–143.
- Perrouy, S., Ailleres, L., Jessell, M.W., Baratoux, L. Bourassa, Y., Crawford, B., 2012. Revised Eburnean geodynamic evolution of the gold-rich southern Ashanti Belt, Ghana, with new field and geophysical evidence of the pre-Tarkwaian deformations. *Precambrian Research* 204–205, 12–39.
- Perrouy, S., Ailleres, L., Jessell, M.W., Baratoux, L. Bourassa, Y., Crawford, B., 2012. Revised Eburnean geodynamic evolution of the gold-rich southern Ashanti Belt, Ghana, with new field and geophysical evidence of the pre-Tarkwaian deformations. *Precambrian Research* 204–205, 12–39.
- Potrel A., Peucat J. J., Fanning C. M., 1998. Archean crustal evolution of the West African craton: example of the Amsaga area (Reguibat Rise). U–Pb and Sm–Nd evidence for crustal growth and recycling. *Precambrian Research* 90:107–117.
- Pouclet, A., Vidal, M., Delor, C., Simeon, Y., Alric, G., 1996. Le volcanisme birimien du nord-est de la Cote-d’Ivoire, mise en evidence de deux phases volcano-tectoniques distinctes dans l’evolution geodynamique du Paleoproterozoique. *Le Bulletin de la Societe geologique de France* 167, 529–541.

Sakyi, P.A., Su, B.X., Anum, S., Kwayisi, D., Dampare, S.B., Anani, C.Y., Nude, P.M., 2014. New zircon U–Pb ages for erratic emplacement of 2213–2130 Ma Paleoproterozoic calc-alkaline I-type granitoid rocks in the Lawra Volcanic Belt of Northwestern Ghana, West Africa. *Precambrian Res.* 254, 149–168.

Sylvester, P.J., Attoh, K., 1992. Lithostratigraphy and composition of 2.1 Ga. Greenstone belts of West Africa craton and their bearing on crustal evolution and the Archean-Proterozoic boundary. *Journal of Geology.* 100, 377–393.

Tagini, B., 1971. Esquisse structurale de la Cote d’Ivoire. In: *Essai de geotectonique regionale.* Universite Lausanne, 302.

Tagini, B., 1972. Carte Geologique de la Cote d’Ivoire 1:2,000,000. SODEMI.

Thorman, C.H., 1976. Implication of the klippen and a new sedimentary unit at the Gibi Mountain, Liberia, West Africa, in the problem of the Pan-african-Liberian age province boundary. *Geological society of American Bulletin,* 87, 851–856

Trompette, R., 1973. Le Précambrien supérieur et le Paléozoïque inférieur de l’Adrar de Mauritanie (bordure occidentale du bassin de Taoudeni, Afrique de l’Ouest). Un exemple de sédimentation de craton. *Etude stratigraphique et sédimentologique.* Trav. Lab. Sci. Terre, St Jerome, Marseille, 7, 702.

Vidal, M., Alric, G., 1994. The Palaeoproterozoic (Birimian) of Haute-Comoe in the West African craton Ivory Coast: a transtensional back-arc basin. *Precambrian Research* 65, 207–229.

Vidal, M., Delor, C., Pouclet, A., Simeon, Y., Alric, G., 1996. Evolution géodynamique de l’Afrique de l’Ouest entre 2, 2 Ga et 2 Ga; le style “archéen” des ceintures vertes et des ensembles sédimentaires birimiens du nord-est de la Cote-d’Ivoire. *Bulletin de la Societe Geologique de France* 167, 307–319.

Vidal, M., Gumiaux, C., Cagnard, F., Pouclet, A., Ouattara, G., Pichon, M., 2009. Evolution of a Paleoproterozoic “weak type” orogeny in the West African Craton (Ivory Coast). *Tectonophysics* 477, 145–159.

Villeneuve, M., Cornée, J.J., 1994. Structure, evolution and paleogeography of the West African craton and the bordering belts during the Neoproterozoic. *Precambrian Research,* 69, 307–326

Villeneuve, M., Dallmeyer, R.D., 1987. $^{40}\text{Ar}/^{39}\text{Ar}$ polyorogenic mineral age record of the Polyphase tectonothermal evolution in the Southern Mauritanide orogen, southeastern Senegal. *Geological Society of America Bulletin,* 98, 602–611

Whitelaw, O.A.L., 1929. The geological and mining features of the Tarkwa-Abosso Goldfield. Gold Coast Geological Survey: Memoir 1, 1-45.

Yacé, I. 1984. Le Précambrien de l'Afrique de l'Ouest et ses corrélations avec le Brésil oriental. Centre International pour la formation et les Echanges Géologiques (CIFEG), Paris, Rapport final du projet PICG 108-144, publication occasionnelle, no 2, 2

Chapter 3

The Julie Deposit

Introduction

The Julie deposit is situated in NW Ghana, within the Julie belt and it is a rare occurrence of granitoid-hosted gold deposit found in that region. The deposit has an average grade of 2.0 gram per tonne (g/t) with a tonnage of 2.21 million tonnes (Mt). As at 2014, the proven reserve was 202,000 Moz (Salvi et al. in press). This chapter describes the geology and geochemistry of the deposit.

The geology and geochemical characteristics of the Julie deposit described in this chapter has been published and is in press with the Journal of African Earth Science with a digital object identifier (DOI) as <http://dx.doi.org/10.1016/j.jafrearsci.2015.06.013>, titled '*Geology and geochemistry of the shear-hosted Julie gold deposit NW, Ghana*' and is part of the West African special issue for the West Africa Exploration initiative (WAXI). The publication presents the structural, geochemical, sulphide crystallography, fluid inclusion data, and provides an insight on the timing of gold occurrence in the area. The deposit is also compared with deposits found in southern Ghana to see if there is any resemblance or contrast.

A second publication (which is in subsection 3.3), is summary of geological information, exploration history, as well as an overview of the geology and ore mineralogy, highlighting how the gold relates to sulphides was submitted and published in Ore Geological Reviews (OGR) as part of the Mineral Atlas monograph (MAM) with a DOI of <http://dx.doi.org/10.1016/j.oregeorev.2015.08.008> with the title '*Shear related gold mineralization in Northwest Ghana: The Julie deposit*'. The MAM is first compendium of mineral deposits in West Africa. It presents basic information about deposit and deposit styles of West Africa. The Mineral Atlas monograph will become a basic tool for many university students and as a basic start reference for exploration companies.

3. 1 Geology and geochemistry of the shear-hosted Julie gold deposit, NW Ghana

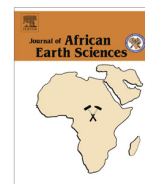
The Leo Man Craton in West Africa is host to numerous economic gold deposits. In some regions, such as the SW of Ghana, are well known for world-class mineralizations and have been extensively studied, gold occurrences elsewhere in the craton have been discovered only in the last half a century or so, and very little is known about them. The Julie gold deposit, located in the Paleoproterozoic Birimian terrane of NW Ghana, is one such case. This deposit is hosted in a series of granitoid intrusives of TTG composition, and consists of a network of deformed, boudinaged quartz lodes (A-type veins) contained within an early D₁ E–W trending shear zone with dextral characteristics. A conjugate set of veins (C-type) perpendicular to the A-type veins contains low grade mineralization. The main ore zone defines a lenticular corridor about 20–50 m in width and about 3.5 km along strike, trending E–W and dipping between 30 and 60°N. The corridor is strongly altered, by an assemblage of sericite + quartz + ankerite + calcite + tourmaline + pyrite. This is surrounded by a second alteration assemblage, consisting of albite + sericite + calcite + chlorite + pyrite + rutile, which marks a lateral alteration that fades into the unaltered rock. Mass balance calculations show that during alteration overall mass was conserved and elemental transfer is generally consistent with sulfidation, sericitization and carbonatization of the host TTG.

Gold is closely associated with pyrite, which occurs as disseminated grains in the veins and in the host rock, within the mineralized corridor. SEM imagery and LA-ICP-MS analyses of pyrites indicate that in A-type veins gold is associated with bismuth, tellurium, lead and silver, while in C-type veins it is mostly associated with silver. Pyrites in A-type veins contain gold as inclusions and as free gold on its edges and fractures, while pyrites from C-type veins contains mostly free gold. Primary and pseudosecondary fluid inclusions from both type veins indicate circulation in the system of an aqueous-carbonic fluid of low to moderate salinity, which entered the immiscibility PT region of the H₂O–CO₂–NaCl system, at about 220 °C and <1 kbar.



Contents lists available at ScienceDirect

Journal of African Earth Sciences

journal homepage: www.elsevier.com/locate/jafrearsci

Geology and geochemistry of the shear-hosted Julie gold deposit, NW Ghana

Prince Ofori Amponsah^{a,b}, Stefano Salvi^{a,*}, Didier Béziat^a, Luc Siebenaller^{a,c}, Lenka Baratoux^{a,d}, Mark W. Jessell^e

^a Université de Toulouse, CNRS, Géosciences Environnement Toulouse, Institut de Recherche pour le Développement, Observatoire Midi-Pyrénées, 14 Av. Edouard Belin, F-31400 Toulouse, France

^b Azumah Resources Ghana limited, PMB CT452, Cantonments, Accra, Ghana

^c ONG-D "Le Soleil dans la Main" asbl, 48, Duerfstrooss, L-9696 Winseler, Luxembourg

^d IFAN Cheikh Anta Diop, Dakar, Senegal

^e Centre for Exploration Targeting, School of Earth and Environment, The University of Western Australia, 35 Stirling Highway, Crawley, WA 6009, Australia

ARTICLE INFO

Article history:

Received 16 February 2015

Received in revised form 19 June 2015

Accepted 22 June 2015

Available online xxx

Keywords:

Birimian

NW Ghana

Gold mineralization

Alteration

ABSTRACT

The Leo Man Craton in West Africa is host to numerous economic gold deposits. If some regions, such as the SW of Ghana, are well known for world-class mineralizations and have been extensively studied, gold occurrences elsewhere in the craton have been discovered only in the last half a century or so, and very little is known about them. The Julie gold deposit, located in the Paleoproterozoic Birimian terrane of NW Ghana, is one such case. This deposit is hosted in a series of granitoid intrusives of TTG composition, and consists of a network of deformed, boudinaged quartz lodes (A-type veins) contained within an early D_{J1} E–W trending shear zone with dextral characteristics. A conjugate set of veins (C-type) perpendicular to the A-type veins contains low grade mineralization. The main ore zone defines a lenticular corridor about 20–50 m in width and about 3.5 km along strike, trending E–W and dipping between 30 and 60°N. The corridor is strongly altered, by an assemblage of sericite + quartz + ankerite + calcite + tourmaline + pyrite. This is surrounded by a second alteration assemblage, consisting of albite + sericite + calcite + chlorite + pyrite + rutile, which marks a lateral alteration that fades into the unaltered rock. Mass balance calculations show that during alteration overall mass was conserved and elemental transfer is generally consistent with sulfidation, sericitization and carbonatization of the host TTG.

Gold is closely associated with pyrite, which occurs as disseminated grains in the veins and in the host rock, within the mineralized corridor. SEM imagery and LA-ICP-MS analyses of pyrites indicate that in A-type veins gold is associated with bismuth, tellurium, lead and silver, while in C-type veins it is mostly associated with silver. Pyrites in A-type veins contain gold as inclusions and as free gold on its edges and fractures, while pyrites from C-type veins contains mostly free gold. Primary and pseudosecondary fluid inclusions from both type veins indicate circulation in the system of an aqueous-carbonic fluid of low to moderate salinity, which entered the immiscibility PT region of the H₂O–CO₂–NaCl system, at about 220 °C and <1 kbar.

© 2015 Elsevier Ltd. All rights reserved.

1. Introduction

The Birimian terrains in southern Ghana (particularly the Ashanti and Sefwi belts) have been the focus of commercial gold exploration and exploitation since the early 1900s. Due to the commercial implications of gold, extensive geological studies have been completed on these belts by many workers including Junner (1932, 1935, 1940), Kesse (1985), Milési et al. (1989,

1992), Eisenlohr and Hirdes (1992), Blenkinsop et al. (1994), Mücke and Dzigbodi-Adjimah (1994), Hünken et al. (1994), Oberthür et al. (1994, 1996, 1997, 1998), Mumin and Fleet (1995), Hammond and Tabata (1997), Klemm et al. (1996), Barritt and Kuma (1998), Yao and Robb (2000), Perrouty et al. (2012). Gold mineralization in southern Ghana is associated with a wide range of metamorphosed rocks. According to Leube et al. (1990) and Taylor et al. (1992), the gold mineralization usually occurs in chemical facies, defined by cherts, manganese and carbon-rich sediments, Fe–Ca–Mg carbonates where sulfide mineral disseminations intermittently developed at the transition between volcanic

* Corresponding author.

E-mail address: stefano.salvi@get.obs-mip.fr (S. Salvi).

<http://dx.doi.org/10.1016/j.jafrearsci.2015.06.013>

1464-343X/© 2015 Elsevier Ltd. All rights reserved.

belts and metasedimentary basins. The gold deposits west of the Ashanti Mine on the Ashanti belt are hosted by granodiorite and tonalite that intrude the metasediments (Allibone et al., 2002). Allibone et al. (2004) showed that most of the gold mineralization in southern Ghana occurs within and adjacent to northwest trending thrust faults that define the regional-scale structural architecture. Gold-ore forming fluids in southern Ghana are usually CO₂ dominated as indicated by the presence of abundant CO₂-N₂ ± CH₄ fluid inclusions associated locally to H₂O-CO₂-NaCl and H₂O-NaCl fluid inclusions (Schwartz et al., 1992; Klemm et al., 1993, 1996; Oberthür et al., 1994; Schmidt-Mumm et al., 1997; Yao et al., 2001).

Discovery of gold in the Birimian of NW Ghana, on the other hand, is much more recent. Here, alluvial and bedrock indications of gold were recognized during the early 1960s when the Gold Coast Geological Survey (Griffis et al., 2002) together with a Russian geological team carried out prospecting and mapping in the area, and outlined prospects in the Wa-Lawra greenstone belt and adjacent Koudougou-Tumu domain and the Julie belt. During further exploration for gold in 2006 and beyond, Azumah Resources Limited discovered 834,000 Oz of measured and indicated gold at 1.53 g/t with a reserve of 202,000 Oz at 2.84 g/t in the Julie deposit, in the Julie belt. To date, there has been no published data on the geology, alteration geochemistry along with the ore forming fluids and process associated with gold mineralization in the Julie deposit, nor on other deposits in NW Ghana.

The objective of this paper is to describe the geology and alteration geochemistry of the Julie deposit and to investigate the conditions of mineralization, in order to understand the mode of formation of the gold mineralization in the Julie deposit. These results are discussed and compared with those of previous studies from other deposits in Southern Ghana.

2. Regional geological setting

The Julie deposit is one of the numerous gold camps in the Wa-East district. This district is located within the Upper West region of Ghana, which lies on the eastern edge of the Paleoproterozoic Birimian terrane of the West African Craton (WAC) (Fig. 1).

This district formed during the 2250–1980 Ma Eburnean tectono-magmatic process that formed the greenstone belts and associated granitoids in the Birimian or Baoule-Mossi domain of the WAC (Feybesse et al., 2006). The Wa-East gold district occurs within the Julie Belt, which is bounded to the north by the Koudougou-Tumu granitoid domain, to the south by the Bole-Bulenga terrane, to the west by the N–S striking Wa-Lawra belt, and to the east by the Bole-Nangodi shear zone (Block et al., in press) (Fig. 2).

The Koudougou-Tumu domain is dominantly composed of 2156 ± 1–2134 ± 1 Ma old (U–Pb zircon ages; Agyei Duodu et al., 2009) tonalite–trondhjemite–granodiorite (TTG) intrusions, often present as orthogneisses, with some gabbroic intrusions. These rocks have been intruded by the 2128 ± 1 Ma and 2086 ± 4 Ma late pulse potassic porphyritic granites (U–Pb zircon ages; Taylor et al., 1992; Agyei Duodu et al., 2009). At the contact with the Koudougou-Tumu granitoid domain, the Julie belt is composed of basalts, gabbros and volcano-sediments.

The boundary between the Wa-Lawra belt (southern extent of the Boromo belt) and the Koudougou-Tumu granitoid domain (Fig. 2) is marked by the Jirapa fault and extends into the Boromo belt in Burkina Faso to the north. The Jirapa fault exhibits sinistral characteristics. The Wa-Lawra belt is predominantly composed of shales, greywackes, volcano-sediments, basalts and granitoids. Detrital zircon U–Pb dating of the volcanosediments in the Wa-Lawra belt gave ages older than 2139 ± 2 Ma (Agyei Duodu

et al., 2009), which indicates that these volcano-sediments are probably older than some of the plutonic rocks in the Koudougou-Tumu domain. These volcano-sedimentary rocks have been intruded by granitoids with ages between 2124 ± 2 Ma and 2104 ± 1 Ma (U–Pb zircon ages; Agyei Duodu et al., 2009). South of the Julie belt, the Bole-Bulenga domain is composed of high grade metamorphic rocks termed as Buki gneisses composed mostly of metagreywackes (de Kock et al., 2011). These rocks have been intruded by tonalite–trondhjemite–granodiorite (TTG) plutons usually exhibiting migmatitic texture and structures, which in turn have been cross-cut by the Bole-Nangodi NE shear zone.

3. Structure and metamorphic framework

The Birimian terrane in Ghana has been interpreted by Baratoux et al. (2011), Allibone et al. (2002), Feybesse et al. (2006), de Kock et al. (2011) and Block et al. (in press) to have a polyphase character. de Kock et al. (2011) proposed a short lived pre-Eburnean event in NW Ghana, which was termed Eoeburnean. The Eoeburnean event operated from 2160 Ma to 2150 Ma. The deformation associated to this event was driven by pluton emplacement and basin folding. In the Bole-Nangodi belt Eoeburnean structures strike N–S. The first Eburnean event according to Allibone et al. (2002) occurred between 2150 and 2110 Ma (according to U–Pb and Pb–Pb zircon ages on rhyolites and granitoids) and was termed Eburnean I. This same event was termed D₁ by Milési et al. (1989). According to Block et al. (in press) D₁ in NW Ghana occurred around 2137 ± 8 Ma (U–Pb monazite ages on the metasediments). The first Eburnean event is characterized by of magmatic accretion, volcanism, Birimian sedimentation and corresponds to a major phase in crustal thickening by nappe stacking and has experienced NE–SW shortening (Feybesse et al., 2006), N–S shortening (Perrouty et al., 2012) in southern Ghana and N–S shortening (Block et al. (in press) in northern Ghana. Metamorphism associated with this event has *P–T* conditions up to 450–650 °C and 4–6 kbar (Harcouët et al., 2007; John et al., 1999) in southern Ghana using the plagioclase–amphibolite geothermobarometry methods after Spear (1980), Plyusnina (1982) and Holland and Blundy (1994). Block et al. (in press), reported greenschist- to amphibolite-facies metamorphism associated with this event in NW Ghana using the *P–T* pseudosection method and geothermometry with a multi equilibria method. The amphibolite-facies regional metamorphism is characterized by pressures up to 11 kbar and temperatures up to 600 °C, whereas the greenschist-facies metamorphism occurred at temperatures between 230 °C and 350 °C and pressures between 1 and 3 kbar.

The second phase known as Eburnean II by Allibone et al. (2002) and D_{2–3} by Feybesse et al. (2006) occurred around 2130–2110 Ma and 2090–1980 Ma (U–Pb and Pb–Pb zircon ages on rhyolites and granitoids). The tectonic style characterizing this event is a NE–SW transcurrent structures (Feybesse et al., 2006) and N- and NE-trending regional scale transcurrent faulting (Baratoux et al., 2011) which affected all lithologies within the Birimian in Ghana and SW Burkina Faso. This event is marked by greenschist-facies metamorphism with *P–T* conditions of 200–300 °C and 2–3 kbars and acts as a fluid pathway for mineralization (Feybesse et al., 2006; Block et al., in press). Gold mineralization has been reported along these transcurrent shear zones by Beziat et al. (2008), Allibone et al. (2002) and Feybesse et al. (2006).

Post Eburnean, late brittle NE–SW faults have been reported by Block et al. (in press) to have cross-cut all Eburnean structures in NW Ghana. These late faults have a limited extension and are steeply dipping normal faults. According to Block et al. (in press) this deformational event is also associated with retrograde metamorphism shown by quartz–chlorite, quartz–white mica and quartz–epidote veins and late brittle faults in-filled by chlorite.

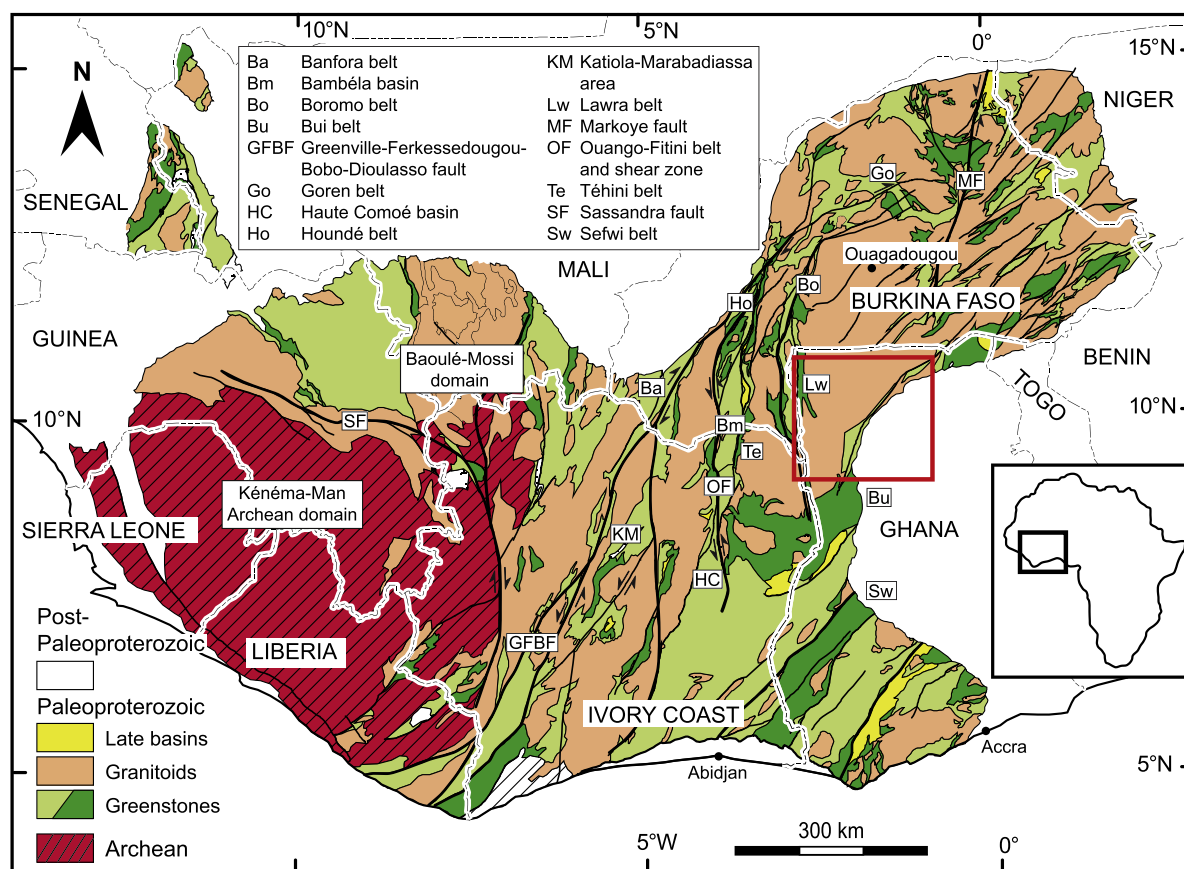


Fig. 1. Simplified geological map of the Leo-Man craton (modified after Block et al., in press) with the area covered by Fig. 2 indicated by the red box. The dark green areas are mafic to felsic lavas and the light green areas are volcanoclastic and sediments. (For interpretation of the references to colour in this figure legend, the reader is referred to the web version of this article.)

4. Materials and analytical methods

Fieldwork consisted of lithological and structural logging and geological mapping. The logging was carried out on 69 bore holes (representing seven N–S fences or sections) drilled within the Julie deposit (Azumah Resources Limited). The field data were collected from mineralized zones, hydrothermally altered zones, and fresh rocks. Twenty-five samples from mineralized and unmineralized zones (both quartz veins and wall rock) were collected from drill core. Petrography and ore microscopy was completed on 20 polished thin sections from the mineralized and unmineralized zones. Six samples of altered and fresh rocks were analyzed for bulk rock data, by ALS Chemex laboratory. Major elements were analyzed by X-ray fluorescence spectrometry (XRF) using a lithium tetraborate fusion technique for digestion, while rare earth elements (REE) and high field strength elements (HFSE: Th, Nb, Y, Zr, Hf) and Co, Cu, Zn, Cr, Ni, V, Mn, Pb, Ba and Sr were analyzed by inductively coupled plasma mass spectrometry (ICP-MS).

A Jeol JSM 6360LV SEM coupled to an energy dispersive X-ray spectrometer (SDD Bruker 129 eV) was used to acquire images in backscattered electron mode (BSE) at the GET laboratory. An acceleration voltage of 20 kV was used to conduct electron scanning of various sulfides on 20 polished thin sections within the mineralized zone to detect the minerals and elements associated with the Au mineralization. Spot analyses of pyrite crystals were performed by LA-ICP-MS at the Géosciences Montpellier laboratory (France), to determine trace element concentrations. Analyses were performed using a Geolas (Microlas) Excimer ArF automated platform

housing a 193 nm Compex 102 nanosecond laser from LambdaPhysik, coupled with a high-resolution ThermoFinnigan (ELEMENT XR) ICP-MS. Data were acquired in the fast E-scan mode at low mass resolution using a flux of 15 J/cm² at a frequency of 5 Hz and working with a spot size of 51 μm. Raw data were processed on-line using the GLITTER software package (e.g., Van Achterbergh et al., 2001), and using several sulfide standards, i.e., pyrrhotite-Po-726 (Sylvester et al., 2005) and in-house chalcopyrite Cpy-RM (Velázquez et al., 2012) as external calibrators, and using ³⁴S as the internal calibrator (e.g., Lorand and Alard, 2011). During analysis, the following isotopes were monitored: ³³S, ³⁴S, ⁵⁶Fe, ⁵⁷Fe, ⁵⁹Co, ⁶⁰Ni, ⁶³Cu, ⁷⁵As, ⁸²Se, ¹⁰⁷Ag, ¹²⁵Te, ¹⁹⁷Au, ²⁰⁸Pb, and ²⁰⁹Bi. Typical detection limits, at the conditions described above, are between 0.01 ppm. Detection limits were calculated as three times the background standard deviation value and were converted to concentration units (ppm) with the yield_{ms} parameter (e.g., Borisova et al., 2010). All calculated concentrations were comparable to the analytical precision limits of the *in-situ* femtosecond quadrupole LA-ICP-MS technique (<15% RSD, e.g., Borisova et al., 2010) and the reference materials homogeneities (<16% RSD, Velázquez et al., 2012).

Petrographic, microthermometric and Raman analyses were conducted on fluid inclusions in 5 doubly-polished thick-sections (150–200 μm) of A-type and C-type quartz veins from the mineralized zone. Petrographic work on the thick sections was performed to ascertain the textural relationship of various fluid inclusion types at room temperature along with their distribution and size. Thermobarometric studies were carried out at the GET laboratory,

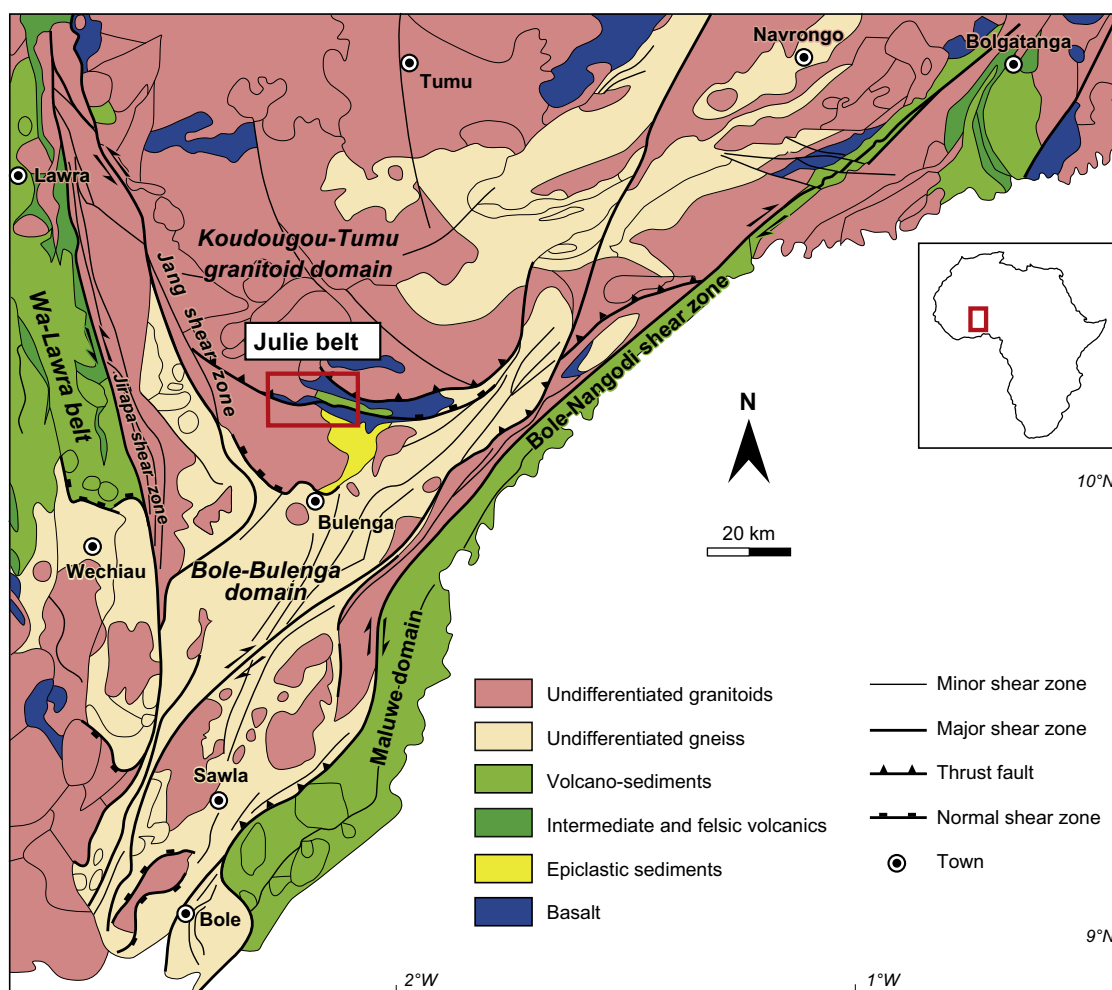


Fig. 2. Regional litho-structural map of NW Ghana (modified after Block et al., in press). The red insert shows the study area (Fig. 3). (For interpretation of the references to colour in this figure legend, the reader is referred to the web version of this article.)

using a Linkam LNPCI94 heating and cooling stage following the procedures described by Roedder (1984) and Shepherd et al. (1985). Calibration was made using $\text{H}_2\text{O}-\text{CO}_2$ fluid inclusions with melting temperature of pure CO_2 of -56.6°C and pure water inclusions with ice melting temperature of 0°C and critical homogenization of 374°C . Raman spectroscopic measurements were made at the CEMES laboratory in Toulouse, using a Labram HR (Horiba Jobin Yvon) Raman spectrometer equipped with a Notch filter and a CCD detector cooled to -130°C by liquid nitrogen. The exciting radiation at 514.535 nm was provided by an Ar^+ 108 laser (type 2020, Spectra-Physics) with a laser power of 200 mW at the source and $\sim 20\text{ mW}$ at the sample. Spectra were collected with a grating of 1800 lines/mm and a confocal $\times 50$ objective, allowing a spectral resolution of 4 cm^{-1} . The acquisition range was between 90 and 4400 cm^{-1} in order to detect the maximum number of possible Raman active vibrational bands of the different dissolved and gaseous phases. Three minutes was typically required to measure the entire spectral range.

5. Geology of the Julie deposit

The Julie gold deposit is currently the highest-grade in NW Ghana. It is located in the Wa-East gold district, which lies within

the Julie belt south of the Koudougou-Tumu granitoid domain. The Wa-East gold district also includes gold camps of Collette, Kjersti, Kandia, Julie west, Baayiri and Danyawu (Fig. 3).

5.1. Lithological description

The Julie deposit is hosted in strongly sheared granitoids of the Julie belt. The rocks are pink in color on both fresh and weathered surfaces in the altered zone and greenish in the least-altered zone. They are medium to coarse grained (Fig. 4), weakly magnetic in altered zones and strongly magnetic in the least-altered zones. They are primarily composed of quartz, plagioclase, hornblende and biotite with accessory minerals consisting of titanite, zircon and magnetite, which are overprinted by greenschist-facies metamorphic assemblages of epidote, calcite, fine-grained biotite and rutile.

To the north of the Julie shear zone are basalts and sediments, consisting mainly of intercalated metamorphosed greywacke, shale and volcanosediments. The sediments are fine to medium grained, black to gray in color and composed of quartz, muscovite, chlorite, biotite and graphite. The basalts are strongly magnetic and composed of plagioclase, green amphibole, calcite, chlorite with minor titanite and magnetite.

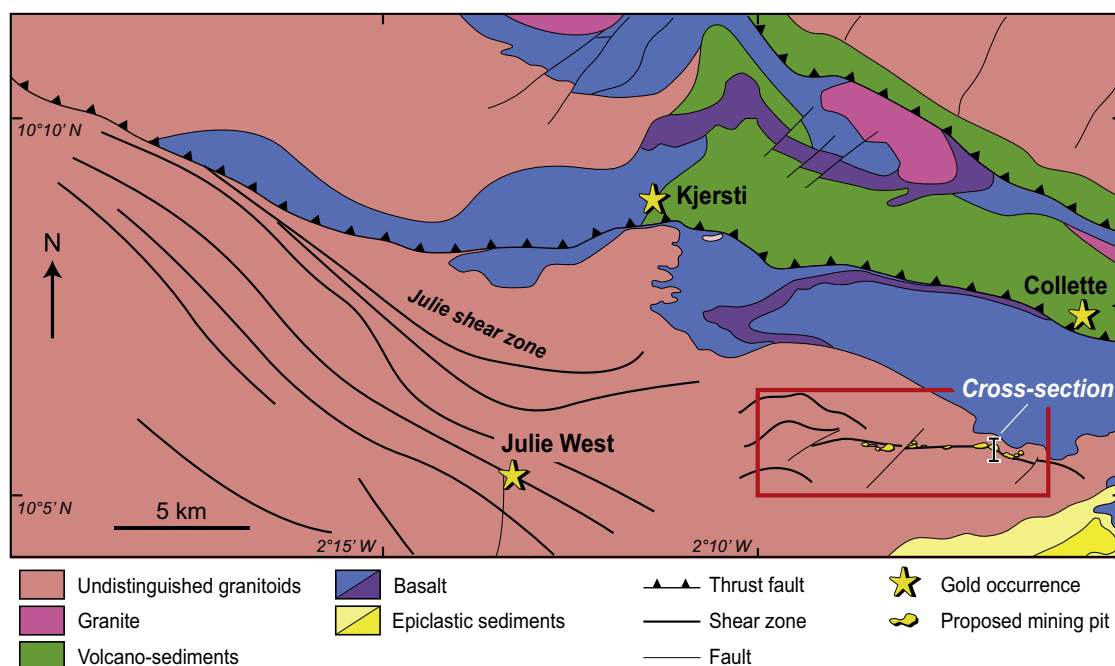


Fig. 3. Simplified geological map of the Wa-East gold district showing various gold occurrences. The Julie deposit is located by the red insert; the location of the cross-section in Fig. 9 is also shown. (For interpretation of the references to colour in this figure legend, the reader is referred to the web version of this article.)

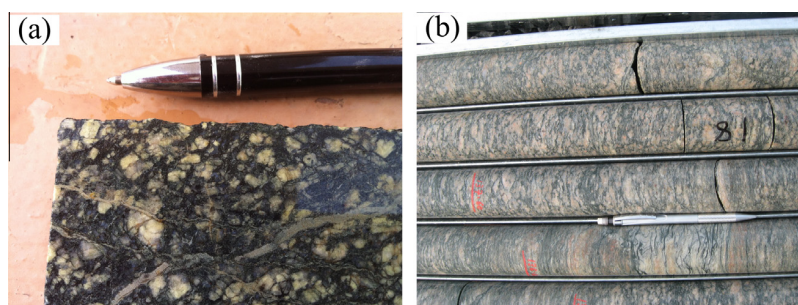


Fig. 4. (a) Fresh undeformed granitoid in drill core outside the mineralization zone in the Julie deposit. (b) The rocks show a weak mineral lineation that intensifies approaching the mineralization zone (bottom of the image).

5.2. Geochemistry

Fresh unaltered granitoid samples from the Julie deposit have SiO_2 content ranging from 51.6 to 67.3 wt.% with Mg# ranging from 44.44 to 61.54. The $(\text{La}/\text{Yb})_n$ ratio varies between 4.39 and 14.54 (Table 1). In the Baker classification diagram (1979; Fig. 5a), the normative composition (Ab–An–Or) of the Julie granitoid samples plots near a triple point separating the compositional fields of tonalite, granodiorite and trondhjemite; as such, they will be referred to as TTG from now on. In classification diagrams of Frost et al. (2001) and Frost and Frost (2008) (Fig. 5b–d), the Julie samples exhibit characteristics of magnesian rocks, calcic to alkalic rocks and they are metaluminous. Rare-earth element (REE) spectra (Fig. 5e) show a net enrichment in LREE relative to HREE and the multi-element spectra (Fig. 5f) show enrichment in LILE (K_2O , Rb and Ba) with respect to HFSE, with well-marked negative anomalies for Nb and Ta.

All the geochemical characteristics of these intrusives are typical of magmatic rocks in active margins (Chappell and White, 1974). These results are confirmed by the Rb vs Y + Nb diagram

of Pearce et al. (1984; Fig. 5g). The signature of the magmatic activity from the Julie deposit falls within the Volcanic Arc Granite (VAG) field (Fig. 5g). It can thus be concluded that the Julie TTG have relative common geochemical characteristics, similar to those of many plutons within the West African Craton that were emplaced during the Eburnean Orogeny (Doumbia et al., 1998; Gasquet et al., 2003; Diop et al., 2006).

5.3. Structural geology

Meso- and micro-structural analysis during geological mapping, drill core logging and microscopic structural work has permitted to identify three main deformational events, which correspond to D_{11} , D_{12} and D_{13} phases. The D_{11} event is the most prominent deformation event and has affected all the rocks in the Wa-East district (Fig. 6). D_{11} in the TTG and basalts is defined by an E–W penetrative metamorphic foliation (S_1) (Fig. 7a and b), which is often parallel to primary bedding (S_0) in the volcano-sediments north of the Julie deposit (Fig. 3).

Table 1
Major and trace element analytical data of granitoids in the Julie deposit.

	JUL_1	JUL_2	JUL_3	JUL_4	JUL_5	JUL_6	JUL_7
<i>wt.%</i>							
SiO ₂	72.2	67.3	61.1	61	54.9	52.3	51.6
TiO ₂	0.4	0.4	0.3	0.4	1	1.1	0.5
Al ₂ O ₃	12.5	14.1	12.8	12.5	14.4	16.1	18.3
Fe ₂ O ₃	3.8	4.9	4.3	4.9	6.7	8.1	4
MnO	0	0.1	0.1	0.1	0.1	0.1	0.1
MgO	1.7	1.9	2.3	2.4	3.6	3.1	2.4
CaO	1.7	4.8	7.3	6.2	5.4	6.1	5.2
Na ₂ O	0.3	4	3.6	3.6	4.3	2.7	6.1
K ₂ O	3.6	1.1	0.2	1.9	2.8	2.9	2.4
P ₂ O ₅	0.1	0.1	0.1	0.1	0.7	0.4	0.1
Total	99.3	100.4	99.4	100.6	99.8	98.5	98
<i>ppm</i>							
As	0.2	0.1	5.4	13.9	0.1	0.2	0.4
S	0	0	0	0.5	0.2	0.2	0.3
Cs	1.5	2.2	0.4	1.1	2.1	1.7	2.8
Li	20	10	10	10	20	20	10
Rb	2	1	7	46	2	1	2
Ba	70	130	60	60	110	50	60
Sr	0	0.6	0.8	0.9	1	0.7	0.7
Pb	9	9	7	6	13	12	14
Cr	3	4	70	40	5	3	4
Ni	631	51	11	17	21	54	23
V	461	1	228	95	6	6	17
Sc	12	13	11	10	11	11	11
Ga	3.9	4	19.8	14.7	5.2	3.4	5.4
Zn	35	53	52	63	102	99	31
U	128	89	1	1	145	159	118
Zr	1.8	5.9	134	157	0.3	1.9	2.2
Hf	19.6	19	4	4.4	61.6	36.2	31.6
Y	1.5	2.2	30.6	16.9	1.6	1.4	2.7
Nb	4.8	5.3	4.9	5.1	17.9	10.7	7.7
Ta	3.8	2.2	1.1	0.6	5.1	3.2	4.8
Th	0.2	0.3	3.1	2.8	0.3	0.2	0.4
Tl	99.3	100.4	0	0.1	99.8	98.6	98
La	6.7	5.9	26.3	19.2	6.9	5.8	8.7
Ce	2.3	1.1	54.3	40.3	3.6	1.2	0.8
Pr	3.5	4.3	6.4	4.5	13.3	8.1	5.5
Nd	79.6	27.8	4.9	5.1	93.8	70.6	61.8
Sm	163	588	5	3	1620	410	807
Eu	2.6	3.8	1.7	1.1	8.2	5.4	4.3
Gd	0.5	0.7	5	3	0.9	0.6	0.9
Tb	0.5	0.5	0.8	0.4	0.6	0.5	0.5
Dy	0.7	1.1	4.8	2.6	3.3	2.1	1.4
Ho	0.2	0.4	0.9	0.6	0.2	0.2	0.5
Er	17.6	15.5	2.9	1.6	21.7	19.3	21.1
Tm	1	1	0.5	0.2	2.5	0.9	1.3
Yb	132	135	2	2	203	130	182
Lu	17	21	0.4	0.3	72	43	29
(La/Yb) _n	5.1	4.5	19.9	14.5	5.2	4.4	6.6
Mg#	44.5	45.4	54.5	18	52.9	44.4	61.5

Mg# = MgO/(MgO + FeO_{total}) * 100.

A stretching mineral lineation (L_1) associated with D_{J1} can be observed within the TTG. The S_1 in the Julie deposit strikes E–W (Fig. 7a) with dips ranging between 35° and 70° to the north, with a stretching mineral lineation (L_1) (Fig. 7c) which is trending 025° and plunges between 35° and 80°. The shear zone in the Julie deposit, is a splay of the Baayiri shear zone (Fig. 3). Within the TTG, in the Julie deposit, D_{J1} is represented by a well-defined E–W oriented S_1 shear zone with ductile and brittle characteristics and no noticeable displacement. It is inferred to be dextral, based on the north-side up sigmoidal shapes in the deformed mineral fabric, and on the shapes of sigmoidal pressure shadows around minerals. Pre- to syn-deformational quartz veins occur within this zone, and have been boudinaged and oriented in the direction of S_1 during the D_{J1} deformation. Striations on the vein wall have a shallow plunge (20–30°) and are north trending.

The second deformational event (D_{J2}) in the study area is marked by crenulations or F_2 isoclinal folds with fold axes verging

toward the north and mainly observed within the volcanosediments. The axial planes of these F_2 folds forms an S_2 foliation that strike N–S with moderate to steep dips (Fig. 7e) and an L_2 (Fig. 7d) mineral lineation trends northward with moderate dips (~50°). D_{J2} marks an E–W compression within the study area.

The last stage of deformation (D_{J3}) is manifested by late brittle faults that occur in the region along a NE–SW trend (Fig. 3) and locally displace the D_{J1} shear in the deposit area (Fig. 6). Their dips range between 36° and 60° to the NW. Striations in the faults trend 130° and plunge 30°.

6. Quartz veins

Mineralization in the deposit is concentrated within and around quartz veins, which are controlled by the regional deformation events. Three sets of quartz veins were identified in the study area, and are referred to as veins A-type, B-type and C-type.

6.1. A-type vein

A-type veins are mostly pre- to syn-deformation and are composed of milky to translucent quartz plus about 5% calcite, chlorite, and tourmaline. They form corridors consisting of swarms of several veins oriented E–W, occurring mainly within the D_{J1} shear zone crosscutting the TTG, in which case the veins and their immediate host are particularly enriched in tourmaline (about 10%; Fig. 8a). These veins have been strongly ductily deformed (Fig. 8b). The gold mineralization in the Julie deposit occurs mainly within these corridors.

6.2. B-type vein

The B-type veins formed within the S_2 foliation plane of the D_{J2} and are oriented N–S. They are deformed, are made up of translucent quartz, accessory calcite, and contain tourmaline (<2%). They have not been found intersecting the TTG, but only the basalt, where they are observed to crosscut A-type veins. These veins are not associated with mineralization.

6.3. C-type vein

Veins of this type were mostly observed within trenches and artisanal mining pits within the TTG. So far, they have not been intersected in drill core. They are oriented N–S (Fig. 7f), locally sub-parallel to the late, D_{J3} -related faults. They are characterized by a vuggy aspect (Fig. 8c) contain chlorite, carbonate and muscovite, and carry minor mineralization in the form of spotty gold commonly associated with euhedral millimeter-scale pyrite within the veins.

7. Ore body geometry and mineralogy

The main ore body at Julie consists of two plunging auriferous corridors (mostly of lenticular shape) made up of A-type veins, that extend over 3.5 km within a 6 km E–W trending S_1 shear zone, with a thickness varying from 20 to 50 m. A secondary mineralization is associated with a series of C-type veins that trend N–S. The strike extent of these lodes cannot be determined because of very poor outcrop. The longest one measured on the Julie deposit is 100 m and has a lenticular shape.

Strong alteration can be observed within and around the mineralized corridors and veins. Although they are much more important volumetrically in the main mineralization, the same alteration was also found in the mineralizations contained in the C-type veins. Mineral assemblages define clear zones with

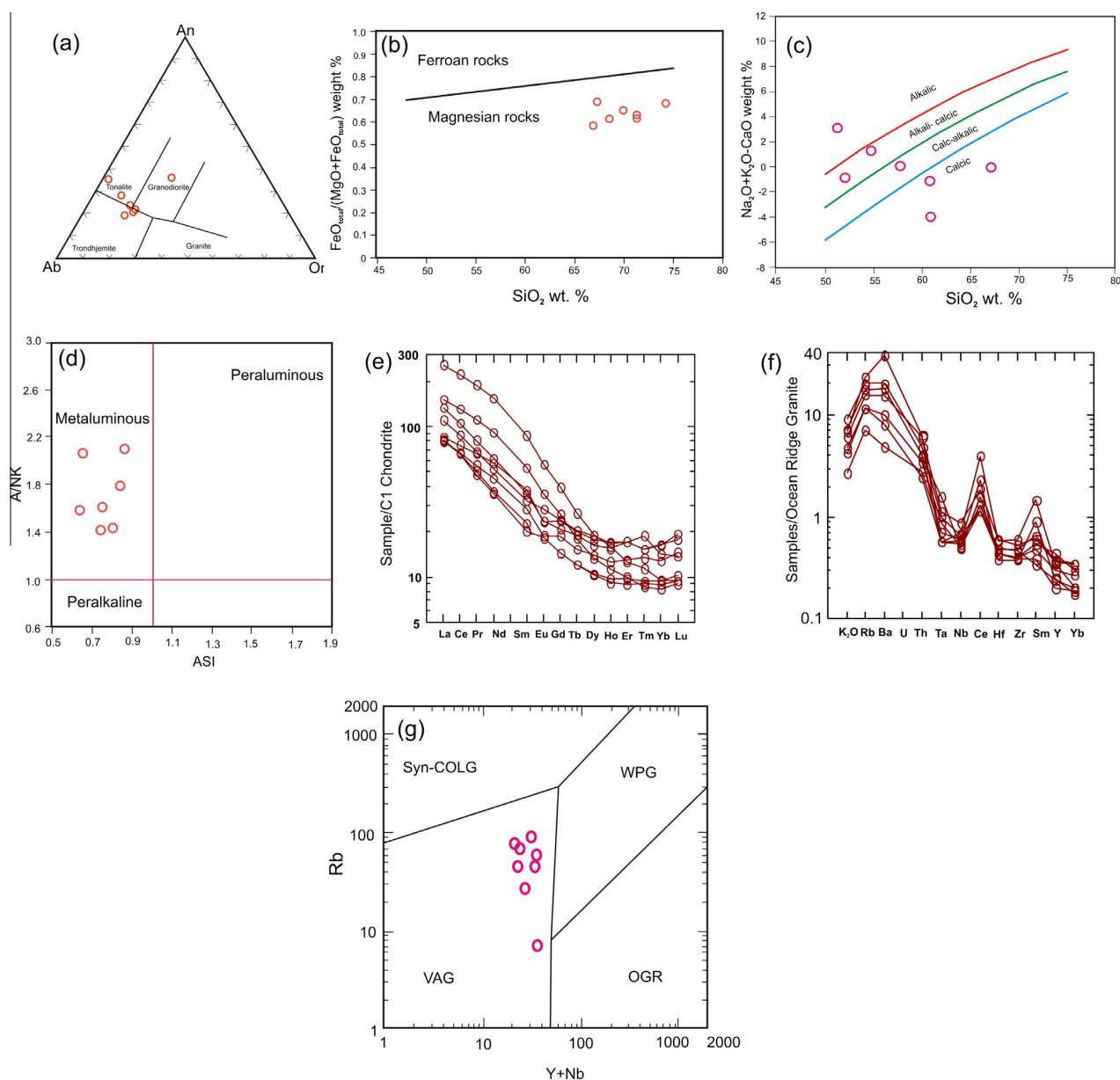


Fig. 5. Geochemical plots for the Julie granitoids. (a) Normative plots of Ab–An–Or (Barker, 1979). (b–d) Geochemical classification diagrams for granitic rocks (Frost et al., 2001; Frost and Frost, 2008); (b) $\text{FeO}_{\text{tot}}/(\text{FeO}_{\text{tot}} + \text{MgO})$ vs weight percent SiO_2 diagram showing the boundary between ferroan rocks and magnesian rocks; (c) $\text{Na}_2\text{O} + \text{K}_2\text{O} - \text{CaO}$ vs SiO_2 showing the range for the alkalic, alkali-calcic, calc-alkalic and calcic rocks; (d) Molecular ratio $\text{Al}/(\text{Na} + \text{K})$ vs Aluminum Saturation Index (ASI) distinguishing metaluminous from peraluminous compositions. (e) Chondrite normalized REE plot. (f) ORG-normalized distribution patterns. (g) Plots of Rb vs $\text{Y} + \text{Nb}$ (Pearce et al., 1984). Syn-COLG: Syncollision granites; VAG: Volcanic Arc Granites; WPG: Within Plate Granites; ORG: Ocean Ridge granites.

gradational contacts as one moves laterally away from the veins (Fig. 9). Because of the better exposure and availability of drill core samples, the alteration is described in more details below for the main ore body (related to the A-type vein networks) only. From the ore zone outwards, these are:

Alteration (1), consisting of sericite + quartz + ankerite + calcite + tourmaline + pyrite, is restricted to the mineralized network of quartz veins and the immediate wall-rock host (Fig. 9), forming an envelope of a maximum width of 50 m. The rocks affected by this alteration type have a bleached appearance (Fig. 8b), as a result of the intense carbonatization, and display S_1 -parallel foliation. Here, sericitization is abundant (Fig. 10a), and calcite and ankerite replace albite. In this zone, magnetite is

entirely replaced by pyrite. This is consistent with the low magnetic susceptibility reading within this zone compared to the values from outside the ore zone. Gold grades associated with this alteration average at about 3 g/t.

Alteration (2) consists of albite + sericite + calcite + chlorite + pyrite + rutile: This zone marks a lateral alteration away from the main mineralization zones. Here, the rock is sericitized, and magmatic plagioclase is replaced by albite (Fig. 10b). Rutile and pyrite partially replace magnetite (Fig. 10c). Gold grades associated with this alteration zone range between 0.83 g/t.

Finally, away from the mineralized zone, a metamorphic assemblage of chlorite–epidote–biotite (Fig. 10d) characterizes the rocks and is considered to represent a greenschist-facies metamorphic

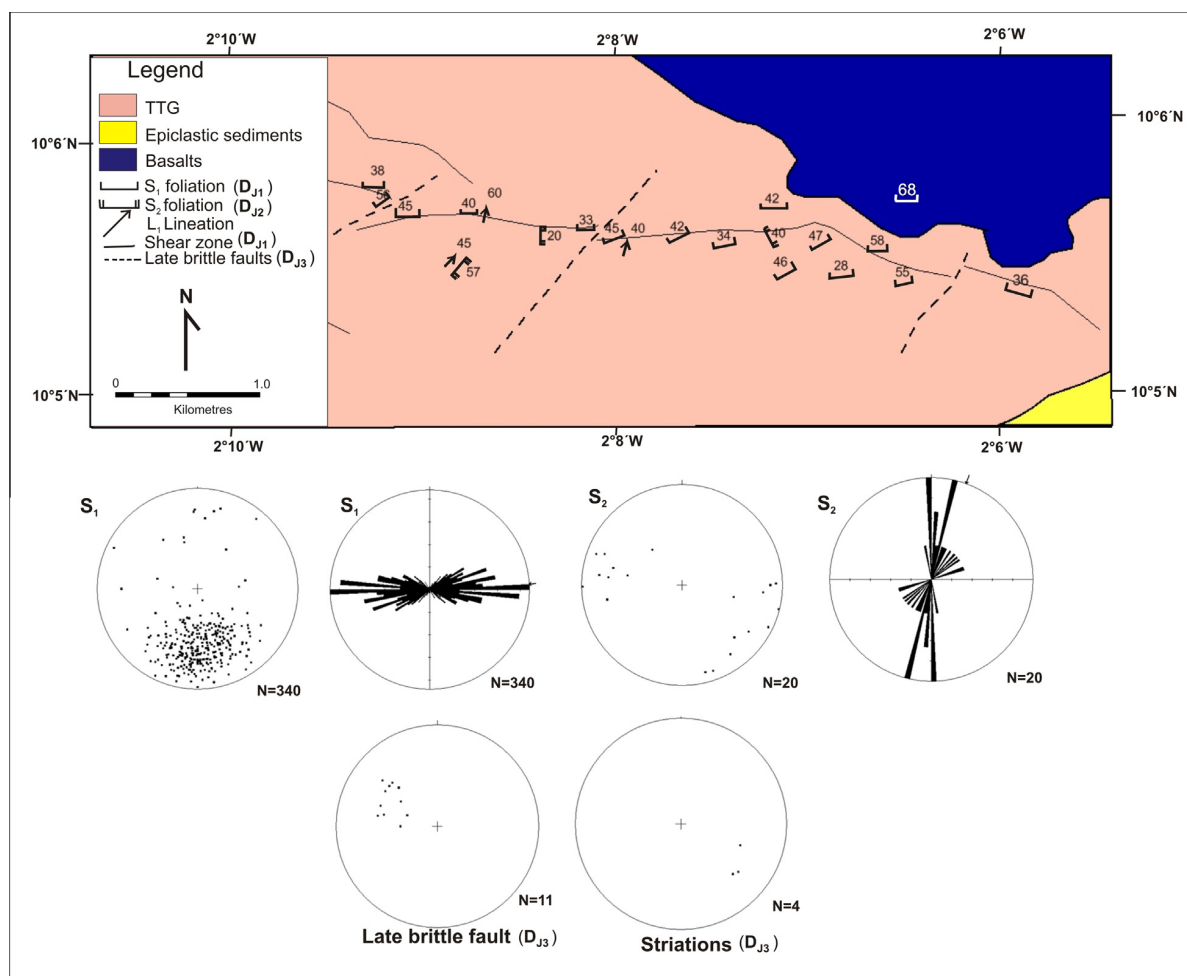


Fig. 6. Geological map of the Julie deposit outlining the structural trends. Diagrams in the bottom half illustrates equal-area lower hemisphere stereoplots and rose diagrams of the structural orientation measured.

overprint. Biotite and chlorite are ubiquitous also within the entire hydrothermal plumbing system.

8. Mass balance considerations

In order to further characterize the alteration, quantitative evaluation of chemical gains and losses within the TTG during the hydrothermal process has been determined using major-oxide and trace-element compositions determined by whole-rock analyses (Table 2). The Grant (1986) isocon method was used to estimate significant changes in composition, mass and volume (Fig. 11). Average compositions for the least altered zones were plotted against samples from the altered zones (averages) by using the EASYGRESGRANT MS-Excel sheet provided in Lopez-Moro (2012). Zirconium and Hafnium were used as immobile elements. This choice resulted from the fact that in this setting Zr was most likely not mobile, and from the presence of euhedral zircons that subsisted the alteration (e.g., Fig. 12b and c). Results (Fig. 11) indicate that mass was generally conserved during alteration (a slight mass gain is recorded in the inner alteration envelope). Au, Te, Bi, S and, to a lesser extent, Ag, increase from the unaltered to the inner alteration envelope (see also Table 2). Here, Al_2O_3 was constant, SiO_2 and CaO were added and Fe_2O_3 , K_2O were leached compared to the least-altered, barren rocks. In the outer alteration envelope

(alteration zone 2) silica was leached and CaO, Fe_2O_3 , K_2O , Na_2O and Al_2O_3 were added to the rock (Fig. 11c and d).

9. Sulfide characterization

Pyrite (Fig. 12) is the principal ore mineral within the mineralized zones, either in the veins, or in the altered host rocks. Gold mineralization occurs in the form of (i) micron-sized gold inclusions (Fig. 12a–c) and larger gold grains within fractures or on the edges of euhedral pyrite, in the A-type vein corridor; and (ii) mostly as free gold in fractures within pyrite (Fig. 12d) associated with C-type veins. In the first case, gold is associated with silver, bismuth, tellurium (Fig. 12c), plus minor amounts of other base metals such as copper and lead, while gold occurrence in pyrite in the C-type veins are associated mostly with silver. To check for the presence of invisible gold within the pyrite structure, we performed several *in-situ* spot analyses by LA-ICP-MS on representative pyrite grains from A-type and C-type veins (Tables 3 and 4). The results document the presence of variable amounts of Au (below detection to 13 ppm), Ag (up to 2 ppm), Te (up to 13 ppm), Pb (up to 9 ppm), As (up to 35.53 ppm), Se (4–15 ppm), and important amounts of Ni (88–799 ppm) and Co (6–696 ppm). LA-ICP-MS analyses performed on pyrite from C-type veins (Table 4) show low amounts of Au and Ag contents within the

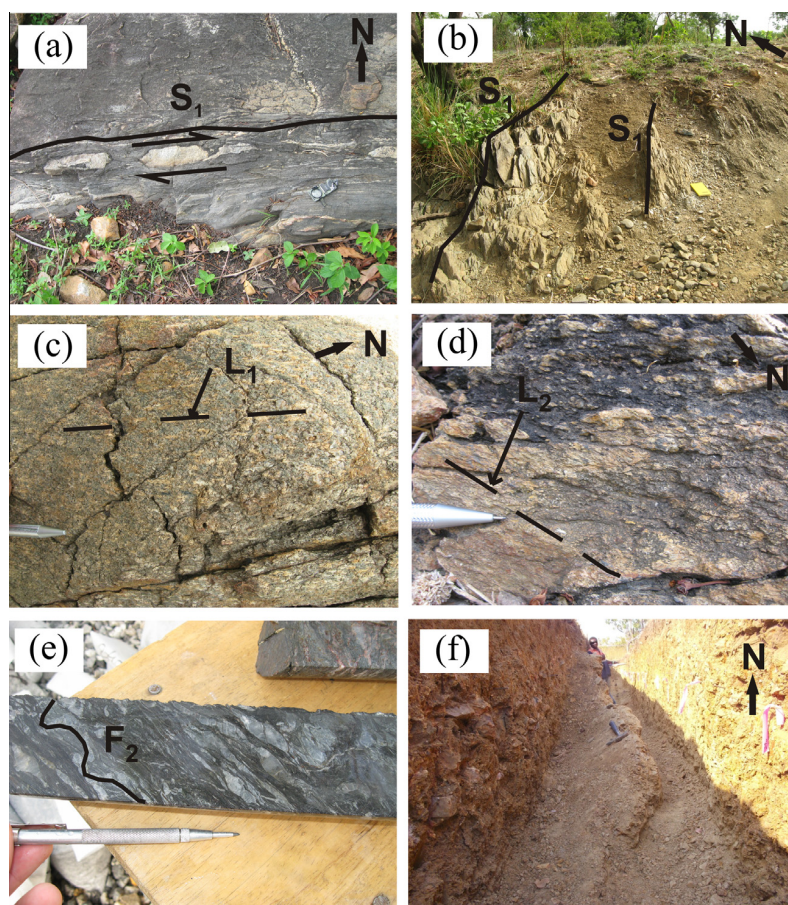


Fig. 7. Field and drill core photographs illustrating representative structures in the deposit area. (a) Extensively sheared TTG exhibiting S_1 foliation fabric in the Julie deposit. The photograph shows E–W oriented syn-kinematic boudins with dextral sense of movement. (b) Steeply dipping E–W trending S_1 foliation within the volcano-sediments. (c) Photograph showing L_1 mineral stretching lineation on the TTG. (d) Photograph showing north trending mineral lineation L_2 . (e) Drill core of sediments showing F_2 fold and E–W trending, boudinaged veins exhibiting dextral characteristics. (f) Photograph of a trench showing a D_{13} -parallel quartz vein. The vein strikes north with a dip of 36° to the west.

pyrite structure, and generally also lower contents of other metals than in A-type veins, except for As that overall has somewhat higher values, Ni that has similar values, and Co that has quite higher values. In A-type quartz veins, the metals that were found by SEM to coexist with gold, correlate among each other (Au and Ag, as well as Ag with Te, Pb, Bi; Table 5).

10. Fluid inclusion study

10.1. Fluid inclusion petrography

Fluid inclusions were analyzed in quartz crystals from eight and six representative samples of the A-type and C-type mineralized veins, respectively. Based on petrographic considerations (cf. Goldstein and Reynolds, 1994), primary fluid inclusions were identified as isolated individuals forming clusters, and were considered for further study together with clearly pseudosecondary fluid inclusions occurring along intra-granular healed fractures.

All primary and pseudosecondary fluid inclusions studied contain an aqueous and a carbonic phase (Fig. 13), identified based on their aspect at room temperature, thermometric behavior and Raman micro-spectrometry. Based on the differences in relative filling of the aqueous and carbonic phases, we could divide these into two main types: Type-1 fluid inclusions are aqueous-carbonic inclusions characterized by high liquid (L) to

vapor (V) ratios (about 75–85% H_2O by volume; Fig. 13a). At room temperature they generally display two phases, i.e., liquid H_2O and a dense CO_2 phase (Fig. 13a), however, CO_2 vapor nucleated upon cooling in most cases. These inclusions displayed total homogenization to the liquid phase. Type-2 fluid inclusions are also aqueous-carbonic, but show three phases at room temperature (L H_2O , L CO_2 and V CO_2 ; Fig. 13b) and are characterized by variable volumetric proportion of the aqueous and carbonic phases, from about 50% to 90% CO_2 (Fig. 13b and d). These inclusions homogenized mostly to the vapor phase on heating. The size of both inclusion types ranges from <5 to $20\ \mu m$. Locally, a small, high-relief, birefringent crystal could be observed in the two fluid inclusion types, and was interpreted as a carbonate based on optical properties. Three fluid inclusion populations containing one or both of these inclusion types were identified in A-type as well as in C-type veins. One consists of mainly Type-1 inclusions, one consists of a mixture of Type-1 and V-rich Type-2 inclusions, and one consists of Type-2 inclusions with variable L/V ratios. The distribution of these populations varied, and fluid inclusion assemblages (FIA) containing all three of these populations are common in all quartz grains studied in A-type as in C-type veins.

10.2. Analytical results and fluid inclusion composition

Raman spectroscopic analyses were performed on all fluid inclusion types, to obtain information of the volatile composition

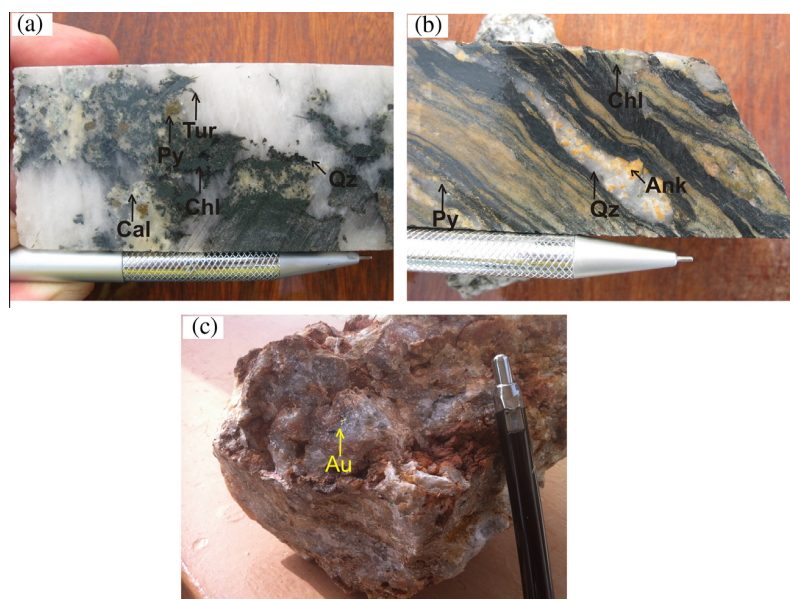


Fig. 8. (a) A-type vein in drill core, showing vein quartz including chlorite, tourmaline, calcite and pyrite. (b) Drill core showing strongly deformed TTG (D_{11}) containing small, boudinaged A-type veins. Sulfides and tourmaline are abundant in the groundmass. (c) A sample of C-type vuggy quartz veins with native gold mineralization (arrow). Cal-calcite, Py-pyrite, Chl-chlorite, Tur-tourmaline, Qz-quartz, Ank-ankerite, Au-gold.

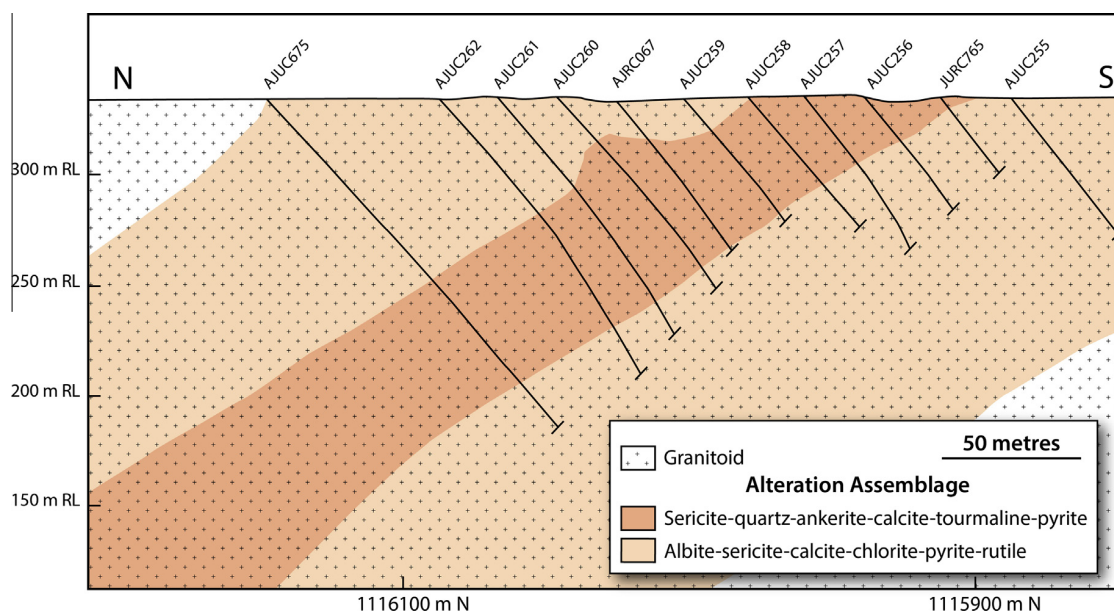


Fig. 9. Cross-section (looking east) of the Julie deposit along 597,100 mE showing one of the main mineralized corridors, along the E–W D_{11} shear dipping 35° north. High-grade mineralization is confined to a 20- to 50 m-thick zone characterized by alteration (1), which forms a corridor of A-type veins. The alteration (2) selvage contains only low grade mineralization.

of the fluids. A total of about 30 fluid inclusions (Type 1 and 2) from both vein sets were analyzed using this technique. Spectra were collected on the L and V phases present in Type-1 fluid inclusions and in Type-2 fluid inclusions with similar L and V content, as well as on the carbonic phase in V-rich Type-2 inclusions (Fig. 13c and d). The results confirm the microthermometric data, i.e., that the inclusions consist of H_2O and CO_2 , and that no other gases are present. The occurrence of a small film of water in the inclusions with the largest V (CO_2) filling was also confirmed by Raman analysis.

The CO_2 solidification temperature (T_n), ice-nucleating temperatures ($T_{n_{ice}}$), melting temperatures for CO_2 ($T_{m_{CO_2}}$) and ice ($T_{m_{ice}}$), clathrate dissolution temperature ($T_{m_{clath}}$), homogenization temperatures of CO_2 ($T_{h_{CO_2}}$) and total homogenization temperatures ($T_{h_{tot}}$) were measured. The salinities of the Type-1 and Type-2 aqueous-carbonic inclusions were determined from the clathrate dissolution temperatures, using the computer programs BULK and ISOC of Bakker (2003).

The microthermometric measurements for the different FIA were similar in A-type and C-type vein samples (Figs. 14 and 15).

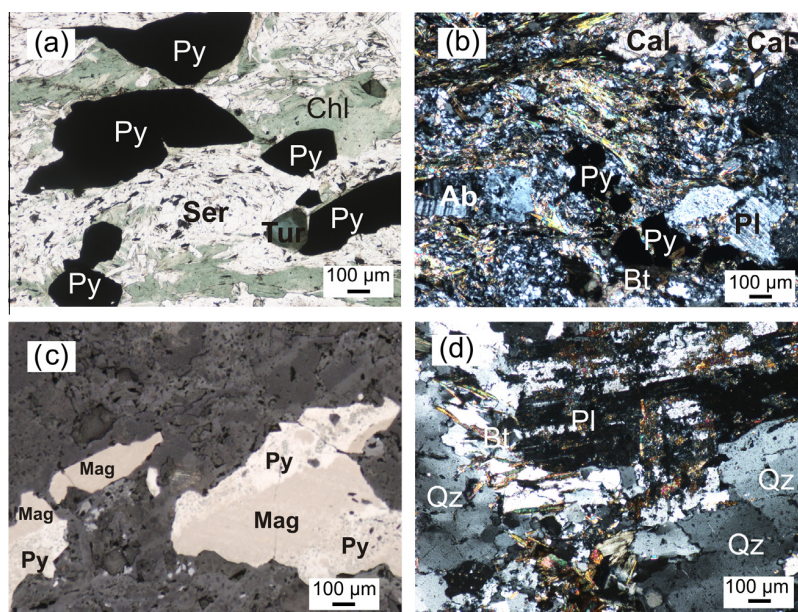


Fig. 10. Photomicrograph of mineral assemblages in TTG hosting A-type veins. (a) Transmitted PPL image of the inner alteration envelope, showing secondary sericite, pyrite, tourmaline, and chlorite. A foliation is defined by alignment of pyrites and the micas. (b) Transmitted XPL image of strongly altered magmatic plagioclase with secondary albite, sericites, pyrite, carbonate, from the outer alteration envelope. (c) Reflected-light image showing magnetite partially replaced by pyrite. This is typical of alteration seen in rocks adjacent to the mineralization zone (alteration 2). (d) Transmitted XPL image of metamorphic assemblage in TTG outside of the mineralized zone. Plagioclase does not show strained textures, suggesting that the rocks outside the mineralization zone did not experience any significant deformation. Ab-albite, Py-pyrite, Bt-biotite, Pl-plagioclase, Qz-Quartz, Cal-calcite, Chl-chlorite, Mag-magnetite, Tur-tourmaline.

The CO₂ solidification temperature (Tn) recorded for Type-1 and Type-2 fluid inclusions ranges between -96.5 °C to -98.5 °C. Melting temperatures for CO₂ in Type-1 and Type-2 inclusions cluster around -56.6 °C, consistent with CO₂ being the main gaseous phase in the inclusions (Figs. 14a, 15a). The ice-melting temperature for Type 1 fluid inclusion ranges from -2.1 to -5.5 °C and that of Type 2 ranges from -0.9 to -2.3 . Clathrate dissolution temperature for Type-1 inclusions ranges from 6.8 to 7.5 °C, whereas for Type-2 inclusions it ranges from 5.0 to 7.9 °C (Figs. 14b, 15b). In both Type-1 and Type-2 inclusions, homogenization of CO₂ took place to the liquid phase, within a narrow range of temperature, from 25.2 to 26.1 °C and 25.1 to 26.6 °C respectively (Figs. 14c, 15c). Total homogenization for Type-1 inclusions varies little, within a range from 210 °C to 228 °C. Type-2 inclusions displayed a wider scatter of Th_{tot} values, between 210 and 275 °C (Figs. 14d, 15d). The carbonate solid melted between 240 and 260 °C. The salinities calculated for Type-1 and Type-2 inclusions range between 4.9 and 8.6 wt.% eq. NaCl and 1.9 to 6.2 wt.% eq. NaCl respectively (Figs. 14e, 15e). Calculated densities are within the range of 0.41–0.99 g cm⁻³, all inclusion types comprised.

11. Discussion and conclusion

Structural studies from drill core logging and field mapping suggest that three local deformational episodes (named D_{J1}, D_{J2} and D_{J3}) have taken place in the Julie deposit. The first episode, D_{J1}, in the deposit area is manifested by an E–W trending dextral shear zone that affected the TTG. The occurrence of this early deformation event correlates well with a regional D₁ deformation of initial N–S directed shortening, described by Block et al. (in press) for the Birimian of NW Ghana. The second deformation event (D_{J2}), is associated with E–W compression generally forming F₂ fold resulting in the formation of sub-vertical schistosity in foliated rocks. It is mainly pronounced in the sediments and is hardly observed in the TTG. This deformation stage is not associated with

hydrothermal activity and correlates well with the regional D₃ deformation described by Block et al. (in press) in NW Ghana. The final deformation stage, D_{J3}, is associated with NE–SW-oriented brittle faulting that displace the early D₁ and D₂ structures. At this stage, it is not clear to which regional event it could correspond.

The principal gold-bearing body in the deposit is contained within a network of A-type vein in the E–W-trending D_{J1} shear zone. The foliation shown by the alteration minerals is parallel to the S₁ foliation plane, consistently with a syn-deformation emplacement of the veins, contemporaneously to D_{J1}. The veins probably started their formation at a high angle to the shear zone, then were successively transposed into the foliation and boudinaged. A second, less important mineralized system, consists of undeformed C-type veins, that have a perpendicular strike to the main ore system. This orientation suggest that they could correspond to a conjugate vein sets, parallel to the σ₃ direction for D_{J1}. They probably formed during the final stages of the shearing episode, in a locally brittle regime within the TTG, thus the veins were not transposed along the E–W shear (e.g., Siebenaller et al., 2013). The presence of the same alteration halos as in A-type veins, and the strikingly similar composition and properties of the fluid inclusions, is consistent with a pene-contemporaneous origin of the two vein sets, rather than the C-type veins being related to the late D_{J3} faults.

The A-type vein corridors are strongly altered, manifested mostly by the presence of sericite, carbonates, quartz and tourmaline within the corridor, and by a second alteration halo surrounding it, where tourmaline was not found and albite is more important. In addition, magnetite is progressively replaced by pyrite, toward the inner envelope. The alteration mineralogy is consistent with the greenschist metamorphic grade prevailing through the region. Geochemical variations associated with alteration are illustrated by the isocon diagrams in Fig. 11. These show that both inner and outer alteration envelopes were accompanied by a small volume

Table 2
Whole-rock geochemical data from the alteration zones in the A-type vein system used for the isocon calculations.

Number of samples	Alteration 1 (mineralized zone)			Alteration 2 (adjacent to mineralized zone)			Least altered	
	4	Gain/loss in wt% or ppm Δ Ci/Co		4	Gain/loss in wt% or ppm Δ Ci/Co		2	
	Average (Ci_A1)	1 σ	Mass gain/loss	Average (Ci_A2)	1 σ	Mass gain/loss	Average (Co)	1 σ
	Mineralized			Outer zone			Unaltered	
<i>Oxides (g/100 g⁻¹)</i>								
SiO ₂	61.05	0.05	0.00	51.95	0.35	-0.15	61.00	6.20
Al ₂ O ₃	12.68	0.18	-0.11	17.25	1.10	0.21	14.28	0.13
Fe ₂ O ₃	4.59	0.33	-0.21	6.04	2.06	0.04	5.79	0.89
CaO	6.78	0.55	0.33	5.68	0.43	0.11	5.10	0.47
MgO	2.36	0.07	-0.14	2.78	0.37	0.01	2.75	0.81
Na ₂ O	3.58	0.03	-0.14	4.43	1.71	0.06	4.16	0.12
K ₂ O	1.03	0.83	-0.47	2.66	0.22	0.38	1.93	1.27
Cr ₂ O ₃	0.01	0.00	-0.50	0.01	0.00	-0.50	0.02	0.01
TiO ₂	0.32	0.05	-0.54	0.79	0.30	0.14	0.69	0.29
MnO	0.10	0.01	0.11	0.11	0.01	0.22	0.09	0.01
P ₂ O ₅	0.13	0.03	-0.69	0.27	0.14	-0.36	0.42	0.32
SrO	0.05	0.02	-0.58	0.07	0.02	-0.42	0.12	0.05
BaO	1.67	0.02	14.18	0.09	0.01	-0.18	0.11	0.12
<i>Trace elements (100⁻³g/100 g⁻¹)</i>								
S	0.25	0.24	1.27	0.23	0.05	1.09	0.11	0.09
Ba	278.60		-0.74	825.3	68.50	-0.23	1068.25	60.00
Ce	47.30	7.00	-0.47	72.9	7.80	-0.18	89.20	48.30
Cr	55.00	15.00	-0.54	55	5.00	-0.54	120.00	10.00
Cs	0.75	0.34	-0.68	1.02	0.26	-0.56	2.31	1.25
Dy	3.70	1.06	-0.11	3.76	0.39	-0.10	4.18	0.65
Er	2.23	0.63	0.05	2.45	0.78	0.15	2.13	0.03
Eu	1.35	0.30	-0.38	1.72	0.35	-0.21	2.19	1.10
Ga	17.25	2.55	-0.07	20.2	0.90	0.09	18.60	3.10
Gd	3.96	1.00	-0.34	4.84	0.58	-0.19	6.01	2.18
Hf	4.20	0.20	-0.09	4.4	1.00	-0.04	4.60	0.60
Ho	0.75	0.20	-0.07	0.76	0.12	-0.06	0.81	0.10
La	22.75	3.55	-0.44	33.9	2.30	-0.16	40.30	21.30
Lu	0.31	0.05	0.00	0.36	0.13	0.16	0.31	0.07
Nb	5.00	0.10	-0.22	7.25	1.45	0.13	6.40	0.50
Nd	20.60	3.80	-0.56	35.65	6.91	-0.23	46.45	25.45
Pr	5.49	0.95	-0.53	9.2	1.50	-0.21	11.62	6.34
Rb	26.55	19.25	-0.56	66.2	4.40	0.09	60.80	33.00
Sm	4.01	0.95	-0.55	6.78	1.30	-0.23	8.82	4.48
Sn	2.00	0.00	0.33	1.5	0.50	0.00	1.50	0.50
Sr	620.50	204.50	-0.44	608.5	60.00	-0.45	1104.00	70.00
Ta	0.85	0.25	0.89	0.6	0.20	0.33	0.45	0.05
Tb	0.61	0.16	-0.23	0.69	0.02	-0.13	0.79	0.22
Th	2.93	0.15	-0.20	4.03	0.81	0.10	3.66	1.44
Tl	0.04	0.01	-0.92	0.5	0.00	0.00	0.50	0.05
Tm	0.36	0.12	0.13	0.31	0.09	-0.03	0.32	0.03
U	0.62	0.00	-0.64	1.1	0.19	-0.37	1.74	0.72
V	161.50	66.50	0.38	138.5	20.50	0.18	117.00	28.00
W	5.50	0.50	0.57	11.5	5.50	2.29	3.50	2.50
Y	23.75	6.85	0.06	21.35	3.85	-0.05	22.50	1.70
Yb	2.01	0.42	0.06	2.07	0.67	0.09	1.90	1.09
Zr	145.50	11.50	-0.14	156	26.00	-0.08	169.00	34.00
As	9.65	4.25	2.11	2.05	0.15	-0.34	3.10	2.80
Bi	3.23	2.63	39.38	0.31	0.10	2.88	0.08	0.03
Hg	0.04	0.00	3.00	0.02	0.00	1.00	0.01	0.00
Sb	17.88	8.43	148.00	0.53	0.15	3.42	0.12	0.03
Se	0.65	0.05	0.44	0.45	0.05	0.00	0.45	0.05
Te	7.38	6.68	146.60	0.35	0.21	6.00	0.05	0.04
Ag	1.20	0.60	1.40	0.5	0.00	0.00	0.50	0.00
Cd	0.50	0.00	0.00	0.5	0.00	0.00	0.50	0.00
Co	10.50	7.50	-0.32	16	10.00	0.03	15.50	1.50
Cu	23.50	14.50	1.47	36.5	20.50	2.84	9.50	1.50
Li	0.50	0.00	-0.97	0.5	10.00	-0.97	15.00	5.00
Mo	0.50	0.00	-0.89	3.5	0.50	-0.22	4.50	2.50
Ni	14.00	3.00	-0.61	38.5	15.50	0.07	36.00	15.00
Pb	6.40	0.50	-0.42	13.5	1.00	0.23	11.00	2.00
Sc	10.50	0.50	-0.13	11	0.00	-0.08	12.00	1.00
Zn	57.50	5.50	-0.26	65	34.00	-0.16	77.50	24.50
Au	3.00	0.01	59.00	0.83	0.01	15.60	0.05	0.01
Density g/cm ³	2.72			2.70			2.68	

Ci_A1 = average concentration for alteration 1; Ci_A2 = average concentration for alteration 2.
Samples used to define the least altered sample are JUL_3 and JUL_5 (Table 1).

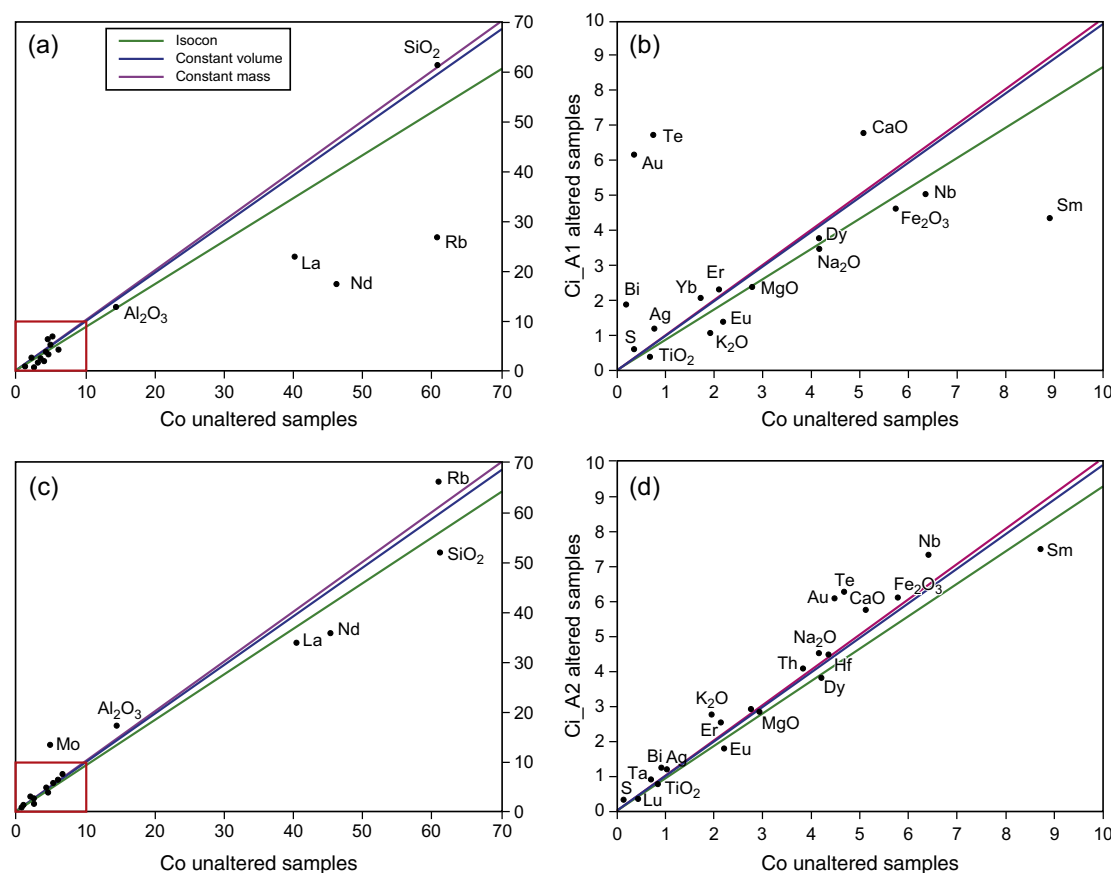


Fig. 11. Isocon diagrams constructed (using the method in Lopez-Moro (2012); based on the theoretical development by Grant (1986) for pairs of unaltered and altered TTG from the main ore zone (A-type veins). The top diagrams (a and b) are for the inner alteration halo (1), where (b) shows a close-up of the red insert in (a). The bottom diagrams (c and d) are for alteration (2), adjacent to the ore zone; (d) is a close-up of the red insert in (c). (For interpretation of the references to colour in this figure legend, the reader is referred to the web version of this article.)

increase, of about 14% and 7% for the inner and outer halos, respectively. Alteration was accompanied by additions of S, Au, Ag, Te, Bi, plus variations in Ca, Si, K, Na, Fe, which are mostly consistent with the sulfidation, sericitization, silicification and carbonatization that affected the host rock. Addition of silica in the inner envelope (alteration-1) was also expected, as it reflects the abundant addition of quartz in the rock and veins. Similarly, albitization accounts for the increase in Na in alteration (2). The leaching of Fe in the inner envelope probably resulted from the extensive replacement of magnetite by pyrite; however, the leaching of K in the same zone is surprising, giving the common presence of sericite. The important width of the alteration zone suggests that the fluid circulated throughout the entire shear corridor, while the veins were local loci of preferential quartz precipitation, during open-space creation. If most fluid circulation had taken place within vein conduits, armoring of a vein by precipitation of minerals on the vein walls would have blocked the hydrothermal fluid, limiting the extent of fluid-rock interaction (e.g., Robert and Brown, 1986; Garofalo, 2004). This is also consistent with the fact that pyrite (and gold) are not limited to the veins but are present across the shear corridor.

Field observation, petrographic work and SEM imagery of both quartz vein sets and TTG, reveal that gold mineralization in Julie is associated with pyrite formation. Gold has been identified in the form of inclusions (less than 5 μm across) and free gold occurring in pyrite or very close to it, whereas variable amounts of gold were found within the structure of pyrite by LA-ICP-MS analysis. The small gold inclusions in the pyrite probably represent

co-precipitation of gold with this sulfide (e.g., Simon et al., 1999; Reich et al., 2005). The fact that free gold is commonly associated with silver and other metals such as Te, Bi, Pb – i.e., the same elements that were found in the pyrite structure – and that these metals correlate well with silver, suggests that some remobilisation may have taken place, i.e., that some leaching of pyrite could have produced secondary concentrations of gold in association with these metals (cf., Velásquez et al., 2014). This was probably a localized phenomenon, that reflects a continuum of precipitation/dissolution, as fluid saturation with respect to gold changed in the mineralizing system, as suggested by the variable amount of invisible gold found in pyrites. The fact that in C-type veins gold did not occur as inclusions but precipitated mostly in fractures, may indicate that in these veins the remobilisation process was dominant.

Insights on depositional conditions can be obtained from the fluid inclusion study. The data collected and the occurrences of the FIA described above, suggest the presence of a H₂O–CO₂–NaCl fluid that entered the immiscible region for this system. FIAs consisting of Type-1 (L-rich) inclusions probably trapped only the liquid phase, FIAs with Type-2 (variable L–V ratios) inclusions represent heterogeneous trapping of vapor with some liquid, given their high V/L filling, and the FIAs with Type-1 and V-rich Type-2 inclusions represent homogeneous trapping of liquid and vapor phases (e.g., Diamond, 2001). The scatter in Th data for Type-2 inclusions is consistent with this interpretation. It follows that the trapping conditions correspond to the homogenization temperatures of the inclusions that trapped the liquid or the vapor end

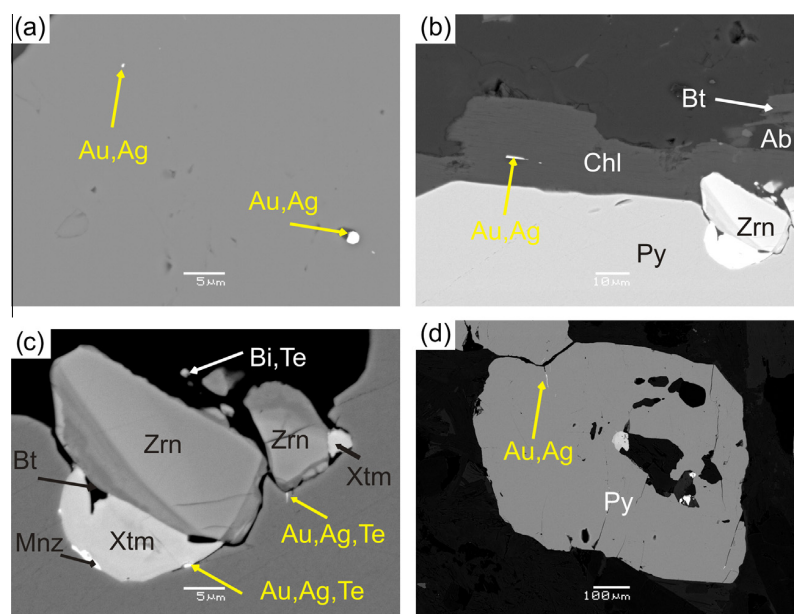


Fig. 12. SEM images of mineralization associated with sulfides. (a) Micron-sized gold inclusions in pyrite. (b) Free gold within chlorite next to pyrite. (a) and (b) are from A-type veins. (c) A close-up of the lower right part of (b) showing gold in association with Ag and Te, on a pyrite edge. Note subhedral zircon, with xenotime (YPO₄), and monazite being partly overgrown by the pyrite. (d) Pyrite grain from a C-type vein showing free gold in fractures. Ab-albite, Au-gold, Ag-Silver, Bt-biotite, Chl-chlorite, Py-pyrite, Mnz-monazite, Xtm-xenotime, Zrn-zircon.

Table 3

LA-ICP-MS measurement on pyrites in the A-type veins. Values in ppm.

Spots	Au	Ag	Sb	Te	Pb	Bi	As	Se	Cd	Ni	Co	Cu	Zn
LOD	0.01	0.01	0.1	0.12	0.1	0.1	0.8	1.4	2.5	0.6	0.2	0.09	0.07
py_1	0.10	0.03	<LOD	0.34	<LOD	0.1	0.8	6.4	<LOD	92.9	50.0	0.09	0.14
py_2	12.78	7.83	<LOD	35.21	2.0	8.0	1.8	7.4	<LOD	327.1	20.0	0.41	0.43
py_3	0.93	2.36	0.1	6.61	2.9	1.1	8.5	15.5	<LOD	88.2	18.2	2.83	0.50
py_4	<LOD	0.62	<LOD	0.69	<LOD	<LOD	1.2	16.1	<LOD	101.2	16.5	0.17	0.86
py_5	<LOD	<LOD	<LOD	0.20	<LOD	<LOD	0.6	7.3	<LOD	235.4	26.8	0.15	0.70
py_6	<LOD	<LOD	<LOD	0.10	<LOD	<LOD	1.3	12.0	<LOD	205.2	6.1	<LOD	0.61
py_7	<LOD	<LOD	<LOD	0.44	<LOD	<LOD	2.1	13.1	<LOD	139.8	93.0	0.11	0.77
py_8	0.05	<LOD	<LOD	0.63	<LOD	0.1	1.4	14.9	<LOD	205.0	49.0	0.19	0.76
py_9	<LOD	<LOD	<LOD	0.43	<LOD	<LOD	2.5	13.6	<LOD	210.5	695.5	0.28	0.84
py_10	0.15	0.05	<LOD	1.83	<LOD	0.2	14.8	10.5	<LOD	260.5	48.8	0.14	0.81
py_11	3.36	1.89	<LOD	8.95	0.4	2.4	9.0	8.1	<LOD	89.3	321.0	0.43	0.91
py_12	0.67	<LOD	0.5	12.76	9.1	7.4	8.4	5.0	<LOD	303.3	105.3	4.88	1.75
py_13	0.09	<LOD	0.1	2.03	0.8	0.4	13.2	4.3	<LOD	798.9	41.4	0.14	0.95
py_14	<LOD	<LOD	<LOD	0.59	0.1	<LOD	11.4	11.9	<LOD	306.2	110.0	0.14	1.09
py_15	<LOD	<LOD	<LOD	0.16	<LOD	<LOD	35.5	13.5	<LOD	234.1	243.7	0.14	0.89

LOD = Limit of detection.

Table 4

LA-ICP-MS measurements on pyrites in the C-type veins. Values are in ppm.

Spots	Au	Ag	Sb	Te	Pb	Bi	As	Se	Cd	Ni	Co	Cu	Zn
LOD	0.01	0.01	0.1	0.12	0.1	0.1	0.8	1.4	2.5	0.6	0.2	0.09	0.07
py_17	0.43	1.29	0.1	6.48	9.0	2.9	16.1	15.4	<LOD	131.8	21.5	1.64	0.82
py_18	0.03	<LOD	<LOD	0.94	0.3	0.8	27.7	8.8	<LOD	360.0	148.9	0.24	1.00
py_19	<LOD	<LOD	<LOD	0.35	0.2	<LOD	5.0	19.1	<LOD	60.3	5.2	0.31	1.07
py_20	<LOD	<LOD	<LOD	0.36	<LOD	0.2	27.3	8.3	<LOD	257.2	1023.5	0.33	1.03
py_21	<LOD	<LOD	<LOD	<LOD	<LOD	<LOD	69.2	5.3	<LOD	261.5	524.3	0.15	1.02
py_22	<LOD	<LOD	<LOD	0.10	<LOD	<LOD	62.9	5.3	<LOD	169.1	268.9	0.15	1.28
py_23	<LOD	<LOD	<LOD	0.07	<LOD	<LOD	13.8	9.7	<LOD	228.2	244.0	0.14	1.19
py_24	<LOD	<LOD	<LOD	0.40	0.2	<LOD	5.6	14.8	<LOD	132.9	1171.8	0.17	0.92
py_25	0.18	0.12	<LOD	1.00	0.1	<LOD	17.5	8.4	<LOD	277.0	418.4	0.17	1.15
py_26	<LOD	<LOD	<LOD	<LOD	<LOD	<LOD	2.4	5.9	<LOD	244.8	590.1	0.19	0.66
py_27	0.18	<LOD	<LOD	0.44	<LOD	0.1	2.0	16.0	<LOD	39.6	1077.1	0.17	0.70
py_28	<LOD	<LOD	<LOD	0.06	<LOD	<LOD	45.5	10.9	<LOD	298.2	794.6	0.18	0.66
py_29	<LOD	<LOD	<LOD	1.00	<LOD	<LOD	323.8	9.1	<LOD	459.7	784.1	0.16	0.78

LOD = Limit of detection.

Table 5

Correlation coefficients of Au and other trace elements in pyrites from the A-type veins. Bold face denotes correlations discussed in the text.

	Au	Ag	Sb	Te	Pb	Bi	As	Se	Cd	Ni	Co	Cu	Zn
Au	1												
Ag	0.75	1											
Sb	-0.02	0.1	1										
Te	0.58	0.97	0.17	1									
Pb	0.33	0.85	0.37	0.95	1								
Bi	0.37	0.88	0.16	0.97	0.97	1							
As	-0.19	-0.22	0.05	-0.19	-0.15	-0.17	1						
Se	-0.18	0.12	-0.35	0.13	0.14	0.2	-0.01	1					
Cd	-0.12	-0.05	0.06	-0.11	-0.07	-0.11	-0.07	0.36	1				
Ni	-0.01	-0.2	0.16	-0.19	-0.19	-0.22	0.28	-0.56	-0.18	1			
Co	-0.13	-0.2	-0.11	-0.18	-0.17	-0.16	0.44	0.1	0.53	-0.08	1		
Cu	-0.02	0	0.93	0	0.19	-0.03	0.04	-0.21	0.27	-0.01	-0.06	1	
Zn	-0.26	-0.19	0.66	-0.07	0.12	-0.03	0.3	-0.17	-0.14	0.31	0.2	0.55	1

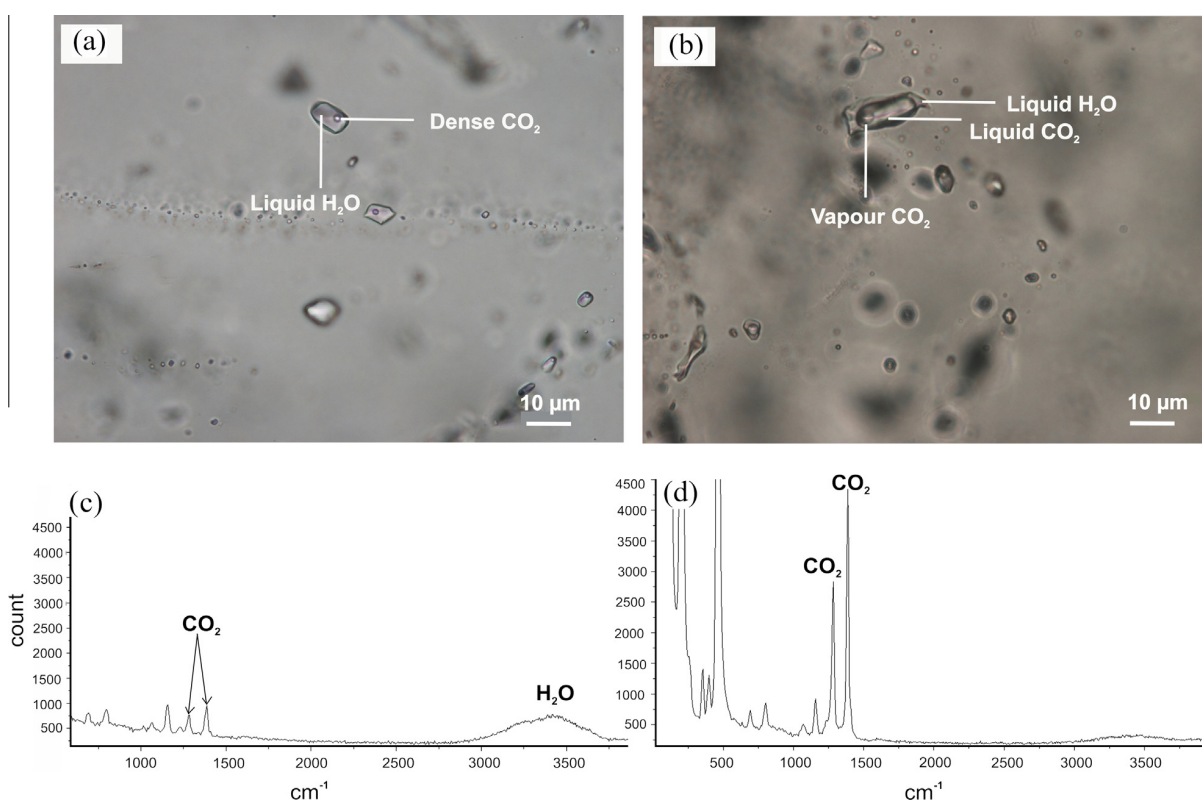


Fig. 13. (a) and (b) are photomicrographs, taken at room temperature, showing representative examples of fluid inclusions from mineralized quartz veins at Julie. (a) An isolated aqueous-rich (Type-1) inclusions near a pseudosecondary plane of similar fluid inclusions; (b) coexisting Type-1 (small inclusion on top of the image) and carbonic-rich (Type-2) fluid inclusions. (c, d) Raman spectra showing signals for the carbonic phase in (c) a Type-1 and (d) a Type-2 fluid inclusion; peaks for H₂O and CO₂ were obtained from both inclusion types.

members (e.g., Wilkinson, 2001). Given the difficulties in measuring Th in V-filled inclusions, we estimate Th of Type-1 inclusions to represent the trapping conditions (Diamond, 2003), at ~220 °C and a pressure of <1 kbar (estimated for liquid–vapor coexistence at the average composition of the fluid inclusions, using ISOC of Bakker (2003)). This temperature is quite low and although could correspond to the low-temperature end of typical orogenic gold-related systems (e.g., Goldfarb et al., 2005; Saunders et al., 2014, and refs therein), it most likely reflects conditions recorded at hydrostatic regimes during pressure drops that are characteristic of these systems (e.g., Sibson and Scott, 1998; Robert et al., 1995). Such pressure fluctuations are excellent mechanisms for precipitating gold and other metals, as well as quartz

(Kouzmanov and Pokrovski, 2012). It is likely that the fluid had a metamorphic rather than an orthomagmatic source, given its relatively low salinity and high content of CO₂. Also, there are no late-stage intrusions in the sector that could have acted as fluid source. The elevated values of Ni and Co measured in pyrite is consistent with a non-plutonic source of the fluid.

The structural history associated with gold mineralization documented in the Julie deposit is different from that known in southern Ghana, where gold mineralization is mainly related to late, brittle–ductile re-activation of faults with an early history of reverse movement with sinistral characteristics compatible to the structural timing of a single mineralizing event (Allibone et al., 2004; Feybesse et al., 2006). Evidence from the Julie deposit shows

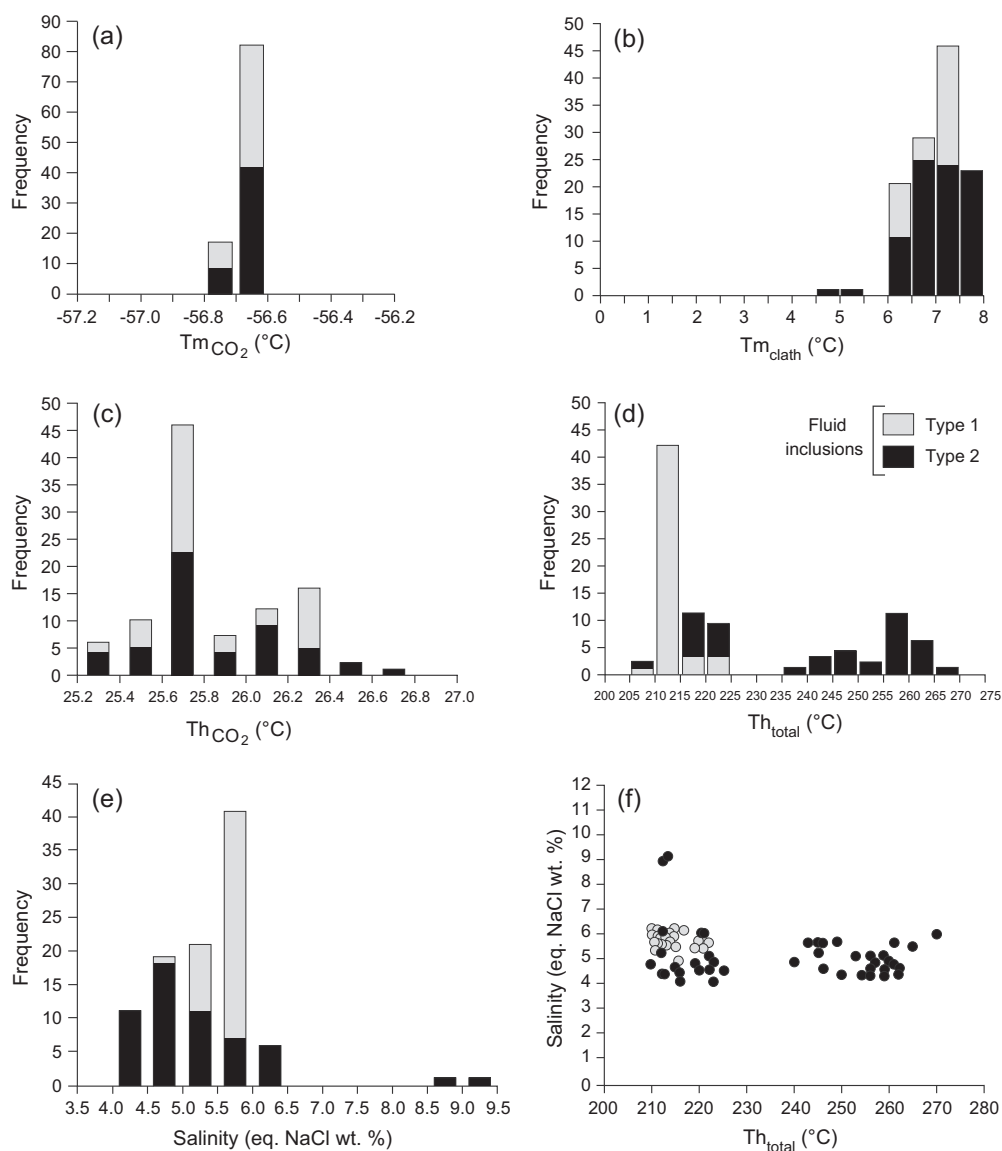


Fig. 14. Diagrams showing microthermometric data for the aqueous-carbonic Type-1 and Type-2 fluid inclusions in mineralized A-type veins. (a) Melting temperatures of CO₂; (b) clathrate dissolution temperatures; (c) homogenization temperatures of CO₂; (d) total homogenization temperatures; (e) calculated salinities. (f) A plot of total homogenization temperature vs salinity data for all fluid inclusions in the mineralized A-type quartz veins.

that gold mineralization is associated with an early dextral ductile shear zone with reverse movement. Another difference consists in the fluid composition. A substantial amount of fluid inclusion work has been done in Ghana, and most of it deals with belts in the south of the country (Schwartz et al., 1992; Klemm et al., 1993, 1996; Oberthür et al., 1994; Schmidt-Mumm et al., 1997; Yao et al., 2001). These show that ore forming fluids are usually CO₂ dominated, with an abundance of CO₂-N₂ ± CH₄ fluid inclusions and only minor H₂O-NaCl and H₂O-CO₂-NaCl fluid inclusions. Similarly to the south of Ghana, distinct carbonic and aqueous-carbonic fluid types, with a strong predominance for the former, were also documented from various deposits elsewhere in the Birimian of West Africa, e.g., in Burkina Faso, where they were rarely found to coexist in the same deposit (Beziat et al., 2008, and references therein), in Mali (Loulo district; Lawrence et al., 2013) and Ivory Coast (Coulibaly et al., 2008). Conversely, the fluids found in gold-mineralized samples at Julie consist exclusively of aqueous-carbonic fluids (H₂O-CO₂-NaCl), and CH₄ was not

identified. To account for the different fluid types in a similar context, most of the authors cited above invoke either water leakage subsequent to quartz deformation during decompression, implying that the ore-bearing fluid originally consisted of a homogeneous mixture of H₂O and CO₂, or that both fluid phases were unmixed before trapping. In the Julie deposit, both types of fluids coexist and fluid inclusion textural relationships and data infer that two separate fluid phases (CO₂ and H₂O) were present at the time of trapping.

The new structural, geochemical and mineralization data presented for the Julie deposit indicate that the mineralization in NW Ghana is different from what has been documented in southern Ghana.

- Gold in NW Ghana, exemplified by the Julie deposit, is mainly associated with a ductile–brittle deformation (D₁) event, while in southern Ghana it is associated with a deformational event characterized by a late brittle event, usually along broad shear

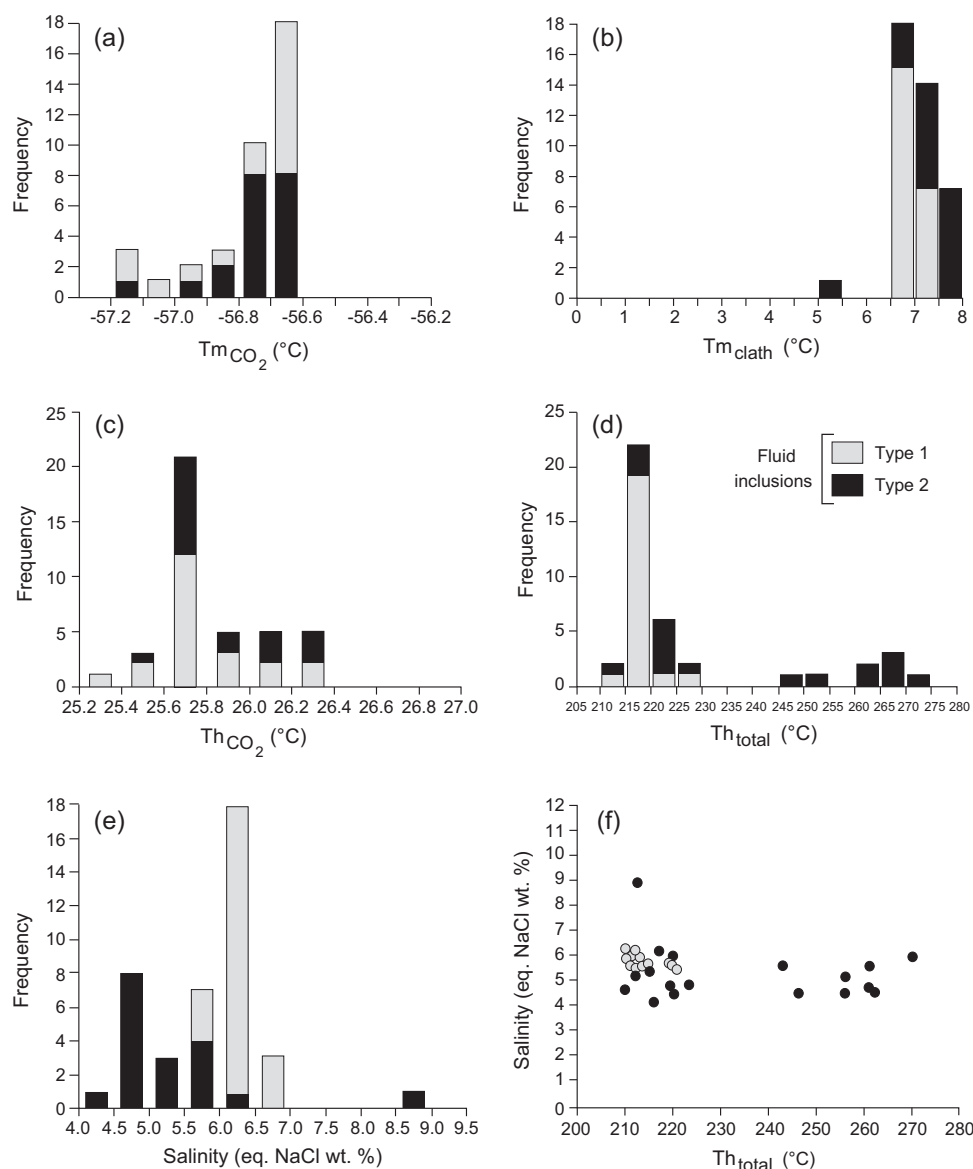


Fig. 15. Diagrams showing microthermometric data for the aqueous-carbonic Type-1 and Type-2 fluid inclusions in mineralized C-type veins. (a) Melting temperatures of CO_2 ; (b) clathrate dissolution temperatures; (c) homogenization temperatures of CO_2 ; (d) total homogenization temperatures; (e) calculated salinities. (f) A plot of total homogenization temperature vs salinity data for all fluid inclusions in the mineralized C-type quartz veins.

zones (Allibone et al., 2004). This suggests different timing relationships between gold formation and deformation in north-western from southern Ghana. The only exception is the Wassa gold deposit where recent investigations show that gold is also associated to D_1 (Parra-Avila et al., 2015; Perrouy et al., in press). Together with the results from the present study, these very recent data are the first to propose early-stage Birimian mineralization that could correspond to the source of later paleo-placer deposits along the Ashanti Belt, such as Tarkwa and Damang.

- The Julie deposit is a rare case of granitoid (TTG)-hosted mineralization together with the Ayanfuri (Ashanti Belt) granite hosted Au-mineralization where similar fluid inclusion assemblages have been identified (Schmidt-Mumm et al., 1997). In SW Ghana most deposits are related to NE–SW oriented shear zones (Oubuasi, Pampe, Bogoso, Benzo, etc., cf., Perrouy et al., in press, and references therein) that have been reactivated.

The Julie deposit is contained within D_1 E–W oriented structures, compared to SW Ghana where D_2 – D_3 NE–SW oriented structures dominate, or SW Burkina Faso where D_2 – D_3 structures are N–S oriented (Baratoux et al., 2011).

Acknowledgements

Azumah Resources Limited the owners of the Julie deposit are particularly thanked for giving the permission to publish this paper and for financing the fieldwork. We wish to gratefully acknowledge AMIRA International and the industry sponsors, including AusAid and the ARC Linkage Project LP110100667, for their support through the WAXI project (P934A). POA would like to thank Nick Franey and Stephen Stone for the continual support throughout the program. Special thanks go to P.M. Nude, Sylvain Block, Scriven Nyarko, Eugene Adubofour-Gyawu, Andrew Chubb and Jerome

Ganne for their useful geological discussion on the Julie deposit. The author wants to thank Andrew Chubb for his input during the early drafting stages of this manuscript, and to Michel Dubois and Cyril Durand for their thorough reviews which contributed to enhance the quality of this work.

References

- Agyei Duodu, J., Loh, G.K., Boamah, K.O., Baba, M., Hirdes, W., Toloczyki, M., Davis, D.W., 2009. Geological map of Ghana 1:1000000. Geological Survey Department of Ghana (GSD).
- Allibone, A., Teasdale, J., Cameron, G., Etheridge, M., Uttley, P., Soboh, A., Appiah-Kubi, J., Adanu, A., Arthur, R., Mamphey, J., Odoom, B., Zuta, J., Tsikata, A., Pataye, F., Famiyeh, S., Lamb, E., 2002. Timing and structural controls on gold mineralization at the Bogoso Gold Mine, Ghana, West Africa. *Econ. Geol.* 97, 949–969.
- Allibone, A., Hayden, P., Cameron, G., Duku, F., 2004. Paleoproterozoic gold deposits hosted by albite- and carbonate-altered tonalite in the Chirano district, Ghana, West Africa. *Econ. Geol.* 99, 479–497.
- Azumah resources Limited, 2012. Julie update. Unpublished internal report.
- Bakker, R.J., 2003. Package FLUIDS 1. Computer programs for analysis of fluid inclusion data and for modelling bulk fluid properties. *Chem. Geol.* 194, 3–23.
- Baratoux, L., Metelka, V., Naba, S., Jessell, M.W., Grégoire, M., Ganne, J., 2011. Juvenile Paleoproterozoic crust evolution during the Eburnean orogeny (2.2–2.0 Ga), Western Burkina Faso. *Precambrian Res.* 191, 18–45.
- Barker, F., 1979. Trondjemite: definition, environment and hypotheses of origin. In: Barker (Ed.), *Trondjemites, Dacites, and Related Rocks*, first ed. Elsevier, New York, pp. 1–12.
- Barritt, S.D., Kuma, J.S., 1998. Constrained gravity models and structural evolution of the Ashanti Belt, Southwest Ghana. *J. Earth Sci.* 26, 539–550.
- Beziat, D., Dubois, M., Debat, P., Nikiema, S., Salvi, S., Tollon, F., 2008. Gold metallogeny in the Birimian craton of Burkina Faso (West Africa). *J. Afr. Earth Sci.* 50, 215–233.
- Blenkinsop, T.G., Schmidt-Mumm, A., Kumi, R., Sangmor, S., 1994. Structural geology of the Ashanti Gold Mine. *Geol. Jahrb.*, D 100, 131–153.
- Block, S., Ganne, J., Baratoux, L., Zeh, L., Parra-Avila, A., Jessell, M., Ailleres, L., Siebenaller, L., 2015. Petrological and geochronological constraints on lower crust exhumation during Paleoproterozoic (Eburnean) orogeny, NW Ghana, West African Craton. *J. Metamorph. Geol.*, 33, 463–494 (in press), <http://dx.doi.org/10.1111/jmg.12129>.
- Borisova, A.Y., Freydir, R., Polvé, M., Jochum, K.P., Candaudap, F., 2010. Multi-elemental analysis of ATHO-G rhyolitic glass (MPI-DING reference material) by femtosecond and nanosecond LA-ICP-MS: evidence for significant heterogeneity of B, V, Zn, Mo, Sn, Sb, Cs, W, Pt, and Pb at the millimetre scale. *Geostand. Geoanal. Res.* 34, 245–255.
- Chappell, B.W., White, A.J.R., 1974. Two contrasting granite types. *Pac. Geol.* 8, 173–174.
- Coulibaly, Y., Boiron, M.C., Cathelineau, M., Kouamelan, A.N., 2008. Fluid immiscibility and gold deposition in the Birimian quartz veins of the Angovia deposit (Yaouré, Ivory Coast). *J. Afr. Earth Sci.* 50, 234–254.
- de Kock, G.S., Armstrong, R.A., Siegfried, H.P., Thomas, E., 2011. Geochronology of the Birim Supergroup of the West African craton in the Wa-Bole region of Westcentral Ghana: implications for the stratigraphic framework. *J. Afr. Earth Sci.* 59, 291–294.
- Diamond, L.W., 2001. Review of the systematics of CO₂–H₂O fluid inclusions. *Lithos* 55, 69–99.
- Diamond, L.W., 2003. Introduction to gas-bearing aqueous fluid inclusions. In: Iain Samson, Alan Anderson, Dan Marshall (Eds.), *Fluid inclusions, analysis and interpretation*. Mineralogical Association of Canada Short Course Series, vol. 32. Mineralogical Association of Canada, 374 p.
- Dioh, E., Béziat, D., Debat, P., Grégoire, M., Ngom, P.M., 2006. Diversity of the Paleoproterozoic granitoids of the Kédougou inlier (eastern Sénégal): petrographical and geochemical constraints. *J. Afr. Earth Sci.* 44, 351–371.
- Doumbia, S., Pouclet, A., Kouamelan, A., Peucat, J.J., Vidal, M., Delor, C., 1998. Petrogenesis of juvenile-type Birimian (Paleoproterozoic) granitoids in Central Côte-d'Ivoire West Africa: geochemistry and geochronology. *Precambrian Res.* 87, 33–63.
- Eisenlohr, B.N., Hirdes, W., 1992. The structural development of the early Proterozoic Birimian and Tarkwaian rocks of southwest Ghana, West Africa. *J. Earth Sci.* 14, 313–325.
- Feybesse, J.-L., Billa, M., Guerrot, C., Duguey, E., Lescuyer, J., Milési, J.P., Bouchot, 2006. The Paleoproterozoic Ghanaian province. Geodynamic model and ore controls, including regional stress modeling. *Precambrian Res.* 149, 149–196.
- Frost, B.R., Frost, C.D., 2008. A geochemical classification for feldspathic igneous rocks. *J. Petrol.* 49, 1955–1969.
- Frost, B.R., Barnes, G.C., Collins, W.J., Arculus, R.J., Ellis, D.J., Frost, C.D., 2001. A geochemical classification of granitic rocks. *J. Petrol.* 42, 2033–2048.
- Garofalo, P.S., 2004. Mass transfer during gold precipitation within a vertically extensive vein network (Sigma deposit –Abitibi greenstone belt – Canada). Part I. Patterns of hydrothermal alteration haloes. *Eur. J. Miner.* 16, 753–760.
- Gasquet, D., Barbey, P., Adou, M., Paquette, J.L., 2003. Structure Sr–Nd isotope geochemistry and zircon U–Pb geochronology of the granitoids of the Dabakala area (Côte d'Ivoire): evidence for a 2.3 Ga crustal growth event in the Paleoproterozoic of West Africa? *Precambrian Res.* 127, 329–354.
- Goldfarb, R.J., Baker, T., Dubé, B., Groves, D.I., Hart, J.R.C., Gosselin, P., 2005. Distribution, character and genesis of gold deposit in metamorphic terranes. *Economic geology*, 100th Anniversary volume, pp. 407–450.
- Goldstein, R.H., Reynolds, T.J., 1994. Systematics of fluid inclusions in diagenetic minerals. *Soc. Sediment. Geol. Short Course* 31, 199.
- Grant, J.A., 1986. The isocon diagram—a simple solution to Gresens' equation for metasomatic alteration. *Econ. Geol.* 81, 1976–1982.
- Griffis, R.J., Barning, K., Agezo, F.L., Akosah, F.K., 2002. Gold Deposits of Ghana. Minerals Commission, Accra, Ghana, p. 438.
- Hammond, N.Q., Tabata, H., 1997. Characteristics of ore minerals associated with gold at the Prestea mine, Ghana. *Mineral. Mag.* 61, 879–894.
- Harcouët, V., Guillour-Frottier, L., Bonneville, A., Bouchout, V., Milesi, J.-P., 2007. Geological and thermal condition before the major paleoproterozoic gold mineralization, as inferred from improved thermal modelling. *Precambrian Res.* 154, 71–87.
- Holland, T., Blundy, J., 1994. Non-ideal interactions in calcic amphiboles and their bearing on amphibole–plagioclase thermometry. *Contrib. Miner. Petrol.* 116, 433–447.
- Hünken, U., Klemd, R., Olesch, M., 1994. Fluid inclusions in quartz-pebbles of Proterozoic Tarkwaian conglomerates in Ghana. *Geol. Jahrb.*, D 100, 313–341.
- John, T., Klemd, R., Hirdes, W., Loh, G., 1999. The metamorphic evolution of the Paleoproterozoic (Birimian) volcanic Ashanti belt (Ghana, West Africa).
- Junner, N.R., 1932. Geology of the Obuasi goldfield. *Gold Coast Geol. Surv., Mem.* 2, 1–71.
- Junner, N.R., 1935. Gold in the gold coast. *Gold Coast Geol. Surv., Mem.* 4, 1–67.
- Junner, N.R., 1940. Geology of the Gold Coast and western Togoland (with revised geological map). *Gold Coast Geol. Surv. Bull.* 11, 1–40.
- Kesse, G., 1985. The Mineral and Rocks Resources of Ghana. A.A. Balkema, Rotterdam, Boston, p. 609.
- Klemd, R., Hirdes, W., Olesch, M., Oberthur, T., 1993. Fluid inclusions in quartz pebbles of gold bearing Tarkwaian conglomerates as a guide to their provenance area. *Miner. Deposita* 28, 334–343.
- Klemd, R., Hünken, U., Olesch, M., 1996. Fluid composition and source of early Proterozoic lode gold deposits of the Birimian volcanic belt, West Africa. *Int. Geol. Rev.* 38, 22–32.
- Kouzmanov, K., Pokrovski, G.S., 2012. Hydrothermal controls on metal distribution in Cu (–Au–Mo) porphyry systems. *Soc. Econ. Geol., Spec. Publ.* 16, 573–618.
- Lawrence, D.M., Treloar, P.J., Rankin, A.H., Boyce, A., Harbidge, P., 2013. A fluid inclusion and stable isotope study at the Loulo mining district, Mali, West Africa: implications for multifluid sources in the generation of orogenic gold deposits. *Econ. Geol.* 108, 229–257.
- Leube, A., Hirdes, W., Mauer, R., Kesse, G.O., 1990. The early Proterozoic Birimian Supergroup of Ghana and some aspects of its associated gold mineralization. *Precambrian Res.* 46–165.
- Lopez-Moro, F.J., 2012. EASYGRESGRANT—A Microsoft Excel spreadsheet to quantify volume changes and to perform mass-balance modeling in metamorphic systems. *Comput. Geosci.* 39, 191–196.
- Lorand, J.-P., Alard, O., 2011. Pyrite tracks assimilation of crustal sulfur in Pyrenean peridotites. *Mineral. Petrol.* 101, 115–128.
- Milési, J.P., Feybesse, J.L., Ledru, P., Dommangeat, A., Ouedraogo, M.F., Marcoux, E., Prost, A., Vinchon, C., Sylvain, J.P., Johan, V., Tegye, M., Calvez, J.Y., Lagny, Ph., 1989. Mineralisations aurifères de l'Afrique de l'ouest, leurs relations avec l'évolution litho-structurale au Protérozoïque inférieur. *Carte géologique au 1/2.000.000. Chronique Rech. Minière* 497, 3–98.
- Milési, J.-P., Ledru, P., Feybesse, J.-L., Dommangeat, A., Marcoux, E., 1992. Early Proterozoic ore deposits and tectonics of the Birimian Orogenic belt, West Africa. *Precambrian Res.* 58, 305–344.
- Mücke, A., Dzigidji-Adjimah, K., 1994. Ore textures and parageneses of the Prestea and Obuasi gold deposit in the Ashanti Belt of Ghana: an ore microscopy study. In *Metallogenesis of Selected Gold Deposits in Africa* (T. Oberthur, edition). *Geol. Jahrb. Reihe* 100, 99–167.
- Mumin, A.H., Fleet, M.E., 1995. Evolution of gold mineralization in the Ashanti Gold Belt, Ghana. Evidence from carbonate compositions and parageneses. *Mineral. Petrol.* 55, 265–280.
- Oberthür, T., Vetter, U., Schmidt-Mumm, A., Weiser, T., Amanor, J.A., Gyapong, W.A., Kumi, R., Blenkinsop, T.G., 1994. The Ashanti Gold Mine at Obuasi, Ghana: mineralogical, geochemical, stable isotope and fluid inclusion studies on the metallogenesis of the deposit. *Geol. Jahrb.*, D 100, 31–129.
- Oberthür, T., Schmidt-Mumm, A., Vetter, U., Simon, K., Amanor, J.A., 1996. Gold mineralization in the Ashanti Belt of Ghana. Genetic constraints of the stable isotope geochemistry. *Econ. Geol.* 91, 289–301.
- Oberthür, T., Weiser, T., Amanor, J.A., Chrystoullis, S.L., 1997. Mineralogical siting and distribution of gold in quartz veins and sulfide ores of the Ashanti mine and other deposits in the Ashanti belt of Ghana: genetic implications. *Miner. Deposita* 32, 2–15.
- Oberthür, T., Vetter, U., Davis, D.W., Amanor, J.A., 1998. Age constraints on gold mineralization and Paleoproterozoic crustal evolution in the Ashanti belt of Southern Ghana. *Precambrian Res.* 89, 129–143.
- Parra-Avila, L.A., Bourassa, Y., Miller, J., Perrouty, S., Fiorentini, M.L., McCuaig, T.C., 2015. Age constraints of the Wassau and Benso mesothermal gold deposits, Ashanti Belt, Ghana, West Africa. *J. Afr. Earth Sci.* <http://dx.doi.org/10.1016/j.jafrearsci.2015.05.017>, in press.
- Pearce, J.A., Harris, N.B.W., Tindle, A.G., 1984. Trace element discrimination diagrams for the tectonic interpretation of granitic rocks. *J. Petrol.* 25, 956–983.
- Perrouty, S., Ailleres, L., Jessell, M.W., Baratoux, L., Bourassa, Y., Crawford, B., 2012. Revised Eburnean geodynamic evolution of the gold-rich southern Ashanti

- Belt, Ghana, with new field and geophysical evidence of the pre-Tarkwaian deformations. *Precambrian Res.* 204–205, 12–39.
- Perrouty, S., Jessell, M.W., Bourassa, Y., Miller, J., Apau, D., Siebenaller, L., Velasquez, G., Baratoux, L., Aillères, L., Didier, B., Salvi, S., 2015. The Wassa mine: a poly-deformed orogenic gold system in southwest Ghana – implications for regional exploration. *J. Afr. Earth Sci.* (in press), <http://dx.doi.org/10.1016/j.jafrearsci.2015.03.003>.
- Plyusnina, L.P., 1982. Geothermometry and geobarometry of plagioclase–hornblende bearing assemblages. *Contrib. Miner. Petrol.* 80, 140–146.
- Reich, M., Kesler, S.E., Utsunomiya, S., Palenik, C.S., Chryssoulis, S.L., Ewing, R.C., 2005. Solubility of gold in arsenian pyrite. *Geochim. Cosmochim. Acta* 69, 2781–2796.
- Robert, F., Brown, A.C., 1986. Archean gold-bearing quartz veins at the Sigma mine, Abitibi Greenstone belt: part II. Vein paragenesis and hydrothermal alteration. *Econ. Geol.* 79, 393–399.
- Robert, F., Boullier, A.-M., Firdaus, K., 1995. Gold-quartz veins in metamorphic terranes and their bearing on the role of fluids in faulting. *J. Geophys. Res.: Solid Earth* 100, 12861–12879.
- Roedder, E., 1984. Fluid inclusions. *Rev. Mineral.* 12, 1–664.
- Saunders, J.A., Hofstra, A.H., Goldfarb, R.J., Reed, M.H., 2014. Geochemistry of hydrothermal gold deposits. In: *Treatise on Geochemistry*, second ed. Elsevier, pp. 386–424.
- Schmidt-Mumm, A., Oberthür, T., Vetter, U., Blenkinsop, T.G., 1997. High CO₂ content of fluid inclusions in gold mineralisations in the Ashanti Belt, Ghana: a new category of ore forming fluids? *Miner. Deposita* 32, 107–118.
- Schwartz, M.O., Oberthür, T., Amanor, J., Gyapong, W.A., 1992. Fluid inclusion re-equilibration and P-T-X constraints on fluid evolution in the Ashanti gold deposit, Ghana. *Eur. J. Mineral.* 4, 1017–1103.
- Shepherd, T.J., Ranbin, A.H., Alderton, D.H.M., 1985. *A Practical Guide to Fluid Inclusion Studies*. Blackie, Glasgow, p. 239.
- Sibson, R.H., Scott, J., 1998. Stress/fault controls on the containment and release of overpressured fluids. Examples from gold-quartz vein systems in Juneau, Alaska; Victoria, Australia and Otago, New Zealand. *Ore Geol. Rev.* 13 (1–5), 293–306.
- Siebenaller, L., Boiron, M.-C., Vanderhaeghe, O., Hibsich, C., Jessell, M.W., André-Mayer, A.-S., France-Lanord, C., Photiades, A., 2013. Fluid record of rock exhumation across the brittle–ductile transition during formation of a Metamorphic Core Complex (Naxos Island, Cyclades, Greece). *J. Metamorph. Geol.* 31, 313–338.
- Simon, G., Huang, H., Penner-Hahn, J.E., Kesler, S.E., Kao, L., 1999. Oxidation state of gold and arsenic in gold-bearing arsenian pyrite. *Am. Mineral.* 84, 1071–1079.
- Spear, F.S., 1980. NaSi–CaAl exchange equilibria between plagioclase and amphibole, an empirical model. *Contrib. Miner. Petrol.* 72, 33–41.
- Sylvester, P.J., Cabri, L.J., Tubrett, M.N., McMahon, G., Laflamme, J.H.G., Peregoedova, A., 2005. Synthesis and evaluation of a fused pyrrhotite standard reference material for platinum group element and gold analysis by laser ablation-ICPMS. In: Törmänen, T.O., Alapieti, T.T. (Eds.), *10th International Platinum Symposium*. Oulu, Geological Survey of Finland, Extended Abstracts, pp. 16–20.
- Taylor, P.N., Moorbath, S., Leube, A., Hirdes, W., 1992. Early Proterozoic crustal evolution in the Birimian of Ghana: constraints from geochronology and isotope geochemistry. *Precambrian Res.* 56, 97–111.
- Van Achterbergh, E., Ryan, C.G., Griffin, W.L., 2001. Data reduction software for LA-ICP-MS. *Miner. Assoc. Can., Short Course Ser.* 29, 239–243.
- Velásquez, G., Béziat, D., Salvi, S., Siebenaller, L., Borisova, A.Y., Pokrovski, G.B., de Parseval, Ph., 2014. Formation and deformation of pyrite and implications for gold mineralization in the El Callao District, Venezuela. *Econ. Geol.* 109, 457–486.
- Velásquez, G., Borisova, A.Y., Salvi, S., Béziat, D., 2012. In situ determination of Au and Cu in natural pyrite by near-infrared femtosecond laser ablation-inductively coupled plasma-quadrupole mass spectrometry: no evidence for matrix effects. *Geostand. Geoanal. Res.* 36, 315–324.
- Wilkinson, J.J., 2001. Fluid inclusions in ore deposits. *Lithos* 55, 229–272.
- Yao, Y., Robb, L.J., 2000. Gold mineralization in Palaeoproterozoic granitoids at Obuasi, Ashanti region, Ghana: ore geology, geochemistry and fluid characteristics. *S. Afr. J. Geol.* 103, 255–278.
- Yao, Y., Murphy, P.J., Robb, L.J., 2001. Fluid characteristics of Granitoid-Hosted gold deposits in the Birimian Terrane of Ghana: a fluid inclusion microthermometric and Raman spectroscopic study. *Econ. Geol.* 96, 1611–1643.

3. 2 Shear related gold mineralization in Northwest Ghana: The Julie deposit

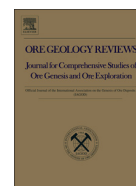
The Julie deposit is currently the largest gold prospect in NW Ghana. It is hosted in sheared granitoids of TTG composition of the Paleoproterozoic Julie greenstone belt. The main mineralization consists of a corridor of gold-bearing quartz veins forming a network of a few tens of metres in thickness, trending E–W and dipping 30–60° N, contained within the main shear zone that affects these rocks. The core of this vein corridor is altered by sericite, quartz, ankerite, calcite, tourmaline and pyrite, and is surrounded by an outer halo consisting of albite, sericite, calcite, chlorite, pyrite and rutile. A second set of veins, conjugate to the first set, occurs in the area. These veins have alteration halos with a similar mineralogy as the main corridor, however, their extent, as well as the size of the mineralization, is less important. In the main corridor, gold forms micron-sized grains that occur in pyrite as inclusions, on its edges, and in fractures crosscutting it. Silver, tellurium, bismuth, copper and lead commonly accompany the gold. Pyrite occurs disseminated in the veins and in the surrounding rocks. Up to several ppm Au occurs in the structure of pyrite from the main mineralization.



ELSEVIER

Contents lists available at ScienceDirect

Ore Geology Reviews

journal homepage: www.elsevier.com/locate/oregeorev

Shear-related gold mineralization in Northwest Ghana: The Julie deposit

Stefano Salvi ^{a,*}, Prince Ofori Amponsah ^{a,b}, Luc Siebenaller ^a, Didier Béziat ^a, Lenka Baratoux ^{a,c}, Mark Jessell ^d

^a Université de Toulouse, CNRS, Géosciences Environnement Toulouse, Institut de Recherche pour le Développement, Observatoire Midi-Pyrénées, 14 Av. Edouard Belin, F-31400 Toulouse, France

^b Azumah Resources Ghana limited, PMB CT452, Cantonments, Accra, Ghana

^c IFAN Cheikh Anta Diop, Dakar, Senegal

^d Centre for Exploration Targeting, School of Earth and Environment, The University of Western Australia, 35 Stirling Highway, Crawley, WA 6009, Australia

ARTICLE INFO

Article history:

Received 18 May 2015

Received in revised form 3 August 2015

Accepted 15 August 2015

Available online xxxx

Keywords:

Orogenic gold

West Africa

Gold in pyrite

Ghana

ABSTRACT

The Julie deposit is currently the largest gold prospect in NW Ghana. It is hosted in sheared granitoids of TTG composition of the Paleoproterozoic Julie greenstone belt. The main mineralization consists of a corridor of gold-bearing quartz veins forming a network of a few tens of metres in thickness, trending E–W and dipping 30–60° N, contained within the main shear zone that affects these rocks. The core of this vein corridor is altered by sericite, quartz, ankerite, calcite, tourmaline and pyrite, and is surrounded by an outer halo consisting of albite, sericite, calcite, chlorite, pyrite and rutile. A second set of veins, conjugate to the first set, occurs in the area. These veins have alteration halos with a similar mineralogy as the main corridor, however, their extent, as well as the size of the mineralization, is less important. In the main corridor, gold forms micron-sized grains that occur in pyrite as inclusions, on its edges, and in fractures crosscutting it. Silver, tellurium, bismuth, copper and lead commonly accompany the gold. Pyrite occurs disseminated in the veins and in the surrounding rocks. Up to several ppm Au occurs in the structure of pyrite from the main mineralization.

© 2015 Published by Elsevier B.V.

1. Introduction and exploration history

In the Birimian terranes of Southern Ghana, commercial gold exploration and exploitation have been active since the early 1900s, notably with the development of world-class deposits in the Ashanti and Sefwi belts, which have received extensive attention in the literature (e.g., Junner, 1932; Milési et al., 1989; Klemd et al., 1996; Allibone et al., 2002; Feybesse et al., 2006; Perrouty et al., 2012, 2015; White et al., 2015; Amponsah et al., in press). Conversely, very little is known of the Birimian mineralization of NW Ghana (Fig. 1), where alluvial and bedrock indications of gold have only been reported since the early 1960s. Nevertheless, it is now recognized that this part of the country hosts an important gold-producing area, known as the Wa-East gold district. Numerous gold camps occur in this district, the most important of which is the Julie deposit. Other examples include Collette, Kjersti, Julie West (Fig. 2), plus Kandia, Baayiri and Danyawu, which lie just outside the area covered by the map in Fig. 2.

The first discoveries of mineralization in this part of Ghana are attributed to the Gold Coast Geological Survey (Griffis et al., 2002). Survey geologists mapped the area and outlined prospects in the Wa-Lawra greenstone belt during the early 1960s, in the adjacent Koudougou-Tumu granitoid domain and in the Julie greenstone belt. A Russian

geological team carried out additional prospecting and geological mapping, also in the 1960s. However, it was not until the 1990s that systematic exploration activities started. Kenor Corporation held the first prospecting licence for the Julie deposit, from September 1996 to May 1999, which was then taken over by Crew Gold Corporation who detained it until February 2010. These companies focussed their work mainly on target generational prospecting, which included interpreting Landsat satellite and airborne geophysical data, geological mapping, and geochemical sampling (mainly soil, grab and auger sampling methods). Surface targets generated by these first-pass geological and geochemical surveying methods were tested further to top of bedrock by rotary air-blast (RAB) and air-core (AC) drilling. From December 2004 to May 2005 a total of about 4815 m of reverse circulation (RC) core were drilled, to assess bedrock mineralization. Crew Gold Corporation identified 312,000 oz (8.8 t) of gold (grading at 2.9 g/t) and estimated mineralization to extend to depths of over 30 m along a 3.5 km strike length (Azumah Resources Limited, 2012). Further exploration was carried out by Azumah Resources Limited in 2006 and beyond, who discovered 834,000 oz (23.6 t) of measured and indicated gold (at 1.53 g/t), with a proven reserve of 202,000 oz (5.7 t) (at 2.84 g/t) in the Julie deposit (Table 1). Azumah acquired the prospecting licence in February 2012. Currently, they have drilled some 43,700 m, to establish trend and continuity of the mineralization first detected by Kenor. In 2013, 2.21 Mt of indicated resources was estimated, making Julie the largest gold resource in NW Ghana.

* Corresponding author.

E-mail address: stefano.salvi@get.obs-mip.fr (S. Salvi).

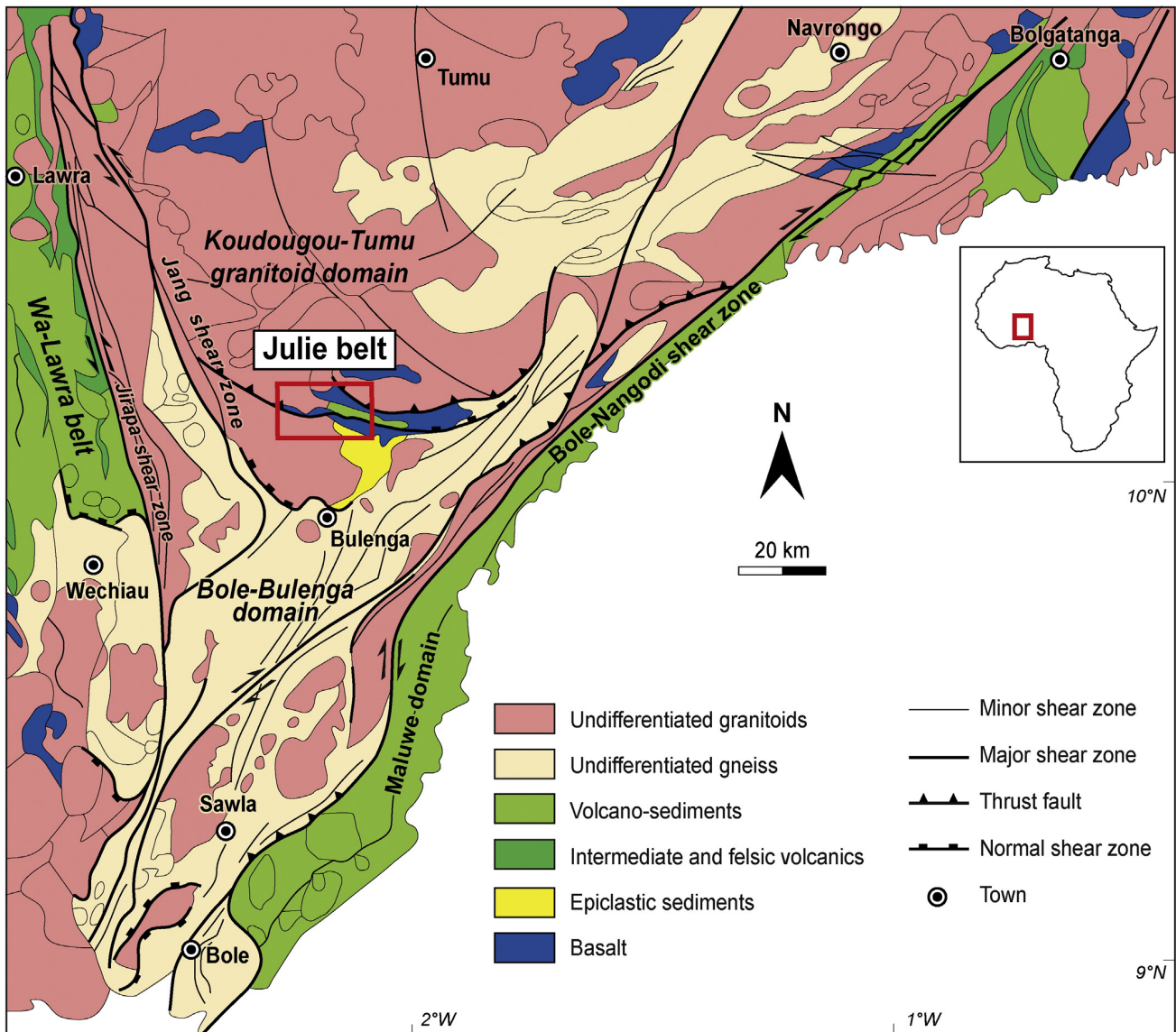


Fig. 1. Regional litho-structural map of Precambrian terranes in NW Ghana (modified after Block et al., 2015), showing the geological context of the Julie belt. The red inset localises the study area. (For interpretation of the references to colour in this figure legend, the reader is referred to the web version of this article.)

2. Regional geological overview

Northwest Ghana lies on the eastern edge of the Paleoproterozoic Birimian terrane of the West African Craton (WAC). The Wa-East gold district occurs within the Julie greenstone belt, an E–W trending structure bounded to the east by the Bole–Nangodi greenstone belt, to the south by the Bole–Bulenga domain, to the west by the Wa–Lawra greenstone belt and to the north by the Koudougou–Tumu granitoid domain (Fig. 1). The Koudougou–Tumu granitoid domain is composed of tonalite–trondhjemite–granodiorite (TTG) intrusions formed between 2155 and 2135 Ma (U–Pb zircon ages; Agyei Duodu et al., 2009). Potassic porphyritic granites, dated at 2128 and 2086 Ma (U–Pb zircon ages; Agyei Duodu et al., 2009; Amponsah et al., 2015), intrude these rocks. The Wa–Lawra belt is composed of shales, volcano-sediments, basalts and granitoids. Geochronological U–Pb dating on detrital zircons in the volcano-sediments gives ages older than 2139 Ma (Agyei Duodu et al., 2009). The Wa–Lawra and Koudougou–Tumu domain are juxtaposed along the crustal scale sinistral Jirapa fault. The Bole–Bulenga domain is composed of high-grade gneisses, intruded by TTG plutons

commonly exhibiting migmatitic textures. The Julie belt is composed of basalts, granitoids, gabbros and volcano-sediments. To date, no geochronological data exist for the rocks from the Julie belt.

Baratoux et al. (2011), de Kock et al. (2011) and Block et al. (2015) highlighted the evidence for multiple deformation phases in the Birimian terranes of NW Ghana. An early, short-lived event (termed Eoburnean) was identified by de Kock et al. (2011), and interpreted to be driven by pluton emplacement and basin folding, between 2160 and 2150 Ma. Block et al. (2015) proposed that the first Eburnean event (D_1) in NW Ghana occurred around 2137 ± 8 Ma (in-situ U–Pb dating on monazite). This event is characterized by intrusions of voluminous granitoid plutons, locally associated with volcanism and sedimentation, allochthonous thrusting, folding and development of penetrative metamorphic fabrics resulting in crustal thickening driven by N–S shortening. Peak metamorphic conditions of D_1 reach upper amphibolite facies (Block et al., 2015). The second Eburnean phase, D_2 , is interpreted to have occurred between 2130 and 2110 Ma (U–Pb dating on rhyolites). This event is characterized by regional scale WNW-trending sinistral and NE-trending dextral transcurrent faulting and

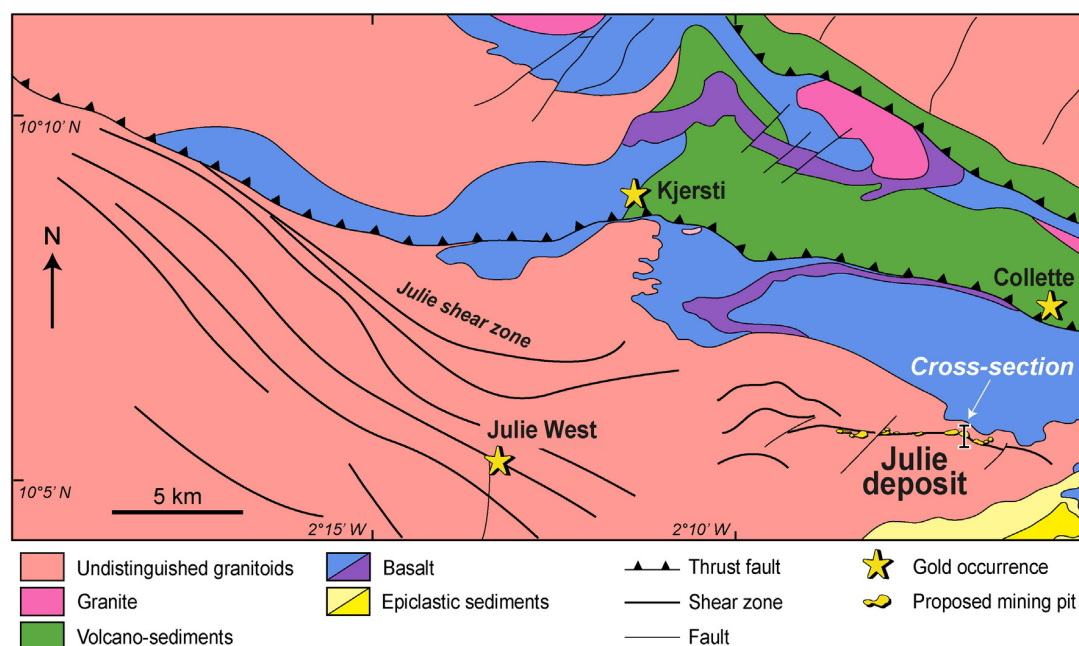


Fig. 2. Simplified map of the Julie Belt, showing several mineralized occurrences in the Wa-East district (modified after Amponsah et al., in press). The Julie deposit, in the lower right of the map, consists of several potentially exploitable workings. The N–S cross-section shown in Fig. 3 is also located.

shearing, which affected most of the rocks within the Wa-Lawra belt, west of the Julie area. Gold mineralization has been reported along these structures (e.g., Allibone et al., 2002; Béziat et al., 2008; Amponsah et al., in press). Block et al. (2015) report late, post-Eburnean brittle NE- and NW-trending faults that crosscut all existing Eburnean structures in the region. These faults are subvertical and of limited extent.

Metamorphic conditions in this region range from greenschist to granulite facies. The highest grades (granulite facies) are observed in the Bole–Bulenga domain, whereas amphibolite facies dominate in the Koudougou–Tumu domain. Rocks in the Julie belt are metamorphosed to greenschist facies, at temperatures between 230 °C and 350 °C and pressures between 1 and 3 kbar, determined by equilibrium mineral assemblages (chlorite–muscovite–epidote–calcite) by Block et al. (2015).

3. Local geology

3.1. Main rock types

The principal lithology in the area of the Julie deposit consists of metamorphosed granitoids that are deformed to various degrees, and

which are in contact with basalt and volcanic sediments, a few km to the north (Fig. 2; see also Fig. 3). The granitoids are metaluminous and their normative composition overlaps the compositional fields of tonalite, granodiorite and trondhjemite (TTG) (Amponsah et al., in press). Their trace geochemistry corresponds to typical magmatic rocks in active margins, with a Rb vs Y + Nb signature corresponding to the volcanic arc granite field of Pearce et al. (1984; cf. Amponsah et al., in press). Texturally, the TTG are medium to coarse grained, and are primarily composed of quartz, hornblende, plagioclase and biotite plus accessory magnetite, zircons and titanite. A greenschist metamorphic assemblage consisting of epidote, calcite, chlorite and rutile overprinted these minerals.

To the north of the Julie shear zone, the basaltic flows alternate with sediments consisting of metamorphosed volcanic sediments with minor intercalated greywacke and shale. The basalts are strongly magnetic and are made up of plagioclase, green amphibole, calcite, chlorite with minor titanite and magnetite. The sediments are fine to medium grained, black to grey in colour, and consist of quartz, muscovites, chlorite, biotite and locally graphite.

3.2. Structural features and quartz veins

Three deformational phases were mapped in the deposit area (D_{J1} , D_{J2} and D_{J3} ; Amponsah et al., in press). In the TTG, the D_{J1} deformation is defined by an E–W-trending penetrative foliation (S_1) that dips between 35° and 70° to the north, representing a brittle–ductile shear zone. This shear reflects a regional scale thrust, and has a general top-to-the-south movement, although E–W to WNW–ESE mylonitic dextral shears can be observed to locally crosscut the ductile fabric and are interpreted as late D_{J1} . Quartz veins are abundant within this shear zone and are commonly boudinaged parallel to it (Fig. 4a). In addition to quartz, the veins contain lower proportions of calcite, ankerite, tourmaline and pyrite. These veins host the main mineralization at Julie. A few isolated, undeformed quartz veins ranging in strike from N–S to NE–SW were observed in exploration trenches and pits. They are interpreted to represent a conjugate set to the E–W (S_1 -parallel) veins (see Section 6). They never extend for more than 100 m along strike, have a vuggy aspect and, in addition to quartz, contain chlorite,

Table 1

General information on the Julie deposit.

Deposit name	Julie
Commodity of exploitation	Au
Location	NW Ghana
Longitude–latitude [dec degrees]	10.205°N–2.189°W
Geographic location	NW Ghana, Upper West Region. The deposit is situated 60.8 km west of the regional capital (Wa).
Geological location	Leo-Man shield of the West African Craton; in the Julie greenstone belt, between the Wa-Lawra and Bole-Nangodi belts.
Deposit status	Prospect under development (mine development stage).
Deposit type	Granitoid hosted; shear-zone related, quartz veins.
Current owner	Azumah Resource Limited
Average grade	2.0 g/t
Tonnage	2.21 Mt of measured and indicated resource; 202,000 oz proven reserves (September, 2014).
Past production	No production to date.

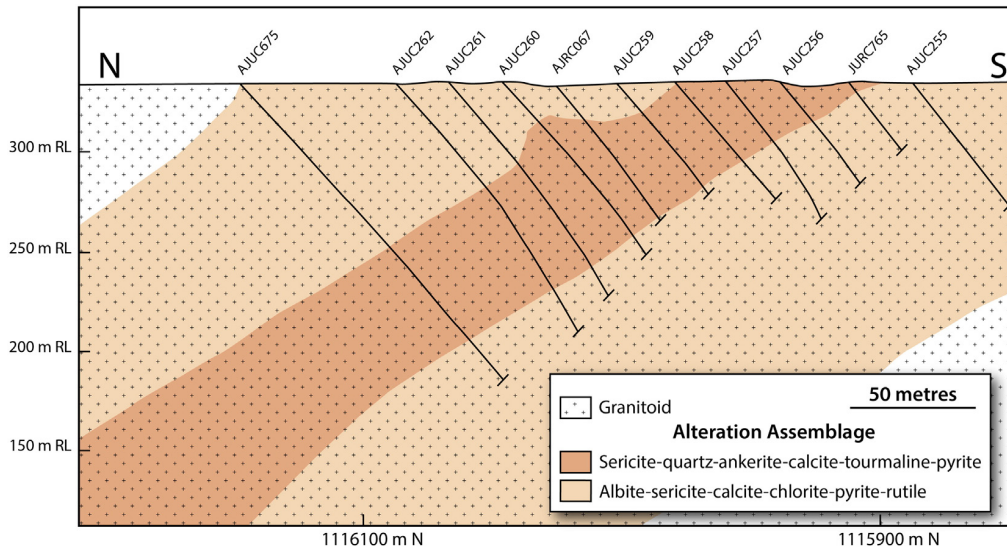


Fig. 3. Cross-section of the Julie deposit along 579,100 m E (see Fig. 2 for location), constructed based on drill core information (single drill holes are labelled on the section). The section shows the main mineralized corridor, which is defined by wall-rock alteration. High-grade mineralization is confined to the inner alteration zone. The external alteration selvage contains low-grade mineralization.

carbonates, muscovite and pyrite (Fig. 4b). These veins also host some mineralization, although to a lesser extent than the E–W veins.

D_{J2} is characterized by an E–W compression, which produced F_2 isoclinal folds with a fold axis verging northwards, and axial planes striking N–S with subvertical dips. This event is not observed in the intrusives at Julie but affected the basalts and volcano-sedimentary units north of the deposit, mostly in the form of crenulation of the D_{J1} fabric. Quartz veins formed within the S_2 foliation plane, but were only observed in the basalt. They are deformed, contain traces of calcite and tourmaline, and are not mineralized.

The latest stage of deformation recognized at Julie, D_{J3} , is characterized by brittle faults that crosscut the D_{J1} and D_{J2} structures, strike NE–SW and dip 30 to 40° to the northwest.

4. Ore body characteristics

Mineralization in the Julie deposit is mostly related to the E–W trending D_{J1} -related S_1 shear zone. The main ore body consists of a network of numerous quartz veins, which form a corridor striking E–W and dipping 30 to 60° to the north (Fig. 3). The ore body extends over 3.5 km along strike and has a thickness varying from 20 to 30 m. It is enclosed by an alteration envelope that gradually changes away from the mineralized zone into the barren rock; an inner zone affects the vein corridor, within a width of about 50 m (Fig. 3), and has particularly-low magnetic susceptibility relative to the barren rock. This alteration consists of sericite + quartz + ankerite + calcite + tourmaline + pyrite. In this zone, the average gold grade is about 3.0 g/t. A second alteration

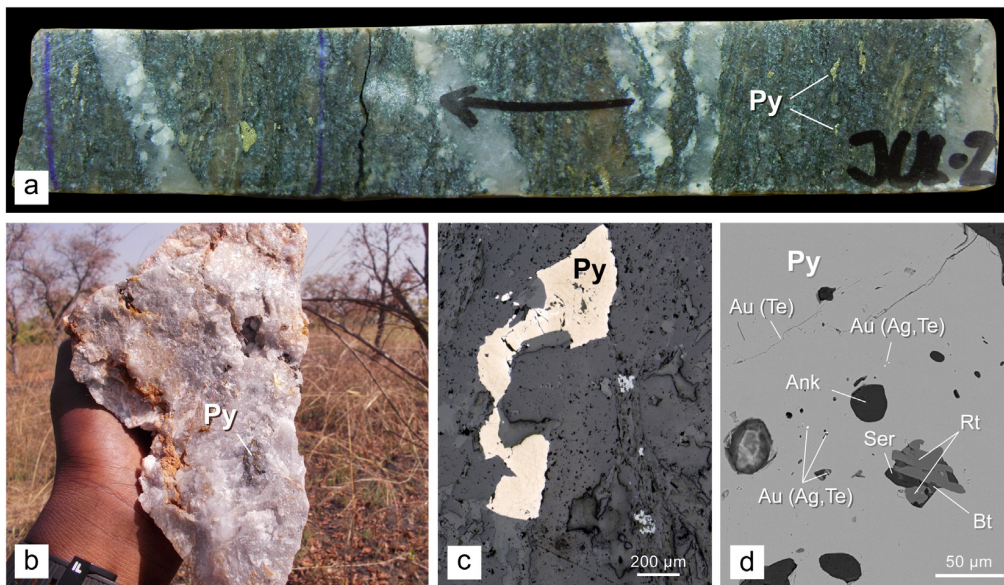


Fig. 4. Macroscopic and microscopic images of samples from the Julie deposit. (a) Drill core of sheared granitoid from the main mineralization zone, showing several quartz veins and pyrite grains (Py) stretched along the main foliation. (b) Hand sample of vuggy quartz from the N–S veins. The sample shows a pyrite agglomerate in quartz. (c) Photomicrograph under reflected light of a pyrite grain deformed parallel to the foliation (vertically with respect to the image) from the main mineralized zone. (d) SEM image showing details of a pyrite grain, also from the main mineralized zone, where gold occurs as micron-sized inclusions and in a fracture. Inclusions of ankerite (Ank), sericite (Ser), rutile (Rt) and biotite (Bt) are also visible.

envelope surrounds this inner zone and consists of albite + sericite + calcite + chlorite + pyrite + rutile (Fig. 3). Here, pyrite partially replaces primary magnetite and albite replaces most feldspars, and gold grades range between 0.1 g/t and 0.4 g/t. Further away from this zone, a metamorphic assemblage of chlorite, epidote and calcite affects the barren rocks.

Gold mineralization also occurs in the N–S trending quartz veins. An alteration envelope, similar to that affecting the main ore, characterizes these veins, although in this case it is much more limited in space. In these veins, gold grades range around 0.2 g/t, although in a few places values up to 3.5 g/t have been measured.

5. Microscopic features of the ore

Mineralization in the D_{J1} -related vein corridor occurs mostly in the form of micron-sized gold grains that form inclusions in pyrite crystals that are commonly deformed, as well as larger grains occurring within fractures in pyrite or along its crystal edges (Fig. 4c, d). In many instances, gold is accompanied by silver, bismuth, tellurium, copper and lead. Gold-bearing pyrite occurs in the quartz veins as well as disseminated in the wall rock, within the alteration selvages described above, and no particular difference was observed between the two. In the N–S trending veins, gold occurs in quartz as rare free grains, although mostly in fractures within pyrite from the veins and the alteration halos, and it is commonly accompanied by minor silver. However, in these veins gold was not found as inclusions in pyrite.

Amponsah et al. (in press) detected the presence of up to 15 ppm Au in pyrites from the main mineralized zone by LA-ICP-MS analyses; the data did not allow to distinguish whether gold is in the structure of this sulphide or forms nanoparticles (cf. Deditius et al., 2011). Only ppb amounts of Au were detected by this technique in a few pyrites from the N–S veins. In addition to gold, other metals detected by LA-ICP-MS in pyrite from the main mineralization include Ag, Te, Pb, Se, Ni and Co.

6. Genetic considerations

The main ore body in the Julie deposit occurs in the form of a network of quartz veins along the E–W trending S_1 shear zone. The hydrothermal alteration that affected the rocks containing the vein network, defines the mineralized corridor. It consists mainly of sericitization, carbonatization and sulphidation. Amponsah et al. (in press) show that these secondary minerals are foliated parallel to the local S_1 foliation plane, which is consistent with a syn-deformation emplacement of the mineralized system, which, in turn, is coherent with the fact that the veins are boudinaged along S_1 . The N–S trending veins are interpreted by these authors as being a conjugate set to the S_1 -parallel veins, i.e., they formed pene-contemporaneously, and represent the σ_3 direction for D_{J1} . They base their argument on their orientations, as well as the fact that both vein sets display the same type of alteration halos and contain fluid inclusions with the same physicochemical characteristics. Nevertheless, the fact that in the N–S veins gold only occurs in fractures, suggests that these veins were under a brittle deformational regime, and recorded only the late stages of mineralization. The D_{J1} event, responsible for the formation of the S_1 shear zone and the mineralization at Julie, has the same kinematic indicators as the regional D_1 of Block et al. (2015) and likely represents a local expression of this regional scale deformation episode.

A study of the fluid inclusions found in the veins indicates the presence of immiscible aqueous and carbonic fluids circulating at about 250 °C and 1 kbar (Amponsah et al., in press). Their composition suggests a metamorphic origin of the mineralizing fluids, rather than orthomagmatic. This is consistent with the alteration mineralogy, which is typical of orogenic gold deposits hosted in metamorphosed volcanic rocks (e.g., Saunders et al., 2014). The PT conditions are interpreted to record hydrostatic regime during drops in pressure

subsequent to the creation of open space during deformation (e.g., Sibson et al., 1988). As suggested by Amponsah et al. (in press) these pressure drops most likely triggered gold precipitation (e.g., Kouzmanov and Pokrovski, 2012), along with other metals and quartz.

7. Summary and conclusions

The Julie deposit, hosted in the Wa-Lawra greenstone belt in NW Ghana, will be potentially the next operating mine in the country and the largest resource in the region. It is hosted in sheared Paleoproterozoic granitoids of TTG composition and the main ore consists of a mineralized corridor, trending E–W and dipping N, formed by a network of quartz veins emplaced along the main shear zone, which is an expression of the regional D_1 deformation episode. Minor gold mineralization was also found in a set of quartz veins that are conjugate to the main veins though formed slightly later, mostly under a brittle regime. Within the main vein corridor, gold occurs almost exclusively within pyrite, as inclusions, in fractures and along its edges. In both vein sets, this sulphide occurs in the veins as well as in the host rock where it is contained within an alteration selvage, which defines the extent of the mineralized body. Invisible gold occurs in pyrite from both vein sets, although only ppb amounts were detected in pyrite from the conjugate veins.

Acknowledgement

This work was financed by the AMIRA WAXI Phase II sponsors (project number P934), including AusAid and the ARC Linkage Project LP110100667, and by Azumah Resources Limited. The latter is also thanked for field assistance, access to their core and data, and for granting permission to publish this paper. We also acknowledge the contribution of Geological Surveys/Department of Mines in West Africa as sponsors in-kind of WAXI. Constructive reviews by German Velásquez and Steven Micklethwaite were appreciated and contributed to improve the quality of the manuscript.

References

- Ageyi Duodu, J., Loh, G.K., Boamah, K.O., Baba, M., Hirdes, W., Toloczyki, M., Davis, D.W., 2009. Geological map of Ghana 1:1 000 000. Geological Survey Department of Ghana (GSD).
- Allibone, A., Teasdale, J., Cameron, G., Etheridge, M., Uttley, P., Soboh, A., Appiah-Kubi, J., Adanu, A., Arthur, R., Mamphey, J., Odoom, B., Zuta, J., Tsikata, A., Pataye, F., Famiyeh, S., Lamb, E., 2002. Timing and structural controls on gold mineralization at the Bogoso Gold Mine, Ghana, West Africa. *Econ. Geol.* 97, 949–969.
- Amponsah, P.O., Salvi, S., Béziat, D., Baratoux, L., Siebenaller, L., Nude, P.O., Nyarko, R.S., Jessell, M.W., 2015. The Bepkong gold deposit, northwestern Ghana. *Ore Geology Reviews* (in this volume).
- Amponsah, P.O., Salvi, S., Béziat, D., Jessell, M.W., Siebenaller, L., Baratoux, L., 2015. Geology and geochemistry of the shear-hosted Julie deposit, NW Ghana. *J. Afr. Earth Sci.* <http://dx.doi.org/10.1016/j.afrearsci.2015.06.013> (in press).
- Baratoux, L., Metelka, V., Naba, S., Jessell, M.W., Grégoire, M., Ganne, J., 2011. Juvenile Paleoproterozoic crust evolution during the Eburnean orogeny (2.2–2.0 Ga), Western Burkina Faso. *Precambrian Res.* 191, 18–45.
- Béziat, D., Dubois, M., Debat, P., Nikiema, S., Salvi, S., Tollon, F., 2008. Gold metallogeny in the Birimian craton of Burkina Faso (West Africa). *J. Afr. Earth Sci.* 50, 215–233.
- Block, S., Ganne, J., Baratoux, L., Zeh, A., Parra, L.A., Jessell, M.W., Aillères, L., Siebenaller, L., 2015. Petrological and geochronological constraints on lower crust exhumation during Paleoproterozoic (Eburnean) orogeny, NW Ghana, West African Craton. *J. Metamorph. Geol.* 33, 463–494. <http://dx.doi.org/10.1111/jmg.12129>.
- de Kock, G.S., Armstrong, R.A., Siegfried, H.P., Thomas, E., 2011. Geochronology of the Birim Supergroup of the West African craton in the Wa-Bole region of west central Ghana: implications for the stratigraphic framework. *J. Afr. Earth Sci.* 59, 291–294.
- Deditius, A.P., Utsunomiya, S., Reich, M., Kesler, S.E., Ewing, R.C., Hough, R., Walshe, J., 2011. Trace metal nanoparticles in pyrite. *Ore Geol. Rev.* 42, 32–46.
- Feybesse, J.-L., Billa, M., Guerrot, C., Duguey, E., Lescuyer, J., Milési, J.P., Bouchot, 2006. The Paleoproterozoic Ghanaian province: geodynamic model and ore controls, including regional stress modeling. *Precambrian Res.* 149, 149–196.
- Griffis, et al., 2002. Gold deposits of Ghana. Ghana Minerals Commission Report (430 pp.).
- Junner, N.R., 1932. Geology of the Obuasi goldfield. Gold Coast Geological Survey. Memoir 2, 1–71.
- Klemd, R., Hünken, U., Olesch, M., 1996. Fluid composition and source of early Proterozoic lode gold deposits of the Birimian volcanic belt, West Africa. *Int. Geol. Rev.* 38, 22–32.
- Kouzmanov, K., Pokrovski, G.S., 2012. Hydrothermal controls on metal distribution in Cu (–Au–Mo) porphyry systems: society of economic geologists. *Spec. Pub.* 16, 573–618.

- Azumah Resource Limited, 2012. Julie status report. Unpublished.
- Milési, J.P., Feybesse, J.L., Ledru, P., Dommangeat, A., Ouedraogo, M.F., Marcoux, E., Prost, A., Vinchon, C., Sylvain, J.P., Johan, V., Tegye, M., Calvez, J.Y., Lagny, Ph., 1989. Mineralisations aurifères de l'Afrique de l'ouest, leurs relations avec l'évolution litho-structurale au Proterozoïque inférieur. Carte géologique au 1/2.000.000. Chronique de la recherche minière 497, 3–98.
- Pearce, J.A., Harris, N.B.W., Tindle, A.G., 1984. Trace element discrimination diagrams for the tectonic interpretation of granitic rocks. *J. Petrol.* 25, 956–983.
- Perrouy, S., Aillères, L., Jessell, M.W., Baratoux, L., Bourassa, Y., Crawford, B., 2012. Revised Eburnean geodynamic evolution of the gold-rich southern Ashanti Belt, Ghana, with new field and geophysical evidence of the pre-Tarkwaian deformations. *Precambrian Res.* 204–205, 12–39.
- Perrouy, S., Jessell, M.W., Miller, J., Bourassa, Y., Apau, D., Siebenaller, L., Baratoux, L., Velásquez, G., Aillères, L., Béziat, D., Salvi, S., 2015. The tectonic context of the Eoeburnean Wassah gold mine – implications for relative timing of mineralising events in southwest Ghana. *J. Afr. Earth Sci.* <http://dx.doi.org/10.1016/j.jafrearsci.2015.03.003>.
- Saunders, J.A., Hofstra, A.H., Goldfarb, R.J., Reed, M.H., 2014. Geochemistry of Hydrothermal Gold Deposits. in *Treatise on Geochemistry*. 2nd Edition. Elsevier, pp. 386–424.
- Sibson, R.H., Robert, F.A., Poulsen, K.H., 1988. High-angle reverse faults, fluid-pressure cycling, and mesothermal gold-quartz deposits. *Geology* 16, 551–555.
- White, A.J.R., Waters, D.J., Robb, L.J., 2015. Exhumation-driven devolatilization as a fluid source for orogenic gold mineralization at the Damang deposit, Ghana. *Econ. Geol.* 110, 1009–1025.

Chapter 4

The Kunche Deposit

Introduction

The economic, but not world-class Kunche gold deposit, is one of the many gold deposits actively explored by Azumah resources Limited on the Wa-Lawra belt and the largest gold deposit on the belt found so far. The deposit has an ore inventory of 750,000 Oz, at an average grade of 1.94 g/t have seen no production till date.

This chapter of the thesis discusses the geology, general structural and alteration control on gold mineralization and the ore genesis. This paper will be submitted to Precambrian Research by January, 2015. The study further examine the textures, mineralogy and overprinting relationship of sulphides hosting the gold mineralization on a crystallographic scale.

4.0 Geological, structural and geochemical controls of Gold Mineralization in the Wa-Lawra belt, NW Ghana: A case study from the Kunche deposit

Prince Ofori Amponsah^{1,2}, Stefano Salvi¹, Mark Jessell³, Luc Siebenaller^{1,5}, Didier Beziat¹, Lenka Baratoux^{1,6}

1. Université de Toulouse, CNRS, Géosciences Environnement Toulouse, Institut de Recherche pour le Développement, Observatoire Midi-Pyrénées, 14 Av. Edouard Belin, F-31400 Toulouse, France

2. Azumah Resources Ghana limited, PMB CT452, Cantonments, Accra

3. Centre for exploration Targeting, School of Earth and Environment, The University of Western Australia, 35 Stirling Highway, Crawley WA 6009

4. University of Ghana, Department of Earth Sciences, P.O. Box LG 58, Legon, Accra.

5. ONG-D “Le Soleil dans la Main” asbl, 48, Duerfstrooss, L-9696 Winseler, Luxembourg.

6. IFAN Cheikh Anta Diop, Dakar, Senegal

Abstract

The Kunche deposit is one of the largest gold deposit discovered so far on the Wa-Lara belt in NW Ghana and the eastern edge of the Paleoproterozoic West African craton. Gold in Kunche is confined within N-NNW trending and steeply dipping D_{K1} anastomosing shear zone and Type-1 quartz veins. The rock body hosting the gold mineralization in Kunche is the volcanoclastic sediments which have been metamorphosed to the greenschist facies. From the space-time correlation of events, the gold in the Kunche deposit can be inferred to have occurred around 2110- 2105 Ma. The ore body in Kunche consist of a single lode with a strike length of 1.1 km. The ore zone is characterized by an alteration assemblage of calcite + chlorite + sericites + quartz + sulphides which occupy an entire width of 20 to 150 m. Gold in the Kunche deposit is associated with the arsenopyrite mineral.

Two types of gold occurrence has been identified in the Kunche deposit. (1) The invisible gold formed as nanoparticle or solid solution with the crystal lattice of the arsenopyrite and (2) the visible gold formed within the fractures formed in the arsenopyrites or in the quartz veins.

SEM imagery done on arsenopyrite reveals that the arsenopyrite carrying the gold mineralization was formed via hydrothermal processes. The arsenopyrite exhibits alteration rims and oscillatory zone which are typically akin to hydrothermal activity. LA-ICP-MS show that the gold in Kunche is associated with trace element such as Ag, Pb, Cu and Zn.

Keywords: Kunche, gold, mineralization

4.1 Introduction

Orogenic gold deposits are formed as a direct result of accretionary and collisional events (Goldfarb et al, 2001; Dubé & Gosselin, 2007; Kouhestani et al., 2014) and demonstrate a high degree of structural control. This deposit type is distributed in deformed metamorphic greenstone belts of all ages (Dubé & Gosselin, 2007). The Birimian terrane greenstone belts and basins in West Africa have been described to have formed in an intra cratonic rift to ocean spreading and accretion related setting (Leube et al., 1990) during the Paleoproterozoic Eburnean event (Abouchami et al., 1990). This accretionary event associated to the Eburnean Orogeny resulted in the formation of various gold deposits in the West African craton (eg. The Ashanti deposit exploited by AngloGold Ashanti, Chirano deposit and the Tarkwa paleoplacers in Ghana, Inata deposit exploited by Avocet and Mana deposit exploited by SEMAFO, both in Burkina and Syama deposit in Mali). One of such greenstone belts, is the Wa-Lawra greenstone belt which has been identified in NW Ghana and has been a prospective area for search of the precious metal, gold (Amponsah et al., 2015; Griffis et al., 2002).

The search for gold in the Wa-Lawra gold district in Wa-Lawra belt has been on-going since the 1960s when the Russian prospecting team reported on bedrock gold mineralization in the area. These reports mentioned occurrences of gold related to quartz veins near the Wa Township, and narrow, discontinuous north-south trending quartz veins near the villages of Duri and Lambussie (Amponsah et al. 2015). Renewed interest in the belt in terms of gold exploration was ignited when AGEM (a joint venture between Ashanti Goldfields and IAM Gold of Canada) discovered significant gold intercepts in the early 1990s (eg. for borehole NRC023, AGEM had 2 m at 1.2 g/t from 47 to 49 m and 13 m at 1.33 g/t from 54 m to 66 m; Amponsah et al, 2015) along the 40 km Kunche-Atikpi shear zone. The activities of AGEM discovered the Kunche, Bepkong, Duri and the Atikpi prospects. All the prospecting licences on the Wa-Lawra belt were taken over by Azumah resources limited by 2006, where till date have defined 750,000 Oz (measured and inferred) of gold in the Kunche deposit.

Although Azumah has defined something substantial to make a mine, the geology and ore controls are poorly constrained. This can only be achieved if the genesis of the ore is clearly defined. This study will address the geology, structural and geochemical controls of the known mineralization in the Kunche deposit and how this can influence or improve the exploration strategies to find more gold in the Wa-Lawra belt.

4.2 Regional Geology

The Birimian units in Ghana form part of the Paleoproterozoic terrane of the West African Craton. The Birimian architecture in Ghana comprises of five NE-SW greenstone belts (thus, the Kibi-Winneba, Ashanti, Sefwi, Bui and Bole-Nangodi belts), and one N-S trending belt (Wa-Lawra belt), with intervening sedimentary basins. These belts are almost 70 km apart from each other. All the Birimian rocks in Ghana were formed in 2250 to 1980 Ma (Feybesse et al., 2006).

The Kunche deposit is situated in the Wa-Lawra gold district of the Wa-Lawra belt in NW Ghana (Fig. 4.1).

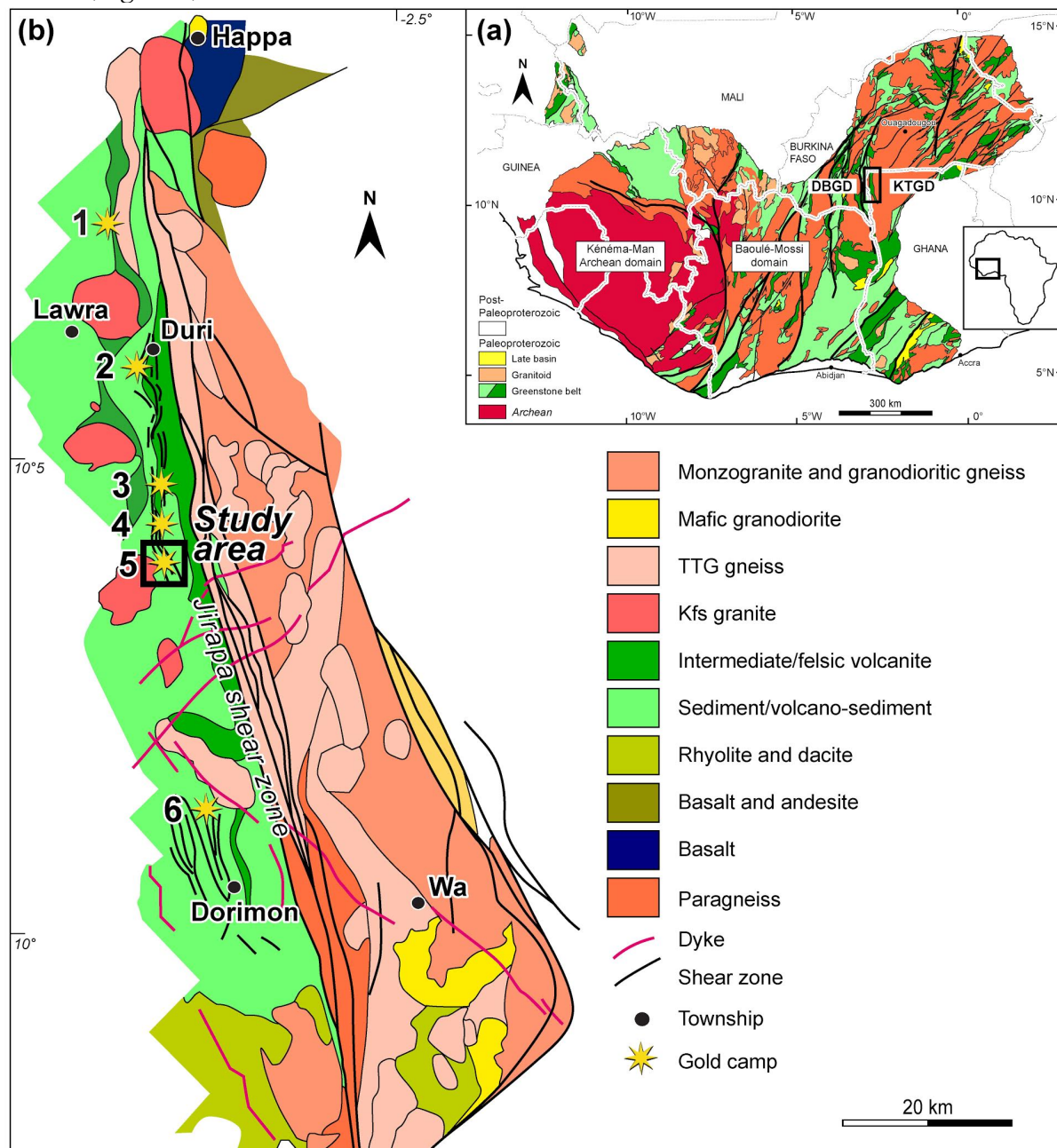


Fig. 4.1. Fig. 1. a) Geological map showing the Kenema-Man domain (modified after Milési et al., 2004), Koudougou-Tumu granitoid domain (KTGD), Dieboucou-Bouna granitoid domain (DBGD) and the Baoulé-Mossi domains of the West African Craton (WAC) with the position of the Wa-Lawra belt in the black insert. b) Geological map of the Wa-Lawra belt (Modified after Block et al., 2015, Amponsah et al., 2015) showing the various gold prospect: 1. Basabli 2. Duri 3. Yagha; 4 – Bepkong, 5. Kunche (the study area) 6. Butele.

The geology of NW Ghana has been described by Block et al. (2015) to be composed of terranes such as the Wa-Lawra belt, the Koudougou-Tumu Granitoid domain, the Julie belt, Bole-Bulenga domain and Bole-Nangodi belt.

The Wa-Lawra belts represents the southernmost portion of the larger Boromo belt (Béziat et al., 2000, Baratoux et al., 2011). It is boarded to the east by the Koudougou-Tumu Granitoid domain, to the south east by the Bole-Bulenga domain, to the south by the Bole-Nangodi belt.

The Wa-Lawra belt is composed of greywackes, shales, andesites, basalts, gabbro, granites, gneisses and can be divided into two parts, thus the eastern and western parts (Block et al., 2015). The western part is composed of 2187 ± 3 Ma high grade para- and ortho gneisses, rhyolites and granitoids (Agyei Duodu et al., 2009). The eastern part is composed of 2139 ± 2 Ma (detrital age of zircons, Agyei Duodu et al., 2009) greywackes, volcanosediments (Agyei Duodu et al., 2009) and early syn-tectonic 2212 ± 1 Ma (Sekyi et al., 2014) and 2153 ± 4 Ma granitoids (Agyei Duodu et al., 2009) which hosts the Wa-Lawra gold district. These rocks have been intruded by late kinematic granitoids 2104 ± 1 Ma (Agyei Duodu et al., 2009; Baratoux et al., 2011, Amponsah et al., 2015; Feng et al., 2015). The boundary between the eastern and western parts is marked by a 100 km sinistral Jirapa shear zones which was formed during the Eburnean Orogeny (Block et al., 2015). This shear zones has deformed the rocks in that region. The Wa-Lawra gold district, for that matter the eastern part of the Wa-Lawra belt is dominated of the greenschist facies metamorphism with P-T conditions of 200-300 °C and 1-3 kbar using fluid inclusion microthermometric methods (Amponsah et al. in press) and P-T multi equilibra method, whilst the western part is dominated by migmatite facies metamorphism (Block et al., 2015).

The Bole-Bulenga domain is composed of high grade metamorphic rocks such as metabasites and paragneisses with migmatitic characteristics. These rocks have been termed as the Buki gneisses by deKock et al. (2011) and have been intruded by 2195 Ma and 2135 Ma granitoids (Agyei Duodu et al., 2009; Block et al., 2015; Feng et al. in press).

The Koudougou-Tumu Granitoid domain adjacent to the Wa-Lawra belt and affected by the sinistral Jang shear zone and is composed of gabbros and gneisses of 2162 ± 1 Ma to 2134 ± 1 Ma. These rocks have been intruded by late 2128 Ma porphyritic granites (Agyei Duodu et al., 2009).

Block (2015) proposed a six deformation events for the rocks in NW Ghana. The first deformation phase, D₁ in NW Ghana is defined by crustal thickening due to N-S shortening, which is marked by thrust faulting and folding which is mostly best observed within the Julie Belt and rocks from the Bole-Bulenga domain. D₂ is marked by N-S extension which is characterized by extensional shear zones along the E-W margin of the Bole-Bulenga domain. D₃ is marked by E-W shortening which is responsible for the N-S S₃ foliation observed within the Wa-Lawra belt and the Bole-Bulenga domain. D₄ is characterized by WNW to ESE compression and is marked by the NNW sinistral Jirapa shear zone. D₅ is characterised by the dextral NE crustal scale strike slip shear zone in the Bole-Nangodi belt. D₆ in NW Ghana is marked by E-W shorting and responsible for all the late N-S brittle faults.

4.3 Methodology

The geological information in the Kunche deposit was obtained from logging of reverse circulation (RC) drilling chips and diamond drill core (DD) drilled by Azumah resources, and field mapping in surrounding areas near the deposit in the Wa-Lawra belt. In all, 60 RC and DD bore-holes were logged, constituting 5 E-W fence lines. A geological map was prepared by projecting the structural measurements and lithological data from the drill core logged to surface and was further constrained by interpreting conductivity and resistivity induced polarisation (IP) images processed by Sagax Afrique S.A in 2012, on behalf of Azumah Resources limited.

The mineralogy and textural relationships of the rock samples were investigated using optical microscopy and back-scattered electron (BSE) images obtained with a JEOL JSM 6360LV scanning electron microscope (SEM) equipped with a silicon drift detector analysis system, at the University of Toulouse, France. Whole-rock major and trace-element compositions were analysed using ICP-AES and ICP-MS, respectively by the ALS Chemex laboratory in Seville, Spain.

Spot analyses of pyrite crystals were performed by LA-ICP-MS at the Géosciences Montpellier laboratory (France), to determine trace element concentrations. Analyses were performed using a Geolas (Microlas) Excimer ArF automated platform housing a 193 nm Compex 102 nanosecond laser from LambdaPhysik, coupled with a high-resolution ThermoFinnigan (ELEMENT XR) ICP-MS. Data were acquired in the fast E-scan mode at low mass resolution using a flux of 15 J/cm² at a frequency of 5 Hz and working with a spot size of 51 µm. Raw data were processed on-line using the GLITTER software package (e.g., [Van Achterbergh et al., 2001](#)), and using several sulphide standards, i.e., pyrrhotite-Po-726 ([Sylvester et al., 2005](#)) and in-house chalcopyrite Cpy-RM ([Velásquez et al., 2012](#)) as external calibrators, and using ³⁴S as the internal calibrator (e.g., [Lorand and Alard, 2011](#)). During analysis, the following isotopes were monitored: ³³S, ³⁴S, ⁵⁶Fe, ⁵⁷Fe, ⁵⁹Co, ⁶⁰Ni, ⁶³Cu, ⁷⁵As, ⁸²Se, ¹⁰⁷Ag, ¹²⁵Te, ¹⁹⁷Au, ²⁰⁸Pb, and ²⁰⁹Bi. Typical detection limits, at the conditions described above, are between 0.01 to 0.1 ppm. Detection limits were calculated as three times the background standard deviation value and were converted to concentration units (ppm) with the *yield_{ms}* parameter (e.g., [Borisova et al., 2010](#)). All calculated concentrations were comparable to the analytical precision limits of the *in-situ* femtosecond quadrupole LA-ICP-MS technique (< 15% RSD, e.g., [Borisova et al., 2010](#)) and the reference materials homogeneities (< 16% RSD, [Velásquez et al., 2012](#)).

4.4 Geology of the Kunche deposit

Gold in the Kunche deposit is restricted to the discrete anastomosing shear zone of highly silicified 2139 ± 2 Ma ([Agyei Duodu et al., 2009](#)) volcanoclastics sediments with quartz-carbonate veins and microdiorite dyke (Fig. 4.2).

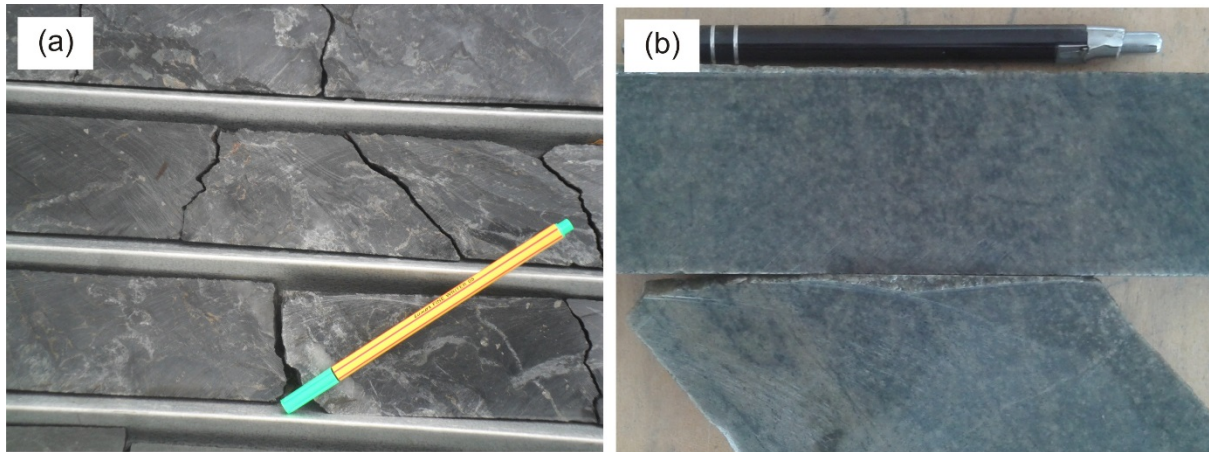


Fig. 4.2. Drill core images of rocks in the Kunche deposit (a) volcaniclastic rock exhibiting weak brecciated texture (b) calcite bleached microdiorite rock

The volcaniclastic sedimentary rocks are grey, fine to medium grained, show graded bedding, display poor sorting and are composed mainly of plagioclase and quartz (exhibits undulose extinction) with rutile as the accessory mineral. These minerals have been superimposed by calcite, sericite and chlorite (Fig. 4.3a).

The microdiorite in the Kunche deposits occurs as dykes, which are mostly sheared. It is composed of phenocrysts of plagioclase and amphibole in groundmass composed primarily of plagioclase and minor mica and accessory rutile, quartz and sphene (Fig. 4.3b). These minerals have been superimposed by calcite as a result of hydrothermal alteration.

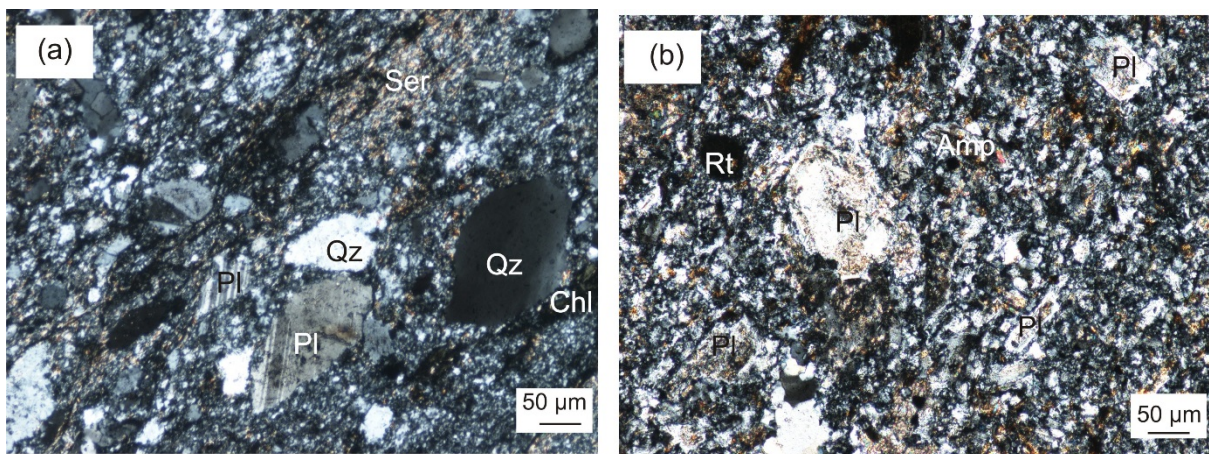


Fig. 4.3. Photomicrograph of rocks in the Kunche deposit (a) the volcaniclastic rock is composed of quartz, plagioclase, sericite and chlorite. The thin section exhibits poor sorting, but the crystals have preferred orientation due to deformation (b) the microdiorite is composed of phenocrysts of plagioclase and ground mass of amphibole and plagioclase with accessory mineral rutile. Qz=quartz, Pl=plagioclase, Chl=chlorite, Amp=amphibole, Ser=sericite, Rt=rutile

4.5 Geochemistry

4.5.1 Volcanoclastic sediments

The volcanoclastic sediments in Kunche (Table 4.1) have a wide range of SiO₂ (45.6 % to 69.8 %) and Al₂O₃ (14.65 % to 24.8 %) and narrow range for TiO₂ (0.33 % to 1.02 %) and Cr₂O₃ (0.01 to 0.04%). The MgO value ranges from 0.68 % to 2.87 %. When the concentration of REE is normalized to the upper crust, the volcanoclastic rocks are highly spiked with high inter element fractionation (Fig. 4.4a).

Th, Sc and REEs elements are valuable in monitoring source rock composition in sediments (Taylor & McLennan, 1985; McLennan & Taylor, 1991). These elements have short residence times in the water column and can therefore be transferred quantitatively into the rock record (Baulauz et al., 2000). Sources of sedimentary rocks can also be inferred from REE patterns. For example basic rocks contain low LREE/HREE ratios with no Eu anomaly, whilst silica rich rocks contains high LREE/HREE ratios with an Eu anomaly (Condie, 1987; 1989). The REE pattern in the Kunche deposit have high LREE/HREE ratios and when normalized to chondrite (Sun & McDonough, 1989) and upper crust shows high positive Eu anomaly (Fig. 4.4b). This indicates that most of the volcanoclastic rocks have an intermediate or calc-alkaline source. Further using the La-Th-Sc ternary diagram to discriminate the source most of the samples were hypotised towards the granodiorite source (Fig. 4.4c).

Table 4.1. Major and trace element analytical data for volcanoclastic sediments in the Kunche deposit

SAMPLE	KUN-1	KUN-2	KUN-3
	Volcaniclastic	volcaniclastics	volcaniclastics
wt. %			
SiO ₂	68.80	45.60	69.80
Al ₂ O ₃	14.65	24.80	14.85
Fe ₂ O ₃	5.31	9.03	2.21
CaO	2.10	1.59	2.12
MgO	2.16	2.87	0.68
Na ₂ O	3.49	2.45	4.45
K ₂ O	1.45	6.34	3.22
Cr ₂ O ₃	0.04	0.04	0.01
TiO ₂	0.55	1.02	0.33
MnO	0.06	0.05	0.02
P ₂ O ₅	0.12	0.15	0.10
SrO	0.03	0.02	0.06
BaO	0.03	0.17	0.12
C	0.09	0.30	0.12
S	0.03	1.87	0.03
LOI	2.10	4.92	1.22

Total	100.89	99.05	99.19
ppm			
Ba	350.00	1645.00	1040.00
Ce	40.60	57.60	53.80
Cr	310.00	320.00	80.00
Cs	6.38	12.95	2.60
Dy	2.66	3.07	0.79
Er	1.42	1.70	0.37
Eu	1.26	1.44	0.75
Ga	15.00	34.00	19.10
Gd	2.95	4.37	1.63
Hf	4.70	5.00	4.00
Ho	0.42	0.55	0.12
La	18.80	26.40	28.50
Lu	0.21	0.29	0.04
Nb	4.10	7.40	3.80
Nd	18.00	26.00	19.60
Pr	4.66	6.51	5.98
Rb	59.60	226.00	101.50
Sm	3.51	5.31	2.93
Sn	2.00	3.00	1.00
Sr	378.00	346.00	519.00
Ta	0.80	0.50	0.40
Tb	0.36	0.50	0.19
Th	3.06	4.58	6.52
Tm	0.18	0.27	0.05
U	0.82	1.42	2.39
V	112.00	245.00	23.00
W	2.00	14.00	4.00
Y	14.80	18.10	3.60
Yb	1.36	1.68	0.23
Zr	183.00	198.00	148.00
As	75.00	250.00	51.70
Bi	0.14	1.03	0.12
Hg	0.02	0.02	0.04
Sb	7.49	26.80	0.37
Se	0.40	26.30	0.20
Te	0.04	9.29	0.01

Tl	0.21	0.23	0.60
Ag	0.50	0.60	0.50
Cd	0.50	0.50	0.50
Co	17.00	33.00	5.00
Cu	27.00	12.00	20.00
Li	40.00	70.00	20.00
Mo	1.00	1.00	18.00
Ni	60.00	120.00	101.00
Pb	7.00	10.00	18.00
Sc	12.00	24.00	2.00
Zn	57.00	70.00	54.00
(La/Yb) _n	9.32	10.59	83.54

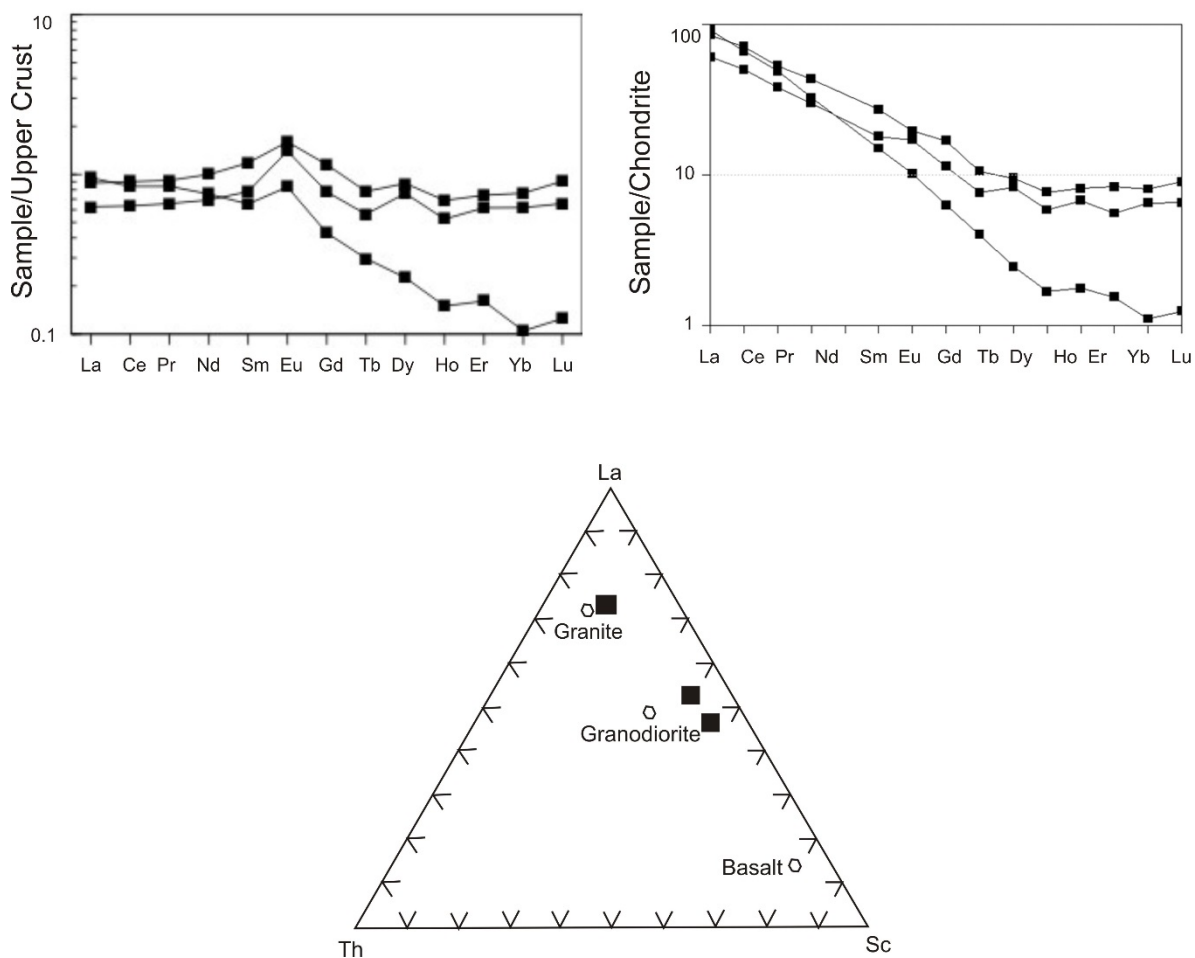


Fig. 4.4. Geochemical plots for the volcaniclastic rocks in the Kunche deposit (a) spider plot of REE normalised against Upper crust in the Bepkong deposit (Sun & McDonough, 1989) (b) Chondrite normalized REE patterns in Kunche (Condie, 1987) (c) La-Th-Sc plot of the analysed volcaniclastic sediment in the Kunche deposit. The volcaniclastic rock plots between

the granite and granodiorite composition. This indicates most likely an intermediate source for the sediments in the area.

4.5.2 Microdiorite

The SiO₂ content for the microdiorite in Kunche deposit ranges from 55 % to 57.1 % and that for Al₂O₃ ranges from 14.6 % to 15.2 % (Table 4.2). The magnesium number (Mg#) for the microdiorite rocks in the Kunche deposit ranges from 34.36 to 40.16. The low Mg# indicates that the microdiorite in Kunche are highly evolved. The microdiorite in Kunche have a flat REE when normalized to chondrite (Fig. 4.5a). Cs, Ba and Rb (total alkali) shows concentrations 100 times higher than the chondrite (Fig. 4.5b).

From the tectonic discrimination diagram, it can be established that the microdiorite were formed in an arc related setting (Fig. 4.5c).

Table 4.2. Major and trace element analytical data for microdiorite in the Kunche deposit

SAMPLE	KUN-4	KUN-5	KUN-6
	lamprophyre	lamprophyre	lamprophyre
wt. %			
SiO ₂	56.50	55.00	57.10
Al ₂ O ₃	15.20	14.80	14.60
Fe ₂ O ₃	5.38	7.09	8.92
CaO	5.67	6.49	3.91
MgO	3.61	4.47	4.67
Na ₂ O	2.57	3.45	0.42
K ₂ O	2.67	0.83	2.78
Cr ₂ O ₃	0.01	0.03	0.03
TiO ₂	0.62	0.91	0.54
MnO	0.09	0.12	0.11
P ₂ O ₅	0.23	0.55	0.22
SrO	0.06	0.13	0.04
BaO	0.08	0.06	0.04
C	1.15	1.01	0.90
S	0.03	0.14	0.27
LOI	6.82	6.34	6.31
Total	99.51	100.27	99.69
Mg#	40.16	38.67	34.36

ppm			
Ba	753.00	549.00	361.00
Ce	66.60	89.80	55.20
Cr	90.00	210.00	220.00
Cs	10.35	2.93	7.01
Dy	2.06	3.73	3.86
Er	0.90	1.86	2.23
Eu	1.50	2.17	1.44
Ga	18.80	17.40	21.80
Gd	3.11	6.05	4.23
Hf	2.90	5.40	3.30
Ho	0.28	0.67	0.80
La	30.30	39.90	26.90
Lu	0.12	0.23	0.33
Nb	3.50	8.40	5.00
Nd	29.20	47.60	26.50
Pr	8.04	11.90	6.94
Rb	109.50	28.90	113.50
Sm	4.39	8.89	5.32
Sn	2.00	2.00	1.00
Sr	721.00	1150.00	325.00
Ta	0.60	0.50	0.30
Tb	0.33	0.76	0.70
Th	3.33	5.14	3.04
Tm	0.12	0.26	0.32
U	0.90	1.91	1.12
V	103.00	158.00	167.00
W	23.00	2.00	202.00
Y	10.50	18.60	21.10
Yb	0.72	1.48	1.97
Zr	128.00	201.00	129.00
As	212.00	29.30	250.00
Bi	0.23	0.14	0.49
Hg	0.02	0.02	0.16
Sb	9.90	0.38	1.67
Se	0.40	0.70	1.40
Te	0.06	0.01	0.86
Tl	0.12	0.50	0.60
Ag	0.50	0.50	6.80
Cd	0.50	0.50	0.50

Co	16.00	24.00	25.00
Cu	8.00	26.00	20.00
Li	80.00	70.00	90.00
Mo	1.00	6.00	2.00
Ni	32.00	67.00	89.00
Pb	12.00	14.00	19.00
Sc	10.00	17.00	15.00
Zn	84.00	85.00	122.00

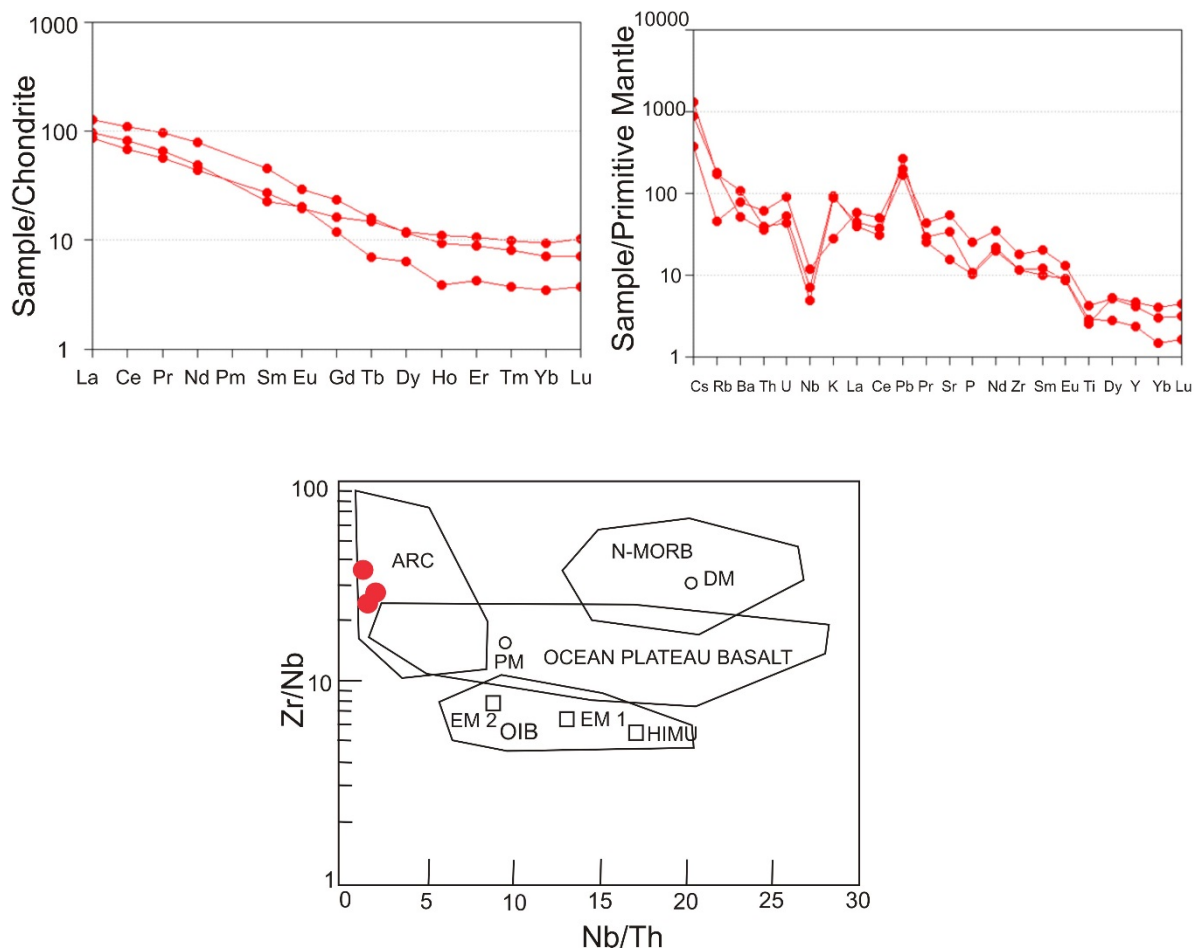


Fig. 4.5. Geochemical plots for microdiorite in the Kunche deposit (a) Chondrite-normalized REE patterns of the Kunche microdiorite (b) Primitive mantle-normalized diagrams of Kunche microdiorite (normalization values from [Sun and McDonough, 1989](#)) (c) Zr/Nb vs. Nb/Th. ARC = arc-related basalts; N-MORB = Normal mid ocean ridge basalt; OIB = oceanic island basalt. Hypothetical mantle sources: DM = shallow depleted mantle; EN = enriched component; PM = primitive mantle; HIMU = high μ (U/Pb) source; EM1 and EM2 = enriched mantle sources (modified after [Condie, 2005](#)).

4.6 Deformation History

Structural analysis of the Kunche deposit is expository to comprehensively understand the genesis of gold mineralization. The Kunche deposit shows the development of three generations of fabric elements representing deformational phases D_{K1} - D_{K3} (Fig. 4.6). The addendum K, is used to denote the local deformation pertaining only to the Kunche deposit and not the structural history of the whole Wa-Lawra belt.

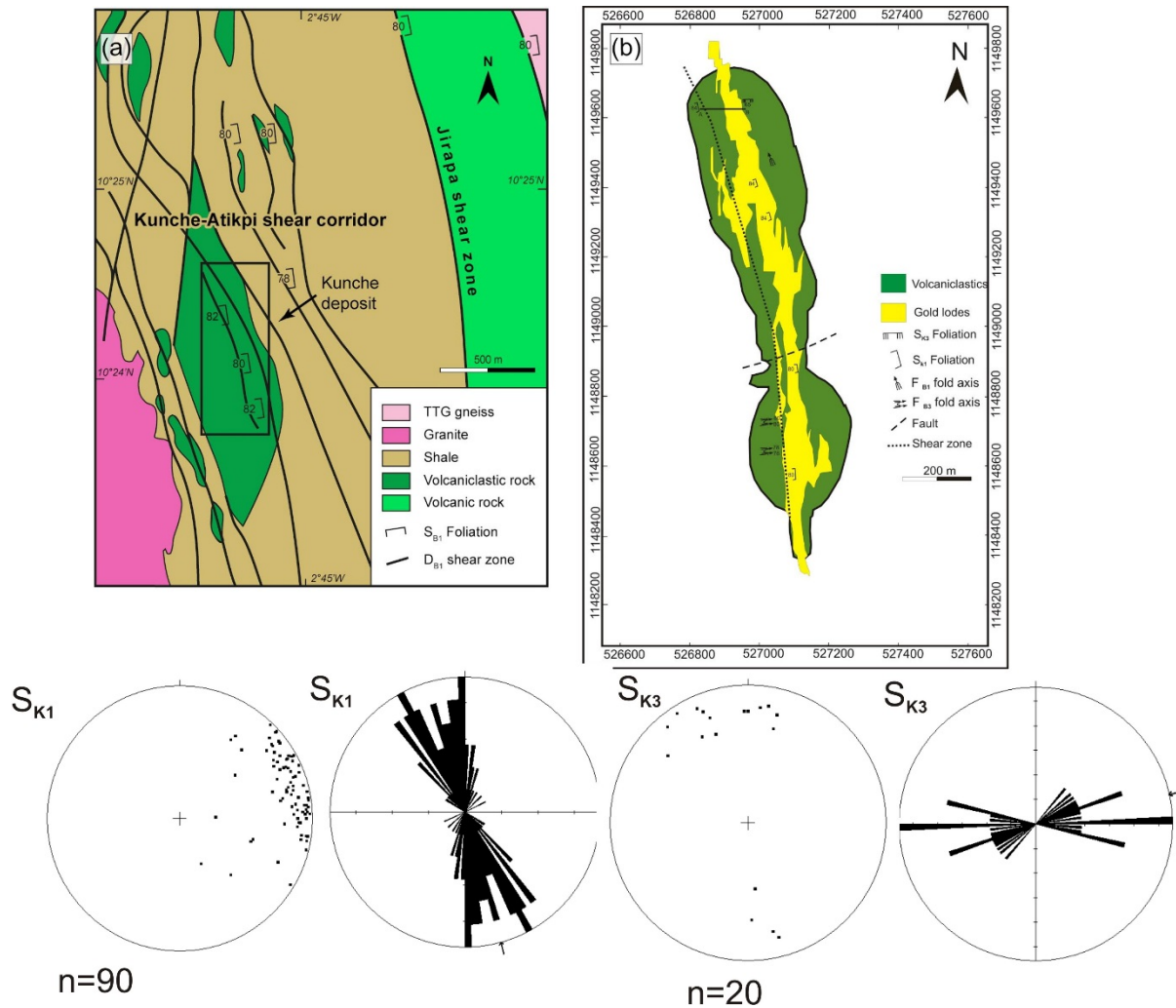


Fig. 4.6. (a) A simplified geological map of a portion of the Kunche-Atikpi shear zone, west of the Jirapa shear zone. In the black insert is the Kunche deposit (location of the subpanel b). (b) The deposit showing the N to NNW anastomosing shear zone and the mineralized corridor. The equal-area lower hemisphere stereo-plots and rose diagram of structural orientation.

4.6.1 D_{K1}

D_{K1} is the oldest deformation in the Kunche deposit and affected all the rocks in the deposit. It is represented by N to NNW oriented sinistral shear zones. The early stage of this

deformational phase observed mainly within the Jirapa shear zone is marked by a N to NNW penetrative foliation or fabric (S_{K1}), with vertical to subvertical dips (Fig. 4.7a) to the west and a N-trending (008°) subhorizontal stretching lineation and plunges ranging from 14° to 20° and parallel to primary bedding S_0 . The S_{K1} is parallel to the primary bedding in the Kunche deposit (Fig. 4.7b). The volcanoclastic sediment in the Kunche deposit exhibit graded bedding with a fining upward sequence and the younging direction to the west. The D_{K1} in the Kunche deposit is also characterized by F_{K1} isoclinal folds (Fig. 4.7a). These isoclinal folds do have subvertical fold axis and axial planes parallel to the S_{K1} penetrative fabrics.

There is a discrete anastomosing shear zone 4 km west of the Jirapa shear zone which may have formed during the waning stages of the D_{K1} event or synchronously with the Jirapa shear zone. The shear zone is characterized by a left stepping dilatational jogs and is denoted as the Kunche-Atikpi shear zone corridor. This shear zone is traceable about 20 km both north and south from the Kunche deposit. The volcanoclastic sediments in the Kunche deposit were deformed by the brittle-ductile anastomosing shear zone with a N to NNW strike and vertical dip.

The dilatational zone in the anastomosing shear zones have created or permitted fluid flow into the sediments. This is evident by the ductile boudinage of quartz vein and veinlets.

4.6.2 D_{K2}

D_{K2} in the Kunche deposit is marked by E-W trending tension gashes (Fig. 4.7d) that crosscut the S_{K1} shear zones and are mostly quartz filled representing en echelon quartz veins. This indicates an E-W shortening (the maximum compressive stress).

4.6.3 D_{K3}

The D_{K3} deformation phase in the Kunche deposit is characterized by east trending axial planes of F_{K3} folds, with vertical fold axis and an E-W trending penetrative S_{K3} axial planar foliation (Fig. 4.7e). These structures over print the S_{K1} foliation in the deposit and mainly observed within the volcanoclastic sediment beds. In the volcanoclastic rocks F_{K3} folds are rare, but an E-W spaced cleavage S_{K3} (Fig. 4.6f) that crosscuts all the structures described above can be found. The D_{K3} deformational phase in the Kunche deposit is also characterized by the late NE and NW brittle faults. They locally displace the D_{K1} shear zones and occur as broken fragments or as offsets in the drill core. They are hard to be found in the field due to the fact that there is no outcrop, but can be easily recognisable in the drill cores.

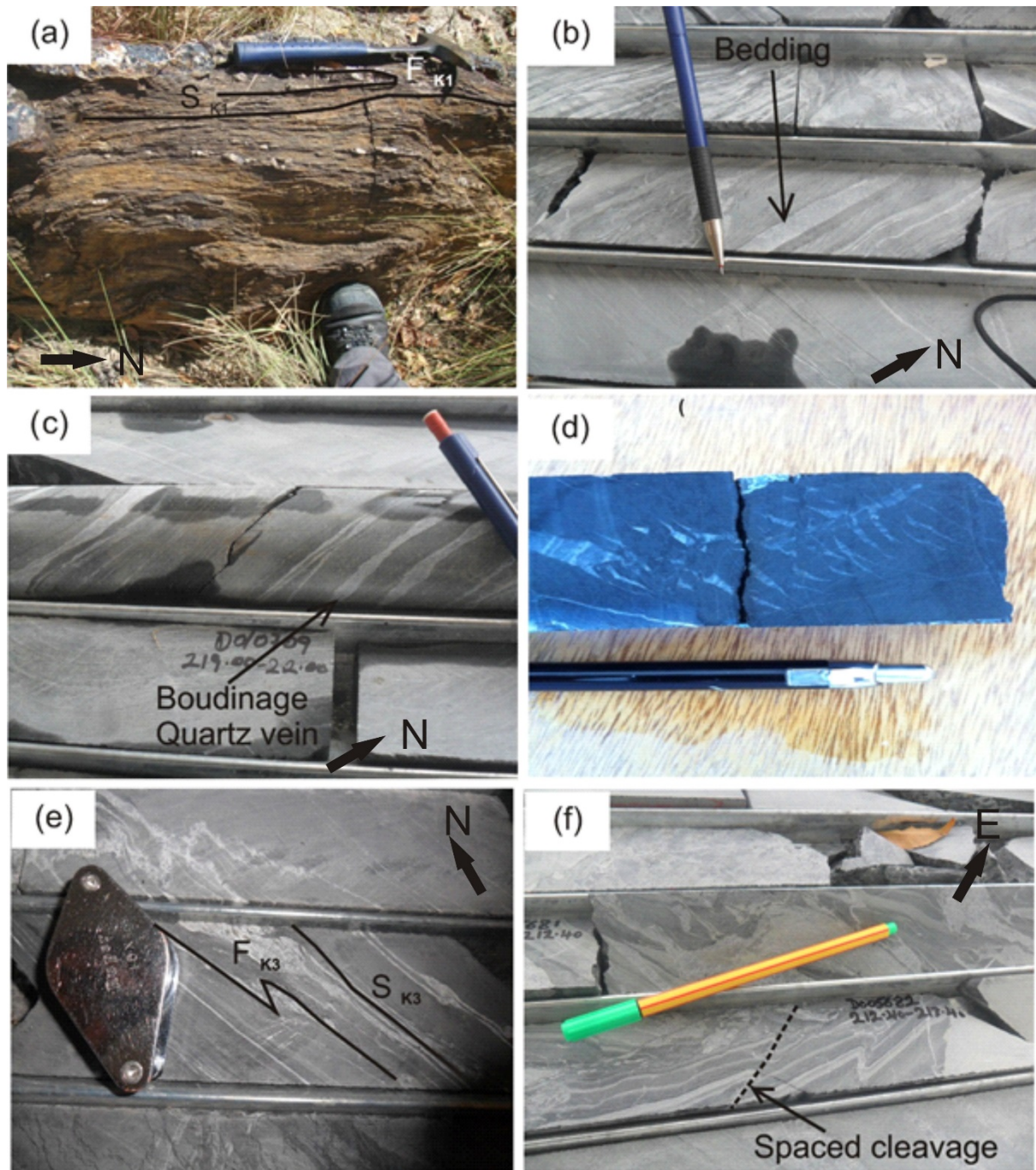


Fig. 4.7. Field and drill core photographs of representative structures in the Kunche deposit (a) Volcaniclastic sediment cropping out within the Kunche-Atikpi shear zone exhibiting N striking S_{K1} foliation and north verging F_{K1} isoclinal fold which is axial planar to S_{K1} (b) drill core showing bedding (c) drill core showing boudinage quartz vein within the dilatational zone of the Kunche-Atikpi shear zone (d) Zoomed in drill core showing the D_{K2} E-W trending tension gashes (e) a drill core exhibiting E-W trending F_{K3} fold with the axial plane acting as the S_{K3} foliation plane (f) E-W spaced cleavages can be observed and this is characteristic of D_{K3} deformation

4.6 Quartz veins

In general, two type of quartz veins were observed within the Kunche deposit. This classification is based on their infill type since there are no clear cut crosscutting features. These are the type 1 and 2.

The Type-1 quartz veins observed within the Kunche deposit occur within the dilatational zone of the D_{K1} anastomosing shear zones. The quartz veins in Kunche are grey (or smoky), generally do not have a vuggy aspect (Fig. 4.8a) except in minor areas where calcite increases and are sheeted. The quartz vein is composed about 90 to 95 % quartz, with 2 % calcite, 2 % chlorite and 1% sericite. The vein contains 4 % of sulphides composed dominantly of arsenopyrite, minor pyrrhotite, galena and chalcopyrite. The sulphides were mostly found nested with fractures in the quartz vein.

The quartz vein mostly strike N-S in the deposit and bends NNW at the northern edge of the deposit and dips ranging between 70° to 80° to the west (Fig. 4.8b). Within the dilatational zones these veins are 20 to 30 m thick.

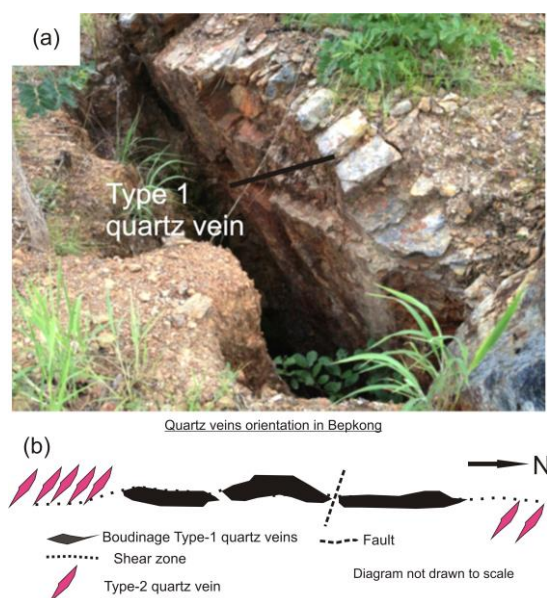


Fig. 4.8. (a) Photograph showing N-S trending type 1 grey quartz vein in an artisanal mining pit (b) Schematic diagram showing orientation of quartz veins in the Kunche deposit

Thin section analysis revealed that the quartz mineral exhibits undulose extinction (Fig. 4.9a), indicating it has accommodated some amount of strain. Textural analysis of the quartz grains indicates they are mainly comb (recrystallized grains) textures. The fine grained recrystallized quartz has serrated edges indicating varying degree of dynamic recrystallization by the mechanism of grain boundary migration and sub grain rotation (Fig. 4.9b).

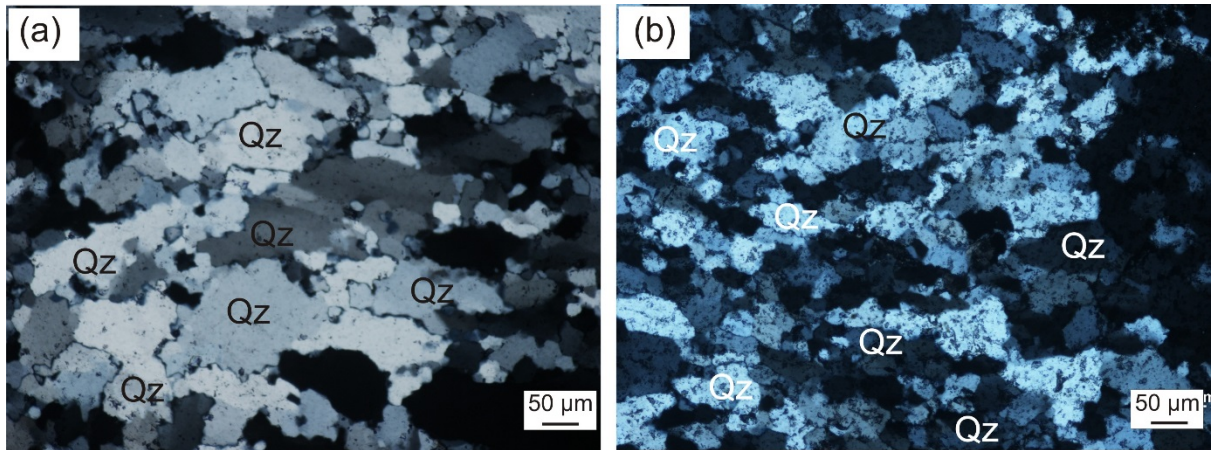


Fig. 4.9. Photomicrographs of a Type-1 quartz vein in the Kunche deposit (a) Type-1 quartz grain exhibiting undulose extinction (b) Type-1 quartz vein showing sheared comb and ribbon-like textures. Fine-grained recrystallized quartz develops along the shear planes, affected by grain boundary migration and sub-grain rotation. Qz=quartz

4.8 Alteration

Alteration in the Kunche deposit is easily noticeable and can be quantitatively recognised by the colour and mineralogy. From drill core logging the hydrothermal alteration exhibits a straight forward pattern, thus the alteration mineral assemblage associated with the ore zone and that associated with the barren rocks. The alteration mineral assemblage associated with the mineralized zone are calcite + chlorite + sericite + quartz + sulphides (Fig. 4.10) and give the rock a greenish colouration. The presence of silica as an alteration product makes the rock very hard. The rocks within the mineralized zone are highly silicified. The sulphides (arsenopyrite, pyrrhotite, chalcopyrite and galena) occur as disseminations mainly within the brittlely deformed country rocks or in the fractures formed within the quartz veins. The thickness of the alteration zone in Kunche is variable, but typically ranges between 20 to 150 m (Fig. 4.11). As one moves within the barren rocks, the rocks do have greenschist facies signatures with sulphides absent.

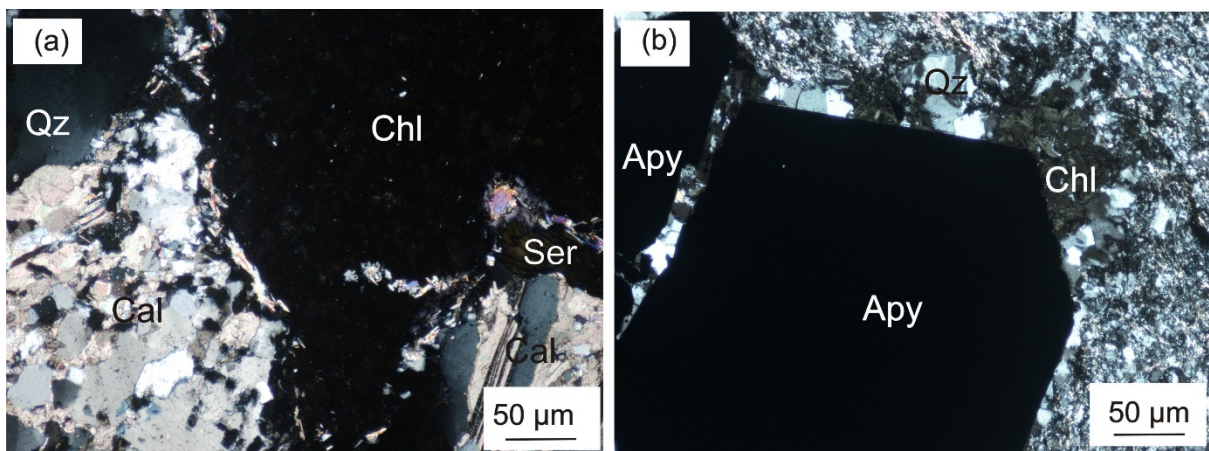


Fig. 4.10. Photomicrograph of alteration mineral assemblage within the ore zone (a) showing the alteration mineral assemblage of calcite, chlorite and quartz (b) alteration assemblage of arsenopyrites, quartz and chlorite. Chl=chlorite, Ser=sericite, Apy= arsenopyrite, Qz=quartz

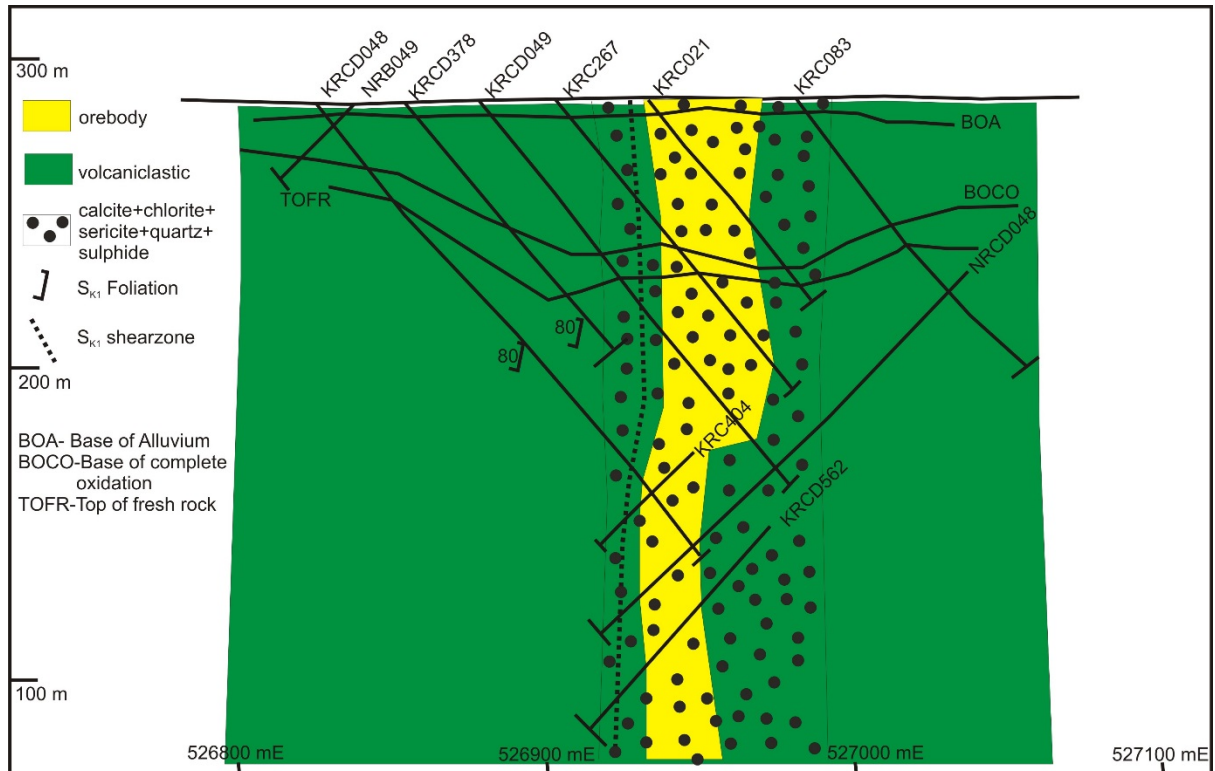


Fig. 4.11. Cross-section (looking north) of the Kunche deposit along 1,149,600mN, showing mineralized shoots within the main ore body, along subvertical D_{K1} shear zones (cf., Fig. 4.6 for location). High-grade mineralization is confined to a 20 m- to 150 m-thick alteration zone defined by an assemblage consisting of chlorite + calcite + sericite + quartz + sulphides.

4.9 Ore body characteristics and geometry

The main mineralization in the Kunche deposit is restricted to the anastomosing shear zone and hosted in a 1.1 km long and 20 to 40 m thick quartz vein system (Fig. 4.12), characterised mainly by dark grey quartz veins and disseminated sulphides. The sulphides are concentrated within the fractures in the vein and the vein selvedge with the volcaniclastic host rock, or within the brecciated zone in the volcaniclastic rocks. The 1.1 km lenticular ore body in the Kunche deposit, is made up of a single ore shoot or lode which is parallel to the anastomosing shear zone. To the north and south of the main ore body is the NE trending minor mineralized lodes that horse tails or splay off the main mineralised body. The ore body trends N, but bends NW wards at the northern section of the deposit. The ore body has been faulted in the central part by a late ENE oriented brittle normal fault with a displacement or fault throw of 20 m.

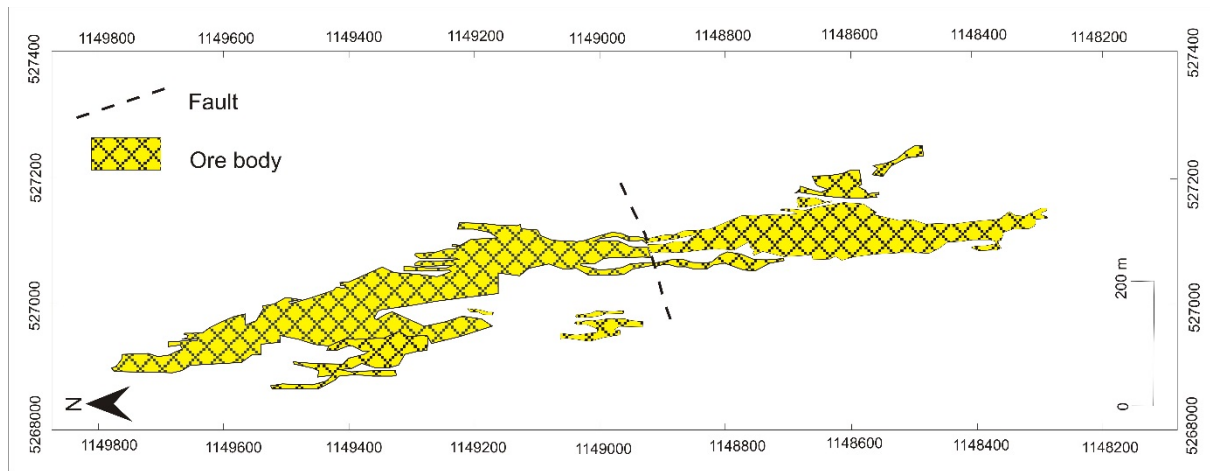


Fig. 4.12. A map showing the 1.1 km mineralized lode in the Kunche deposit projected to surface. It shows a single lode, faulted in its central portion of the deposit, with the minor lode splaying of the main lode in both the northern and southern portion.

4.10 Ore Mineralogy

The ore minerals in the Kunche deposit is composed of arsenopyrites, chalcopyrites, pyrrhotites and galena. The ore minerals mostly occur as disseminations within the hydrothermal altered country rock, especially the silicified zones. These sulphide minerals occupy about 3 to 6 % of the ore zone, but increases as one gets to areas where the brecciation is intense.

The arsenopyrite is the most dominant and wide spread sulphide mineral within the brittle mineralized zone. The arsenopyrite are coarse grained (sometimes contain inclusions of the country rock), occurs as rhomb shaped euhedral crystals (Fig. 4.13) and sometimes can grow up to 2 mm in the brecciated rock or in the quartz veins. The arsenopyrite sometimes occur as matted euhedral acicular grains (Fig. 4.13b). The pyrrhotite mainly grow on the crystals of the arsenopyrites or grow along the fractures within the arsenopyrite crystal and in some instances replaces the arsenopyrites. The chalcopyrite do occur as fine grained inclusions (2-5 μm ; Fig. 4.13c, d), within the pyrrhotite grains embayed in the margin or in the core of the arsenopyrite.

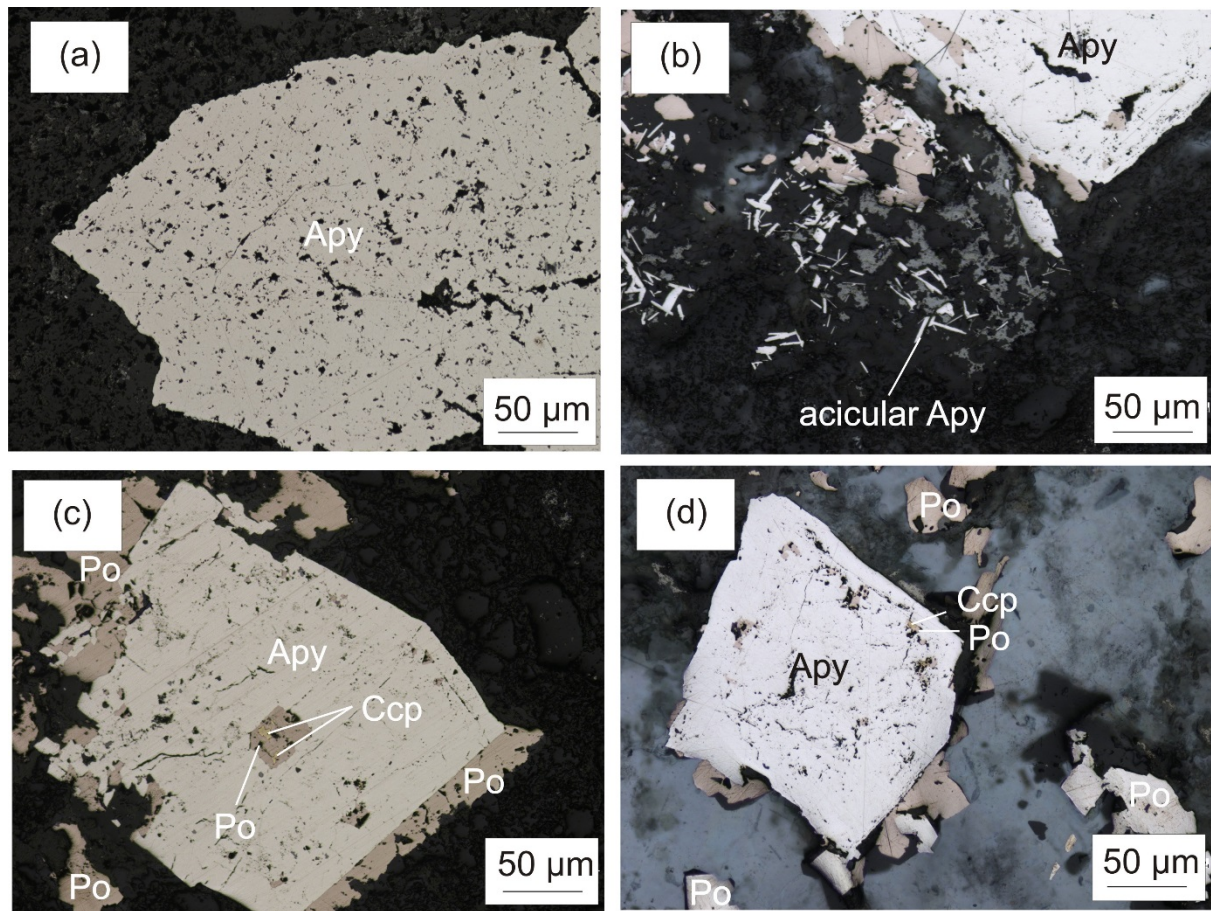


Fig.4.13 Photomicrographs of sulphides within the Kunche deposit (a) Euhedral arsenopyrite with inclusion of the country rock (b) The photomicrograph shows euhedral arsenopyrite at the top. Beneath the euhedral arsenopyrite is a euhedral matted acicular arsenopyrite (c) arsenopyrite with pyrrhotite growing on top of it or formed within the fractures in the arsenopyrite. Embedded in the core of the arsenopyrite is pyrrhotite with chalcopyrite inclusion (d) Euhedral arsenopyrite with pyrrhotite growing on top of the arsenopyrite crystal and within fractures found at the margins of the arsenopyrite. Apy=arsenopyrite, Ccp=chalcopyrite, Po= pyrrhotite.

BSE SEM images, the arsenopyrite crystal exhibits intra grain, grain boundary alteration rim as well as crystallographic zoning (Fig. 4.14a) and growth rims (Fig 4.14b). Gold in the Kunche deposit is associated mainly with the arsenopyrite. BSE SEM images showed that gold is always accompanied with silver and are both chemically bounded with the sulphides (Fig. 4.14c, d). The gold also form as micro sizes with fractures in the arsenopyrite (Fig. 4.14d)

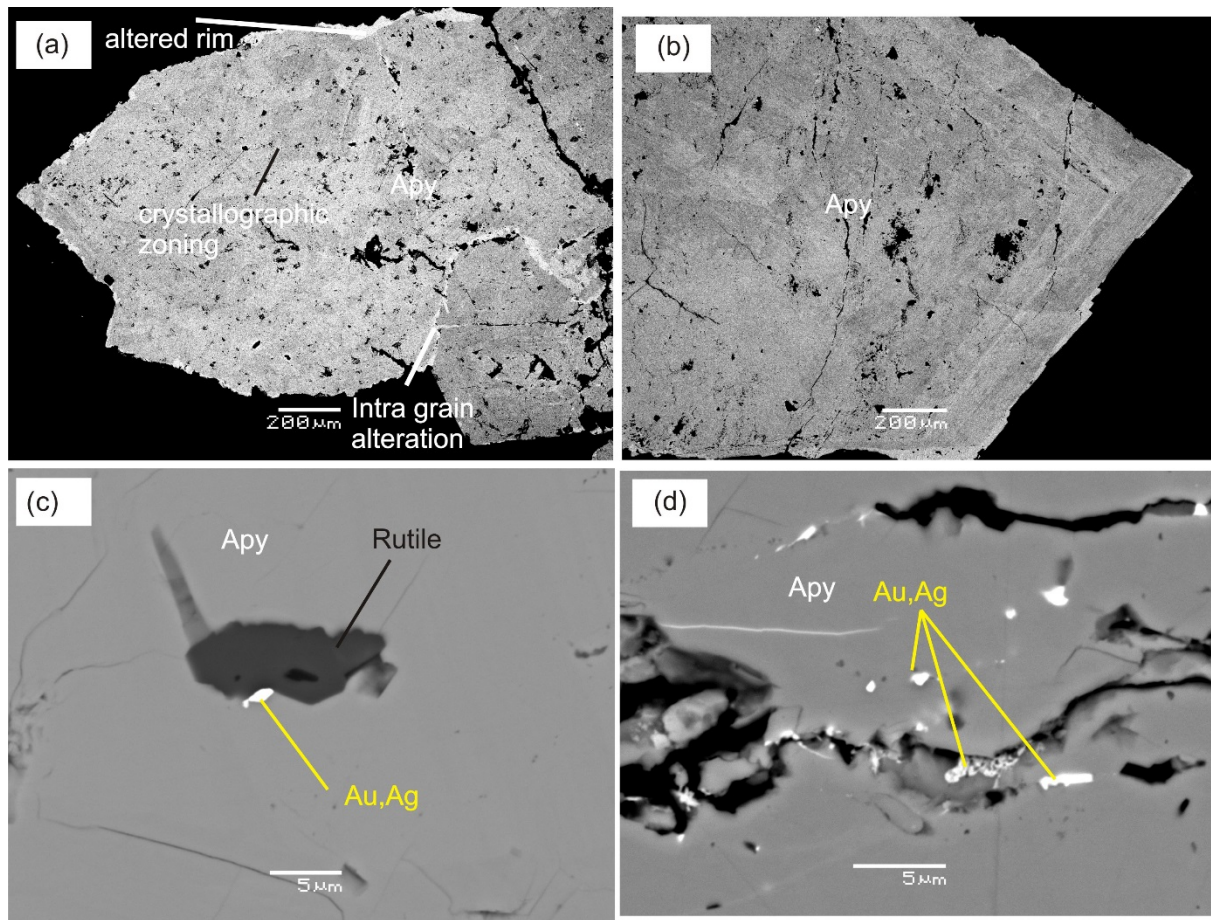


Fig 4.14. BSE SEM images of arsenopyrites in the Kunche deposit (a) Arsenopyrite exhibiting intra grain alteration, crystallographic zoning and hydrothermal altered rims (b) Euhedral arsenopyrite exhibiting growth rings (c) gold associated with rutile in a fracture in the arsenopyrite (d) arsenopyrite showing micron size inclusion of Au, Ag within fractures

From LA-IC-PMS done on eighteen arsenopyrite grains (Table 4.3) in the Kunche deposit revealed the presence of trace amount of Au (3.84-19.61ppm), Ag (0.11-0.86ppm), Sb (656-1995.65ppm), Pb (0.20-0.27 ppm), As (14176658-2123187 ppm) and the most abundant element in the Kunche deposit, Ni (96.47-2110.30 ppm), Co (1.89- 1309.22 ppm), Cu (0.65-2.94 ppm) and Zn (0.75-5.87 ppm). Gold in the Kunche deposit shows positive correlation with Ag and Cu (Table 4.4).

Table 4.3. LA-ICP-MS on arsenopyrites in the Kunche deposit

spots	Au	Ag	Sb	Pb	As	Ni	Co	Cu	Zn
LOD	0.01	0.01	0.1	0.10	0.8	0.6	0.2	0.09	0.07
Apy_1	7.86	0.31	656.62	0.27	1456046.00	128.13	5.53	1.05	0.81
Apy_2	4.40	0.17	1449.67	<LOD	1404947.00	96.47	1.89	1.43	0.82
Apy_3	7.58	0.33	748.75	<LOD	1347354.38	266.15	60.25	1.47	0.75
Apy_4	16.24	0.37	1201.64	<LOD	1319488.63	129.27	52.64	1.10	5.87
Apy_5	10.00	0.46	630.62	<LOD	1679860.38	144.31	10.37	1.35	1.05
Apy_6	3.84	0.25	865.08	<LOD	1431428.25	118.77	6.55	1.04	0.80
Apy_7	4.76	0.25	840.02	0.20	1417665.38	127.34	4.62	1.01	2.44
Apy_8	7.77	0.40	1073.53	<LOD	1571126.00	130.34	8.24	1.15	0.91
Apy_9	13.30	0.47	1028.67	<LOD	1653153.75	145.26	8.59	1.24	1.19
Apy_10	6.23	0.22	1374.10	<LOD	1603611.25	119.69	3.63	1.55	2.70
Apy_11	19.13	0.54	935.45	<LOD	1696231.63	971.93	282.40	1.35	1.15
Apy_12	19.61	0.86	1778.56	0.26	1434620.13	167.38	10.81	2.94	1.34
Apy_13	8.92	0.11	1777.58	<LOD	1394680.75	138.74	19.97	0.65	1.71
Apy_14	6.23	0.24	1738.34	<LOD	1608862.50	207.86	32.19	1.24	0.84
Apy_15	3.36	0.15	1334.56	<LOD	1511525.88	330.21	1309.22	0.99	1.10
Apy_16	14.10	0.25	1414.90	<LOD	1698370.63	2110.30	610.87	1.11	0.97
Apy_17	14.57	0.34	702.07	0.26	1637013.50	146.23	34.47	1.09	0.85
Apy_18	16.99	0.25	1995.67	0.26	2123187.25	441.62	57.11	1.39	1.10

LOD=Limit of detection

Table 4.4. Correlation coefficient of Au and other trace elements in the arsenopyrite. Bold face denotes correlations discussed in the text.

	Au	Ag	Sb	Pb	As	Ni	Co	Cu	Zn
Au	1.00	0.67	0.19	0.33	0.40	0.35	-0.12	0.44	0.19
Ag		1.00	-0.11	0.32	0.02	-0.02	-0.24	0.77	0.19
Sb			1.00	-0.06	0.28	0.13	0.11	0.28	0.07
Pb				1.00	0.23	-0.18	0.29	0.29	-0.13
As					1.00	0.35	0.07	0.02	-0.31
Ni						1.00	0.45	-0.06	-0.16
Co							1.00	-0.18	-0.11
Cu								1.00	-0.07
Zn									1.00

4.11 Mineral paragenesis

The paragenetic sequence in the Kunche deposit is associated with the onset of the D_{K1} deformation and the related mineral assemblage is summarized in the figure below. The silicate minerals such as the plagioclase, quartz, sericite, and muscovite are believed to have formed early in the paragenetic sequence and associated with the regional metamorphism (Fig. 4.15). The ore forming stages was still associated with the regional metamorphic minerals plus the formation of the sulphides (arsenopyrite, pyrrhotite, chalcopyrite and galena).

Minerals	Regional metamorphism	Ore stage (D_{K1})	Late stage (D_{K2} - D_{K3})
Plagioclase	_____	_____	_____
Quartz	_____	_____	_____
Muscovite	_____	_____	_____
Chlorite	_____	_____	_____
Calcite	_____	_____	_____
Sericite		_____	
Arsenopyrite		_____	
Pyrrhotite		_____	
Chalcopyrite		_____	
Galena		_____	
Gold		_____	
Silver		_____	
Rutile	_____	_____	_____

Fig.4.15. A paragenetic scheme in the Kunche deposit showing the relative abundance of minerals during the regional metamorphic stage, ore forming stage and after the ore forming stage

4.12 LA-ICP-MS profile character of the arsenopyrite

Inspection of the LA-ICP-MS output profiles from the spot analysis show that all of the arsenopyrite measured had some measurable quantity of gold (Fig. 4.16), with relatively little variation in their gold concentrations.

The gold pattern (Fig. 4.16) are relative smooth with no spikes, which gives an indication that the invisible gold in the arsenopyrite occurs primarily in a form of solid solution or as nanoparticles. Iron and arsenic in the time-resolved depth profile in the arsenopyrite are very flat with no spikes (Fig. 4.16a, b, c). This show that iron and arsenic are in solid solution over several hundreds of concentration. Lead (Pb) vary in several order of magnitude and can be attributed to the inclusion of galena within the arsenopyrite.

All the samples measured contained considerable quantities of Ag (Table 4.3). Ag trends in the time-resolved depth profile is parallel to that of Pb, which indicates that Ag may occur as S-Pb compound. Ni and Co are usually trace element usually associated with arsenopyrite and their flat responds in the time-resolved depth profile shows they are present in the arsenopyrite. Zn is detectable in most of the arsenopyrite analysed and shows spikes in the time-resolved depth profile indicating the presence of chalcopyrite. Chalcopyrite were also observed within thin-section. Sb also shows a flat responds in the time depth profile, which indicates the also occur as solid solution within the arsenopyrite.

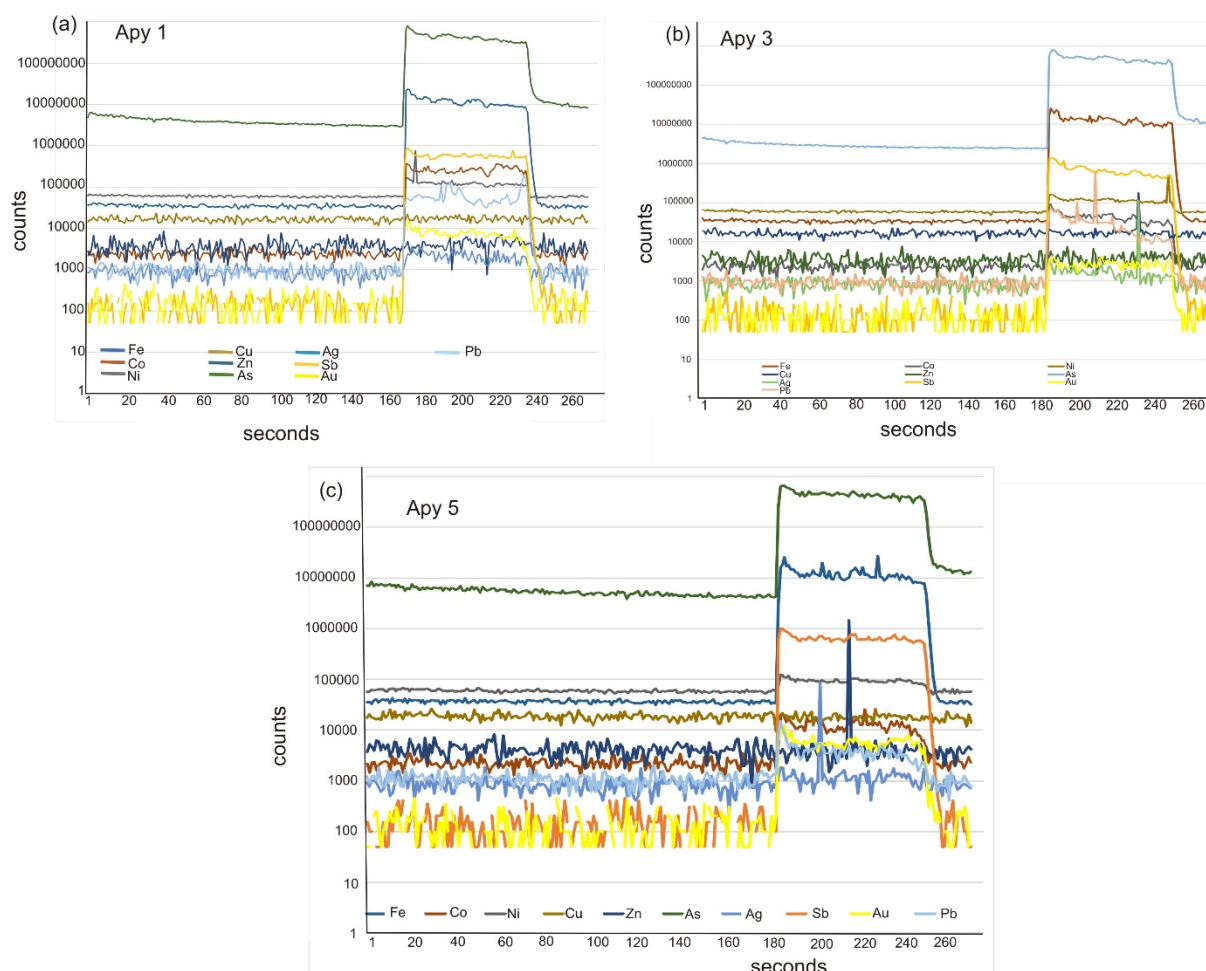


Fig. 4.16. Representative time-resolved depth spectra for arsenopyrite analysed within the Kunche deposit indicating the occurrence of gold and other element. Fe and As exhibits flats responds which is typical of major elements in arsenopyrite. The parallel trends of Au and Ag suggest they formed as nanoparticles or in solid solution.

4.13 Discussion

The combination of petrographic, structural analysis and inferred chronological ages from Block (2015) has permitted for the correlation of events with regards to gold mineralization and structural controls in the Kunche deposit.

Block (2015) ascribed greenschist metamorphic facies to the sediments on the Wa-Lawra belt (temperature and pressure of 250-300 and <4 kbar respectively, using the chlorite-phengite equilibria method). This assertion is in line with the mineral assemblage of chlorite, mica, sericite, quartz observed within the volcanoclastic sediment carrying the gold in the Kunche deposit. The lower temperature and pressure metamorphic characteristics is also observed in the quartz crystals in the type 1 quartz veins. The quartz crystals progressively grow by grain boundary migration and exhibit a lobate shapes in ribbon forms (Fig. 4.9). Similar low temperature characteristics of quartz have been described by Passchier & Trouw (2009).

Structural analysis from drill core logging and geological mapping within the Kunche deposit suggest three phases of deformations (D_{K1} - D_{K3}). These deformation events recognised at local scale will be discussed in relation to the regional deformation events. The regional structural events have been described by Baratoux et al. (2011) who worked on the larger Boromo belt in Burkina Faso and Block (2015) who worked on the whole NW Ghana.

The first deformational episode D_{K1} on the deposit scale affected all the volcanoclastic and microdiorite rocks and is characterized by early N to NNW oriented sinistral shear zones observed within the major crustal scale Jirapa shear zone with vertical to subvertical dips. West of this major shear zone is located the discrete anastomosing shear zone characterized by a left stepping dilatational jog, which was probably formed at the later stages of this deformation event. The dilatational zone in the anastomosing shear zones have permitted fluid flow into the sediments and is responsible for the gold mineralization in the deposit. From the table below, the D_{K1} in the Kunche deposit correspond to D_4 and D_1 regional events described by Block (2015) and Baratoux et al. (2011) respectively.

Table. 4.4. Table comparing the structures observed within the Kunche deposit and that of the regional deformation sequence proposed by Block (2015) and Baratoux et al., (2011)

Study	D ₁	D ₂	D ₃	D ₄	D ₅	D ₆
Block (2015) NW Ghana	D ₁ = N-S directed shortening, E-W penetrative fabric (S ₁) with shallow to steep dips. Low angle thrust faulting and folding	D ₂ = N-S directed shortening, S ₂ foliation with moderate dips with plunging lineation down dip	D ₃ =E-W directed shortening and S ₃ schistose foliation	D ₄ =ENE to WSW shortening with sinistral strike slip shearing	D ₅ = E-W brittle deformation	D ₆ =E-W brittle deformation, tension and brittle strike and slip faults
Baratoux et al. (2011) Boromo belt	D ₁ = N-NNE oriented S1 foliation. F1 fold with axial plane parallel to S1					
	D ₂ consist of steeply dipping NNE to ENE anastomosing shear zone with dextral characteristics					
	D ₃ consist of crenulation cleavages, chevron kink folds, E-W space cleavages, and the late brittle strike slip faults					
Kunche deposit	D _{K1} =N to NNW steeply dipping sinistral anastomosing shear zone and denotes ENE-WSW shortening. FK1 fold with axial plane parallel to the shear zone SK1 foliation. Syn-tectonic quartz vein. Gold is present					
	D _{K2} = E-W trending tension gashes. This indicates E-W shortening					
	D _{K3} = F _{K3} isoclinal folds and crenulation cleavages overprinting S _{K1} . E-W space cleavages and late NE-NW brittle fault.					

D_{K2} is characterized by an en echelon of E-W tension gashes filled with quartz vein, chlorite and white mica. This deformation can be attributed to the regional D_6 deformation described by Block (2015), and is characterized by brittle structures consistent with an east-west shortening, such as E-W quartz tension gashes, sometimes chlorite, white mica or epidote-bearing, and conjugate brittle strike-slip faults.

4.13.1 Structural controls and timing of gold mineralization in the Kunche deposit

There is a strong spatial relationship between gold mineralization and the 40 km anastomosing shear zone. Therefore, understanding the relationship between gold mineralization and the structural history in the Kunche deposit is essential in the development of a metallogenic model for the deposit.

Gold in the Kunche deposit is controlled by dilatational jogs within the sinistral anastomosing shear zone within the favourable volcanoclastic rock which has permitted fluid into the system. The mineralization phase is associated with chlorite + sericite + calcite + quartz + sulphide alteration in the anastomosing shear zones (D_{K1} event), which developed under an E-W shortening direction. The sulphides within the mineralized zone do occur as disseminations. This disseminated style of mineralization and the alteration mineral assemblage described in Kunche is typical of orogenic gold describe worldwide (Groves et al., 1998) formed in greenschist facies (Goldfarb et al., 2005). Geochronological constrains on deformation based on the work of Block (2015) and Agyei Duodu et al. (2009) on the regional deformation in NW Ghana and the parallelism of Type-1 vein associated with D_{K1} , shows that the gold mineralization can be inferred to have formed between 2110-2105 Ma (Fig. 4.17). So far, gold mineralization is not associated with the late 2104 Ma (U-Pb dating on zircon) undeformed intrusives in the Wa-Lawra belt. The age of late granitoid intrusives have help constrained the upper limit of the timing of mineralization in Kunche not later than 2105 Ma. The undeformed (euhedral shape) nature of the sulphides carrying the gold, means they might have formed during the later or waning stages of the D_{K1} event.



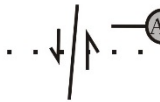


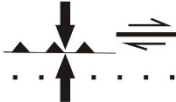
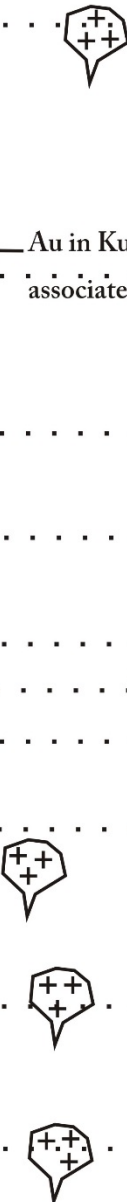
Domains in NW Ghana	Deformation history and kinematics	Timing of deformation event
<u>Wa-Lawra belt 2104 Ma</u> late granitoid intrusive	D6  D5  D4  Au in Kunche, associated with As.	2110 - 2105 Ma ?? inferred ages
	D3 	2123 to 2111 Ma
<u>Wa-Lawra belt 2139 Ma</u> sedimentation-volcanosediments shales, greywackes	D2  D1 	2130 Ma 2145 to 2125 Ma
<u>Julie belt (2168-2140 Ma)</u> -granitoids/granite/ rhyodacite <u>BBD 2190 Ma</u> migmatitic paragneiss with metabasite <u>KTGD 2200 Ma</u> migmatitic orthogneiss		

Fig 4.17. Space to time correlation between regional deformation (based on ages and deformation defined by Block, 2015) and gold mineralization in the Kunche deposit.

Pressure shadows around sulphides were mostly found and oriented along the D_{K1} shear foliation. The Z-shaped face controlled N-NNW oriented antitaxial pressure shadows and fringes developed around the arsenopyrites shows that the sight of sulphide and vein development were within a dilatation zone. This phenomenon of pressure shadows developed in dilational zones has been described by Passchier & Trouw (2009). The Z-shape pressure shadow gives an indication that the kinematics governing the deformation in the D_{K1} event is sinistral (Fig 4.18). The development of antitaxial strain fringes and pressure shadow shows that D_{K1} has experienced co-axial progressive deformation around the core of the sulphide mineral. The progressive deformational character for antitaxial strain development has also

been described by Passchier & Trouw (2009). D_{K2} - D_{K4} overprinted the early mineralization structures. Within a regional structural disposition, the gold mineralization is associated to the D_{1-2} described by Baratoux et al. (2011) and D_4 described by Block et al. (2015).

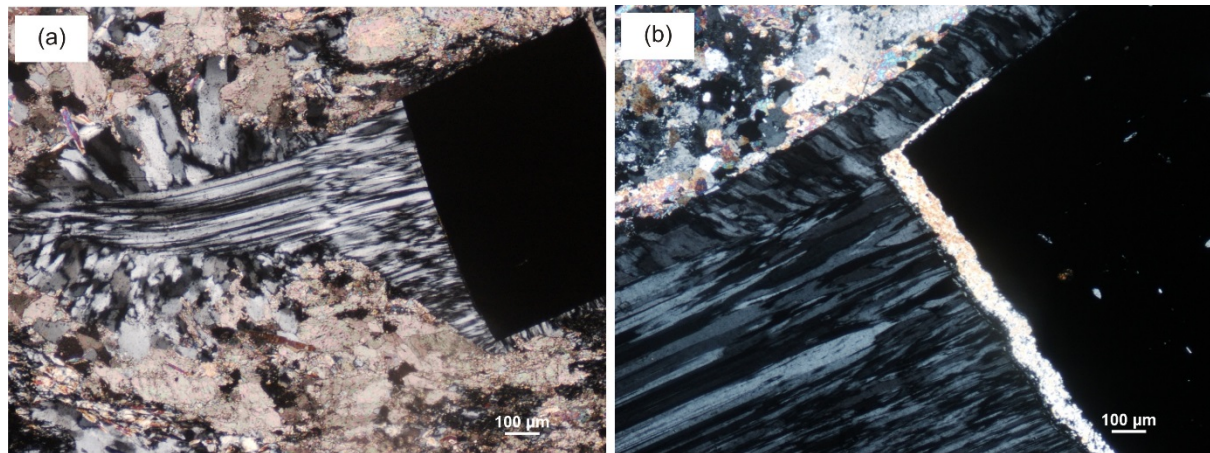


Fig. 4.18. Photomicrograph of pressure shadow in the mineralization zone in the Kunche deposit showing a face controlled antitaxial z-shape pressure shadow

4.13.2 Insight on ore genesis

The analysis of sulphide minerals textures provides useful information and understandings into the origin, history of the deposits as well as its exploitability and probable problems in the mineral processing. According to Barton & Skinner (1979), usually the most important sulphides that retain the original depositional conditions are the refractory types (eg. Arsenopyrites, sphalerite and pyrites) whereas sulphides such as galena, chalcopyrite and pyrrhotite readily adjust to composition during cooling. In order to understand the original depositional conditions in the Kunche deposit, the refractory arsenopyrite was taken into consideration. The arsenopyrites in the Kunche deposits showing evidence of crystallographic zoning, intra-grain and grain boundary alteration rims. These alteration characteristics shows that these sulphide type was formed during the hydrothermal alteration process.

From the overprinting relationship of the various sulphides observed within the mineralized zone within the three stages of the hydrothermal history can be deduced. Thus the initial pyrrhotite grain which have been overgrown by the stage two arsenopyrite with invisible gold. The final stage of the hydrothermal alteration event is composed of chalcopyrite, galena, pyrrhotite, visible gold and the growth of the arsenopyrite rims.

From LA-ICP-MS, the arsenopyrite is composed of chalcophile and siderophile elements such as Au, Ag, Sb, Pb, As, Ni, Co, Cu and Zn. According to the time-resolution depth profiles, these trace metals are either form as invisible solid solution in the crystal lattice of the sulphides or as nanoparticles in the sulphides. Au, Ag, Pb, Cu, Zn are the most abundant trace metallogenic elements in the Kunche deposit. The distribution of Au and Ag in the time-resolution depth profile are smooth indicating invisible gold do occur in solution or as nanoparticles within the arsenopyrite and show a positive correlation. Pb, Cu, Zn either do occur as solid solution or as inclusion within the arsenopyrite structure.

From this study gold in the Kunche deposit have two modes of occurrence; (1) as invisible solid solution or nanoparticles within the sulphide structure and (2) as visible micron-size

grains within the fractures of the arsenopyrite or as visible grains along the micro fractures in type 1 quartz vein.

4.13.3 Source of gold

Based on the geochemical studies from the Kunche deposit, we can conclude the source of gold in the Kunche deposit is from hydrothermal process in the volcanoclastic sediments. From the geochemistry of the volcanoclastic rocks the initial rock was not rich in ore forming metals such as Au, Ag, Zn, Cu, Pb but were simply elevated during the hydrothermal event as shown by LA-ICP-MS data from the arsenopyrite. Also the alteration characteristics such as alteration rim, oscillatory zoning have all shown gold was formed during the hydrothermal activity in Kunche as the sediments underwent greenschist facies metamorphism, and at these relatively low temperatures the chalcophile arsenic is soluble in aqueous fluids and have strong affinities with S and formed arsenopyrites (Zhang et al., 2014). From LA-ICP-MS sulphide contain large concentration of As and can easily form complexes with Au⁰ and Au¹⁺ gold during hydrothermal process. Arsenopyrite sulphide intake as Au⁰ and Au¹⁺ has been reported by Cabri et al. (2000).

4.14 Conclusions

The present study discusses several important aspects of the genesis of gold mineralization in the Kunche deposit in the Wa-Lawra belt which have hitherto not been investigated. This paper contributes to the understanding of the structures controlling gold mineralization in the deposit as well as understanding the ore genesis in the deposit.

Gold mineralization in the Kunche deposit is structurally controlled by the initial D_{K1} anastomosing shear zone and Type-1 quartz veins. Gold associated with trace elements such as Pb, Zn, Cu and Ag. Gold do occur as invisible nanoparticle or solid solution with the arsenopyrite sulphide or as visible gold in fractures of the sulphides.

Acknowledgement

Azumah Resources Limited the owners of the Kunche deposit are particularly thanked for giving the permission to publish this paper and for financing the fieldwork. We wish to gratefully acknowledge AMIRA International and the industry sponsors, including AusAid and the ARC Linkage Project LP110100667, for their support through the WAXI project (P934A). POA would like to thank Nick Franey and Stephen Stone for the continual support throughout the program.

Reference

- Abouchami, W., Boher, M., Michard, A., Albarede, F., 1990. A major 2.1 Ga event of mafic magmatism in West Africa: an early stage of crustal accretion. *Journal of Geophysical Research* 95, 17605–17629.
- Agyei Duodu, J., Loh, G.K., Boamah, K.O., Baba, M., Hirdes, W., Toloczyki, M., Davis, D.W., 2009. Geological map of Ghana 1:1 000 000. Geological Survey Department of Ghana (GSD).
- Amponsah, P.O., Salvi, S., Beziat, D., Baratoux, L., Siebenaller, L., Nude, P.M., Nyarko, R.S., Jessell, M.W., in press. The Bepkong deposit, Northwestern Ghana. *Ore Geology Reviews*. <http://dx.doi.org/10.1016/j.oregeorev.2015.06.022>
- Baratoux, L., Metelka, V., Naba, S., Jessell, M.W., Grégoire, M., Ganne, J., 2011. Juvenile Paleoproterozoic crust evolution during the Eburnean orogeny (2.2-2.0Ga), Western Burkina Faso. *Precambrian Research* 191, 18-45.
- Barton. P. B., Skinner. B.J., 1979. Sulfide Mineral Stabilities. In H. L. Barnes (ed.), *Geochemistry of Hydrothermal Ore Deposits*. 2nd ed. Wiley-Interscience. New York.
- Baulauz, B., Mayoyo, M.J., Frenandez-Nieto, C., Lopez, J.M.G., 2000. Geochemistry of the Precambrian and Palaeozoic siliciclastic rocks from the Iberian range (NE Spain): Implication for source area weathering, sorting, provenance and tectonic setting. *Chemical Geology*, 168, 135-150.
- Béziat, D., Bourges, F., Debat, P., Lompo, M., Martin, F., Tollon, F., 2000. A Palaeoproterozoic ultramafic-mafic assemblage and associated volcanic rocks of the Boromo greenstone belt: fractionates originating from island-arc volcanic activity in the West African craton. *Precambrian Research* 101, 25–47.
- Block, 2015. Evolution géodynamique du craton ouest Africain au nord du Ghana. University of Toulouse III. Unpublished PhD Thesis.
- Block, S., Baratoux, L., Jessell, M., Ailleres, L., Bruguier, O., Zeh, A., Bosch, D., Caby, R., Ganne, J., Mensah E., (submitted). Lower crust exhumation during Paleoproterozoic (Eburnean) orogeny, NW Ghana, West African Craton: interplay of coeval contractional deformation and extensional gravitational collapse. *Precambrian Research*.
- Borisova, A.Y., Freyrier, R., Polvé, M., Jochum, K.P., Candaudap, F., 2010. Multi-elemental analysis of ATHO-G rhyolitic glass (MPI-DING reference material) by femtosecond and nanosecond LA-ICP-MS: Evidence for significant heterogeneity of B, V, Zn, Mo, Sn, Sb, Cs, W, Pt, and Pb at the millimetre scale. *Geostandards and Geoanalytical Research*, 34, 245–255.

Cabri, L.J., Newville, M., Gordon, R.A., Crozier, E.D., Sutton, S.R., McMahon, G., Jiang, D.T., 2000. Chemical separation of gold in arsenopyrite. *Canadian mineralogist*, 38, 1265-1281.

Condie K.C., 1987. Early Proterozoic volcanic regime in southwestern North America. In: *Geochemistry and mineralization of Proterozoic suites* (eds. Pharaoh, T.C., Beckinsale, R.D., and Richard D.). Geological Society special publication 33, 211-218.

Condie K.C., 1989. *Plate Tectonics and Crustal Evolution*. 3rd ed. Oxford, New York, Beijing, Frankfurt, Sao Paulo, Sydney, Tokyo, Toronto: Pergamon Press, 476.

Condie, K.C., 2005. TTGs and adakites: are they both slab melts? *Lithos* 80, 33-44.

de Kock, G.S., Armstrong, R.A., Siegfried, H.P., Thomas, E., 2011. Geochronology of the Birim Supergroup of the West African craton in the Wa-Bole region of westcentral Ghana: implications for the stratigraphic framework. *Journal of African Earth Sciences* 59, 1-40

Dubé, B., and Gosselin, P., 2007, Greenstone-hosted quartz-carbonate vein deposits, in Goodfellow, W.D., ed., *Mineral Deposits of Canada: A Synthesis of Major Deposit-Types, District Metallogeny, the Evolution of Geological Provinces, and Exploration Methods*. Geological Association of Canada, Mineral Deposits Division, Special Publication 5, 49-73.

Feng, X., Amponsah, P. O., Martin, R., Ganne, J., Jessell, M.W., 2015. 3-D numerical modelling of the influence of pre-existing faults and boundary conditions on the distribution of deformation: example of North-Western Ghana. *Precambrian Research* (in press). <http://dx.doi.org/10.1016/j.precamres.2015.06.006>

Feybesse, J.-L., Billa M., Guerrot C., Duguey E., Lescuyer, J., Milési, J.P., Bouchot., 2006. The Paleoproterozoic Ghanaian province: Geodynamic model and ore controls, including regional stress modeling. *Precambrian Research* 149, 149-196.

Goldfarb, R.J., Baker, T., Dubé, B., Groves, D.I., Hart, C.J.R., Robert, F., and Gosselin, P., 2005, World distribution, productivity, character, and genesis of gold deposits in metamorphic terranes, in Hedenquist, J.W., Thompson, J.F.H., Goldfarb, R.J., and Richards, J.P., eds., *Economic Geology One Hundredth Anniversary*. Society of Economic Geologists, 1905-2005, 407-450.

Goldfarb, R.J., Groves, D.I., and Gardoll, S., 2001a. Orogenic gold and geologic time: A global synthesis. *Ore Geology Reviews*, 18, 1-75.

Griffis, R.J., Barning, K., Agezo, F.L., Akosah, F.K., 2002. *Gold Deposits of Ghana*. Minerals Commission, Accra, Ghana, 438.

Groves, D.I., Goldfarb, R.J., Gebre-Mariam, M., Hagemann, S.G., and Robert, F., 1998. Orogenic gold deposits: A proposed classification in the context of their crustal distribution and relationship to other gold deposit types. *Ore Geology Reviews*, 13, 7-27.

- Kouhestani, H., Oman-Rashidnejad, N., Rastad, E., Mohajjed, M., Goldfarb, R.J., Ghaderi, M., 2014. Orogenic gold mineralization at the Chah Bagh deposit, Muteh gold district, Iran. *Journal of Asian Earth Science*, 91, 89-106
- Leube, A., Hirdes, W., Mauer, R., Kesse, G.O., 1990. The early Proterozoic Birimian Supergroup of Ghana and some aspects of its associated gold mineralization. *Precambrian Research* 46, 139-165.
- Lorand, J.-P., Alard, O., 2011. Pyrite tracks assimilation of crustal sulfur in Pyrenean peridotites. *Mineralogy and Petrology*, 101, 115-128.
- McLennan, S.M., Taylor, S.R., 1991. Sedimentary rocks and crustal evolution: tectonic setting and secular trends. *Journal of Geology*, 99, 1-21.
- Milési, J.P., Feybesse, J.L., Pinna, P., Deschamps, Y., Kampunzu, H., Muhongo, S., Lescuyer, J.L., Le Goff, E., Delor, C., Billa, M., Ralay, F., Heinry, C., 2004. Geological map of Africa 1:10,000,000, SIGAfrigue project. In: 20th Conference of African Geology, BRGM, Orleans, France, 2-7 June, <http://www.sigafrique.net> (last accessed 14/12/2010).
- Passchier, C.W., Trouw, R.A.J., 2005. *Microtectonics*. Springer-Verlag Berlin, Heidelberg, 366.
- Sakyi, P.A., Su, B.X., Anum, S., Kwayisi, D., Dampare, S.B., Anani, C.Y., Nude, P.M., 2014. New zircon U-Pb ages for erratic emplacement of 2213-2130 Ma Paleoproterozoic calc-alkaline I-type granitoid rocks in the Lawra Volcanic Belt of Northwestern Ghana, West Africa. *Precambrian Res.* 254, 149-168.
- Sun, S.S., McDonough, W.F., 1989. Chemical and isotopic systematics of oceanic basalts: implication for mantle composition and processes. In: Saunders, A.D., Norry, M.J. (Eds.), *Magmatism in Ocean Basins*, Geological Society of London Special Publication, vol. 42, pp. 313-345.
- Taylor, S.R., McLennan, S.M., 1985. *The continental crust: its composition and evolution*. Blackwell, Oxford, press, 312.
- Van Achterbergh, E., Ryan, C.G., Griffin, W.L., 2001. Data reduction software for LA-ICP-MS. *Mineralogical Association of Canada, Short Course Series* 29, 239-243.
- Velásquez, G., Borisova, A.Y., Salvi, S., Béziat, D., 2012. In situ determination of Au and Cu in natural pyrite by near-infrared femtosecond laser ablation-inductively coupled plasma-quadrupole mass spectrometry. No evidence for matrix effects. *Geostandards and Geoanalytical Research* 36, 315-324.
- Zhang, J., Deng, J., Chen, H-Y., Yang, L-Q., Cooke, D., Danyushevsky, L., Gong, Q-J., 2014. LA-ICP-MS trace element analysis of pyrite from Chang'an deposit, Sanjiang region, China: Implication for ore forming process. *Gondwana Research*, 26, 557-575.

Chapter 5

The Bepkong Deposit

Introduction

This chapter on a whole, presents the geological information of the Bepkong deposit. It takes into consideration the geology which incorporates the lithology, geological structures, gold mineralization and the relationship between the gold mineralization and deformation.

It further highlights the structural control and alteration geochemistry governing the gold mineralization as well as the thermobarometric properties (temperature and pressure) in which the gold were formed, using fluid inclusions and arsenopyrite geothermobarometry approach.

This chapter also present a relatively rare case of gold only present within arsenopyrite within an array of sulphides (pyrite, arsenopyrite, chalcopyrite, and pyrrhotite) present in the deposit. It also present a fine scale information on gold and other metal contents in the sulphides by way of BSE SEM imagery and LA-ICP-MS analysis. This study was submitted to the Journal of African Earth Science in November 2015.

This chapter also includes a publication which summarize of geological information, exploration history, as well as an overview of the geology and ore mineralogy, highlighting how the gold relates to sulphides was submitted and published in Ore Geological Reviews (OGR) as part of the Mineral Atlas monograph (MAM) with a DOI of <http://dx.doi.org/10.1016/j.oregeorev.2015.06.022> with the title '*The Bepkong gold deposit, Northwestern Ghana*'. The MAM is first compendium of mineral deposits in West Africa. It presents basic information about deposit and deposit styles of West Africa. The Mineral Atlas monograph will become a basic tool for many university students and as a basic start reference for exploration companies.

5.0 Gold mineralization in the Wa-Lawra greenstone belt, NW Ghana; The Bepkong deposit

Prince Ofori Amponsah^{1,2}, Stefano Salvi¹, Béziat Didier¹, Lenka Baratoux^{1,5}, Luc Siebenaller^{1,6}, Mark Jessell³, Prosper Mackenzie Nude⁴ Eugene Adubofour Gyawu²

1. Université de Toulouse, CNRS, Géosciences Environnement Toulouse, Institut de Recherché pour le Développement, Observatoire Midi-Pyrénées, 14 Av. Edouard Belin, F-31400 Toulouse, France
2. Azumah Resources Ghana limited, PMB CT452, Cantonments, Accra
3. Centre for exploration Targeting, School of Earth and Environment, The University of Western Australia, 35 Stirling Highway, Crawley WA 6009
4. University of Ghana, Department of Earth Sciences, P.O. Box LG 58, Legon, Accra.
5. IFAN Cheikh Anta Diop, Dakar, Senegal
6. ONG-D "Le Soleil dans la Main" asbl, 48, Duerfstrooss, L-9696 Winseler, Luxembourg.

Abstract

The Bepkong gold deposit is one of several gold mineralizations that occur in the Paleoproterozoic Wa-Lawra greenstone belt of northwest Ghana. These deposits lay along the Kunche-Atikpi shear zone, an offshoot of the larger Jirapa shear zone. The ore in the Bepkong deposit consists of steeply dipping lenticular bodies contained in volcanoclastics and graphitic shales that are deformed by D_{B1} anastomosing structures. The ore zone is defined by four distinct mineralized ore bodies, trending N-S and plunging steeply to the south. Their shape and thickness are variable, with a general strike length of 560 m and an overall thickness of 300 m. An alteration mineral assemblage characterises the ore, and consists of chlorite-calcite-sericite-quartz-arsenopyrite. Pyrite is also abundant, but it is not limited to the altered rocks and occurs throughout the area.

At Bepkong, gold is associated solely with arsenopyrite, which occurs disseminated in the mineralized corridor in the wall rock between the veins and in fractures in type-1 quartz veins. SEM imagery and LA-ICP-MS analysis show that there are two stages of gold precipitation. The first stage is in the form of invisible gold in the structure of arsenopyrite (Apy1), the second stage occurs as remobilization of stage-one gold and precipitation in fractures and zones of overgrowth on arsenopyrite (Apy 2). Both stages of gold mineralization is associated with hydrothermal activity. LA-ICP-MS analysis showed that both Apy1 and Apy2 are compositionally different and were formed at various stages during the mineralization event. Apy1 is enriched in Ni and Co, while Apy2 is depleted in these elements but contains abundant Pb, Ag, As and Sb.

Based on the As geothermometer (ref), the development of arsenopyrite 1 and invisible gold in the Bepkong deposit occurred at a temperature of 275 °C and that of arsenopyrite 2 and visible gold occurred at 290 °C for a pressure range of 1 to 3 kbars.

Primary and pseudosecondary fluid inclusion in the type-1 vein quartz, indicate a circulation of a CH_4 - CO_2 - H_2O fluid with low salinities, which entered immiscibility at 320°C and 1 kbars.

Keywords: Gold mineralization, mineralization, NW Ghana, Bepkong deposit

5.1 Introduction

Greenstone belts all over the world have been classic prospective regions for orogenic gold deposits for many decades now (Davis & Zaleski, 1998), and account for about 13% of the world's total gold production (15,920 metric tonnes of Au; Dubé & Gosselin, 2007) with many world-class occurrences such as the Kalgoorlie in Australia, the Abitibi region in Canada, the Ashanti deposits in Ghana, and Mother Lode in the USA (cf., Groves et al., 1998). These deposits are usually associated with first-order regional shear zones and are commonly situated on second- or third-order faults that splay off these first-order structures (Groves et al. 1987; Eisenlohr et al. 1989). In southern Ghana, gold mineralization has been identified with greenstone belts and has been reported to occur along broad shear zones and in narrow faults immediately adjacent to less deformed rocks (Appiah, 1991; Eisenlohr &

Hirdes, 1992; Allibone et al., 2002; 2004). This region hosts some of the largest deposits of this kind, as exemplified by the Obuasi mine (AngloGold Ashanti), the Ahafo mine (Newmont Mining Corporations), the Damang mine (Goldfields Limited), the Bibiani mine (Noble Mineral resources), the Bogoso/Prestea and Wassa mines (Golden Star Resources), which total over 60 million ounces of gold. Therefore, the majority of geological studies on gold mineralization in Ghana have focussed on them (Junner, 1932, 1935, 1940; Kesse 1985; Milési et al., 1989, 1992; Leube et al., 1990; Blenkinsop et al., 1994; Davis et al., 1994; Oberthür et al., 1994, 1996, 1998; Mumin and Fleet, 1994; Hammond and Tabata 1997; Klemm & Hirdes, 1997; Barritt & Kuma, 1998; Yao & Robb, 2000; Feybesse et al., 2006; Perrouy et al., 2012; White et al., 2015).

However, with gold mining being the major driver of the Ghanaian economy, profitable (<1million ounces) albeit not exceptional gold deposits cannot be overlooked, making the Birimian in NW Ghana an important area to study. In this region, numerous gold exploration prospects have been identified, particularly in the N-S Wa-Lawra greenstone belt. These include the Kunche, Bepkong, Atikpi, Yagha, Basabli and Duri prospects (Fig. 1), although only Kunche (309,000 Oz measured and indicated resource) and Bepkong (113,000 Oz measured and indicated resource) are of economic importance. These two deposits are at a stage of advanced exploration to pre-production, by the Azumah Resources Limited Company. This paper investigates the relationships between gold mineralization and deformation in the Bepkong deposit. It highlights the geological and structural controls on gold mineralization and reconstructs the ore genesis via mineralogical, geochemical and fluid inclusion studies.

5.2 Regional geology of the Wa-Lawra Belt

The N-S trending Wa-Lawra belt in NW Ghana is part of the Paleoproterozoic Birimian terrane of the West African Craton (WAC; Fig. 5.1) and is the only N-S trending belt in Ghana (Kesse, 1985; Samokin & Lashmanov, 1991; Pobedash, 1991; Roudakov, 1991). The Wa-Lawra belt is the southern portion of the larger Boromo belt in Burkina Faso (Béziat et al., 2000; Baratoux et al. 2011).

The Wa-Lawra belt is composed of metamorphosed shales, greywackes, volcano-sediments, basalts, dacites, andesites, granites, para and ortho-gneisses and granitoids (Fig. 5.1). According to Feybesse et al. (2006), the Birimian rocks in Ghana were formed between 2250 to 1980Ma.

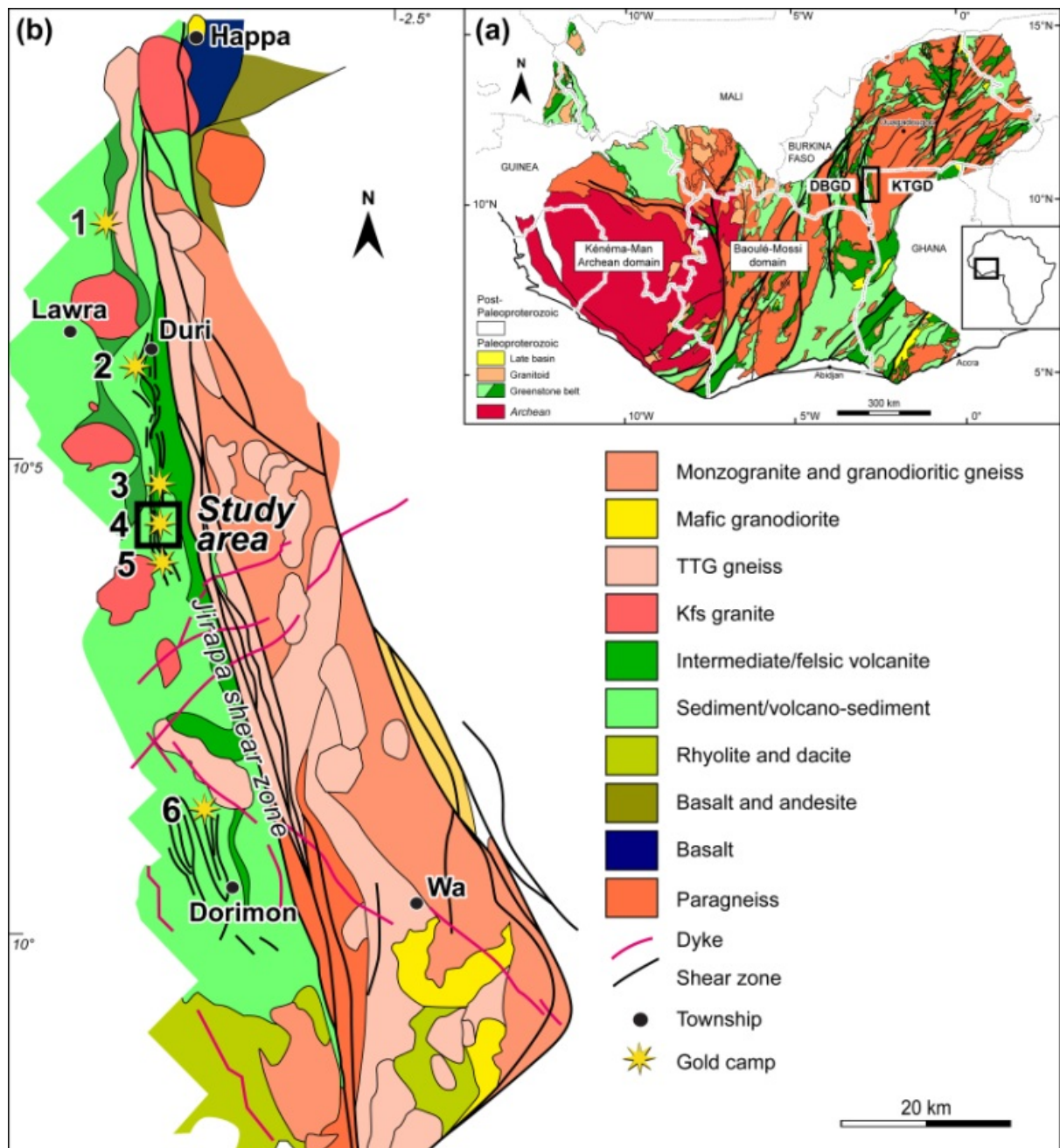


Fig. 5.1. a) Geological map of the Leo-Man Craton, in the southern part of the WAC (modified after Milési et al., 2004), highlighting the positions of the Kenema-Man domain, Baoulé-Mossi domain, Koudougou-Tumu granitoid domain (KTGD), and Diebougou-Bouna granitoid domain (DBGD). The black insert localises the Wa-Lawra belt. b) Geological map of the Wa-Lawra belt (Modified after Block et al., 2015, Amponsah et al., 2015) locating the Bepkong deposit (4) plus several other gold prospects: 1. Basabli 2. Duri 3. Yagha; 5. Kunche 6. Butele.

Regionally, the Wa-Lawra belt is bounded to the west by the Dieboungou-Bouna granitoid domain in Burkina Faso and to the east by Koudougou-Tumu- granitoid domain (KTGD). The contact between the Wa-Lawra belt and the KTGD is marked by the Jang shear zone (Fig. 5.1).

The Wa-Lawra belt can be subdivided into two, eastern and western, parts. The boundary between the eastern and western parts is marked by the crustal scale sinistral Jirapa shear zone (Block et al., 2015) which extends into Burkina Faso. The western part of the Wa-Lawra belt is composed mainly of sediments (shales, greywackes, and volcanisediments), volcanic rocks and intruded granitoids and the eastern part is mainly composed of granites, para and orthogneisses, rhyolites and granitoids.

According to Baratoux et al. (2011) the volcanics and any other pyroclastic flow in the belt were emplaced around 2200 Ma to 2160 Ma. Detrital zircon age dating of the volcanisediments in the Wa-Lawra belt gave ages older than 2139 ± 2 Ma and syn-tectonic to late kinematic granitoid intrusion in the belt were emplaced between $\sim 2153 \pm 4$ to 2104 ± 1 Ma respectively (Agyei Duodu et al., 2009).

The volcanic suites and sediments west of the Jirapa fault have been metamorphosed under green-schist facies conditions whilst the granitoids and para-ortho gneisses to the east have undergone amphibolite facies metamorphism. The metamorphic mineral assemblages associated to the greenschist facies metamorphism consist of chlorite, calcite and epidote whilst the amphibolite facies are garnet, plagioclase, clinopyroxene and hornblende (Block et al. 2015).

Polyphase deformation character has been proposed by Baratoux et al. (2011) and Block et al. (2015) for the Boromo belt including the Wa-Lawra belt. The first deformation event in N Ghana corresponds to N-S shortening under upper greenschist at the limit with blueschist to amphibolite facies conditions (Block et al., 2015). This early deformation event was recorded in southern Ghana (Perrouy et al., 2012) and northern Burkina Faso (Tshibubudze & Hein, 2013; McCuaig et al., in review) but no unequivocal evidence was found in SW Burkina Faso (Baratoux et al., 2011). The D₂ deformation phase (D₁ according to Baratoux et al., 2011) formed N to NNW trending S₂ penetrative foliation, which was transected by S₃ transcurrent shear zones which affected all the Birimian volcanic and volcano-sedimentary units and structured most of the syn-tectonic and early magmatic rocks. The D₂ event is marked by vertical dipping metamorphic penetrative foliation which is often parallel to primary bedding within the sediments. The metamorphic grade varies between the greenschist and amphibolite facies. Extensive domains reaching migmatite facies during D₂ were found in the Bole region in north-western Ghana (Block et al., 2015). The D₃ shear zones are either N-S oriented sinistral or N-E oriented dextral with shallow dipping lineations. Gold mineralization has been reported along these shear zones. The majority of the D₃ shear zones formed under lower to upper greenschist facies conditions. Amphibolite facies ductile shear zones occur at the contact aureoles of syn-kinematic granitoids (Baratoux et al., 2011). The S₃ shear zones are generally brittle to brittle-ductile compared to most of S₂ which is mostly ductile and schistose in nature, suggesting S₃ shear zones operated at lower temperatures with respect to the D₂ event. The D₂ and D₃ are associated to E-W and WNW-ESE shortening, respectively. These E-W shortening form E-W tension gashes which sometimes contain

chlorite, white mica or epidote minerals as well as NE-oriented steeply dipping brittle faults. These late brittle structures have only limited extension.

5.3 Methodology

Gold mineralization at the Bepkong deposit is not cropping out, and the area is entirely covered with transported alluvium and colluvium. All geological information was obtained from logging of reverse circulation (RC) drilling chips (which form the majority of the holes) and diamond drill core (DD) (only a very limited number of these exist) drilled by Azumah resources, and field mapping in surrounding areas within the Wa-Lawra belt. In all, 70 RC and DD bore-holes were logged, constituting 7 E-W fence lines. A geological map was prepared by projecting the structural measurements and lithological data from the drill core logged to surface and was further constrained by interpreting conductivity and resistivity induced polarisation (IP) images processed by Sagax Afrique S.A in 2012, on behalf of Azumah Resources limited.

The mineralogy and textural relationships of the rock samples were investigated using optical microscopy and back-scattered electron (BSE) images obtained with a JEOL JSM 6360LV scanning electron microscope (SEM) equipped with a silicon drift detector analysis system, at the University of Toulouse, France. Whole-rock major and trace-element compositions were analyzed using ICP-AES and ICP-MS, respectively by the ALS Chemex laboratory in Seville, Spain.

Spot analyses of pyrite crystals were performed by LA-ICP-MS at the Géosciences Montpellier laboratory (France), to determine trace element concentrations. Analyses were performed using a Geolas (Microlas) Excimer ArF automated platform housing a 193 nm Compex 102 nanosecond laser from LambdaPhysik, coupled with a high-resolution ThermoFinnigan (ELEMENT XR) ICP-MS. Data were acquired in the fast E-scan mode at low mass resolution using a flux of 15 J/cm² at a frequency of 5 Hz and working with a spot size of 51 µm. Raw data were processed on-line using the GLITTER software package (e.g., [Van Achterbergh et al., 2001](#)), and using several sulphide standards, i.e., pyrrhotite-Po-726 ([Sylvester et al., 2005](#)) and in-house chalcopyrite Cpy-RM ([Velásquez et al., 2012](#)) as external calibrators, and using ³⁴S as the internal calibrator (e.g., [Lorand & Alard, 2011](#)). During analysis, the following isotopes were monitored: ³³S, ³⁴S, ⁵⁶Fe, ⁵⁷Fe, ⁵⁹Co, ⁶⁰Ni, ⁶³Cu, ⁷⁵As, ⁸²Se, ¹⁰⁷Ag, ¹²⁵Te, ¹⁹⁷Au, ²⁰⁸Pb, and ²⁰⁹Bi. Typical detection limits, at the conditions described above, are between 0.01 to 0.1 ppm. Detection limits were calculated as three times the background standard deviation value and were converted to concentration units (ppm) with the *yield_{ns}* parameter (e.g., [Borisova et al., 2010](#)). All calculated concentrations were comparable to the analytical precision limits of the *in-situ* femtosecond quadrupole LA-ICP-MS technique (< 15% RSD, e.g., [Borisova et al., 2010](#)) and the reference materials homogeneities (< 16% RSD, [Velásquez et al., 2012](#)).

Fluid inclusion studies were preceded by careful petrography to identify fluid inclusions assemblages (FIA). Primary and secondary fluid inclusions were identified in 30-µm thick polished thin sections and doubly-polished slices of 150 µm thickness using the criteria of [Roedder \(1984\)](#) and [Goldstein & Reynolds \(1994\)](#). Microthermometric measurements were performed at the University of Toulouse, following the procedures outlined by [Roedder](#)

(1984) and Shepherd et al. (1985), using a Linkam THMGS 600 heating–freezing stage mounted on a BX-51 Olympus microscope. The stage was calibrated against synthetic pure H₂O inclusions (0 and +374.1°C) supplied by SynFlinac and with natural pure CO₂ inclusions (–56.6°C) from Campeirio (Ticino, Switzerland). Measurements below 0°C are accurate to ±0.1°C, whereas at the highest temperature measured (~380 °C), they are accurate to ±1°C. Cryogenic experiments were carried out before heating, to reduce the risk of decrepitating the inclusions. Salinity (expressed as wt. % equivalent NaCl), bulk composition, and density data were calculated using the computer modelling tool of Bakker and Brown (2003) and Flnacor computer software (Brown & Hagemann, 1995).

Raman spectroscopic measurements were made at the CEMES laboratory in Toulouse, using a Labram HR (Horiba Jobin Yvon) Raman spectrometer equipped with a Notch filter and a CCD detector cooled to –130°C by liquid nitrogen. The exciting radiation at 514.535 nm was provided by an Ar+ 108 laser (type 2020, Spectra-Physics) with a laser power of 200 mW at the source and ~20 mW at the sample. Spectra were collected with a grating of 1800 lines/mm and a confocal ×50 objective, allowing a spectral resolution of 4 cm⁻¹. The acquisition range was between 90 and 4,400 cm⁻¹ in order to detect the maximum number of possible Raman active vibrational bands of the different dissolved and gaseous phases. Three minutes was typically required to measure the entire spectral range.

5.4 Local Geology- the Bepkong deposit

Within the Wa-Lawra belt, the Bepkong deposit is located on the N-S anastomosing Kunche-Atikpi shear zone (Amponsah et al., 2015), about 4.4 km west of the major N-S trending crustal-scale strike-slip Jirapa shear zone.

5.4.1 Main Lithologies

Rocks found in the Bepkong deposit are strongly sheared, metamorphosed graphitic shales (Fig. 5.2a), volcanics (Fig. 5.2b) with graphitic interbeds, and microdiorite dykes (Fig. 5.2c). The shales and volcanics are locally interlayered.



Fig. 5.2. Drill core images of rocks in the Bepkong deposit (a) Fresh deformed shale in the Bepkong deposit (b) Volcaniclastic rock in the Bepkong deposit exhibiting some spaced cleavages (c) highly sheared microdiorite rock.

The shale is dark grey, fine grained and non-magnetic. It is mostly made up of quartz, graphite, and minor plagioclase with accessory minerals such as rutile (Fig. 5.3a, b). A secondary assemblage of calcite, chlorite and sericite superimpose these minerals. The volcanoclastic rock is grey, fine grained and are primarily composed of quartz and euhedral plagioclase feldspars, with accessory rutile (Fig. 5.3c, d). These minerals have been superimposed by a hydrothermal assemblage of calcite, chlorite and sericite. Replacement of the plagioclase feldspar by secondary calcite (Fig. 5.3c) is a common feature of the volcanoclastics in the Bepkong deposit. The volcanoclastic sediments exhibits graded beds.

The microdiorite which usually occurs as sheared dyke in the Bepkong deposit is composed primarily of phenocrysts of plagioclase and amphibole in groundmass composed primarily of plagioclase and minor white mica and accessory rutile, quartz and sphene (Fig. 5.3e, f). These minerals have been superimposed by calcite as a result of hydrothermal alteration.

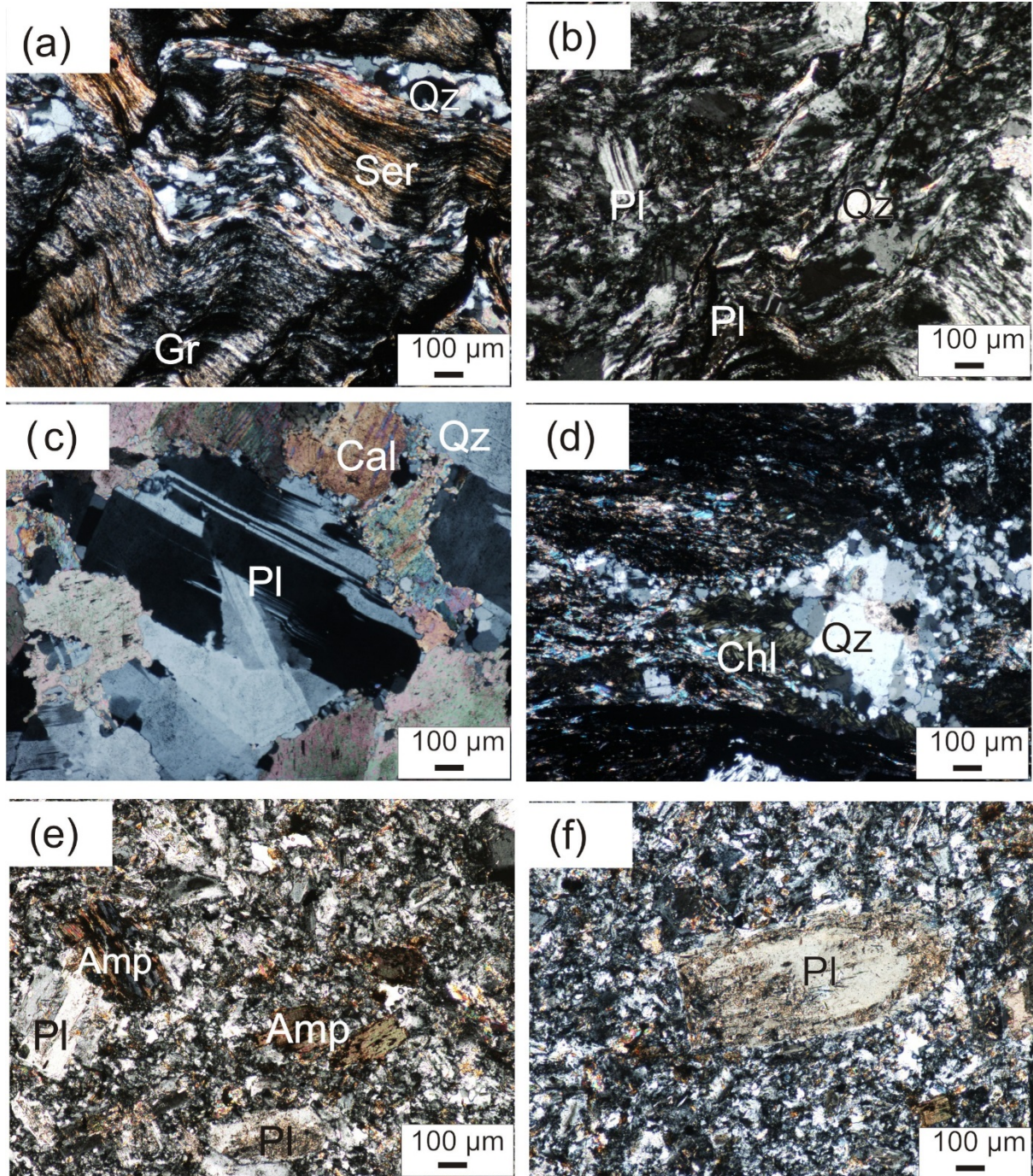


Fig. 5.3. Representative photomicrograph of rocks in the Bepkong deposit (a) Shale composed of quartz, sericites and graphite. Minerals in the thin section have a preferred orientation and are crenulated (b) Shale composed of plagioclase and quartz also exhibiting crenulation cleavages (c) Volcaniclastic rock showing euhedral plagioclase, calcite and quartz (d) Volcaniclastic rock showing alteration minerals such as chlorite, quartz (e) microdiorite exhibiting phenocryst of plagioclase and amphibolite in a ground mass of plagioclase, micas and accessory quartz (f) microdiorite showing poikilitic plagioclase. Amp-amphibole, Cal-calcite, Qz-quartz, Chl-Chlorite, Pl-plagioclase, Gr-graphite

5.4.1.1 Geochemistry Shales

From the major element analyses in Table 5.1, the SiO₂ content in the shales ranges from 59% to 47% with a wide variety of Al₂O₃ content ranging from 14.8% to 21%. Al₂O₃/Na₂O ratio suggests the compositional maturity index of Bepkong varies from 5.5 to 20. The SiO₂/MgO ratio ranges from 9.0 to 18.4 and indicates a probable acidic to intermediate provenance for the shales. The REE pattern in shales when normalised to the chondrite (Sun & McDonough, 1989; Fig. 5.4a) it shows relatively flat REE with a slight negative Eu anomaly. The LREE are more enriched compared to the HREE with the ratios of (La/Sm)_n and (La/Gd)_n ranging from 0.31-3.02 to 1.55- 4.8 respectively.

Using the La-Th-Sc diagram (Fig. 5.4b) in determining the source composition of the shales in Bepkong, it shows that the shales may have probably been derived from a more to a granodioritic source.

Volcaniclastic sediments

The volcaniclastics in the Bepkong deposit have SiO₂ ranging from 87.8 to 58.5 wt. % and Al₂O₃ ranges from 3 to 18.1 wt. %. On the basis of total alkali vs. silica (the TAS classification diagram; Fig. 4c) by Le Bas et al. (1986) most of the volcaniclastic rocks in Bepkong are subalkaline and were derived from acidic and intermediate rocks. The Na₂O/K₂O ratios are low to intermediate, with the values ranging from 0.40 to 2.35. The Volcaniclastics in Bepkong show positive Eu anomaly, which may indicate that, this rock had stable plagioclase forming from the original melt. When normalized to chondrites, the volcaniclastics are enriched in LREE compared to the HREE.

Table 5.1. Major and trace element data in sediments (shales and volcaniclastics) at Bepkong

Sample_ID	BEP-4	BEP-5	BEP-6	BEP-7	BEP-8	BEP-9	BEP-10	BEP-11
Rock type	Volc	Volc	Volc	Volc	Sh	Sh	Sh	Sh
<i>wt. %</i>								
SiO ₂	73.8	57.7	87.8	58.5	59	60.2	50.9	47.9
Al ₂ O ₃	14.6	11	2.95	18.1	17.15	16.55	21	14.8
Fe ₂ O ₃	1.55	7.36	2.65	5.71	9.79	7.81	9.34	8.33
CaO	1.61	8.13	2	1.5	1.23	1.94	1.1	7.03
MgO	0.48	2.95	0.91	2.82	3.93	3.27	4.24	5.35
Na ₂ O	4.59	0.62	0.68	4.05	1.87	3.01	1.05	1.97
K ₂ O	1.95	1.56	0.33	2.59	2.09	1.78	3.86	1.85
Cr ₂ O ₃	0.01	0.02	0.01	0.03	0.02	0.04	0.04	0.03
TiO ₂	0.19	0.37	0.18	0.63	0.65	0.61	0.81	0.6
MnO	0.02	0.28	0.05	0.06	0.12	0.08	0.06	0.2
P ₂ O ₅	0.06	0.07	0.09	0.12	0.12	0.13	0.13	0.2
SrO	0.06	0.08	0.03	0.03	0.02	0.03	0.03	0.03
BaO	0.08	0.03	0.01	0.05	0.04	0.04	0.08	0.04
LOI	2.37	9.33	2.88	0.16	5.24	5.04	6.88	0.04

Total	101.37	99.5	100.57	0.56	101.27	100.53	99.52	0.12
Al ₂ O ₃ /Na ₂ O	3.18	17.74	4.34	4.47	9.17	5.5	20	7.51
SiO ₂ /MgO	153.75	19.56	96.48	20.74	15.01	18.41	12	8.95
Na ₂ O/K ₂ O	2.35	0.40	2.06	1.56	0.89	1.69	0.27	1.06

ppm

Ba	744	322	54.6	4.43	346	351	701	10.9
Ce	46.8	31.2	12.5	98.62	48.4	40.8	56.6	99.23
Cr	20	190	70	621	160	310	280	423
Cs	4.73	3.96	0.85	59.3	5.05	4.36	9	39.1
Dy	0.67	6.22	1.01	310	3.25	2.82	4.43	220
Er	0.29	3.9	0.55	7.32	2	1.79	2.54	5.16
Eu	0.55	1.04	0.37	4.01	1.19	1.01	1.21	2.8
Ga	19.2	17.7	3.2	2.4	20.9	19.3	27.4	1.38
Gd	1.38	4.84	1.19	1.19	3.85	3.18	4.49	1.24
Hf	3.4	2.3	1.1	23.5	3.3	3.4	4.6	16
Ho	0.12	1.45	0.21	4.53	0.69	0.62	0.92	3.12
La	26.1	14.6	6	5.4	22.4	19.2	26.4	2.3
Lu	0.04	0.48	0.11	0.72	0.34	0.31	0.41	0.48
Nb	5.8	3.7	1.6	27.1	5.3	4.8	7.2	17.3
Nd	15.8	15.8	5.9	0.32	22.8	19.7	27.6	0.19
Pr	4.83	3.93	1.49	9.2	6.07	5.16	7.05	3.7
Rb	97.3	74	13.1	24.3	85.3	74.6	156	18.7
Sm	2.38	3.97	1.46	6.72	4.88	4.05	5.45	4.63
Sn	2	1	<1	121.5	1	1	2	82.6
Sr	480	785	251	4.9	220	260	243	3.47
Ta	0.7	0.3	0.1	3	0.4	0.4	0.5	2
Tb	0.17	0.96	0.2	367	0.56	0.49	0.73	396
Th	10.45	2.33	0.94	1.1	3.33	3.15	4.17	1.1
Tl	<0.5	<0.5	<0.5	0.62	<0.5	<0.5	0.6	0.43
Tm	0.04	0.55	0.08	6.08	0.27	0.26	0.39	1.67
U	4.43	0.8	0.35	0.38	1.05	1.06	1.51	0.23
V	14	141	22	1.9	152	143	189	0.57
W	28	8	11	154	4	5	14	161
Y	3.4	39.6	5.7	15	18.9	15.9	24.6	2
Yb	0.25	3.38	0.53	22.7	2.04	1.84	2.49	15.6
Zr	119	83	37	1.94	119	125	174	1.32
As	250	42.2	250	193	80.1	89.7	250	92
Bi	0.57	0.3	0.43	250	0.17	0.11	0.49	57.3
Hg	0.03	0.02	0.02	0.42	0.04	0.01	0.03	0.11
Sb	0.63	0.38	2.28	0.04	0.31	0.63	2.08	0.02
Se	0.3	0.9	2.2	47.2	0.3	0.3	1.5	8.11
Te	0.32	0.12	0.3	2.3	0.05	0.04	0.48	0.4

Ag	0.5	0.5	0.6	0.5	0.5	0.5	0.5	0.5
Cd	0.5	0.5	0.5	0.5	0.5	0.5	0.5	0.5
Co	4	24	17	20	30	27	35	32
Cu	19	37	57	43	68	48	103	12
Li	10	60	10	50	90	80	80	80
Mo	14	5	4	1	1	2	12	1
Ni	80	89	66	66	101	104	162	70
Pb	23	21	27	18	9	6	12	12
Sc	2	14	3	15	20	19	22	23
Zn	41	98	52	97	115	96	167	86
(La/Sm) _n	6.84	2.29	2.56	0.5	2.86	2.96	3.02	0.31
(La/Gd) _n	15.88	2.53	4.23	3.81	4.88	5.07	4.93	1.55

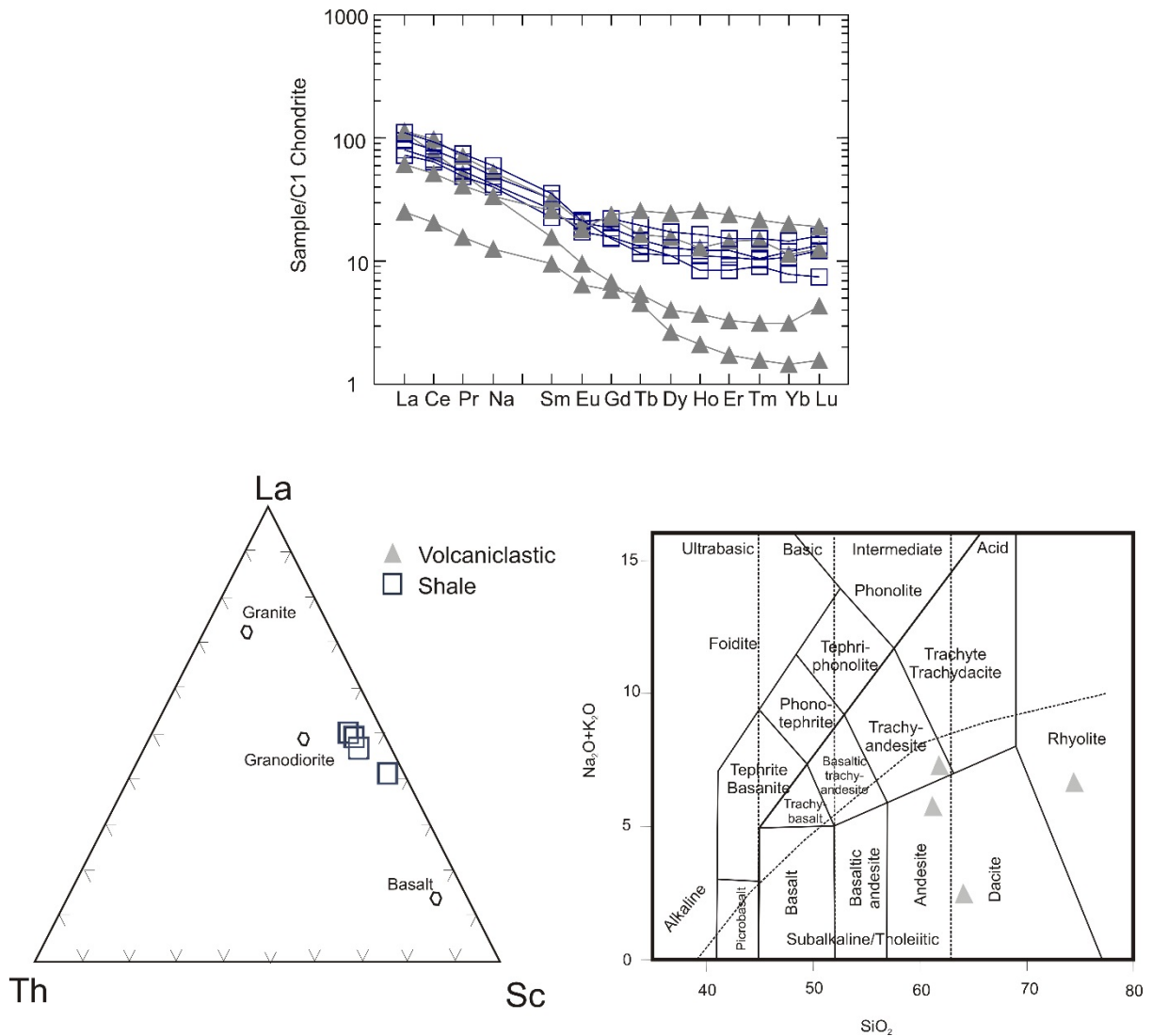


Fig 5.4. Geochemical plots for the sediments in the Bepkong deposit (a) Chondrite normalized REE patterns in Bepkong (Sun & McDonough, 1989) (b) La-Th-Sc plot of the analysed shales in the Bepkong deposit (Cullers & Podkovyrov, 2002). Most of the shales plot close to the granodiorite composition. This indicates most likely a silicic source for the

sediments in the area (d) Total alkali versus silica (TAS) diagram (Le Bas et al., 1986) for the volcanoclastic rocks in Bepkong.

Microdiorite

From Amponsah et al. (2015), these rocks were termed Lamprophyres, but with the study of thin section images and whole rock geochemistry, these rocks are microdiorite. The microdiorite in Bepkong have SiO_2 ranging from 55 to 53.3 wt% and Al_2O_3 ranging from 14.1 to 15.8 wt% with a Mg# ranging from 37.3 to 40.2 (Table 5.2). The microdiorite in Bepkong do not have a mafic character and this is indicated by the Ni (67 to 32 ppm), Cr (210 to 80 ppm) and Co (24 to 26 ppm) values (Table 5.2). The low Mg# indicates that the microdiorite in Bepkong are from are highly altered. The alkali Cs, Ba and Rb shows concentrations 100 times higher than the chondrite (Fig. 5.5a) with the $(\text{La}/\text{Yb})_n$ ranges from 18.3 to 33.4. When the samples were normalized with the chondrites, it is relatively flat, with a minor positive Eu anomaly (Fig. 5.5b). From the tectonic discrimination diagram and petrography, it can be concluded that, the microdiorite are formed in an arc related setting (Fig. 5.5c). Based on the geochemical analyses, Abitty et al. (2015), have established that most of late stage post collisional magmatic rocks in NW Ghana were derived from potassic calc alkaline volcanism and this can be extended to the microdiorite in Bepkong.

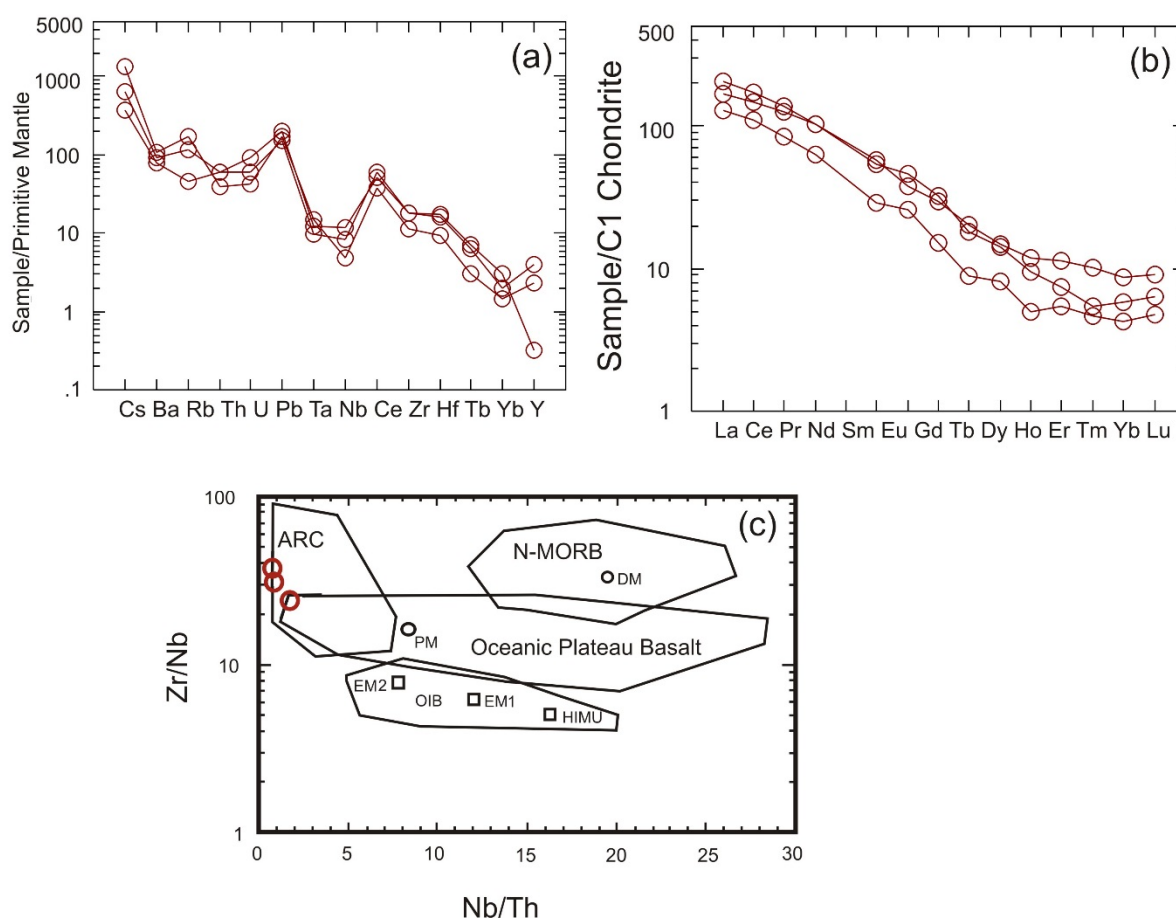


Fig. 5. Geochemical plots for microdiorite in the Bepkong deposit (a) Primitive mantle-normalized diagrams of the Bepkong microdiorite (normalization values from Sun & McDonough, 1989) (b) Chondrite-normalized REE patterns of the Bepkong microdiorite

(Sun & McDonough, 1989) (c) Zr/Nb vs. Nb/Th. ARC = arc-related basalts; N-MORB = Normal mid ocean ridge basalt; OIB = oceanic island basalt. Hypothetical mantle sources: DM = shallow depleted mantle; EN = enriched component; PM = primitive mantle; HIMU = high μ (U/Pb) source; EM1 and EM2 = enriched mantle sources (modified after Condie, 2005).

Table 5.2. Major and trace element analytical data for microdiorite in the Bepkong deposit
M_d-Microdiorite

Sample_ID	BEP-1	BEP-2
Rock type	M _d	M _d
<i>wt. %</i>		
SiO ₂	55	53.3
Al ₂ O ₃	14.8	14.05
Fe ₂ O ₃	7.09	6.56
CaO	6.49	5.96
MgO	4.47	3.91
Na ₂ O	3.45	2.81
K ₂ O	0.83	1.74
Cr ₂ O ₃	0.03	0.01
TiO ₂	0.91	0.87
MnO	0.12	0.12
P ₂ O ₅	0.55	0.48
SrO	0.13	0.07
BaO	0.06	0.07
LOI	6.34	8.33
Total	100.27	98.28
Mg#	38.67	37.34
<i>ppm</i>		
Ba	549	634
Ce	89.8	106
Cr	210	80
Cs	2.93	4.96
Dy	3.73	3.63
Er	1.86	1.23
Eu	2.17	2.65
Ga	17.4	16.2
Gd	6.05	6.61
Hf	5.4	4.9
Ho	0.67	0.54
La	39.9	48.7
Lu	0.23	0.16
Nb	8.4	6
Nd	47.6	48.1

Pr	11.9	12.9
Rb	28.9	73.1
Sm	8.89	8.26
Sn	2	2
Sr	1150	663
Ta	0.5	0.4
Tb	0.76	0.68
Th	5.14	5.02
Tl	<0.5	0.06
Tm	0.26	0.14
U	1.91	1.27
V	158	123
W	2	4
Y	18.6	18.2
Yb	1.48	0.99
Zr	201	205
As	29.3	64.5
Bi	0.14	0.18
Hg	0.02	0.02
Sb	0.38	10.85
Se	0.7	0.6
Te	0.01	0.04
Ag	0.5	0.5
Cd	0.5	0.5
Co	24	20
Cu	26	29
Li	70	50
Mo	6	1
Ni	67	59
Pb	14	11
Sc	17	12
Zn	85	88
(La/Yb) _n	18.31	33.41
(La/Sm) _n	2.8	3.68
(La/Gd) _n	5.53	6.18

5.4.2 Deposit scale structures

The combination of reverse circulation (RC) chips logging, drill core logging, and surface mapping in and around the deposit area and interpretations of ground geophysical IP data, have helped with identification of three main deformational episodes in the Kunche-Atikpi shear zone (Fig. 5.6) where the Bepkong deposit is hosted. These deformation phases are D_{B1} , D_{B2} and D_{B3} . The subscript B is used to denote that the structures or structural history described in this section pertains to local scale deformation in the Bepkong deposit.

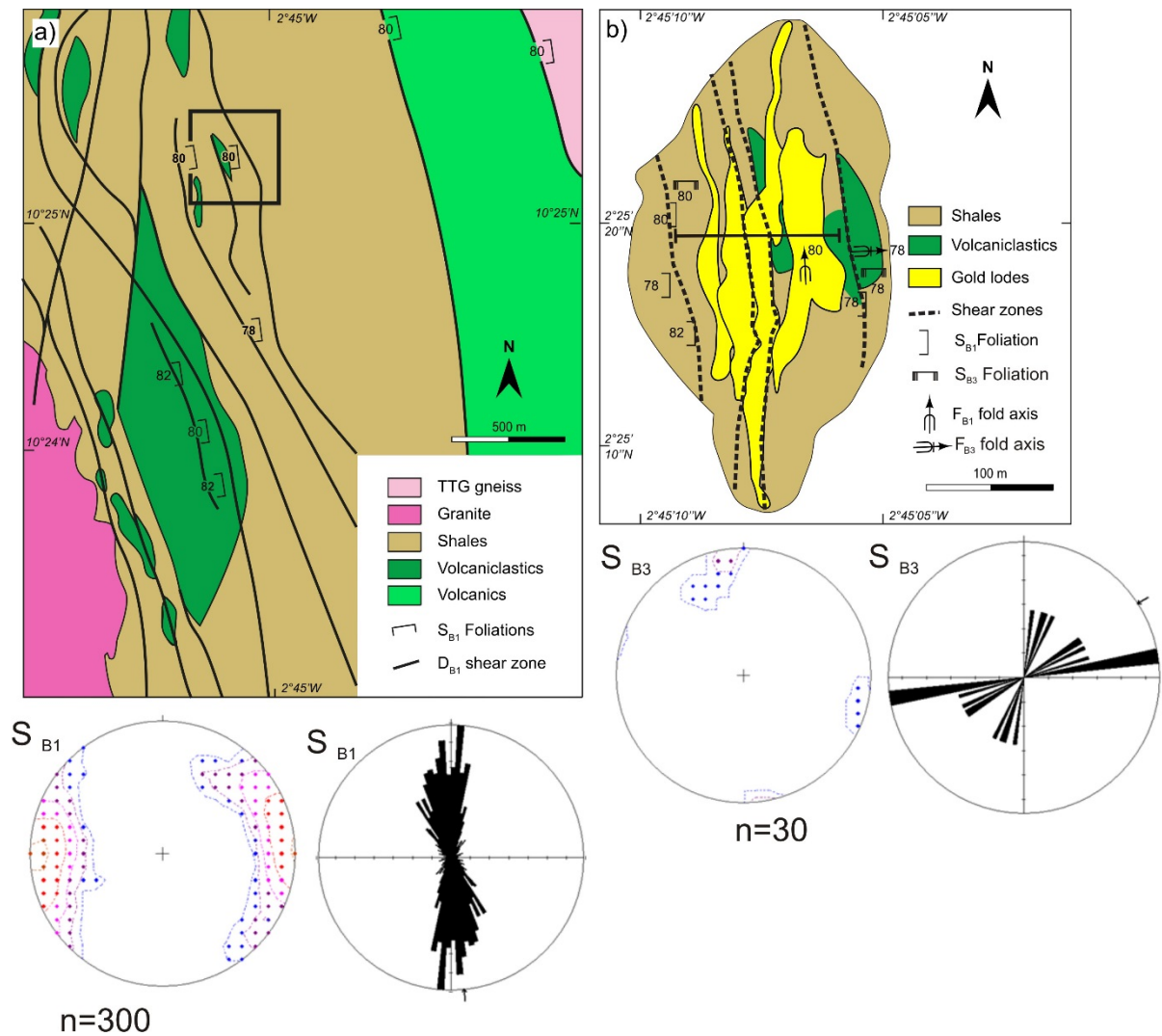


Fig. 5.6. (a) A simplified geological map of a portion of the Kunche-Atikpi shear zone, west of the Jirapa shear zone. In the black insert is the Bepkong deposit (location of the subpanel b). (b) The deposit showing the N to NNW anastomosing shear zone and the mineralized corridor. The diagrams in the bottom half illustrates equal-area lower hemisphere stereonet plots and rose diagram of structural orientation.

5.4.2.1 D_{B1} deformational phase

D_{B1} in the area is represented by N to NNW oriented steeply dipping sinistral transcurrent shear zone which denotes a WNW shortening. This deformational phase affected all the sediments, and the syn- D_{B1} magmatic plutons (Fig. 5.7a, b). This deformational event is manifested by N to NNW striking and vertical dipping penetrative foliation (S_{B1}) with a sub-horizontal stretching lineation (Fig. 5.7c) which trends 008° and plunges 20° and parallel to S_0 bedding in the sediments.

S_{B1} is generally parallel to primary bedding in the sediments. This deformation characteristic is mainly observed within the Jirapa shear zone. 4 km west of the Jirapa fault, D_{B1} on a deposit scale is characterized by discrete anastomosing shear zones. The anastomosing shear zone is formed as a result of strain or deformation partitioning owing to the presence of lithologies with variable strength. This anastomosing shear zone is characterized by left-stepping dilatational jogs and has been denoted the Kunche-Atikpi shear zone in the study area. The anastomosing shear zones have developed an intense N to NNW striking and steeply dipping (78° to 80°) S_{B1} foliation. This deformation is also marked by F_{B1} isoclinal folds (Fig. 5.7d) with vertical fold axes and axial planes parallel to the S_{B1} foliation with dips ranging from 76° to 82° to the west. These anastomosing shear zone systems are visible at the deposit scale and have created dilatational zones which have permitted fluid movement within the sediments. This is evidenced by the syn-tectonic boudinaged quartz veins observed parallel to the foliation. The veins and veinlets usually exhibit asymmetric boudinage (Fig. 5.7e) characteristics along the anastomosing shear fabric suggesting a sinistral sense of shear. The shales and volcanoclastic rocks in the Bepkong deposit exhibit brittle and ductile characteristics and this can be attributed to the rheological properties of the rocks as well as the temperature changes during deformation.

5.4.2.2 D_{B2} deformational phase

D_{B2} in the Bepkong deposit is marked by an E-W trending tension gashes (Fig. 5.7f, g) that crosscut the S_{B1} shear zone and are mostly quartz filled representing an echelon of quartz veins. This indicates an E-W shortening (the maximum compressive stress). The tension gashes are generally Z-shaped with a left lateral motion, indicating a sinistral sense of shear.

4.2.2 D_{B3} deformational phase

The D_{B3} deformational phase observed in the Bepkong deposit is marked by an F_{B3} isoclinal, space cleavages and late brittle faults. F_{B3} isoclinal folds and crenulation cleavages (Fig. 5.7h) overprint the initial S_{B1} foliation and quartz veins filling D_{B1} shear zones. These F_{B3} are defined by vertical fold axes and an ENE-WSW axial planar S_{B3} foliation. E-W spaced cleavages cross-cut all the structures described above. The late NE and NW brittle faults (5.7i) locally displace the D_{B1} shear zones and occur as broken fragments or as offsets in the drill core. They are hard to be found in the field due to the fact that there is no outcrop, but can be easily recognizable in the drill cores.

This deformational phase is denoted by N-S shortening.

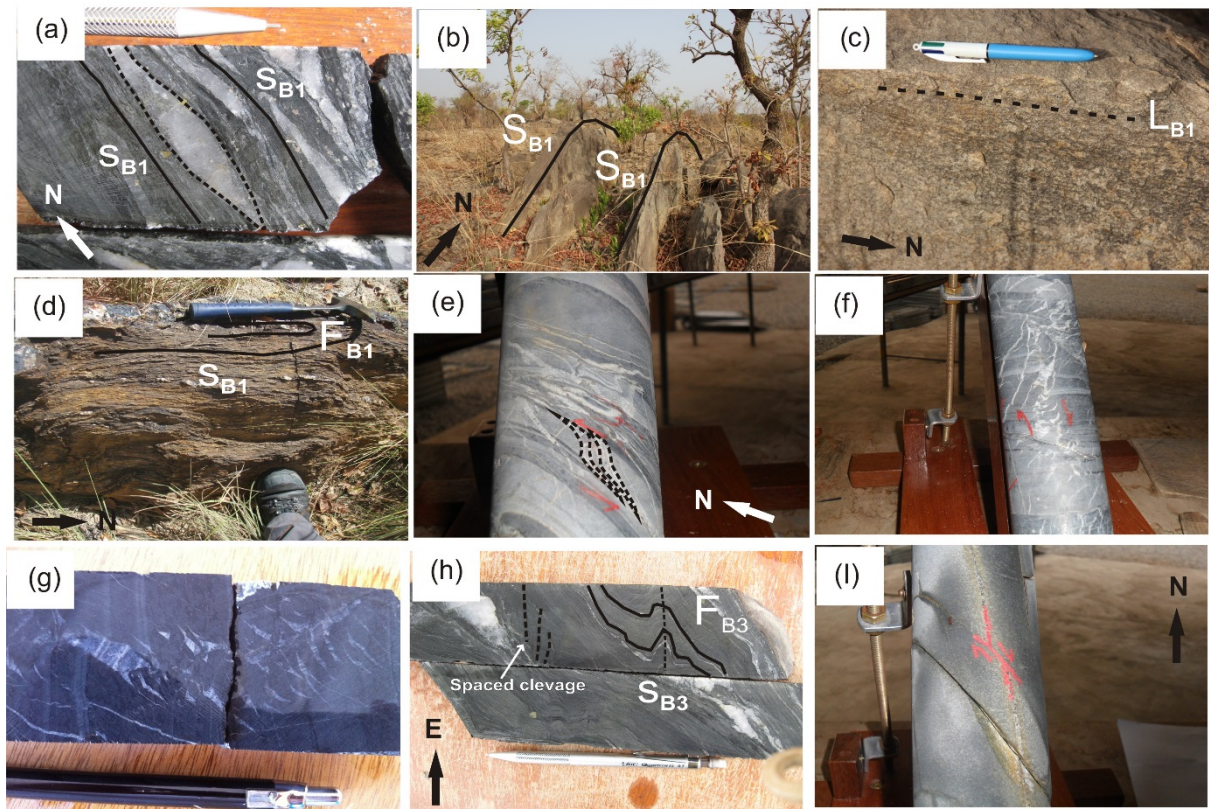


Fig. 5.7. Field and drill core photographs of representative structures in the Bepkong deposit a) S_{B1} foliation observed within a drill core with a boudinaged quartz vein which is flanked by S_{B1} foliation related to the D_{B1} deformational event (b) N-S penetrative S_{B1} foliation in the syn-tectonic magmatic plutons (c) North trending subhorizontal stretching lineation formed on an S_{B1} foliation plane in the magmatic plutons (d) Volcaniclastic rock cropping out within the Kunche-Atikpi shear zone exhibiting N striking S_{B1} foliation and north verging F_{B1} isoclinal fold which is axial planar to S_{B1} (e) an asymmetric boudinaged vein exhibiting a sinistral sense of shear along the shear fabric in the D_{B1} deformational event (f) D_{B2} E-W tension gashes cross-cutting the S_{B1} foliation (g) Zoom at the drill core showing the D_{B2} E-W trending tension gashes (h) a drill core exhibiting E-W trending F_{B3} fold axis with the axial plane acting as the S_{B3} foliation plane. E-W spaced cleavages can be observed and this is characteristic of D_{B2} deformation. (i) Drill core showing the D_{B3} NW brittle fault

5.4.3 Quartz veins

A single generation of quartz vein was identified and described by Amponsah et al., (2015) at the Bepkong deposit. However, further drilling has permitted the identification of a second system of veins, associated with tension gashes. The quartz veins described in this subsection have been classified based solely on their infill type, as there is no clear-cut crosscutting relationship between them. They are designated of Type-1 and Type-2, respectively.

5.4.3.1 Type-1

Type-1 veins are milky in nature, crystalline, have variable thickness (Fig. 5.8a) and are synchronous with the anastomosing D_{B1} shear zone. The Type-1 veins are boudinaged (Fig. 5.8b) and brecciated (Fig. 5.8c), which gives an indication that they formed under brittle-

ductile conditions. These veins were formed within the left stepping deformational jog during late stages of the D_{B1} deformation, which created open fracture systems. Within the dilatational zones of the anastomosing D_{B1} shear these veins range from 0.4 to 3 m in thickness. Outside the dilatational zones they range from 0.1 to 0.2 m. The deformed quartz vein has quartz as the dominant mineral and within the dilatational zones; these veins are composed of calcite (5 %), ankerite (3 %), chlorite (3 %) and sericite (1%). Sulphides are mainly represented by pyrites, which makes up about 2% of the total vein volume. Arsenopyrite (2%) and pyrrhotite (0.5%) are formed at the vein selvage with the country rock (Fig. 5.8b) but not within the vein or sometimes they nest together with chlorite and sericite within as fracture fills in the vein (Fig. 5.8d). These veins occur within the ore zone of the Bepkong deposit. Outside the ore zone the Type-1 quartz veins are composed mainly of quartz, pyrite and calcite. The veins show no vuggy aspects.



Fig. 5.8. Photograph of drill core showing the various characteristic of Type-1 quartz veins observed within the Bepkong deposit (a) Drill core showing 3 m of crystalline Type-1 quartz veins within the dilatational zone of the anastomosing D_{B1} shear zone. Within these veins are ankerite (Ank) and quartz (Qz) (b) Boudinage Type-1 quartz veins folded by the F_{B3} fold within the Bepkong deposit. Pyrite (Py), calcite (Cal), Chlorite (Chl) and the arsenopyrite (Apy) are at the selvages of the veins. (c) Veins exhibiting breccia. The breccias are mainly inclusions from the country rock and give an indication of a brief change in the fluid temperature and pressure in an overall ductile regime within the deposit (d) Type-1 Quartz veins showing fractures. The fractures have been filled with arsenopyrite and secondary minerals such as chlorite, calcite, and sericite. (e) Schematic diagram of quartz vein orientation in the Bepkong deposit.

Thin section analysis revealed that Type-1 quartz veins are composed of quartz, chlorite, sulphides and sericite. The pyrite usually exhibits quartz fringes to a well-developed pressure shadow in the direction of shearing. The quartz exhibits undulose extinction, indicating it has accommodated some amount of strain. Textural analysis of the quartz grains indicates they are mainly buck (large porphyroblast; Fig. 5.9a) and comb (recrystallized grains). The fine grained recrystallized quartz has serrated edges (Fig. 5.9b) indicating varying degree of dynamic recrystallization by the mechanism of grain boundary migration and subgrain rotation. The calcite and ankerite mostly exhibit interstitial textures within the grain boundaries of the quartz grain.

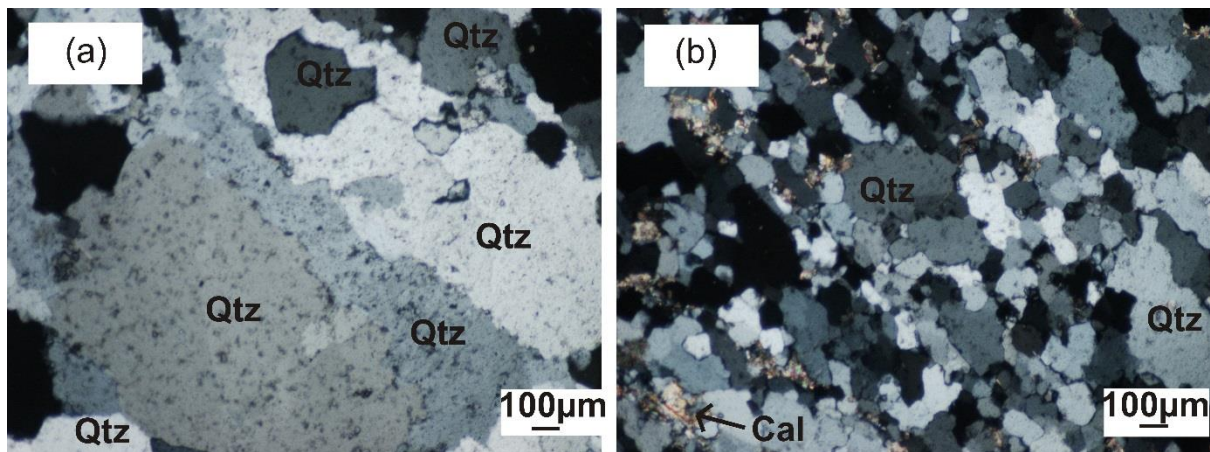


Fig. 5.9. Photomicrographs of a Type-1 quartz vein in the Bepkong deposit (a) Type-1 quartz vein exhibiting buck textures (b) Type-1 quartz vein showing sheared comb and ribbon-like textures with preferential orientation, and interstitial calcite. Fine-grained recrystallized quartz develops along the shear planes, affected by grain boundary migration and subgrain rotation. Qtz-Quartz, Cal-Calcite

5.4.3.2 Type-2 quartz veins

The Type-2 quartz veins are associated with D_{B2} deformation. They are en echelon quartz veins that fill D_{B2} tension gashes (Fig. 5.7f, g, 5.8e). These veins are mainly quartz dominated, milky and with traces of calcite. These veins are typically 5 to 20 cm thick and are not associated with any sulphides, ankerite nor sericite. These veins contain no gold mineralization

5.4.4 Alteration, ore body geometry and mineralogy

5.4.4.1 Alteration

The pervasive alteration affects the sediments host of the Bepkong gold deposit is straightforward, and can easily be observed on a macroscopic scale as one moves across the ore zone into the country rock. The obvious alteration associated with the ore zone is the combination of arsenopyrite and pyrites which occur as disseminations within the quartz

veins and wall rock and forming haloes around the veins. Chlorite, calcite, ankerite, quartz and sericite are the key alteration minerals associated with the disseminated sulphides in the ore zone. This alteration assemblage type represents carbonization, chloritization, silicification and sericitization. This alteration zone has an irregular width, but with its thickest part being 300 m. The uneven size of the alteration is attributed mainly to the change in permeability and porosity of the host rock shales and volcanoclastics. This alteration zone is bounded by the graphitic alteration zone. Calcite and pyrite is ubiquitous within the rock suites in the Bepkong deposit.

5.4.4.2 Ore body geometry and mineralization style

Gold mineralization in the Bepkong deposit is limited to dilational zones within the anastomosing N-NNW D_{B1} shear zones associated with sulphide bearing volcanoclastic rocks and shales with quartz veins which have been altered by chlorite + calcite + sericite + ankerite + quartz + sericite. The dilation zone that hosts disseminated sulphides in variably strained shales and volcanoclastic rocks is 300 m wide with a strike length of 560 m. Four distinct parallel lenticular shaped mineralized ore body with variable thickness have been identified in the Bepkong deposit. The mineralized lodes trend N-S and plunge steeply to the south with mineralization still open at depth after been modelled to a depth of 200m (Amponsah et al., 2015; Fig. 5.10). Gold mineralization is associated with the arsenopyrites that occur within the wall rock next to the quartz vein.

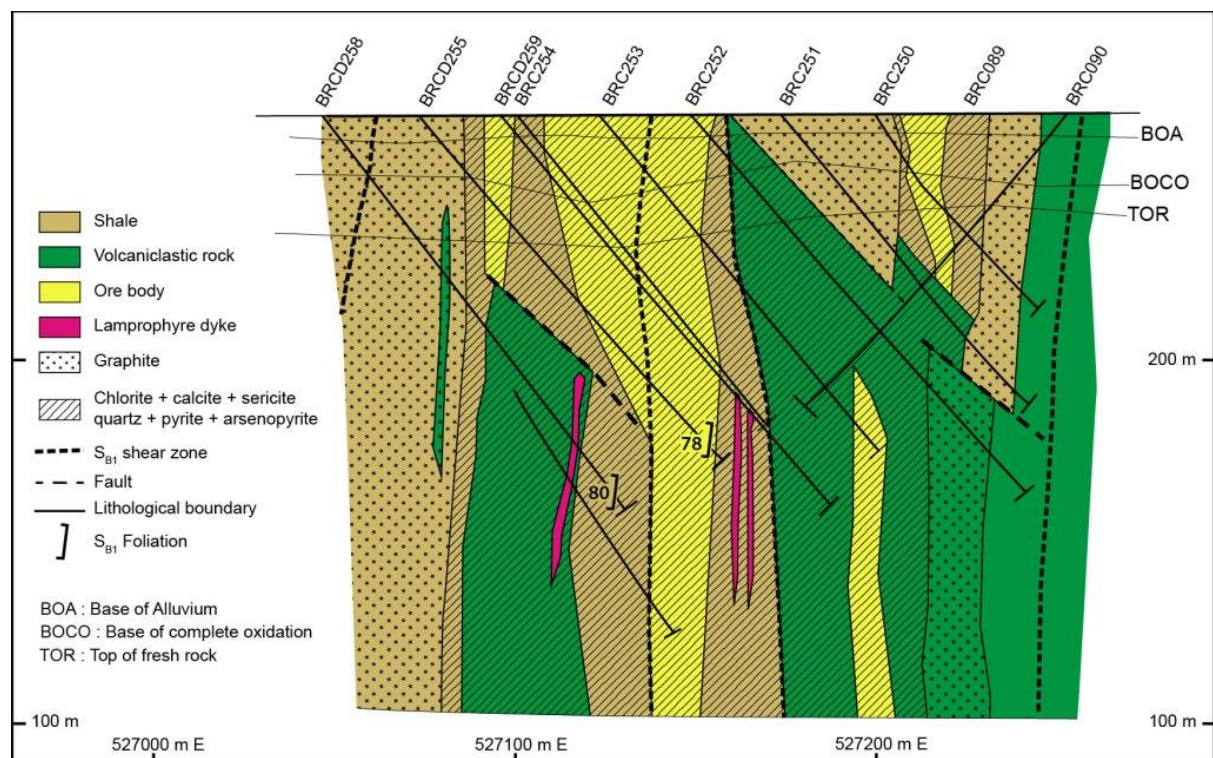


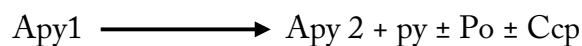
Fig. 5.10. A cross-section (looking north) of the Bepkong deposit along 1,152,175mN, showing mineralized shoots within the main ore body, along subvertical D_{B1} shear zones (cf., Fig. 5.6 for location). High-grade mineralization is confined to a 100 m- to 150 m-thick

alteration zone defined by an assemblage consisting of chlorite + calcite + sericite + quartz + sulphides. Graphitic layers within the shale and the volcanoclastic rocks limit the mineralized hydrothermal conduits (modified after Amponsah et al., 2015).

5.4.4.3 Ore mineralogy

The principal ore minerals which occurs as disseminations within the mineralized zone in Bepkong are arsenopyrite (Apy), pyrite (Py), minor pyrrhotite (Po) and chalcopyrite (Ccp) (Fig. 5.12). The arsenopyrites, minor pyrrhotite and chalcopyrite occur within the altered host rock and quartz vein selvages and fractures whilst pyrite is ubiquitous in the entire rock package in Bepkong. The sulphides in the Bepkong deposit can be group into two generations based on the overprinting relationship. Thus, generation one is composed of arsenopyrite 1 (Apy 1) and generation two is composed of arsenopyrite (Apy 2), Pyrite (Py), minor pyrrhotite (Po) and chalcopyrite (Ccp). Pyrrhotite are not observed under thin section but occurs as minor inclusion SEM imagery. Not all the Apy2 arsenopyrite contain pyrrhotite and chalcopyrite inclusion.

Based on the overprinting relationship of the sulphides in the Bepkong deposit, the evolution or paragenetic sequence of the sulphides is as follows;



Apy 1, Apy 2, pyrrhotite and chalcopyrite are sulphides restricted to the wall around the veins in the dilational zone, or limited to the fractures within the veins or at the selvages whilst Py1 is ubiquitous within the Bepkong deposit but is more pronounced within the shales. Gold mineralization in Bepkong is only associated with arsenopyrite (thus Apy1 and Apy 2) and free gold occurs within fractures in the quartz veins (Fig. 5.11).

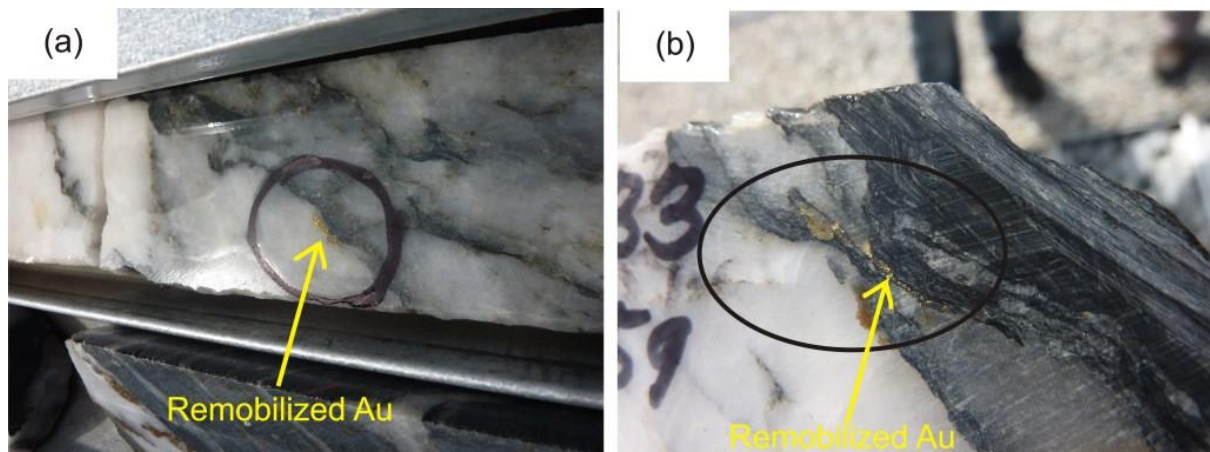


Fig. 5.11. (a) Gold formed within the fractures of quartz vein filled with alteration minerals within the Bepkong deposit (b) gold forms within a fracture and along the selvages of the quartz vein

Arsenopyrite 1 (Apy 1)

This make up about 2 % of the total arsenopyrite population within the deposit. Apy 1 are coarse grained and form anhedral to euhedral crystals (Fig. 5.12a) and occurs as fragmented residual crystals and are homogenous under thin section. This is mainly confined only to the mineralization zones within the volcanoclastics and graphitic shales and occurs as disseminations. It has crystals varying from 0.2 mm to 0.6 mm. Apy1 usually contains inclusions of wall rock materials and had no particular orientation. Apy1 is chemically composed of 22.4 % S, 35.4 % Fe and 39.1 % As and traces of Pb, Bi, Sb and Ag.

Pyrite (Py1)

This sulphide type is mainly subhedral to euhedral in shape (Fig. 5.12c) and occurs as disseminated isolated crystals in all the rocks in the deposit but those that occur in the mineralized zone grow around the early formed Apy1 (Fig. 5.12b). The crystals sizes of this sulphide type ranges from 0.5mm to 35mm. Some of pyrite crystal contain some wall rock materials and exhibits no growth zone. From microprobe analysis Py1 is chemically composed of 54% S, 45.7 % Fe, 0.3% and traces of Ag, As and Bi.

Arsenopyrite 2 (Apy 2)

This arsenopyrite type is subhedral to euhedral in shape (Fig. 5.12d) as occur as dissemination within the fractures of the quartz lodes and adjacent wall rock and the most abundant arsenopyrite type observed within the Bepkong deposit. These arsenopyrites contain no inclusion of country rock materials. The crystal size ranges from 0.4 to 15 mm. From SEM imagery, the arsenopyrite exhibit zonation by way of growth zone and exhibit inter-grain and intra-grain alteration rim. This phenomenon is not readily observed under the microscope. Apy 2 is composed of 23.8 % S, 36 % Fe and 41% As with trace amount of Pd, Sb, Bi and Ag.

Chalcopyrite (Ccp) and pyrrhotite (Po)

The chalcopyrite generally anhedral and subhedral in shape with sizes up to 10 μm . They occur as inclusions mostly within the rim or growth zones of Apy 2 (Fig. 5.12d). Their inclusion within the arsenopyrite growth zone indicated they also crystallization during the hydrothermal alteration activity. The Ccp is chemically composed of 33 % S, 28 % Fe, 32 % Cu with traces of Ag, Bi, As and Sb.

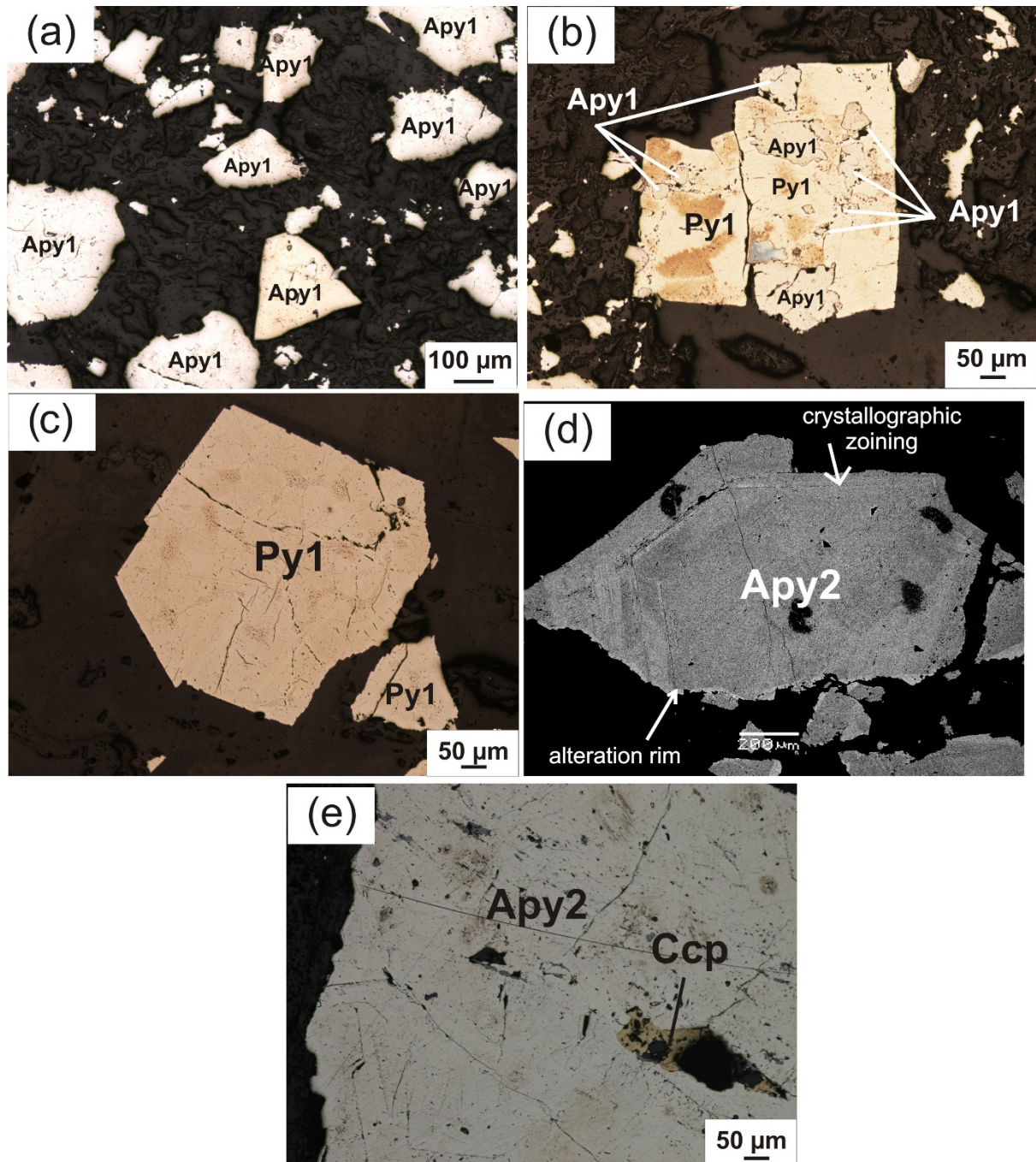


Fig. 5.12. Photomicrograph of the various sulphides observed in the Bepkong deposit. (a) Fragmented residual arsenopyrite 1(Apy1) (b) broken up arsenopyrites (Apy1) overgrown by euhedral pyrite (py1) (c) disseminated euhedral isolated crystal of pyrite (Py1) (d) SEM image of arsenopyrite 2showing the growth zones and grain boundary alteration rim (Apy 2) (e) arsenopyrite1 (Apy 2) with the inclusion of chalcopyrite (Ccp)

5.4.4.4 Trace element Geochemistry of sulphides

The composition of trace elements of the various generation of sulphides were determined by means of LA-ICP-MS. Summary of the results is in Table 5.3. Elemental associations attributed to the various sulphides will be discussed here.

Type	Co	Ni	Cu	Zn	As	Se	Ag	Cd	Sb	Te	Au	Pb	Bi	Co/Ni
LOD	0.20	0.60	0.09	0.07	0.80	1.40	0.01	2.50	0.10	0.12	0.01	0.10	0.10	
Py1	<LOD	<LOD	0.09	0.41	2106.47	29.38	<LOD	<LOD	<LOD	<LOD	<LOD	<LOD	<LOD	<LOD
Py1	<LOD	6.97	0.20	0.84	3355.85	44.62	<LOD	<LOD	<LOD	0.28	0.03	<LOD	<LOD	<LOD
Py1	1.68	90.49	0.15	0.80	4040.42	54.91	<LOD	<LOD	<LOD	0.25	0.28	0.19	<LOD	<LOD
Py1	<LOD	2.99	1.62	1.84	1492.38	25.31	0.06	<LOD	1.00	0.16	<LOD	4.61	0.74	<LOD
Apy1	222.44	342.55	4.35	1.15	1111477.00	305.59	1.94	0.62	361.16	45.29	3.03	84.24	27.47	0.65
Apy1	128.67	712.08	13.57	2.54	1414491.00	301.48	6.77	0.60	330.84	35.86	2.74	97.12	19.05	0.18
Apy1	68.48	262.59	56.32	0.90	1817457.00	506.71	1.98	0.96	372.88	407.26	1.34	61.79	36.51	0.26
Apy1	66.74	198.54	2.27	0.95	1734507.00	425.94	1.67	0.80	414.67	101.16	1.20	29.99	24.57	0.34
Apy1	48.59	323.00	14.69	2.07	1487687.00	281.83	0.52	1.03	306.59	26.28	2.02	54.96	8.75	0.15
Apy1	55.76	153.95	3.92	5.02	1464240.00	412.16	1.39	0.81	429.53	137.34	0.64	41.61	23.78	0.36
Apy1	262.39	1507.39	38.03	0.47	1030642.00	551.42	0.46	0.44	270.28	45.98	0.47	17.66	6.90	0.17
Apy1	262.13	2079.09	15.20	0.51	995740.00	284.28	2.89	1.04	369.17	34.32	0.37	567.19	17.94	0.13
Apy2	1.20	10.74	20.99	1.71	2317479.00	1247.68	0.73	1.07	266.12	39.67	0.60	46.82	6.96	0.11
Apy2	16.60	99.41	7.34	2.29	2407810.00	1147.21	1.35	1.44	872.49	904.05	1.60	64.17	35.74	0.17
Apy2	6.41	14.20	11.37	2.95	3065886.00	1147.59	3.07	1.45	911.58	310.96	1.66	336.41	141.39	0.45
Apy2	2.47	9.91	6.27	3.46	4501282.00	2449.05	42.04	13.75	772.84	233.76	1.05	8402.28	162.61	0.25
Apy2	1.30	39.19	3.07	3.78	2522397.00	1013.81	0.47	1.06	1166.93	799.00	0.34	16.27	20.16	<LOD
Apy2	2.13	44.21	2.68	1.48	2196299.00	770.10	0.98	0.76	477.15	464.48	5.95	46.02	23.95	0.05

Type	Co	Ni	Cu	Zn	As	Se	Ag	Cd	Sb	Te	Au	Pb	Bi	Co/Ni
Apy2	7.02	51.47	4.79	4.16	2954130.00	763.22	1.08	0.81	502.99	477.08	4.92	51.50	26.69	0.14
Apy2	3.13	382.68	5.43	4.75	3621238.00	964.51	1.35	1.45	1225.29	146.45	0.84	80.65	39.84	<LOD
Apy2	0.42	210.68	4.42	2.56	3170022.00	1009.65	0.31	1.76	1445.76	67.64	0.19	9.26	20.13	<LOD
Apy2	0.43	33.75	4.63	5.70	2908388.00	1364.64	0.36	1.30	816.79	246.97	0.45	4.69	4.17	<LOD
Apy2	1.93	19.54	3.63	2.24	2450511.00	933.72	1.08	0.84	775.35	178.89	1.46	18.72	17.37	0.10

LOD - Limit of detection

Pyrite (Py1)

The pyrite in the Bepkong deposit generally gave low concentration of trace elements. Invisible Au and Ag concentration ranges from 0.01 to 0.28 ppm, with a mean value of 0.08 ppm and 0.06 to 0.13 ppm with an average of 0.04 ppm respectively. It shows low concentrations of Ni, Co, Sb, Se, Pb and Cu.

Arsenopyrite 1 (Apy1)

The arsenic concentration in Apy 1 is generally low compared to Apy 2 (Table 5.3), with its concentration ranging from 995740 to 1817457 ppm. This sulphide type is rich in Ni (198 to 2079 ppm), Co (48.59 to 262 ppm) and deficient in Sb (270-429 ppm), Pb (17 to 97 ppm) and Au (0.37 to 3.03 ppm).

Arsenopyrite 2 (Apy 2)

This sulphide shows elevated concentration of arsenic (2196299-4501282 ppm), Sb (502-1445 ppm), Se (770-2449 ppm), Pb (4-8402 ppm) and Au (0.6-5.95 ppm) and highly deficient in Ni (19 to 382.6 ppm) and Co (0.42- 16 ppm). Apy 2 is devoid of almost Ni and Co as supposed to Apy 1. Lead and gold concentrations in both arsenopyrites are relatively the same (Fig. 5.13c, e). Apy 2 have higher Sb and Se concentrations compared to Apy 1 (Fig. 5.13d, f).

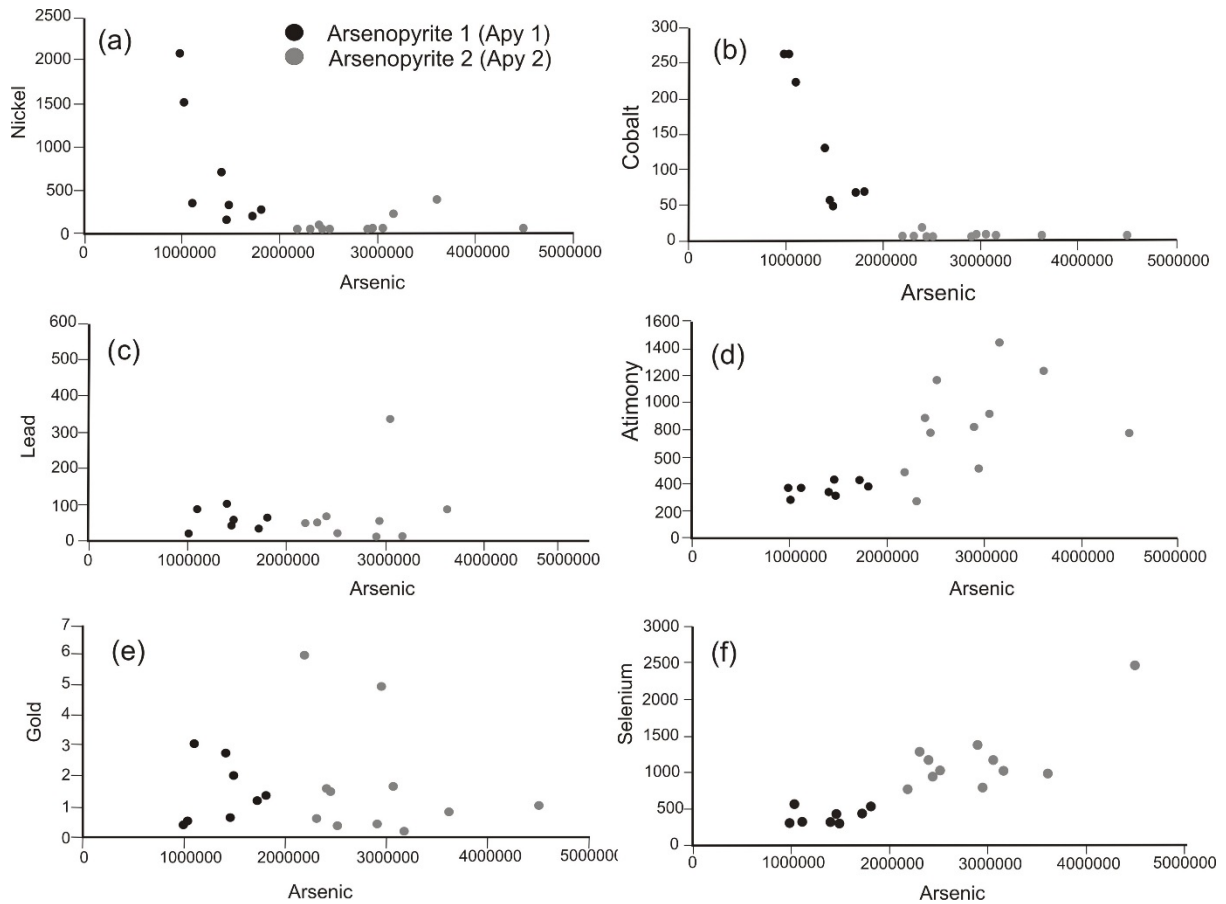


Fig. 5.13. Bivariate diagram showing trace element variations in arsenopyrite 1 and 2 (units in ppm).

5.4.4.5 Gold occurrence in Arsenopyrite

Arsenopyrites (Apy1 and Apy2) in the Bepkong deposit are the main carriers of gold in the Bepkong deposit. LA-ICP-MS analysis on pyrites showed that the pyrite were deficient in gold mineralization (Fig. 5.14a; Table 5.3). Apy 2 exhibited growth zone within its crystal structure (Fig. 5.14b), with usually pyrrhotite mineral caught within the growth zones and sometimes within the core (Fig. 5.14c). This sulphide type was extensively fractured. Gold mineralization was found within outer growth zone of the arsenopyrite as well as within the fractures (Fig. 5.14d)

Apy1 generally did not exhibit growth zone. Gold mineralization that occurs within the core of Apy1 occurred as invisible gold. Invisible gold found within the core of Apy1 do occur with albite and rutile. This indicated that gold mineralization occurred at the formative temperatures of the albite during the formation of the period of the country rock.

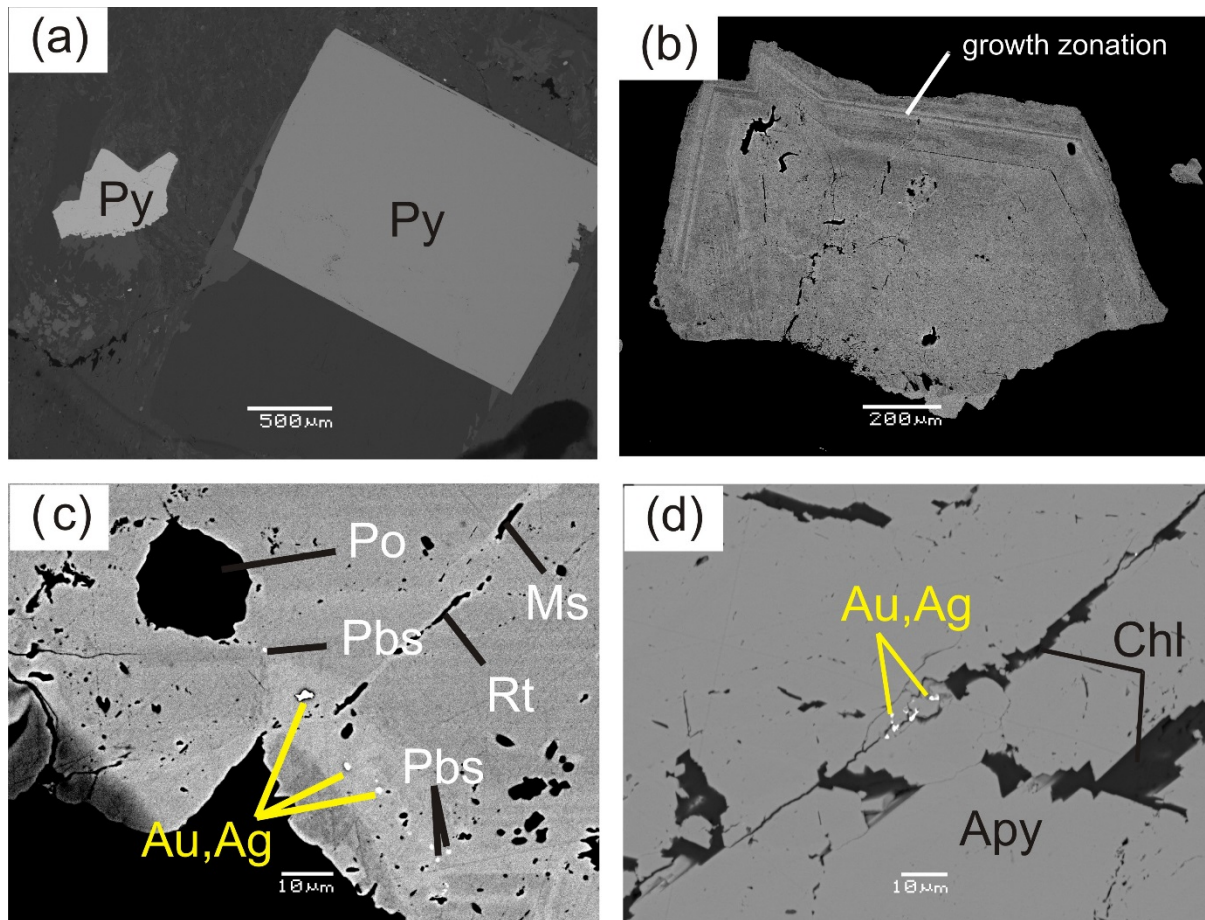


Fig. 5.14. BSE SEM images of pyrite and arsenopyrites from the ore zone in Bepkong (a) unmineralized euhedral pyrite within the mineralized zone (b) Apy2 exhibiting growth rims, formed during the hydrothermal fluid flow within the Bepkong deposit (c) micro size visible gold precipitated within the growth rims of Asp2. Inclusion of Pyrrhotite within the growth rims (d) Apy2 grain from type 1 quartz vein showing visible gold formed within the fractures. The fractures are also filled with hydrothermal chlorite and rutile. Au-gold, Ag-silver.

5.4.5 Arsenopyrite geothermometry

In order to holistically understand the temperature-pressure history of mineralization in the Bepkong deposit, sulphides geothermometry together with fluid inclusion studies are used, with the latter described in the section below. From Table 4 below, the sulphides present in the Bepkong deposit are either rich in arsenic, iron and sulphur.

Stability experiments of systems such as Fe-As-S and Cu-Fe-S have been used by earlier workers such as Clark (1960 a, b), Sugaki et al. (1975) and Kretschmar & Scott (1976) to determine the temperatures and pressures condition for arsenopyrite formation and alteration. In spite of arsenopyrite geothermometry being an empirical thermometer and therefore not fully quantitative, it can be used to estimate mineralization temperatures (Kretschmar & Scott, 1976; Sharp et al., 1985).

In order to use the stability diagrams of Sharp et al. (1976), Clark (1960a, b) and Kretschmar & Scott (1976) to determine temperatures, the sulphides and the sulpharsenides must attain equilibrium conditions and differential reequilibrations have not taken place (Morey et al., 2008). BSE SEM imagery done of Apy1 and Apy2, shows that Apy1 is not zoned whilst that of Apy2 exhibit oscillatory zoning. From Table 5.4 below, there is no clear compositional difference between core and the rim of the type 2 arsenopyrite (Apy2) studied. It is therefore permissible to conclude that arsenopyrite were not chemically zoned but chemically homogenous. Similarly, Table 5.4 shows that type 1 arsenopyrite (Apy1) is chemically the same as type 2 arsenopyrites (Apy2) and both arsenopyrite are sulphur rich. The same chemical composition of Apy1 and Apy2 shows that the diffusional reequilibrations have not affected the arsenopyrites been analysed.

To determine the temperature in the Bepkong deposit, microprobe analyses were done on mineralised arsenopyrite. The elements analysed were S, Fe, Au, Cu, Ag, Pb, Bi, As, Sb. Elements Au, Cu, Ag, Pb, Bi, Sb when combined gave a total concentration of less than 1 wt. % and where therefore considered as minor element and not relevant for the geothermometry analysis. For temperature estimations, the atomic % of As is plotted on a ($f(S_2)$ – Temperature diagram of Kretschmar & Scott (1976) and sharp et al (1985). From the stability diagram in Fig. 5.17, the stability of arsenopyrite and invisible gold is attained at 275 °C, and that of visible gold, arsenopyrite and pyrrhotite is attained at 290 °C.

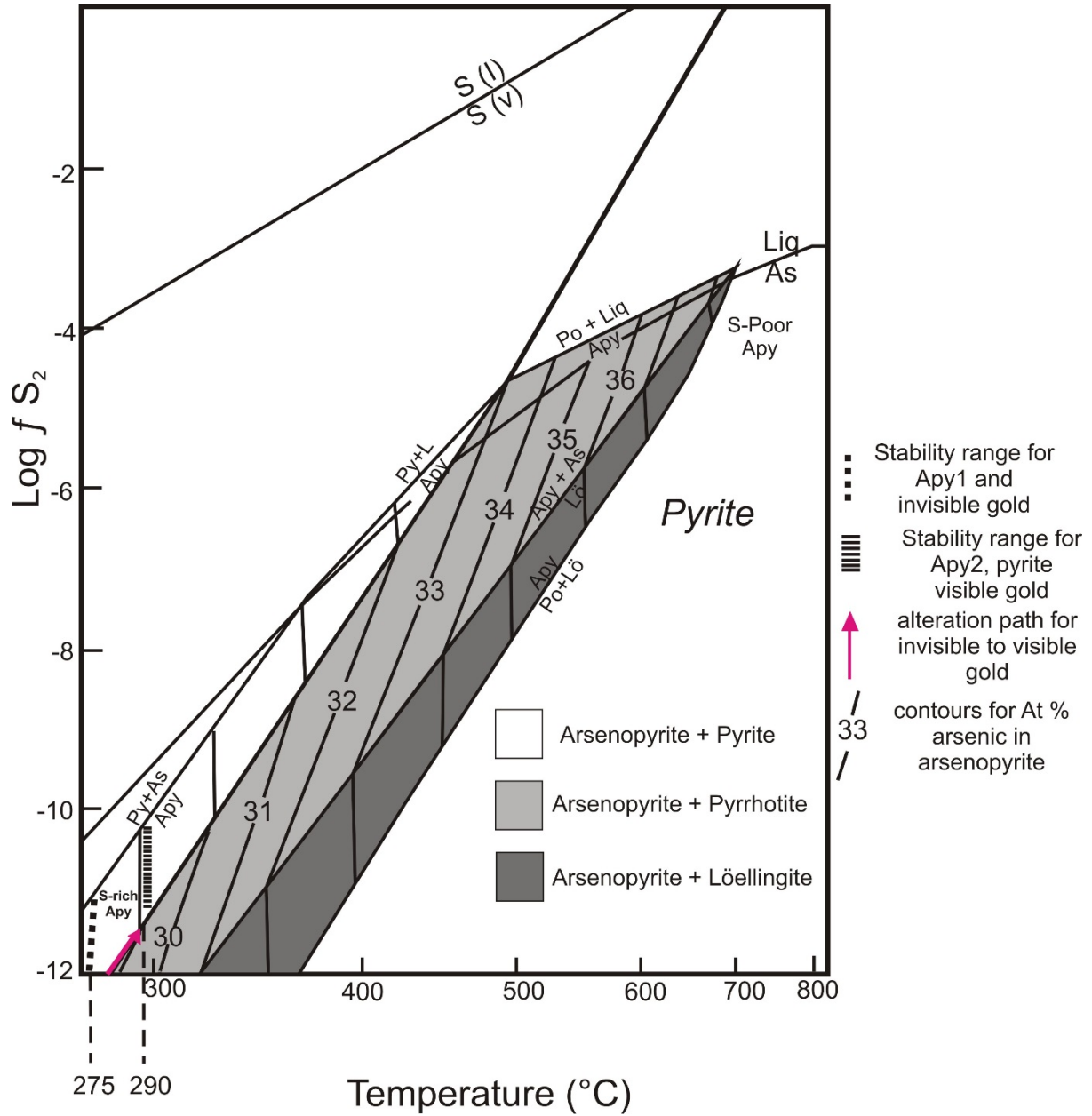


Fig. 5.17. The stability and phase relationship of arsenopyrite based on Sharp et al. (1985) and Kretschmar and Scott (1976). The average composition of Apy1 and Apy2 from table 4 were used.

Table 5.4. The composition of coexisting phases in arsenopyrite based on 41 independent electron microprobe analysis in the Bepkong deposit

Microprobe analysis for co-existing phases in arsenopyrite					Analytical results in At. %		
Sample Name	Apy type	sample location	S	Fe	Apy	Total	
Sample 2	1		38.00	33.90	28.00	100.00	
	2	Core	37.10	33.90	29.00	100.00	
	2	Core	37.20	33.90	28.80	100.00	
	2	Rim	38.20	33.80	28.00	100.00	
	2	Rim	38.10	33.60	28.30	100.00	
Sample 3	1		37.60	33.90	28.50	100.00	
	1		37.10	33.80	29.10	100.00	
Sample 4	2	Core	37.60	33.80	28.60	100.00	
Sample 5	1		37.40	33.80	28.80	99.90	
Sample 6	1		37.30	33.90	28.70	99.90	
	1		38.00	34.00	28.00	100.00	
	1		37.40	33.90	28.70	100.00	
	1		37.10	33.80	29.00	100.00	
	1		36.70	33.90	29.40	100.00	
Sample 7	1		36.80	33.90	29.20	100.00	
	2	Rim	38.30	33.80	28.80	100.00	
	2	Core	37.00	33.80	29.20	100.00	
	2	Core	37.30	33.70	29.00	100.00	
	2	Core	37.30	33.70	29.00	100.00	
Sample 8	2	Core	37.30	34.10	28.40	100.00	
	2	Core	37.50	34.10	28.40	100.00	
	2	Core	37.30	34.00	28.70	100.00	
	2	Core	37.30	34.00	28.70	100.00	
	2	Core	37.30	34.00	28.70	100.00	

Microprobe analysis for co-existing phases in arsenopyrite

Sample Name	Apy type	sample location	Analytical results in At. %			
			S	Fe	Apy	Total
	2	Core	36.90	33.90	29.10	100.00
	2	Rim	37.20	33.70	29.10	99.90
	2	Rim	36.30	33.80	29.90	100.00
	2	Rim	36.80	33.70	29.50	100.00
Sample 10	1		38.20	33.60	28.20	100.00
Sample 11	1		37.30	33.90	28.70	100.00
	1		37.30	33.70	28.90	100.00
	1		37.40	33.70	28.90	100.00
Sample 12	1		37.40	33.90	28.70	100.00
	1		37.90	33.60	28.50	100.00
	1		37.30	33.50	29.20	100.00
	1		36.70	34.00	29.30	100.00
	1		36.90	33.80	29.30	100.00
	1		37.40	33.80	28.70	100.00
Sample 14	1		36.90	34.00	28.90	99.90
	1		37.20	33.80	28.90	99.90
Sample 15	2	Core	37.60	33.60	28.80	100.00
	2	Rim	37.00	33.90	29.10	100.00
	2	Rim	36.90	33.80	29.30	100.00
	2	Rim	37.40	33.60	29.00	100.00
Mean			37.32	33.81	28.86	99.99

5.4.6 Fluid inclusions

Fluid inclusion studies were done on quartz crystals (Fig. 5.18) in type 1 mineralized quartz veins within the dilatational zone of the anastomosing D_{B1} shear zone and from pressure shadows (Fig. 5.18e) around the sulphides in the mineralized zone in the type 1 veins. Petrographic studies as outlined by Goldstein & Reynolds (1994) and subsequent measurement of fluid inclusions thermometric properties were centred on closely associated groups and trails of primary and pseudosecondary inclusions based on the genetic classification by Roedder (1984).

Primary fluid inclusions (Fig. 5.18a) used for the fluid inclusion analysis were observed mainly within quartz crystals from the D_{B1} type 1 quartz veins and also pressure shadow around sulphide minerals in the type 1 quartz vein. They occur as isolated inclusions with size ranging from 20 μm to 35 μm with about 70 % decrepitated.

Trails of pseudosecondary inclusions (Fig. 5.18c) were observed in both in the quartz crystals in the D_{B1} quartz veins and quartz crystals from pressure shadow in the mineralized zone. The fluid inclusion planes crosscut the grain boundaries (transphase) of the quartz crystals as a result of healing of fractures.

Two types of fluid inclusion were identified base on the number of phases and degree of filling at room temperature, phase variations during heating and freezing runs and Raman spectroscopic analysis (Fig. 5.19).

Type 1 fluid inclusions

Type 1 are $\text{CH}_4\text{-H}_2\text{O} \pm \text{SO}_2$ fluid inclusions (Fig. 5.18f) and the least abundant within the mineralized zone in Bepkong. They usually occur as clusters or in a trail within the pressure shadow around the sulphide in the mineralized zone. This fluid inclusion type are V-rich fluid inclusion with very little L, with some the $\text{CH}_4 \pm \text{SO}_2$ vapour bubble generally occupying about 100 % of the total fluid inclusion. The inclusions show irregular shapes and sizes ranging from 2 to 5 μm .

Type 2 fluid inclusions

Type 2 are $\text{CH}_4\text{-CO}_2\text{-SO}_2\text{-H}_2\text{O}$ fluid inclusions (Fig. 18b, d) and the most abundant fluid inclusion type. These are two phase L+V inclusion type with the V $\text{CH}_4\text{-CO}_2\text{-SO}_2$ vapour bubble occupying about 30 to 40 % of the total fluid inclusion and with the $\text{LH}_2\text{O-SO}_2$ occupying the rest. This fluid inclusion type occurs as isolated primary inclusions or in trails with their size ranging from 5 to 30 μm . The general degree of filling of the vapour bubble at room temperature ranges from 10 to 90 %.

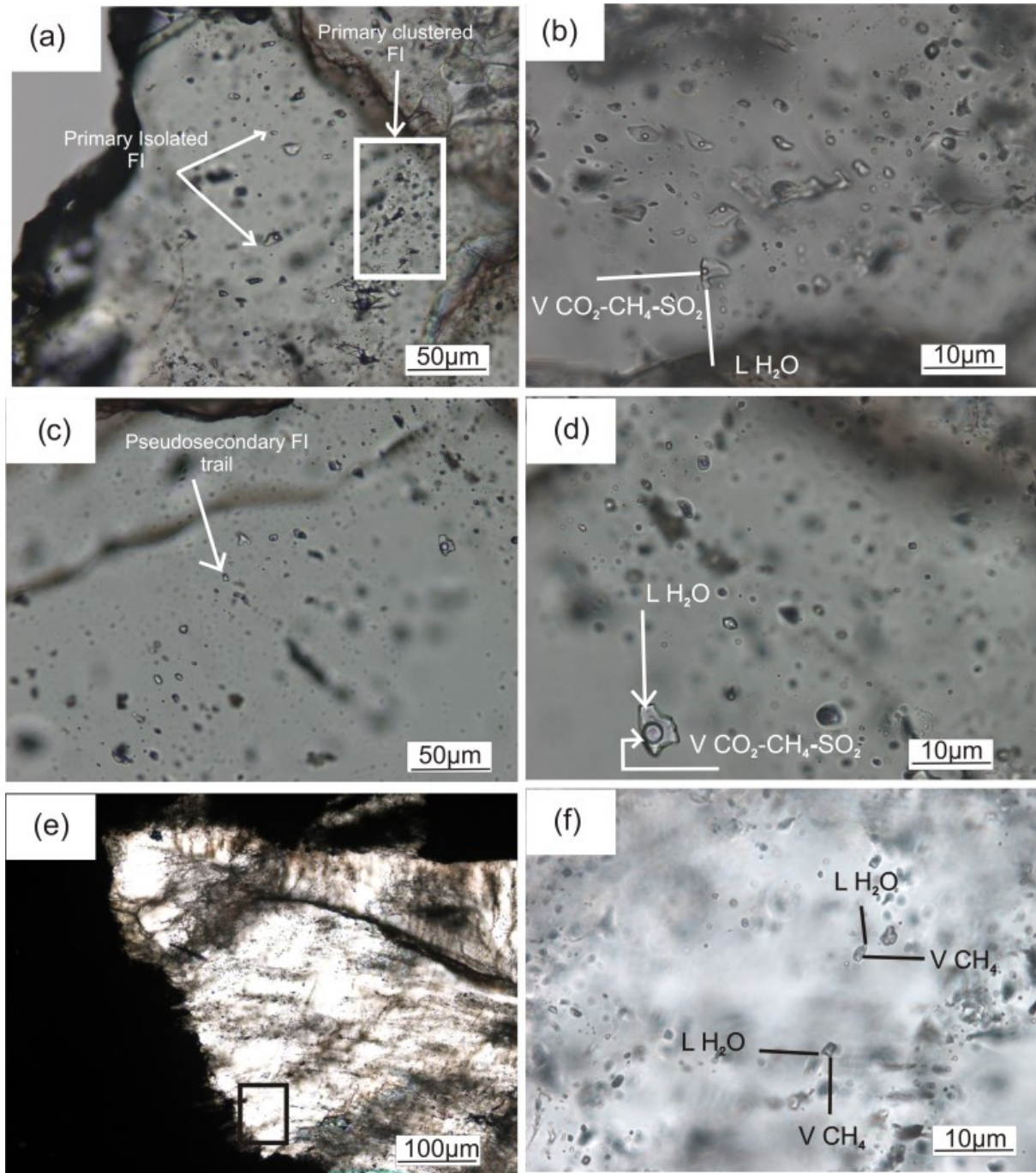


Fig. 5.18. Photomicrograph showing fluid inclusions in type 1 quartz crystals found in D₂ anastomosing mineralized vein and pressure shadows in the Bepkong deposit. (a) Quartz crystal showing cluster of primary fluid inclusion (in the white box) and isolated primary fluid inclusion (b) shows close up of the white insert in (a) Showing type 2 primary cluster fluid inclusion (c) intragranular pseudosecondary fluid inclusion trail (d) zoomed in fluid inclusion trail showing type 2 characteristics (e) pressure shadow showing sites of type 1 fluid inclusions. The black box shows sites of isolated fluid inclusion (f) shows a zoom section of (e) showing isolated type 1 fluid inclusion

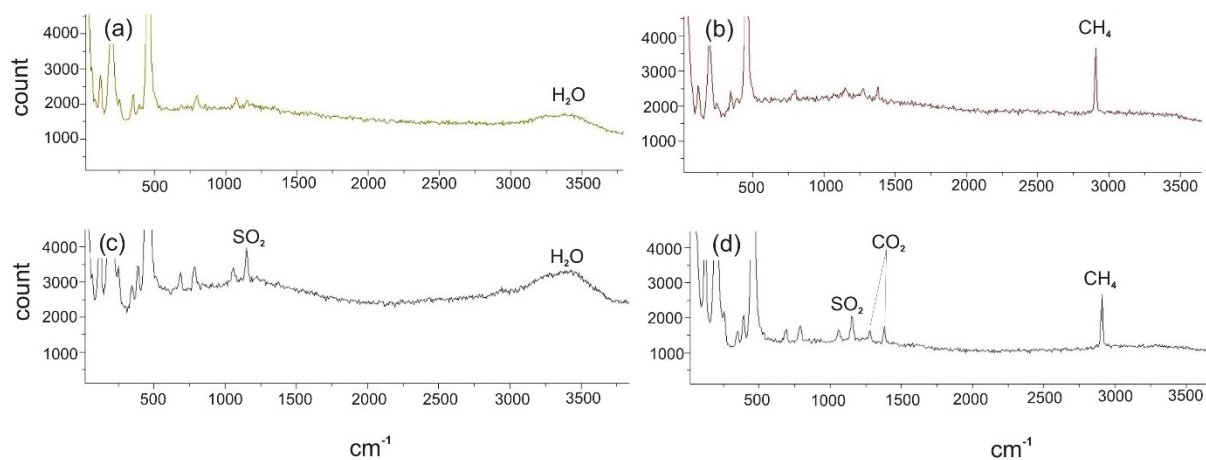


Fig. 5.19. Raman spectra signals of type 1 and type 2 fluid inclusions in the Bepkong deposit (a) the liquid phase of type 1 inclusion only showing the presence of H₂O (b) the vapour phase of type 1 inclusion showing the presence of CH₄ (c) liquid phase of type 2 fluid inclusion showing the presence of SO₂ and H₂O (d) The vapour phase of type 2 inclusion showing the presence of CO₂, SO₂ and CH₄.

Fluid composition and microthermometric results

Raman spectroscopic analysis were done on all the fluid inclusion type, to obtain the volatile composition of the fluids. Spectra obtained from the V phase in type 1 and L and V phase in type 2 shows that, the V-phase in type 1 is composed of CH₄ ± SO₂, whilst the L and V phase in type 2 fluid inclusion is composed of H₂O ± SO₂ and CH₄-CO₂-SO₂ respectively (Fig. 5.19).

A total of 40 fluid inclusion each for both type 1 and type 2 fluid inclusions were analysed in the type 1 quartz vein and 15 fluid inclusion were analysed from the pressure shadow. The lower temperature phase (thus, the total freezing temperatures, ice nucleation temperatures, melting temperatures and clathrate dissolution temperatures) were measured first to curtail the possibility of the fluid inclusion decrepitation during the heating experiments (homogenization temperatures and total homogenization temperatures).

The supercritical methane bubble in the type 1 fluid inclusion separates into a L an V phase at temperatures less than -80 °C and when cooled to the temperature of the liquid nitrogen during the heating runs it attains its triple points between -184.4 °C to -180 °C (Fig. 5.20a). About 90 % of the fluid studied gave values close to the triple point of pure CH₄, which is -182.5 °C (van den Kerkhof, 1990). The measurement below the triple point of the pure CH₄ are due to the presence of minor amounts of SO₂, as detected by Raman spectroscopy; the data above this value probably result from difficulty in observing the phase transition precisely, due to the very low temperature, close to the physical limit of the stage. CH₄ homogenization temperatures ranged from -84.2 °C to -80 °C (Fig. 5.20b), with most

inclusions displaying critical behaviour (T_h pure $\text{CH}_4 = -82.6^\circ\text{C}$). The data above this value are due to the presence of minor amounts of SO_2 . Clathrate melting temperatures ranging from 14° to 17°C were recorded (Fig. 5.20c), which lay within the range of clathrate melting temperatures for CH_4 (10° to 19°C ; Diamond, 2003). Total homogenization temperatures ranging from 310° to 370°C were measured (Fig. 20d). The densities calculated using Flicor computer program (Brown & Hagemann, 1995) for the type 1 inclusion ranges from $0.448\text{--}0.451\text{ g/cm}^3$.

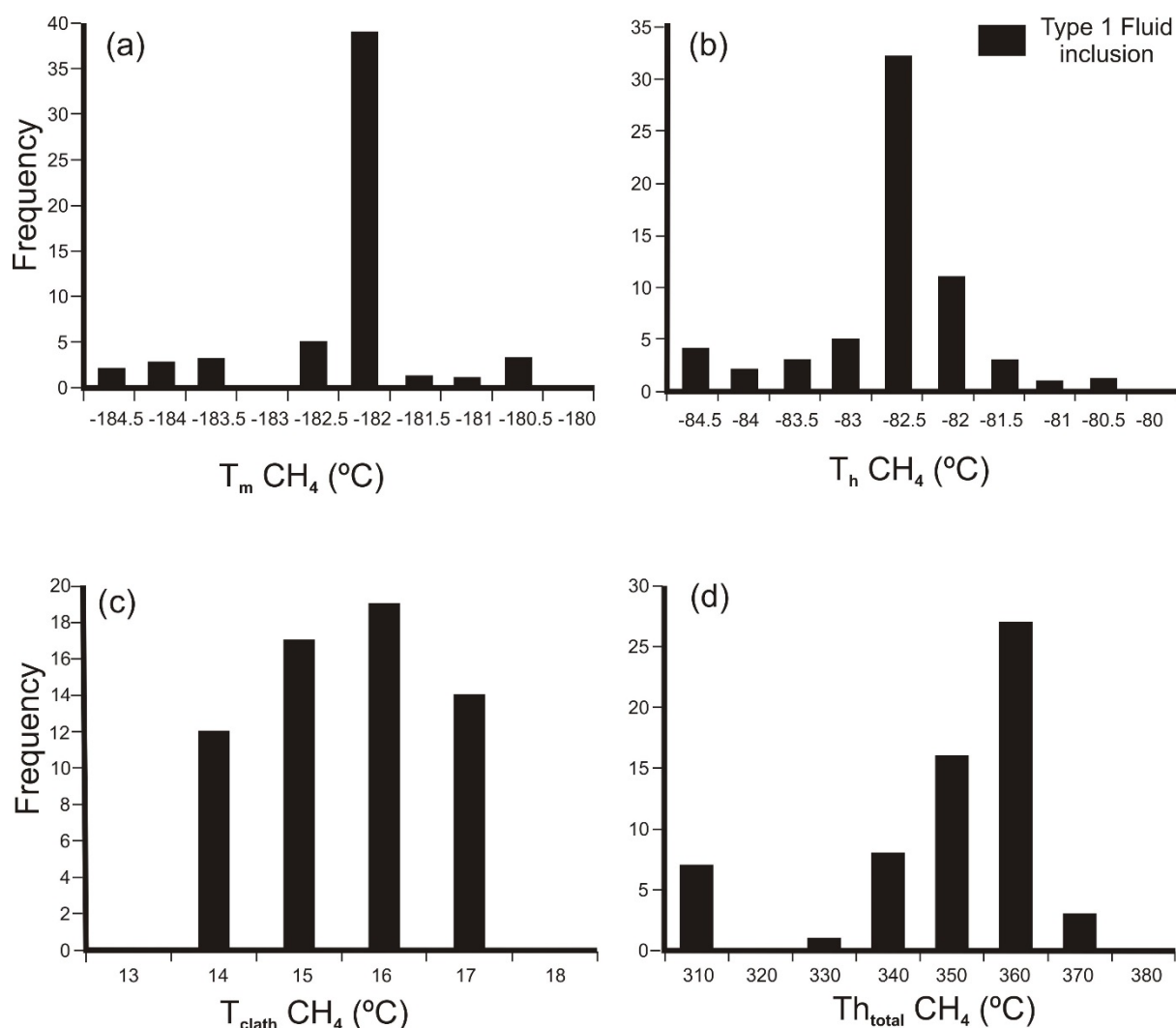


Fig. 5.20. Diagrams showing the microthermometric data for type 1 fluid inclusions in the Bepkong deposit (a) melting temperatures of CH_4 (b) homogenization temperature for CH_4 (c) Clathrate dissolution temperatures for CH_4 (d) Total homogenization temperatures for CH_4 .

For the Type 2 dominant fluid inclusion triple point temperatures range between -56.8° to -74°C . These temperature ranges are above the triple point of pure CO_2 suggesting varying amount of CH_4 and SO_2 . Clathrate melting temperature occurred from 8° to 16°C . Critical temperatures measured were from 18 to 25°C with total homogenization ranging from $320\text{--}342^\circ\text{C}$. X_{CH_4} , X_{CO_2} and X_{SO_2} ranges from 0.61 to 0.36 , 0.03 to 0.4 and 0.01 to 0.29 respectively for most of the samples measured. The composition of the type 2 fluid inclusion was

determined from the Raman spectroscopy measurements. Salinities measured for type 2 fluid inclusions ranges from 2.27 to 3.42 wt. % eq. NaCl and densities from 0.39g/cm³ to 0.58g/cm³ (Table 5.5) using BULK and ISOC of Bakker (2003).

Table 5.5. Summary of fluid inclusions microthermometric measurement from the mineralized type 1 quartz vein in the Bepkong deposit

Quartz vein type	Host mineral	environment	Inclusion type	Size μm	Degree of filling at room temperature	Tm CH ₄	Thclath	Th	Thtotal
type 1	quartz	Primary inclusion that occurs as cluster within the fluid inclusion plane in the quartz crystal	type 1 CH ₄ ± SO ₂ n=15	2-5	100	-184 to -180 mean = -182.6 n	14 to 17 mean=16	-84.2 to -80 mean= -82.6	310-360
type 1	quartz	Isolated Primary inclusion that occurs within the fluid inclusion plane in the quartz crystal	type 1 CH ₄ ± SO ₂ n=25	2-10	100	-183 to -181 mean = -182.5	15 to 17 mean=16	-83 to -80 mean= -82.6	310-370
type 1	quartz	Isolated Primary inclusion that occurs within the fluid inclusion plane in the quartz crystal in the pressure shadow	type 1 CH ₄ ± SO ₂ n=15	2-5	95-100	-183 to -181 mean = -182.5	14 to 17 mean=16	-84.2 to -80 mean= -82.6	310-370
type 1	quartz	Primary inclusion that occurs as cluster within the fluid inclusion plane in the quartz crystal	type 2 CH ₄ -CO ₂ -SO ₂ n=25	30	40	-56.8 to -74	8 to 16 mean= 16	18 to 25 mean 22	320 to 320
type 1	quartz	Isolated Primary inclusion that occurs within the fluid inclusion plane in the quartz crystal	type 2 CH ₄ -CO ₂ -SO ₂ n=15	10	10	-56.8 to -70	8 to 14 mean= 10	19 to 25 mean 22.5	321 to 324
type 1	quartz	Isolated Primary inclusion that occurs within the fluid inclusion plane in the quartz crystal	type 2 CH ₄ -CO ₂ -SO ₂ n=10	20	90	-56.8 to -74	8 to 16 mean= 14	20 to 24 mean 22	320 to 320

n = the number of measurement made

5.5 Discussion

Structural control on gold mineralization and timing relationships

The initial pervasive deformation (D_{B1}), which is observed at the deposit scale is characterized by N-S trending anastomosing shear zones that define an initial S_{B1} foliation with steep dips and the main structural event that occurred in the Wa-Lawra belt. The anastomosing pattern is as a result of strain partitioning due to the rheological difference between the shales and the volcanoclastic rocks. This deformation style observed here is comparable to the regional initial D_1 and D_2 deformation for region studied by Baratoux et al. (2011) and D_4 by Block, (2015). The F_{B1} and the L_{B1} are all parallel to S_{B1} and are all probably part of the same transcurrent sinistral system.

The F_{B1} folds are asymmetric, non-cylindrical, and tight to isoclinal fold with their orientation on the curvilinear axis at about 5 to 22° with F_{B1} axial plane plunging north. These folds were formed during the D_{B1} deformation event as a result of continual WNW-ESE shortening.

The anastomosing shear zone have created several dilatational zones or jogs during the D_{B1} deformational phase on the Wa-Lawra belt. The Bepkong deposit sits on one of these dilatational zones. These dilatational zones have created discrete open system within an overall partly open wall rock system that permitted channelized fluid flow with substantial inflow of fluids from the in and out of the wall rock, hence the sulphidation observed within the wall rocks.

Amponsah et al. (2015) observed that the parallelism of type 1 veins of ore shoots within the D_{B1} shear zones and occurrence of gold in altered rock around the deformed type 1 quartz veins clearly states that the anastomosing shear zone controls the gold mineralization in the Bepkong deposit. The maximum age for the deposition of the volcano-sedimentary units of the Wa-Lawra belt is 2139 ± 2 Ma (U-Pb zircon ages; Agyei Duodu et al., 2009). The onset of the D_{B1} (i.e., regional D_4) took place after 2130 Ma, which is defined by a U-Pb age constraint on D_2 , from metamorphic monazite (Block, 2015). The D_{B1} deformation event took place relatively late in the Eburnean tectonic history in Northern Ghana.

Two stages of gold mineralization

From gold assay results from Azumah resources database and LA-ICP-MS analysis shows that gold in the Bepkong deposit is associated with disseminated arsenopyrites of two generations hosted within the shales and volcanoclastic rock. Gold is not found in relation to pyrite. The early stage of mineralization associated with Apy1 occur as invisible gold within the lattices of the sulphide and the second stage as visible gold present within the rims and fractures found within Apy2 or present within fractures found within the type 1 quartz vein or the wall rock adjacent to the type 1 quartz vein. Gold formation in the Bepkong deposit is also associated with D_{B1} event, where gold bearing hydrothermal fluid infiltrated the dilatational zones which lead to the pervasive alteration by chlorite + sericite + ankerite +

quartz + calcite + sulphides within the vicinity of type 1 quartz vein and the wall rock adjacent to the vein. The chemical state of gold in a solid solution is a complex with the oxidation state of Au³⁺ or a combination of Au⁰ or Au¹⁺ (Arehart et al., 1993; Simon et al., 1999 and reference there in) and the intake of gold into the arsenopyrites is usually in the form of Au⁰ and Au¹⁺ forms (Cabri et al., 2000; Morey et al., 2008). From SEM imagery all the arsenopyrites formed within the Bepkong deposit are a product of hydrothermal alteration. This is because, the all the arsenopyrite type exhibits grain boundary alteration rim and particularly Apy2 shows oscillatory zonation with the core and rims characterize by compositional variation in their As content when analysed with the LA-ICP-MS. The rims of Apy2 are more enriched in As compared to the core (Table 5.3) which suggest that the growth zone of Apy2 occurred within the hydrothermal event. The formation of visible gold within the oscillatory or growth zone of the arsenopyrite shows that remobilization of the visible gold is associated with the growth rim and fracturing during the hydrothermal alteration event. From the LA-ICP-MS analysis done on the sulphides (thus Py1 and Apy1), there were elemental variation associated or unique to each sulphide. The Apy1 is rich in Co and Ni and deficient As, St, Sb, Pb, whilst Apy2 is rich in Au, Pb, As, St, Sb and deficient in Ni and Co. This means Apy2 was formed in an environment deficient in Ni and Co whilst Pb, As, St and Sb were added to the system as well as visible gold.

Arsenopyrite zonation and temperatures estimates for gold mineralization using microprobe analysis

Microprobe analysis in Table 5.4, has proved that there is no chemical variation within the core and rim of the oscillatory zone Apy2 and similarly Apy1 and Apy 2 are chemically the same. This same phenomenon was observed by Lowell & Gasparrini (1982), when the authors analysed the rim and core of arsenopyrite from the Topaz Greisen vein in the south eastern Missouri, even though Kretschmar & Scott (1976) said the absence of chemical variation is an uncommon phenomenon. The small difference in the As and S values as well as As/S ratios for both Ap1 and Apy2, shows that the arsenopyrite used were in equilibrium. This observation is consistent with the observation made by Morey et al. (2008). From the average at.% values for As in both type 1 and type 2 arsenopyrites plotted on the stability diagram in Fig. 5.17 shows that there is the is an general increase in sulphur fugacity from -11 to -10.5 and temperature from 275 to 290 °C respectively for the transition between Apy1 to Ap2 + Py ± Po ± Ccp. This means that the require temperature to form the Apy1 + invisible gold to Ap2 + Py + visible gold ± Po ± Ccp is only approximately 15 °C and increase in sulphur fugacity in the scale of 0.5. The association of uniform increase temperature and sulphur fugacity is consistent with the notion that the solubility of gold in arsenopyrite decrease with increasing temperature (Morey et al., 2008). Arsenic At% values are low in the arsenopyrite in Bepkong when compared to arsenopyrite that have earlier remnant of pyrrhotite inclusion embedded within the core of arsenopyrites from the Boorara and Bardoc shear systems (Morey et al., 2008). From the sulphur fugacity and temperature diagram after Sharp et al. (1985) shows the pressure range for the gold to form ranges from 1 to 3 kbars.

Fluid trapping mechanism

From the microthermometric measurements and Raman spectroscopy analysis on fluid inclusion in the Bepkong deposit revealed two different fluid inclusion types. Type 1 is CH₄-H₂O rich and type 2 is CH₄-CO₂-SO₂-H₂O rich with type 2 been the most abundant in the Bepkong deposit.

From the calculated X_{CH₄}, X_{SO₂} and X_{CO₂} mole fraction form the most abundant type 2 fluid inclusion, as well as the pure CH₄-rich fluid inclusion, it can be said, the Bepkong deposit is CH₄ inclusion rich. CH₄-H₂O may be probably the main primary fluid inclusion during the **early** stage of mineralization. This is particularly true due to the abundance of graphite in the shales observed within the deposit area. This corresponds well with other CH₄ rich fluid inclusion in low grade metamorphic organic rich sediment reported by Mullis (1987) and Fan et al. (2000). CO₂-SO₂ introduction into the fluid system in Bepkong might be **late** and may have driven solely from the metamorphism of the graphitic shale.

Given the fluid inclusion population observed in the Bepkong deposit and their distribution, ie., abundance of vapour-rich inclusions that can contain up to 100% vapour, does not coexisting with liquid-rich type-2 L-V inclusions assemblages. It is most likely that the fluid was immiscible (i.e., phase separation had taken place) at the time of fluid inclusion entrapment. The total homogenization temperature for the supercritical type-1 CH₄-rich inclusion is 370°C and well above the solvus of CH₄ and will stay as V-rich CH₄ (Fig.1). As the ambient temperature and pressure drop to 320 to 324°C as a result of the initiation of the D_{B1} anastomosing shear zone and fluid ascending to higher crustal levels, or the expansion of the solvus due to the interaction of fluid with graphitic host rock, the fluid would separate into phase (or exsolve from the original Type-1) forming the type 2 (CH₄-CO₂-SO₂-H₂O) abundant fluid inclusion type. Phase separation have been proposed as an important mechanism for depositing high grade gold into quartz veins under sub-amphibolite facies conditions (Robert and Kelly, 1987, Walsh et al., 1998, Guha et al., 1991).

Conclusion

From this studies it can be concluded that the gold in the Bepkong deposit is controlled by the long lived D_{B1} anastomosing shear zone and alteration assemblage of chlorite + sericite + ankerite + quartz + calcite + sulphides. The gold in Bepkong occurs as both invisible and visible gold during the hydrothermal process. The invisible gold occur within the first generation arsenopyrite and the visible gold is associated with the oscillatory zones and hydrothermal alteration rim and fractures within the Apy2. From the arsenopyrite geobarometry it can be concluded that the invisible gold in the Bepkong deposit formed at a temperature of about 275 °C and visible gold at about 290 °C with a pressure between 0.5 to 3 kbars. Fluid inclusions data reveals that fluid circulated within the dilatational zone at temperature between 320°C.

Acknowledgement

Azumah Resources Limited the owners of the Bepkong deposit are particularly thanked for giving the permission to publish this paper and for financing the fieldwork. We wish to gratefully acknowledge AMIRA International and the industry sponsors, including AusAid and the ARC Linkage Project LP110100667, for their support through the WAXI project (P934A). POA would like to thank Nick Franey and Stephen Stone for the continual support throughout the program. Special thanks go to Scriven Nyarko, Eugene Adubofour-Gyawu, Andrew Chubb, Sylvain Block and Vitus Bomaansan for their useful geological discussion on the Bepkong deposit. The author wants to thank Nick Franey for his thorough review of an earlier version of this manuscript.

5.6 Reference

- Abitty, E. K., Dampare, S. B., Nude, P. M., Asiedu D. K., (in press). Geochemistry and petrogenesis of the K-rich 'Bongo-type' granitoids in the Paleoproterozoic Bole-Nangodi greenstone belt of Ghana. *Journal of African Earth Sciences*. <http://dx.doi.org/10.1016/j.jafrearsci.2015.08.011>
- Agyei Duodu, J., Loh, G.K., Boamah, K.O., Baba, M., Hirdes, W., Toloczyki, M., Davis, D.W., 2009. Geological map of Ghana 1:1 000 000. Geological Survey Department of Ghana (GSD).
- Allibone, A., Hayden, P., Cameron, G., Duku, F., 2004. Paleopaleozoic gold deposits hosted by albite- and carbonate-altered tonalite in the Chirano district, Ghana, West Africa. *Economic Geology* 99, 479–497.
- Allibone, A., Teasdale, J., Cameron, G., Etheridge, M., Uttley, P., Soboh, A., Appiah-Kubi, J., Adanu, A., Arthur, R., Mamphey, J., Odoom, B., Zuta, J., Tsikata, A., Pataye, F., Famiyeh, S., Lamb, E., 2002. Timing and structural controls on gold mineralization at the Bogoso Gold Mine, Ghana, West Africa. *Economic Geology* 97, 949–969.
- Amponsah, P.O., Salvi, S., Beziat, D., Baratoux, L., Siebenaller, L., Nude, P.M., Nyarko, R.S., Jessell, M.W., 2015. The Bepkong deposit, Northwestern Ghana. *Ore Geology Reviews*. <http://dx.doi.org/10.1016/j.oregeorev.2015.06.022>
- Appiah, H., 1991. Geology and mine exploration trends of Prestea goldfields, Ghana. *Journal of African Earth Sciences, and the Middle East* 13, 235–241.
- Arhart, G. B., Chryssoulis, S.L., Kesler, S.E., 1993. Gold and arsenic in iron sulphides from sediment hosted disseminated gold deposits: Implication for depositional process. *Economic Geology*, 88, 171-185.
- Bakker, R.J., Brown, P.E., 2003. Computer modelling in fluid inclusion research. In: *Fluid Inclusions, Analysis and Interpretation* (edits Samson, I., Anderson, A., Marshall, D.). Short Course, Mineralogical Association of Canada, Ottawa, Canada, 175– 212.
- Baratoux, L., Metelka, V., Naba, S., Jessell, M.W., Grégoire, M., Ganne, J., 2011. Juvenile Paleoproterozoic crust evolution during the Eburnean orogeny (2.2-2.0Ga), Western Burkina Faso. *Precambrian Research* 191, 18-45.
- Barritt, S.D., Kuma J.S., 1998. Constrained gravity models and structural evolution of the Ashanti Belt, Southwest Ghana. *Journal of Earth Sciences* 26, 539-550.
- Béziat, D., Bourges, F., Debat, P., Lompo, M., Martin, F., Tollon, F., 2000. A Palaeoproterozoic ultramafic-mafic assemblage and associated volcanic rocks of the Boromo greenstone belt: fractionates originating from island-arc volcanic activity in the West African craton. *Precambrian Research* 101, 25–47.

Blenkinsop, T.G., Schmidt Mumm, A., Kumi, R., Sangmor, S., 1994. Structural geology of the Ashanti Gold Mine. *Geologisches Jahrbuch D* 100, 131–153.

Block, S., Jessell, M.W., Ailleres, L., Baratoux, L., Bruguier, O., Zeh, A., Bosch, D., Caby, R., Mensah, E., 2015. Lower crust exhumation during Paleoproterozoic (Eburnean) orogeny, NW Ghana, West African Craton: interplay of coeval contractional deformation and extensional gravitational collapse. *Precambrian Research*. Doi: 10.1016/j.precamres.2015.10.014

Block, 2015. Evolution géodynamique du craton ouest Africain au nord du Ghana. University of Toulouse III. Unpublished PhD Thesis.

Borisova, A.Y., Freydier, R., Polvé, M., Jochum, K.P., Candaudap, F., 2010. Multi-elemental analysis of ATHO-G rhyolitic glass (MPI-DING reference material) by femtosecond and nanosecond LA-ICP-MS: Evidence for significant heterogeneity of B, V, Zn, Mo, Sn, Sb, Cs, W, Pt, and Pb at the millimetre scale. *Geostandards and Geoanalytical Research*, 34, 245–255.

Brown, P.E., and Hagemann, S.G., 1995. MacFlincon and its application to fluids in Archean lode-gold deposits. *Geochimica et Cosmochimica Acta*, 59, 3943–3952.

Cabri, L.J., Newville, M., Gordon, R.A., Crozier, E.D., Sutton, S.R., McMahon, G., Jiang, D.T., 2000. Chemical separation of gold in arsenopyrite. *Canadian mineralogist*, 38, 1265–1281.

Clark, L. A., 1960a. The Fe-As-S system: Phase relations and applications *Economic Geology*. 56, Part I:1345-1381 Part II: 1631-1652.

Clark, L. A., 1960b. Arsenopyrite As/S ratio as a possible geobarometer. *Bulletin of Geological Society of America* 71, 1844 (Abstract).

Cullers, R.L., Podkovyrov, V.N., 2002. The source and origin of terrigenous sedimentary rocks in the Mesoproterozoic UI group, southern Russia. *Precambrian Research*, 17, 157-183

Davis, D.W., Hirdes, W., Schaltegger, U., Nunoo, E.A., 1994. U–Pb age constraints on deposition and provenance of Birimian and gold-bearing Tarkwaian sediments in Ghana, West Africa. *Precambrian Research* 67, 89–107.

Davis, W.J., Zaleski, E., 1998, Geochronological investigations of the Woodburn Lake group, western Churchill Province, Northwest Territories: preliminary results: *in* Radiogenic Age and Isotopic Studies, Geological Survey of Canada Report 11, 89-97.

Diamond, L.W., 2003. Introduction to gas-bearing aqueous fluid inclusions. In: Iain Samson, Alan Anderson, Dan Marshall (Eds.), *Fluid inclusions, analysis and interpretation*. Mineralogical Association of Canada Short Course Series, vol. 32. Mineralogical Association of Canada, 374.

Dubé, B., Gosselin, P., 2007. Greenstone-hosted quartz-carbonate vein deposits, in Goodfellow, W.D., edits, *Mineral Deposits of Canada: A Synthesis of Major Deposit-Types*,

District Metallogeny, the Evolution of Geological Provinces, and Exploration Methods. Geological Association of Canada, Mineral Deposits Division, Special Publication 5, 49-73.

Eisenlohr, B. N., Hirdes, W., 1992. The structural development of the early Proterozoic Birimian and Tarkwaian rocks of southwest Ghana, West Africa. *Journal of Earth Sciences* 14, 313-325.

Eisenlohr, B.N., Groves, D.I., Partington, G.A., 1989. Crustal scale shear zones and their significance to Archean gold mineralization in Western Australia. *Mineralium Deposita*, 24, 1-8.

Fan, H-R, Groves, I.G., Mikucki, E.J., McNaughton, N.J., 2000. Contrasting fluid types at the Neveoria gold deposit in the Southern Cross greenstone belt, Western Australia: Implications of Auriferous fluids depositing ores within an Archean band Iron-formation. *Economic Geology*, 95, 1527-1536

Feybesse, J.-L., Billa M., Guerrot C., Duguey E., Lescuyer, J., Milési, J.P., Bouchot., 2006. The Paleoproterozoic Ghanaian province: Geodynamic model and ore controls, including regional stress modeling. *Precambrian Research* 149, 149-196.

Goldstein, R.H., Reynolds, T.J., 1994. Systematics of fluid inclusions in diagenetic minerals. *Society for Sedimentary Geology Short Course* 31, 199.

Groves, D.I., Barley, M.E., Ho, S., 1988. Nature, genesis and tectonic setting of mesothermal gold mineralization in the Yilgarn Block, Western Australia. In: Keays, R.R., Ramsay, W.R.H., Groves, D.I. Edits, *the Geology of Gold Deposits: The Perspective in 1988*. *Economic Geology Monograph* 6, 71-85.

Groves, D.I., Goldfarb, R.J., Gebre-Mariam, M., Hagemann, S.G., and Robert, F., 1998. Orogenic gold deposits: A proposed classification in the context of their crustal distribution and relationship to other gold deposit types. *Ore Geology Reviews*, 13, 7-27.

Hammond, N.Q., Tabata, H., 1997. Characteristics of ore minerals associated with gold at the Prestea mine, Ghana. *Mineralogical Magazine* 61, 879-894.

Junner, N. R. 1932. *Geology of the Obuasi goldfield*. Gold Coast Geological Survey, Memoir 2, 1- 71.

Junner, N.R., 1935. *Gold in the Gold Coast*. Gold Coast Geological Survey Memoir 4, 1-67.

Junner, N.R., 1940. *Geology of the Gold Coast and western Togoland (with revised geological map)*. Gold Coast Geological Survey Bulletin 11, 1-40.

Kesse, G., 1985. *The mineral and rocks resources of Ghana*. A.A. Balkema, Rotterdam, Boston, 609.

Klemd, R., Hirdes, W., 1997. Origin of an unusual fluid compositions for early Proterozoic placer and lode-gold deposits of West Africa. *South Africa Journal of Geology* 100, 405-415.

- Kretschmar, U., Scott, S. D., 1976. Phase relations involving arsenopyrite in the system Fe-As-S and their applications. *Canadian Mineralogist* 14, 364-386.
- LeBas, M.J., LeMaitre, R.W., Streckeisen, A., and Zanettin, B., 1986, A chemical classification of volcanic rocks based on the total alkali-silica diagram: *Journal of Petrology* 27, 745-750.
- Leube, A., Hirdes, W., Mauer, R., Kesse, G.O., 1990. The early Proterozoic Birimian Supergroup of Ghana and some aspects of its associated gold mineralization. *Precambrian Research* 46, 139-165.
- Lorand, J.-P., Alard, O., 2011. Pyrite tracks assimilation of crustal sulfur in Pyrenean peridotites. *Mineralogy and Petrology*, 101, 115-128.
- Lowell, G. R., Gasparini, C., 1982. Composition of Arsenopyrite from the Topaz Greisen veins in southeastern Missouri. *Mineral Deposita* 17, 229-238.
- McCuaig, T.C., Fougereuse, D., Salvi, S., Siebenaller, L., Rarra-Avila, L., Seed, R., Bezait, D., Andre-Mayer, A-S. The Inata Deposit, Belahouro District, northern Burkina Faso. *Ore Geology Reviews* (In Review).
- Milési, J.P., Feybesse, J.L., Pinna, P., Deschamps, Y., Kampunzu, H., Muhongo, S., Lescuyer, J.L., Le Goff, E., Delor, C., Billa, M., Ralay, F., Heinry, C., 2004. Geological map of Africa 1:10,000,000, SIGAfric project. In: 20th Conference of African Geology, BRGM, Orleans, France, 2-7 June, <http://www.sigafrique.net> (last accessed 14/12/2010).
- Milesi, J.-P., Feybesse, J.L., Ledru, P., Dommagnet, A., Ouedraogo, M.F., Marcoux, E., Prost, A., Vinchon, C., Sylvain, J.P., Johan, V., Tegye, M., Clavez, J.Y., Lagny, Ph., 1989. Mineralisations aurifères de l'Afrique de l'ouest, leurs relations avec l'évolution litho-structurale au Paleoproterozoïque inférieur. *Chron. Rech. Min.* 497, 3-98.
- Milési, J.-P., Ledru, P., Feybesse, J.-L., Dommagnet, A., Marcoux, E., 1992. Early Proterozoic ore deposits and tectonics of the Birimian Orogenic belt, West Africa. *Precambrian Research*, 58, 305-344.
- Morey, A.A., Tomkins, A.G., Bierlein, F.P., Wienberg, R.F., Davidson, G.J., 2008. Bimodal distribution of gold in pyrites and arsenopyrites: Examples from the Archean Boorara and Bordoc shear systems, Yilgarn Craton, Western Australia. *Economic Geology*, 103, 599-614.
- Mullis, J., 1987. Fluid inclusion studies during very low-grade metamorphism, *in* Frey M., ed., *Low temperature metamorphism*. Glasgow, Blackie, 162-199.
- Mumin, A.H., Fleet, M.E., 1994. Evolution of gold mineralization in the Ashanti Gold Belt, Ghana. Evidence from carbonate compositions and paragenesis. *Mineralogy and Petrology* 55, 265-280.

- Oberthur, T., Schmidt Mumm, A., Vetter, U., Simon, K., Amanor, J.A., 1996. Gold mineralization in the Ashanti Belt of Ghana. Genetic constraints of the stable isotope geochemistry. *Economic Geology* 91, 289–301.
- Oberthür, T., Vetter, U., Davis, D. W., Amanor, J.A., 1998. Age constraints on gold mineralization and Paleoproterozoic crustal evolution in the Ashanti belt of Southern Ghana. *Precambrian Research* 89, 129–143.
- Oberthür, T., Vetter, U., Schmidt Mumm, A., Weiser, T., Amanor, J.A., Gyapong, W.A., Kumi, R., Blenkinsop, T.G., 1994. The Ashanti Gold Mine at Obuasi, Ghana: mineralogical, geochemical, stable isotope and fluid inclusion studies on the metallogenesis of the deposit. *Geologisches Jahrbuch D* 100, 31–129.
- Perrouy, S., Ailleres, L., Jessell, M.W., Baratoux, L. Bourassa, Y., Crawford, B., 2012. Revised Eburnean geodynamic evolution of the gold-rich southern Ashanti Belt, Ghana, with new field and geophysical evidence of the pre-Tarkwaian deformations. *Precambrian Research* 204–205, 12–39.
- Pobedash, I. D., 1991. Report on the Geology and Minerals of the south-western part of the Wa Field Sheet. Ghana Geological Survey archive. Report 51, 95.
- Robert, F., Kelly, W.S., 1987. Ore forming fluids in the Archean gold bearing quartz veins at the Sigma mines, Abitibi, greenstone belt, Quebec, Canada. *Economic geology*, 82, 1464–1482.
- Roedder, E. 1984. Fluid inclusions. *Mineralogy Reviews* 12, 1–664.
- Roudakov, V. M., 1991. Report on the Geology and Minerals of the north-western part of the Wa Field Sheet. Ghana Geological Survey archive report 50, 95.
- Samokhin, A. A., Lashmanov, V. I., 1991. Geology and Minerals of the northern part of the Bole Field Sheet. Ghana. Ghana Geological survey archive report 53, 118.
- Sharp, D.Z., Essene, E. J., Kelly, W.C. (1985). A re-examination of arsenopyrite geothermometer: pressure considerations and applications to natural assemblages. *Canadian mineralogist* 23, 517–534.
- Shepherd, T.J., Ranbin, A.H., Alderton, D.H.M., 1985. *A Practical Guide to Fluid Inclusion Studies*. Blackie, Glasgow, 239.
- Simon, G., Huang, H., Penner-Hahn, J.E., Kesler, S.E., and Kao, L., 1999. Oxidation state of gold and arsenic in gold-bearing arsenian pyrite. *American Mineralogist*, 84, 1071–1079.
- Sugaki, A., Shima, H., Kitakaze, A., Harada, H., 1975. Isothermal phase relations in the system Cu-Fe-S under hydrothermal conditions at 350°C and 300 °C. *Economic Geology* 70, 806–823.

Sun, S.S., McDonough, W.F., 1989. Chemical and isotopic systematics of oceanic basalts: implication for mantle composition and processes. In: Saunders, A.D., Norry, M.J. (Eds.), *Magmatism in Ocean Basins*, Geological Society of London Special Publication, vol. 42, pp. 313-345.

Sylvester, P.J., Cabri, L.J., Tubrett, M.N., McMahon, G., Laflamme, J.H.G., Peregoedova, A., 2005. Synthesis and evaluation of a fused pyrrhotite standard reference material for platinum group element and gold analysis by laser ablation-ICPMS, in Törmänen, T.O., and Alapieti, T.T., eds., *10th International Platinum Symposium*. Oulu, Geological Survey of Finland, Extended Abstracts, 16–20.

Tshibubudze, A., Hein, K. A. A. 2013. Structural setting of gold deposits in the Oudalan-Gorouol volcano-sedimentary belt east of the Markoye Shear Zone, West African Craton. *Journal of African Earth Sciences*, 80, 31–47.

Van Achterbergh, E., Ryan, C.G., Griffin, W.L., 2001. Data reduction software for LA-ICP-MS. *Mineralogical Association of Canada, Short Course Series 29*, 239–243.

Velásquez, G., Borisova, A.Y., Salvi, S., Béziat, D., 2012. In situ determination of Au and Cu in natural pyrite by near-infrared femtosecond laser ablation-inductively coupled plasma-quadrupole mass spectrometry. No evidence for matrix effects. *Geostandards and Geoanalytical Research* 36, 315–324.

White, A.J.R., Waters, D.J., Robb, L.J., 2015. Exhumation-driven devolatilization as a fluid source for orogenic gold mineralization at the Damang deposit, Ghana. *Economic geology*, 110, 1009-1025.

Yao, Y., Robb, L.J., 2000. Gold mineralization in Palaeoproterozoic granitoids at Obuasi, Ashanti region, Ghana: ore geology, geochemistry and fluid characteristics. *South African Journal of Geology* 103, 255–278.

5.7 The Bepkong gold deposit, northwestern Ghana

The Bepkong gold deposit is located in the Wa–Lawra belt of the Paleoproterozoic Baoulé–Mossi domain of the West African Craton, in NW Ghana. It occurs in pelitic and volcano-sedimentary rocks, metamorphosed to greenschist facies, in genetic association with zones of shear interpreted to form during the regional D_3 deformational event, denominated D_{B1} at the deposit scale. The ore zone forms a corridor-like body composed of multiple quartz \pm carbonate veins surrounded by an alteration envelope, characterized by the presence of chlorite, calcite, sericite, quartz and disseminated pyrite, arsenopyrite plus subordinate pyrrhotite and chalcopyrite. The veins contain only small proportions of pyrite, whereas most of the sulphides, particularly arsenopyrite, occur in the altered host rock, next to the veins. Pyrite is also common outside of the ore zone. Gold is found in arsenopyrite, where it occurs as invisible gold and as visible – albeit micron-size – grains in its rims, and as free gold within fractures cross-cutting this sulphide. More rarely, free gold also occurs in the veins, in fractured quartz. In the ore zone, pyrite forms euhedral crystals surrounding arsenopyrite, but does not contain gold, suggesting that it formed at a late stage, from a gold-free hydrothermal fluid.



ELSEVIER

Contents lists available at ScienceDirect

Ore Geology Reviews

journal homepage: www.elsevier.com/locate/oregeorev

The Bepkong gold deposit, Northwestern Ghana

Prince Ofori Amponsah^{a,b}, Stefano Salvi^{a,*}, Didier Béziat^a, Lenka Baratoux^{a,c}, Luc Siebenaller^{a,d}, Prosper Mackenzie Nude^e, Richard Scriven Nyarko^b, Mark W. Jessell^f

^a Université de Toulouse, CNRS, Géosciences Environnement Toulouse, Institut de Recherche pour le Développement, Observatoire Midi-Pyrénées, 14 Av. Edouard Belin, F-31400 Toulouse, France

^b Azumah Resources Ghana Limited, PMB CT452, Cantonments, Accra, Ghana

^c IFAN Cheikh Anta Diop, Dakar, Senegal

^d ONG-D "Le Soleil dans la Main" asbl, 48, Duerfstrooss, L-9696 Winseler, Luxembourg

^e University of Ghana, Department of Earth Sciences, P.O. Box LG 58, Legon, Accra, Ghana

^f Centre for Exploration Targeting, School of Earth and Environment, The University of Western Australia, 35 Stirling Highway, Crawley, WA 6009, Australia

ARTICLE INFO

Article history:

Received 9 April 2015

Received in revised form 25 June 2015

Accepted 29 June 2015

Available online xxxx

Keywords:

Bepkong deposit

Northwestern Ghana

Gold mineralization

ABSTRACT

The Bepkong gold deposit is located in the Wa–Lawra belt of the Paleoproterozoic Baoulé-Mossi domain of the West African Craton, in NW Ghana. It occurs in pelitic and volcano-sedimentary rocks, metamorphosed to greenschist facies, in genetic association with zones of shear interpreted to form during the regional D₃ deformational event, denominated D_{B1} at the deposit scale. The ore zone forms a corridor-like body composed of multiple quartz ± carbonate veins surrounded by an alteration envelope, characterized by the presence of chlorite, calcite, sericite, quartz and disseminated pyrite, arsenopyrite plus subordinate pyrrhotite and chalcopyrite. The veins contain only small proportions of pyrite, whereas most of the sulphides, particularly arsenopyrite, occur in the altered host rock, next to the veins. Pyrite is also common outside of the ore zone. Gold is found in arsenopyrite, where it occurs as invisible gold and as visible – albeit micron-size – grains in its rims, and as free gold within fractures cross-cutting this sulphide. More rarely, free gold also occurs in the veins, in fractured quartz. In the ore zone, pyrite forms euhedral crystals surrounding arsenopyrite, but does not contain gold, suggesting that it formed at a late stage, from a gold-free hydrothermal fluid.

© 2015 Elsevier B.V. All rights reserved.

1. Introduction and exploration history

In recent years, renewed attention has been paid to the mining potential of the Paleoproterozoic greenstone belts of the West African Craton (WAC). This part of Africa is well known for its world-class mineralization, mostly in the Ashanti Belt of Southern Ghana, which is host to giant gold deposits such as Obuasi, Damang and Wassa. While these deposits have been relatively well studied (e.g., Fougereuse et al., in press; White et al., 2015; Perrouty et al., 2015, and references therein), much less has been published on other regions of the WAC. This and other contributions in this special issue are an effort to fill this gap, by providing comprehensive geological information on a number of poorly known mineralizations, such as those in the northwest of Ghana (e.g., Salvi et al., in this issue).

Reports on gold mining in Northwestern Ghana date back to the early 1960s, when the Gold Coast geological survey reported numerous gold occurrences during their geological field mapping in the area. Further discoveries of gold in bedrock were reported roughly in the same period by a Russian geological team who carried out geological mapping and prospecting in the area, and outlined prospects in the Wa–Lawra

greenstone belt (Griffis et al., 2002). These reports mentioned occurrences of gold related to quartz veins near the Wa Township, and narrow, discontinuous north–south trending quartz veins near the villages of Duri and Lambussie.

The first methodical exploration on the Wa–Lawra belt was undertaken by BHP-Utah Minerals in the early 1990s. They completed a regional bulk leach extractable gold (BLEG) soil survey of the entire Wa–Lawra belt along a 2 km traverse, with a sampling spacing of 200 m. This exercise defined various prospects along the Wa–Lawra belt, including the Kunche, Duri, Basabli, Atikpi and Yagha deposits. In the late 1990s, these prospects were tested by various geochemical approaches (stream sediments, soils, laterite and anthill sampling) at a local scale, and the geology was mapped, by AGEM (a joint venture between Ashanti Goldfields and IAMGOLD of Canada) who held prospecting rights during that period. AGEM refined the various anomalies by undertaking further trenching, rotary air blast (RAB) programmes and minimum reverse circulation (RC) drilling programmes (about 8 holes) and identified the Kunche–Atikpi shear zone, a 40-km long mineralized structure parallel to the main Jirapa fault, in which the Bepkong deposit is situated. Despite intercepting mineralization (eg. for borehole NRC023, AGEM had 2 m at 1.2 g/t from 47 to 49 m and 13 m at 1.33 g/t from 54 m to 66 m), the company farmed out the tenements to Semafo in 1999. The latter did little work,

* Corresponding author.

E-mail address: stefano.salvi@get.obs-mip.fr (S. Salvi).

Table 1
General information on the Bepkong deposit.

Deposit name	Bepkong
Commodity of exploitation	Au
Location	NW Ghana
Longitude–latitude [dec. degrees]	10°25'N–2°45'W
Geographic location	The deposit is situated 50 km NNW of the regional capital (Wa) of the Upper West region in NW, Ghana.
Geological location	West African Craton; Leo-Man shield; Baoulé-Mossi domain; Wa–Lawra belt
Deposit status	Prospect under development (mine development stage)
Deposit type	Sediment hosted; sheared zone hosted, quartz veins
Current owner	Azumah Resources Limited
Average grade	1.84 g/t
Tonnage	1.9 Mt of measured and indicated resource; 113,000 oz proven reserves (September, 2014)
Past production	No production to date

except outlining few low-level geochemical anomalies within the Kunche–Atikpi shear zone. Semafo allowed the tenements in the area to lapse that year.

On the 2nd of March 2005 the tenements were granted to Carlie Mining Cooperation and were immediately transferred to Azumah Resources Limited, on the 5th of March 2005. From 2005 to 2007, Azumah Resources focussed its exploration on target generation, which included various multimedia geochemical sampling (soil, auger, rock sampling and occasionally stream sediments) in the deposit area. These studies defined various low-level gold anomalies. One auger hole returned a value of 1300 ppb and that led to the discovery of the Bepkong deposit. This target was further tested for bedrock mineralization from 2007 to 2012 with air core (AC), reverse circulation (RC) and diamond drilling (DD) methods (Azumah Resources Limited, 2012a). From 2012 to 2014, Azumah Resources Limited has defined both measured and indicated resources of 1.9 Mt proven reserves of 113,000 oz in the Bepkong deposit (Azumah Resources Limited, 2012b). At present, the deposit is at an advanced-exploration to near-mining stage (Table 1).

2. Regional geological overview

The Bepkong gold deposit is located in the Wa–Lawra greenstone belt in Northwestern Ghana, and is part of the Paleoproterozoic Birmanian terranes of the WAC (Fig. 1). This belt is the only N–S trending belt in Ghana (Kesse, 1985; Samokhin and Lashmanov, 1991; Pobedash, 1991; Roudakov, 1991), whereas all other belts trend NE–SW (Griffis

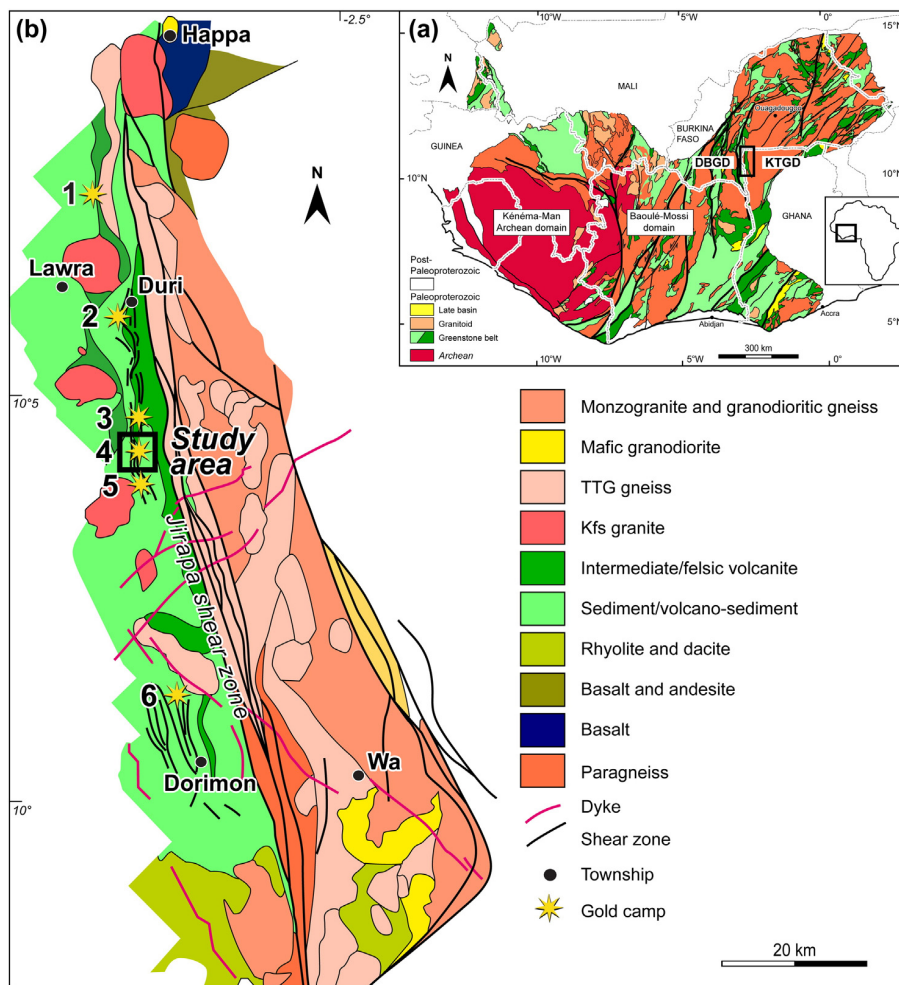


Fig. 1. a) A geological map of the West African Craton (WAC) showing the main lithostratigraphic terrains: the Kenema-Man domain, the Baoulé-Mossi domain, the Koudougou–Tumu granitoid domain (KTGD), and the Dieboukou–Bouna granitoid domain (DBGD). The position of the Wa–Lawra belt (Fig. 1b) is located by the black box. b) Detailed geological map of the Wa–Lawra belt (modified after Block et al., 2015) showing its various gold camps on the Kunche–Atikpi shear zone (see Fig. 2), west of the Jirapa shear zone: 1. Basabli, 2. Duri, 3. Yagha, 4. Bepkong, 5. Kunche and 6. Butele. The study area, located, is shown in detail in Fig. 2.

Please cite this article as: Amponsah, P.O., et al., The Bepkong gold deposit, Northwestern Ghana, Ore Geol. Rev. (2015), <http://dx.doi.org/10.1016/j.oregeorev.2015.06.022>

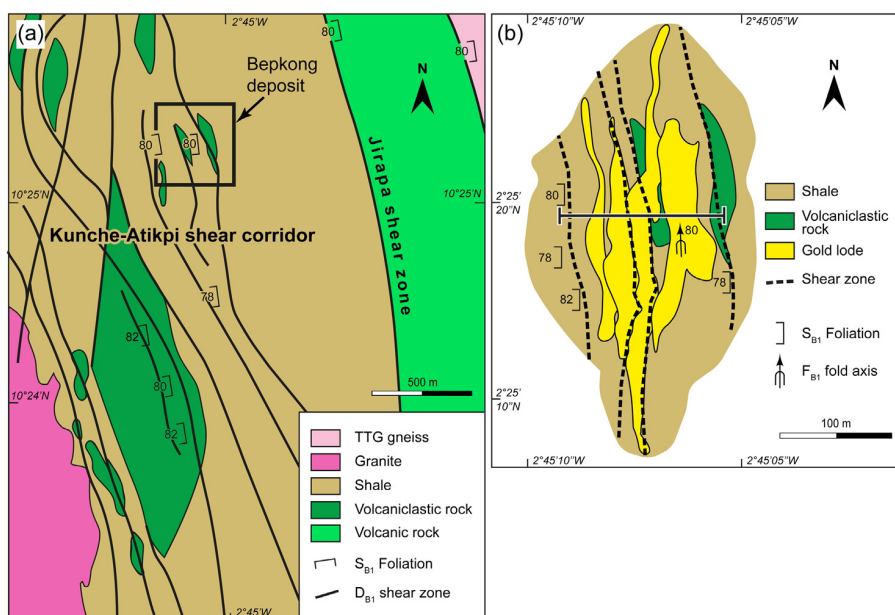


Fig. 2. (a) A simplified geological map of a portion of the Kunche–Atikpi shear zone corridor, west of the main Jirapa shear zone, showing several anastomosing D_{B1} shears. The black inset shows the location of subpanel b. (b) A close-up map of the Bepkong deposit showing the N- to NNW-trending shears that are part of the Kunche–Atikpi structure. The shape of the gold lodes and D_{B1} fabric indicators are also shown. The horizontal line locates the cross-section in Fig. 3.

et al., 2002). The Wa–Lawra belt extends further northwards into Burkina, as part of the Boromo belt (Béziat et al., 2000; Griffis et al., 2002; Baratoux et al., 2011).

The Wa–Lawra belt is bounded to the east by the Koudougou–Tumu granitoid domain and their contact is marked by the Jang fault. To the west of it occurs the Dieboungou–Bouna granitoid domain in Burkina Faso and Ivory Coast (Fig. 1a). The Wa–Lawra belt is divided into eastern and western halves by the crustal-scale Jirapa shear zone (Fig. 1b), a large structure that exhibits sinistral characteristic (Block et al., 2015) and also extends into Burkina Faso. The western half of the belt consists mostly of shale, volcaniclastic and volcano-sedimentary rocks, basalt and granitoids; the eastern half consists mostly of granite, paragneiss and orthogneiss, rhyolite and granitoids. According to Feybesse et al. (2006),

the Birimian units in Ghana were formed between 2250 and 1980 Ma. Based on a review of published ages, Baratoux et al. (2011) propose the emplacement of the volcanic and pyroclastic flows in the belt at about 2200 Ma to 2160 Ma. Detrital zircon dating of the volcano-sediments in the Wa–Lawra belt gave ages older than 2139 Ma and emplacement of the syn-tectonic and late granitoid intrusions in the belt was dated at ~2153 and 2104 Ma, respectively (Agyei Duodu et al., 2009).

Block et al. (2015) proposed a polyphase deformational history for Northwestern Ghana, which includes the Wa–Lawra belt. In this scenario, three main phases of deformation were identified, which are: i) a D_1 episode, which is expressed mostly by a penetrative foliation (S_1) bearing high-grade metamorphic assemblages that affected the Birimian volcano-sedimentary and sedimentary units. This deformation

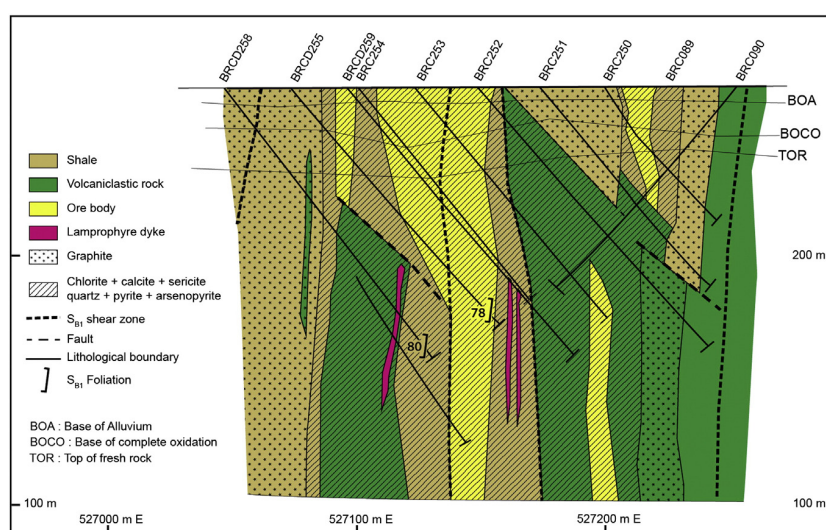


Fig. 3. A cross-section (looking north) of the Bepkong deposit along 1,152,175 N, showing mineralized shoots within the main ore body, along subvertical D_{B1} shear zones (cf. Fig. 2 for location). High-grade mineralization is confined to a 100 m- to 150 m-thick alteration zone defined by an assemblage consisting of chlorite + calcite + sericite + quartz + sulphides. Graphitic layers within the shale and the volcaniclastic rocks limit the mineralized hydrothermal conduits.

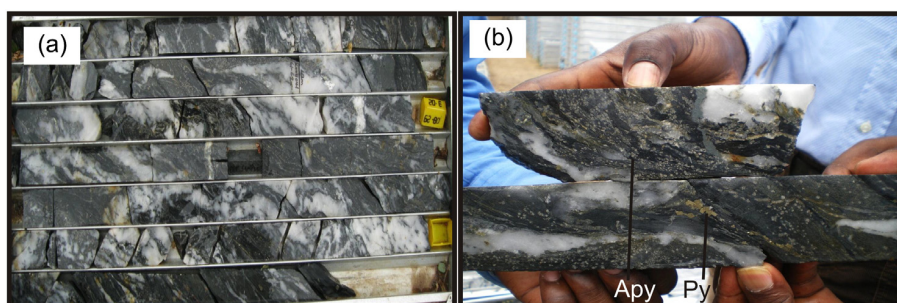


Fig. 4. Photographs of drill core from a mineralized zone in the Bepkong deposit showing (a) a typical syn-tectonic set of veins, and (b) disseminated pyrite (Py) and arsenopyrite (Apy) in the rock adjacent to the veins.

phase is related to N–S crustal shortening and was not registered by the volcanic and volcano-sedimentary rocks at the Bepkong deposit. ii) The second deformation phase (D_2) is responsible for the exhumation of high-grade units and is characterized by N–S stretching. Localized shallow-dipping shear zones with down-dipping lineation were found at the contacts of units with contrasting metamorphic grade. This deformation phase was not found in the Bepkong deposit either. iii) A D_3 deformational phase, consisting of anastomosing, NE- to NNW-trending steeply dipping transcurrent shear zones (S_3). The early stages of this event are marked by a vertical-dipping penetrative foliation parallel to primary bedding, while discrete shear zones developed during later stages. This illustrates a transition from ductile to brittle behaviour corresponding to amphibolite to upper-greenschist metamorphic facies during early D_3 , and to greenschist facies during the late stages. The D_3 of Block et al. (2015) is consistent with an E–W to NE–SW shortening and corresponds to the D_1 and D_2 events in Southwestern Burkina Faso (Baratoux et al., 2011). The S_3 shear zones exhibit dextral or sinistral characteristics, depending on their orientation. This deformation event is predominant in the Bepkong area, and we denominate it D_{B1} at the deposit scale.

Close to the Jirapa shear zone and to the west of it, where the Bepkong deposit is located, the D_{B1} schistosity is very intense, forming the anastomosing Kunche–Atikpi shear zone corridor (Fig. 2a), which exhibits steep dips to the west and trends from NNW to N. The deposit is crossed by several structures that are part of this shear system (Fig. 2b). E–W tension gashes crosscutting these S_{B1} shear zones were found in the deposit area and are best observed in drill core. They are preserved either as quartz veins or are filled with chlorite, white mica, and epidote. These late faults are brittle, have a normal displacement, have subvertical dips and a limited extension. They can be ascribed either to the late stages of the D_{B1} deformation event or to a D_{B2} event, still under an E–W shortening tectonic regime.

The volcanic suites and the sediments in the Wa–Lawra belt, west of the Jirapa fault, registered greenschist facies metamorphism, while

paragneiss and orthogneiss to the east of it were formed at amphibolite facies conditions. Diagnostic greenschist facies metamorphic assemblages observed include chlorite–calcite–epidote plus sericite, actinolite and albite while amphibolite facies minerals are garnet, clinopyroxene, staurolite and hornblende (Block et al., 2015).

3. Ore body characteristics

3.1. Host rocks

The rocks hosting the gold mineralization in the Bepkong deposit are strongly sheared metamorphosed shales and volcanoclastic units. These are locally interlayered, include graphitic interbeds and are crosscut by lamprophyre dykes. Mineralization is not visible on the outcrop, as the area is entirely covered with allochthonous alluvium and colluvium, plus at least 10 m of laterite, which overlies a saprolite horizon that extends to about 40 m depths.

3.2. Mineralization

Gold mineralization is restricted to a zone of dilation within anastomosing D_{B1} shear zones (Fig. 2a). The mineralized zone forms a body up to 300 m wide for a strike length of 560 m that extends across variably strained units of the volcanoclastic rocks and shales. So far, four parallel, mineralized shoots of lenticular shape and variable thickness (up to 20 m) have been defined (Fig. 2b). They trend N–S and plunge steeply to the south with mineralization still open at depth. Mineralization could be modelled to a depth of 200 m, and occurs in the form of a tight network of quartz veins, generally between 30 cm and 1 m in thickness, with steep dips (70° W to subvertical). A geological section showing key geological features of the ore body is presented in Fig. 3. The veins are strongly deformed, and commonly form a quartz breccia or are boudinaged (Fig. 4a), but do not have vugs, indicating brittle–ductile transitional conditions. Quartz in the veins is milky, and is accompanied by

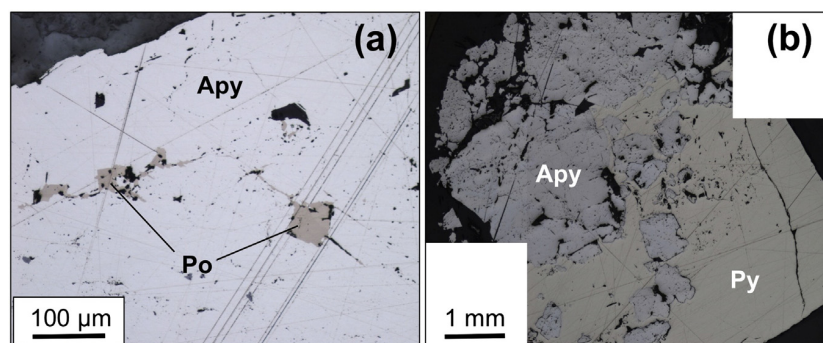


Fig. 5. Photomicrographs of thin sections under reflected light, showing sulphide textures. (a) Arsenopyrite (Apy) with inclusion of pyrrhotite (Po). (b) Collage of two fields of view showing broken-up arsenopyrite overgrown by euhedral pyrite (Py).

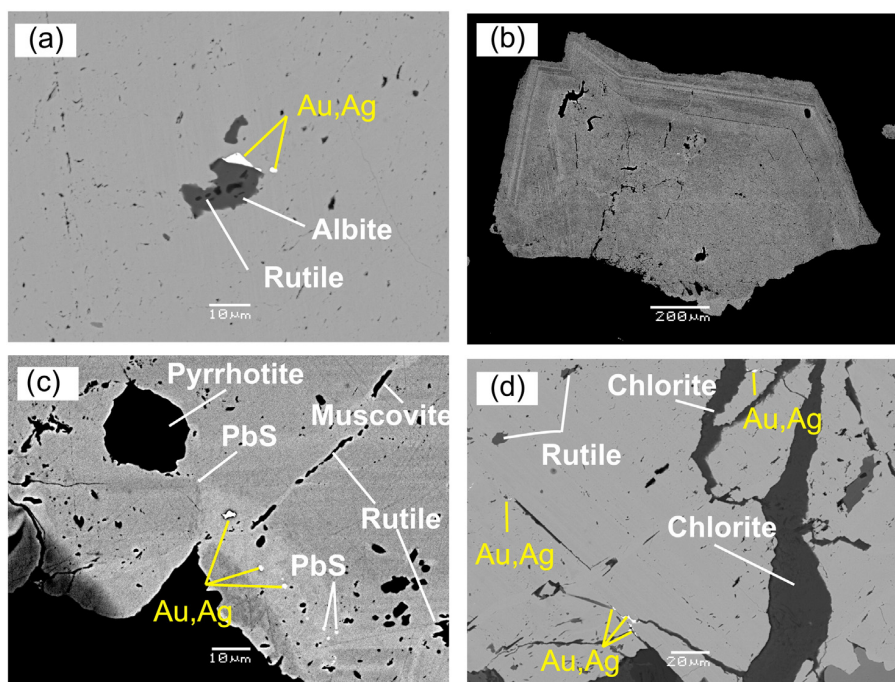


Fig. 6. BSE SEM images of arsenopyrite from the ore zone. (a) Micron-size inclusions of gold with albite and rutile. (b) Subhedral arsenopyrite exhibiting rhythmic growth zones. The bright BSE bands are defined by an abundance of Ni and Co. (c) Micron-size gold grains within the rim of an arsenopyrite grain. Other mineral inclusions include pyrrhotite, rutile and muscovite. (d) An arsenopyrite grain showing gold grains within fractures. Secondary chlorite fills the fractures in this field of view.

calcite (5%), chlorite (3%) and sericite (1%). Pyrite, and rarely arsenopyrite, occur as disseminated, relatively large crystals in the veins, but in relatively low proportions (less than about 4% by volume). Both sulphides are present in much higher amounts next to the veins, in the altered selvages (Fig. 4b). Gold grades (drill hole assays) in the deposit reach about 5 g/t with an average of 1.8 g/t, but the veins themselves are much lower grade, mostly between 0.1 and 0.3 g/t.

3.3. Alteration

Pervasive alteration affects all sediments hosting the mineralized lodes in the Bepkong deposit. It is readily recognisable macroscopically by the presence of widespread pyrite and arsenopyrite, which, as mentioned, occur disseminated in the vein corridors, mostly in the wall rock haloes around the veins. Other alteration minerals include calcite, chlorite, quartz and sericite. This alteration fades away rapidly perpendicularly across the ore zone, into the barren country rocks, where the rocks are basically unaltered and contain only minor or no carbonates. The alteration has a width that drifts around 100 m, with the largest parts reaching 300 m, and appears to be confined by the less permeable graphitic beds in the host rock.

3.4. Microscopic features of the ore

In the Bepkong area pyrite is ubiquitous, whereas arsenopyrite is restricted to the altered rocks, only to within a close range to the veins

Table 2
LA-ICP-MS analyses of sulphides in the ore zone. Values are averages of *n* analyses.

	<i>n</i>	Co	Ni	Se	Ag	Sb	Te	Au	Pb	Bi
LOD		0.2	0.6	1.4	0.01	0.1	0.12	0.01	0.1	0.1
Py	5	0.6	25	39	0.06	0.5	0.19	0.16	2.4	0.4
Apy core	4	122.2	661	415	0.79	335.5	69.87	1.04	38.1	13.1
Apy rim	5	3.4	21	1537	15.19	950.5	447.91	1.02	2918.3	108.1

All values are in ppm.

Abbreviations: LOD = limit of detection, Py = pyrite and Apy = arsenopyrite.

(generally less than 30 cm). Both sulphides vary in size from <1 mm to about 40 mm. Pyrrhotite and, less commonly, chalcocopyrite, are found as small inclusions within the arsenopyrite (Fig. 5a). In the ore zone, subhedral to euhedral pyrite can be observed to overgrow and locally replace arsenopyrite. In many cases, the latter forms fragmented residual crystals, suggesting that pyrite replacement took place after an episode of brittle deformation (Fig. 5b).

Grains of native gold were found by SEM observations, mostly in porous areas in the outer edges of arsenopyrite in the form of particles of a few microns in size. Small amounts of silver were usually detected within these gold grains by EDS-SEM, and small grains of galena, rutile, chlorite, muscovite and quartz could be identified within small distances (Fig. 6). Free gold also occurs within fractures in arsenopyrite (Fig. 6d) and, less commonly, in fractured quartz crystals within the veins themselves. In pyrite, however, gold was not detected by SEM observation.

Representative LA-ICP-MS analyses were performed on pyrite and arsenopyrite (Table 2; see Amponsah et al., in press, for analytical parameters). These data reveal the presence of variable amounts of Ni and Co in the arsenopyrite, defining growth zones that are detectable by BSE-SEM imaging (Fig. 6b). The data indicate that they are enriched in crystal cores (up to 660 ppm Ni was measured). The presence of such high amounts of these elements is consistent with formation of arsenopyrite in the host rock rather than in the veins, which is likely enriched in these metals. Important quantities of Pb, Te, Sb and Se were also detected by LA-ICP-MS analyses in arsenopyrite, particularly in the rims where they average at 3000, 450, 950 and 1500 ppm, respectively. Silver and Bi concentrations are also higher in arsenopyrite rims, at 15 and 110 ppm, respectively. “Invisible” gold (cf., Cook and Chryssoulis, 1990) was detected in cores and rims of arsenopyrite, where it ranges from 0.2 to 6 ppm (with an average of about 1 ppm); no difference in contents was detected between cores and rims. Only ppb amounts of Au and Ag were measured in pyrite, along with minor amounts of the other metals (Table 2). In pyrite within the veins gold was below detection limits.

4. Timing of mineralization

The D_{B1} deformation is the main structural event that affected the Wa–Lawra belt. Field relationships such as the parallelism of the vein shoots with the shear zone (Fig. 3) and the occurrence of gold in the altered rocks around the deformed quartz veins clearly indicate that the anastomosing S_{B1} shear structures controlled gold mineralization at Bepkong, by providing a pathway for fluid flow. The maximum age for the deposition of the volcano-sedimentary units of the Wa–Lawra belt is 2139 ± 2 Ma (U–Pb zircon ages; Agyei Duodu et al., 2009). The D_{B1} deformation event took place relatively late in the Eburnean tectonic history in Northern Ghana and corresponds to the later stages of deformation defined by Block et al. (2015) at a regional scale. The onset of the D_{B1} (i.e., regional D_3) took place after 2130 Ma, which is defined by a U–Pb age constraint on D_2 , from metamorphic monazite (Block et al., 2015). The D_3 dextral shear zones in Western Ghana may be as young as 2088 ± 1 Ma (Hirdes et al., 1992; Jessell et al., 2012).

The fact that the veins were folded, boudinaged and brecciated, indicates a probable early formation during the shearing episode and that they were reworked during a relatively long-lived deformational regime. The presence of gold in an invisible form in the core and rims and as discrete grains within arsenopyrite, as well as its occurrence in fractures through this sulphide, indicates an early onset of the mineralization and that this probably continued through the evolving deformation conditions. Nevertheless, the hydrothermal system became barren before the onset of pyrite precipitation, as indicated by the absence of gold in pyrite. The latter sulphide probably did not precipitate until the waning stages of deformation, as suggested by the euhedral shapes of the crystals enclosing fractured arsenopyrite.

The presence of relatively permeable volcanoclastic rocks, locally intercalated with more impermeable graphitic horizons, favoured the formation of a contained hydrothermal corridor within the S_{B1} shear zone. The association of native gold with secondary minerals such as chlorite, sericites and calcite are consistent with the occurrence of the mineralization under greenschist facies metamorphic conditions, which dominated during the late stages of D_{B1} deformation.

Acknowledgements

We would like to thank the Azumah geologists for the interesting discussion about the geology of the deposit. We gratefully acknowledge AMIRA International (P934A) and the industry sponsors, including AusAid and the ARC Linkage Project LP110100667, for their support through the WAXI project. POA would like to extend his gratitude to Nick Franey and Stephen Stone for their continual support throughout the programme. Constructive remarks from G. Vélásquez and Y. Bourassa helped improve the quality of this ms.

References

- Agyei Duodu, J., Loh, G.K., Boamah, K.O., Baba, M., Hirdes, W., Toloczky, M., Davis, D.W., 2009. Geological map of Ghana 1:1 000 000. Geological Survey Department of Ghana (GSD).
- Amponsah, P.O., Salvi, S., Béziat, D., Jessell, M.W., Siebenaller, L., Baratoux, L., 2015. Geology and geochemistry of the shear-hosted Julie deposit, NW Ghana. *J. Afr. Earth Sci.* <http://dx.doi.org/10.1016/j.jafrearsci.2015.06.013> (in press).
- Azumah Resource Limited, 2012a. Kunche-Bepkong region status report. Unpublished internal report.
- Azumah Resources Limited, 2012b. Feasibility study, Wa-Gold project. Unpublished internal report.
- Baratoux, L., Metelka, V., Naba, S., Jessell, M.W., Grégoire, M., Ganne, J., 2011. Juvenile Paleoproterozoic crust evolution during the Eburnean orogeny (2.2–2.0 Ga), Western Burkina Faso. *Precambrian Res.* 191, 18–45.
- Béziat, D., Bourges, F., Debat, P., Lompo, M., Martin, F., Tollon, F., 2000. A Palaeoproterozoic ultramafic–mafic assemblage and associated volcanic rocks of the Boromo greenstone belt: fractionates originating from island-arc volcanic activity in the West African craton. *Precambrian Res.* 101, 25–47.
- Block, S., Ganne, J., Baratoux, L., Zeh, L., Parra-Avila, A., Jessell, M., Aillères, L., Siebenaller, L., 2015. Petrological and geochronological constraints on lower crust exhumation during Paleoproterozoic (Eburnean) orogeny, NW Ghana, West African Craton. *J. Metamorph. Geol.* 33, 463–494.
- Cook, N.J., Chryssoulis, L., 1990. Concentrations of “invisible gold” in the common sulfides. *Can. Mineral.* 28, 1–16.
- Feybesse, J.-L., Billa, M., Guerrot, C., Duguey, E., Lescuyer, J., Milési, J.-P., Bouchot, V., 2006. The Paleoproterozoic Ghanaian province: geodynamic model and ore controls, including regional stress modeling. *Precambrian Res.* 149, 149–196.
- Fougerouse, D., Micklethwaite, S., Ulrich, S., Miller, J., McCuaig, T.C., Godel, B., Adams, D., 2015. Evidence for two stages of mineralization in West Africa’s largest gold deposit: Obuasi, Ghana. *Econ. Geol.* (in press).
- Griffis, R.J., Barning, K., Agezo, F.L., Akosah, F.K., 2002. Gold Deposits of Ghana. Minerals Commission, Accra, Ghana, p. 438.
- Hirdes, W., Davis, D.W., Eisenlohr, B.N., 1992. Reassessment of Proterozoic granitoid ages in Ghana on the basis of U/Pb zircon and monazite dating. *Precambrian Res.* 56, 89–96.
- Jessell, M.W., Amponsah, P.O., Baratoux, L., Asiedu, D.K., Loh, G.K., Ganne, J., 2012. Crustal-scale transcurent shearing in the Paleoproterozoic Sefwi-Sunyani-Comoe region, West Africa. *Precambrian Res.* 212–213, 155–168.
- Kesse, G., 1985. *The Mineral and Rocks Resources of Ghana*. A.A. Balkema, Rotterdam, Boston, p. 609.
- Perrouy, S., Jessell, M.W., Miller, J., Bourassa, Y., Apau, D., Siebenaller, L., Baratoux, L., Velásquez, G., Aillères, L., Béziat, D., Salvi, S., 2015. The tectonic context of the Eoeburnean Wassa gold mine – implications for relative timing of mineralising events in southwest Ghana. *J. Afr. Earth Sci.* <http://dx.doi.org/10.1016/j.jafrearsci.2015.03.003>.
- Pobedash, I.D., 1991. Report on the geology and minerals of the south-western part of the Wa field sheet. Ghana Geological Survey Archive, Report 51, p. 95.
- Roudakov, V.M., 1991. Report on the geology and minerals of the north-western part of the Wa field sheet. Ghana Geological Survey Archive, Report 50, p. 95.
- Salvi, S., Amponsah, P.O., Siebenaller, L., Béziat, D., Baratoux, L., Jessell, M., 2015. The Julie Gold Deposit, An Appealing Resource in Northwestern Ghana (in this issue).
- Samokhin, A.A., Lashmanov, V.I., 1991. Geology and minerals of the northern part of the Bole Field Sheet, Ghana. Ghana Geological Survey Archive, Report 53, p. 118.
- White, A.J.R., Waters, D.J., Robb, L.J., 2015. Exhumation-driven devolatilization as a fluid source for orogenic gold mineralization at the Damang deposit, Ghana. *Econ. Geol.* 110, 1009–1025.

Chapter 6

Discussion and Conclusion

6.1 Discussion

Genetic models for gold mineralization have a great influence on exploration strategies. To create models for the three deposit studied it is important to define the major characteristics associated with these deposit. This will serve as the premise for the conceptualization or development of the genetic models.

6.1.1 Host Rocks

The rocks hosting the gold mineralization in the Julie deposit are granitoids and the Kunche and Bepkong deposit sedimentary rocks. The sedimentary sequence hosting the Kunche deposit is a monotonous volcanoclastic package, whereas in the Bepkong deposit graphitic shales alternate with the volcanoclastic sediments. The sediments in both Kunche and Bepkong deposit have been intruded by microdiorites.

The granitoids hosting gold mineralization in the Julie deposit are associated with TTG's, are calcic to alkali rich and metaluminous. The geochemical characteristic of these granitoids is typical of magmatic rocks found in active margins. The geochemical signatures of the magmatic activity falls within the volcanic arc granite field (Amponsah, et al., 2015).

The shales hosting the gold mineralization in the Bepkong deposit have an acidic to intermediate provenance and from La-Th-Sc diagram (Fig. 5.4c), the shales were derived from a granodiorite source. The volcanosediments in the Bepkong deposit are derived from acidic to intermediate rocks. The volcanoclastic sediments in the Kunche deposit also have intermediate and calc alkaline sources. The microdiorites that intrude the sediments in both deposit have the same signature. The rock have a low Mg number and are highly evolved and are thought to have formed in an arc related setting.

6.1.2 Structures

Gold mineralization in three deposits studied in the Wa-Lawra region have a spatial relationship with shear zones and greenschist metamorphism, the structural control on gold mineralization can be discussed in relation to the regional deformation events described in Block (2015) and Baratoux et al. (2011) which has been summarized in Table 6.1.

Table 6.1. Table summarizing the regional structural events by Block (2015), Baratoux et al. (2011) compared with that of the Julie, Bepkong and Kunche deposits in NW Ghana.

Study	D ₁	D ₂	D ₃	D ₄	D ₅	D ₆
Block (2015) NW Ghana	D ₁ = N-S directed shortening. E-W penetrative fabric (S ₁) with shallow to steep dips. Low angle thrust faulting and folding	D ₂ = N-S directed shortening. S ₂ foliation with moderate dips with plunging lineation down dip	D ₃ =E-W directed shortening and S ₃ schistose foliation	D ₄ =ENE to WSW shortening with sinistral strike slip shearing	D ₅ = E-W brittle deformation	D ₆ =E-W brittle deformation, tension and brittle strike and slip faults
Baratoux et al. (2011) Boromo belt			D ₁ = N-NNE oriented S1 foliation. F1 fold with axial plane parallel to S1	D ₂ consist of steeply dipping NNE to ENE anastomosing shear zone with dextral characteristics		D ₃ consist of crenulation cleavages, chevron kink folds, E-W space cleavages, and the late brittle strike slip faults
Amponsah et al. (2015) Julie deposit	D ₁₁ = E-W penetrative metamorphic foliation (S ₁₁) with dips ranging from 35° to 70° to the north. E-W shear zone related to low angle thrust fault. Pre to syn deformational quartz vein. Au is present in the quartz vein					D ₁₃ is manifested by late brittle NE trending faults which displace the E-W shear zones

Amponsah et al. (2015) Bepkong deposit	<p>D_{B1}= N to NNW steeply dipping sinistral shear zone which denotes ENE-WSW shortening. FB1 fold with axial plane parallel to the shear zone SB1 foliation. Syn-tectonic quartz vein. Gold is present</p>	<p>D_{B3} = FB3 isoclinal folds and crenulation cleavages overprinting SB1. E-W spaced cleavages and late NE-NW brittle fault</p> <p>D_{B2} =E-W trending tension gashes. E-W shortening direction</p>
Kunche deposit	<p>D_{K1}=N to NNW steeply dipping sinistral anastomosing shear zone and denotes ENE-SWS shortening. FK1 fold with axial plane parallel to the shear zone SK1 foliation. Syn-tectonic quartz vein. Gold is present</p>	<p>D_{K3}= F_{K3} isoclinal folds and crenulation cleavages overprinting S_{K1}. E-W space cleavages and late NE-NW brittle fault.</p> <p>D_{K2}= E-W trending tension gashes. This indicates E-W shortening</p>

The ages of the deformations in NW Ghana (Fig. 6.1) were constrained by Block et al., (2015), using the U-Pb dating methods on zircons and monazites, generally lacking chemical zonation and oriented in the direction of the dominant structural grain associated with a particular deformation event. From the regional structural analysis done by Block (2015) D_{J1} correlates to the regional D_1 which occurred between 2145 to 2125 Ma (Fig. 6.1). D_{J2} also correlates to the regional D_1 described by Block (2015). D_{J3} correlates with the regional D_6 by Block (2015) and regional D_3 of Baratoux et al. (2011). The initial deformation event in the Kunche and Bepkong deposit (D_{B1} and D_{K1}) corresponds to the regional D_4 described by Block (2015) and D_1 and D_2 by Baratoux et al. (2011).

From the structural analysis done for the three deposits studied, the structural architecture of the Julie deposit is different from that of the Bepkong and Kunche deposit. The only similarity is that, the three deposit have experienced three stages of deformation, but even with that, there is a difference when it comes to the age constraint of the deformational events. The first and second stage of deformation (D_{J1} and D_{J2}) in the Julie deposit preceded (2145 – 2130 Ma) or are older than the first two deformational stages in the Kunche and Bepkong deposits (2110-2105 Ma). The early structure (D_{J1}) in the Julie deposit is controlled by N-S shortening and defined an E-W penetrative metamorphic foliation (S_1), which is often parallel to primary bedding (S_0) in the volcano-sediments north of the Julie deposit and with intermediate dips (30 to 50°). A corridor consisting of swarm of several pre- to syn-deformational boudinage milky quartz vein are oriented E-W occurring mainly within the shear zones.

The kinematics that controlled the early structure in the Kunche and Bepkong deposit is an ENE-WNW directed shortening. This created a N to NNW anastomosing shear zone with vertical dips (70-80°). These anastomosing shear zone systems visible at the deposit scale and have created dilatational zones which have permitted fluid movement within the sediments. This is evidenced by the syn-tectonic boudinaged type-1 quartz veins observed parallel to the foliation. Gold mineralization in the Julie deposit is associated with quartz veins controlled by the E-W shear zone associated with the D_{J1} event.

From the space-time correlation between deformation and gold mineralization, gold in the Julie deposit can be constrained to have occurred from 2145 to 2125 Ma. Gold in the Kunche and Bepkong deposits were controlled by the initial stage anastomosing shear zones. The shear zone created dilatational zones which permitted the fluid flow and hence the site favourable for gold mineralization in the Wa-Lawra belt. From the space time correlation for the timing of deformation event (Fig. 6.1), gold mineralization in the Kunche and Bepkong deposit occurred between 2110-2105 Ma.

From the characteristics described above, although gold is associated with the first structural event in the deposits studied, the gold in Julie occurred much earlier than that of Kunche and Bepkong. Kunche and Bepkong are governed by the same structures. Architecture wise the prevailing structures in the Julie deposit is different from that of Kunche and Bepkong. The dominant structural grain in the Julie deposit is oriented in the E-W direction with intermediate dips whilst that of the Kunche and Bepkong deposit is N-NNW with vertical dips.

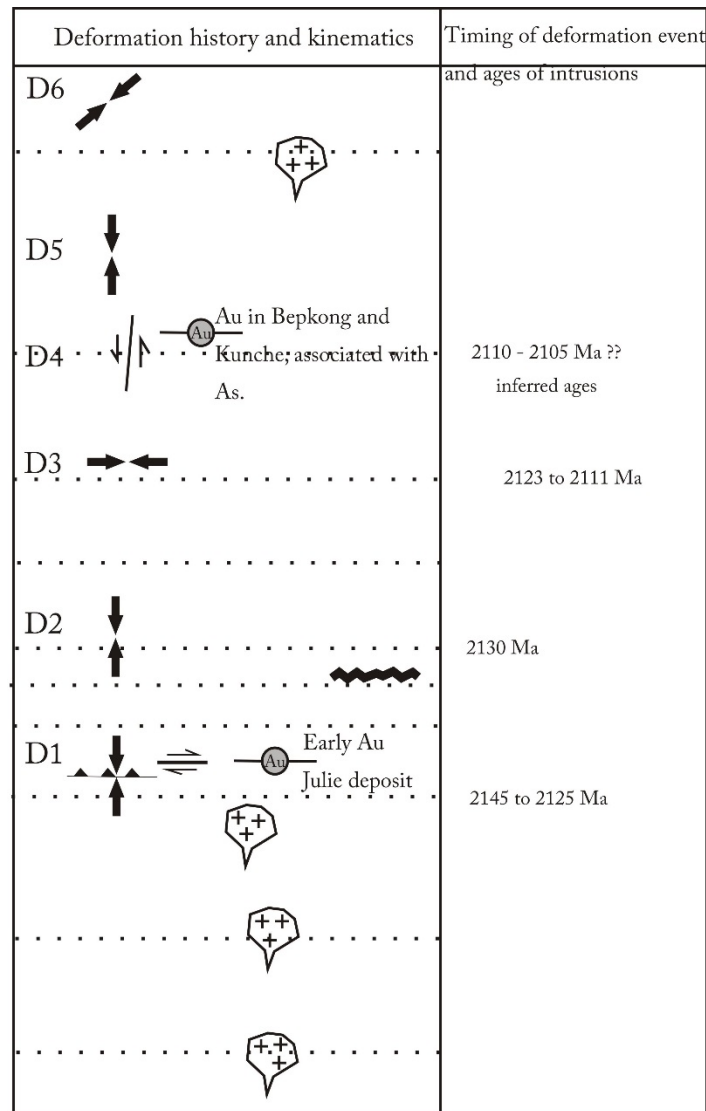


Fig. 6.1. Image showing the time and space correlation of events in NW Ghana. These events were obtained from the geochronological studies done by [Block et al. \(2015\)](#) in NW Ghana.

6.1.3 Mineralization style and alteration

The mineralization style in the Julie deposit have been described by [Amponsah, et al. \(2015\)](#) as a sheared hosted quartz lode with disseminated sulphides. The ore body in Julie consist of two plunging auriferous corridor made up of quartz veins that extend 3.5 km with a thickness of 20 to 50 m. The mineralized corridor in the Julie deposit is characterized by strong alteration. The alteration assemblage in the mineralized zone is composed of sericite + quartz + ankerite + calcite + tourmaline + pyrite. This alteration assemblage forms an envelope around the mineralized quartz veins and the immediate wall rock host. Gold grades associated with this alteration assemblage is 3.0 g/t. A second alteration assemblage laterally away from the mineralized zone was observed and consists of mineral assemblage of albite + sericite + calcite + pyrite and rutile. Gold mineralization associated with the second alteration assemblage is 3.0 g/t.

The ore body in Kunche is composed of a N to NNW oriented 1.1 km long and a 20 to 40 m thick of a single lode. The lode is characterized by grey quartz veins with disseminated sulphides. The alteration mineral assemblage governing the mineralized zone is composed of calcite + chlorite + sericites + quartz + sulphides. As one moves from the mineralized zone to the unmineralized zone, the alteration quickly fades away.

The ore bodies in Bepkong consist of four N-S trending quartz lodes with a strike length of 560 m. The alteration mineral assemblage governing the mineralized zone is chlorite + calcite + ankerite + quartz + sericite + sulphides (arsenopyrite, pyrrhotite, and chalcopyrite). This alteration zone is bounded by a graphitic alteration zone. Calcite and pyrite is ubiquitous within the Bepkong deposit.

From the description of the ore geometry and alteration assemblages the Julie deposit is very different from the Kunche and Bepkong deposit. The alteration assemblage governing the mineralized zone in both Kunche and Bepkong are similar.

6.1.4 Fluid inclusions

Fluid inclusions analysis was only performed for the Julie and Bepkong deposits. Samples of sufficient quality for fluid inclusion analysis were not found in the Kunche deposit.

The fluid inclusion types that exist in the Julie deposit is the two phase aqueous carbonic inclusion in a $\text{CO}_2\text{-H}_2\text{O-NaCl}$ system, with low to moderate salinities ranging from 1.9 to 8.6 wt.% eq. NaCl. Densities of the fluid ranges from 0.41 to 0.99 gcm^{-3} . Fluid inclusion data for Julie suggest that the temperature for ore forming were trapped around 220°C and a pressure of <1 kbar. The data collected and the occurrences of the FIA described, suggest the presence of a $\text{H}_2\text{O-CO}_2\text{-NaCl}$ fluid that entered the immiscible region for this system.

Two types of fluid inclusion dominated in the Bepkong deposit. These are the least abundant $\text{CH}_4\text{-H}_2\text{O}$ and the abundant $\text{CH}_4\text{-CO}_2\text{-H}_2\text{O-SO}_2$ fluid inclusion. Mineralized fluids in the Bepkong deposit were trapped around 320°C with salinities ranging from 2.27 to 3.24 wt.% eq. NaCl. Both fluid mixing and immiscibility produced the fluid population observed within the Bepkong deposit.

The sources of the fluid for both deposit studied were different. The fluid that dominated in the Julie deposit was CO_2 , which reach immiscibility at 220 °C whilst the initial fluid in Bepkong was dominated with CH_4 , which attain immiscibility with H_2O and CO_2 . This means the systems which for precipitated the gold in the deposits are very different and have no relationship to each other.

6.1.5 Sulphide characterization

Pyrite is the principal ore mineral in the mineralized quartz veins and altered granitoids. From SEM imagery, gold in the Julie deposit occurs as micron-sized gold inclusion and as larger gold grains within the fractures or edges of the pyrite minerals. LA-ICP-MS analysis

shows the presence of trace elements such as Ag, Fe, Pb, Se, Ni and Co. Au in Julie correlated well with Te, Pb and Bi.

The principal ore minerals in the Bepkong deposit is composed of arsenopyrite, chalcopyrite and pyrrhotite. Gold is only associated with the arsenopyrite. From SEM imagery and LA-CP-MS gold in Bepkong occur as (1) invisible gold within the arsenopyrite crystal lattice and (2) visible gold within the fractures of the arsenopyrite or the oscillatory growth zones. Trace metals such as Co, Ni, Cu, Zn, As, Pb and Ag were observed within the arsenopyrite. Ag correlated well with gold.

The principal ore mineral in the Kunche deposit are arsenopyrite, pyrrhotite, chalcopyrite and galena. The sulphide minerals occur as disseminations within the quartz vein and country rock. Gold in the Kunche deposit occur as invisible gold which occur as solid solution or nanoparticles within the crystal lattice or as visible gold within the fractures in the arsenopyrites. LA-ICP-MS shows trace amount of metal such as As, Ag, Pb, Co, Cu and Ni.

Arsenopyrite in both the Kunche and Bepkong deposits exhibits oscillatory zoning, with alteration rim, which gives an indication that the arsenopyrite were formed during the hydrothermal alteration.

From the trace elements studied in both deposits, gold in the Julie occur as a bismuth-telluride (Ag-Bi-Te). Although hydrothermal alteration, is the most dominant process for which gold precipitated, the presence of Bi and Te, shows some magmatic associations. Also gold in the Kunche and Bepkong deposit do occur mainly Au-Ag.

6.2 Genetic Model

6.2.1 The Kunche and Bepkong deposits

The similarities in character in the Kunche and Bepkong deposit have made it possible to conceptualize a genetic model for gold mineralization in the Wa-Lawra belt. Also the lithology plays an important role in the gold formation process. A two stage process has been proposed for gold mineralization in the Wa-Lawra belt (specifically the Kunche and Bepkong deposit).

Stage 1

The early stage represent the initiation of the anastomosing shear zone (D_{B1} -Bepkong, D_{K1} -Kunche) formation. The anastomosing shear zone was formed as a result of strain partitioning owing to the presence of lithologies with variable strength (thus different rock responds differently to the same stress rate). The graphitic shales deformed in a ductile fashion (Fig. 6.2a), whilst the volcanoclastic rock responded by deforming in a brittle manner, by causing the rock to brecciate (Fig. 6.2b).

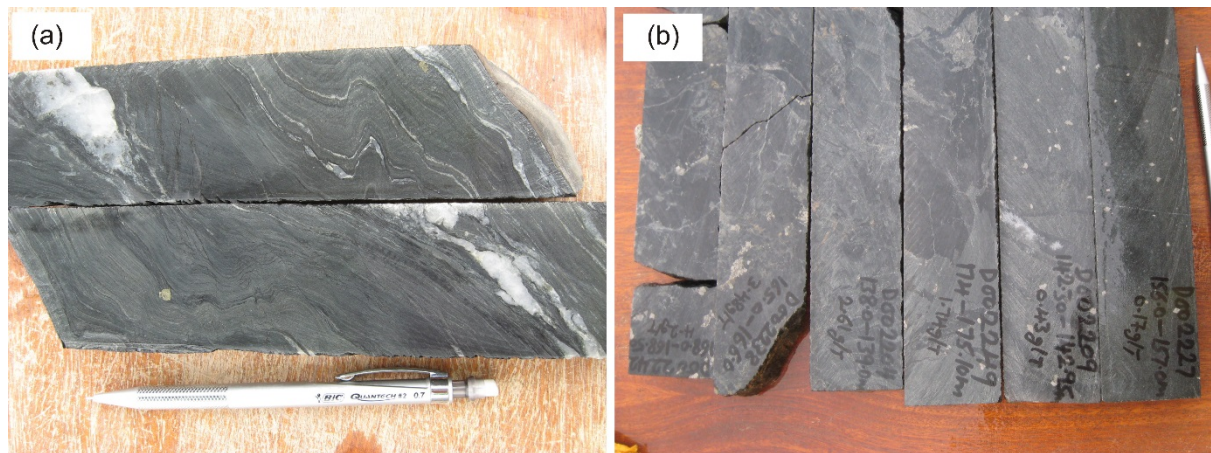


Fig. 6.2. Drill core of sediments in the Wa-Lawra belt (a) borehole showing graphitic shale deformed in a ductile fashion showing folding (b) borehole showing volcanoclastic rock affected by brittle deformation (brecciation).

The anastomosing shear zones created dilatational sites which act as permeable sites for hydrothermal fluid flow. Although the shear zones enable and enhance permeability for hydrothermal fluid flow (Kerrick, 1996), the ductile regime experienced by the graphitic shales does not really permit large volumes of hydrothermal fluid circulation, as is the case of Bepkong which is dominated by graphitic shales. The brecciated volcanoclastic sediments in both the Kunche and Bepkong deposits have created fractures and open space which favours the circulation of hydrothermal fluids and creating in-fill veins. The hydrothermal fluid drained within the anastomosing shear zone alters the country rock and causes modification within the mineralogy of the rocks within the shear zone. In both Kunche and Bepkong the original mineralogy of the rocks has been superimposed by chlorite, calcite sericites and sulphides. The initial arsenopyrite (which occurs as homogenous fragmented residual crystals), with invisible gold which occurs as solid solution or nanoparticles within the arsenopyrite crystal structure, accompanies the hydrothermal fluid which occurs as dissemination along the dilatational sites along the anastomosing shear zones. During this stage, dykes of microdiorite were also emplaced within the shear zones. These dykes are generally not mineralized, except in situation where rare quartz veinlets occur in them. These rare quartz veinlets usually contain small grain of gold (the grade is usually low, thus between 0.01-0.2 g/t and not economic). Rutile is also a mineral that is formed at this stage as a result of the release of Ti into the shear zone. The temperatures at which fluids circulated at this stage is about 370 °C with a pressure >1kbar. The fluids at this stage were CH₄ rich and do occur as supercritical fluid inclusions or inclusions with V-phase covering over 95% of the fluid inclusion.

Stage 2

An intense shearing continues as a result of the long lived D_{K1} or D_{K2} deformations, the earlier shear zones became increasingly deformed and the competent volcanoclastic materials underwent progressive brecciation which in turn created more favourable sites for the circulation of the increase hydrothermal flow. The early stage arsenopyrite which had a significant invisible gold concentration as a result of the stage 1 process, became enriched with more arsenic (with concentration increasing from 1,000,000 ppm to about 2,000,000 ppm and more; see Table 5.3), iron, silver and sulphur at this stage. The arsenopyrites grew, and this is exhibited by the growth rims or oscillatory zones (Type 2 arsenopyrite) observed in

the arsenopyrite at this stage. The ribbon nature of the quartz veins and the growth zones observed in the arsenopyrite, represent many episode of fluid infiltration into the mineralizing site. Gold remobilized and formed visible micro-size gold particles which are observed within the growth rim or fractures formed within the arsenopyrite as a result of the shearing. Visible gold up to about 150 microns in size can be observed within fractures in the quartz veins that have been infiltrated by the hydrothermal fluids. Sulphides such as chalcopyrite, pyrrhotite, and galena came into equilibrium at this stage and grew together with the type-2 arsenopyrite, resulting in intermingled sulphides within the altered country rock or quartz veins. Fluid inclusion at this stage demonstrate P and T values ranging from 320-324 °C and <1 kbar respectively. During this stage phase separation occurred in which the initial V-rich CH₄ fluid inclusion formed a 2 phase L-V CO₂-CH₄-SO₂-H₂O rich fluids with low salinities.

6.2.2 Implication on gold endowment within the two deposit in the Wa-Lawra belt

From the above model and characteristics described for the Kunche and Bepkong deposits, it is clear that the shear zone, hydrothermal alteration and host lithology play a major role in the gold endowment of the two deposits. Shear zones have long been recognised as favourable site for focussing fluid flow into the upper crust (Cox et al., 2001; Chernicoff et al., 2002; Bierlien et al., 2006), but in areas of ductile deformation, permeability is limited, whilst in areas where the rocks which respond more brittlely, greater fluid circulation is permitted (Bonnemaison & Marcoux, 1990).

The Bepkong deposit is composed graphitic shales which are interlayered with volcanoclastics. The graphitic shale is the dominant rock type in the deposit and responds plastically to the stress imposed by the shear zone whilst the minor volcanoclastic sediment responds brittlely to the same stress. The thickness and strike of the volcanoclastic sediment is more restricted hence the brittle openings in the Bepkong deposit are limited or restricted. This phenomenon, reduces the overall fluid circulation that should be focussed with the shear zone, hence the relatively small size of the deposit.

However for the Kunche deposit, which is composed of entirely volcanoclastic sediments, the brittle failure that these rocks undergoes creates a lot of dilatancy which permits greater fluid flow and hence the deposition of more disseminated sulphides and gold. The ore body in Kunche has a 1.1 km strike whilst that of Bepkong is 560 m, and has three times the reserves of gold at present.

Therefore structural architecture, the rheological properties of the rocks, the time of vein formation in the two deposits in the Wa-Lawra belt, provides an insight to the overall disparity in the gold endowment between the Kunche and Bepkong deposit.

6.2.3 Genetic model for gold mineralization in the Julie deposit

Shear zones also played an important role in the gold mineralization within the Julie deposit. From LA-ICP-MS analysis invisible gold was observed within the deposit (Table 3; Amponsah et al., 2015), which suggests a similar two stage or phase of gold mineralization model can be proposed for gold mineralization in the Julie deposit.

Stage 1

This stage marked the commencement of the 6.5 km E-W shear zone related to low angle thrust fault in the Julie belt. The granodiorite rock in the Julie deposit at this stage became intensely deformed creating a mylonitic fabric (Fig 8b; Amponsah et al., 2015) within the rocks. The permeable plumbing system created by the shear zone allowed hydrothermal fluids to circulate within it forming an infill quartz vein. At this stage pyrite formed along with invisible gold. The pyrite and magnetite mineral formed at this stage were deformed and exhibits sigma or sigmoidal porphyroblast (Fig. 6.3) and demonstrate a dextral shear sense.



Fig 6.3. Borehole showing mylonised granodiorite with the early stage pyrite deformed showing a sigmoidal features.

The hydrothermal fluid at this stage altered the country rock and introduced minerals such as sericite, calcite, chlorite, tourmaline and ankerite into the mineralized corridor. The most dominant hydrothermal fluid type was CO₂ rich.

Stage 2

As the deformation continued, more voids were created and more fluid is allowed into the system forming infill quartz veins up to about 50 m thick. At the waning stage of shear zone

formation, more euhedral pyrites precipitated out of solution or completely replaced the magnetite in the system and the initial invisible gold is remobilized into micron-sized gold grains. These micron-sized visible gold grains are usually hosted in fractures within the pyrite mineral or at the grain boundaries of the pyrite mineral. Also at this stage free gold is found within the hydrothermal alteration minerals that formed within the mineralized zone. The fluids dominating at this stage were aqueous-carbonic rich fluid, which entered into immiscibility around 220 °C at a pressure <1 kbar.

6.3 Resituating the three gold deposit in NW Ghana into craton-scale mineral systems context

Gold systems in the West African Craton occurs over a wide geographic extent (Miller et al., 2013) and are mostly shear zone or fault hosted gold deposits (orogenic type), intrusive related copper porphyry deposits or paleo placers. The gold deposits in the WAC are mostly found within the Paleoproterozoic Birimian domain. Examples of the Intrusive related types are the Morila deposit in Mali (McFarlane et al., 2011), the Massawa gold deposit in Senegal (Treloar et al., 2014), whilst examples of thrust and shear related orogenic gold are, Obuasi (Fougerouse et al., 2015), Syama (Traore et al., accepted ms), Wassa (Perrouty et al., 2012; Parra-Avila et al., 2015), Kalana, Damang (White et al., 2015), Pampe deposits (Miller et al., 2013) and that of the Paleoplacer is the Tarkwa deposit (Sestini, 1973; Bossiere et al., 1996; Miller et al., 2013). Gold deposits in WAC are associated with a large range of host rocks (volcano-sedimentary belts with associated intrusives) which have mostly been metamorphosed up to the greenschist facies. The rocks that host the three deposits studied here are within the range of rocks which host known gold deposits in the WAC. The Julie deposit is host in granitoids as is the Ayanfuri deposit in the Ashanti belt, the Subika deposit (Yao & Robb, 2000; Yao et al., 2001) on the Sefwi belt and the Banfora west deposit in Burkina Faso.

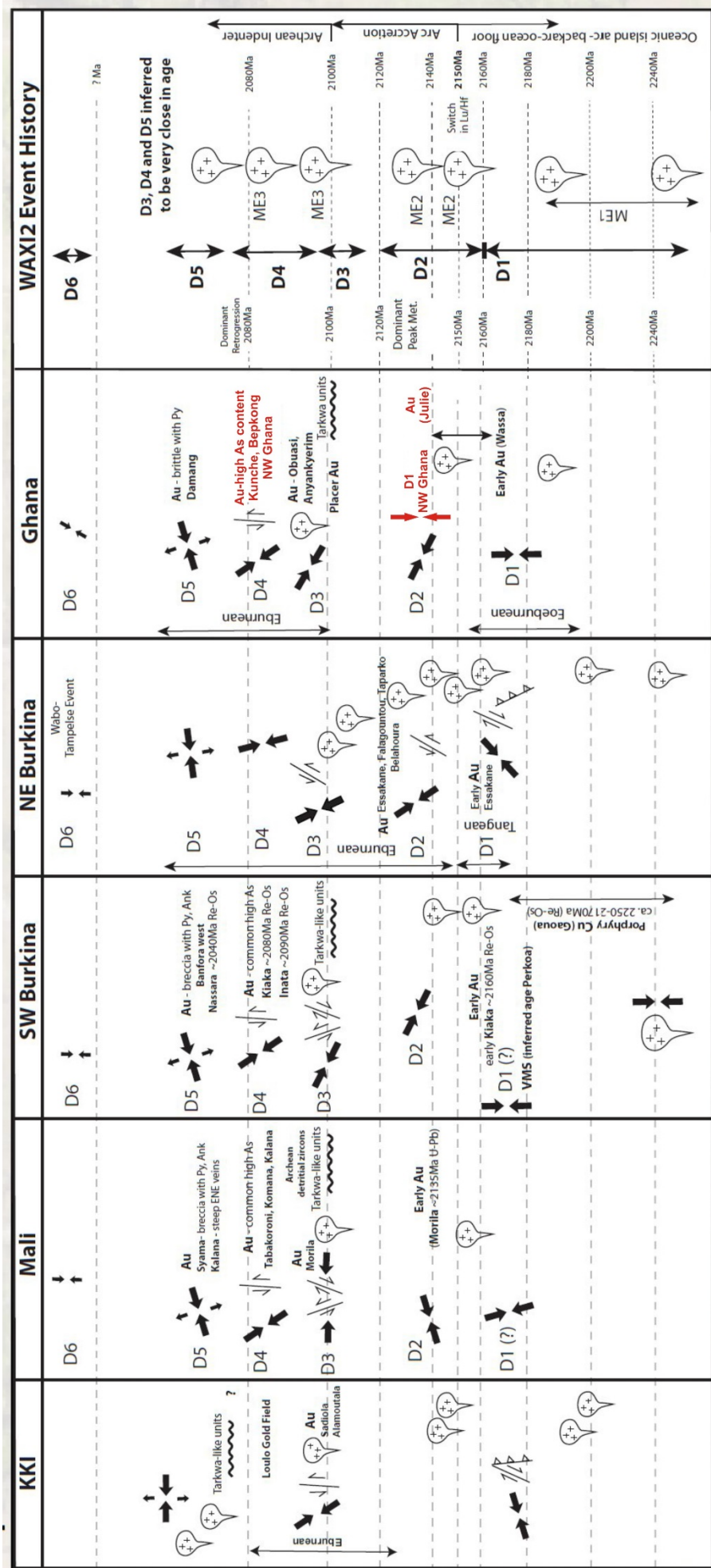


Fig. 6.4. Space-time correlation of events and mineralized system across the West African craton (after Miller et al., 2013)

The Bepkong and Kunche are hosted in sediments (volcaniclastics and graphitic shales), as are the Obuasi (Fougerouse et al., 2015), Siguiri (Lebrun et al., 2015; Markwitz et al., 2015), Sadiola (Masurel et al., submitted), Kalana deposits (Miller et al., 2013) all belonging to the WAC.

6.3.1 Space and time constrains

Gold systems in the WAC according to Feybesse et al. (2006) occurred between 2250 to 2100 Ma. From the space-time correlation of event created by Miller et al. (2013; Fig, 6.4), gold systems in the WAC are associated with several of the different deformation events (multiphase) the craton have experienced.

According to table 6.4 D_1 in the WAC is constrained to have occurred between 2180- 2160 Ma, D_2 between 2150- 2120 Ma, D_3 occurred around 2100 Ma, D_4 occurred between 2100-2080 Ma, whilst D_5 and D_6 are presently unconstrained (Miller et al., 2013).

D_{J1} relates to D_1 in NW Ghana (Block, 2015) which occurred around 2145 to 2125 Ma. The ages of D_{J1} or D_1 in NW Ghana is late when correlated with the general D_1 on a craton wide scale. It actually correlates with the ages that constrain the craton wide D_2 . The N-S shortening which is responsible for the mineralization in the Julie belts correlates well with the general kinematics that affected D_1 in southern Ghana which host the Wassa deposit (Perrouy et al., 2012) and SW Burkina which host the early mineralization in the Kiaka deposit (Miller et al., 2013).

The D_{B1}/D_{K1} which correlates with D_4 in NW Ghana (Block, 2015) which host the Bepkong and Kunche deposits occurred around 2110 to 2105 Ma. This age does not correlate with the ages for craton wide D_4 (Miller et al., 2013) which occurred around 2100-2080 Ma, but with the ages of craton wide D_3 , D_4 , D_5 being close (thus 2120-2080 Ma) the gold in Bepkong and Kunche and be related with Archean indenter regime (Miller et al., 2013). The kinematics associated with D_4 (D_{B1}/D_{K1}) in NW Ghana correlates well with the general craton wide D_4 kinematics and the craton wide transcurrent and transpressional shear activity.

The timing of gold mineralization the Julie, Kunche, Bepkong deposits in NW Ghana, correlates well with the general time constraint of craton wide gold mineralization proposed by Feybesse et al. (2006).

6.3.2 Structures

Gold mineralization in the West African craton has been recognised by many authors (Allibone et al., 2002; 2004; Feybesse et al., 2006; Perrouy et al., 2012) to be associated with thrust faults and shear zones which usually define the regional structural architecture. For examples the early gold mineralization within the WAC (thus the Wassa and Essakane deposits; Perrouy et al., 2012; Miller et al., 2013) are associated with thrust tectonic with its related shearing. The early gold mineralization in NW Ghana (the Julie deposit) is associated with early thrust tectonics (Block et al., 2015) with related shear zones (Amponsah et al., 2015). The Kunche and Bepkong deposits are associated with N to NNW shearing, however the craton scale gold mineralization which occurred between D_3 and D_4 (Miller et al., 2013), is associated with N to NE shearing. Examples are the Loulo (Lawrence et al., 2013),

Tabakoroni, Kalana (Miller et al., 2013), Syama (Traore et al., accepted ms), Banfora west (Miller et al., 2013), Kiaka (Fontaine et al., submitted), Inata (Sawadogo et al., 2014) and Obuasi (Fougerouse et al., 2015) deposits which are all associated with the N- NE shear zones (Miller et al., 2013). The structures hosting the three deposit in NW Ghana are structures that host other deposit in the WAC. This situates the three deposits studied within the normal scheme for the Eburnean orogenic event that affected West Africa.

6.3.3 The nature of the fluids

Fluid inclusions have been studied across the West Africa craton, but the majority of the studies are concentrated in Ghana and Burkina Faso. According the summary in table 6.1, the major fluids that circulated in gold systems during the time of gold precipitation is CO₂-CH₄-N₂ with subordinate CO₂-H₂O and H₂O-NaCl. This fluid system was registered in almost all the deposits across the craton. The fluid that circulated during gold precipitation in Julie deposit in NW Ghana is CO₂ rich. Thus the fluid was composed of aqueous-carbonic type and carbonic rich fluid inclusions. This is almost the same as the fluids observed within the Ayanfuri deposit, where CO₂ was dominated in a granitoid hosted deposit. Fluid inclusion that dominated in the Bepkong deposit were CH₄-CO₂-H₂O-SO₂ fluids. This fluid system is also observed is different from the normal CH₄-CO₂-N₂ fluid systems seen in most of the sediment hosted gold deposit within the WAC. So far SO₂ has not been reported in any of the deposits across the WAC. This makes the Bepkong deposit quite different from other sediment-hosted deposits across the craton. From the timing of gold mineralization, structural control of the gold mineralization it is concluded that all the deposits formed within the Eburnean orogeny, thereby one can say CH₄-CO₂-H₂O-SO₂ fluid systems also existed during gold formation in the WAC.

Table 6.1. Summary of fluid inclusion characteristics across gold deposit within the WAC.

Deposit	Type	CO ₂ -CH ₄ -N ₂	CO ₂ -H ₂ O	H ₂ O-NaCl	N ₂
Ashanti (Ghana)	Quartz	Major	Subordinate	Subordinate	
Schwartz et al. (1992)	vein	0.77-1.11 g/cm ³	0-2.2 wt.% eq. NaCl Th= 271-360°C	0.4-5.2 wt.% eq. NaCl Th= 271-360°C	
Tarkwaian (Ghana)	Quartz	Major	<5%	uncommon	
Klemd et al. (1993)	pebble	0.35-1.15 g/cm ³		5-12 wt.% eq. NaCl Th= 140-380°C	
Ashanti (Ghana)	Quartz	Major		uncommon	surmised
Schmidt Munn et al. (1997)	vein	0.65-1.06 g/cm ³		Th= 72 to 280°C	
Prestea Mine (Ghana)	Quartz	Major	uncommon	uncommon	
Schmidt Munn et al. (1997)	vein	0.85-0.98 g/cm ³	Th= 270 to 334°C	10-13 wt.% eq. NaCl Th= 138 to 223°C	
Konongo (Ghana)	Quartz	Major		uncommon	
Schmidt Munn et al. (1997)	vein	0.95-1.02 g/cm ³		Th= 82 to 188°C	
Ayanfuri(Ghana)	Quartz	Pure CO ₂	<8 wt.% eq. NaCl Th= 186 to 334°C	5-5.6 wt.% eq. NaCl Th= 183 to 284°C	
Schmidt Munn et al. (1997)	vein				
Abosso-Damang(Ghana)	Quartz	Major	uncommon	uncommon	
Schmidt Munn et al. (1997)	vein	0.80-1.00 g/cm ³	Th= 278°C	Th= 104-122°C	
Morilla (Mali)	Quartz	Major		Major	
Hammond et al. (2011)	vein	0.53-32.7 wt.% eq NaCl		Th=197-407°C	
Diabatou(Burkina Faso)	Quartz	Major		14-19 wt.% eq. NaCl	<5%
Klemd et al. (1997)	vein	0.22-0.99 g/cm ³		Th= 160 to 190°C	0.35-0.65 g/cm ³
Larafella (Burkina Faso)	Quartz		Th= 160-323°C	Th= 150-310°C	
Klemd & Ott (1997)	vein				
Granitoid hosted(Ghana)	Quartz	Major	0-6 wt.% eq. NaCl	<10	
Yoa et al. (2001)	vein	0.3-0.92 g/cm ³	Th= 121 to 387°C	1-8 wt.% eq. NaCl Th= 181 to 316°C	
Sansu mine(Ghana)	Quartz	Major			
Yoa et al. (2001)	vein	0.3-0.92 g/cm ³			
Guibare(Burkina Faso)	Quartz		<6.6 wt.% eq. NaCl	Th= 135 to 184°C	
Dubios et al. (2001)	vein		Th= 280 to 330°C		
Loraboue(Burkina Faso)	Quartz	0.7-1g/cm ³		<3 wt.% eq. NaCl	
Dubios et al. (2001)	vein			Th= 150 to 200°C	
Yaoure-Angovia (Ivory Coast)	Quartz	>72%	8%	18%	
Coulibaly et al. (2007)	vein	0.69-1.04 g/cm ³	2.5-10 wt.% eq. NaCl Th= 267 to 345°C	0-8 wt.% eq. NaCl Th= 158 to 339°C	1% 0.45-0.6 g/cm ³
Julie deposit (Ghana)	Quartz	minor Pure CO ₂	Major		
Amponsah et al. (2015)	vein	4.9-8.6 wt.% eq. NaCl	1.9-6.2 wt.% eq. NaCl		
This study		Th= 210 to 228°C	Th= 210 to 275°C		
Bepkong deposit (Ghana)	Quartz	Major CO ₂ -CH ₄ ±SO ₂	Minor CH ₄ ±SO ₂		
This study	vein	2.27-3.42 wt.% eq. NaCl Th=320-324°C	Th=310-370°C 0.448-0.451g/cm ³		

6.4 Exploration Guide in the Wa-Lawra region

From the above mentioned features described for the three deposits, added with multi-element geochemistry (rock chip sampling, soil sampling, trenching) and geophysics can be useful guide to exploration. The following tips can be a useful guide for exploration in the Wa-Lawra region.

1. Identification of second order shear zones in the Julie belt, and identification of dilatational sites within the anastomosing shear zones filled with boudinage quartz veins in the Wa-Lawra belt can be a very useful information in planning exploration strategies.
2. Identification of mechanically competent rocks within the shear zone is vital for gold formation. These rocks responds brittlely and creates more opening for fluid flow.
3. The presence of sulphides, especially pyrites in the Julie deposit and arsenopyrites within the sediments in the Wa-Lawra belt is very vital for exploration. Also the presence of chalcopyrite, pyrrhotite, galena and pyrite are also useful pathfinders for gold exploration in the Wa-Lawra belt, since they are always intermingled with the arsenopyrite
4. Hydrothermal alteration in the country rock is also another useful guide in identifying gold mineralized corridor in the Wa-Lawra region. For the sediments in the Wa-Lawra belt, the alteration mineral assemblage that defines the mineralizing corridor is chlorite + sericite + calcite + sulphide in the country rock. The alteration assemblage that envelopes the mineralization zone in the Julie belt consist of sericite + quartz + ankerite + calcite + tourmaline +pyrite. The second alteration assemblage laterally away from the mineralized corridor before moving into barren greenschist rocks consist of albite + sericite + calcite + chlorite + pyrite + rutile. Identifying these alteration assemblages is a useful tool for gold exploration in the Wa-Lawra region.
5. The association of gold with other metals can also be a useful tool for exploration in the region. In the Julie belt gold is usually associated with Ag, Te, Bi and Pb. In the Wa-Lawra belt the gold is associated with Ag, As, with minor amount of Ni and Co. These elements can be used as a strong pathfinder element for gold mineralization.

6.5 Conclusion

The Kunche, Bepkong and Julie deposit are the major and the most economical gold deposits currently discovered in the Wa-Lawra region. A common feature to these three deposit are that, they are associated with areas of high deformation (shearzones) but the nature of their wall rock is different. The Kunche deposit is hosted in volcanics, the Bepkong deposit is hosted in volcanics and graphitic shales while the Julie deposit is hosted in granitoids.

The gold mineralization in the three deposits are associated with various disseminated sulphides found within quartz veins and the country rock adjacent to the veins. The quartz veins in the three deposits do have varying thicknesses but are all boudinaged. Gold in the Julie deposit is present as micro-size inclusion in pyrite, the main and only sulphide present in the Julie deposit. SEM imagery and LA-ICP-MS done on the pyrite shows that the micro-size gold are localised in fractures within the pyrite and correlate well with metals such as Ag, Pb, Te and Bi. Gold in the Kunche and Bepkong deposits are present as invisible (usually as solid solution or nanoparticles within the crystal lattice) and visible gold in the arsenopyrite mineral. Other sulphides such as chalcopyrites and pyrrhotite are also present in the mineralized zone in the Kunche and Bepkong deposit. SEM imagery, shows the gold in these two deposits are found within fractures in the arsenopyrites whilst LA-ICP-MS shows that the gold is associated with Ag.

There is significant difference in the nature of mineralizing fluids, and the trapping T/P conditions within the Julie and Bepkong deposit. In the Julie deposit, the mineralizing fluids are rich in CO₂, and exhibit low to moderate salinity with an H₂O–CO₂–NaCl system. The fluids were trapped in a P/T condition around 220 C and <1 kbar. The fluids in Bepkong are rich in CH₄, with low salinity within a CH₄-CO₂-SO₂-H₂O system. Gold trapping P/T conditions is around 320°C and 1 kbars.

The three deposits, gold mineralization is associated with shear zones marked by the development of quartz vein system oriented N to NNW in the Kunche and Bepkong deposit and E-W in the Julie deposit. The timing of gold mineralization in the Julie deposit is around 2145-2125 Ma whilst that of the Kunche and Bepkong deposit is around 2110- 2105 Ma.

All the three gold deposits in the Wa-Lawra region are associated with shearzones. However, the Kunche and Bepkong deposit are alike with regards with the relative timing of deformation and gold mineralization, structural architecture, metal associated with the mineralization, and gold do occur as invisible and visible gold. These two deposit differs from the Julie deposits in terms of the characteristics described above.

However, these three deposits studied have characteristics similar to orogenic gold and therefore can be considered as orogenic gold.

6.6 References

- Allibone, A., Hayden, P., Cameron, G., Duku, F., 2004. Paleoproterozoic gold deposits hosted by albite- and carbonate-altered tonalite in the Chirano District, Ghana, West Africa. *Economic Geology and the Bulletin of the Society* 99, 479–497.
- Allibone, A., Teasdale, J., Cameron, G., Etheridge, M., Uttley, P., Soboh, A., Appiah-Kubi, J., Adanu, A., Arthur, R., Mamphey, J., Odoom, B., Zuta, J., Tsikata, A., Pataye, F., Famiyeh, S., Lamb, E., 2002. Timing and structural controls on gold mineralization at the Bogoso Gold Mine, Ghana, West Africa. *Economic Geology* 97, 949–969.
- Amponsah, P. O., Salvi, S., Béziat, D., Jessell, M., Siebenaller, L., Baratoux, L., 2015. Geology and geochemistry of shear hosted Julie gold deposit, NW Ghana. *Journal of African Earth Science* (In press). <http://dx.doi.org/10.1016/j.jafrearsci.2015.06.013>.
- Baratoux, L., Metelka, V., Naba, S., Jessell, M.W., Grégoire, M., Ganne, J., 2011. Juvenile Paleoproterozoic crust evolution during the Eburnean orogeny (2.2-2.0Ga), Western Burkina Faso. *Precambrian Research* 191, 18-45.
- Bierlein, F.P., Murphy, F.C., Wienberg, R.F, Lees, T., 2006. Distribution of orogenic gold deposits in relation to fault zones and gravity gradients: targeting tools applied to the Eastern Goldfields, Yilgarn Craton, Western Australia. *Miner Deposita*. DOI 10.1007/s00126-005-0044-4.
- Block, S, 2015. Evolution geodynamique du craton Ouest Africain au nord du Ghana. PhD thesis, University of Toulouse III (unpublished)
- Block, S., Jessell, M.W., Ailleres, L., Baratoux, L., Bruguier, O., Zeh, A., Bosch, D., Caby, R., Mensah, E., 2015. Lower crust exhumation during Paleoproterozoic (Eburnean) orogeny, NW Ghana, West African Craton: interplay of coeval contractional deformation and extensional gravitational collapse. *Precambrian Research*. Doi: 10.1016/j.precamres.2015.10.014
- Bonnemaison, M., Marcoux, E., 1990. Auriferous mineralization in some shear-zones: A three-stage model of metallogenesis. *Mineralium Deposita*, 25, 96-104.
- Bossiere, G., Bonkougou, I., Peucat, J-J., Pupin, J-P., 1996. Origin and age of Palaeoproterozoic conglomerates and sandstones of the Tarkwaian Group in Burkina Faso, West Africa. *Precambrian Research*, 80, 153-172.
- Chernicoff, C.J., Richards, J.P., Zappettini, E.O., 2002. Crustal lineament control on magmatism and mineralization in northwestern Argentina: geological, geophysical, and remote sensing evidence. *Ore Geology Reviews* 21:127–155.

- Cox, S.F., Knackstedt, M.A., Braun, J., 2001. Principles of structural control on permeability and fluid flow in hydrothermal systems. *Society of Economic Geology Reviews*, 14.1–24
- Feybesse, J.-L., Billa M., Guerrot C., Duguey E., Lescuyer, J., Milési, J.P., Bouchot., 2006. The Paleoproterozoic Ghanaian province: Geodynamic model and ore controls, including regional stress modeling. *Precambrian Research* 149, 149-196.
- Fontaine, A., Andre-Mayer, A.S, Eglinger, A., Ada K., Reisberg, L., Le Mignot E., Ganne, J., **Poujol, M** (submitted). The Kiaka gold deposit (Burkina Faso): A record of Paleoproterozoic (Eburnean) orogeny in West Africa. *Economic Geology*.
- Fougerouse, D., Micklethwaite, S., Miller, J.M., Ulrich, S., McCuaig, T.C., 2015. The Obuasi gold deposit: A West African giant. *Ore Geology Reviews*, in press, doi:dx.doi.org/10.1016/j.oregeorev.2015.06.019
- Lawrence, M.D., Treloar, P.J., Harbidge, P., Holliday, J., 2013. The Geology and Mineralogy of the Loulo Mining District, Mali, West Africa: Evidence for Two Distinct Styles of Orogenic Gold Mineralization. *Economic Geology*, 108, 199-227,
- Lebrun, E.O., Thébaud, N., Miller, J., Ulrich, S., McCuaig, C.T., 2015. The world-class orogenic gold Siguiri district, Siguiri Basin (Guinea, West Africa). *Ore Geology Reviews*, in press, doi:dx.doi.org/10.1016/j.oregeorev.2015.08.013
- Markwitz, V., Hein, K. A.A., Jessell, M. W., Miller, J., 2015. Metallogenic portfolio of the west Africa craton, *Ore Geology Reviews*, doi: 10.1016/j.oregeorev.2015.10.024
- Miller, J., Bezait, D., Salvi, S., Siebenaller, L., Markwitz, J., Davis, K., Hien, K., McCuaig, T.C., Le Mignot, L., Andre-Mayer, A-S., Reisberg, L., Bourassa, Y., Baratoux, L., Jessell, M., Metalka, V., Perrouty, S., Fougerouse, D., 2013. Mineral System variations across the craton. Poster presentation, WAXI conference, Senegal, 2013.
- Masurel, Q., Thebaud, N., Miller, J., McCuaig, T.C., Ulrich, S., Cameron, G., Hein, K.A.A., submitted. Sadiola Hill, a carbonate-hosted world-class gold deposit in Mali. *Ore Geology Reviews*.
- Parra-Avila, L.A., Bourassa, Y., Miller, J., Perrouty, S., Fiorentini, M.L., McCuaig, T.C., 2015. Age constraints of the Wassa and Benso mesothermal gold deposits, Ashanti Belt, Ghana, West Africa. *Journal of African Earth Sciences*, in press, doi:dx.doi.org/10.1016/j.jafrearsci.2015.05.017
- Perrouty, S., Ailleres, L., Jessell, M.W., Baratoux, L. Bourassa, Y., Crawford, B., 2012. Revised Eburnean geodynamic evolution of the gold-rich southern Ashanti Belt, Ghana, with new field and geophysical evidence of the pre-Tarkwaian deformations. *Precambrian Research* 204-205, 12-39.

Sawadogo, P., Bamba, O., Sawadogo, S., Belem, T., 2014. Geomechanical study of the Inata gold mine pits rock slopes, Burkina Faso (West Africa). *International Journal of Scientific Engineering and Research*, 2, 20-27.

Sestini, G., 1973. Sedimentology of a Paleoplacer: The Gold-bearing Tarkwaian of Ghana. In: *Ores in Sediments*. Amstutz, G.C. and Bernard, A.J. (Eds.), Springer Berlin Heidelberg, 3: 275-305.

Traore, D. Y., Siebenaller, L., Beziat, D., Salvi, S., Miller, J., Bouare, M. L., (accepted ms). Gold mineralization along the Syama shear-zone, southern Mali (West Africa). Part 2: Tectonic setting and Ore mineralogy. *Ore Geology Reviews*.

Treloar, P.J., Lawrence, D.M., Senghor, A., Boyce, A., Harbidge, P., 2014. The Massawa gold deposit, Eastern Senegal, West Africa: an orogenic gold sourced from magmatically derived fluids? From Jenkin, G.R.T., Lusty, P.A.J., McDonald, I., Smith, M.P., Boyce, A.J., Wilkinson, J.J (eds), 2015. *Ore deposits in an evolving Earth*. Geological Society of London, 93, 135-160.

White, A.J.R., Waters, D.J., Robb, L.J., 2015. Exhumation-driven devolatilization as a fluid source for orogenic gold mineralization at the Damang deposit, Ghana. *Economic geology*, 110, 1009-1025.

Yao, Y., Murphy, P.J., Robb, L.J., 2001. Fluid Characteristics of granitoid-hosted gold deposits in the Birimian terrane of Ghana: a fluid inclusion microthermometric and Raman spectroscopic study. *Economic Geology*, 96, 1611-1643.

Yao Y and Robb L J, 2000. Gold mineralization in Palaeoproterozoic granitoids at Obuasi, Ashanti region, Ghana: Ore geology, geochemistry and fluid characteristics: in *South Africa Journal of Geology*, 103, 255-278

6.7 Conclusion générale

Les gisements de Kunche, Bepkong et Julie sont les trois principaux gisements d'or de la région Wa-Lawra. Une caractéristique commune à ces trois gisements est qu'ils sont associés à des zones de très forte déformation (shear-zone) mais la nature de leurs roches encaissantes est différente. Ces dernières sont de nature volcanoclastique à Kunche, volcanoclastique et shale graphiteux à Bepkong et granite à Julie.

Dans les trois gisements, la minéralisation aurifère, associée à divers sulfures, se rencontrent au sein de filons de quartz et aux épontes de ceux-ci. Ces filons de quartz se présentent sous forme de lentilles montrant des épaisseurs variables traduisant un boudinage. A Julie, les grains d'or se présentent en inclusion dans la pyrite, unique sulfure du gisement, mais le plus souvent localisés dans les fractures de la pyrite et souvent associés à des tellurures d'or, d'argent et de bismuth. Les analyses LA-ICP-MS réalisées sur les pyrites hôtes montrent également cette association de l'or à ces mêmes éléments (Ag, Bi, Pb et Te). A Kunche et Bepkong, l'or est présent à la fois sous la forme « invisible » (soit en substitution dans le réseau de la pyrite et de l'arsénopyrite, soit sous forme de nanoparticules) et visible sous forme d'inclusions uniquement au sein des cristaux d'arsénopyrite ; cette dernière est associée à la chalcoppyrite et à la pyrrhotite dans les zones minéralisées. Les images MEB montrent que l'or est localisé dans les fractures de l'arsénopyrite et les analyses LA-ICP-MS réalisées sur les arsénopyrites montrent une très forte corrélation avec Ag, Sb, Ni et Co.

Des différences importantes s'observent également au niveau de la nature des fluides et de leur condition P-T de piégeage. A Julie, les fluides minéralisateurs sont riches en CO₂, et montrent une salinité faible à modérée (système H₂O-CO₂-NaCl) ; ils seraient piégés dans des conditions P/T autour de 220°C et <1 kbar. A Bepkong, les fluides sont riches en CH₄, avec une faible salinité (système CH₄-CO₂-SO₂-H₂O) et indiqueraient des températures de piégeage de l'or visible autour de 320°C et 1 kbar.

Dans les trois gisements, la minéralisation aurifère est associée à une zone de cisaillement (shear-zone) marquée par le développement d'un important réseau de veines de quartz orientées N-NNO à Kunche et Bepkong, orientées E-W à Julie. A Julie, la mise en place de la minéralisation se ferait autour de 2145-2125 Ma, mais autour de 2110- 2105 Ma pour Kunche et Bepkong.

Au final, les gisements de Bepkong et Kunche présentent entre eux de très fortes similitudes et diffèrent nettement tant par l'âge, la nature de la roche encaissante, le style des déformations et des minéralisations du gisement de Julie.

Toutefois, ces trois gisements présentent toutes les caractéristiques de gisements d'or dit « orogéniques » et peuvent être considérés comme appartenant à cette catégorie de gisements.

APPENDIX

Appendix A

3-D numerical modelling of the influence of pre-existing faults and boundary conditions on the distribution of deformation: Example of North-Western Ghana

High-strain zones bound and separate the high-grade tectono-metamorphic terranes from low-grade greenstone belts in the North-Western parts of Ghana. These belts are bounded by granitoid domains characterized by two main episodic pulses of magmatic intrusive events, which occurred between 2213 Ma and 2086 Ma. High-strain zones are thought to play a significant role in creating fluid pathways, particularly for partially molten material from lower crustal sources to the upper crust. In this study, a three-dimensional thermo-mechanical model has been used to explore the evolution of high-strain zones and relief under compressional and simple shear boundary conditions. Different orientations of a system of branched strike-slip faults were tested. The effects of the frictional angle and density contrast on the evolution of relief were also compared in this study. The resulting model indicates domains of tensile vs. compressional strain as well as shear zones. This shows that the internal fault zones as well as the host rock in between the faults behave as relatively weaker domains than the external regions. Under both applied compressive and simple shear boundary conditions, these weakened domains constitute preferential zones of tensile and shear strain accommodations in the upper crust, which may favour infilling by deeper partially molten rocks. This processes is suggested by the authors as the most likely processes to have occurred in pre-existing branched shear zones systems in North-Western Ghana during the Eburnean orogeny (around 2.20–2.10 Ga).

The orientations of faults in these models play an important role in controlling the evolution of relief and localized deformation. In particular, greatest the largest relief is obtained when faults dip parallel to each other and when they are inclined at depth, as they thus facilitate strain rotation and material transfer from depth. The host rock density does not play a primary role in producing relief compared to variations in friction angle at crustal scale of our model. Relief increases by 200–300 m when the host rock density is increased by 200 kg/m³, whereas relief reduces by about 1200 m when decreasing the host rock friction from $\varphi = 20^\circ$ to 10° . This study suggests a model for interpreting the evolution and locus of exhumation of partially molten rocks in North-Western Ghana.



ELSEVIER

Contents lists available at ScienceDirect

Precambrian Research

journal homepage: www.elsevier.com/locate/precamres



3-D numerical modelling of the influence of pre-existing faults and boundary conditions on the distribution of deformation: Example of North-Western Ghana

Xiaojun Feng^{a,*}, Prince O. Amponsah^a, Roland Martin^a, Jérôme Ganne^a, Mark W. Jessell^{a,b}

^a Geosciences Environnement Toulouse, Observatoire Midi Pyrénées, 14 av. E. Belin, 31400 Toulouse, France

^b Centre for Exploration Targeting, The University of Western Australia, 35 Stirling Highway, Crawley, Perth, WA 6009, Australia

ARTICLE INFO

Article history:

Received 17 January 2015
Received in revised form 11 June 2015
Accepted 14 June 2015
Available online xxx

Keywords:

3D numerical modelling
Eburnean orogeny
Strike-slip faults
Deformation
West African Craton

ABSTRACT

High-strain zones bound and separate the high-grade tectono-metamorphic terranes from low-grade greenstone belts in the North-Western parts of Ghana. These belts are bounded by granitoid domains characterized by two main episodic pulses of magmatic intrusive events, which occurred between 2213 Ma and 2086 Ma. High-strain zones are thought to play a significant role in creating fluid pathways, particularly for partially molten material from lower crustal sources to the upper crust. In this study, a three-dimensional thermo-mechanical model has been used to explore the evolution of high-strain zones and relief under compressional and simple shear boundary conditions. Different orientations of a system of branched strike-slip faults were tested. The effects of the frictional angle and density contrast on the evolution of relief were also compared in this study. The resulting model indicates domains of tensile vs. compressional strain as well as shear zones. This shows that the internal fault zones as well as the host rock in between the faults behave as relatively weaker domains than the external regions. Under both applied compressive and simple shear boundary conditions, these weakened domains constitute preferential zones of tensile and shear strain accommodations in the upper crust, which may favour infilling by deeper partially molten rocks. This processes is suggested by the authors as the most likely processes to have occurred in pre-existing branched shear zones systems in North-Western Ghana during the Eburnean orogeny (around 2.20–2.10 Ga).

The orientations of faults in these models play an important role in controlling the evolution of relief and localized deformation. In particular, greatest the largest relief is obtained when faults dip parallel to each other and when they are inclined at depth, as they thus facilitate strain rotation and material transfer from depth. The host rock density does not play a primary role in producing relief compared to variations in friction angle at crustal scale of our model. Relief increases by 200–300 m when the host rock density is increased by 200 kg/m³, whereas relief reduces by about 1200 m when decreasing the host rock friction from $\varphi = 20^\circ$ to 10° . This study suggests a model for interpreting the evolution and locus of exhumation of partially molten rocks in North-Western Ghana.

© 2015 Elsevier B.V. All rights reserved.

1. Introduction

It has been previously established that pre-existing shear zones in the crust may be reactivated and act as preferential loci for strain accommodation, when the principal stress field changes or rotates under external boundary conditions (D'Alessio and Martel, 2004; Fialko et al., 2005; Fialko, 2006; Gerbault et al., 2003; Middleton

and Copley, 2013; Nieto-Samaniego, 1999; Scholz, 2007; Sibson, 1977; Tong et al., 2014; Walsh et al., 2002; Zhang et al., 2009). It has also been suggested that shear zones play a significant role in providing fluid pathways for partially molten materials from lower crustal levels to the upper crust (Neves et al., 2000; Pereira et al., 2013; Snoke et al., 1999; Vigneresse and Tikoff, 1999; Weinberg et al., 2006).

Even at constant obliquity of far-field motion, the development of high-strain shear zones results in highly variable structures and fabrics. Whereas numerical modelling studies of oblique tectonics in the crust (e.g. Braun and Beaumont, 1995; Braun and Yamato,

* Corresponding author. Tel.: +33 0664699991.
E-mail address: fxjuncumt@gmail.com (X. Feng).

2010; Gerbault et al., 2002; Le Pourhiet et al., 2012) are still constrained by computational limitations, a large number of analogue modelling studies have investigated aspects of localized deformation in three-dimensional strike-slip settings (e.g., see review by Dooley and Schreurs, 2012, and references therein; Leever et al., 2011). Such numerical and analogue studies reproduce quite well field observations such as evolving Riedel shears, connection with P shears and the building of positive or negative flower structures. All of these structures mentioned above depend on lateral and basal boundary conditions, the initial geometries and the mechanical properties of the modelled crustal material. The orientation, magnitude and shape (flattening vs constriction, etc.) of finite strain ellipsoids tend to change continually as a result of the increasing simple shear component with respect to the coaxial components of deformation (Fossen and Tikoff, 1998; Sanderson and Marchini, 1984; Leever et al., 2011; Dooley and Schreurs, 2012). Further complications arise with heterogeneous deformation, non-steady-state deformation and strain partitioning. Within a shear zone, strain may either increase in intensity towards the central part of the zone, or be preferentially partitioned as a localized simple shear component within the broader high strain zone. In such partitioned shear zones, parts of the terranes may actually move faster than the relative plate motion, while other sections may move slower than or even in an antithetical direction to plate motion (Fossen and Tikoff, 1998; Dooley and Schreurs, 2012). This highlights the difficulty in reconstructing initial geometries and boundary conditions that produce high-strain shear zones, and then in understanding the strain field allowing deeper fluids to flow throughout the solid upper crust.

The crustal dynamics of an interacting fault system represent a complex problem due to varying orientation (Peltzer et al., 2001) and strike-slip instability along fault (Xing et al., 2007) over geological time scales. The spatial and temporal pattern of deformation is controlled by the orientations of pre-existing fault zones with respect to far-field boundary conditions (e.g., Buck and Lavier, 2001; Sibson and Xie, 1998; Tranos, 2012). In particular, new shear zones and localized deformation may develop through time (Alberti, 2010; Avouac and Burov, 1996; Giger et al., 2008; Jessell et al., 2012; Rice, 1993). Two interacting faults can be mutually constrained over a time period, during which faults weaken and also impact on the surrounding host rocks (Imber et al., 2004), possibly initiating new failures (Buck and Lavier, 2001; Leever et al., 2011). Conversely, varying boundary conditions simulate how different paleostress fields affect strain localization of interacting faults over geological time (Naylor et al., 1986; Ueta et al., 2000).

In this study we have investigated the role NE-SW trending crustal scale shear zone architecture plays in controlling the loci of exhumation during the Eburnean Orogeny in the Birimian of North-Western Ghana. According to Block et al. (2015), the high grade Bole-Bulenga terrane in North-Western Ghana, is composed mostly of gneisses, metabasites and monzogranites and located between the craton scale N-S Jirapa and the NE-SW Bole-Nangodi shear zones (Fig. 1). These high strain shear zones separate the high grade tectono-metamorphic Bole-Bulenga terrane from adjacent low grade greenstone belts (i.e. Wa-Lawra and Julie belts) which is mostly characterized by early thrust and late stage kinematic shear deformation. The minimum pressure difference between high grade amphibolite–migmatite facies Bole-Bulenga terrane (lower crust) and the adjacent greenschist facies belts (upper crustal materials) is about 3 kbar, corresponding to over 10 km in thickness.

Although Block et al. (2015) highlighted the significance of extension for exhumation in the Bole-Bulenga terrane; they also indicated that extension is certainly not the only process accounting for the exhumation of lower crust. In addition, Sakyi et al. (2014) concluded that the oldest pulses of granitic emplacement in the Wa-Lawra belt are around 2212 ± 1 Ma. This indicates that the

emplacement of Birimian granitoids in the study area should have commenced much earlier than previous studies have mentioned. All these uncertainties show that insights into the exhumation mechanisms for high grade rocks along and in between these two faults are of interest in this region. Generally, the spatial–temporal evolution of high-strain zones relating to pre-existing branched faults systems is still not completely understood. Simultaneously, fault zones in this area of Ghana are generally treated as vertical or sub-vertical (Adjei, 1992; Harcouët-Menou et al., 2009; Lompo, 2010). These uncertainties associated with the interpretation and geometry of the fault zones provided the motivation to test the influence of fault orientations on the distribution of high-strain zones reactivated in a specific kinematic setting.

The aim of this paper is not to re-produce the exact evolutionary history of geological structures in North-Western Ghana, but rather to use this geology as a basic example for assessing how the orientations of a paired fault zone system influences the distribution of high-strain zones and relief. In this study, we assume that the pre-existing faults interact with hard linkage (Gupta and Scholz, 2000), rather than interacting only through their stress fields (soft linkage), and the choice of soft linkages would significantly alter the results, but were not studied here. We use a three-dimensional thermo-mechanical model to explore the distribution of high-strain zones and relief associated with pre-existing weak domains, by testing various orientations of a system of two strike-slip faults under pure shear as well as simple shear boundary conditions. We also test the relative effects of friction angle and density contrast on the evolution of relief. These tests may shed light on exhumation process of high grade rocks associated with strain, as well as the topographic evolution in North-Western Ghana. According to tomographic models and velocity group dispersion analysis, in the Kaapvaal, Congo, Cameroon and West African/(WAC) cratons, the depth of the Moho has been estimated as 40 km and even deeper towards the south-west margin of the WAC or at about 43–48 km in the Congo Basin (Fishwick and Bastow, 2011; Lebedev et al., 2009; Pasyanos and Nyblade, 2007; Seber et al., 2001; Tokam et al., 2010) while it can reach as high as 30 km in northern Africa (Marone et al., 2003). Similar or complementary data of the Precambrian lithosphere structure has also been detailed in Lebedev et al. (2009). A compilation of Moho depths for the West African Craton (Jessell et al., 2015) reveals considerable uncertainty, and we have taken a thinner crust depth around 30 km in the present 3D modelling studies assuming that this was more or less the Proterozoic Moho depth.

2. Geological setting

2.1. Summary of the Birimian in the West African Craton

Most modern orogenic belts, such as the Alpine or Himalayan chains, display greenschist and blueschist facies metamorphism (Avé Lallemant and Guth, 1990; Maruyama et al., 1996; Ota and Kaneko, 2010), whereas the existence of modern-style plate subduction in ancient orogenic belts remains the subject of debate (Ganne et al., 2011; Stern, 2007, 2008; Condie and Kröner, 2008). Precambrian terranes also display widespread greenschist rocks, characterized by the development of a subvertical foliation, which is also axial-planar to elongated synforms and antiforms in greenstone lithologies (Cagnard et al., 2006a,b, 2007; Rey and Houseman, 2006). Such tectonic features are exemplified by the upper crustal portions of the Archaean crust in India (Chardon et al., 2009; Hansen et al., 1995; Jagadeesh and Rai, 2008; Mall et al., 2012). These Precambrian deformation events are proposed to have occurred in a regime of moderate regional convergence, which involved dominantly horizontal and locally vertical motions of material in the

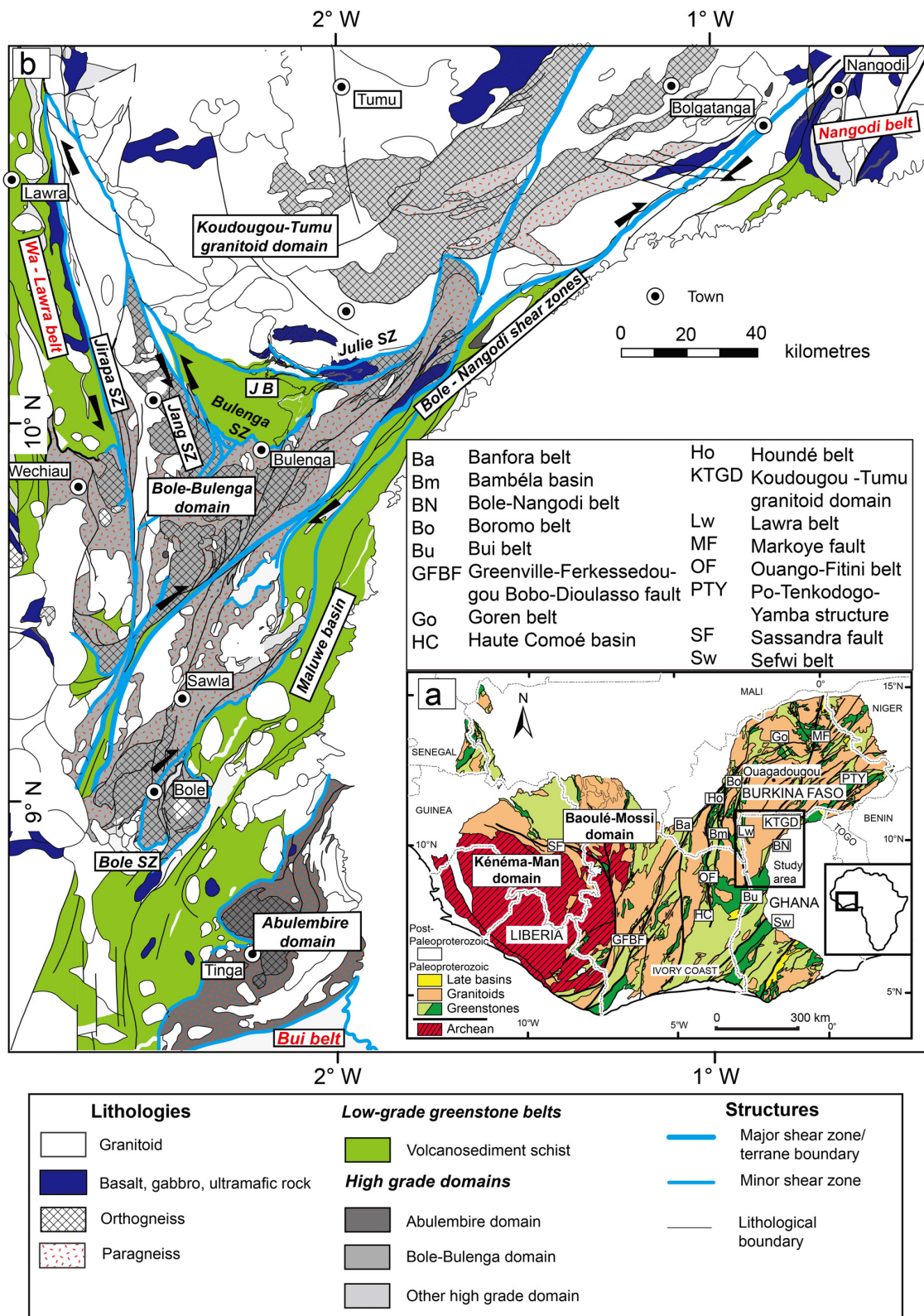


Fig. 1. (a) Simplified geological map of the Leo-Man Craton of the southern part of the West African Craton (WAC) with the zone of interest outlined. Paleoproterozoic greenstones are divided into two groups, light green represents intermediate to acid volcanoclastic and volcano-sediment, and dark green represents mafic to intermediate lavas and volcanic products, with granitoids in orange. (b) Geological setting of the study area (after Block et al., 2015). High-strain zones (blue lines) separate or limit the high-grade tectono-metamorphic terranes from low-grade greenstone belts, high-grade rock assemblages are mainly observed between the Jirapa shear zone and Bole-Nangodi shear zones. (For interpretation of the references to colour in this figure legend, the reader is referred to the web version of the article.)

Please cite this article in press as: Feng, X., et al., 3-D numerical modelling of the influence of pre-existing faults and boundary conditions on the distribution of deformation: Example of North-Western Ghana. Precambrian Res. (2015), <http://dx.doi.org/10.1016/j.precamres.2015.06.006>

upper portions of the crust (down-dip mineral lineation), accompanied by localized strike-slip motion (Block et al., 2015; Ganne et al., 2014).

The southern part of the West African Craton (WAC; Fig. 1) is dominated by Birimian terranes of Palaeoproterozoic age (ca. ~2.20–2.00 Ga, Castaing et al., 2003a,b and references therein), which extend to the east and to the north of the Liberian Archaean cratonic nucleus (Fig. 1). The Birimian formations consist of linear or arcuate narrow volcanic belts (greenstones sensu stricto) often associated to narrow volcano-sedimentary basins (greenstones sensu lato). They are intruded by several generations of granitoids (Dioh et al., 2006; Doumbia et al., 1998; Gasquet et al., 2003; Hirdes et al., 1996 and references therein). The Birimian basins is composed of, a thick sequence of tholeiitic basalts, covered by a detrital sedimentary pile which includes inter-bedded calc-alkaline volcanic rocks. Recent studies have shown that the geodynamic settings of the Birimian units was initially formed in an immature volcanic arc setting (Dioh et al., 2006) or plateaus (Boher et al., 1992; Lompo, 2009), and were later deformed and metamorphosed during the Eburnean orogeny, between ~2.15 Ga and 2.00 Ga (Egal et al., 2002). Despite stimulating debate in the last 30 years, the geodynamic setting of the Birimian sequences is not well constrained, in part because there are large uncertainties and growing discussion surrounding the use of geochemical information as an efficient tool for unravelling geodynamical settings in the past.

Structurally, the number of deformation phases characterizing the Eburnean orogeny is still under debate (Feybesse et al., 2006 and refs therein). In summary, the first Eburnean deformation phase (D1) took place between ca. ~2.20 Ga and 2.10 Ga. This phase of deformation is associated with crustal thickening via nappe stacking and burial of rocks (Allibone et al., 2002; Ledru et al., 1991; Vidal et al., 1996), operated under an E-W to WNW-oriented compression (Baratoux et al., 2011). Block et al. (2015) suggest that some aspects of this phase of deformation occurred in high pressure – low temperature conditions. D2 is a tectono-metamorphic deformational phase responsible for most of the large structures observed in the Birimian Province (Greenstones basins were deformed into linear to arcuate belts or transcurrent shear zones) and occurred synchronously with some granitoid emplacement. Transition of D1 to the subsequent D2 deformation phase is likely to have occurred at around 2.13 Ga in Ghana, following a major pulse of granitoid emplacement at ca. 2.15 Ga (Feybesse et al., 2006; Block et al., 2015).

2.2. Geological summary in North-Western Ghana

The geology of North-Western Ghana straddles the Upper West region, Upper East region and the Northern regions of Ghana and lies near the eastern margin of the Paleoproterozoic Baoulé-Mossi domain of the West African Craton (WAC). Block et al. (2015) divided the geology of North-Western Ghana into various domains. Thus the Wa-Lawra belt, the Koudougou-Tumu domain, the Bole-Bulenga domain, the Julie belt and the Bole-Nangodi belt.

The E-W oriented Julie belt is located in the central portion of North-Western Ghana (Fig. 1). Bounded to the north of the Julie belt is the Koudougou-Tumu domain and to the south by the Bole-Bulenga domain and to the east, the Bole-Nangodi belt. Bounded to the west of the Koudougou-Tumu domain is the Wa-Lawra belt.

The Wa-Lawra belt is further divided into the eastern and western halves by the crustal scale Jirapa shear zone which usually exhibits sinistral characteristics (Fig. 1). The eastern half is composed of mainly 2139 ± 2 Ma (detrital zircon ages) metamorphosed sedimentary rocks (volcanosediments, greywackes, shales) and early syn-tectonic 2212 ± 1 Ma (Sakyi et al., 2014) and 2153 ± 4 Ma (Agyei Duodu et al., 2009) granitoids. These rocks have been intruded by the 2104 ± 1 Ma late kinematic granitoids (Agyei

Duodu et al., 2009; Baratoux et al., 2011; Block et al., 2015). The rocks in the eastern half has experienced up to green schist metamorphism (Block et al., 2015). The western half is composed of the 2187 ± 3 Ma mainly high grade gneisses and granitoid (Agyei Duodu et al., 2009). These rocks here have been metamorphosed up to amphibolite facies.

The boundary between the Wa-Lawra belt and the Koudougou-Tumu domain is marked by the Jang fault (Block et al., 2015). The Koudougou-Tumu domain is composed of mainly of the 2162 ± 1 Ma to 2134 ± 1 Ma gneisses and gabbro, which has been intruded by the 2128 Ma late porphyritic granites (Agyei Duodu et al., 2009).

The Julie belt is composed of low grade basalts, silicic volcanosediments and granitoids mostly with tonalitic affinities (Amponsah et al., 2015). Dating done on the silicic volcanosediments showed that some of the rocks crystallized at 2129 ± 7 Ma (Block et al., 2015). This indicates that some part of the belt formed at least at 2130 Ma. The foliation in volcanosediments and granitoids within this fault shows a stretching lineation plunging down-dip and towards higher grade rocks (Block et al., 2015).

The Bole-Bulenga terrane is composed of high grade metamorphic rock termed as Buki gneisses by De Kock et al. (2011). According to Block et al. (2015), the Bole-Bulenga terrane is composed of paragneisses and metabasites usually migmatitic in nature. These rocks have been intruded by orthogneisses with crystallization ages between 2195 Ma and 2135 Ma.

Bounded to the south of the Bole-Bulenga terrane and east of the Julie belt is the Bole-Nangodi belt. Their boundary is marked by the NE-SW trending crustal scale Bole-Nangodi shear zones. This belt is composed of volcanoclastic rocks, greywackes, shales, granites, granitoids and gneisses with crystallization ages between 2196 ± 1 Ma and 2118 ± 3 Ma (Agyei Duodu et al., 2009; De Kock et al., 2011).

Structurally, De Kock et al. (2011) proposed an initial short lived pre-Eburnean event which occurred between 2160 Ma and 2150 Ma in North-Western Ghana. This deformational event is associated with plutonic emplacement and basin contraction. D1 is characterized by shortening and mostly marked by thrust faulting (Baratoux et al., 2011). S1 penetrative metamorphic foliation observed within this deformation event is evidenced within the high grade and low grade rocks in the Bole-Bulenga terrane and Julie belt respectively. D2 is marked by N-S-directed extension which is characterized by extensional shear zones along the northern and southern margins (acting as transition zones with greenstone belts) of the Bole-Bulenga domain (Block et al., 2015).

Recent investigations performed by Block et al. (2015) in the North-Western parts of Ghana highlighted the presence of large scale (>50 km wide) migmatitic complexes in the Bole-Bulenga terrane formed at ca. 2.13 Ga. They are associated with medium-pressure amphibolite facies rocks that are very similar to those observed by Ganne et al. (2011) in the thermal aureoles of granitic plutons in Burkina Faso, Senegal and Niger. They reveal a clockwise P-T-t path, melting at pressure over 10.0 kbar, then followed by decompression and heating to peak temperature of 750 °C at 5–8 kbar.

Ganne et al. (2014) proposed that a relatively homogeneous temperature profile existed at ca. 2.15–2.10 Ga, characterized by a moderate temperature gradient of 20–30 °C/km (that does not correspond to a hot orogeny) (Chardon et al., 2009). Accordingly, a partially molten zone would have formed at a depth of 25 km in the crust, fuelled by progressive burial and heating of felsic material. Once mixed in the lower crust, these melts could have been partially redistributed towards the upper crust, contributing to gravitational instabilities in the middle crust. They proposed that exhumation of this partially molten material, characterized by strong lateral metamorphic gradients, was mainly controlled by simultaneous

Table 1

Model parameters common to all experiments. $^*\rho_{\text{fault}}$, $^*\Delta T$ and $^*\varphi$ indicate the values that change according to different models.

Parameter	Symbol	Value-units
Thickness	H_{upper}	20 km
	H_{lower}	10 km
	$^*\rho_{\text{upper}}$	2800 kg/m ³
Density	ρ_{lower}	3000 kg/m ³
	$^*\rho_{\text{fault}}$	2600 kg/m ³
Dislocation creep power law pre-exponential factor	A	MPa ⁻ⁿ /s
Dislocation creep power law exponent	n	–
Power law creep activation energy	Q	kJ/mol
Temperature gradient	$^*\Delta T$	20 °C/km
Gas constant	R	8.314 J mol ⁻¹ K ⁻¹
Heat capacity	C_p	1000 J/kg K
Thermal diffusivity	γ	m ² /s
Thermal expansion	λ	K ⁻¹
Gravitational acceleration	g	9.81 m/s ²
Friction angle	$^*\varphi$	2.5–36.5°
Cohesion for Drucker–Prager	σ_c	1–20 MPa
Viscosity limit	η	1e+20 < η < 1e+23 Pa s

Table 2

Rheological properties of crustal layers. The non-Newtonian power law is used for the upper and lower crusts, whereas we employ a constant viscosity for fault zones, yielding a viscosity contrast of about 1/1000 compared to upper crust portions (Malservisi et al., 2003).

Layer	A (MPa ⁻ⁿ /s)	n	Q (kJ/mol)
Upper crust	2.0×10^{-4}	3.4	260
Lower crust	1.3×10^{-3}	2.4	219
Fault		1×10^{20} Pa s	

folding/shortening and gravitational instabilities in the juvenile crust, with the exception of North-Western Ghana where this partially molten material was extruded into the upper crust. It has been blocked and ceased at around 15 km depth in the crust, we might call retention zones, perhaps related to the presence of a competent overlying upper crust (Ganne et al., 2014; Vigneresse and Clemens, 2000).

3. Numerical method and model setup

The mechanical problem is modelled using the numerical code Underworld (Moresi et al., 2003, 2007), which can simulate visco-plastic rheologies in a three-dimensional cartesian geometry. Underworld uses a Lagrangian particle-in-cell finite element scheme which has been extensively used in geological modelling (Lemiale et al., 2008; Mason et al., 2010; Moresi and Mühlhaus, 2006; OzBench et al., 2008; Zlotnik et al., 2013). The governing equations of momentum (1), mass (approximately incompressible materials) (2) and energy (3) conservation are expressed as follows (Moresi et al., 2003, 2007; De Smet et al., 1998):

$$\frac{\partial \sigma_{ij}}{\partial x_j} = \rho g_i \quad (1)$$

$$\nabla \cdot u = 0 \quad (2)$$

$$\rho C_p \frac{DT}{Dt} + (u \cdot \nabla)T = \frac{\partial}{\partial x_i} \left(\frac{k_i \partial T}{\partial x_i} \right) + \rho H \quad (3)$$

where σ is the Cauchy stress tensor, u is the velocity, and ρ is the density (which depends on material composition), g is the gravitational acceleration, x_i are the spatial coordinates, k_i is the thermal conductivity and is calculated by the equation $k_i = \gamma \rho C_p$, $\gamma = 10^{-6}$ m²/s is the thermal diffusivity, C_p is the heat capacity at constant pressure and H is the radiogenic heat production per unit mass.

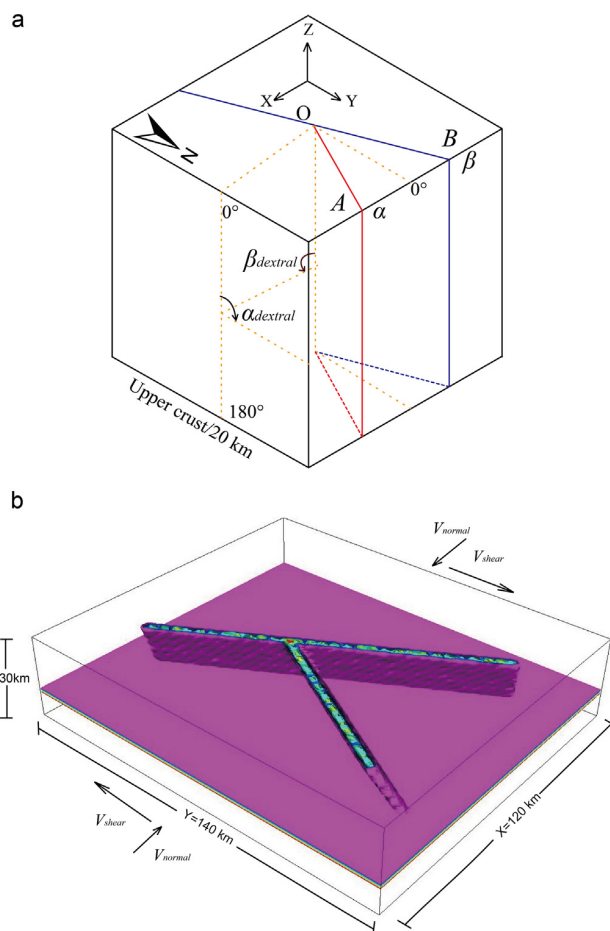


Fig. 2. Schematic geometry and boundary conditions. The domain is 140 km long (Y direction), 120 km wide (X direction) and 30 km thick (Z direction), and contains two neighbouring faults in the upper crust. In figure (a), planes A and B in red and dark blue represent fault A and fault B. The faults' intersection is referred to as point O. In figure (b), the purple plane represents the interface between the upper and lower crust. Boundary conditions are displayed with black arrows. Compressional velocities (V_{normal}) are applied normal to YZ section (East–West direction), whereas simple shear (V_{shear}) is simulated along these YZ borders. The base of the model is fixed, while the surface is set either to free, free-slip or free-remeshing surface boundary conditions. Four angles (α , β , α_{dextral} , β_{dextral}) are used to describe faults' orientations. The angles α , β represent the azimuth of the fault planes. The angles α_{dextral} , β_{dextral} are counted clockwise around the azimuth direction of the fault expressed between N0 and 180°. In all cases, α is fixed to 30° (as in figure (b)). (For interpretation of the references to colour in this figure legend, the reader is referred to the web version of the article.)

The depth dependent Drucker–Prager yield criterion (Eq. (4)) is used to describe the solid yield behaviour of the crust, in which P is the local pressure. φ is the effective friction angle and σ_p is the effective cohesion, by allowing for strain-weakening of materials (Moresi and Mühlhaus, 2006)

$$\tau_{\text{yield}} = P \cdot \tan \varphi + \sigma_p \quad (4)$$

Rock deformation is temperature sensitive and at higher temperatures they preferentially deform by dislocation creep, commonly described by a temperature-dependent non-Newtonian power law viscosity (e.g. Ranalli, 1995 and references therein):

$$\eta_m = 0.25 \cdot (0.75A)^{-(1/n)} \cdot \dot{\epsilon}^{((1/n)-1)} \cdot \exp(Q/nRT) \quad (5)$$

where $\dot{\epsilon}$ is the second invariant of the strain rate, Q is the activation energy, R is the universal gas constant, A is a pre-exponential constant, and n is a power law exponent.

Table 3

Parameters for each model, varying with respect to the reference value (model 1-1).

Exp#	Boundary condition	α	β	$\alpha_{dextral}$	$\beta_{dextral}$	Surface boundary condition	Friction of upper crust	Density contrast ($\rho_{upper} - \rho_{fault}$)
1-1	Compression	30	330	150	30	Remesh	30	200
1-1-1	Compression	30	330	150	30	Free	30	200
1-1-2	Compression	30	330	150	30	Free-slip	30	200
1-2	Compression	30	330	150	30	Remesh	30	100
1-3	Compression	30	330	150	30	Remesh	30	50
1-4	Compression	30	330	150	30	Remesh	30	0
1-5	Compression	30	330	150	30	Remesh	30	400
2-2	Compression	30	330	30	150	Remesh	30	200
2-3	Compression	30	330	30	30	Remesh	30	200
2-4	Compression	30	330	60	150	Remesh	30	200
2-5	Compression	30	315	120	30	Remesh	30	200
2-5-1	Compression	30	315	120	0	Remesh	30	200
2-5-2	Compression	30	315	120	150	Remesh	30	200
2-6	Compression	30	330	60	30	Remesh	30	200
2-7	Compression	30	330	120	30	Remesh	30	200
2-8	Compression	30	330	150	30	Remesh	20	200
2-9	Compression	30	330	150	30	Remesh	10	200
2-10	Compression	30	330	150	150	Remesh	30	200
2-11	Compression	30	330	120	150	Remesh	30	200
2-12	Compression	30	330	150	30	Remesh	15	200
S-1	Simple shear	30	330	150	30	Remesh	30	200
S-2-4	Simple shear	30	330	60	150	Remesh	20	200
S-5	Simple shear	30	330	0	30	Remesh	30	200
S-5-1	Simple shear	30	330	0	30	Remesh	20	200
S-5-2	Simple shear	30	330	0	30	Remesh	10	200
S-2-5	Simple shear	30	315	120	30	Remesh	20	200
S-2-6	Simple shear	30	330	60	30	Remesh	20	200
S-2-7	Simple shear	30	330	60	30	Free	20	200
S-2-8	Simple shear	30	330	60	30	Free-slip	20	200
S-2-9	Simple shear	30	330	120	30	Remesh	20	200
V-5	Simple shear	30	330	0	0	Remesh	20	200
V-C	Compression	30	330	0	0	Remesh	20	200

With progressive loading, elementary stresses increase. We note $\tau = \sqrt{(1/2)\tau_{ij}\tau_{ij}}$ the square root of the second invariant of the stress tensor. When τ is less than the yield stress τ_{yield} , the viscosity remains equal to the material viscosity $\eta = \eta_m$. However, when τ equals yield stress τ_{yield} , the additional plastic deformation is accounted for through reducing the viscosity to an effective viscosity:

$$\eta = \frac{\tau_{yield}}{2\dot{\epsilon}} \quad \text{for } \tau = \tau_{yield} \quad (6)$$

The rheological parameters for the non-Newtonian power-law are given in Table 2.

For the initial thermal conditions, we fixed a temperature $T = 20^\circ\text{C}$ at the top surface ($Z = 30\text{ km}$) and $T = 620^\circ\text{C}$ at the bottom of the computational domain ($Z = 0$), assuming a reference temperature gradient of 20°C/km . Other physical and thermal properties are given in Table 1.

The model domain is composed of a 20 km thick upper crust and a 10 km thick lower crust. In the upper crust, two neighbouring faults A and B (20 km thick) are defined with specific orientations ($\alpha, \alpha_{dextral}, \beta, \beta_{dextral}$). The schematic model is given in Fig. 2. The size of the domain is 140 km long (Y direction), 120 km wide (X direction) and 30 km thick (Z direction), and is modelled at a resolution of $2\text{ km} \times 2\text{ km} \times 1\text{ km}$. We use a random initial particle layout with 30 particles in each cell, and record their positions and other fields' variables at each computing step. All experiments described below were run at similar resolution on an Altix ICE 8200, 2.8 GHz, and 8 Mb per processor cluster.

Four possible conditions to simulate surface: (1) a free surface (Arnold et al., 2001; González et al., 2008; Hall et al., 2003; Schellart, 2008), (2) a sticky air-layer (viscosity set to $\sim 10^{19}\text{ Pa s}$; density set to 1 kg/m^3) overlying the surface to stop particles from escaping from the computing domain (Burov and Gerya, 2014; Gerya and Stöckhert, 2005; Gerya et al., 2008; Ueda et al., 2012) (3) a free-slip surface (Eberle et al., 2002; Mason et al., 2010; OzBench et al., 2008;

Schellart et al., 2010; Stegman et al., 2006; Zlotnik et al., 2013) or (4) a free remeshing surface (Foryan and Rasmussen, 1989; Koshizuka et al., 1998; Moresi et al., 2003; Shyy et al., 2012). We tested the option (1), (3) and (4) in this study. A free surface is completely free, without constraining horizontal and vertical velocities, but within codes such as Underworld, passive markers (particles) are lost with their stored historical data when they escape from the computational domain. The model also needs to refill with new particles in cells that become empty. A free-slip surface in turn does not allow for vertical motion and therefore over constrains this boundary. A free re-meshing surface as the one we have implemented here is one that couples a free surface with a re-meshing technique (Moresi et al., 2003), and which can carry the particles (passive markers) out of the ranges of the old mesh. Their history is stored into a new mesh according to their vertical velocities. We update/re-generate and deform the Eulerian mesh at every solution step. Particles and nodes carry various data used for outputs and subsequent step calculations. The particles located near the surface of the computing domain tend to escape when they store an upward velocity. The outline of the mesh is thus re-meshed and moved to ensure that these escaping particles remain inside the computational domain. Thanks to this procedure, the model can better model topographic evolution under various external boundary conditions, in compression (see case 1-1, case 1-1-1 and case 1-1-2 in Table 3) and simple shear (cases S-2-6, S-2-7, and S-2-8 depicted in Table 3).

In this paper, we test compressional (21 models) and simple shear with periodic boundary conditions (11 models, see the configurations given in Table 3) applied from each YZ wall side, applied at a rate of 5 mm/year respectively for about 4.5 Ma (shortening: 45 km) and 19 Ma (bulk shear strain $\gamma = 1.5$).

4. Results

A total of 32 models have been constructed to test the influence of various orientations of the pre-existing faults on the distribution

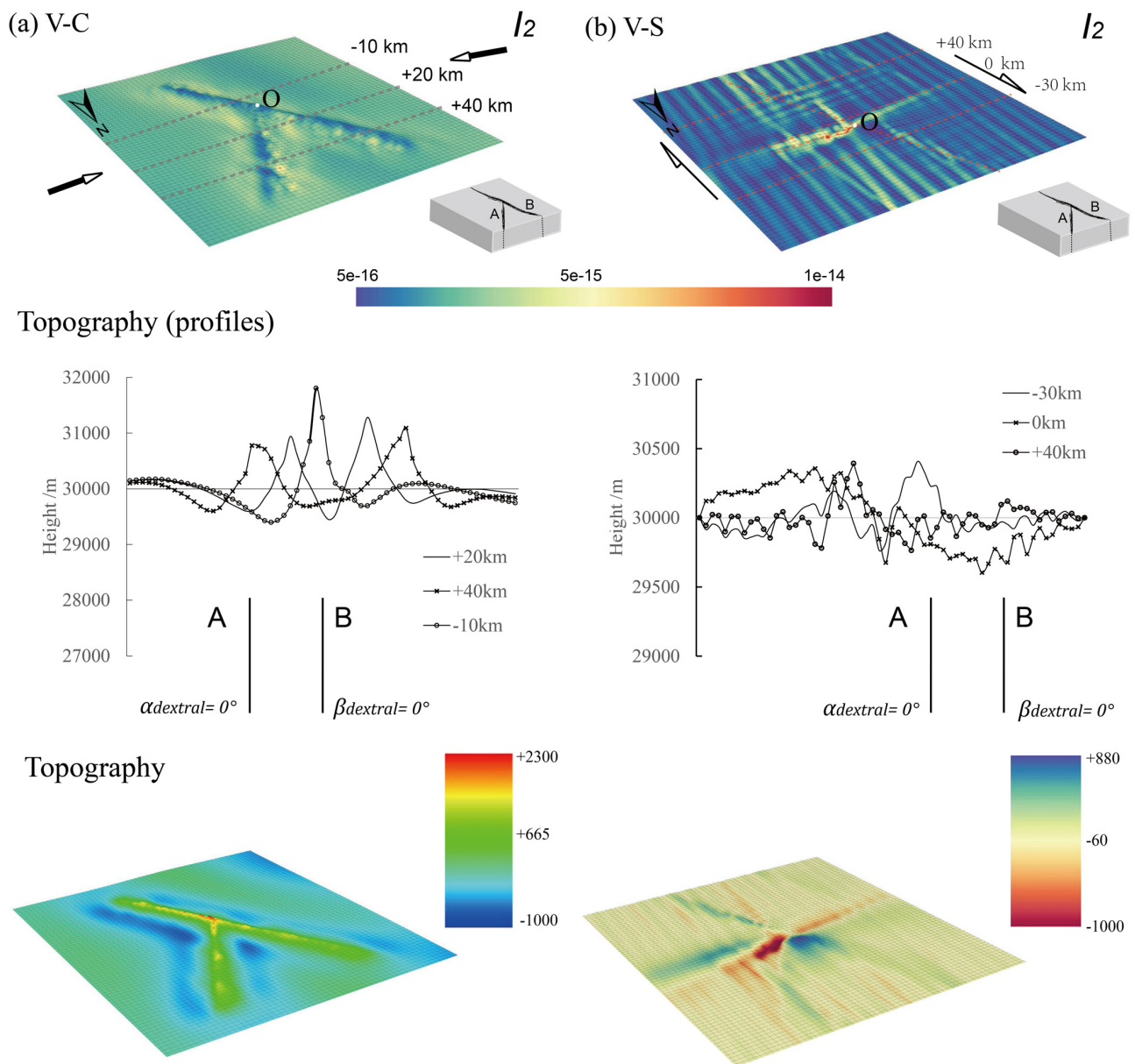


Fig. 3. Contour plots of the second (I_2 , s^{-1} , first row) invariants of strain rate and topographic profiles (second and third rows). For boundary conditions in compression (a) and simple shear (b). The intersection point of both faults is marked as point O in Fig. 2a. Topographic profiles of case V-C are displayed at $Y = +20$ km, $Y = +40$ km and $Y = -10$ km, at $Y = -30$ km, $Y = 0$ km and $Y = +40$ km for case V-S, which are indicated by dashed lines in the first row.

of localized deformation and topographic evolution. The parameters are all listed in Table 3.

4.1. Influence of faults orientations

Firstly, we test the simplest system of two vertical faults under compressional (case V-C) and simple shear (case V-S) boundary conditions. The results under compressional boundary conditions are displayed in Fig. 3a, and show that deformation is evenly distributed along faults. Relief at the top surface of the model is approximately symmetrical along profiles at $Y = 20$ km and $Y = 40$ km, and reaches a maximum height of about 2 km along profile $Y = -10$ km when only fault B is present. When both faults are present, the highest relief reaches about 2300 m close to the faults intersection

zone (point O, $Y = 0$). Maximum subsidence occurs along the south segment of fault B and in between both faults (about 500 m).

For the case V-S under simple shear boundary conditions (Fig. 3b), fault A which has an unfavourable orientation to the shearing direction will rotate synchronously to accommodate shear strain. The relief reaches a maximum height of 880 m and subsidence attains about -800 m around the intersection zone.

In Figs. 4–6, the results indicate that the angle of orientations of the pre-existing faults $\alpha_{dextral}$, $\beta_{dextral}$ controls the distribution of strain and relief. For experiments 2-6 and 2-4 in compression, the dip of fault A ($\alpha_{dextral} = 60^\circ$) is double that of fault B ($\beta_{dextral} = 30^\circ/150^\circ$), and deformation mostly focuses on the foot-wall of fault A, and less along fault B (Figs. 4a and 5a). The topographic profile of fault B in Fig. 4a with $\beta_{dextral} = 30^\circ$ shows

Please cite this article in press as: Feng, X., et al., 3-D numerical modelling of the influence of pre-existing faults and boundary conditions on the distribution of deformation: Example of North-Western Ghana. Precambrian Res. (2015), <http://dx.doi.org/10.1016/j.precamres.2015.06.006>

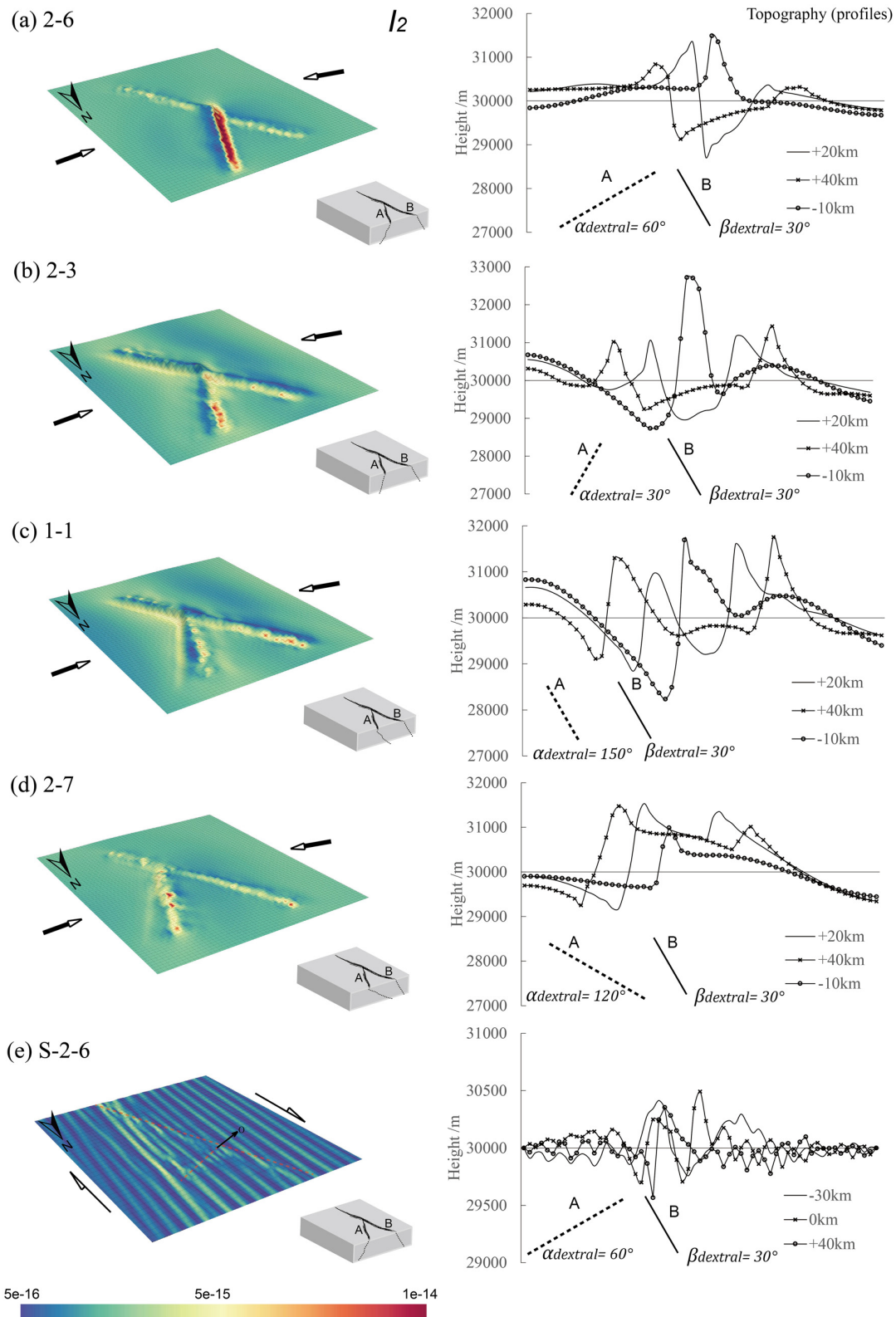


Fig. 4. The second (I_2 , s^{-1} , left column) invariants of strain rate and topography (right column) when using different fault A orientations at $\alpha_{dextral} = 30^\circ$, 60° , 120° , and 150° respectively (Fig. 2), fixing $\beta_{dextral}$ to 30° . In figure (a)–(d), compressional boundary conditions are applied. In figure (e), simple shear boundary conditions are applied. Topographic profiles using the free-remeshing surface boundary condition with legend displayed in Fig. 3. The dashed and solid lines labelled A and B in the right column represent the orientations of fault A and B, respectively. For other model details including model names and parameters, see details in Tables 1–3.

Please cite this article in press as: Feng, X., et al., 3-D numerical modelling of the influence of pre-existing faults and boundary conditions on the distribution of deformation: Example of North-Western Ghana. Precambrian Res. (2015), <http://dx.doi.org/10.1016/j.precamres.2015.06.006>

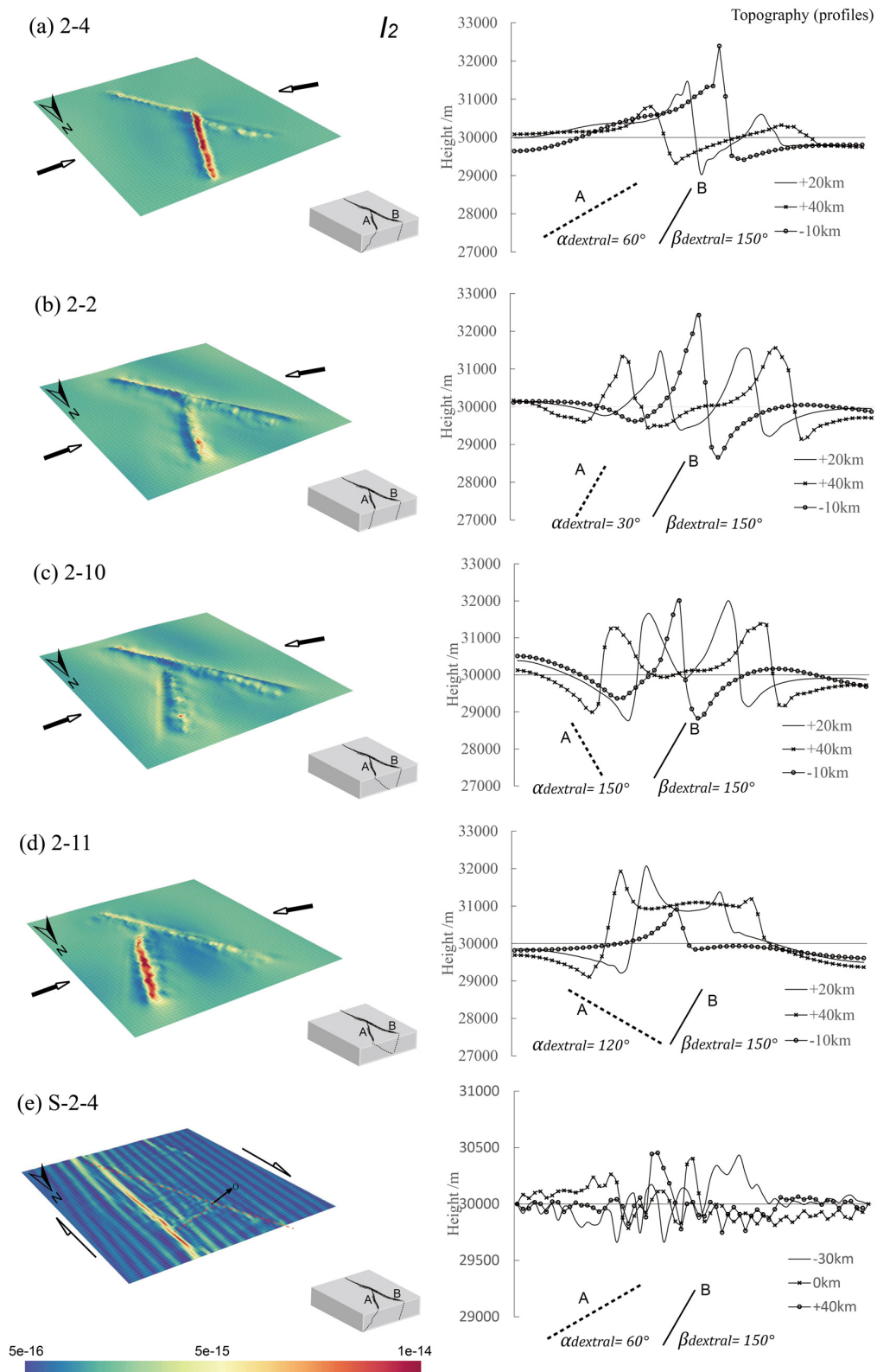


Fig. 5. The second (I_2 , s^{-1} , left column) invariants of strain rate when using different fault A orientations at $\alpha_{dextral} = 30^\circ, 60^\circ, 120^\circ$, and 150° respectively (Fig. 2), fixing $\beta_{dextral}$ to 150° compared to Fig. 4. In figure (a)–(d), compressional boundary conditions are applied. In figure (e), simple shear boundary conditions are applied. The right column shows topographic profiles using the free-remeshing surface boundary condition. Legends for topographic profiles are same as Figs. 3 and 4.

Please cite this article in press as: Feng, X., et al., 3-D numerical modelling of the influence of pre-existing faults and boundary conditions on the distribution of deformation: Example of North-Western Ghana. Precambrian Res. (2015), <http://dx.doi.org/10.1016/j.precamres.2015.06.006>

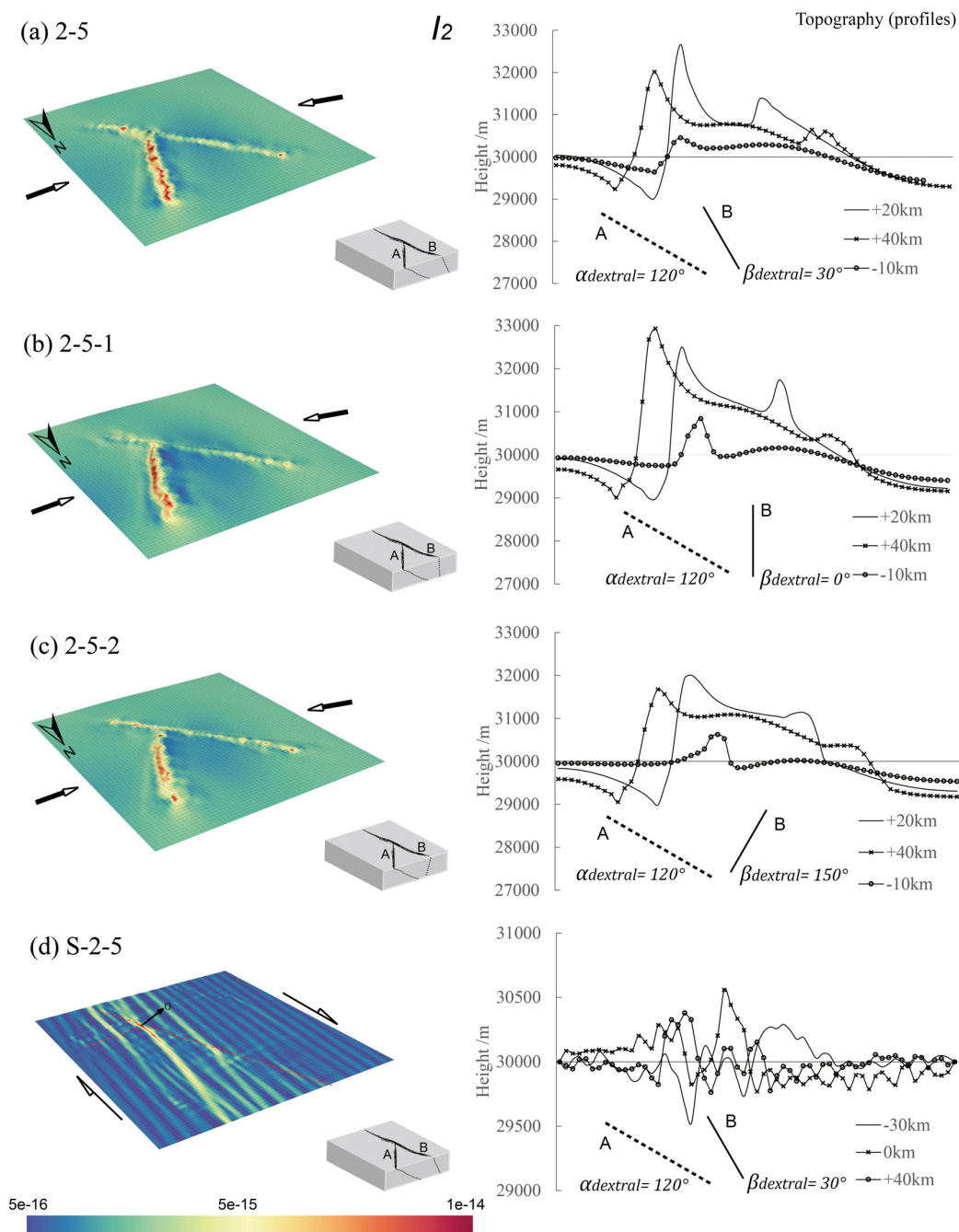


Fig. 6. The second (I_2 , s^{-1} , left column) invariants of strain rate and topography when varying the orientations of fault B $\beta_{dextral} = 0^\circ, 30^\circ$, and 150° (Fig. 2), and fixing $\alpha_{dextral}$ to 120° compared to Figs. 4 and 5. In figure (a)–(d) compressional boundary conditions are applied, whereas figure (e) displays the results for applied simple shear boundary conditions. See Fig. 3 and Table 3 for additional legend detail.

greater subsidence compared to Fig. 5a, where $\beta_{dextral} = 150^\circ$. Surface uplift primarily focuses in the hanging walls of fault A and B, and decreases when moving away from the intersection zone, as indicated by vertical sections along $Y = +20$ km, $+40$ km and -10 km in Fig. 3a.

Still in compression, we tested the dip of fault A (Figs. 4a–d and 5a–d), and varied $\alpha_{dextral}$ from 30° to 150° and $\beta_{dextral} = 30^\circ/150^\circ$, the variation in the tested dip resulted in different strain localization and topographic evolution. In case 2-7 ($\alpha_{dextral} = 120^\circ, \beta_{dextral} = 30^\circ$), subsidence occurs immediately above the intersection of fault A with the topography, and is located

adjacent to the main uplifting topography, which exceeds 1 km in height at a distance of about 10 km away from the southern side of the intersected zone. The orientation of fault A ($\alpha_{dextral}$) influences the subsidence associated with fault B, as shown in Fig. 5 by cases 2-4, 2-2, 2-10 and 2-11 ($\beta_{dextral} = 150^\circ$). The models produce a roughly symmetric topography when dips $\alpha_{dextral}$ and $\beta_{dextral}$ are identical, e.g., cases 2-3 and 2-10. Maximum subsidence of -1.5 km occurs in cases 1-1, where faults dip become parallel ($\alpha_{dextral} = 150^\circ$ and $\beta_{dextral} = 30^\circ$).

Note that in all these experiments, the negative segment (southern segment of point O, in Fig. 2a) contains only fault B. This

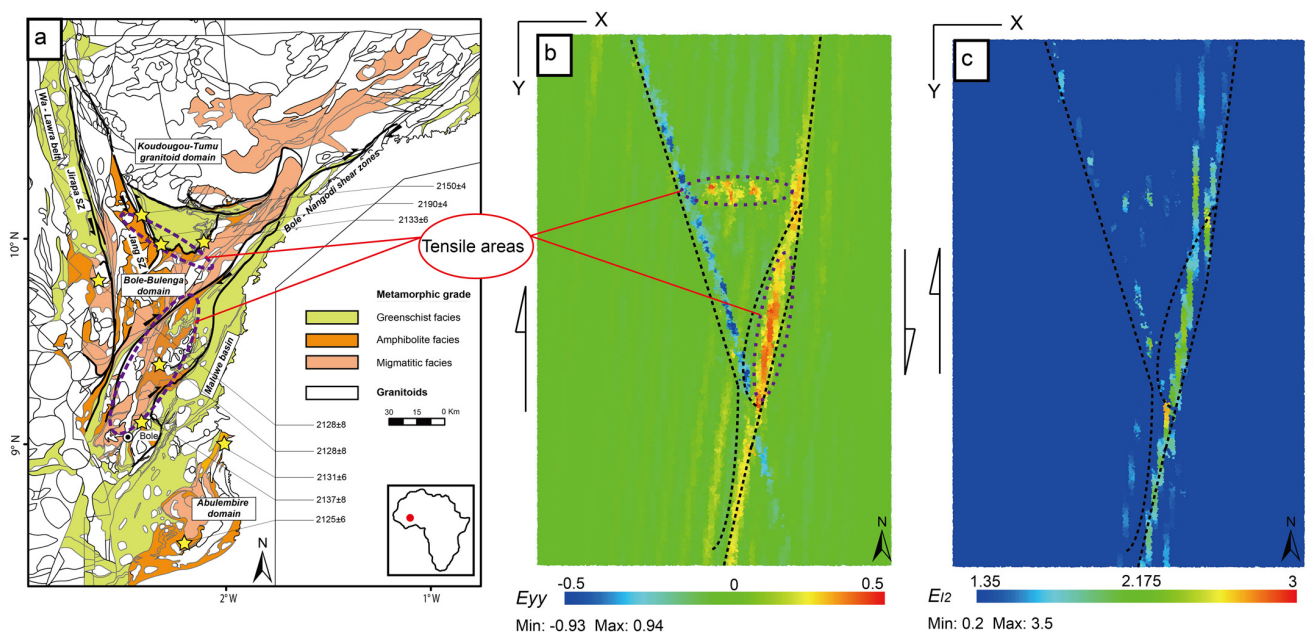


Fig. 7. (a) Metamorphic map of North-Western Ghana in the West African Craton and radiometric ages, modified from Block et al. (2015) and Baratoux et al. (2011). (b) The accumulation (E_{yy}) of strain rate component ϵ_{yy} , which is used as a proxy to indicate the finite strain zones (tensile and compressional areas) under simple shear boundary conditions. The dashed lines bound the major deformed regions. (c) The accumulation (E_{I_2}) of the second invariant of the strain rate (I_2, s^{-1}). Dotted ellipses are used to indicate the major N-S tensile domains in the study area (figure (a)) by Block et al., 2015 and numerical results in the model (figure (b)). (For interpretation of the references to colour in the text, the reader is referred to the web version of the article.)

motivated another series of comparisons (Fig. 6), in which fault A's orientation is set fixed and equal to $\alpha_{dextral} = 120^\circ$, while fault B's orientation $\beta_{dextral}$ were varied at $0^\circ, 30^\circ$ and 150° . The resulting models indicate that surface uplift decreases with increasing $\beta_{dextral}$, with maximum height reaching about 3000 m at the faults' intersection zone (point O). In contrast, when the fault flips as for case $\beta_{dextral} > 90^\circ$, relief only reaches about 2000 m with uplift spatially distributed instead of being concentrated around point O.

Four cases in simple shear boundary conditions (Figs. 3b, 4e, 5e and 6d) are tested with variable dips and orientations similar to cases displayed in Figs. 3a, 4a, 5a and 6a. Angle $\alpha_{dextral}$ has a dominating role, with largest strain zones focusing in the internal domain in between both faults when $\alpha_{dextral} = 60^\circ$ (Figs. 4e and 5e). In turn, angle $\beta_{dextral}$ mainly influences the distribution of deformation and relief at the surface along fault B with the highest topographic point or relief reaching 500 m under simple shear (case S-2-6).

4.2. A strain pattern compatible to North-Western Ghana

Case S-2-6 produces a compatible strain pattern with field observation, characterized by two main structures bound the internal high strain domain. We have chosen to display the cumulated values over time (E_{yy} and E_{I_2}) of the strain rate component ϵ_{yy} in N-S direction and the second (I_2) invariant of the strain rate tensor respectively. This helps to identify domains in tensile (Figs. 7b and S1) and shear (Fig. 7c) for case S-2-6. E_{yy} values obtained, was within the interval $[-0.93, 0.94]$, and E_{I_2} ranged between the interval $[0.2, 3.5]$ over 19 Ma under simple shear boundary conditions. Tensile zones focus in the internal domain in between both faults and parallel to the eastern shearing direction ($E_{yy} > 0$, green to red). Compressional zones concentrate around the inherited fault B ($E_{yy} < 0$, green to blue). Shear zones ($E_{I_2} < 1.8$, light blue to red) focus along the inherited fault B and mainly overlap with the tensile areas (parallel to the eastern shearing direction, $E_{I_2} > 2$).

Supplementary Fig. S1 related to this article can be found, in the online version, at <http://dx.doi.org/10.1016/j.precamres.2015.06.006>

The angle ψ (Fig. 8) between the external shearing orientations and the misoriented fault A increases with time (rotating about 60° over 19 Ma, indicated by the grey lines with red arrows in Fig. 8b). The oriented fault B rotates about 15° over 19 Ma (indicated by the dotted black line with blue arrow in Fig. 8b).

4.3. Influences of rock density and host rock friction

Here we use a reference model case 1-1 (under compression, $\alpha_{dextral} = 150^\circ$ and $\beta_{dextral} = 30^\circ$, Fig. 4c). Figs. 9 and 10 show that a more resistant surrounding host rock causes greater localized deformation and higher elevations along faults A and B. Cases 2-12 and 2-9 with lower host rock friction (thus closer to the internal faults friction) generate four new shear bands rooting at the base of the model domain, nearly independent from the pre-existing faults. As expected, the shear bands angle increases towards 45° with decreasing rock friction (e.g. Lemiale et al., 2008). We also document the influence of host rock friction under simple shear boundary conditions (case S-5, S-5-1 and S-5-2). These tests illustrate how a smaller contrast in friction between internal (faults) and external (host) domains tends to destroy the initial geometry and perhaps even the continuity (e.g. coherency) of pre-existing fault systems, relating with the effects of the Drucker-Prager yield criterion and lithostatic pressure.

Density variations do not play a primary role in building topography compared to the effect of host rock friction at the scale of a crustal system. When increasing by 200 kg/m^3 the host rock density, topographic height respectively increases by 200 m and 300 m at the highest uplifted point at the intersection of faults A and B (point O). Fig. 10 shows that using a friction angle 30° or 20° produce a similar height (elliptic domain in light green). While when setting a host rock friction angle to 20° and 10° (respectively in blue and light red ellipses), topography height drops by about 1200 m. In

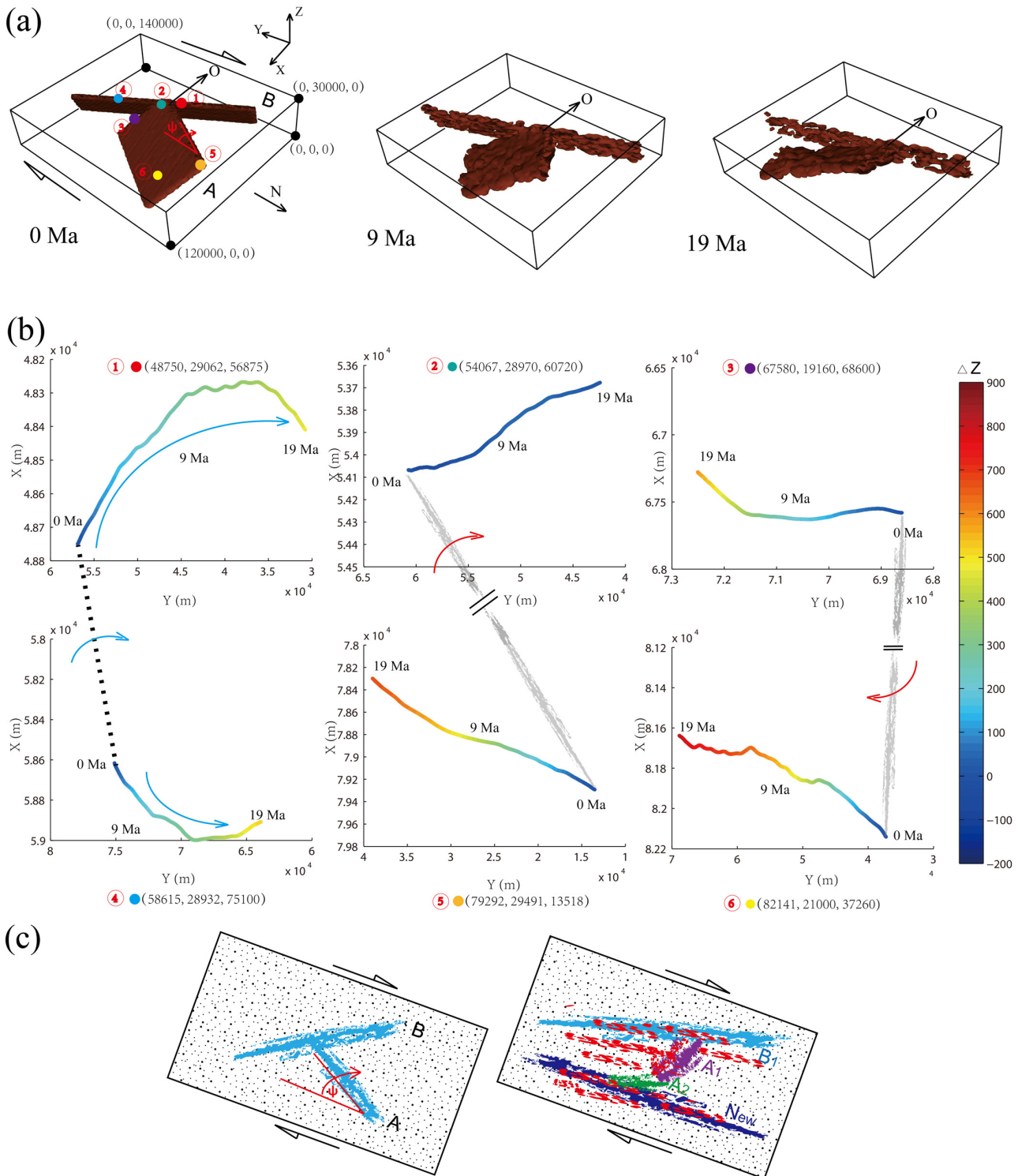


Fig. 8. Analysis of crustal rocks motion under simple shear boundary conditions (case S-2-6). (a) The evolution of faults geometries at 0 Ma, 9 Ma, and 19 Ma. (b) Coordinates of six representative points, initial positions are displayed by a filled colour circle in (figure (a)). Red and blue circles display passive markers (particles) located along fault B (near surface), while green, orange, purple and yellow circles are particles located in fault A. Red and blue arrows sketch the main trends of faults through time. The light grey and dotted lines represent the initial position of fault A and B (joining markers), indicating fault rotation through time. The colour bar for lines in figure (b) represents the uplifted trajectory (ΔZ) of these particles. (c) Sketch showing the evolution of faults geometries. The red dots sketch the possible channels of the upwelling molten material (Figs. 7, 8 and S1). (For interpretation of the references to colour in this figure legend, the reader is referred to the web version of the article.)

Please cite this article in press as: Feng, X., et al., 3-D numerical modelling of the influence of pre-existing faults and boundary conditions on the distribution of deformation: Example of North-Western Ghana. Precambrian Res. (2015), <http://dx.doi.org/10.1016/j.precamres.2015.06.006>

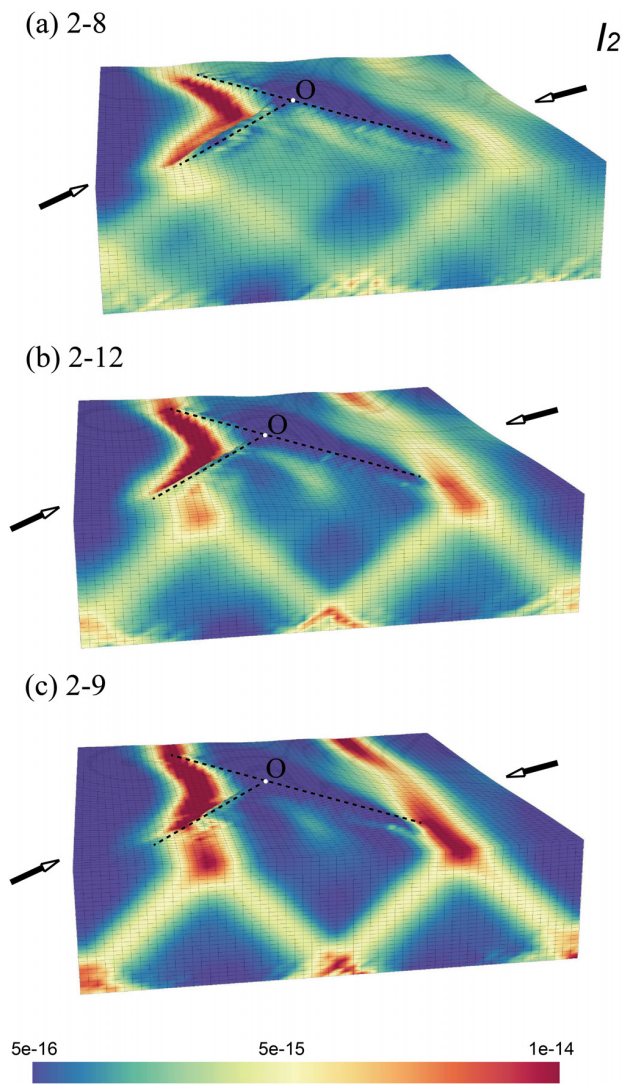


Fig. 9. The second (I_2, s^{-1}) invariants of strain rate influenced by host rock friction angle under compressional boundary conditions. To the difference with the reference model (case 1-1, friction angle = 30° ; Fig. 4c), upper crust friction angles of 20° , 15° , 10° (from top to bottom).

comparison, a variable density of the fault rocks tested in cases 1-2, 1-3, 1-4, produces roughly similar topography (slightly inclined lines in Fig. 10).

4.4. Effect of the top surface boundary condition

In Fig. 11 we have selected four near-surface passive markers (physical particles) to trace field data. The results show that the physical particles, when accounting for a free surface boundary condition, lose their historic data after about 12.5 Ma in simple shear, and after about 1–2 Ma in compression due to escaping (Fig. 11a and d). In the case with a top free-slip boundary condition, the uplifting process is greatly constrained by the fixed vertical motion at the surface (Fig. 11b and e). These tests show the advantages of implementing a free-remeshing surface boundary condition when modelling the evolution of Earth's surface using particle in cell (PIC) method.

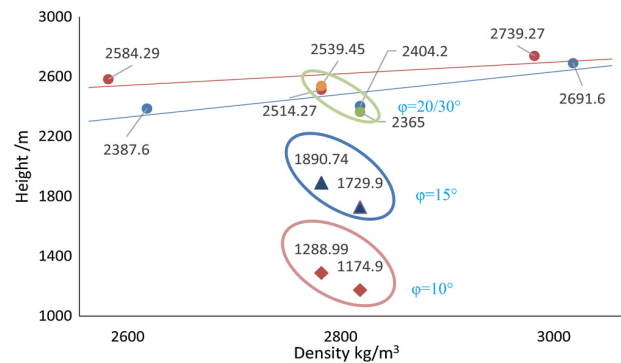


Fig. 10. Relief influenced by host rock friction angle and density contrast under compressional boundary conditions. A representative point at the faults' intersection (point O), as well as the maximum uplifted height of each model. Topographic height respectively increases by 200 m and 300 m at point O when increasing by 200 kg/m^3 the host rock density. Topographic height when using host rock friction angles of 30° or 20° produce similar heights (elliptic domain in light green in figure (d)). Setting a friction angle to 15° and 10° (respectively covered by the blue and light red ellipses), drops the topography by about 600 m. In all experiments, the contrast in density has a smaller effect on topography than the host rock friction angle. (For interpretation of the references to colour in this figure legend, the reader is referred to the web version of the article.)

5. Discussion

5.1. Strain and relief

The second invariant of the strain rate highlights shearing domains (greatest in red, in Figs. 3–7, 9 and 12), following several previous studies that have proposed that high-strain zones (shear and tension zones) could play a significant role in the draining of residual fluids from deeper retention zones at the strain rate of 10^{-15} s^{-1} to $\sim 10^{-10} \text{ s}^{-1}$ indicated by structure (Fernández and Castro, 1999), analogue (Benn et al., 1998) and numerical models (Cruden, 1998; Berdiel et al., 1997), feeding the upper crust with partially molten lower crustal rocks (Fossen and Tikoff, 1998; Neves et al., 1996, 2000; Pereira et al., 2013; Snoko et al., 1999; Weinberg et al., 2006).

Effective strength heterogeneities due to pre-existing faults trigger strain rotation and produce preferential sites for shear strain with respect to the surrounding rocks (e.g. Mair and Abe, 2008; Nieto-Samaniego, 1999). Our numerical models show that high-strain zones focus along and in between both faults A and B. The highest uplifted point is close to the intersection region which may focus fluids flow (Lawley et al., 2013), the peak fluid velocities increase 20–47% when the fault zone intersections enlarge apertures only about 1–8% (Person et al., 2012). Large localized deformation appears at the two faults' intersection zone and along faults using the free-remeshing surface boundary condition. Models with top-free boundary conditions lose a large amount of data due to particles escape out of the domain, whereas those with free-slip boundary conditions limit the accuracy in modelling surface processes because the vertical motion of the surface is prevented, in particular around high strain/uplifted zones (Fig. 11).

Our models, similarly to analogue models which yet assume different initial and boundary conditions, reproduce large block rotations at large amounts of strike-slip motion. Under compression, the host rock domain in between the two faults concentrate shear deformation relatively faster (about 2–5 times) than other domains (case 1-1, in Figs. 4 and 12), which is consistent with the description by Fossen and Tikoff (1998). They discussed the distribution of wrenching into shearing and vertical components, with both constriction and extrusion domains whatever the obliquity of the boundary conditions. In our models, large shearing

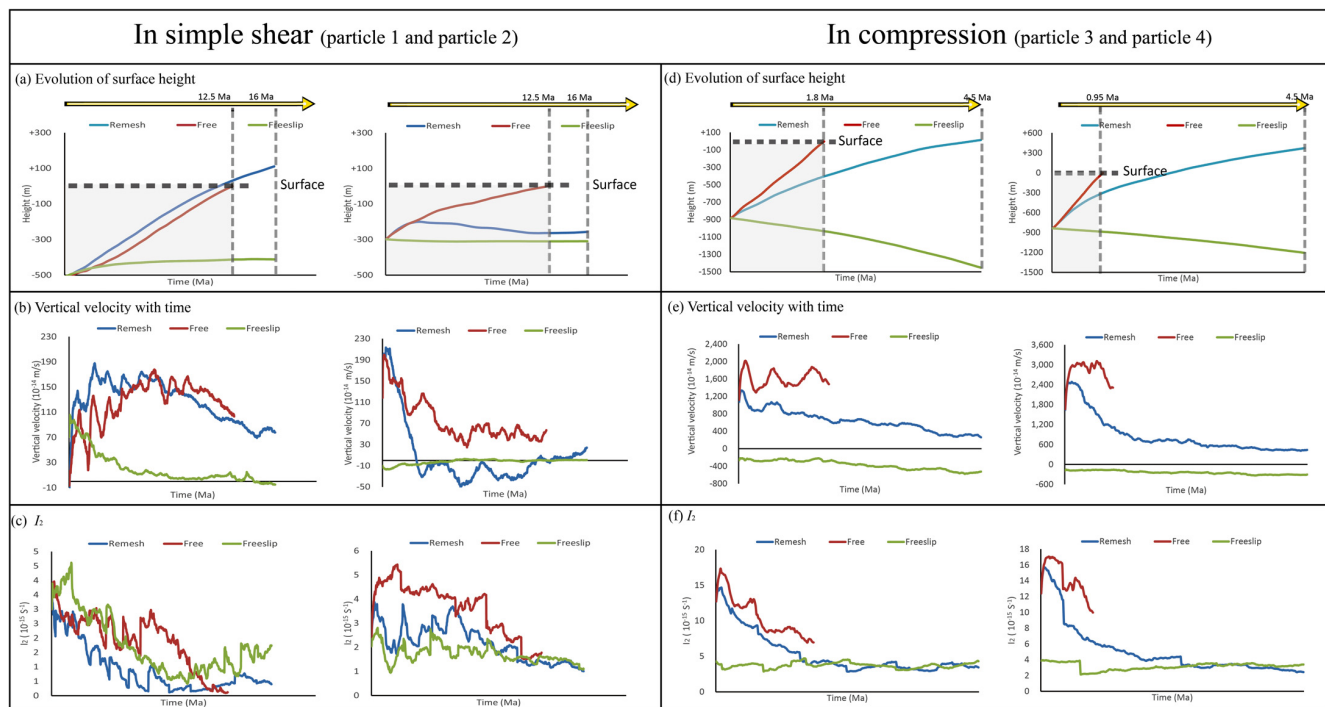


Fig. 11. Effect of top surface boundary conditions (cell particles) in case S-2-6 (left column: simple shear) and case 1-1 (right column: compression) by recording properties of tracers when using a free re-meshing surface, free and free-slip top surface boundary conditions, respectively, see Table 3 for details. Four near-surface particles were selected to trace data (surface height in figure (a) and (d), vertical velocity in figure (b) and (e) and the second invariant of strain rate I_2 in figure (c) and (f)) through time. Their coordinates (Figs. 2 and 8a) in metres are (X, Z, Y): particle 1 (79,292, 29,491, 13,518), particle 2 (73,352, 29,701, 99,471), particle 3 (96,320, 29,115, 28,924), and particle 4 (76,560, 29,163, 93,712). Physical particles under free surface boundary conditions lose their historic data after about 12.5 Ma in simple shear (particle 1 and particle 2) and after about 1.0–2.0 Ma in compression (particle 3 and particle 4) due to their escaping from the mesh domain. For models under free-slip top boundary conditions, surface uplift is over constrained by the imposed 0 vertical motion condition (figure (b) and figure (e)).

deformations develop along and in between faults at depth, which may consequently act as favourable areas to channel molten material from the lower crust and upwelling into the upper crust (Fig. 12) (Rosenberg and Handy, 2000; Katz et al., 2006; Koyi et al., 2013; Lawley et al., 2013; Mourgues et al., 2012). In addition, heterogeneous shearing zones evolving with time at depth would influence the geometry of pathway for channelling partially molten material. Based on our numerical results, we have sketched the evolving deformation and rotation (towards the vertical line) process in compression (Fig. 12b).

For models under simple shear boundary conditions (Figs. 3b, 4e, 5e and 6d), pre-existing faults mainly accommodate strain distribution, as long as they are not too radically misoriented with respect to the external shearing conditions, such as fault B in Fig. 2. When faults are radically misoriented, such as fault A in Fig. 2, they tend to rotate with the overall strain (and stress) field and synchronously accommodate less strain than optimally oriented faults. The noise of simple shear models occurs because the sample boundary is never perfectly flat (as in the real world situation) due to numerical fluctuations in the particle locations, and to a mild interference effect between the array of particles and the underlying grid (Moresi et al., 2001).

Relief is controlled by the rock hardness, homogeneity, external boundary conditions, mantle convection and the geometry of faults systems (Amadei and Stephansson, 1997; Bois et al., 2012; Brown and Scholz, 1985; Brown et al., 1986; Moucha and Forte, 2011). A recent numerical model developed by Braun et al. (2014), showed that rock density also plays an important role in shaping relief at the scale of the Earth. Considering pre-existing faults, structure development and topographic uplift have been shown to be controlled by the reactivation of pre-existing

faults under renewed boundary conditions associated with the rotation of principal forces (Ju et al., 2014; Tong et al., 2014; Wibberley et al., 2008). Testing different orientations show a direct relation with the distribution of uplifted areas. In comparison to the effect of the friction angle, the density contrast does not play a primary role in shaping the relief at the scale of the study area in these models (similarly to sand prism in analogue models, Graveleau et al., 2011, 2012 and references therein).

5.2. Reconstruction: model application to the Bole-Bulenga terrane

High-strain zones (tensile zones in Figs. 7b and S1, corresponding to N-S-directed extension, shear zones in Fig. 7c) mainly focus parallel to the eastern shearing direction and internal domains of both structures, which is similar with the distribution of high grade rock in the Bole-Bulenga terrane in Fig. 3a.

From deformation phase D1 (dominantly characterized by E-W to WNW-directed shortening, evidence from western Burkina Faso by Baratoux et al., 2011) to the subsequent D2 (characterized by N-S directed extension, Block et al., 2015), changes in the direction of principal forces must occur in the study area, resulting in a transition deformation phase for accumulating strain from far field boundary conditions. We suggest that our modelled pre-existing faults grew and developed during this short stage (case S-2-6). Fault A becomes a non-favoured location to accommodate strain from its eastern side (right-hand) as angle ψ increases through time. A large amount of localized deformation will tend to occur parallel to the eastern shearing direction (Figs. 7 and S1). This newly produced tensile and shear zone together with the favourably

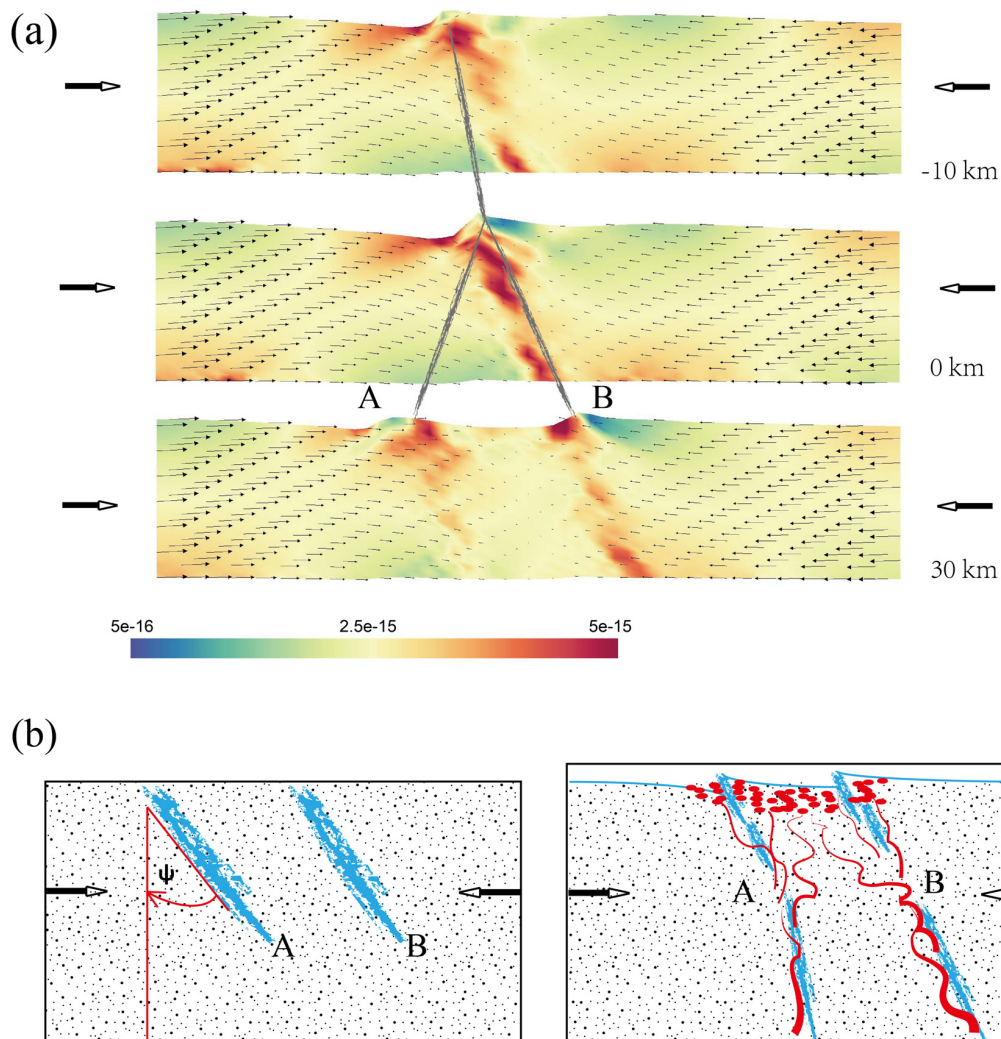


Fig. 12. Profiles of the second (I_2, s^{-1}) invariant of strain rate with velocity vectors (case 1-1) after about 4.5 Ma under compressional boundary conditions, and along selected profiles at $Y = -10$ km, 0 km and 30 km. The outlines of fault A and B are plotted in light grey above these sections. (e) Sketch showing the evolution of faults geometries (in blue) under compressional boundary conditions according to the numerical results. The angle ψ in figure (b) indicates that fault A rotates clockwise with time (towards vertical). The red dots and lines represent inferred favourable areas that would channel partially molten material/fluids from the lower crust and extrude in the upper crust. (For interpretation of the references to colour in this figure legend, the reader is referred to the web version of the article.)

oriented fault B form a compatible strain pattern with the field, characterized by two main high-strain zones with the bounded internal high-strain domain (A1 particles in purple, sketched in Fig. 8c). Fluids or partially molten materials may store in the deepest root of the pre-existing shear zones (Morand, 1992; Berdiel et al., 1997; D’Lemos et al., 1992; Pirajno, 2010). By taking fault

rotation into consideration, this suggests that they may passively migrate and rotate together (Fig. 8b) with the solid matrix under external boundary conditions through geological time, preferentially intruding into the upper crust, which can probably be interpreted as a potential contribution to exhumation in the study area.

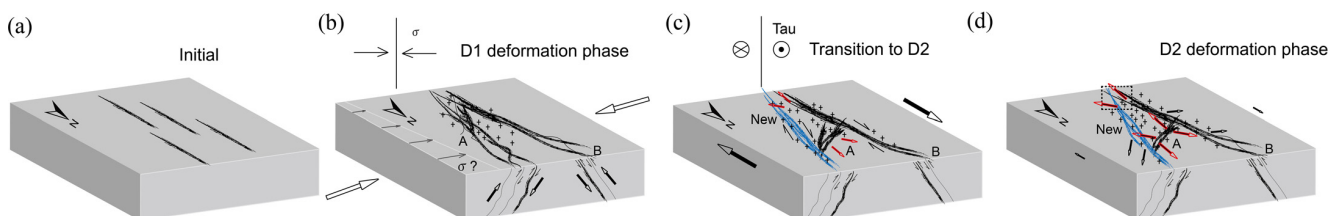


Fig. 13. Reconstruct and sketch the tectonic scenario during D1–D2 deformation phase for the study area. Figures (a)–(d) correspond to initial condition, D1 phase, late-D1 – early D2 transition phase and post-D2 phase, respectively (Block et al., 2015; Baratoux et al., 2011). The crosses in the figures represent weak domains, the red arrows represent the stretching direction according to the findings of Block et al. (2015). During its N-S-directed extensional process, the fault New in blue transects the internal domains, merges and intersects with the inherited fault B (indicated by the dotted box). (For interpretation of the references to colour in this figure legend, the reader is referred to the web version of the article.)

Please cite this article in press as: Feng, X., et al., 3-D numerical modelling of the influence of pre-existing faults and boundary conditions on the distribution of deformation: Example of North-Western Ghana. Precambrian Res. (2015), <http://dx.doi.org/10.1016/j.precamres.2015.06.006>

These cumulative high-strain zones may exhume part of partially molten materials from the lower crust during this transition stage. This is evident by the broad range of crystallization age in the field (in Fig. 7a, 2195 Ma to ~2125 Ma). More importantly, these high-strain zones make a significant contribution to offering preferred/potential zones (tensile and shearing zones) for the major exhumation event during the following post-D2 N-S stretching deformation phase. This theoretical model is consistent with the findings of Block et al. (2015). The P-T paths of samples collected in the Bole-Bulenga terrane indicate that during this late D2 deformation phase, high grade rocks were largely exhumed through the upper crust (>10 km) along the reverse, normal and transcurrent shear zones. According to the numerical results, we reconstruct and sketch the tectonic scenario during D1–D2 deformation phase (Baratoux et al., 2011; Block et al., 2015) for the study area in Fig. 13.

6. Limitations and perspectives

As discussed in Fossen and Tikoff (1998), it is difficult to track the evolution of strain orientations and magnitude within high-strain shear zones, because by definition shearing and constrictional components evolve in time, this becomes worse if the medium is heterogeneous and if deformation is partitioned. The numerical models presented here show how delicate it is to represent the long term evolution of strain components in numerical models, and we aim at improving these representations of strain components in future numerical approaches (e.g. strain ellipsoids as in Gerbault et al., 2002, or lines of maximum finite strain tensor as in Le Pourhiet et al., 2012), in order to better identify constrictional and tensile structural domains. We deliberately did not introduce any melting process in order to first understand the appropriate requirements on the mechanical state of the solid upper crust, although this is a focus of future studies. A number of analogue models have explored this question via significantly different experimental setups in which the modelled crustal layers are underlain by mechanical discontinuities such as strike-slip basement faults or basal weak zones (see reviews by Dooley and Schreurs, 2012, and references therein). It would be delicate but interesting to explore with analogue models the influence of pre-existing systems of weak fault zones as those we have considered here.

In addition, we mostly discussed the role of crustal strength variations and density contrast in producing relief at crustal scale using a viscous material (Cook and Royden, 2008). In the near future, in order to fulfil a completed topography, a crust-mantle coupled interaction should be taken into consideration for including dynamic topography.

7. Conclusion

In this paper, we use a three-dimensional thermo-mechanical model to explore the distribution of high-strain domains associated with pre-existing shear zones, by testing various orientations of a system of two strike-slip faults under pure shear as well as simple shear boundary conditions. We have also tested the effects of the friction angle and density contrast on the evolution of relief.

We reconstructed the evolution of deformation in North-Western Ghana around 2.20–2.10 Ga, the result shows that the Bole-Bulenga terrane may undergo a major transition in association with changes in the directions of principal forces from deformation phase D1 to D2. These cumulative high-strain zones may exhume part of partially molten materials from the lower crust during this stage, this can probably be evidenced by the broad range of crystallization age in the field (In Fig. 7a, 2195 Ma to ~2125 Ma). More

importantly, these high-strain zones make a significant contribution to offering preferred/potential zones (tensile and shearing zones) for the major exhumation event during the following post-D2 N-S stretching deformation phase.

The resulting model shows the formation of domains of tensile vs. compressional strain as well as shear zones, shows that the internal fault zones as well as the host rock in between the faults behave as relatively weaker domains than external regions.

The orientations of faults play an important role in controlling the evolution of relief. Greatest magnitudes of relief are obtained when faults dip parallel to each other and when they are inclined at depth, as they thus facilitate strain rotation and material transfer from depth. Relief increases by 200–300 m when the host rock density is increased by 200 kg/m³, whereas relief reduces by about 1200 m when decreasing the host rock friction from $\phi = 20^\circ$ to 10° at crustal scale.

Acknowledgements

This work was granted access to the high-performance computing resources of both the French supercomputing centre, CCRT of the French Nuclear Agency, under allocation #2014-046351 awarded by GENCI (Grand Equipement National de Calcul Intensif), and the regional computing centre, CALMIP in Toulouse, France, under allocation #P1403. We would like to thank Muriel Gerbault for kindly providing many helpful comments and discussions at different stages of the project. We also thank the development teams at the Victorian Partnership for Advanced Computing (VPAC) and Monash University for technical assistance with the software Underworld. We gratefully acknowledge John Mansour and Luke Mondy for improving a previous version of the code. Sylvain Block is warmly thanked for providing radiometric ages of some samples and comments. Figures are plotted using open source package Visit developed by the Lawrence Livermore National Laboratory. X.F. thanks the Chinese Scholarship Council for his PhD scholarship. Constructive and valuable comments by Laurent Ailleres, an anonymous reviewer and Editor Peter Cawood are gratefully acknowledged.

References

- Adjei, 1992. The significance of NE-SW parallel fractures in the West African Craton. In: *Proceedings of the International Conferences on Basement Tectonics*, vol. 7, pp. 49–60.
- Agyei Duodu, J., Loh, G.K., Boamah, K.O., 2009. Geological Map of Ghana 1:1 000 000. Geological Survey Department of Ghana (GSD).
- Alberti, M., 2010. Analysis of kinematic correlations in faults and focal mechanisms with GIS and Fortran programs. *Comput. Geosci.* 36, 186–194.
- Allibone, A., Teasdale, J., Cameron, G., Etheridge, M., Uttley, P., Soboh, A., Lamb, E., 2002. Timing and structural controls on gold mineralization at the Bogoso gold mine, Ghana, West Africa. *Econ. Geol.* 97, 949–969.
- Amadei, B., Stephansson, O., 1997. *Rock Stress and Its Measurement*. Springer Science Business Media.
- Amponsah, P.O., Salvi, S., Béziat, D., Jessell, M.W., Siebenaller, L., Baratoux, L., 2015. *Geology and geochemistry of the shear-hosted Julie deposit, NW Ghana*. *J. Afr. Earth Sci.* (in press).
- Arnold, J., Jacoby, W.R., Schmeling, H., Schott, B., 2001. Continental collision and the dynamic and thermal evolution of the Variscan orogenic crustal root – numerical models. *J. Geodyn.* 31, 273–291.
- Avé Lallemand, H.G., Guth, L.R., 1990. Role of extensional tectonics in exhumation of eclogites and blueschists in an oblique subduction setting: Northeastern Venezuela. *Geology* 18, 950–953.
- Avouac, J.P., Burov, E.B., 1996. Erosion as a driving mechanism of intracontinental mountain growth. *J. Geophys. Res.* 101, 17747–17769.
- Baratoux, L., Metelka, V., Naba, S., Jessell, M.W., Grégoire, M., Ganne, J., 2011. Juvenile Paleoproterozoic crust evolution during the Eburnean orogeny (<2.2–2.0 Ga), western Burkina Faso. *Precambrian Res.* 191, 18–45.
- Berdiel, T.R., Gapais, D., Brun, J.P., 1997. Granite intrusion along strike-slip zones in experiment and nature. *Am. J. Sci.* 297, 651–678.
- Benn, K., Odonne, F., De Saint Blanquat, M., 1998. Pluton emplacement during transpression in brittle crust: new views from analogue experiments. *Geology* 26, 1079–1082.

- Block, S., Ganne, J., Baratoux, L., Zeh, A., Parra-Avila, A.L., Jessell, M., Ailleres, L., Siebnaller, L., 2015. Petrological and geochronological constraints on lower crust exhumation during Paleoproterozoic (Eburnean) orogeny, NW Ghana, West African craton. *J. Metamorph. Geol.* 33, 463–494.
- Boher, M., Abouchami, W., Michard, A., Albarede, F., Arndt, N.T., 1992. Crustal growth in West Africa at 2.1 Ga. *J. Geophys. Res.* 97, 345–369.
- Bois, T., Bouissou, S., Jaboyedoff, M., 2012. Influence of structural heterogeneities and of large scale topography on imbricate gravitational rock slope failures: new insights from 3-D physical modeling and geomorphological analysis. *Tectonophysics* 526–529, 147–156.
- Braun, J., Beaumont, C., 1995. Three-dimensional numerical experiments of strain partitioning at oblique plate boundaries: implications for contrasting tectonic styles in the southern Coast Ranges, California, and central South Island, New Zealand. *J. Geophys. Res. Atmos.* 1001, 18059–18074.
- Braun, J., Yamato, P., 2010. Structural evolution of a three-dimensional, finite-width crustal wedge. *Tectonophysics* 484, 181–192.
- Braun, J., Simon-Labric, T., Murray, K.E., Reiners, P.W., 2014. Topographic relief driven by variations in surface rock density. *Nat. Geosci.* 7, 534–540.
- Brown, S.R., Scholz, C.H., 1985. Broad bandwidth study of the topography of natural rock surfaces. *J. Geophys. Res.* 90, 12575–12582.
- Brown, S.R., Kranz, R.L., Bonner, B.P., 1986. Correlation between the surfaces of natural rock joints. *Geophys. Res. Lett.* 13, 1430–1433.
- Buck, W.R., Lavier, L.L., 2001. A tale of two kinds of normal fault: the importance of strain weakening in fault development. *Geol. Soc. Lond. Spec. Publ.* 187, 289–303.
- Burov, E., Gerya, T., 2014. Asymmetric three-dimensional topography over mantle plumes. *Nature* 513, 85–89.
- Cagnard, F., Brun, J.P., Gapais, D., 2006a. Modes of thickening of analogue weak lithospheres. *Tectonophysics* 421, 145–160.
- Cagnard, F., Durrieu, N., Gapais, D., Brun, J.P., Ehlers, C., 2006b. Crustal thickening and lateral flow during compression of hot lithospheres, with particular reference to Precambrian times. *Terra Nova* 18, 72–78.
- Cagnard, F., Gapais, D., Barbey, P., 2007. Collision tectonics involving juvenile crust: the example of the southern Finnish Svecofennides. *Precambrian Res.* 154, 125–141.
- Castaing, C., Billa, M., Milési, J.P., Thiéblemont, D., Le Metour, J., Egal, E., Donzeau, M., (BRGM) (Coordonnateurs) et Guerrot, C., Cocherie, A., Chevremont, P., Tegey, M., Itard, Y., (BRGM), Zida, B., Ouédraogo, I., Koté, S., Kaboré B.E., Ouédraogo C., (ANTEA), 2003a. Notice explicative de la carte géologique et minière du Burkina Faso à 1/1 000 000.
- Castaing, C., Le Metour, J., Billa, M., (Coordonnateurs) Donzeau, M., Chevremont, P., Egal, E., (BRGM) Zida, B., Ouédraogo, I., Koté, S., Kaboré B.E., Ouédraogo C., (BUMIGEB), Thiéblemont, D., Guerrot, C., Cocherie, A., Tegey, M., Milési J.P., Itard, Y., (BRGM), 2003b. Carte géologique et minière du Burkina Faso à 1/1 000 000.
- Chardon, D., Gapais, D., Cagnard, F., 2009. Flow of ultra-hot orogens: a view from the Precambrian, clues for the Phanerozoic. *Tectonophysics* 477, 105–118.
- Condie, K.C., Kröner, A., 2008. When did plate tectonics begin? Evidence from the geologic record. *Geol. Soc. Am. Spec. Pap.* 440, 281–294.
- Cook, K.L., Royden, L.H., 2008. The role of crustal strength variations in shaping orogenic plateaus, with application to Tibet. *J. Geophys. Res.* 113, B8407.
- Cruden, A.R., 1998. On the emplacement of tabular granites. *J. Geol. Soc. Lond.* 155, 853–862.
- D'Alessio, M.A., Martel, S.J., 2004. Fault terminations and barriers to fault growth. *J. Struct. Geol.* 26, 1885–1896.
- De Kock, G.S., Armstrong, R.A., Siegfried, H.P., Thomas, E., 2011. Geochronology of the Birim Supergroup of the West African craton in the Wa-Bolè region of west-central Ghana: implications for the stratigraphic framework. *J. Afr. Earth Sci.* 59, 1–40.
- D'Lemos, R.S., Brown, M., Strachan, R.A., 1992. Granite magma generation, ascent and emplacement within a transpressional orogen. *J. Geol. Soc.* 149, 487–490.
- Dioh, E., Béziat, D., Debat, P., Grégoire, M., Ngom, P.M., 2006. Diversity of the Palaeoproterozoic granitoids of the Kédougou inlier (eastern Sénégal): petrographical and geochemical constraints. *J. Afr. Earth Sci.* 44, 351–371.
- Dooley, T.P., Schreurs, G., 2012. Analogue modelling of intraplate strike-slip tectonics: a review and new experimental results. *Tectonophysics* 574–575, 1–71.
- Doumbia, S., Poulet, A., Kouamelan, A., Peucat, J.J., Vidal, M., Delor, C., 1998. Petrogenesis of juvenile-type Birimian (Paleoproterozoic) granitoids in Central Côte-d'Ivoire, West Africa: geochemistry and geochronology. *Precambrian Res.* 123, 47–65.
- Eberle, M.A., Grasset, O., Sotin, C., 2002. A numerical study of the interaction between the mantle wedge, subducting slab, and overriding plate. *Phys. Earth Planet. Inter.* 134, 191–202.
- Egal, E., Thiéblemont, D., Lahondère, D., Guerrot, C., Costea, C.A., Iliescu, D., Delor, C., Goujou, J.C., Lafon, J.M., Tegey, M., Diaby, S., Kolié, P., 2002. Late Eburnean granitization and tectonics along the western and northwestern margin of the Archean Kénéma-Man domain (Guinea, West African Craton). *Precambrian Res.* 117, 57–84.
- Feybesse, J.L., Billa, M., Guerrot, C., Duguey, E., Lescuyer, J.L., Milesi, J.P., Bouchot, V., 2006. The paleoproterozoic Ghanaian province: geodynamic model and ore controls, including regional stress modeling. *Precambrian Res.* 149, 149–196.
- Fernández, C., Castro, A., 1999. Pluton accommodation at high strain rates in the upper continental crust. The example of the Central Extremadura batholith, Spain. *J. Struct. Geol.* 21, 1143–1149.
- Fialko, Y., Rivera, L., Kanamori, H., 2005. Estimate of differential stress in the upper crust from variations in topography and strike along the San Andreas Fault. *Geophys. J. Int.* 160, 527–532.
- Fialko, Y., 2006. Interseismic strain accumulation and the earthquake potential on the southern San Andreas fault system. *Nature* 441, 968–971.
- Fishwick, S., Bastow, I., 2011. Towards a better understanding of African topography: a review of passive-source seismic studies of the African crust and upper mantle. *Geol. Soc. Lond. Spec. Publ.* 357, 343–371.
- Foryan, J.M., Rasmussen, H., 1989. Numerical methods for viscous flows with moving boundaries. *Appl. Mech. Rev.* 42, 323–341.
- Fossen, H., Tikoff, B., 1998. Extended models of transpression and transtension, and application to tectonic settings. *Geol. Soc. Lond. Spec. Publ.* 135, 15–33.
- Ganne, J., De Andrade, V., Weinberg, R.F., Vidal, O., Dubacq, B., Kagambega, N., Naba, S., Baratoux, L., Jessell, M., Allibon, J., 2011. Modern-style plate subduction preserved in the Palaeoproterozoic West African craton. *Nat. Geosci.* 5, 60–65.
- Ganne, J., Gerbault, M., Block, S., 2014. Thermo-mechanical modeling of lower crust exhumation—constraints from the metamorphic record of the Palaeoproterozoic Eburnean orogeny, West African Craton. *Precambrian Res.* 243, 88–109.
- Gasquet, D., Barbey, P., MAdou, B., Paquette, J., 2003. Structure, Sr–Nd isotope geochemistry and zircon U–Pb geochronology of the granitoids of the Dabakala area (Côte d'Ivoire): evidence for a 2.3 Ga crustal growth event in the Palaeoproterozoic of West Africa? *Precambrian Res.* 127, 329–354.
- Gerbault, M., Davey, F., Henrys, S., 2002. Three-dimensional lateral crustal thickening in continental oblique collision: an example from the Southern Alps, New Zealand. *Geophys. J. Int.* 150, 770–779.
- Gerbault, M., Henrys, S., Davey, F., 2003. Numerical models of lithospheric deformation forming the Southern Alps of New Zealand. *J. Geophys. Res.* 108 (B7), 2341, <http://dx.doi.org/10.1029/2001JB001716>
- Gerya, T., Stöckhert, B., 2005. Two-dimensional numerical modeling of tectonic and metamorphic histories at active continental margins. *Int. J. Earth Sci.* 95, 250–274.
- Gerya, T.V., Perchuk, L.L., Burg, J.-P., 2008. Transient hot channels: perpetrating and regurgitating ultrahigh-pressure, high-temperature crust–mantle associations in collision belts. *Lithos* 103, 236–256.
- Giger, S.B., Cox, S.F., Tenthorey, E., 2008. Slip localization and fault weakening as a consequence of fault gouge strengthening – insights from laboratory experiments. *Earth Planet Sci. Lett.* 276, 73–84.
- González, G., Gerbault, M., Martinod, J., Cembrano, J., Carrizo, D., Allmendinger, R., Espina, J., 2008. Crack formation on top of propagating reverse faults of the Chuculay Fault System, northern Chile: insights from field data and numerical modelling. *J. Struct. Geol.* 30, 791–808.
- Graveleau, F., Hirtz, J.E., Dominguez, S., Malavieille, J., 2011. A new experimental material for modeling relief dynamics and interactions between tectonics and surface processes. *Tectonophysics* 513, 68–87.
- Graveleau, F., Malavieille, J., Dominguez, S., 2012. Experimental modelling of orogenic wedges: a review. *Tectonophysics* 538, 1–66.
- Gupta, A., Scholz, C.H., 2000. A model of normal fault interaction based on observations and theory. *J. Struct. Geol.* 22, 865–879.
- Hall, C.E., Gurnis, M., Sdrolias, M., Lavier, L.L., Müller, R.D., 2003. Catastrophic initiation of subduction following forced convergence across fracture zones. *Earth Planet Sci. Lett.* 212, 15–30.
- Hansen, E.C., Newton, R.C., Janardhar, A.S., Lindenberg, S., 1995. Differentiation of Late Archean Crust in the Eastern Dharwar Craton, Krishnagiri–Salem Area, South India. *J. Geol.* 103, 629–651.
- Harcouët-Menou, V., Guillou-Frottier, L., Bonneville, A., Adler, P.M., Mourzenko, V., 2009. Hydrothermal convection in and around mineralized fault zones: insights from two- and three-dimensional numerical modeling applied to the Ashanti belt, Ghana. *Geofluids* 9, 116–137.
- Hirdes, W., Davis, D.W., Lüdtke, G., Konan, G., 1996. Two generations of Birimian (Paleoproterozoic) volcanic belts in northeastern Côte d'Ivoire (West Africa): consequences for the Birimian controversy. *Precambrian Res.* 80, 173–191.
- Imber, J., Tuckwell, G.W., Childs, C., Walsh, J.J., Manzocchi, T., Heath, A.E., Bonson, C.G., Strand, J., 2004. Three-dimensional distinct element modelling of relay growth and breaching along normal faults. *J. Struct. Geol.* 26, 1897–1911.
- Jagadeesh, S., Rai, S.S., 2008. Thickness, composition, and evolution of the Indian Precambrian crust inferred from broadband seismological measurements. *Precambrian Res.* 162, 4–15.
- Jessell, M.W., Amponsah, P.O., Baratoux, L., Asiedu, D.K., Loh, G.K., Ganne, J., 2012. Crustal-scale transcurrent shearing in the Paleoproterozoic Sefwi-Sunyani-Comoé region, West Africa. *Precambrian Res.* 212–213, 155–168.
- Jessell, M.W., Begg, G.C., Miller, M.S., 2015. The geophysical signatures of the West African Craton. *Precambrian Res.* (under review).
- Ju, W., Hou, G., Zhang, B., 2014. Insights into the damage zones in fault-bend folds from geomechanical models and field data. *Tectonophysics* 610, 182–194.
- Katz, R.F., Spiegelman, M., Holtzman, B., 2006. The dynamics of melt and shear localization in partially molten aggregates. *Nature* 442, 676–679.
- Koshizuka, S., Nobe, A., Oka, Y., 1998. Numerical analysis of breaking waves using the moving particle semi-implicit method. *Int. J. Numer. Methods Fluids* 26, 751–769.

Please cite this article in press as: Feng, X., et al., 3-D numerical modelling of the influence of pre-existing faults and boundary conditions on the distribution of deformation: Example of North-Western Ghana. *Precambrian Res.* (2015), <http://dx.doi.org/10.1016/j.precamres.2015.06.006>

- Koyi, H., Schmeling, H., Burchardt, S., Talbot, C., Mukherjee, S., Sjöström, H., Chemia, Z., 2013. Shear zones between rock units with no relative movement. *J. Struct. Geol.* 50, 82–90.
- Lawley, C., Imber, J., Selby, D., 2013. Structural controls on orogenic and mineralization during transpression: Lupa Goldfield, Southwestern Tanzania. *Econ. Geol.* 108, 1615–1640.
- Le Pourhiet, L., Huet, B., May, D.A., Labrousse, L., Jolivet, L., 2012. Kinematic interpretation of the 3D shapes of metamorphic core complexes. *Geochim. Geophys. Geosyst.* 13, Q09002, <http://dx.doi.org/10.1029/2012GC004271>
- Lebedev, S., Boonen, J., Trampert, J., 2009. Seismic structure of Precambrian lithosphere: new constraints from broad-band surface-wave dispersion. *Lithos* 109, 96–111.
- Leever, K.A., Gabrielsen, R.H., Sokoutis, D., Willingshofer, E., 2011. The effect of convergence angle on the kinematic evolution of strain partitioning in transpressional brittle wedges: insight from analog modeling and high-resolution digital image analysis. *Tectonics* 30, TC2013, <http://dx.doi.org/10.1029/2010TC002823>
- Ledru, P., Pons, J., Milési, J.P., Feybesse, J.L., Johan, V., 1991. Transcurrent tectonics and polycyclic evolution in the Lower Proterozoic of Senegal-Mali. *Precambrian Res.* 50, 337–354.
- Lemiale, V., Mühlhaus, H.-B., Moresi, L., Stafford, J., 2008. Shear banding analysis of plastic models formulated for incompressible viscous flows. *Phys. Earth Planet. Inter.* 171, 177–186.
- Lompo, M., 2009. Geodynamic evolution of the 2.25–2.0 Ga Palaeoproterozoic magmatic rocks in the Man-Leo Shield of the West African Craton. A model of subsidence of an oceanic plateau. *Geol. Soc. Lond. Spec. Publ.* 323, 231–254.
- Lompo, M., 2010. Paleoproterozoic structural evolution of the Man-Leo Shield (West Africa). Key structures for vertical to transcurrent tectonics. *J. Afr. Earth Sci.* 58, 19–36.
- Mair, K., Abe, S., 2008. 3D numerical simulations of fault gouge evolution during shear: grain size reduction and strain localization. *Earth Planet. Sci. Lett.* 274, 72–81.
- Mall, D.M., Chandrakala, K., Sudhir Kumar, A., Sarkar, D., 2012. Sub-crustal LVZ below Dharwar craton, India: an evidence for mantle metasomatism and tectonothermal activity in the Archean crust. *Precambrian Res.* 208–211, 161–173.
- Malservici, R., Gans, C., Furlong, K., 2003. Numerical modeling of strike-slip creeping faults and implications for the Hayward fault, California. *Tectonophysics* 361, 121–137.
- Marone, F., Van Der Meijde, M., Van Der Lee, S., Giardini, D., 2003. Joint inversion of local, regional and teleseismic data for crustal thickness in the Eurasia–Africa plate boundary region. *Geophys. J. Int.* 154, 499–514.
- Maruyama, S., Liou, J.G., Terabayashi, M., 1996. Blueschists and eclogites of the world and their exhumation. *Int. Geol. Rev.* 38, 485–594.
- Mason, W., Moresi, L., Betts, P.G., Miller, M.S., 2010. Three-dimensional numerical models of the influence of a buoyant oceanic plateau on subduction zones. *Tectonophysics* 483, 71–79.
- Middleton, T.A., Copley, A., 2013. Constraining fault friction by re-examining earthquake nodal plane dips. *Geophys. J. Int.* 196, 671–680.
- Morand, V.J., 1992. Pluton emplacement in a strike-slip fault zone: the Doctors Flat Pluton, Victoria, Australia. *J. Struct. Geol.* 14, 205–213.
- Moresi, L., Mühlhaus, H., Dufour, F., 2001. An overview of numerical methods for Earth simulations. In: *Exploration Geodynamics Chapman Conference* 19, pp. 113–119.
- Moresi, L., Dufour, F., Mühlhaus, H.B., 2003. A Lagrangian integration point finite element method for large deformation modeling of viscoelastic geomaterials. *J. Comput. Phys.* 184, 476–497.
- Moresi, L., Mühlhaus, H.B., 2006. Anisotropic viscous models of large-deformation Mohr–Coulomb failure. *Philos. Mag.* 86, 3287–3305.
- Moresi, L., Quenette, S., Lemiale, V., Mérieux, C., Appelbe, B., Mühlhaus, H., 2007. Computational approaches to studying non-linear dynamics of the crust and mantle. *Phys. Earth Planet. Inter.* 163, 69–82.
- Moucha, R., Forte, A.M., 2011. Changes in African topography driven by mantle convection. *Nat. Geosci.* 4, 707–712.
- Mourgues, R., Bureau, D., Bodet, L., Gay, A., Gressier, J.B., 2012. Formation of conical fractures in sedimentary basins: experiments involving pore fluids and implications for sandstone intrusion mechanisms. *Earth Planet. Sci. Lett.* 313–314, 67–78.
- Naylor, M., Mandl, G., Supesteijn, C.H., 1986. Fault geometries in basement-induced wrench faulting under different initial stress states. *J. Struct. Geol.* 8, 737–752.
- Neves, S.P., Vauchez, A., Archanjo, C.J., 1996. Shear zone-controlled magma emplacement or magma-assisted nucleation of shear zones? Insights from northeast Brazil. *Tectonophysics* 262, 349–364.
- Neves, S.P., Vauchez, A., Feraud, G., 2000. Tectono-thermal evolution, magma emplacement, and shear zone development in the Caruaru area (Borborema Province, NE Brazil). *Precambrian Res.* 99, 1–32.
- Nieto-Samaniego, Á.F., 1999. Stress, strain and fault patterns. *J. Struct. Geol.* 21, 1065–1070.
- Ota, T., Kaneko, Y., 2010. Blueschists, eclogites, and subduction zone tectonics: insights from a review of Late Miocene blueschists and eclogites, and related young high-pressure metamorphic rocks. *Gondwana Res.* 18, 167–188.
- OzBench, M., Regenauer-Lieb, K., Stegman, D.R., Morra, G., Farrington, R., Hale, A., May, D.A., Freeman, J., Bourgoin, L., Mühlhaus, H., Moresi, L., 2008. A model comparison study of large-scale mantle-lithosphere dynamics driven by subduction. *Phys. Earth Planet. Inter.* 171, 224–234.
- Pasyanos, M.E., Nyblade, A.A., 2007. A top to bottom lithospheric study of Africa and Arabia. *Tectonophysics* 444, 27–44.
- Pereira, M.F., Chichorro, M., Fernández, C., Silva, J.B., Matias, F.V., 2013. The role of strain localization in magma injection into a transtensional shear zone (Variscan belt, SW Iberia). *J. Geol. Soc.* 170, 93–105.
- Peltzer, G., Crampé, F., Hensley, S., Rosen, P., 2001. Transient strain accumulation and fault interaction in the Eastern California shear zone. *Geology* 29, 975–978.
- Person, M., Hofstra, A., Sweetkind, D., Stone, W., Cohen, D., Gable, C.W., Banerjee, A., 2012. Analytical and numerical models of hydrothermal fluid flow at fault intersections. *Geofluids* 12, 312–326.
- Pirajno, F., 2010. Intracontinental strike-slip faults, associated magmatism, mineral systems and mantle dynamics: examples from NW China and Altay-Sayan (Siberia). *J. Geodyn.* 50, 325–346.
- Ranalli, G., 1995. *Rheology of the Earth*. Springer Science & Business Media, pp. 413.
- Rey, P.F., Houseman, G., 2006. Lithospheric scale gravitational flow: the impact of body forces on orogenic processes from Archaean to Phanerozoic. *Geol. Soc. Lond. Spec. Publ.* 253, 153–167.
- Rice, J., 1993. Spatio-temporal complexity of slip on a fault. *J. Geophys. Res.* 98, 9885–9907.
- Rosenberg, C.L., Handy, M.R., 2000. Syntectonic melt pathways during simple shearing of a partially molten rock analogue (Norcamphor-Benzamide). *J. Geophys. Res.* 105, 3135–3149.
- Sakyi, P.A., Su, B.X., Anum, S., Kwayisi, D., Dampare, S.B., Anani, C.Y., Nude, P.M., 2014. New zircon U–Pb ages for erratic emplacement of 2213–2130 Ma Paleoproterozoic calc-alkaline I-type granitoid rocks in the Lawra Volcanic Belt of Northwestern Ghana, West Africa. *Precambrian Res.* 254, 149–168.
- Sanderson, D.J., Marchini, W.R.D., 1984. Transpression. *J. Struct. Geol.* 6, 449–458.
- Schellart, W.P., 2008. Kinematics and flow patterns in deep mantle and upper mantle subduction models: influence of the mantle depth and slab to mantle viscosity ratio. *Geochim. Geophys. Geosyst.* 9, Q03014, <http://dx.doi.org/10.1029/2007GC001656>
- Schellart, W., Stegman, D., Farrington, R., 2010. Cenozoic tectonics of western North America controlled by evolving width of Farallon slab. *Science* 80, 316–319.
- Scholz, C.H., 2007. *Fault mechanics*. Treatise Geophys. 6, 441–483.
- Seber, D., Sandvol, E., Sandvol, C., Brindisi, C., Barazangi, M., 2001. Crustal model for the Middle East and North Africa region: implications for the isostatic compensation mechanism. *Geophys. J. Int.* 147, 630–638.
- Shyy, W., Udaykumar, H.S., Rao, M.M., Smith, R.W., 2012. *Computational Fluid Dynamics with Moving Boundaries*. Taylor & Francis, Inc., Bristol, PA.
- Sibson, R.H., 1977. Fault rocks and fault mechanisms. *J. Geol. Soc.* 133, 191–213.
- Sibson, R.H., Xie, G.Y., 1998. Dip range for intracontinental reverse fault ruptures: truth not stranger than fiction? *Bull. Seismol. Soc. Am.* 88, 1014–1022.
- De Smet, J.H., Van Den Berg, A.P., Vlaar, N.J., 1998. Stability and growth of continental shields in mantle convection models including recurrent melt production. *Tectonophysics* 296, 15–29.
- Snoke, A.W., Kalakay, T.J., Quick, J.E., Sinigoi, S., 1999. Development of a deep-crustal shear zone in response to syntectonic intrusion of mafic magma into the lower crust, Ivrea-Verbano zone, Italy. *Earth Planet. Sci. Lett.* 166, 31–45.
- Stegman, D.R., Freeman, J., Schellart, W.P., Moresi, L., May, D., 2006. Influence of trench width on subduction hinge retreat rates in 3-D models of slab rollback. *Geochim. Geophys. Geosyst.* 7, Q03012, <http://dx.doi.org/10.1029/2005GC001056>
- Stern, R.J., 2007. When and how did plate tectonics begin? Theoretical and empirical considerations. *Chin. Sci. Bull.* 52, 578–591.
- Stern, R.J., 2008. Modern-style plate tectonics began in Neoproterozoic time: an alternative interpretation of Earth's tectonic history. *Geol. Soc. Am. Spec. Pap.* 440, 265–280.
- Tokam, A.P.K., Tabod, C.T., Nyblade, A.A., Julià, J., Wiens, D.A., Pasyanos, M.E., 2010. Structure of the crust beneath Cameroon, West Africa, from the joint inversion of Rayleigh wave group velocities and receiver functions. *Geophys. J. Int.* 183, 1061–1076.
- Tong, H., Koyi, H., Huang, S., Zhao, H., 2014. The effect of multiple pre-existing weaknesses on formation and evolution of faults in extended sandbox models. *Tectonophysics* 626, 197–212.
- Tranos, M.D., 2012. Slip preference on pre-existing faults: a guide tool for the separation of heterogeneous fault-slip data in extensional stress regimes. *Tectonophysics* 544–545, 60–74.
- Ueda, K., Gerya, T.V., Burg, J.P., 2012. Delamination in collisional orogens: thermo-mechanical modeling. *J. Geophys. Res.* 117, B08202, <http://dx.doi.org/10.1029/2012JB009144>
- Ueta, K., Tani, K., Kato, T., 2000. Computerized X-ray tomography analysis of three-dimensional fault geometries in basement-induced wrench faulting. *Eng. Geol.* 84, 233–246.
- Vidal, M., Delor, C., Poulet, A., Simeon, Y., Alric, G., 1996. Evolution géodynamique de l'Afrique de l'Ouest entre 2.2 Ga et 2 Ga; le style archéen des ceintures vertes et des ensembles sédimentaires birimiens du nord-est de la Côte-d'Ivoire. *Bull. Soc. Géol. Fr.* 167, 307–319.
- Vigneresses, J.L., Tikoff, B., 1999. Strain partitioning during partial melting and crystallizing felsic magmas. *Tectonophysics* 312, 117–132.
- Vigneresses, J.L., Clemens, J.D., 2000. Granitic magma ascent and emplacement: neither diapirism nor neutral buoyancy. *Geol. Soc. Lond. Spec. Publ.* 174, 1–19.

Please cite this article in press as: Feng, X., et al., 3-D numerical modelling of the influence of pre-existing faults and boundary conditions on the distribution of deformation: Example of North-Western Ghana. *Precambrian Res.* (2015), <http://dx.doi.org/10.1016/j.precamres.2015.06.006>

- Walsh, J.J., Childs, C., Imber, J., Manzocchi, T., Watterson, J., Nell, P.A.R., 2002. Strain localisation and population changes during fault system growth within the Inner Moray Firth, northern North Sea. *J. Struct. Geol.* 25, 307–315.
- Weinberg, R.F., Mark, G., Reichardt, H., 2006. Magma ponding in the Karakoram shear zone, Ladakh, NW India. *Geol. Soc. Am. Bull.* 121, 278–285.
- Wibberley, C.A.J., Yielding, G., Di Toro, G., 2008. Recent advances in the understanding of fault zone internal structure: a review. *Geol. Soc. Lond. Spec. Publ.* 299, 5–33.
- Xing, H.L., Makinouchi, A., Mora, P., 2007. Finite element modeling of interacting fault systems. *Phys. Earth Planet. Inter.* 163, 106–121.
- Zhang, Y., Gartrell, A., Underschlutz, J.R., Dewhurst, D.N., 2009. Numerical modelling of strain localisation and fluid flow during extensional fault reactivation: implications for hydrocarbon preservation. *J. Struct. Geol.* 31, 315–327.
- Zlotnik, S., Jiménez-Munt, I., Fernández, M., 2013. Coupled mantle dripping and lateral dragging controlling the lithosphere structure of the NW-Moroccan margin and the Atlas Mountains: a numerical experiment. *Lithos* 189, 16–27.

Appendix B

Julie structural measurement

S_{JL} structural measurement on the Julie Prospecting Licence			
Easting	Northing	Dip	Dip direction
597407	1115868	64	334
597418	1115746	29	029
597546	1115704	40	164
597547	1115746	44	165
597091	1115654	38	327
597139	1115691	40	338
596894	1115701	28	322
596924	1115909	42	338
596925	1115903	58	332
597034	1115826	34	334
596614	1115629	54	330
596627	1115771	72	324
596664	1115651	40	332
596671	1116004	23	330
596707	1115908	34	326
596709	1116039	45	022
596718	1115603	54	308
596756	1115760	47	332
596759	1116047	44	005
596784	1115565	44	322
596169	1115789	63	332
596172	1115942	42	004
596207	1115681	54	308
596209	1115681	54	308
596226	1116134	30	342
596226	1115955	42	318
596226	1115955	42	318
596276	1115886	38	334
596299	1116139	70	310
596358	1115697	57	310

596423	1115890	32	320
596449	1115926	49	338
596462	1115904	40	060
596503	1116184	37	358
596503	1116184	37	358
596507	1115595	26	320
596520	1116067	60	356
596524	1115901	42	338
596543	1116129	28	024
596562	1115924	40	322
596564	1115587	46	350
596571	1115619	33	300
596585	1115931	38	350
596025	1115903	58	332
596039	1115997	40	216
596058	1115885	40	340
596113	1115807	70	014
596156	1116038	62	300
596167	1115833	46	296
595885	1115957	34	340
597671	1115570	55	330
595646	1115954	44	335
593658	1115697	57	310
593027	1116309	45	348
593026	1116308	45	326
593012	1116313	60	16
593011	1116313.5	62	360
593008	1116315	52	005
593001	1116316	38	337
592979	1116333	56	004
592974	1116334	54	354
595068	1115954	45	341
595082	1115956	40	336
594871	1115936	33	018
594870	1115929	35	344
594870	1115925	40	351
594870	1115915	40	332

594407	1115894.5	20	094
595665	1115884	38	007
595666	1115884	32	356
595666	1115881	42	350
595664	1115879	25	016
595666	1115878	30	024
595651	1115853	40	356
596957	1115927	10	336
596979	1115902	36	012
596984	1115906	30	007
597002	1115961	31	345
595850	1115231	60	312
591304	1118531	58	339
591290	1118536	70	350
591362	1118539	61	350
591357	1118533	70	003
591955	1119870	59	320
591940	1119883	52	030
591801	1120125	69	350
591803	1120116	83	329
591752	1120101	59	006
591734	1120067	57	009
591957	1119869	65	326
591955	1119870	59	320
591940	1119883	52	030
592182	1120009	62	318
592483	1120007	80	324
592442	1120140	60	360
592447	1120142	64	350
592497	1120149	60	002
592210	1120088	73	348
592123	1120143	60	321
592922	1122475	53	052
592064	1122492	59	035
592003	1122557	55	015
591874	1122686	46	035
591882	1122680	51	025

591896	1122673	55	034
591906	1122667	73	025
591924	1122662	58	009
591958	1122634	78	013
591967	1122630	84	013
592006	1122645	75	033
592037	1122671	64	024
592029	1122677	38	044
592300	1120833	35	349
592305	1120830	32	004
592304	1120815	37	001
592111	1120656	62	025
592131	1120655	55	025
592138	1120655	69	020
592150	1120673	55	030
592177	1120677	68	012
592311	1120630	54	340
592331	1120633	60	005
592435	1120618	73	030
592442	1120613	64	042
592466	1120609	58	015
592341	1120624	56	045
592322	1120625	75	006
593058	1122610	48	033
593062	1122612	51	015
593067	1122608	45	006
593082	1122608	56	014
593096	1122605	56	001
593118	1122602	53	025
593104	1122593	50	005
593213	1121383	48	335
589137	1121492	50	340
589155	1121485	48	350
589205	1121462	59	010
589230	1121454	48	355
589000	1121514	45	355
588868	1121421	60	358

588865	1121420	61	350
588721	1121419	65	345
588709	1121420	55	345
588684	1121422	64	342
588661	1121414	67	342
589297	1121357	70	350
589308	1121346	40	325
589401	1121321	40	015
589364	1121197	20	055
589441	1121283	40	360
589471	1121253	40	260
589476	1121225	45	030
589432	1121458	40	350
589452	1121557	40	020
589386	1121573	35	015
589263	1121550	55	010
589229	1121525	60	360
589187	1121502	40	360
589181	1121568	60	355
589211	1121619	60	010
589547	1121548	40	360
589605	1121433	35	015
581683	1121431	40	010
589695	1121487	60	340
589637	1121461	80	340
589976	1121456	70	355
589874	1121451	60	020
589676	1121166	30	350
589635	1121094	40	015
589609	1121055	40	040
589565	1120985	60	360
589560	1120932	50	025
589649	1120893	65	330
589847	1120907	40	060
589943	1121299	50	350
589969	1121332	60	360
592153	1118523	66	005

592146	1118508	76	001
592117	1118523	48	000
592113	1118520	74	009
592099	1118519	60	003
592082	1118522	68	178
592080	1118521	66	177
592069	1118520	68	192
592066	1118522	78	012
592062	1118523	78	353
592030	1118528	60	000
591995	1118522	65	006
591973	1118519	66	005
591972	1118524	82	004
591916	1118531	70	020
591892	1118538	60	346
591874	1118541	70	029
591868	1118542	64	000
591451	1118546	74	018
591446	1118548	82	020
591440	1118549	72	004
591362	1118541	70	010
591351	1118539	63	004
591332	1118540	70	006
591325	1118536	74	016
591321	1118543	71	358
591309	1118539	78	012
591302	1118538	60	345
591301	1118539	61	359
591293	1118539	66	356
591214	1118531	82	116
591206	1118524	64	358
591205	1118522	74	018
589330	1121442	50	006
589320	1121441	48	340
589313	1121442	38	028
589313	1121441	46	012
589311	1121441	46	007

589303	1121447	56	013
589271	1121440	54	024
589225	1121450	34	360
589228	1121456	57	009
589174	1121477	50	009
589168	1121483	58	030
589170	1121483	51	040
589161	1121485	60	016
589159	1121485	58	013
589156	1121486	56	351
589123	1121495	62	358
589123	1121496	42	353
589112	1121506	36	006
589113	1121506	41	356
589159	1121465.5	50	352
589136	1121481	50	015
589112	1121498	32	002
589105	1121502	55	16
589115	1121477	52	360
589103	1121504	49	006
589094	1121510	62	006
589073	1121509	54	005
589069	1121515	61	24
589063	1121494	50	326
589155	1121446	68	018
589015	1121531	55	344
588972	1121527	63	353
588957	1121532	64	357
588946	1121531	70	343
588951	1121499	60	353
588973	1121446	48	346
588960	1121430	45	332
588977	1121485	42	314
589011	1121494	54	357
594810	1121001	45	015
594786	1121031	64	005
594803	1121060	55	010

594836	1120992	45	010
595704	1120956	66	335
596643	1121020	42	330
596710	1121035	52	330
596690	1121050	59	346
596690	1121051	67	005
596631	1121002	68	008
597047	1121046	74	002
597036	1121046	70	005
597092	1120879	63	012
597101	1120830	80	357
589000	1121515.5	52	002
589033	1121491	54	004
589062	1121447	64	353
589078	1121444	64	353
588769	1122683	55	360
588955	1122714	50	352
589338	1122592	60	186
588876	1122590	40	342
589070	1122484	52	306
587692	1122493	72	352
587692	1122493	34	104
588475	1121222	22	354
588486	1121234	28	354
588484	1121248	30	340
588603	1121220	55	358
588631	1121201	30	360
588651	1121210	65	009
588437	1121221	25	020
588450	1121225	34	267
588445	1121229	40	026
588442	1121236	32	335
588440	1121251	48	310
588446	1121281	15	025
588448	1121285	48	340
588449	1121294	50	344
588466	1121284	65	330

588463	1121278	60	352
588414	1121352	30	020
588390	1121404	55	334
588392	1121400	45	320
588397	1121403	68	320
588397	1121403	45	355
588403	1121407	50	322
588404	1121404	50	145
588408	1121400	50	326
588465	1121475	60	355
588478	1121373	60	340
588456	1121380	35	330
588434	1121407	50	340
588433	1121406	50	330
588432	1121432	50	335
588518	1121441	60	340
588510	1121438	50	330
588486	1121448	60	360
588468	1121434	70	338
588450	1121433	60	355
588418	1121450	45	350
588413	1121452	50	360
588415	1121460	55	346
588413	1121466	34	360
588393	1121510	40	338
588388	1121509	48	350
598540	1119436	52	015
598553	1119406	20	045
593213	1121380	58	045
596629	1120059	50	022
596618	1120064	50	016
596311	1120165	36	330
592901	1121121	58	340
592894	1121123	60	346
588130	1121978	70	060
588130	1121978	80	220
587867	1121770	72	196

587864	1121770	88	360
587847	1121782	66	010
587832	1121784	62	360
587788	1121794	86	026
587801	1121791	55	010
587758	1121786	70	040
587752	1121787	70	040
587551	1121901	60	020
587553	1121920	52	350
587550	1121923	46	347
587993	1122008	62	017
587910	1121255	84	350
587899	1121263	50	338
587890	1121260	65	352
587867	1121248	40	360

S_{J2} foliation in the Julie deposit

Latitudes	Longitude	Dip direction	Dip
10.089893	-2.036433	345	79
10.089012	-2.03666	340	80
10.095452	-2.036909	315	63
10.096067	-2.040944	305	70
10.114275	-2.0333	325	73
10.123374	-2.182434	97	72
10.139566	-2.184563	140	38
10.129643	-2.164411	104	60
10.135325	-2.163773	269	83
10.122661	-2.131377	283	44
10.129699	-2.13193	79	65
10.129699	-2.13193	284	89
10.138368	-2.127293	96	63
10.145649	-2.108368	89	89
10.168005	-2.171936	275	70
10.09855	-2.151461	112	72
10.092838	-2.134113	270	77
10.059948	-2.10938	110	80
10.064565	-2.090921	296	85
10.115387	-2.206236	100	46

Kunche deposit measurement

The coordinates associated with this data can be obtained from Azumah Resources Limited database

S_{K1} foliation measurement in Kunche

Hole_ID	Depth	Dip	Dip_Direction
KRCD378	123.08	80	247
KRCD378	124.86	85	243
KRCD378	125.95	79	245
KRCD378	127.04	77	252
KRCD378	128.9	77	256
KRCD378	130.07	77	263
KRCD378	151.4	44	232
KRCD409	153.2	78	274
KRCD409	158.9	82	280
KRCD409	165	84	268
KRCD409	186.6	22	268
KRCD450	138.7	60	213
KRCD450	147.7	59	222
KRCD454	115.34	88	228
KRCD454	119.35	86	249
KRCD454	124.66	48	318
KRCD454	126.63	31	335
KRCD454	128.41	48	286
KRCD454	131.15	47	288
KRCD454	141.4	75	258
KRCD454	141.6	88	261
KRCD454	148.23	68	273
KRCD454	150.62	80	228
KRCD454	161.54	72	232
KRCD456	142.51	84	232
KRCD456	151.77	80	260
KRCD456	157.81	66	260
KRCD456	160.09	88	262
KRCD456	162.91	86	241

KRCD456	165.22	79	272
KRCD456	166.45	78	254
KRCD456	169.23	88	241
KRCD475	142.17	85	270
KRCD475	142.48	87	278
KRCD475	144.38	76	244
KRCD475	144.7	78	232
KRCD475	146.25	70	294
KRCD475	147.5	88	268
KRCD475	150.05	84	233
KRCD475	153.42	88	258
KRCD475	157.35	88	246
KRCD475	159.15	78	270
KRCD475	178.3	78	266
KRCD475	179.18	75	268
KRCD475	183.44	85	266
KRCD475	184.19	84	264
KRCD475	184.9	87	265
KRCD475	185.9	86	255
KRCD475	186.78	87	228
KRCD475	187.78	86	264
KRCD475	188.72	88	224
KRCD475	194.95	87	280
KRCD475	195.5	88	284
KRCD555	209.96	84	240
KRCD555	210.5	82	241
KRCD555	210.7	81	241
KRCD555	212.93	64	214
KRCD555	224.5	84	240
KRCD555	226.4	72	238
KRCD555	227.13	70	241
KRCD555	229.74	76	235
KRCD555	238.56	68	259
KRCD555	240.37	72	255
KRCD555	265.06	80	250
KRCD555	267.11	62	254
KRCD555	267.3	74	254

KRCD562	266.16	86	267
KRCD562	267.4	82	267
KRCD566	151.05	78	244
KRCD566	177.16	87	301
KRCD566	179.95	78	231
KRCD567	138.15	82	278
KRCD567	140.57	86	278
KRCD567	168.501	74	264
KRCD567	168.801	80	272
KRCD567	169.851	72	256
KRCD567	170.7	78	238
KRCD567	171.221	82	250
KRCD567	172.5	68	248
KRCD574	87.52	73	244
KRCD574	92.63	74	240

S_{K3} measurements from Kunche

Hole_ID	Depth	Dip	Dip_Direction
KRCD299	184.09	73	186
KRCD455	165.84	70	178
KRCD456	170.43	70	347
KRCD456	204.54	60	358
KRCD456	215.64	75	345
KRCD534	188.2	50	160
KRCD534	190.72	60	152
KRCD534	191.26	58	160
KRCD560	187.6	40	354
KRCD563	159.34	76	158
BRCD039	124.25	75	190
BRCD039	126.35	35	195
BRCD039	145	60	195
BRCD079	108.5	65	130
KRCD164	137.5	50	180
KRCD299	146.08	84	147
KRCD555	192.4	80	156
KRCD555	195.3	80	140

Bepkong deposit measurement

S _{B1} foliation for the Bepkong deposit							
Hole_ID	Depth	Dip	Dip_Direction	Hole_ID	Depth	Dip	Dip_Direction
BRCD078	214.58	22	265	BRCD203	180.44	70	104
BRCD078	215.01	15	205	BRCD203	181.42	64	113
BRCD078	215.67	8	60	BRCD203	185.62	64	109
BRCD079	126.9	76	95	BRCD203	187.36	66	106
BRCD078	219.73	56	210	BRCD203	203.43	60	296
BRCD079	86.2	75	90	BRCD203	207.73	60	205
BRCD079	86.35	76	90	BRCD203	214.7	62	280
BRCD079	100.05	85	205	BRCD203	234.93	69	295
BRCD079	101.7	86	235	BRCD207	98	68	105
BRCD079	103.5	65	230	BRCD207	100.05	76	272
BRCD079	105.4	85	255	BRCD207	101	72	277
BRCD079	128.35	85	92	BRCD207	136	64	210
BRCD079	108.8	85	85	BRCD207	136.8	66	305
BRCD079	120.95	87	310	BRCD207	137.27	58	202
BRCD079	121.8	85	290	BRCD207	143	78	90
BRCD079	122.4	76	315	BRCD207	144	62	198
BRCD079	130.52	87	255	BRCD207	144.56	62	214
BRCD079	131.35	85	250	BRCD207	170.8	78	96
BRCD079	132	78	270	BRCD207	171.5	77	100
BRCD079	147.3	88	248	BRCD207	173.6	72	96
BRCD079	147.4	87	255	BRCD207	175.8	78	98
BRCD079	149.8	74	250	BRCD207	176.4	78	93
BRCD079	152.95	78	225	BRCD207	178	80	88
BRCD185	128.23	82	253	BRCD207	179.3	36	290
BRCD185	129.16	85	251	BRCD223	78.24	74	99
BRCD185	131.08	83	263	BRCD223	79.38	73	285
BRCD185	131.88	69	243	BRCD223	80.4	74	292
BRCD185	132.7	68	230	BRCD223	81.72	54	272
BRCD185	133.66	75	246	BRCD223	82.28	44	278
BRCD185	134.41	63	232	BRCD223	82.43	54	280
BRCD185	135.61	51	220	BRCD223	83.14	62	284
BRCD185	139.14	62	260	BRCD223	83.97	60	273
BRCD185	140.29	89	83	BRCD223	84.14	58	270
BRCD187	103.13	69	312	BRCD223	84.63	53	265
BRCD187	103.93	46	318	BRCD223	85.52	72	272
BRCD187	106.15	58	330	BRCD223	87.36	88	275
BRCD187	108.56	75	229	BRCD223	149.2	7	270
BRCD187	111.27	65	291	BRCD224	96.23	88	236
BRCD187	112.8	85	283	BRCD224	107.93	88	274

BRCD187	114.5	70	257	BRCD224	132.22	83	314
BRCD187	115.62	79	230	BRCD224	138.68	84	87
BRCD187	116.55	65	222	BRCD224	140.03	80	278
BRCD187	117.15	51	216	BRCD224	141.31	71	233
BRCD187	117.95	51	222	BRCD249	96.23	88	236
BRCD187	119.13	60	225	BRCD249	132.22	83	314
BRCD187	119.92	74	240	BRCD249	138.68	84	87
BRCD187	120.7	76	261	BRCD249	140.03	80	278
BRCD187	121.7	75	294	BRCD249	141.31	71	233
BRCD187	122.23	78	294	BRCD249	143.4	74	68
BRCD187	123.51	80	302	BRCD249	146.07	78	79
BRCD187	129.38	70	305	BRCD249	149.47	86	80
BRCD187	134.74	65	243	BRCD255	109	78	274
BRCD187	136.7	64	231	BRCD255	109.97	87	74
BRCD187	138.03	72	105	BRCD255	116.61	77	84
BRCD187	138.97	58	211	BRCD255	126.21	74	290
BRCD187	139	68	234	BRCD255	130.89	82	304
BRCD187	139.96	72	257	BRCD255	141.16	69	300
BRCD187	141.57	64	250	BRCD255	142.8	82	305
BRCD187	142.63	78	234	BRCD255	145.11	82	78
BRCD187	143.26	70	247	BRCD255	158.08	77	318
BRCD187	144.15	67	136	BRCD258	105	86	124
BRCD199	128.75	76	235	BRCD258	105.8	86	128
BRCD199	129.8	65	221	BRCD258	106.4	86	145
BRCD199	130.74	65	229	BRCD258	120.8	84	342
BRCD199	131.5	83	255	BRCD258	121.11	86	346
BRCD199	131.74	64	231	BRCD258	148.96	84	103
BRCD199	132.45	73	255	BRCD258	151	78	122
BRCD199	133.17	70	240	BRCD258	163.64	68	222
BRCD199	134.1	60	219	BRCD258	175.44	84	292
BRCD199	135.05	75	253	BRCD258	176.22	68	240
BRCD199	136.7	66	245	BRCD258	183.27	82	282
BRCD199	140.55	85	282	BRCD259	92.17	79	110
BRCD199	145.3	65	255	BRCD259	93.26	83	279
BRCD199	146.23	77	254	BRCD259	100.35	79	276
BRCD199	151.13	73	269	BRCD259	121.09	86	260
BRCD199	156.03	80	272	BRCD259	130.69	87	272
BRCD199	157.78	87	272	BRCD263	94.28	78	258
BRCD199	162.1	86	275	BRCD263	95.26	72	261
BRCD199	164.63	81	200	BRCD263	96.24	68	263
BRCD199	165.64	89	279	BRCD263	97.34	79	259
BRCD199	166.65	78	99	BRCD263	97.96	66	258

BRCD199	167.53	72	100	BRCD263	99.14	74	258
BRCD199	168.26	84	280	BRCD263	100.29	82	258
BRCD199	169	80	102	BRCD263	100.91	84	257
BRCD199	170.16	80	284	BRCD263	104.92	82	288
BRCD199	170.9	84	278	BRCD263	105.77	74	287
BRCD199	171.65	79	287	BRCD263	106.77	84	278
BRCD199	172.6	81	276	BRCD263	110.48	78	287
BRCD199	176.92	89	266	BRCD263	111.4	72	284
BRCD199	177.7	72	270	BRCD263	112.85	66	282
BRCD199	179.4	75	270	BRCD263	114.13	74	278
BRCD199	182.85	75	103	BRCD263	138.2	68	252
BRCD199	183.85	73	281	BRCD263	139.41	71	240
BRCD199	184.67	76	283	BRCD263	142.14	54	200
BRCD199	187.34	70	101	BRCD265	123.73	74	100
BRCD202	135.62	78	265	BRCD265	124.67	10	282
BRCD202	137.62	85	273	BRCD265	134.96	83	100
BRCD202	138.17	89	261	BRCD265	145.12	84	100
BRCD202	140.2	81	246	BRCD302	128.15	86	94
BRCD202	141.24	88	266	BRCD302	135.2	82	245
BRCD202	142.36	88	281	BRCD302	138	82	255
BRCD202	152.79	89	261	BRCD302	139.53	64	216
BRCD202	154.18	80	249	BRCD302	140.4	64	210
BRCD202	155.85	88	258	BRCD302	142.8	82	253
BRCD202	156.81	72	271	BRCD302	146.29	84	262
BRCD202	159.16	88	246	BRCD302	147.37	82	244
BRCD202	160.21	89	246	BRCD302	151.9	80	244
BRCD202	161.64	72	272	BRCD302	155.35	62	240
BRCD202	163.3	79	276	BRCD302	161.82	79	243
BRCD202	164.52	85	255	BRCD302	166.49	87	273
BRCD202	166.15	89	263	BRCD302	168.36	84	94
BRCD202	167.31	86	269	BRCD302	175.44	84	134
BRCD202	181.27	86	259	BRCD302	184.57	80	109
BRCD202	182.8	87	256	BRCD302	192.43	82	94
BRCD202	184.51	79	277	BRCD305	130.8	78	58
BRCD202	194.97	81	272	BRCD305	135.3	86	84
BRCD202	196.32	73	272	BRCD305	139.76	82	64
BRCD202	200.02	83	270	BRCD305	140.6	80	70
BRCD202	201.07	83	278	BRCD305	170.65	84	78
BRCD202	202.25	85	261	BRCD305	172.96	82	63
BRCD202	205.75	85	263	BRCD305	175.27	81	62
BRCD202	212.39	80	262	BRCD305	184.86	68	297
BRCD203	123.24	70	101	BRCD305	186.63	88	66

BRCD203	127.85	69	231	BRCD305	191.36	88	87
BRCD203	146.44	78	268	BRCD305	194.08	89	225
BRCD203	149.09	77	218	BRCD370	103.35	90	258
BRCD203	150.08	86	271	BRCD370	108.86	88	258
BRCD203	155.54	72	115	BRCD370	112.5	81	60
BRCD203	157.39	71	108	BRCD370	137.89	89	262
BRCD203	162.64	75	112	BRCD370	158.58	87	230
BRCD203	179.4	64	119	BRCD416	188.36	82	279
BRCD450	252.81	80	244	BRCD416	190.37	77	303
BRCD450	259.69	85	117	BRCD416	195.69	83	266
BRCD450	278.6	78	242	BRCD416	217.26	27	218
BRCD450	280.36	79	290	BRCD416	230.42	82	264
BRCD450	283.42	88	140	BRCD416	246.23	74	222
BRCD450	286.7	82	105	BRCD416	247.89	70	202
BRCD451	209.38	83	274	BRCD416	271.34	82	256
BRCD453	153.76	76	271	BRCD416	284.99	89	271
BRCD453	217.3	80	322	BRCD416	291.61	87	266
BRCD724	243.73	70	284	BRCD434	143	64	275
BRCD725	294.29	83	261	BRCD434	149.65	71	246
BRCD725	325.87	64	252	BRCD434	157.6	82	260
BRCD725	331.6	70	265	BRCD434	209.15	67	243
BRCD450	205.27	66	280	BRCD450	173.31	65	244
BRCD450	215.83	65	277	BRCD450	193.99	74	248

S_{B3} foliation in the Bepkong deposit

Hole_ID	Depth	Dip	Dip_Direction
BRCD078	220.05	75	95
BRCD450	166.57	82	112
BRCD187	113.68	83	115
BRCD079	96.8	70	180
BRCD078	217.04	10	130
BRCD079	96.45	30	125
BRCD079	108.5	65	130
BRCD203	237.18	71	186
BRCD203	237.39	82	187
BRCD203	238.43	74	183
BRCD203	239.56	51	198
BRCD203	239.92	40	165
BRCD203	241.24	86	196
BRCD203	241.86	81	178
BRCD203	241.98	73	166
BRCD203	244.26	65	170
BRCD203	247.91	65	194
BRCD203	250.43	81	185
BRCD187	131.93	84	130
BRCD187	131.15	83	115